Detailed Puncture Analyses of Various Tank Car Designs

Final Report – Revision 1

January, 2010

Prepared by:
Steven W Kirkpatrick, Ph.D.

Applied Research Associates, Inc.

2672 Bayshore Parkway, Suite 1035
Mountain View, CA 94043

Table of Contents

List of Figures

List of Tables

Acknowledgements

Executive Summary

Over the last few years, there has been significant attention on the potential for release of hazardous materials from railroad tank cars. This attention is primarily a result of a series of three accidents or derailments between 2002 and 2005 involving the release of hazardous material. In response, a research program was initiated to develop strategies for improving railroad tank cars so they can maintain tank integrity for more severe accident conditions than current equipment. The research was initiated by The Dow Chemical Company (Dow), Union Pacific Railroad, and Union Tank Car Company, working under a Memorandum of Cooperation with the Federal Railroad Administration, and Transport Canada, and the U.S. Transportation Security Administration.

The Next Generation Rail Tank Car (NGRTC) Project was organized to include a Core Team (consisting of representatives from the five signatories to the Memorandum of Cooperation) and a group of Lead Contractors. The Core Team and Lead Contractors worked together to: 1) evaluate and select candidate materials, components, subsystems and systems with the potential to provide large performance improvements in the safety and security of rail tank cars; 2) select conceptual tank car designs incorporating appropriate materials, components and systems for improved safety and security; and 3) develop and use appropriate models, analytical techniques and testing protocols to demonstrate the efficacy of the tank car concepts. The goal of the NGRTC program was to develop a conceptual tank car that had a five to ten times improvement in the impact energy required to puncture the tank car.

A key effort in this program is the development and application of detailed finite element models of tank car equipment which can accurately predict the puncture resistance under different impact conditions. These analysis tools were developed and validated for the puncture of the baseline tank cars for both side and head impact conditions (described in Sections 4 and 5 of this report). The models were subsequently applied to assess the puncture resistance of various tank car designs.

This report describes the results of the NGRTC project to develop strategies for improving railroad tank cars so they can maintain tank integrity for more severe accident conditions than current equipment. Primary emphasis is on the finite element analyses of the impact and puncture behaviors of both current and future tank car designs. The scope of this effort includes the development of detailed finite element models for tank cars and the use of those models for various impact scenarios to assess puncture energies. A summary of the testing performed under the NGRTC program is also provided in this report, since it was critical for the development and validation of the puncture modeling capability.

Baseline Tank Car Impact Model

The first task in this research was to develop and validate a modeling capability that can be used to analyze the impact response of a tank car. The model developed for the 105J500 chlorine tank car is shown in Figure 1. The model includes all of the primary tank car structures including the jacket and jacket standoffs, commodity tank, manway, bolsters, stub sills, and the addition of the outriggers attached to the draft gear to prevent a post-test rollover of the target tank caused by the rebound off the reaction wall in the impact testing.
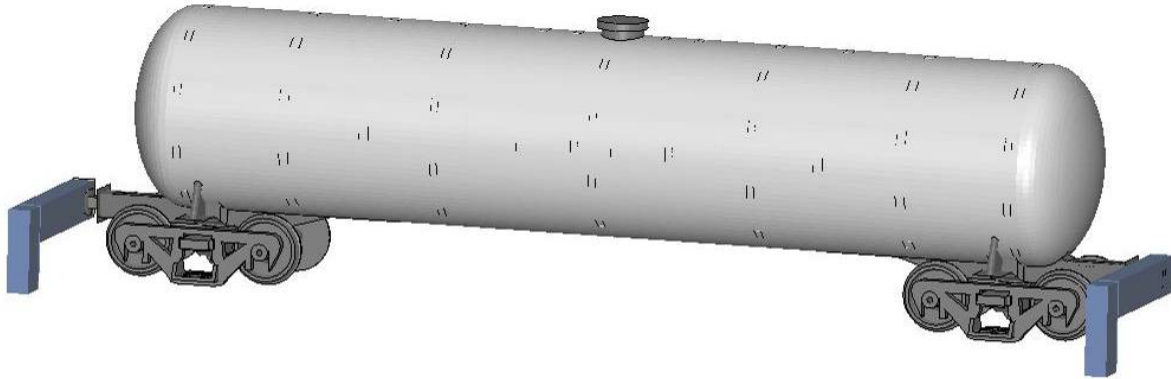
Figure 1. Updated model of a 105J500W pressure tank car.

Another feature of the tank impact model was the addition of an explicit model of the lading. The lading model consists of a low strength viscoelastic material that fills the same volume as the slurry lading in the test tank cars. The sloshing of the lading model can be seen in the cutaway view of the predicted impact response shown in Figure 2. This lading modeling approach was established to capture the momentum transfer of the coupled fluid-structure response but minimize effects such as sloshing at the fluid free surface that can cause numerical stability problems.
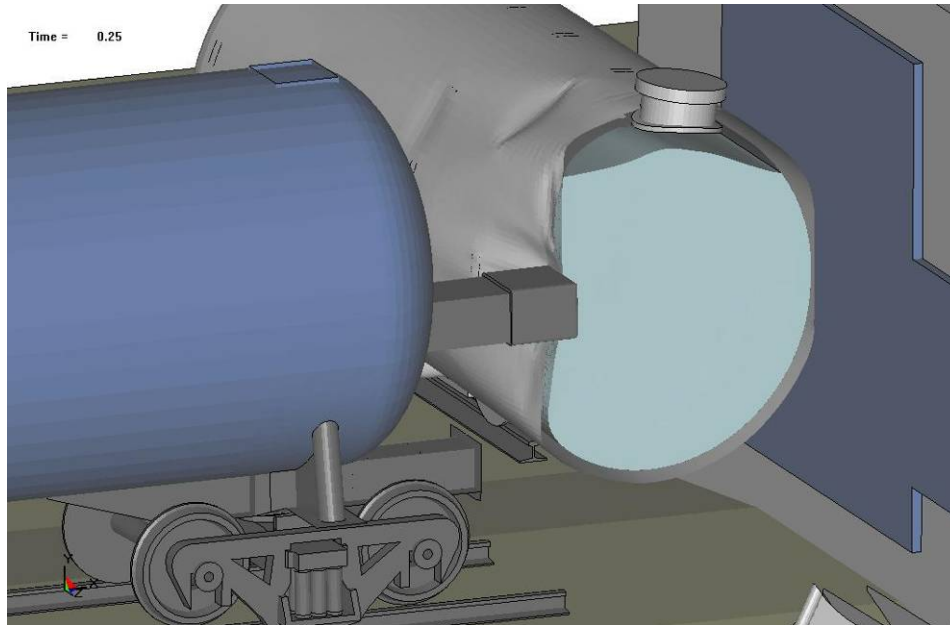
Figure 2. Calculated Test 1 impact response with cutaway showing lading.

Full-scale impact tests were performed on tank cars and the results were used to validate the models. The tests were fully instrumented with accelerometers, string potentiometers, pressure gauges, and strain gauges. These measurements were compared to the model predictions to validate the model. Overall, very good agreement was obtained between the prediction and test for the various measurements made. An example of the agreement is the comparison of the predicted and measured force-deflection curves, shown in Figure 3. This force-deflection curve is an important characteristic of the tank car for a given impact scenario. The area under the force-deflection curve is the impact energy that is dissipated (the primary measure used to assess the puncture protection levels). The comparison of the force-deflection behaviors shows good agreement between the calculation and the test.
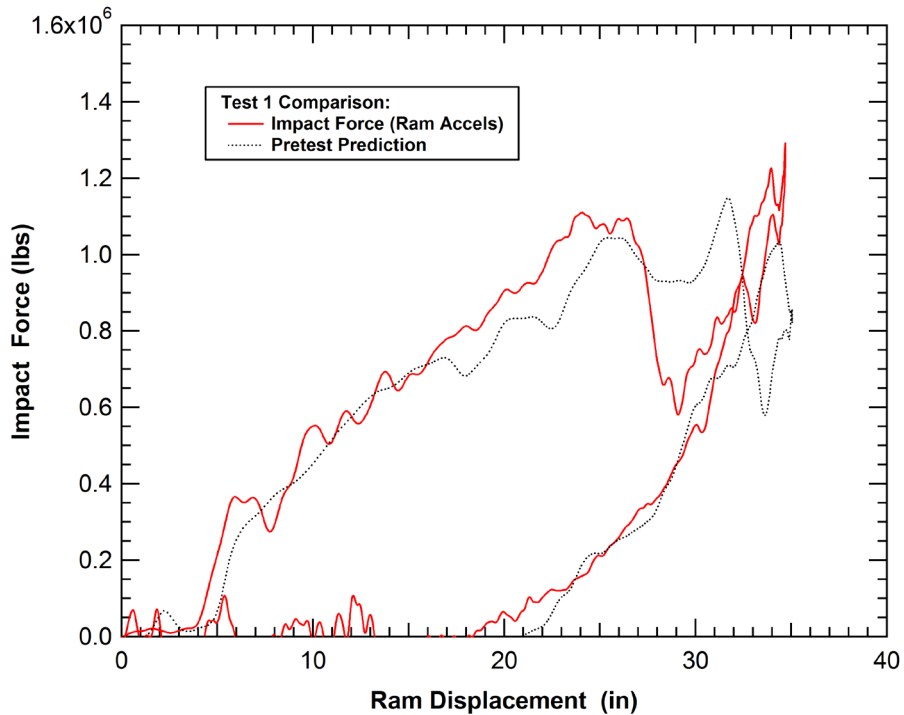
Figure 3. Comparison of the measured and predicted Test 1 force-deflection curves.

Material Damage and Failure Behaviors

The other necessary component of a predictive tank car puncture modeling capability is a detailed model that can be used to determine the impact damage and failure of the tank and protective system materials. An extensive program of laboratory materials testing was performed to characterize the tank car materials of interest. The tests included various material characterization tests, such as notched tensile tests and combined tension/shear tests, used to calibrate the material constitutive and failure behavior. Strain rate effects on the tank car materials were investigated and found to not have a significant effect on the tank puncture behavior. Additional component tests, such as punch tests and bend tests, were performed to validate the constitutive models.

The material damage and failure model applied is the Bao-Wierzbicki (BW) model that defines the material damage development based on the current stress state in the material and the plastic strain increments. The critical strain function is that proposed in the BW criterion and contains multiple branches depending on the range of stress state, as shown in Figure 4. The critical strain in each branch are governed by the equation

$$\varepsilon_c\left(\sigma_{mean}/\sigma_{eq}\right)=\begin{cases}\infty & \left(\sigma_{mean}/\sigma_{eq}\right)\le -\dfrac{1}{3}\\[2mm]\dfrac{A}{1+3\left(\sigma_{mean}/\sigma_{eq}\right)} & -\dfrac{1}{3}\le\left(\sigma_{mean}/\sigma_{eq}\right)\le 0\\[2mm]9(B-A)\left[\left(\sigma_{mean}/\sigma_{eq}\right)\right]^2+A & 0\le\left(\sigma_{mean}/\sigma_{eq}\right)\le\dfrac{1}{3}\\[2mm]\dfrac{B}{3\left(\sigma_{mean}/\sigma_{eq}\right)} & \dfrac{1}{3}\le\left(\sigma_{mean}/\sigma_{eq}\right)\end{cases}$$

And the parameters *A* and *B* can be determined by a series of tests under different stress conditions including notched tensile tests, with specimens of varying notch radii, and tensile-shear tests with different ratios of tension to shear stress.
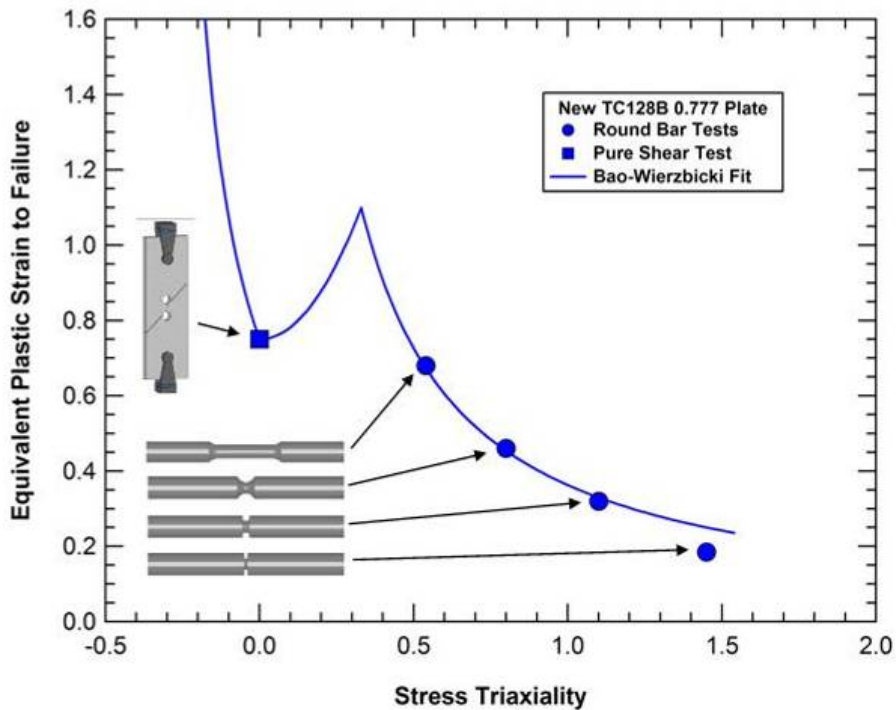
Figure 4. Bao-Wierzbicki failure surface and tests used for model calibration.

Although these material tests were used to develop the constitutive and failure model parameters, the resulting constitutive models were used to simulate the tests. This provides a validation that the material parameters were properly incorporated into the analyses and that the constitutive and failure model is capable of simulating the range of material behaviors under different loading conditions. The first of these material test series was the notched round bar (NRB) test (shown here on TC128B). A comparison of the calculated and measured stress-strain behavior across the notch for the three different radii specimens is shown in Figure 5. The comparison shows

that the constitutive and damage model were capable of reproducing both the increase in stress level and reduction in ductility that occur as the notch radius is reduced. The BW failure parameters used provide a good correlation to the observed failures of the specimens.
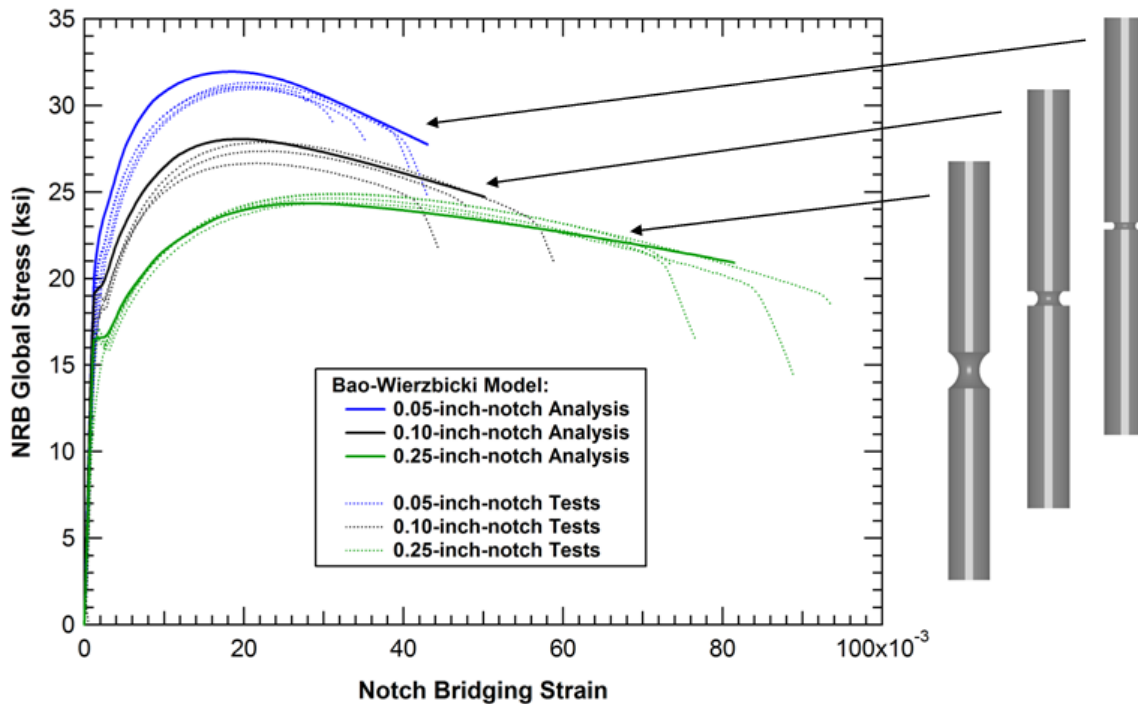
Figure 5. Validation of the notched round bar test behavior for TC128B.

A similar comparison of the calculated and measured load-displacement behaviors for the combined tension/shear tests are shown in Figure 6. The comparison shows again that the constitutive and damage model were capable of reproducing both the decrease in load level and increase in displacement that occur as the orientation was rotated from pure tension to pure shear. The BW failure parameters used provide a good correlation to the observed failures of the specimens.
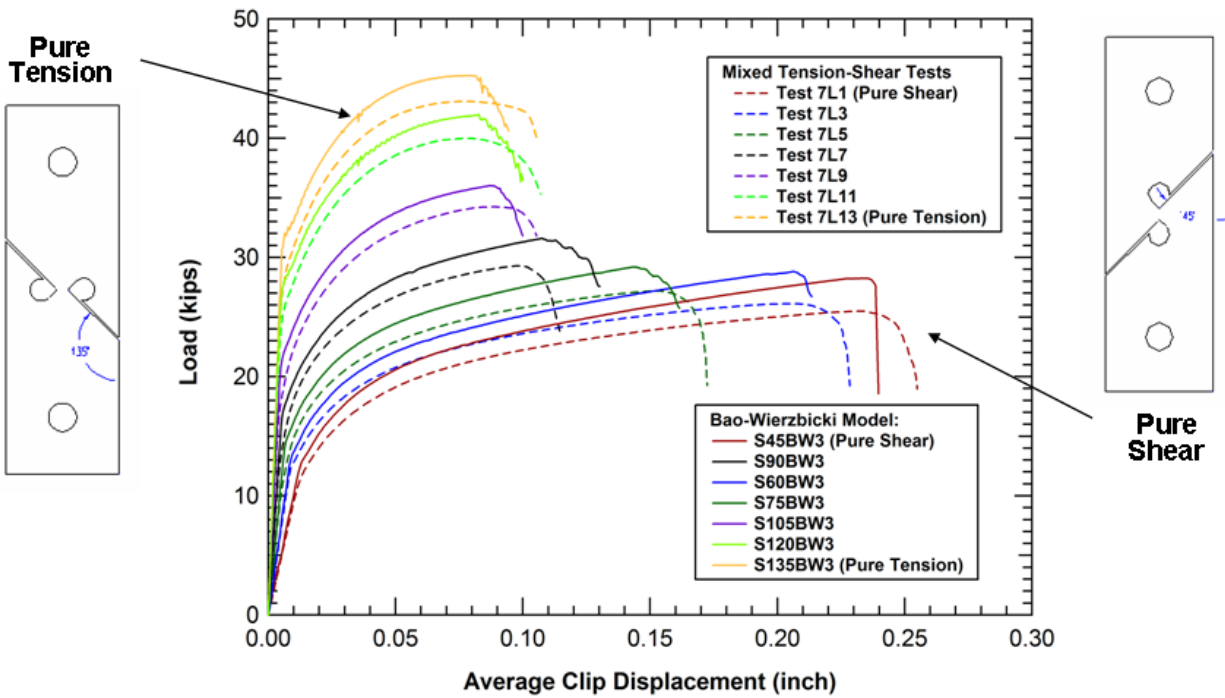
Figure 6. Validation of the combined tensile shear test behavior for TC128B.

For the various steels evaluated in this program, the component punch test was the primary laboratory material test used to validate the constitutive and failure models. An example of a model and simulation of a punch test on a 0.488-inch-thick TC128B plate is shown in Figure 7. The corresponding comparison of measured and calculated punch force-displacement curves for a series of three different tests on the TC128B plate is provided in Figure 8. In addition to the force-deflection curve, the final profile of the plate specimens after the punch tests were digitized and compared to the analyses. Again, the overall agreement between the testing and analyses was good. This agreement provides a further validation that the BW failure model is appropriate for predicting puncture of the tank cars.
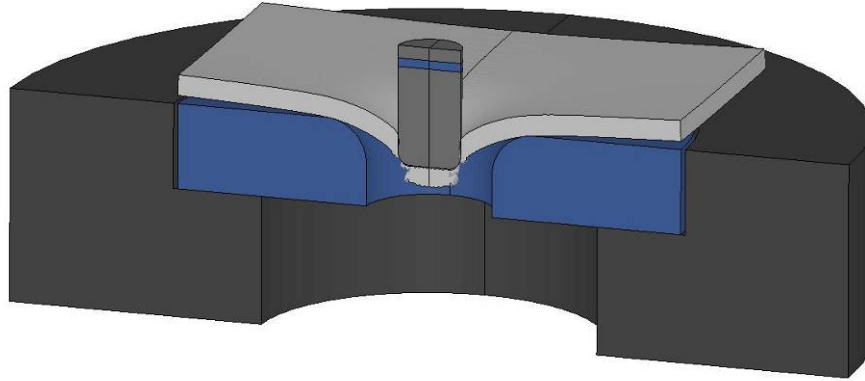
Figure 7. Simulation of the punch test on the thin TC128B plate material.
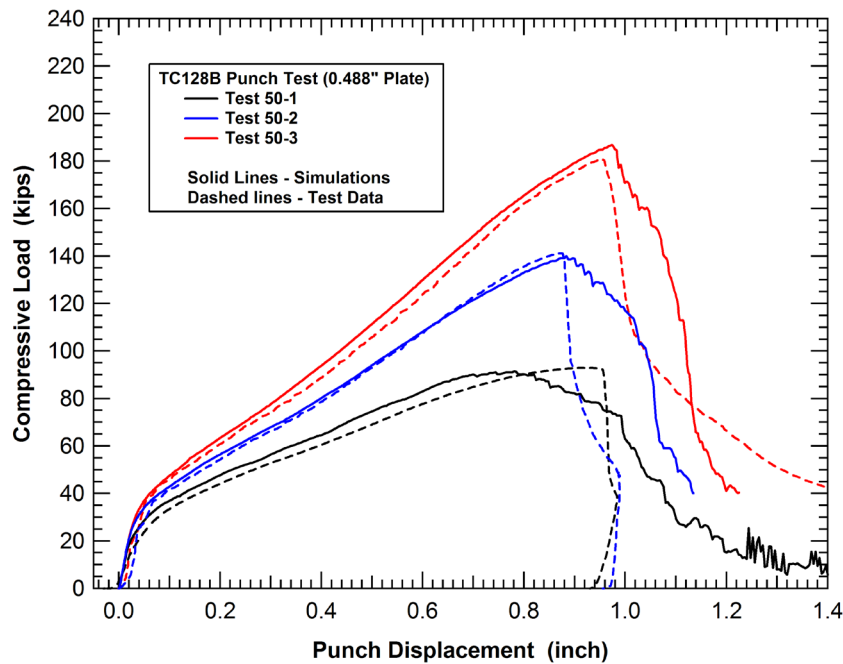
Figure 8. Force-deflection curves for three punch test configurations on TC128B.

Tank Car Puncture Modeling

The BW failure modeling capability was combined with the tank car model to complete the tank car puncture prediction capability. The tank model was also simplified in these analyses to have half-symmetry by removing the manway, bolsters and lading. The simulation of the full scale tank car impact test (Test 2 - above the puncture threshold) was performed using the tank puncture model, as shown in Figure 9. The model shown was reflected vertically about the symmetry plane (seen as a line in the figure) for improved visualization of the impact behavior. The impactor in this analysis was a rigid 6x6 inch ram with a 0.50-inch radius around the edges

and a total weight of 286,000 lbs. The small rectangular patch of elements under the impactor (already punctured in Figure 9) is the fracture zone where the BW failure model was applied. The remainder of the tank structure was again modeled with 4-node shell elements and a tied shell-to-solid constraint was used at the interface of the two model regions.

The comparison of the measured and calculated force-deflection behavior for Test 2 with the tank puncture model is provided in Figure 10. The comparison shows overall good agreement between the calculation and test. The peak load at which the tank was punctured was very accurately captured by the model. The measured puncture force was 940,000 lbs and the calculated puncture force was 915,000 lbs. The primary discrepancy of the test and model was a slightly more compliant behavior in the model seen at the large displacements. This difference in compliance could primarily be attributed to the removal of the manway from the tank model in this analysis. As a result of the larger displacements in the analysis, the calculated puncture energy of 1.26 million ft-lbs is higher than the measured puncture energy of 0.87 million ft-lbs.
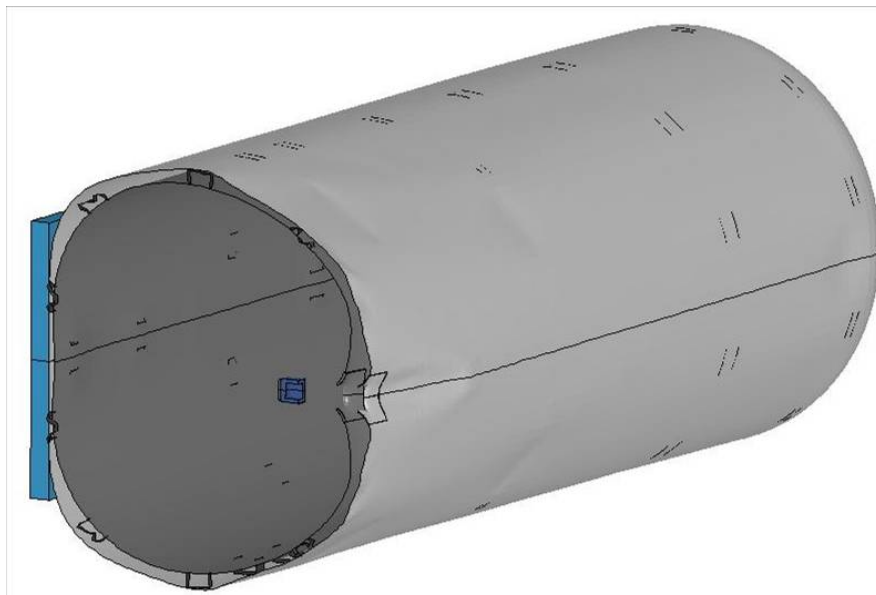
Figure 9. Simplified tank model analysis with Bao-Wierzbicki failure assessment.
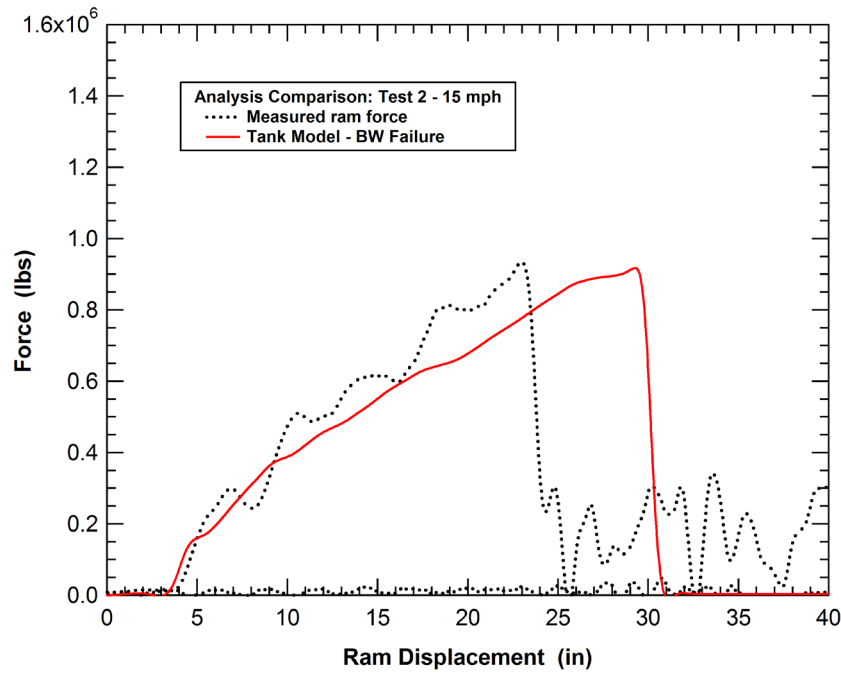
Figure 10. Tank puncture model Test 2 analysis with Bao-Wierzbicki failure assessment.

This combined tank car impact and puncture modeling capability was applied to evaluate a wide range of tank/jacket and head/head shield geometries. The side impact condition was a normal impact centered on the belt line of the tank. The head impact condition was an offset impact point approximately 29 inches vertically downward from the center of the head.

An example head impact and puncture analysis is shown in Figure 11. The head impact analyses included the head, head shield, and a sufficient length of the side shell and jacket to allow for buckling to initiate in the jacket support from the loads transmitted by the head shield, as seen in Figure 11.

(a) Initial impact conditions   **(b) Puncture response of the head**
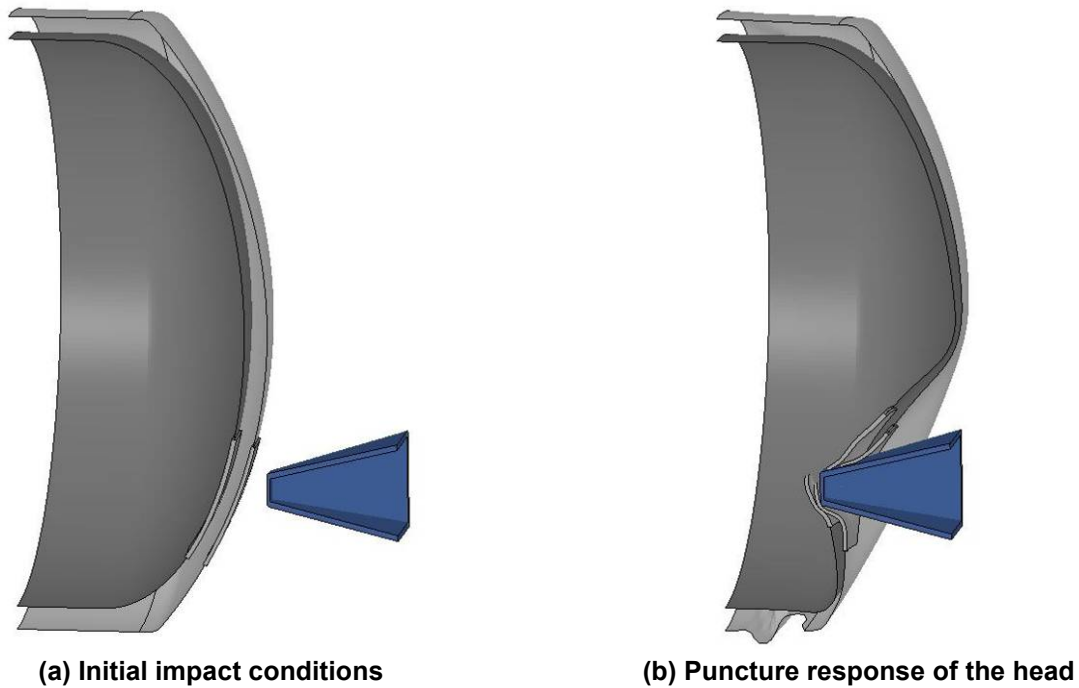
Figure 11. Calculated puncture behavior of a head and head shield.

The calculated head and shell puncture forces as a function of the combined head and head shield thickness are shown in Figure 12. All of the analyses included in the figure are performed with the 6x6 inch impactor. The figure shows the analyses are mostly consistent with a linear relationship between puncture force and total thickness of the protective layers.

The linear relationship between the puncture force and total tank system thickness provides an indication of the primary failure mechanism initiating the tank puncture. The geometry of the ram impacting and indenting a pressurized tank shell is shown in Figure 13(a). A force balance analysis in the direction of the impact on a patch of tank shell material is shown in Figure 13(b). The forces resisting the impact loads are the pressure on the inside surface of the contact patch and the shear stress around the perimeter of the contact patch. For a 100 psi tank pressure and a 6x6 inch impactor, the pressure load is less than 4 kips on the contact patch. Thus, the average shear stress is approximately equal to the impact force divided by the product of the impactor face perimeter and tank thickness.
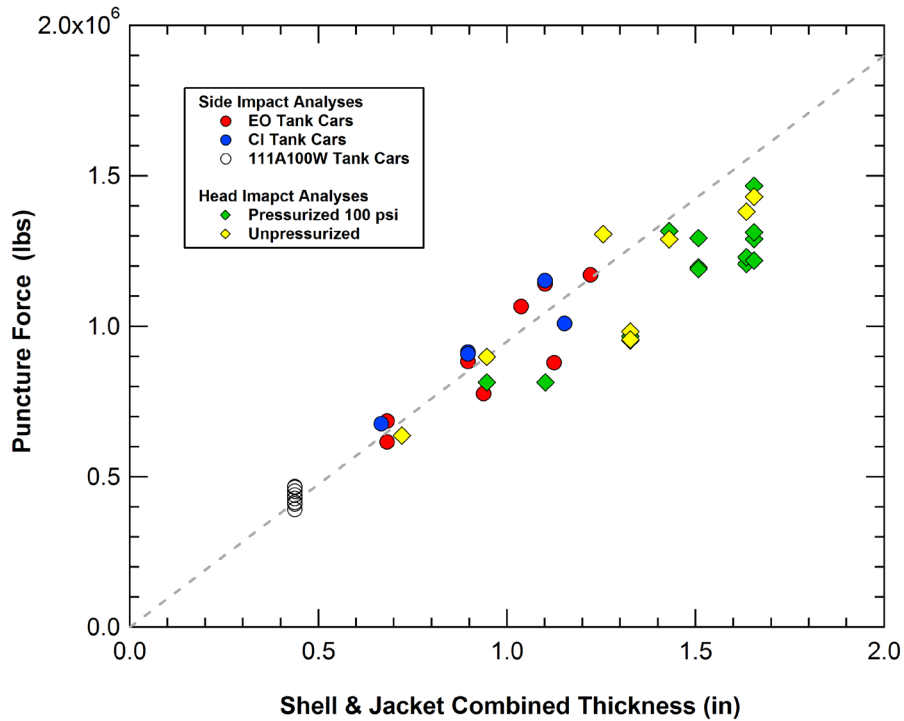
Figure 12. Calculated puncture forces as a function of system thickness.

The slope of the linear fit in Figure 12 corresponds to an average shear stress in the tank layers around the perimeter of the impactor of 39 ksi. By comparison, the yield and ultimate stress levels of the TC128B in pure shear are 33 ksi and 49 ksi, respectively (approximately 58% of the stress values in pure tension using a Von Mises yield criterion). Thus, the failure mode is primarily exceeding the shear capacity around the perimeter of the impact patch.

The calculated puncture forces for pressurized heads and the thicker head systems tended to fall slightly below the linear fit in Figure 12. The proposed mechanism for these lower forces is that, for the stiffer head systems, the offset impact creates a larger stress concentration along the upper edge of the impactor face and the failure initiates at that location at a lower total force. The more compliant head systems allow for a larger dent to form and the impactor develops a more uniform stress distribution in the impact patch around the ram face perimeter.

F

(a) Geometry of the tank indentation

F

τ τ

P_i
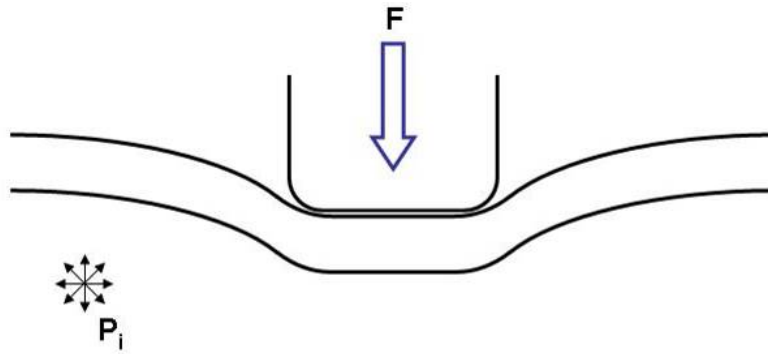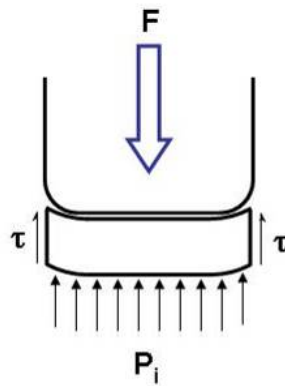
(b) Free body diagram for the tank contact patch

Figure 13. Loading and failure mechanism for the tank impact and puncture.

The calculated puncture energies for all of the side and head impact analyses are plotted against the combined thickness of the system in Figure 14 (6x6 inch impactor only). When comparing all of the puncture energies the data falls into four separate groups that are distinguished by the impact type (side or head) and the tank pressure. Again, the comparison indicates that the total thickness is the relative parameter that determines puncture energy for a given impact condition and pressure level, indicating that a retrofit design with an increased jacket thickness should provide equivalent protection to a thicker commodity tank systems with equivalent combined shell and jacket thicknesses.
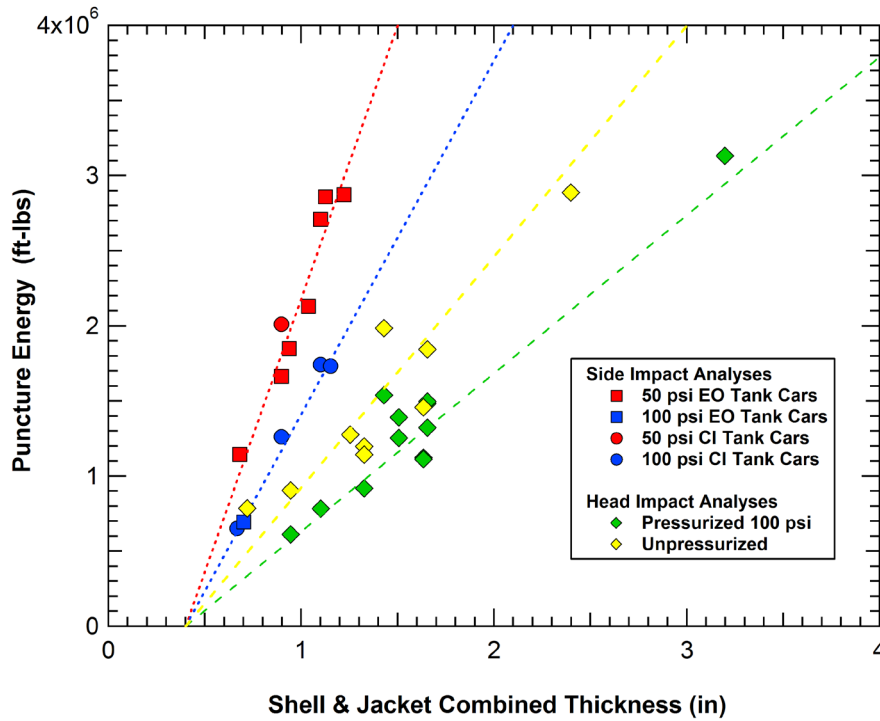
Figure 14. Calculated puncture energies as a function of system thickness.

The above correlation of the system thickness and puncture energy can be converted to assess system requirements for a given impact scenario. The relationship between the impact speed and impact energy for the 295,000 lb ram car is provided in Figure 15. This impact energy is proportional to the mass of the object so a 286,000 ram car would have energies that are three percent lower than those in Figure 15. This relationship between speed and impact energy can be combined with the linear fits between system thickness and puncture energy (shown in Figure 14) to determine the required system thickness to resist puncture for a specified impact speed.

Examples of the pressurized (100 psi) Cl tank car thickness requirements to resist a puncture of the 6x6 inch impactor at various impact speeds is shown in Figure 16 for both side and head impacts. The figure shows that as the impact speed increases, the system thickness required begins to increase rapidly. A 25 mph side impact would require approximately three inches of steel to prevent puncture and a 30 mph head impact would require more than six inches of steel. Obviously, these protection levels are not achievable with a traditional tank car design approach while maintaining a tank car that is economically viable as a result of both the initial tank car cost and the drastically reduced lading capacity.
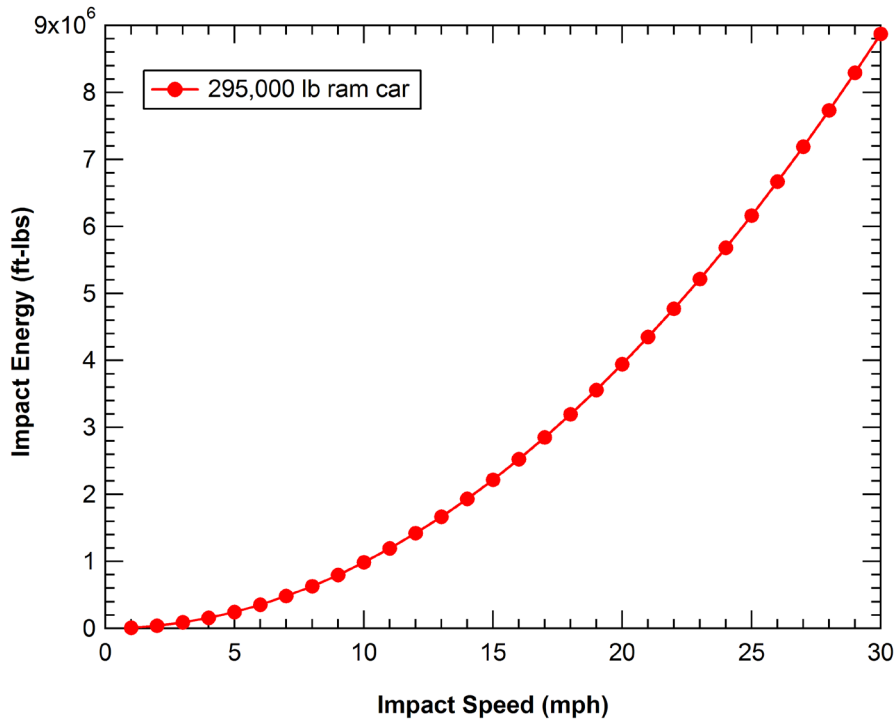
Figure 15. Relationship between impact speed and kinetic energy for the ram car.
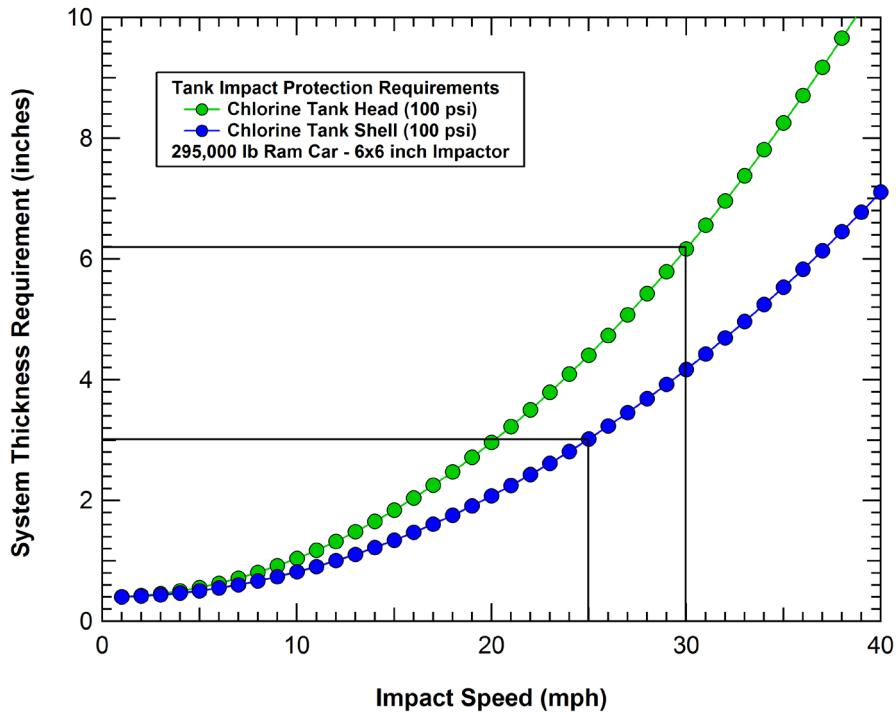
Figure 16. Puncture prevention thickness requirements for various impact speeds.

The analyses demonstrate that the 25 and 30 mph impact protection levels are not feasible for the 6x6 inch impactor. However, the analyses demonstrate that they may be achievable with a larger ram size. The puncture energies from analyses of side impacts on 500 lb and 600 lb tanks using 6-inch, 9-inch, and 12-inch square impactors are shown in Figure 17. The figure shows that the 25 mph ram car impact (6 million ft-lb impact energy from Figure 15) is approximately equivalent to the puncture energy of the 600 lb tank car impacted by the 12x12 inch ram.
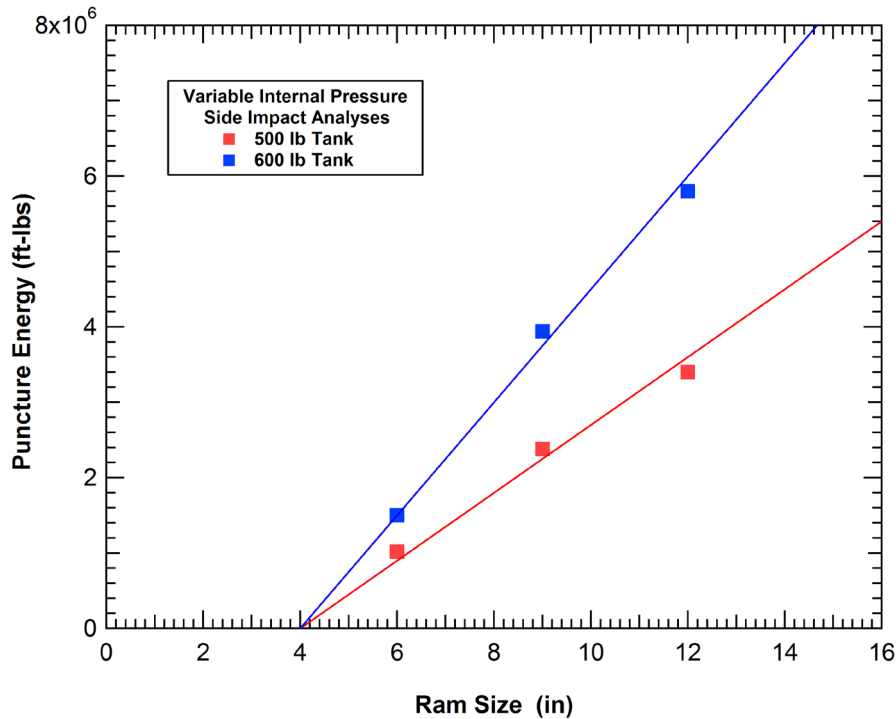
Figure 17. Summary of puncture energies for chlorine tank cars for various impactor sizes.

Retrofit Tank Cars

A topic of interest for increasing the puncture resistance of tank cars is the relative efficiency of adding material to the jacket as opposed to adding material to the commodity tank. This is critical for assessing the capability to retrofit existing tank cars to meet equivalent puncture resistance levels of a thicker tank car with a higher tank test pressure.

The assessment of retrofit options was performed using the shell and head puncture analyses. A summary of the analyses of the 500 lb Cl tank with various jacket thicknesses is provided in Figure 18. The graph provides a fit to the analyses to illustrate the relationship between the retrofit jacket thickness and the puncture energy. The comparison shows that a 0.375-inch thick retrofit jacket is required for the 500 lb Cl tank to provide a similar level of puncture resistance

as a 600 lb tank car with the 11 gauge jacket (as confirmed by the analysis with the 0.375-inch jacket).
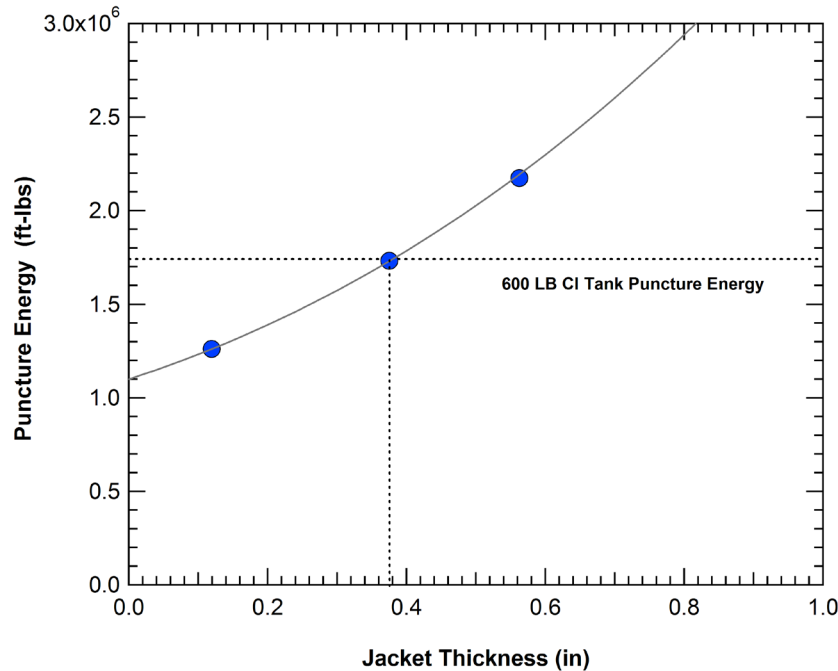
Figure 18. The effects of jacket thickness on puncture energy for a 500 lb Cl tank.

Similarly, a summary of the analyses of the 300 lb EO tank with various jacket thicknesses is provided in Figure 19. The comparison illustrates that an approximately 0.4375-inch thick retrofit jacket would be required for a 300 lb EO tank to provide a similar level of puncture resistance as the 500 lb EO car. However, the puncture energy levels calculated for the 500 lb and 600 lb Cl tank cars are also indicated in Figure 19. We see from the comparison that the 300 lb EO tank car retrofit with a 0.375-inch jacket has a puncture energy that is higher than that of the 600 lb chlorine car as a result of the lower pressures in EO tanks. Thus, the 0.375-inch retrofit jacket in EO cars will provide a protection level equivalent to or better than that of retrofit designs of other commodities.

A summary of the analyses of the pressurized 500 lb tank head with the various head shield thicknesses is provided in Figure 20. The puncture energy levels calculated for the 600 lb head with the baseline jacket and head shield are also indicated in the figure. The comparison shows that an approximately 0.60-inch retrofit head shield thickness would be required for a 500 lb head to provide a similar level of puncture resistance as the 600 lb head with a 0.50-inch A516-70 head shield.
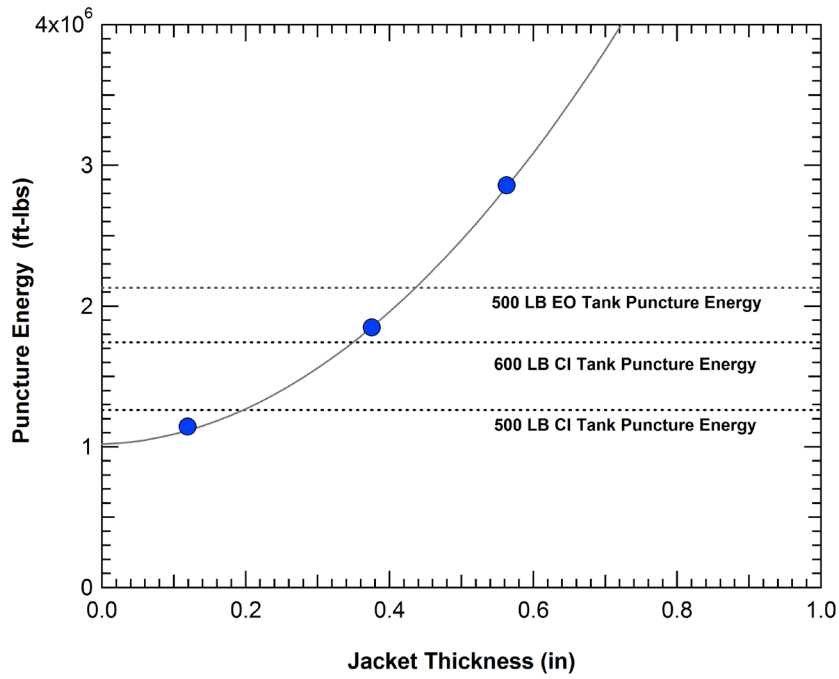
Figure 19. The effects of jacket thickness on puncture energy for a 300 lb EO tank.
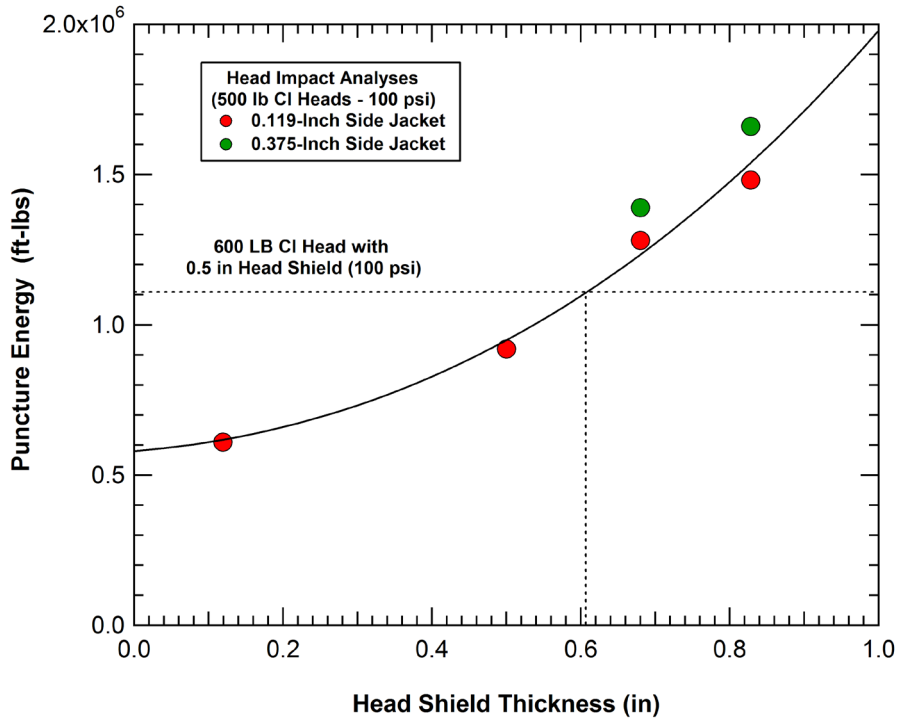
Figure 20. The effects of head shield thickness on puncture energy for a 500 lb head.

Analyses of Advanced Protection Systems

The modeling capabilities developed in this program were applied to analyze a series of advanced tank car protective structure concepts. Included in these were multi-layered foam systems and engineered metal structures (EMS) systems. Example head impact puncture analyses on both a layered foam system and a corrugated EMS system are shown in Figure 21. A variety of designs were investigated both with analyses and with a full scale head test on each of the concepts shown in Figure 21. However, neither of the foam or EMS systems was optimized.
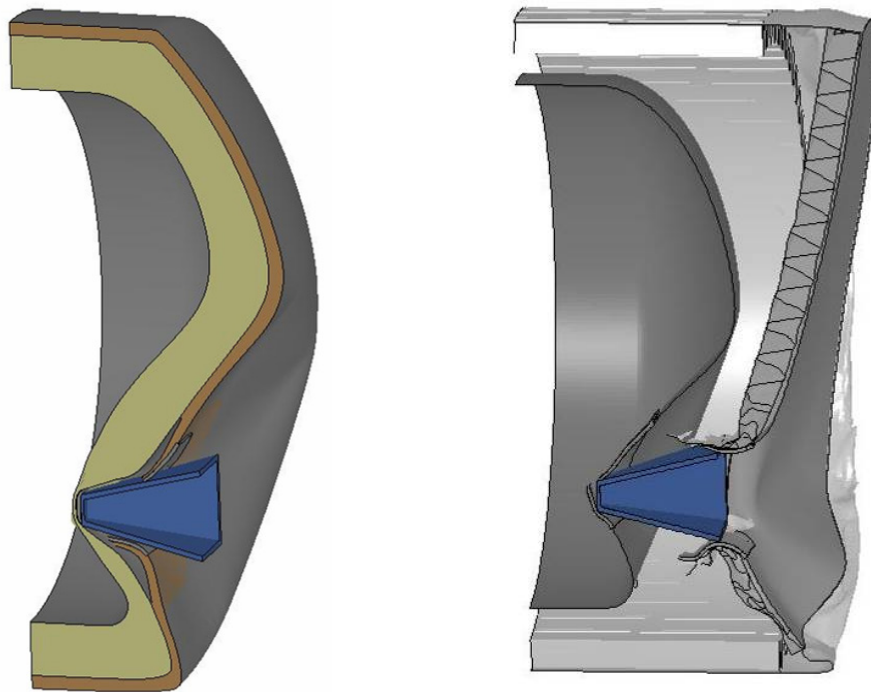
(a) Layered foam protection system   **(b) Corrugated EMS protection system**
Figure 21. Analyses of advanced protection concepts.

The failure mode of the advanced systems was similar to that of the baseline tank systems when impacted by the 6x6 inch impactor. When the load acting on a layer of the advanced protective system exceeded the shear capacity of the layer, the layer would be punctured. For many of the advanced concepts, the system design would increase the stiffness of the support for the outer layers. The increased support structure stiffness would result in outer layer penetration at reduced ram displacements. As a result, the protection system and commodity tank would be penetrated independently at lower peak forces and lower puncture energies than could be obtained in an optimized system.

The performance of advanced protective systems was typically improved when the thickness of the outer layer was increased to resist puncture and the stiffness of the supporting structure was reduced to increase the displacements of the system before the puncture level was exceeded. These effects are seen by considering the three protections concepts shown in Figure 22. The concepts include two different corrugated EMS designs and a single monolithic plate, all of which have approximately equivalent weight. The different corrugated EMS designs illustrate the approach of moving weight from the inner face sheet and core structure to lower the system stiffness and increasing the outer face sheet thickness to improve the penetration resistance. The maximum extrapolation of this concept is to move all of the EMS weight into a single thicker outer jacket.
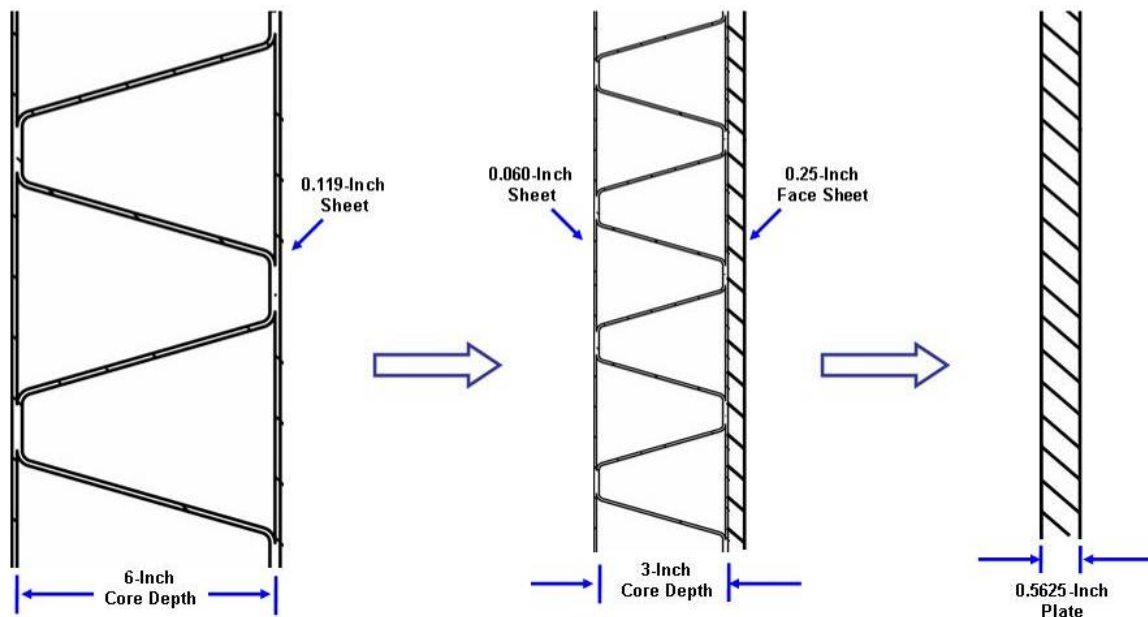
Figure 22. Alternative tank protection concepts.

The calculated puncture behavior of the three protection options are compared in Figure 23. The ram punctures the baseline 6-inch corrugated EMS structure at a load of approximately 200,000 lbs and a ram displacement of approximately 6 inches. Thus, the energy dissipation of this EMS structure is quite small. The ram punctures the modified 3-inch corrugated EMS structure at a load of approximately 600,000 lbs and a ram displacement of approximately 12 inches. Thus, the energy dissipation of this EMS structure is approximately 5 times that of the original 6-inch EMS concept. Alternatively, the 0.5625-inch-thick jacket is not penetrated until a force of approximately 1.1 million lbs and an impactor displacement of approximately 30 inches. Thus, the jacket absorbs significantly more impact energy than either of the corrugated EMS structures for the 6-inch impactor.
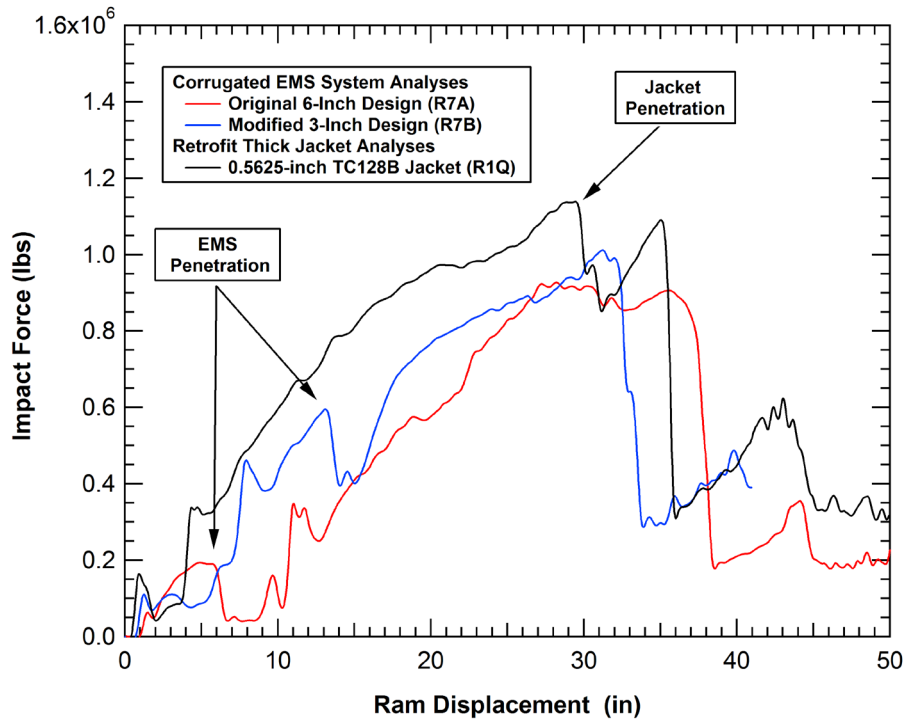
Figure 23. Comparison of the force-deflection behaviors for the corrugated EMS concepts.

The calculated forces to puncture the outer layer of foam and EMS systems are added to the plot of the puncture force versus system thickness in Figure 24. The difference in the data for the advanced systems is that the thickness used is the layer thickness only (e.g. outer head shield or outer face sheet thickness) rather than the sum of the total tank and jacket layer thicknesses. The comparison shows that the foam and EMS structures had the effect of making each layer act independently rather than coming in contact and working together to resist the high shear stresses around the edge of the impactor. As a result, the maximum achievable puncture forces were reduced and the systems do not reach the desired puncture energies.
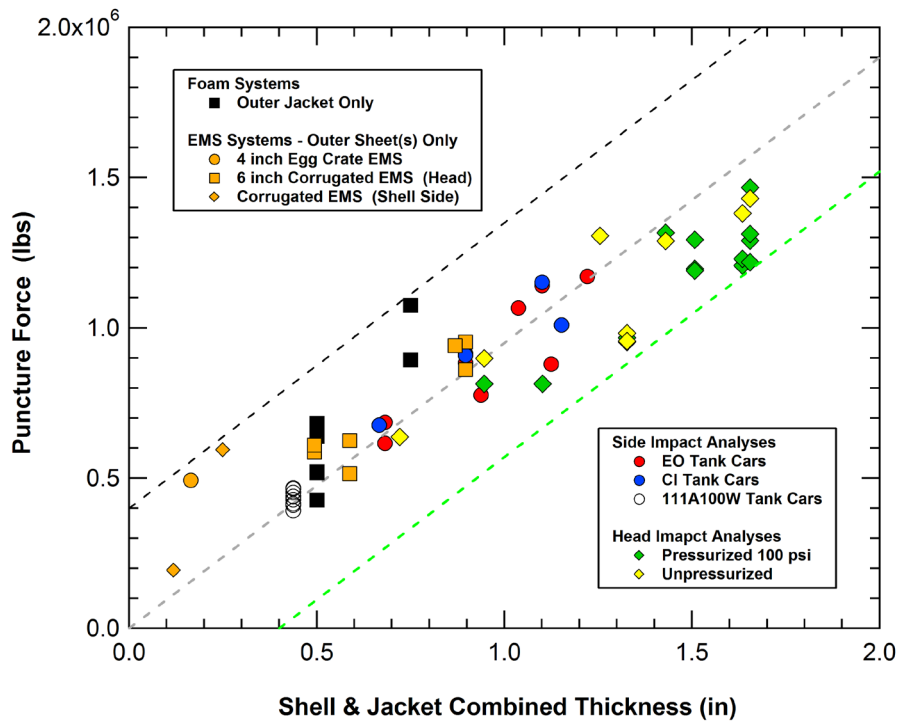
Figure 24. EMS puncture forces as a function of outer layer thickness.

Although the systems with a monolithic jacket performed better than the corrugated EMS structures in this example, the conclusion can not be generalized to all EMS designs and impact scenarios. The EMS structures would be expected to perform significantly better under a more distributed loading. Other benefits of the EMS concepts are that the structural stiffness can be used to efficiently carry the train service loads in a "tank within a tank" design. Further analysis of other EMS concepts (e.g. core geometries, materials) and more general impact conditions would be required to obtain an optimized design.

A similar set of observations was obtained from the analysis of layered foam systems. In general, the systems analyzed did not outperform a single monolithic plate of equivalent protection system weight for the 6x6 inch impactor. However, the performance for larger impactors and the optimum foam and interface properties to maximize performance were not fully explored. In addition, low density foams can contribute to improved thermal insulation. If a foam system can maintain a lower average shipping temperature (and thus a lower average tank pressure), the overall tank puncture energy could potentially be increased.

Composite Material Protection Systems

The above analyses indicate that a tank protection system developed using only typical tank car materials (steels) will have difficulty reaching the five to ten times protection goals of the

NGRTC program. To achieve a five times increase in the puncture energy of tank cars while maintaining a comparable level of utility will require non traditional tank car design approaches and advanced materials. These potential materials for advanced protection concepts include polymeric composite materials.

Tank car concepts with composite protection systems were not evaluated as thoroughly as the layered foam and EMS concepts. However, some preliminary evaluations were performed to assess the potential of composites for puncture resistance.

A summary of the normalized peak punch test loads for different materials plotted against aerial density is shown in Figure 25. Effectively, the normalized punch loads are the shear stress around the punch perimeter scaled by the material density. As a result, the punch shear resistance is compared on an equivalent weight basis rather than an equivalent thickness basis. The data in the figure were taken from the punch tests performed on steels in the NGRTC program and composite punch tests reported in open literature sources for a woven S-2 glass fiber SC-15 polymeric matrix composite system.
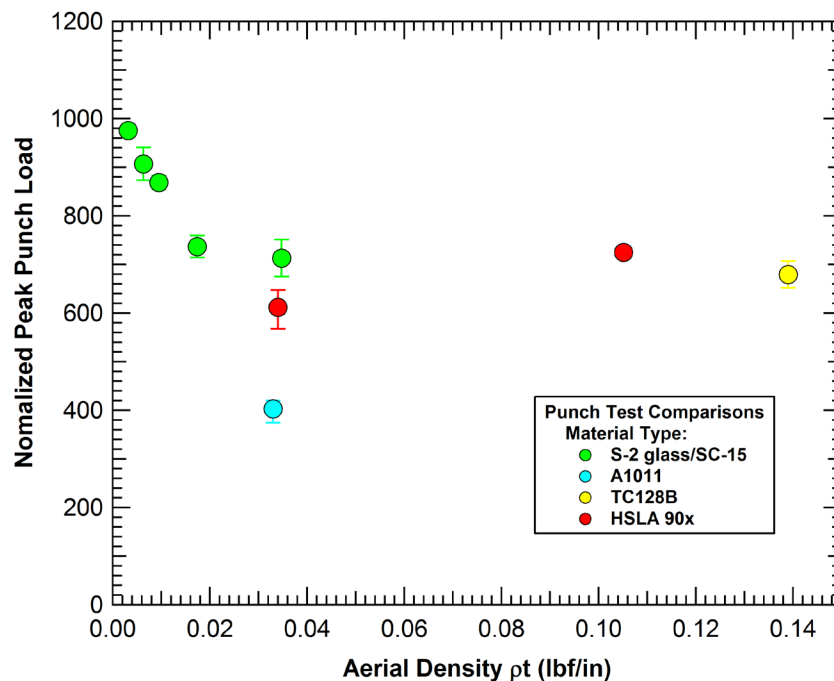
Figure 25. Normalized peak punch test loads versus aerial density for various materials.

The comparisons in Figure 25 are not perfect due to some differences in the punch test protocols between steels and composites. However, the comparison indicates that there is potential for modest puncture resistance improvements using composite materials. At the largest aerial density testing for the composite, a direct comparison can be made with 11 gauge A1011 and

HSLA 90XF with a similar aerial density. The composite out performs A1011 by approximately 70% and HSLA 90x by roughly 10%. Further improvements in the performance of the composite system could likely be obtained by optimizing the composite material and/or layup for these types of impact conditions. However, we have not yet identified any composite systems that could achieve a puncture resistance that approach a two times improvement over a comparable weight steel system.

Impact Performance Summary

A summary of the current state of tank car side impact performance is provided in Figure 26. From the full scale side impact Test 2, the 105J500W tank car puncture energy was slightly less than one million ft-lbs. This corresponds to a 10 mph impact with a 286,000 lb ram car and the 6x6 inch impactor. From analyses, the puncture energies of the 105J300W and 105J600W tank cars are approximately 30 percent less and 40 percent greater than the 105J500W tank car, respectively.

The goal of the Next Generation Railroad Tank Car Project was to increase the puncture energy of the tank car by five to ten times over the baseline 105J500W tank car design. This target is outlined by the red box in Figure 26. The proposed TIH tank car standard falls within this range, requiring a puncture energy that is 6 times that of the baseline tank car. However, the levels that were found to be achievable with the first generation concepts in the NGRTC project are more consistent with two to three times the puncture energy of the baseline design.
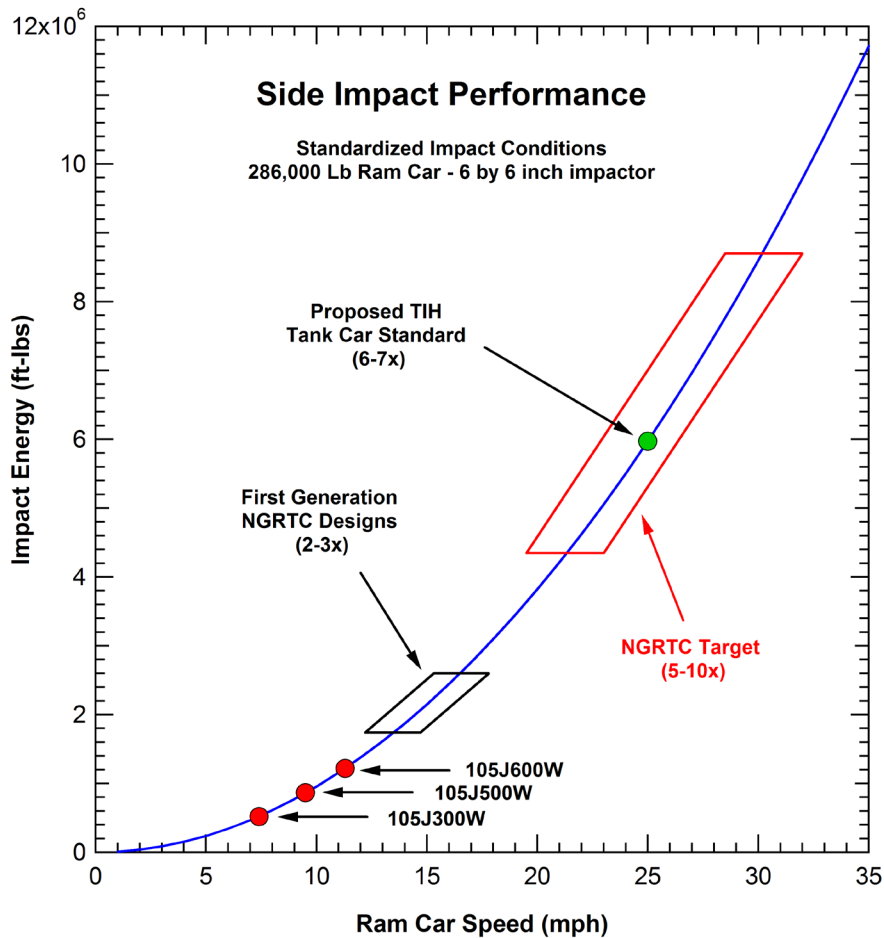
Figure 26. Summary of side impact puncture performance and goals.

A similar summary of the current state of tank car head impact performance is provided in Figure 27. The calculated puncture energy for a pressurized (100 psi) 105J500W tank head with an 11-gauge head jacket is 610,000 ft-lbs (analysis described in Section 5.3.2). This corresponds to an 8 mph impact with the 286,000 lb ram car and the 6x6 inch impactor. For comparison, the puncture energy of a 105J600W tank head with a 0.50 inch full height head shield is 1.1 million ft-lbs.

The goal of the Next Generation Railroad Tank Car Project was to increase the puncture energy of the tank car by five to ten times over the baseline 105J500W tank head as outlined by the red box in Figure 27. The proposed TIH tank car standard is above this range, requiring a puncture energy that is approximately 14 times that of the baseline tank head. However, the levels that were found to be achievable with the first generation concepts in the NGRTC project are more consistent with 2.5 to 4 times the puncture energy of the baseline design.
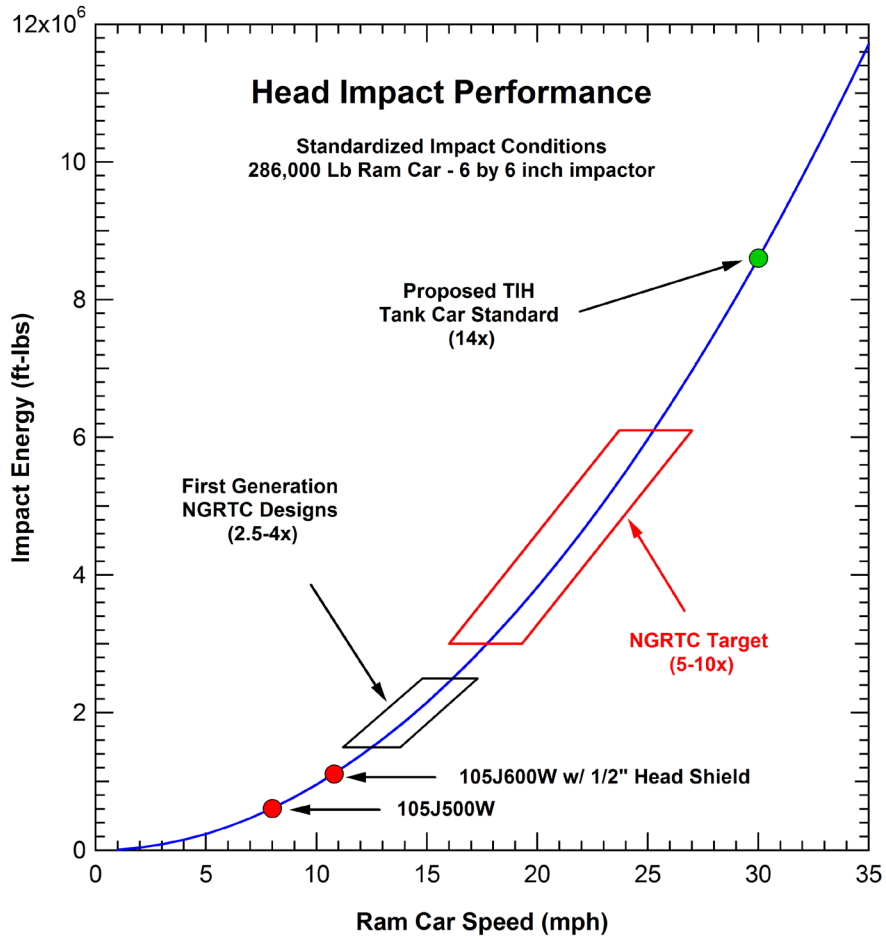
Figure 27. Summary of head impact puncture performance and goals.

Detailed Puncture Analyses of
Various Tank Car Designs

1   Introduction

There is ongoing research to develop strategies for improving railroad tank cars so they can maintain tank integrity for more severe accident conditions than current equipment. Research results are being used to develop improved tank car designs. In addition, this research was performed to support the rail freight operations to prepare for the proposed rulemaking by the Federal Railroad Administration (FRA).

A key effort in this program is the development and application of detailed finite element models of tank car equipment which can accurately predict the puncture resistance under different impact conditions. To date, these analysis tools have been developed and validated for the puncture of the baseline tank cars for both side and head impact conditions (described in Sections 4 and 5 of this report). These validated tools were applied to assess the puncture resistance of various tank car designs.

This report describes finite element analyses of the impact and puncture behaviors of both current and future tank car designs. The scope of this effort includes the development of detailed finite element models for tank cars and the use of those models for various impact scenarios to assess puncture energies.

1.1   Problem Definition and Approach

Accident statistics show that the rail industry's safety performance has generally improved over the last few decades. The FRA's Railroad Accident and Incident Reporting System (RAIRS) show that the number of accidents per year with at least one car releasing hazardous materials has decreased significantly over the past 25 years, as shown in Figure 28 [1]. However, a series of three recent accidents or derailments involving the release of hazardous material have focused attention on the structural integrity of railroad tank cars. These events include (1) Minot, ND, on January 18, 2002; (2) Macdona, TX, on June 28, 2004; and (3) Graniteville, SC, on January 6, 2005 [2-4].

To better define the collision threat, studies have been performed to both evaluate the accident statistics [e.g. 5-7] and analyze the kinematics of freight trains in derailments and collisions [e.g. 8, 9]. Evaluation of the derailments and collisions has shown that these are complex events with a wide range of collisions between the various cars in the train. A 40 mph derailment of a large freight train may involve thirty or more cars and the derailment event would last on the order of a minute before the train comes completely to rest. An example of a derailment simulation for a 36-car train model is shown in Figure 29. Impacts on tank cars will include both head impacts

and side impacts from objects as small as a broken rail to very blunt objects, such as another tank head. Thus, the objective of the tank car development efforts included increased protection in both head and side impacts for a range of impact conditions.
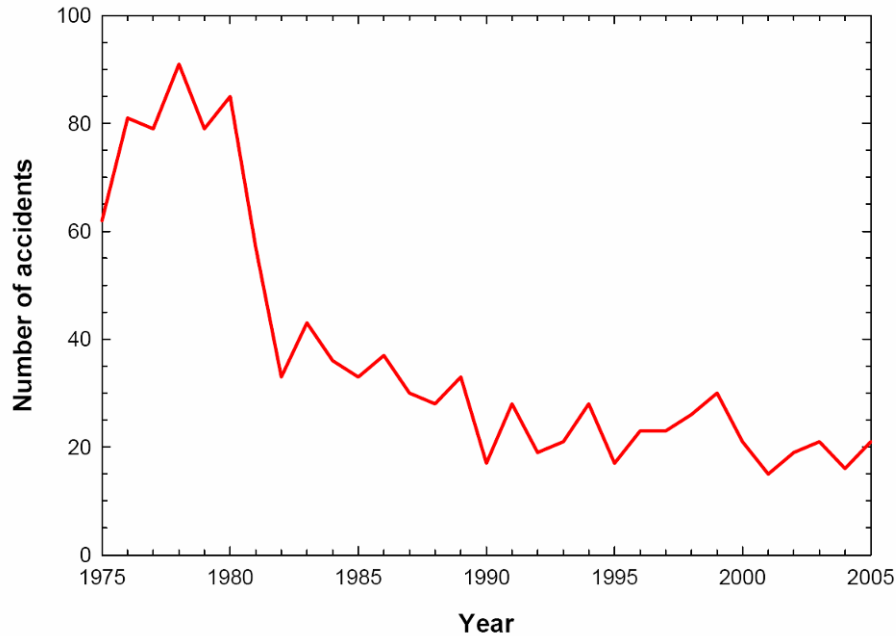
Figure 28. Number of Accidents with at Least One Car Releasing Hazardous Materials [1].

To develop an improved tank car design, the physics of the tank impact response need to be understood. For the purposes of the analyses performed here, the impactor is assumed to be a rigid object. As the impactor strikes the tank, the tank starts to deform. As it deforms, it will develop resisting forces. For a given tank configuration (e.g. tank thickness, internal pressure level) and a given impact condition (e.g. head or side impact, centered or offset impact location) the tank will have a characteristic force-deflection curve, such as that shown in Figure 30. The shape of this force-deflection curve is relatively independent of the size of the impactor. The area under the force-deflection curve is equal to the amount of impact energy that has been dissipated. If the impact speed is sufficiently low, the total energy will be dissipated and the impactor will be safely stopped. If the impact speed is sufficiently high, the forces developed will exceed the strength of the tank material and the tank will be punctured. The point at which this failure of the tank is initiated will depend strongly on the size of the impactor.

Hopper Car Model

Tank Car Model
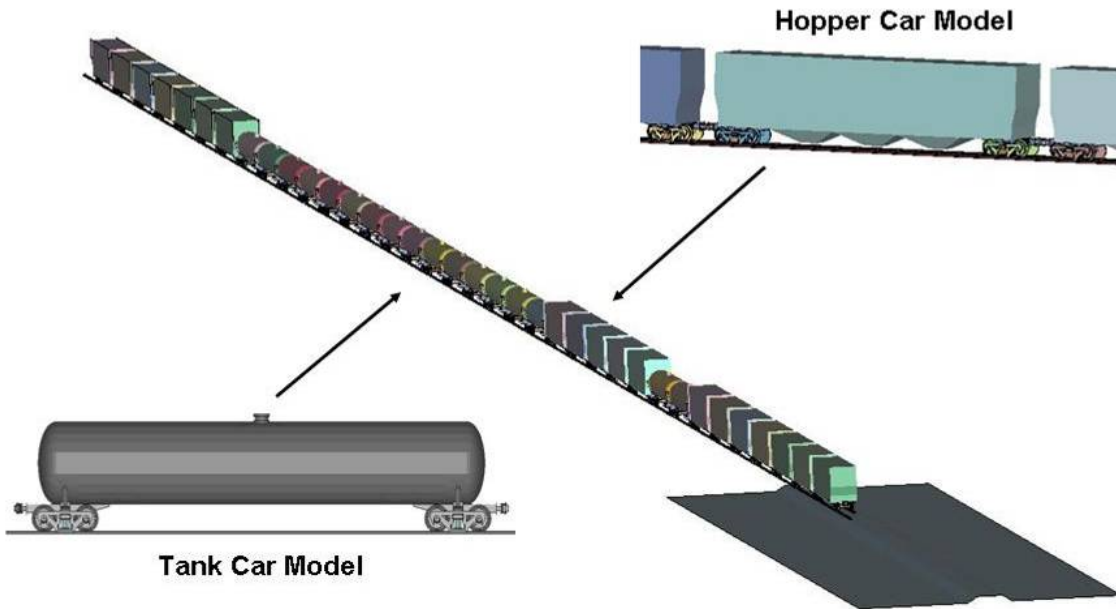
(a) 36-car train derailment model
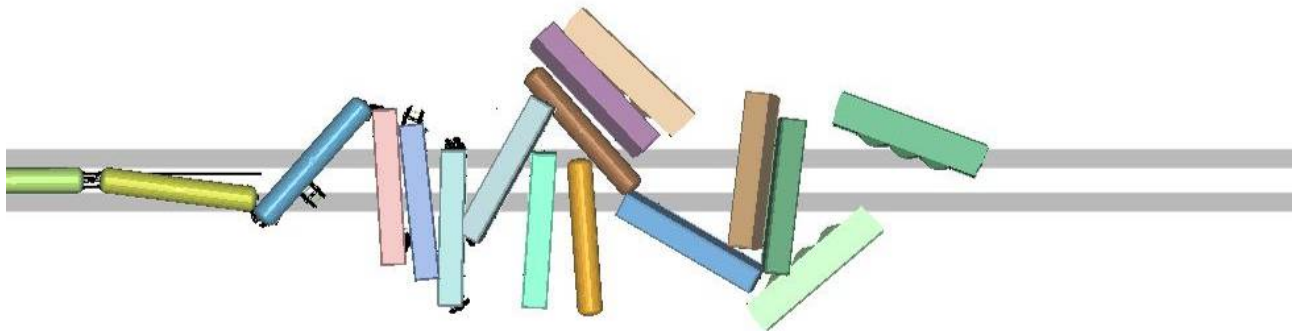
(b) Calculated response 25 seconds after derailment

Figure 29. Calculated derailment behavior for the 36-car train model [9].

To absorb additional energy prior to puncture, you can increase the force levels required to deform the tank, increase the displacements that can be experienced prior to puncture initiation, or a combination of both larger forces and larger displacements. The protection strategies are to add external energy absorbing structures and protective layers. These structures may have a larger standoff distance to extend the total displacement and energy dissipation prior tank rupture. Other protection strategies may be to (1) reinforce the tank system (increasing forces), or (2) blunt the impact loads (increasing the allowable tank displacements prior to rupture).
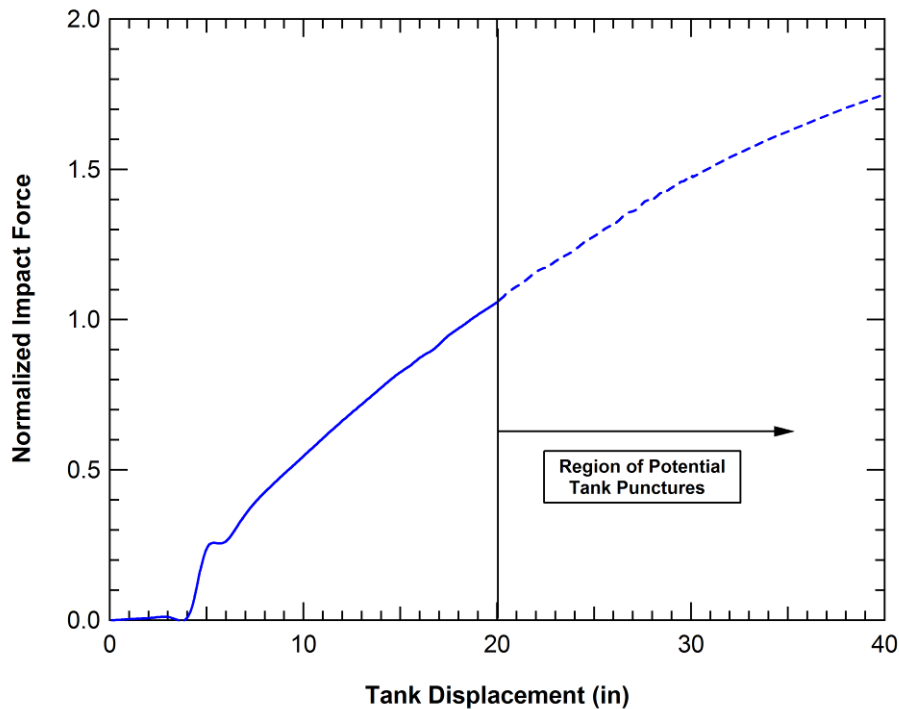
Figure 30. Characteristic force-deflection curve for a tank impact.

1.2 Tank Car Design Constraints

A good summary of the overall tank car design constraints is provided by Tyrell, et al. in Reference 11. A summary of the primary constraints is provided here.

Any new developments for tank car designs will still need to satisfy the basic current tank car design requirements for all conventional aspects (service, manufacturing, inspection, test, and maintenance). The baseline car chosen for this study is a DOT 105J500W car, the same class of tank car used in the full-scale crash tests. The tank cars used in the NGRTC test program were chlorine tank cars. This baseline car is constructed to Association of American Railroads (AAR) plate B clearance standards [10]. The envelope for equipment built to plate B standards is shown in Figure 31. The clearance standard dictates the maximum car height, width, and truck center spacing for compliant cars. For plate B, the maximum allowable height of any portion of the car is 15 feet-1 inch above top-of-rail. At the maximum allowable width of 10 feet-8 inches, truck centers cannot exceed 41 feet-3 inches.

For a car with the maximum distance between truck centers, the length of structure outboard of the trucks must also be considered in the car's design. The swingout at the ends of the car cannot exceed the swingout at the center of the car on a 13 degree curve [10]. A car built to plate B with maximum distance between truck centers has a swingout at the center of the car of 5.75

inches. By extending the length of the car outboard of the trucks until this same swingout is achieved at the end of the car, a maximum overall car length of 57 feet-10 inches can be achieved [11].

The baseline car's tank has an outer diameter of 8 feet-6.3 inches and a nominal capacity of 17,300 gallons. This tank has a 12.875-inch clearance on either side before encountering the maximum allowable car width. This clearance effectively limits the maximum amount of energy absorbing material that can be placed around the tank.
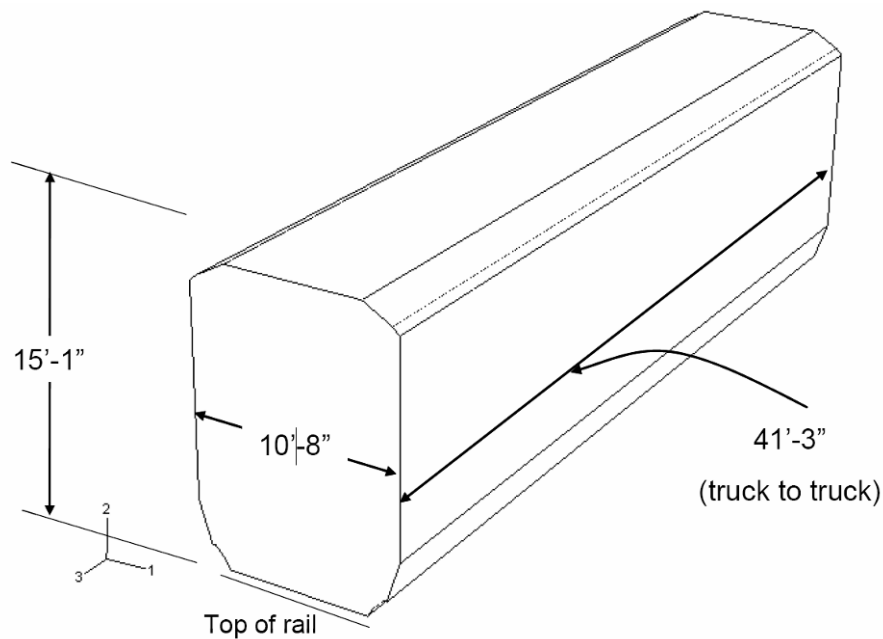
Figure 31. Maximum Dimensions for Plate B [11].

One concern associated with the addition of new structure to the car is the additional weight that this will contribute. For the improved crashworthiness tank car, the maximum allowable weight is 286,000 lb. The new design includes many of the same features of a conventional tank car, including the tank assembly, truck assemblies, safety appliances, and an equal lading capacity of 90 tons of chlorine. In addition, the new design will include a strengthened tank, energy absorbing material, and a structural frame to bear the service loads.

Table 1 shows the weights of components common to both conventional and improved crashworthiness tank cars. These preliminary values are given to estimate the amount of weight that is available for new structure. Based on the weights of existing tank car components and the 286,000 lb limit, approximately 39,000 lb are available for new structure (after removal of the existing tank jacket and head shields). This available weight comes from increasing the car

weight and from incorporating the functions of the baseline car's jacket and the stub sill/body assemblies into alternative components.

Table 1. Weight Breakdown of Tank Car Components [11].

Component	Weight (lbf)
Bare tank (0.777-inch thick)	38,280
Truck Assemblies (2)	20,580
Coupler/Draft gear Assemblies (2)	2,300
Air Brake Assembly	1,310
Fittings and Housing Assembly	1,300
Manway	1,300
Ladders, Handholds, & Railings	1,100
Handbrake Assembly	420
Paint and Markings	100
Chlorine	180,000
Subtotal	246,690
Available for New Structure	39,310

2   Model Development and Preliminary Impact Analyses

2.1   Introduction

In this section, we provide a brief history of the tank car model development, preliminary impact analyses, and model validation for current tank car designs.

2.2   Tank Car Model Development

A diagram of a general purpose tank car is shown in Figure 32 showing the terminology applied in this report [5]. Missing from the figure is any description of an external jacket or head shield that were included in the bulk of the impact analyses.
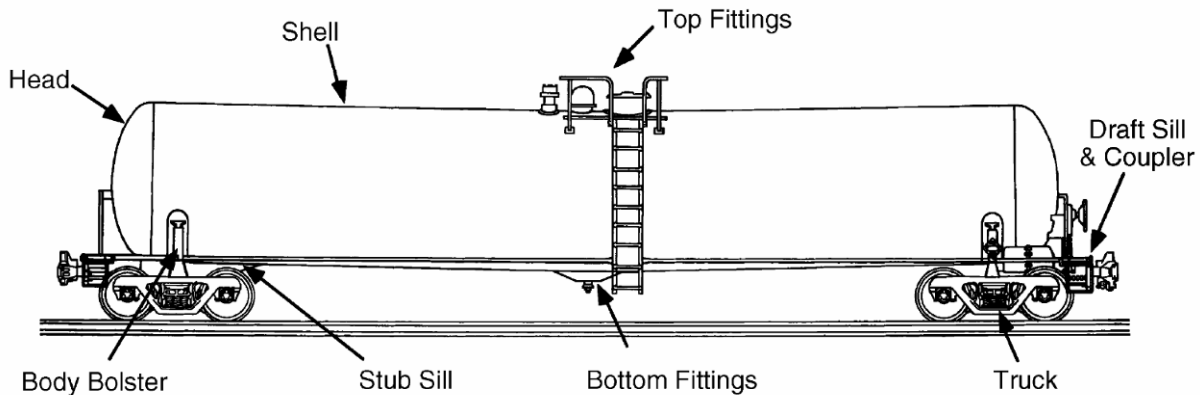
Figure 32. Diagram of a typical North American general purpose tank car [5].

The tank car model used in these analyses was based on a previous finite element model of a DOT 112A340W pressure tank car generated to analyze the loads and stresses in the tank car as a result of service and salvage operating conditions [12-14]. The LS-DYNA finite element code was used for the tank car analyses described in this report [15]. LS-DYNA, developed and maintained by the Livermore Software Technology Corporation (LSTC), is an explicit nonlinear three-dimensional finite element code for analyzing the large deformation dynamic response of solids and structures. LS-DYNA has many features ideally suited to the analysis of vehicle collisions and is well accepted in the crashworthiness community as a state-of-the-art code. Equipment manufacturers commonly use LS-DYNA in the design of passenger rail car and automotive crash safety. The model for the tank car was developed using the TrueGrid preprocessor code [16].

Two external views of the original DOT 112A340W tank car model are shown in Figure 33. The structure includes the tank with ellipsoidal heads, manway, stub sill, bolster, and truck structures. The geometry of the tank car structures in the model were based on a design originally developed

by Union Tank Car. Figure 33(b) gives a detailed view of the original car end structures in the model and the associated model mesh resolution.

(a) Tank car model   **(b) Detail of the tank car mesh**
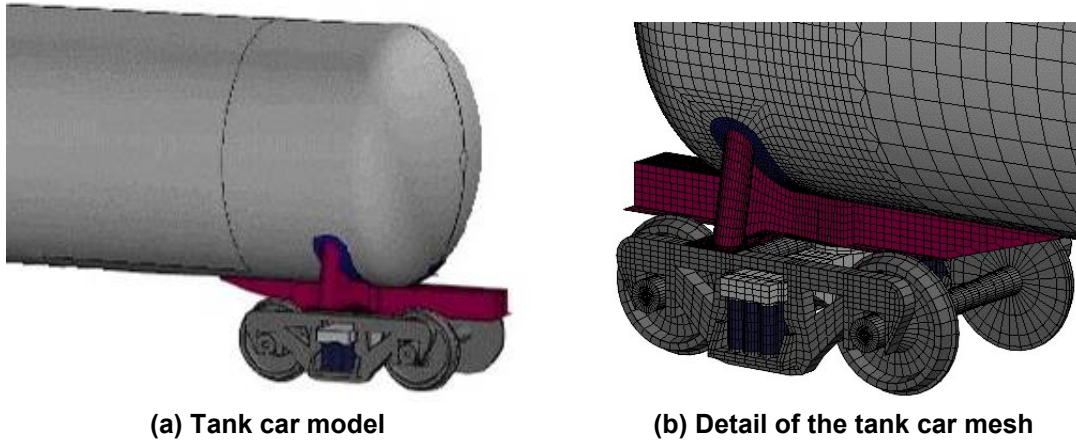
Figure 33. Original model generated for an 112A340W pressure tank car.

Subsequent development and application of the tank car model was performed in a study to assess the conditions for puncture and catastrophic rupture in the Minot, North Dakota Derailment [17-18]. For these impact analyses, the model was modified to be a 105J300W primarily by adjusting the tank wall thickness to match the values measured and reported in the NTSB Materials Laboratory Factual Report [19]. For this application, the external insulation and jacket were not included in the model. The stub sill geometry was also modeled in greater detail to allow for the inclusion of a model for the coupler and draft gear. The final modification made to the model was to significantly increase the mesh resolution in the impact zone. The model was refined to have approximately 2-inch elements in the impact zone to resolve the damage distributions caused by impact. The updated tank car model is shown in Figure 34.

The starting point for the model used in this study was that of the tank car geometry shown in Figure 34. However, additional data on specific tank car designs were used to update the models used in this study. Modifications include the addition of a jacket and standoffs and the modification of the tank dimensions (diameter, length, head and shell thicknesses) to match the specific parameters of the various tank designs of interest.

(a) Overall view   (b) Truck and draft gear geometry

(c) Tank mesh
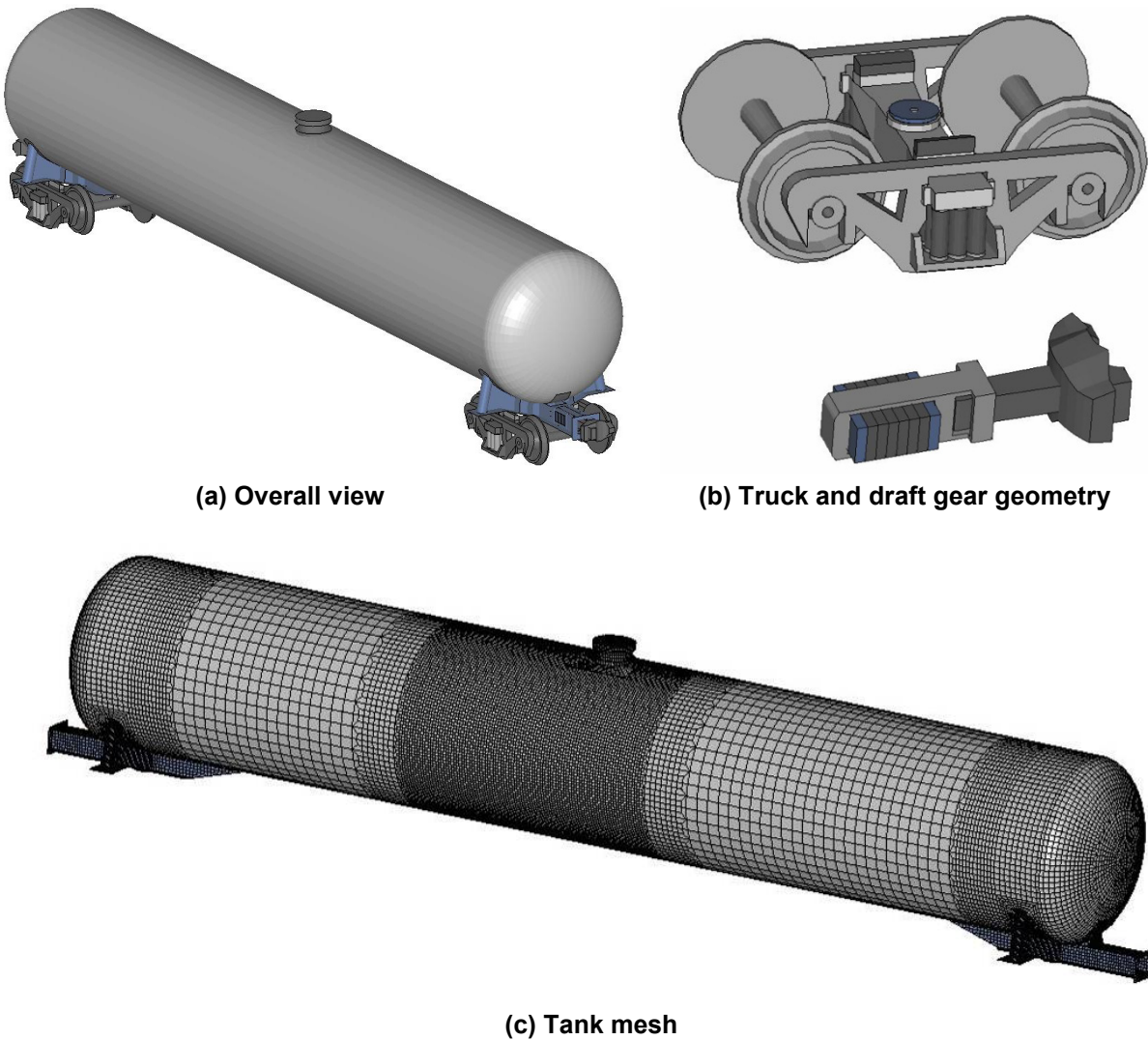
Figure 34. Updated model generated for a 105J300W pressure tank car.

2.3   Side Impact Analyses and Model Validation

This section describes the impact test results and corresponding analyses that were used to validate the models for the detailed impact dynamics. Comparisons to these tests were also used to evaluate modeling simplifications that can be applied in subsequent developments of improved tank car designs. All of the analyses performed here (and in the remainder of the report) were developed using an inch-lbf-s system of units and corresponding plots will be in units consistent with this system (e.g. stress in psi, etc).

2.3.1 Test 1 - 14 mph Side Impact (17x23 impactor)

The first validation of the tank car model was performed for the impact Test 1 from the Next Generation Rail Tank Car project on April 26, 2007, at the Transportation Technology Center, Inc. (TTCI) in Pueblo, Colorado [20]. This test involved a side impact with a blunt and rigid indenter into the side of a type 105 chlorine tank car design. The test was performed by impacting a ram car into the side of a ballasted chlorine tank car that was backed by a rigid impact barrier. The desired impact speed was 14 mph and the ram car speed was measured optically at 13.9 mph using speed trap reflectors placed within 6 feet of the impact point.

Additional parameters for Test 1 were as follows:
- Tank Car Number 3069
- Tank Car Weight (estimated) 265,000 pounds
- Tank Shell: 0.777-inch-thick normalized TC128B
- Insulation and Thermal Protection: ceramic fiber and fiberglass
- Jacket: 11 gauge A1011 steel at 4-inch standoff distance
- Slurry Density 11.6 lb/gallon
- Outage 10.4 percent
- Capacity 17,391 gallons
- Internal Pressure 100 psi
- Ram Car Weight: 285,600 pounds
- Ram Car Speed: 13.9 miles per hour
- Ram Car Energy (derived): 1.86 million foot-pounds

This test and the subsequent Test 2 (described below) were designed to bound the regime between no puncture (but with large deformations of the tank) and puncture of the tank. The instrumentation in the impact tests were designed to measure the necessary accelerations, strains, displacements, and pressure measurements to validate the tank car models. In many areas, sensors were placed to assure redundancy in the critical information.

Figure 35 shows tank car 3069 and the ram car staged in position for the April 26 test. The ram was aligned to impact at mid height at the center of the tank. The rigid ram had approximate frontal dimensions of 23 by 17 inches, with 1-inch-radius edges and corners. The target tank car was supported on trucks resting on short stub sections of track normal to the direction of travel of the ram car. The target tank car was also backed by a rigid barrier to react to the impact loads.

Figure 36 shows the ram and target cars during the impact test for tank car 3069. As a result of the impact speed of 14 mph, the rigid ram dented both the jacket and the shell of the chlorine tank car but the tank was not ruptured. The tank car stayed upright throughout the test, but it did derail from the stub rail sections. Following the primary impact there was a significant rebound of the ram car from the tank car with a rebound speed of 7.6 mph. The tank car also experienced

a rebound from the wall after impact. The rebound of the car was countered by outriggers installed in the draft pockets of the car. Structural inspection after the impact showed no visible damage to the stub sills or their weld joints to the tank. The ram car brakes triggered and set as anticipated, which kept the ram car from rolling forward (downhill) for a second impact.

Figure 35. Ram car and target tank car staged prior to Test 1.

Figure 36. Shell side impact behavior in Test 1 for Tank Car 3069

The post-test condition of the tank included large dents in both the jacket and tank shell. Figure 37 shows the post-test dents in the jacket and commodity tank. The post-test permanent dent in the jacket was approximately 14 inches deep and in the tank shell it was approximately 10 inches deep. The impact also caused one of the weld joints on the jacket near the impact area to fail. The back of the tank car was also deformed by the reaction against the rigid impact barrier.

Figure 37. Post-test dents in the jacket and shell of Tank Car 3069

Comparison of Test 1 with Pretest Predictions

The tank car model was further modified to match the tank car structures used in the full-scale impact test program. The updated model of the 105J500 chlorine tank car is shown in Figure 38. The modifications include the addition of the jacket and jacket standoffs, correction of the commodity tank length, diameter, and thickness, and the addition of the outriggers attached to the draft gear to prevent a post-test rollover of the target tank caused by the rebound off the reaction wall. The mesh was also refined in the impact zone.

Another modification was the addition of an explicit model of the lading. The lading model consists of a low strength viscoelastic material that fills the same volume as the slurry added to the test tank. The sloshing of the lading model can be seen in the cutaway view of the predicted impact response shown in Figure 39. This lading modeling approach was established to capture the momentum transfer of the coupled fluid-structure response but minimize effects such as sloshing at the fluid free surface that can cause numerical stability problems.
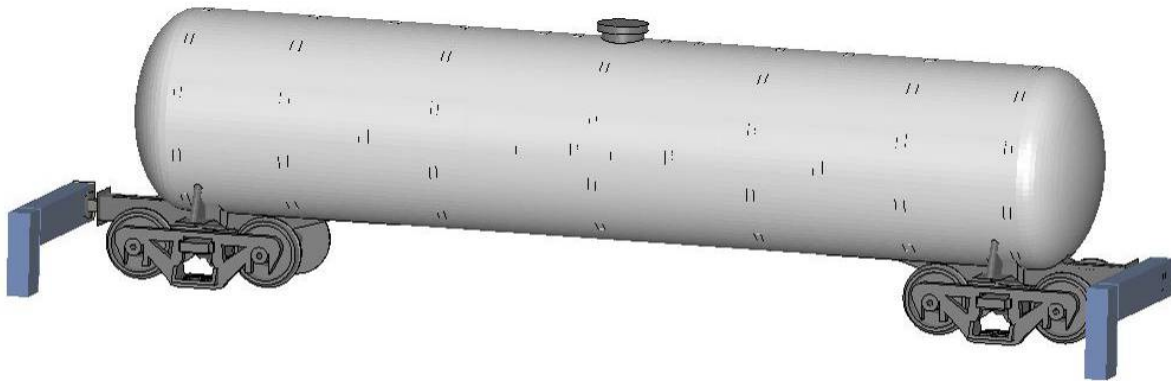
(a) Complete tank car model
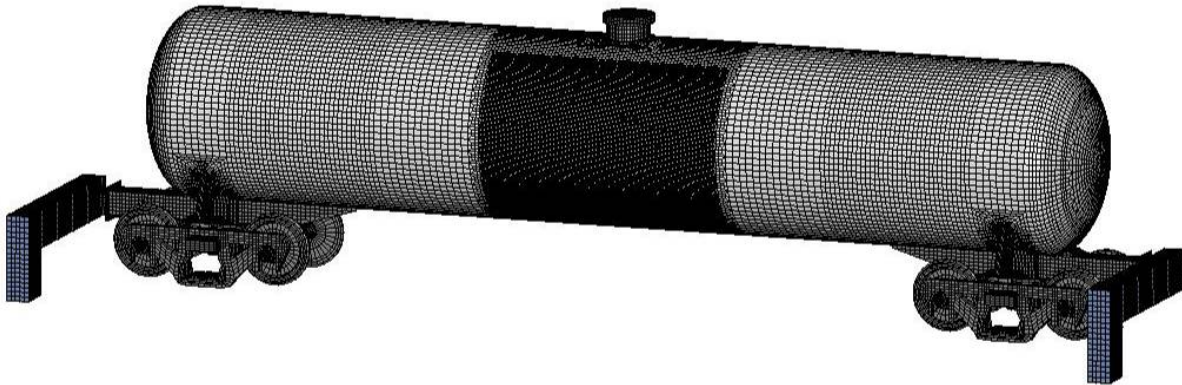
(b) Tank mesh
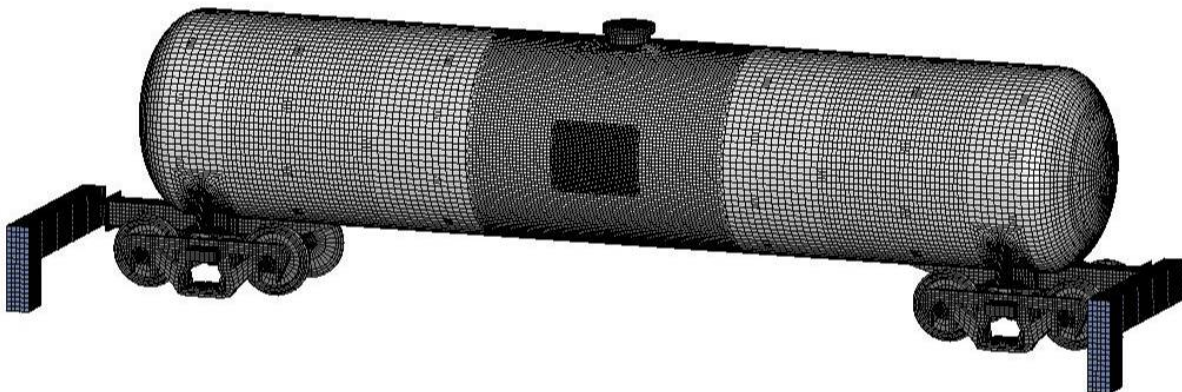
(c) Jacket mesh
Figure 38. Updated model generated for a 105J500W pressure tank car.
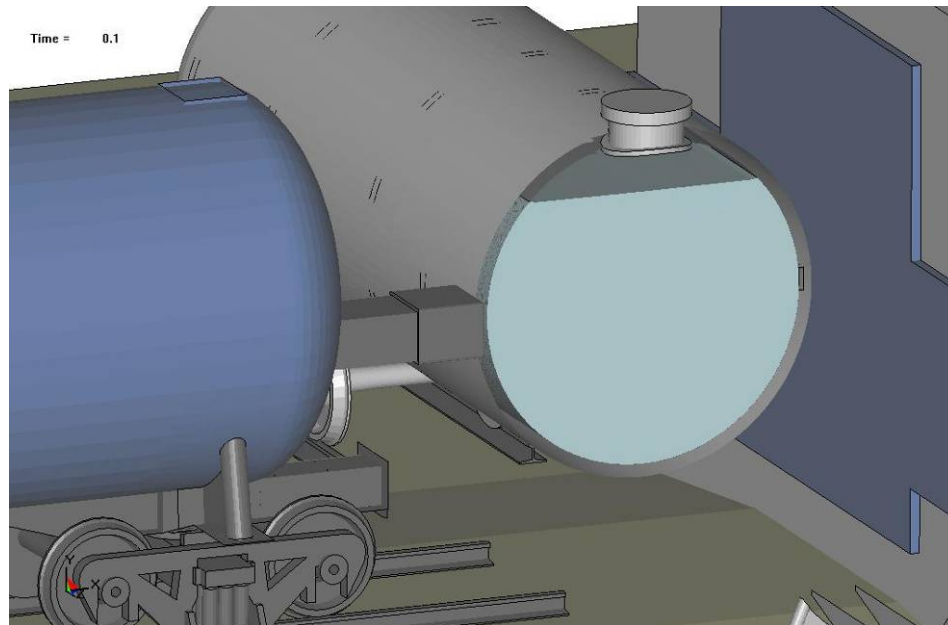
(a) Before impact (time=0.1 s)
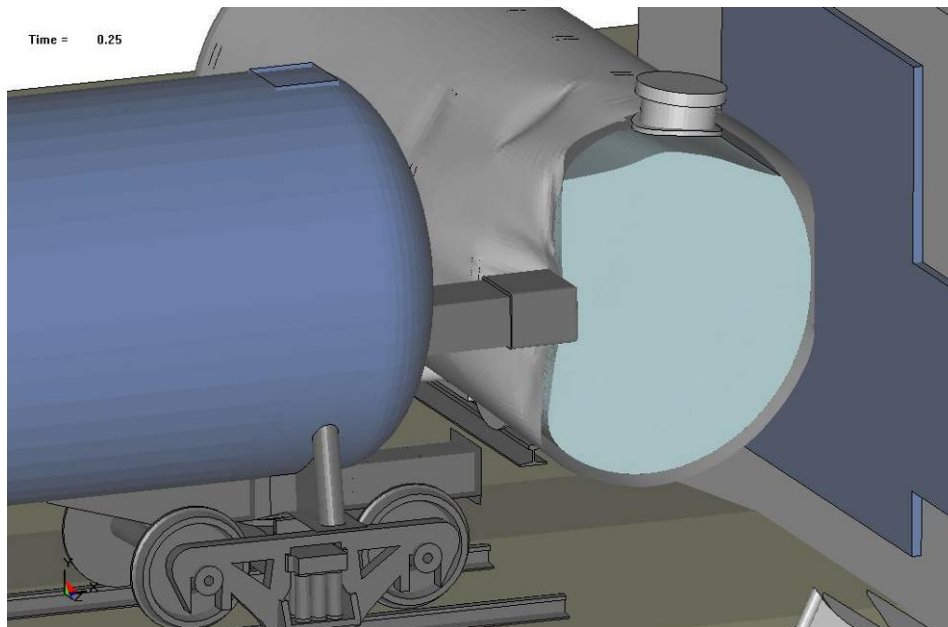
(b) Near maximum displacement (time=0.25 s)

Figure 39. Calculated Test 1 impact response with cutaway showing lading.

A comparison of the predicted and measured ram car acceleration and displacement time histories are shown in Figure 40. The comparison shows that both the characteristics of the double peak acceleration response and the quantitative comparisons of maximum acceleration and displacements agree well between the calculation and the test.
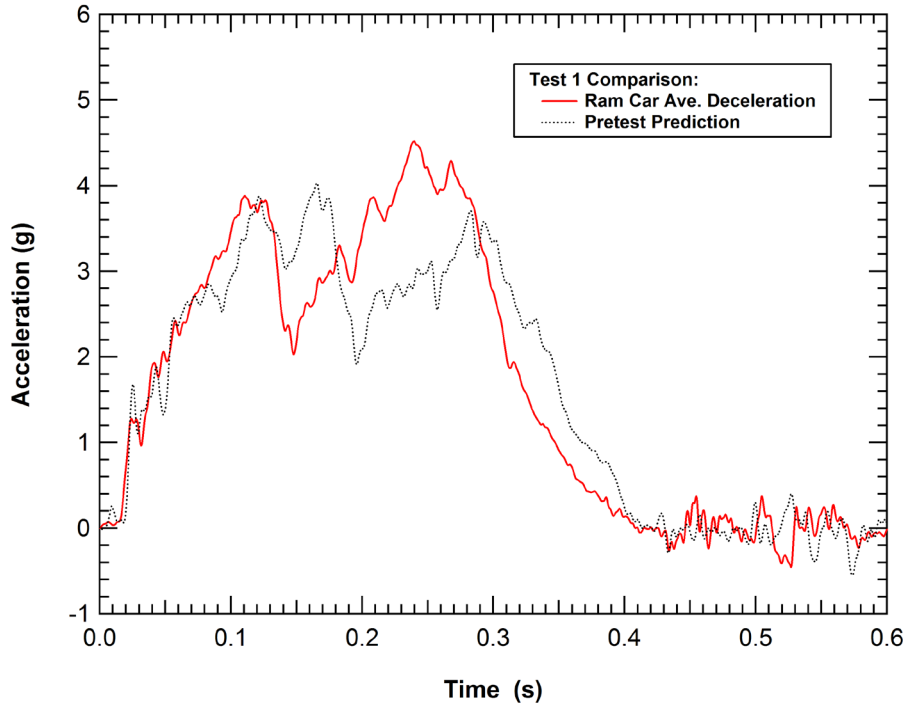
(a) Acceleration history
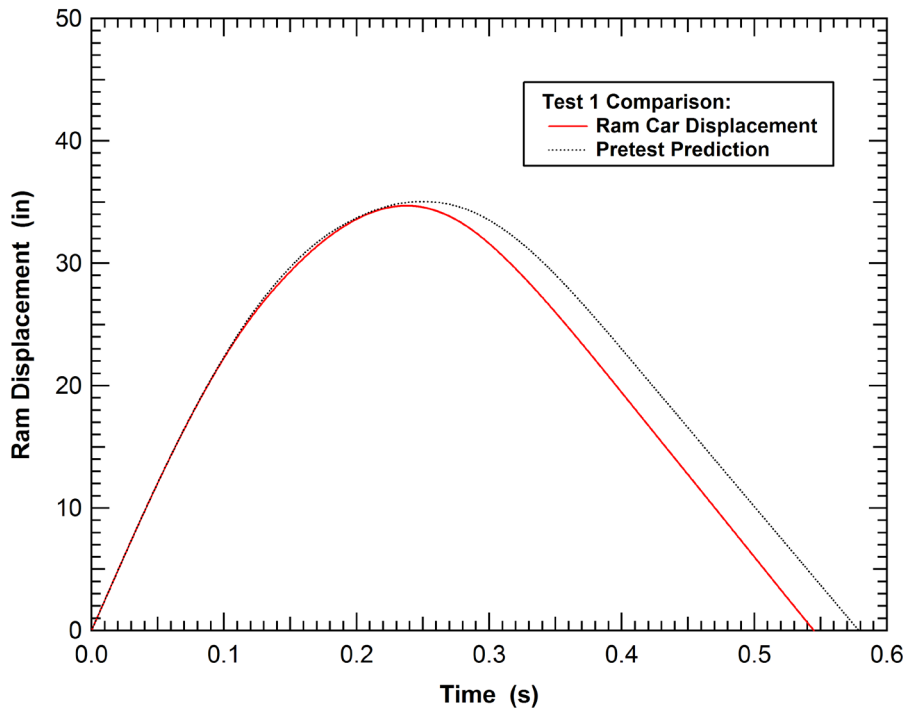
(b) Integrated displacement history

Figure 40. Comparison of the measured and predicted ram car motions.

A series of string potentiometers were included inside the tank to measure the tank distortions during the test. These measurements include a series of 5 string potentiometers spaced longitudinally on 18-inch centers across the spring line (horizontally between tank belt lines) and centered on the impact location. In addition, a vertical string potentiometer was placed on the center line of the tank. All of the string potentiometers successfully collected measurements of the tank distortions with the exception of the vertical gauge that failed early in the impact response.

A comparison of the predicted and measured tank deformations are shown in Figure 41. The solid lines are the predictions and the dashed lines are the measurements. Overall, very good agreement was obtained between the prediction and test. The 35-inch maximum ram displacement, shown previously in Figure 40, corresponds to a 26-inch peak spring line displacement of the tank. The difference between these two values is primarily a result of the compaction of the space between the tank and jacket both on the impact face and on the far side of the tank car between the tank and the impact wall.
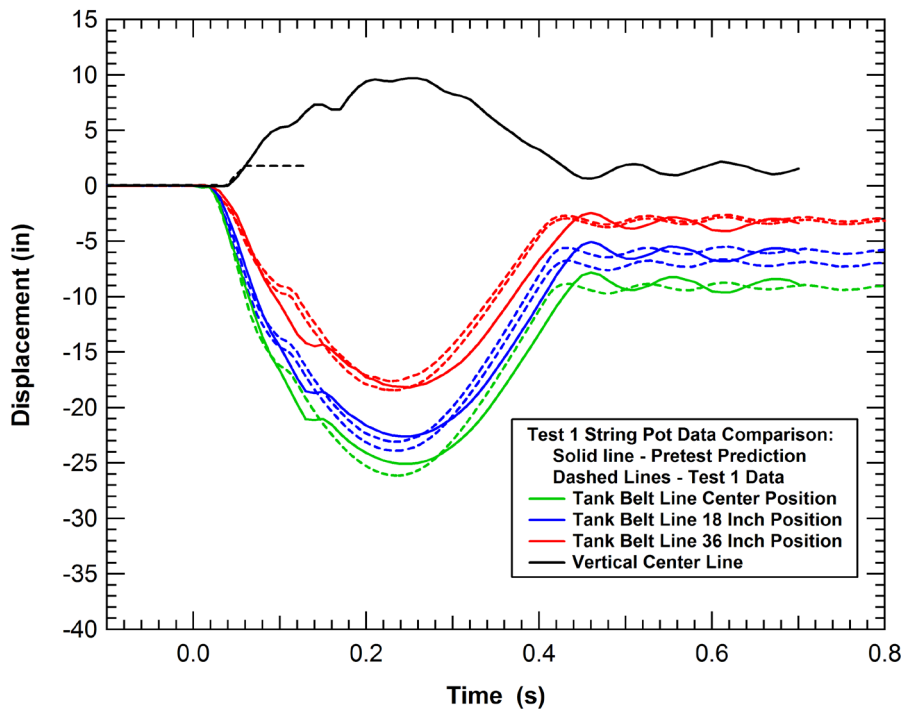
Figure 41. Comparison of the measured and predicted Test 1 tank displacements.

The ram car accelerations and displacements, shown in Figure 40, can be combined to calculate the force-deflection behavior for the target tank car. The comparison of the predicted and measured force-deflection curves is shown in Figure 42. This force-deflection curve is an important characteristic of the tank car for a given impact scenario. Although it is a

characteristic of the tank car and impact condition, it is measured based on the motions of the ram car which acts primarily as a rigid body. The area under the force-deflection curve is the impact energy that is dissipated and the primary approach that will be applied to improve the puncture resistance of tank cars is to add protective structures that increase the area under the curve prior to tank puncture initiation. The comparison of the force-deflection behaviors shows good agreement between the calculation and the test.
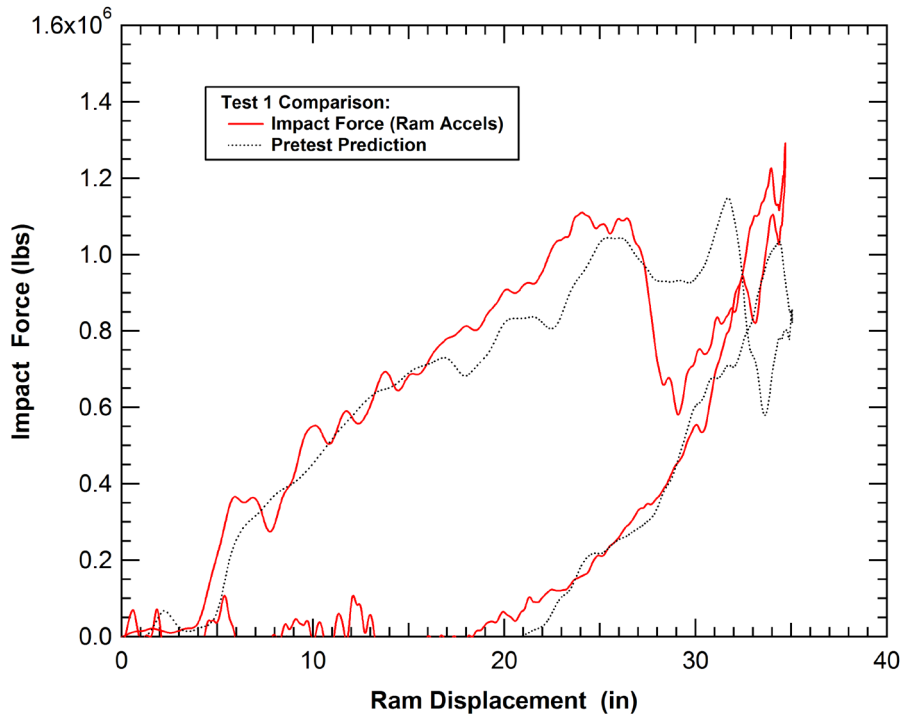
Figure 42. Comparison of the measured and predicted Test 1 force-deflection curves.

The above comparison of the pretest prediction and impact test serves as a validation of the model for the tank collision dynamics and impact deformation behavior. The responses include the initial impact, the reaction of the impact loads against the wall, and the post-impact rebound from the wall. Additional details of the impact behavior captured in the model included the target tank roll motion and lifting forces on the ram car caused by the lateral support of the target tank truck on the stub rail sections and the action of the outriggers resisting a post-test rollover behavior.

Test 1 Internal Pressure

The internal pressure in the pretest analysis was calculated by using the tank as a control volume and imposing an ideal gas pressure-volume relationship for the gas in the outage region of the tank. As a result, the internal pressure at any given time will be uniform everywhere in the tank and determined by the instantaneous tank volume. In the test, the pressure was measured at

various locations submerged in the slurry lading. The positions included the front and back belt line positions as well as locations at the bottom of the tank. Three pressure gauges were distributed longitudinally at each of these circumferential locations (12 gauges total).

A comparison of example measured pressure histories at three different circumferential locations is shown in Figure 43. The measurements indicated that there was both a hydrostatic pressure increase in the tank from the indentation as well as hydrodynamic pressures from the sloshing of the lading within the tank.
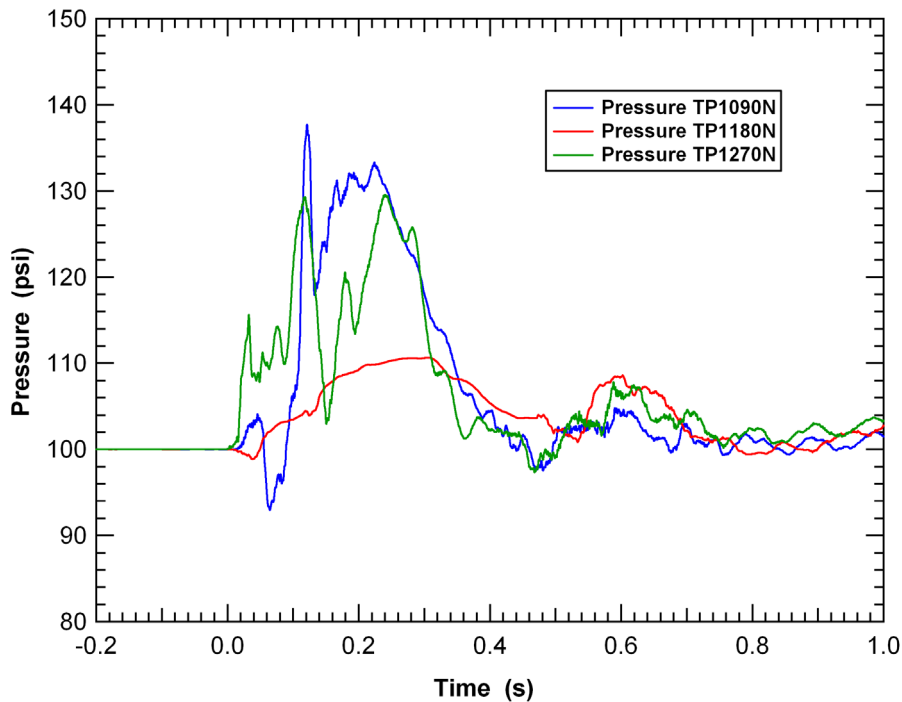
Figure 43. Measured Test 1 tank pressures at various positions in the lading.

A comparison of the predicted hydrostatic internal pressure and the average of the measured pressures is shown in Figure 44. The average of the measured pressures is slightly higher than predicted. However this discrepancy is probably a result of the hydrodynamic effects that are included in the pressure measurements. Overall, comparison indicates that the Test 1 impact response and tank indentation will produce a hydrostatic pressure increase of between 10 and 20 percent. This magnitude of pressure increase is not expected to have a large effect on the impact response and puncture energy.
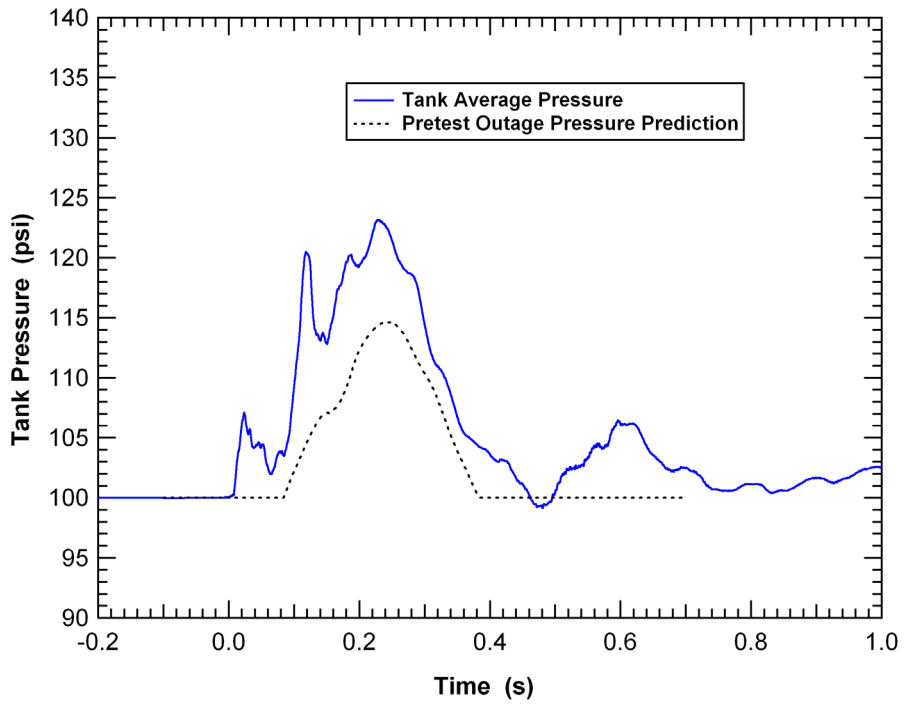
Figure 44. Comparison of the measured and predicted Test 1 tank pressure.

2.3.2   Test 2 - 15 mph Side Impact (6x6 Impactor)

Description of Test Conditions

The full-scale side impact Test 2 was performed on July 11, 2007 at the Transportation Technology Center [21]. The test was a side impact with a tapered and rigid indenter into the side of a type 105 chlorine tank car of modern design. The test was performed by sending a ram car into the side of a ballasted chlorine tank car that was backed by a rigid impact barrier. An impact speed of 15 mph (+0.5/-0 mph) was specified for this test. The actual impact speed was 15.2 mph. The target tank car was modified for this test by lowering the tank position and mounting rigid support skids to the bolster as shown in Figure 45.

Figure 45. Test 2 target Tank Car 3074 mounted on support skids.

The ram car was also modified prior to Test 2 by lowering the position of the ram arm and adding a new ram head with a much smaller contact area, as shown in Figure 46. The ram arm was lowered (as was the target tank car) to more closely align the height of the centers of gravity (CG) of the target tank, ram car, and the line of impact. The modified ram face was 6x6 inches square and had half-inch radiuses on all edges and corners.

A primary objective of these modifications to the target tank car and ram car were to create a test procedure with much more controlled and repeatable impact dynamics that eliminate the post-impact roll of the target tank. The modified ram would also significantly lower the required impact speed to puncture the target tank and would help to establish an upper bound on the puncture conditions within safe limits for the test facility, given the uncertainties in required puncture energy. The impact wall was originally designed based on static 2,700,000 lb load at 3

foot height in combination with 300,000 lb load at a 16 foot height (maximum design moment of 12,900,000 ft-lbs). Recent analysis [22] assessed that the barrier possesses sufficient strength to sustain a 3,000,000-lb impact at 65 in. above top of rail (moment of 16,250,000 ft-lbs).

Figure 46. Modified ram car and ram head used in Test 2

The pretest and post-test conditions of the tank car are shown in Figure 47. As expected, the rigid ram punctured the tank car and left an opening approximately equal to the cross-section dimensions of the ram, about 21 inches wide by 32.5 inches high. High-speed video of the impact event showed that the car stayed upright throughout the test and exhibited very little body roll. Full instrumentation was installed to measure accelerations, strains, and displacements on both the ram and the tank cars and high quality data was collected in the test for model validation.

Additional parameters for Test 2 were as follows:
- Tank Car Number 3074
- Tank Car Weight (estimated): 265,000 pounds
- Tank Shell: 0.777-inch-thick normalized TC128B
- Insulation and Thermal Protection: ceramic fiber and fiberglass
- Jacket: 11 gauge A1011 steel at 4-inch standoff distance
- Slurry Density: 11.6 lb/gallon
- Outage: 10.4 percent
- Capacity: 17,401 gallons
- Internal Pressure: 100 psi
- Ram Car Weight: 285,400 pounds
- Ram Car Speed (official): 15.2 mph
- Ram Car Energy (derived): 2.14 million foot-pounds

(a) Pretest target tank car

(b) Post-test tank damage

Figure 47. Puncture response observed in the full-scale impact Test 2.

The average of the measured longitudinal displacements for the ram car is shown in Figure 48. After impact, the impact decelerations rapidly increase over the initial 0.1 seconds to a peak level of approximately 3.3 g. At that time the tank is punctured and the ram car acceleration rapidly drops to a very low level. Starting at a time of approximately 0.3 seconds, the aft support structures on the ram arm engage the tank and the ram car is brought to rest at a time of slightly over 0.6 seconds. The remainder of the acceleration pulse is the rebound of the ram car from the target tank car.
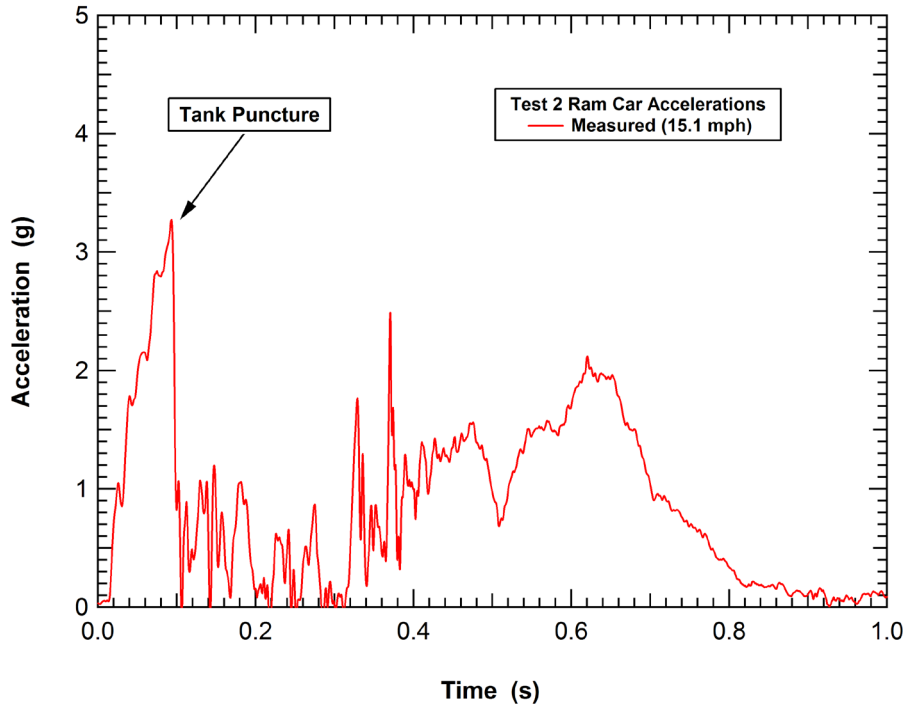
Figure 48. Measured Test 2 ram car average longitudinal acceleration.

The measured displacement histories for the ram car and impacted tank shell are shown in Figure 49. The ram car displacements were found from integration of the ram car impact acceleration history shown in Figure 48. The tank displacements are the measurements from the five string potentiometers that span the tank spring line. At the time of the puncture initiation (just under 0.1 seconds), the ram has 24 inches of displacement and the center tank spring line string potentiometer measured 19 inches of deformation. Again, the primary difference in these two displacements is the compaction of the space between the jacket and the tank shell on the impact side of the tank.

The ram car acceleration, shown in Figure 48, can be multiplied by the mass of the ram car to obtain the impact force history. This force history is plotted against the ram car displacement in Figure 50. Similarly, this force displacement history can be integrated to obtain the energy dissipation up to the point of puncture as shown in the figure. The Test 2 tank car punctured at a peak force of 935,000 lbs and a puncture energy of 870,000 ft-lbs.

The measured pressure histories at the three different circumferential locations are shown in Figure 51. The comparison of the measurements at different locations indicated that the hydrodynamic pressures from the sloshing of the lading were more significant than the hydrostatic pressure increase in the tank. The hydrostatic pressure increase is estimated to be less than 10 psi at the time of the tank puncture.
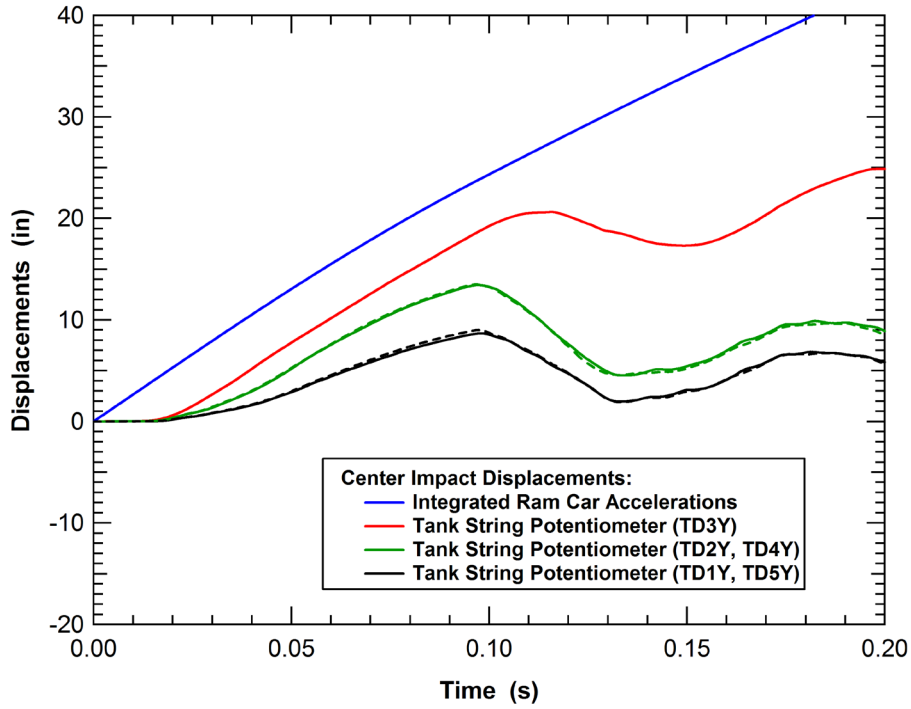
Figure 49. Measured Test 2 ram car and tank displacements.
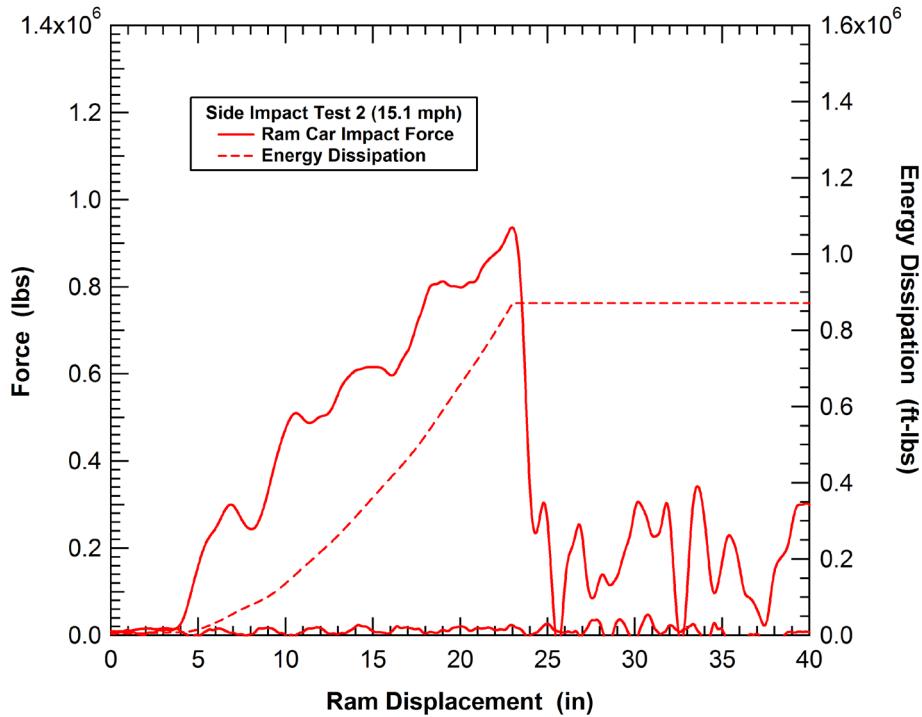
Figure 50. Measured Test 2 force-displacement behavior and energy dissipation.
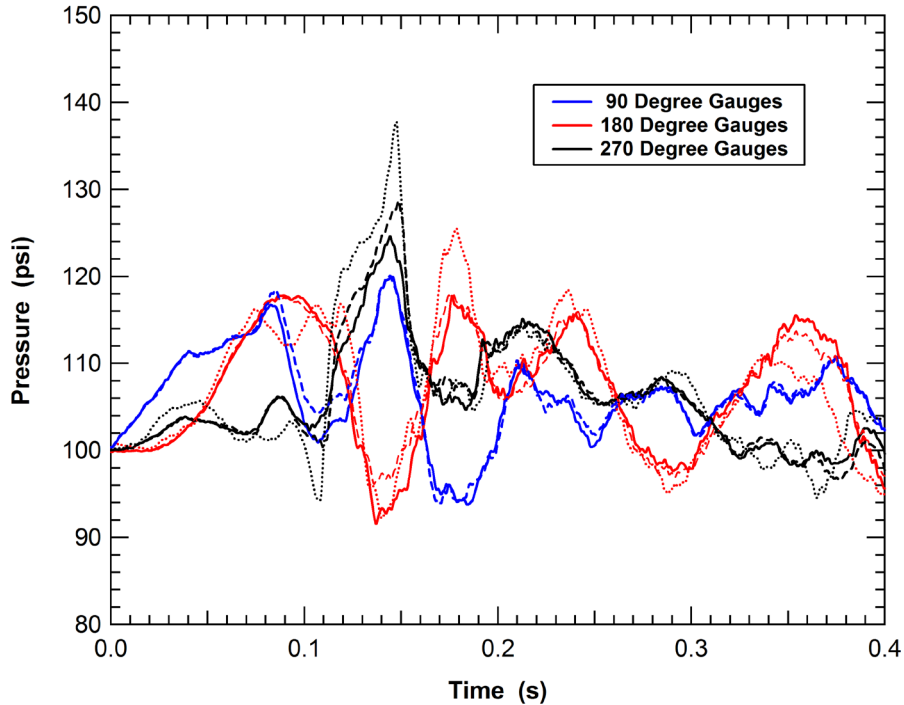
Figure 51. Measured Test 2 tank car internal pressures.

Comparison of Test 2 with Pretest Predictions

Additional modifications were made to the tank car and ram car models to match the test conditions. These include the attachment of the skids to the target tank as shown in Figure 52(a) and the creation of a more detailed ram car model and new ram head as seen in Figure 52(b). The new ram car model was important to accurately simulate the collision dynamics that are influenced by the relative inertial properties of both the ram car and target tank car (e.g. the relative CG heights).

At the time Test 2 was performed, a detailed fracture model was not yet incorporated for prediction of the puncture energies. The development of the fracture model and application to predict puncture energies are described in Sections 3 and 4 of this report. At the time of the test, the predictions were performed where failure of the tank was suppressed and the calculated damage levels were used to assess whether the puncture initiation was likely.

An example of the pretest prediction of the tank damage for Test 2 is shown in Figure 53. The maximum plastic strain in this test was predicted under the ram and the strain level at the inside surface of the tank for a 14 mph impact was approximately 50%. From this strain level it was determined that there was a high confidence that the impact speed selected for Test 2 would result in a puncture of the target tank.
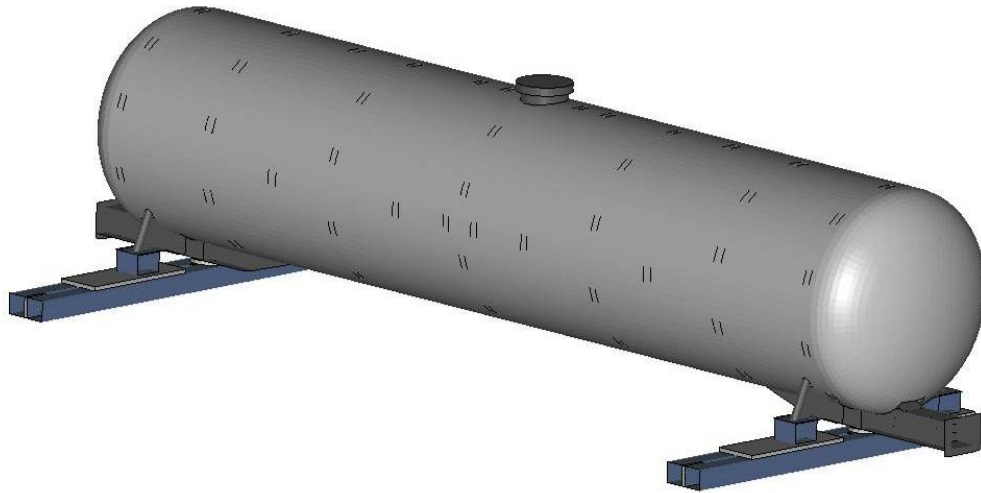
(a) Updated tank car model
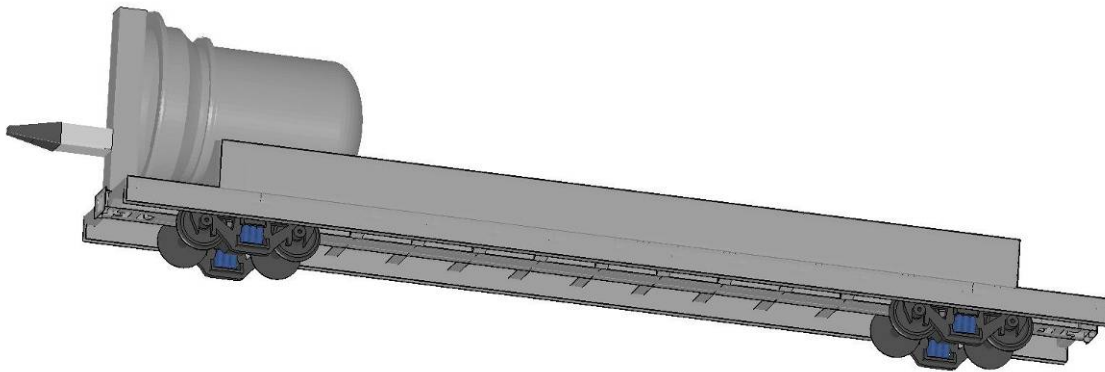
(b) New ram car model

Figure 52. Updated target tank car and ram car models for Test 2.

The pretest prediction of the force-deflection characteristics is compared to the measured Test 2 force-deflection curve in Figure 54. Again, the agreement is excellent up to a post-impact ram displacement of approximately 23 inches, at which time the ram punctures the tank wall and the measured force drops dramatically. This comparison, along with the Test 1 comparison and the evaluation of many other quantitative measures from both tests, validate the ability of these models to accurately capture the impact response up to the point of fracture initiation. The development and addition of the fracture modeling capabilities is described in the following section.

Time =   0.52
Contours of Effective Plastic Strain
max ipt. value
 min=-0.000212409, at elem# 143490
 max=0.516112, at elem# 72229

Fringe Levels

1.000e-001
9.000e-002
8.000e-002
7.000e-002
6.000e-002
5.000e-002
4.000e-002
3.000e-002
2.000e-002
1.000e-002
0.000e+000
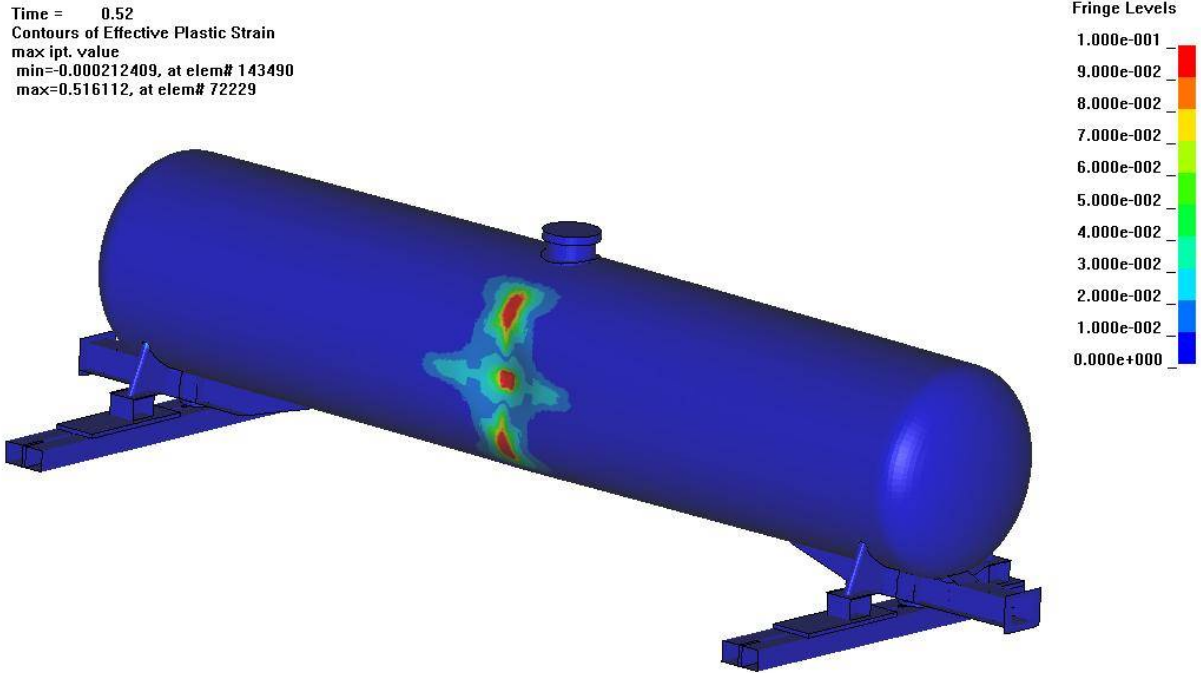
Figure 53. Predicted tank damage for the Test 2 impact conditions.
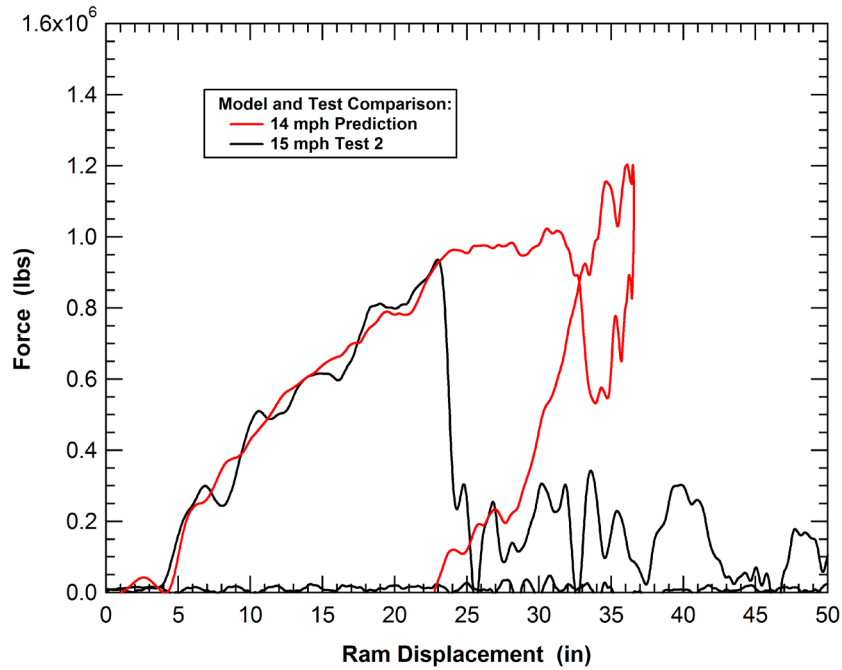
Figure 54. Comparison of measured and calculated Test 2 force-displacement response.

3   Material Constitutive and Damage Models

3.1   Introduction

The tank car impact analyses require a model for the material constitutive and damage behaviors to accurately predict the puncture threshold under various impact conditions. A piecewise linear elastic-plastic constitutive model was modified for this purpose to include a version of the Bao-Wierzbicki (BW) failure criterion [23-25]. This model is has been applied by other researchers to assess tank car puncture conditions [26] and is capable of reproducing both the nonlinear stress-strain behavior of the material as it deforms into the plastic regime and the fracture and failure behavior that depends on the state of stress and plastic strain history in the material. The material parameters used in these constitutive models were developed from the material test data on TC128B steel, developed under the NGRTC program [27-34].

The following sections describe the development of the constitutive and damage parameters used in the subsequent tank car puncture analyses.

3.2   Material Stress-Strain Behavior

The first step in the development of a constitutive model is the development of the nonlinear stress strain behavior. This governs the mechanical response of the material and prescribes the internal forces (stress) that are developed as the material is deformed (strained).

3.2.1   TC128B Material Properties

A tabular stress-strain curve was developed based on testing of different samples of TC128B [27]. A series of standard tensile tests were performed on different batches of TC128B, as shown in Figure 55. The data is consistent within each batch of material but significant variation can be found in tank car material obtained from different sources. The new material that was tested was at the upper range of strength for TC128B and the material recovered from the tank cars used in the test were more consistent with previous test data [14, 19]. As a result, the material recovered from the tank car used as the Test 2 target vehicle was used as the baseline material for the analyses in this report.

The data shown in Figure 55 is the measured engineering stress-strain behavior. Engineering stress was obtained by dividing the measured loads by the original cross-sectional area of the specimen. Similarly, engineering strain was obtained by dividing the change in the specimen gauge-section length by the original length.

The constitutive model in the finite element analyses requires that the engineering data be converted to a true stress and true strain. This conversion accounts for the changing cross

section of the specimen as it was deformed. The specimen cross section changes (shrinks) significantly during the test, and the engineering stress does not yield the "true" stress in this cross section. Similarly, the engineering strain is not representative of the material behavior, especially when a general three-dimensional state of strain exists. As a result, the engineering stress decreases as some materials approach failure, implying a weakening of the material. In reality, the stress in the cross section is increasing due to the reduction in the cross-sectional area (i.e. necking).
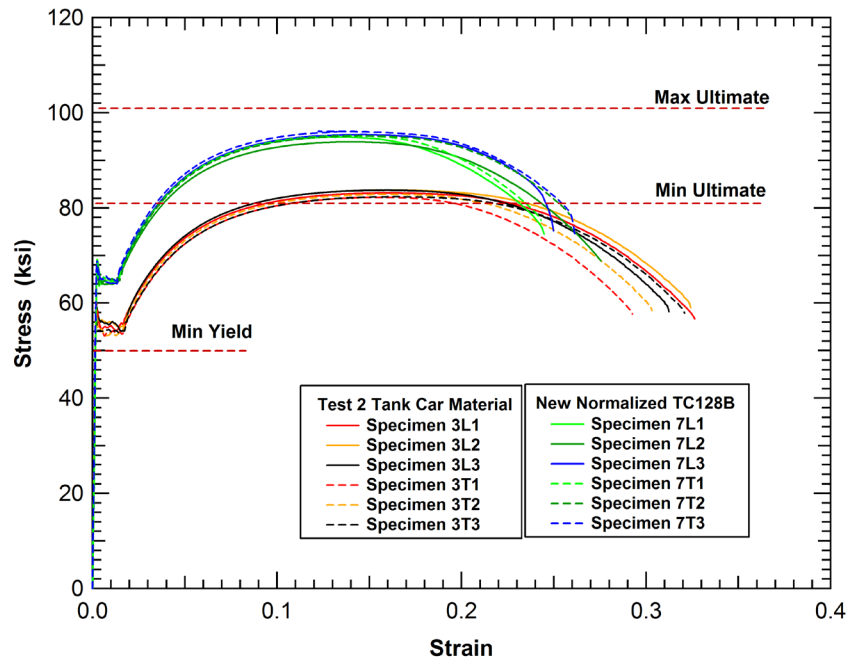
Figure 55. Material testing data for different TC128B materials.

There are several different ways to measure stress and strain based on the coordinate system used [28]. Some are based on material (Lagrangian) coordinates and some on spatial (Eulerian) coordinates. These give rise to terms such as "Green" and "Almansi" strain tensors. These are important in writing a computer code to solve large strain problems. An alternate approach is to define a "true" or "natural" stress and strain. The true stress is based on the load divided by the actual cross-sectional area of the specimen and is equal to the engineering stress multiplied by a term to correct for the change in cross section.

$$\sigma_T = \sigma_{eng}(1+e) \qquad (1)$$

where σ_T and σ_{eng} are the true and engineering stresses, respectively, and e is the engineering strain.

Prior to the onset of localization (necking), the natural or true strain, ε_T, is defined as

$$\varepsilon_T = \ln(\frac{l}{l_o}) = \ln(1 + e) \tag{2}$$

This definition comes about from defining the incremental true or "natural" strain as the current "change in length" divided by the current length, or

$$d\varepsilon_T = \frac{dl}{l} \tag{3}$$

This is in contrast with the definition of engineering strain that references the change in length, Δl, divided by the original length, l_0, or

$$e = \frac{\Delta l}{l_0} \tag{4}$$

After the onset of localization, the determination of the true strain in the necked region becomes more complex and requires measurement of the local neck geometry.

The TC128B engineering test results are compared to the converted true stress and true strain data in Figure 56. The true stress curves from the tests do not include a correction for the necking behavior. As a result, they are only valid up to the onset of necking at a true strain of approximately 15%. The actual true-stress and true strain curves for the material continue to strain harden throughout the loading if the effects of necking were corrected. An extrapolated true stress curve that corrects for the effects of the necking behavior is added to Figure 56 (solid black line). It is this extrapolated curve that is used in the material constitutive model.
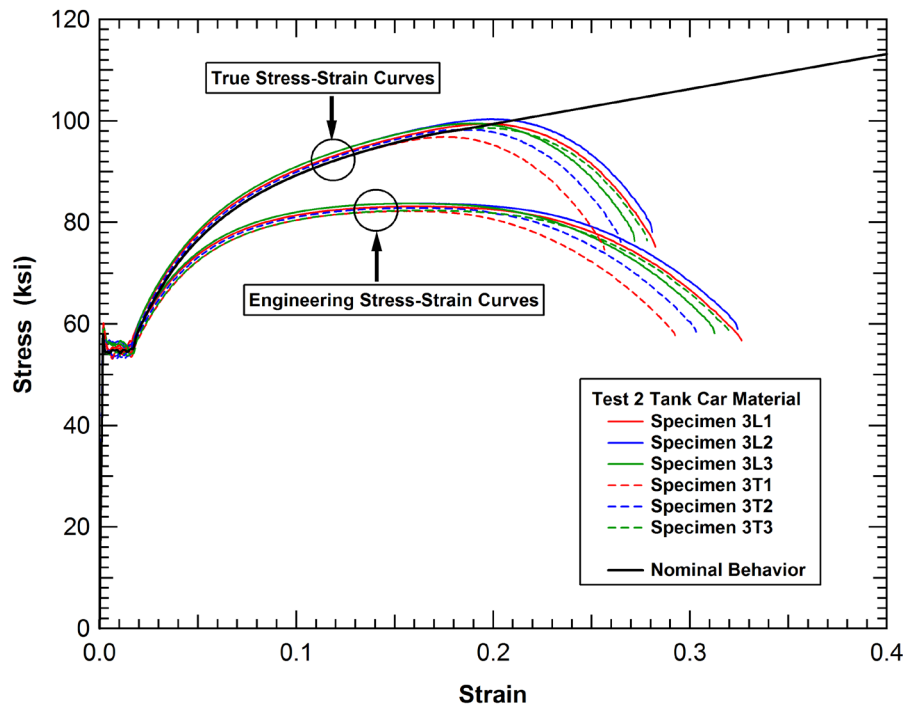
Figure 56. Comparison of engineering and true stress-strain data for TC128B.

The final step in obtaining the tabular stress-strain parameters for the TC128B constitutive model was to fit a smooth set of points to the extrapolated true-stress data. This final tabular fit for the TC128B is shown in the true stress versus plastic strain curve in Figure 57. The specific values for the tabular stress-strain curve are also listed in Table 2. As a validation that this curve accurately captures the true stress-strain behavior of the material, a tensile specimen model was generated and the constitutive parameters were applied to simulate the tensile test response. The calculation was analyzed to determine the engineering stress-strain behavior consistent to the tests (e.g. using equivalent gauge section length). A plot of the calculated engineering behavior compared to the test data is shown in Figure 58. The data shows that the constitutive parameters accurately reproduce the material behaviors including the onset and development of necking in the specimen.
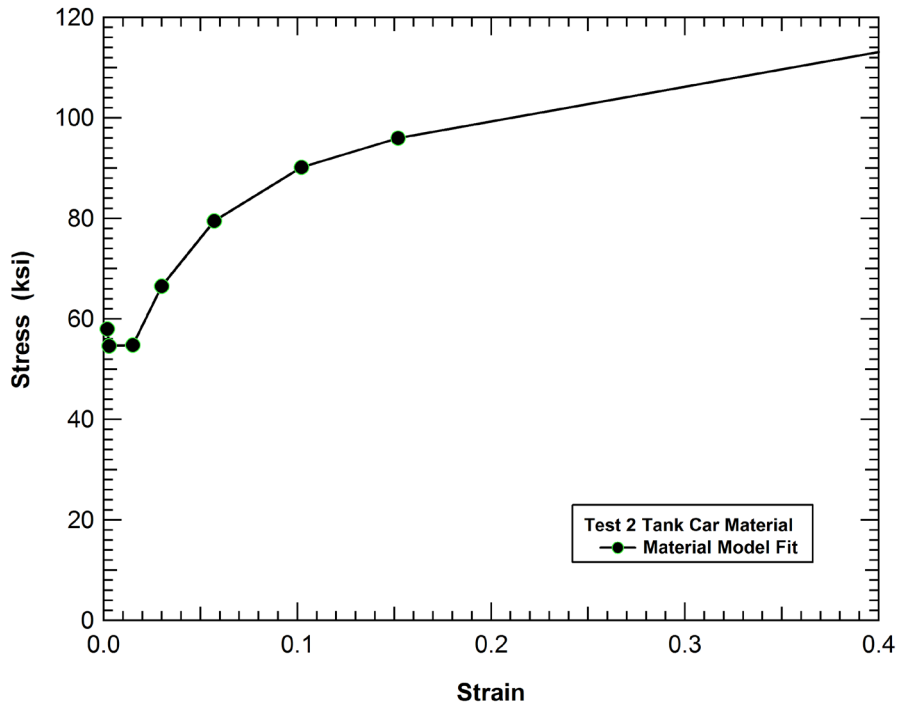
Figure 57. Tabular true stress curve developed for the TC128B constitutive model.
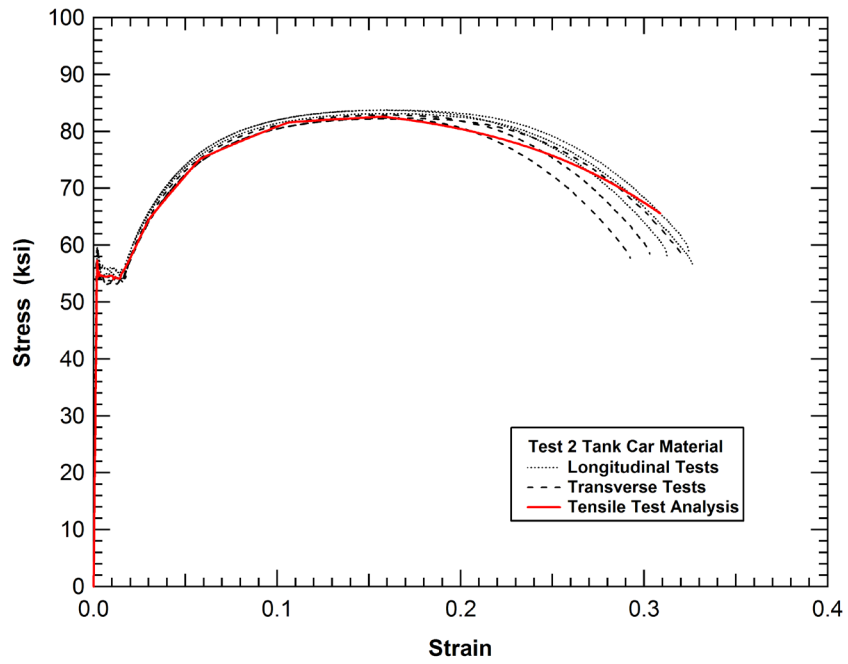
Figure 58. Comparison of the measured and calculated TC128B tensile test.

Table 2. Tabular TC128B stress-strain curve values

Point No.	Plastic Strain (in/in)	True Stress (ksi)
1	0.00e+00	58.0
2	8.22e-04	54.6
3	1.30e-02	54.8
4	2.76e-02	66.5
5	5.41e-02	79.5
6	9.87e-02	90.2
7	1.49e-01	96.0
8	1.15e+00	165.0

3.2.2 Strain Rate Effects

Elevated strain rates can influence the strength and ductility of structural materials. For most rail crashworthiness applications, these strain rate effects are small compared to the effects of the baseline (static) strength and failure modeling. In addition, strain rate effects can have very different trends on different material characteristics such as yield stress and failure strain. This makes inclusion of rate effects more difficult for problems including material failure, such as a tank puncture analysis. The rate effects for TC128B were investigated to assess the potential magnitude of the effects on tank car impact and puncture behaviors. The final result was that strain rate effects on tank car puncture conditions were small and not included in the analyses described in this report. However, the assessment of strain rate effects is provided here for completeness.

An example of high rate testing to establish the rate effects on yield stress for structural steels is shown in Figure 59 [35]. The effects were relatively small for strain rates from below 10^{-2} to approximately 10^3 per second. For the tank car impact analyses the strain rates were expected to be on the order of 10 per second and the associated rate effects were expected to be small.

A series of tests was performed on TC128B as a part of a separate research program [36] and the data was subsequently reevaluated for the NGRTC program [37]. The rate effects on the TC128B yield and ultimate stress are shown in Figure 60. The data spans stain rates from below 10^{-2} to approximately 10 per second. The data shows a much stronger effect of strain rates than observed for other structural steels.
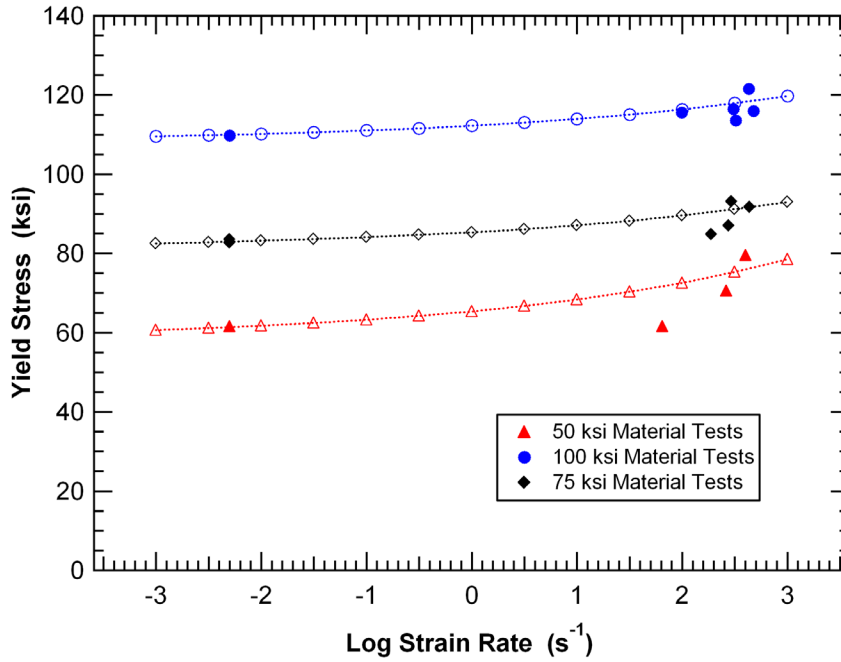
Figure 59. Example strain rate effects data for structural steels.
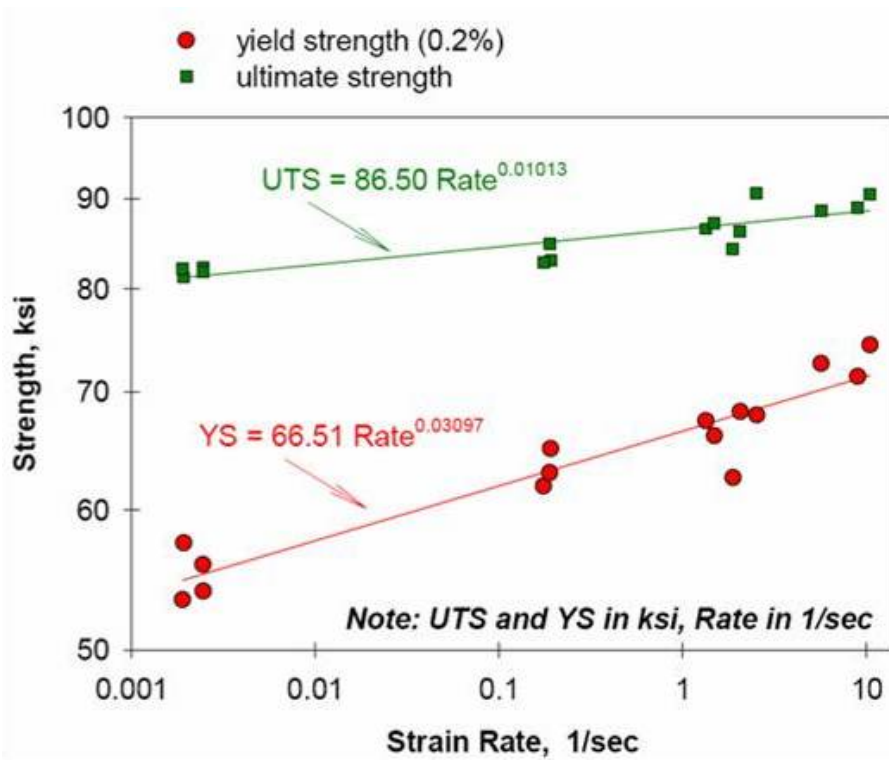
Figure 60. Evaluation of TC128B strain rate effects data [37].

The strain-rate effects on the yield strength were included in the constitutive model for the preliminary tank car analyses with the Cowper-Symonds rate effect model [38]. The functional form for the rate effects on strength is governed by the equation:

$$\sigma_y(\dot{\varepsilon}) = \sigma_y \left[1 + \left(\frac{\dot{\varepsilon}}{C} \right)^{1/p} \right] \tag{5}$$

where σ_y is the yield strength, $\dot{\varepsilon}$ is the strain rate, and C and p are the Cowper-Symonds parameters.

The Cowper-Symonds rate effects parameters, from Equation (5), were fit to the TC128B data for rates between 10^{-1} to approximately 10 per second. The value fit to the parameters C and p were 4000 and 5, respectively. The comparison of the model fit to the rate effects test data is shown in Figure 61. In the figure, the black line is the fit using the Cowper-Symonds model, while the corresponding red line is a fit to the experimental data. The comparison shows that the Cowper-Symonds model is capable of modeling the rate effects for only a limited range of data and would over predict the strength of the material at both higher and lower rates. Preliminary analyses using this model calculates tank and head impact behaviors that were overly stiff and as a result, this model was abandoned.
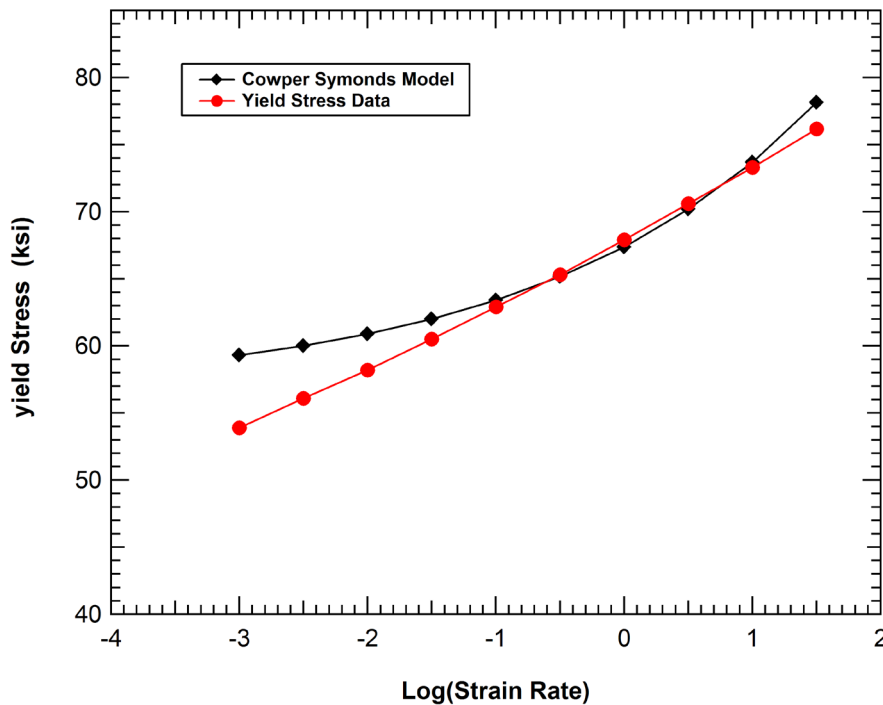
Figure 61. Yield stress rate effects data and Cowper-Symonds model fit.

The data at various strain rates on specimens cut from two different TC128B plates are shown in Figure 62. The comparison of the stress-strain curves show that the data is more complex than would be captured by most simple rate effects models. The rate effects are observable in the initial yield or ultimate stress but are much smaller in different sections of the curves. In addition, the high rate tests have a lower ductility that would not be captured in the models. Overall, the strain energy dissipation capacity (area under the curves) appears to be nearly identical at all of the measured rates.

As a result of the limitations of the Cowper-Symonds model for this application, a new rate-effects model was added to the user-defined constitutive model. This new model scales the yield stress by the ratio of the strain rate to a reference rate to a power specified by an input parameter according to the equation:

$$\sigma_y(\dot{\varepsilon}) = \sigma_y \left(\frac{\dot{\varepsilon}}{\dot{\varepsilon}_{ref}} \right)^C \tag{6}$$

This approach will allow for a simple fit to the data over the full range of rates as shown in Figure 60. However, it cannot reproduce the effects such as the different slopes of the rate effects in the yield and ultimate behaviors or the loss in ductility at high rates. As a result, the rate effects were not included in most of the subsequent tank car impact analyses.
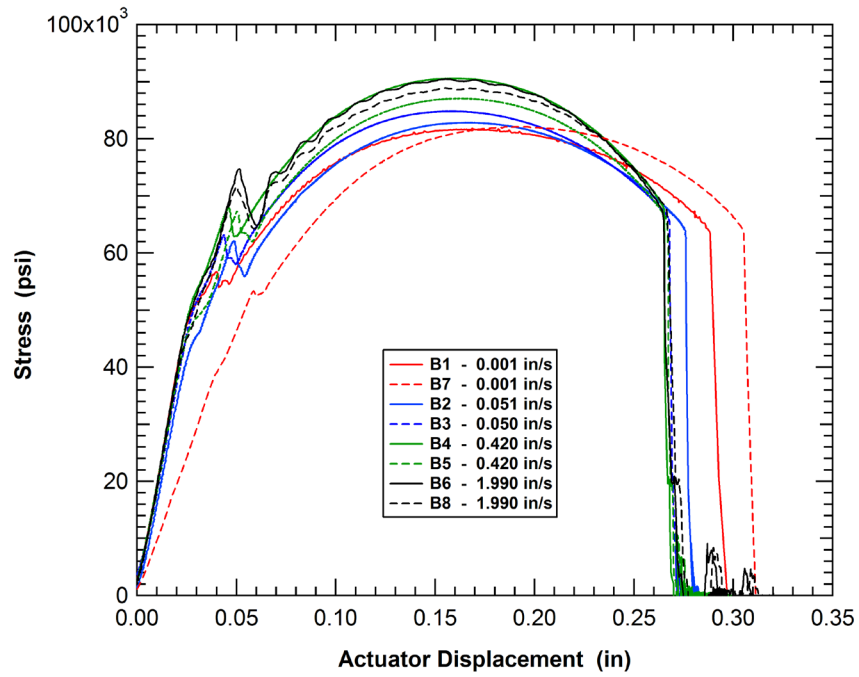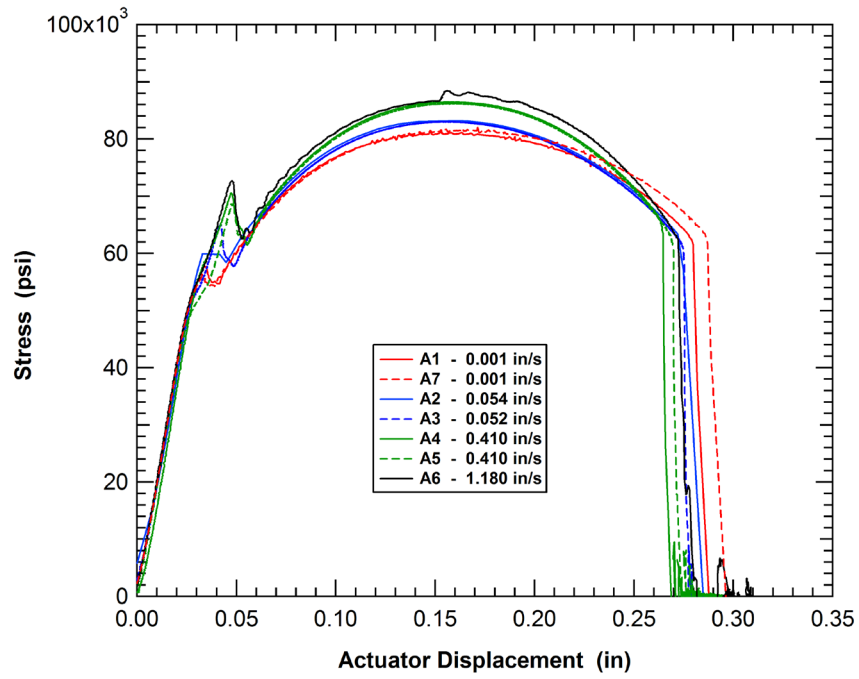
Figure 62. Measured TC128B tensile stress-strain curves at various strain rates.

3.2.3 Properties of Other Tank Car Materials

In addition to TC128B, a range of other structural steels are currently used in tank car designs or proposed for use in future designs. These range from low strength A1011 steel, currently used as a tank car jacket material, to HSLA 90XF steel, proposed as a candidate material for protection structures in future tank car designs. The true stress-strain curves used in the constitutive models for these materials are shown in Figure 63. The approach used to develop constitutive models for these materials was identical to that described for the TC128B above. However, the failure behaviors of these alternative materials were not all characterized as thoroughly as for TC128B. This detailed characterization of the failure behavior for TC128B is described in the following sections of this report.
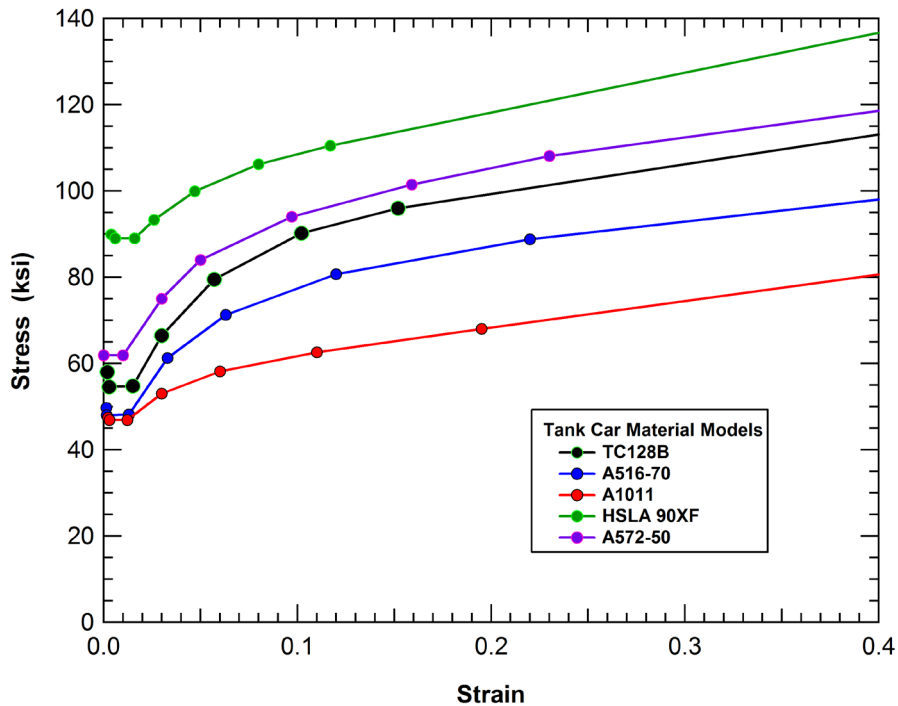
Figure 63. Tabular true stress curve developed for the various tank car steels.

3.3 Bao-Wierzbicki Failure Surface

Accurate prediction of the puncture energies of tank cars for various impact conditions requires the addition of a detailed damage and failure assessment capability to the material model. These damage mechanics, or so-called local fracture mechanics approaches (LFM), provide enhanced capabilities for tank car design and puncture assessment. LFM models the microstructural deformation and failure processes leading to fracture in terms of continuum parameters averaged over a small volume of material [39-46]. In contrast to classical linear elastic and elastic-plastic

fracture mechanics (LEFM and EPFM, respectively), which characterize fracture in terms of the boundary conditions of the fracture process zone while ignoring the details of the processes occurring in that zone, LFM focuses on the evolution of the process zone itself. Although LFM may initially seem more complex to formulate and more difficult to apply than LEFM/EPFM, it is more versatile and more general than the latter approaches. LFM is also ideally suited to implementation into finite element analyses where damage can be evaluated at the local element level.

The key mechanism that needs to be included in the ductile local fracture model for tank car puncture analyses is the influence of the stress state on the rate of damage development as the material is undergoing plastic deformation. The primary stress state factor that controls the rate of damage development is the stress triaxiality, defined as the ratio of the mean stress to the equivalent stress ($\sigma_{mean}/\sigma_{eq}$). The mean stress (or hydrostatic stress) is the average of the three principal stresses (stresses on 3 orthogonal axes perpendicular to the principal planes upon which no shear stress exists). The equivalent stress, also referred to as the effective stress or the Von Mises stress is defined as

$$\sigma_{eq} = \frac{1}{\sqrt{2}}\left[\left(\sigma_1 - \sigma_2\right)^2 + \left(\sigma_2 - \sigma_3\right)^2 + \left(\sigma_3 - \sigma_1\right)^2\right]^{1/2} \tag{7}$$

where σ_1, σ_2, and σ_3 are the three principal stresses.

There are many models that include the effects of stress triaxiality on damage development and ductility. Several of these have previously been applied within LS-DYNA to analyze various ductile fracture problems [e.g. 47-49] including the use of the Gurson-Tvergaard model [50-52] for the puncture assessment of pressure tank cars [53]. These models have the ability to include the stress triaxiality effects on ductility for tensile loading as illustrated in Figure 64. The deficiency with many of these previous local damage models is that they do not include the changes in damage development and failure for low triaxiality where the tensile damage and failure behavior transitions into a shear dominated fracture behavior. The concern that shear fracture behavior is important for tank car puncture assessment led to the selection of the Bao-Wierzbicki (BW) model in this effort.
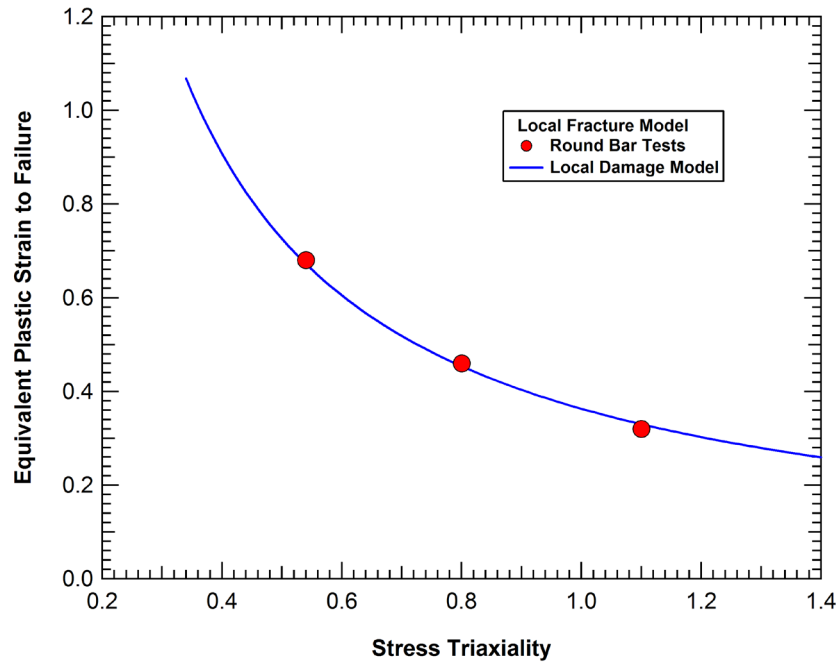
Figure 64. Local damage criterion for tensile ductile fracture analyses.

As implemented, the BW model is a basic form of a ductile fracture criterion [43]. It assumes that failure at a material location occurs when the damage within a surrounding characteristic volume (V_{MIC}) exceeds a critical value. The damage development and failure criterion can be written in the form

$$D = \int \frac{d\varepsilon_{eq}^p}{\varepsilon_c \left(\sigma_{mean}/\sigma_{eq}\right)} = 1 \quad \text{over } V_{MIC} \tag{8}$$

where D is the normalized damage parameter; $d\varepsilon_{eq}^p$ is an increment in equivalent plastic strain; and $\varepsilon_c\left(\sigma_{mean}/\sigma_{eq}\right)$ is the critical failure strain as a function of the stress triaxiality. The characteristic volume (V_{MIC}) in this application is the element size which was maintained with a characteristic element length of approximately 0.040 inch (1 mm) in the fracture zone. Damage accumulation occurs with plastic deformations and the damage is tracked locally in each element in the model. When the damage level in any element exceeds the failure criterion (D=1), the local failure is propagated in the model by element erosion.

The critical strain function is that proposed in the BW criterion and contains multiple branches depending on the range of stress state as shown in Figure 65. The critical strain in each branch are governed by the equation

$$\varepsilon_c\left(\sigma_{mean}/\sigma_{eq}\right)=\begin{cases}\infty & \left(\sigma_{mean}/\sigma_{eq}\right)\leq-\dfrac{1}{3}\\[2mm]\dfrac{A}{1+3\left(\sigma_{mean}/\sigma_{eq}\right)} & -\dfrac{1}{3}\leq\left(\sigma_{mean}/\sigma_{eq}\right)\leq0\\[2mm]9(B-A)\left[\left(\sigma_{mean}/\sigma_{eq}\right)\right]^2+A & 0\leq\left(\sigma_{mean}/\sigma_{eq}\right)\leq\dfrac{1}{3}\\[2mm]\dfrac{B}{3\left(\sigma_{mean}/\sigma_{eq}\right)} & \dfrac{1}{3}\leq\left(\sigma_{mean}/\sigma_{eq}\right)\end{cases} \qquad (9)$$

And the parameters *A* and *B* can be determined by a series of tests under different stress conditions including notched tensile tests with specimens of varying notch radii [54] and tensile-shear tests with different ratios of tension to shear stress.
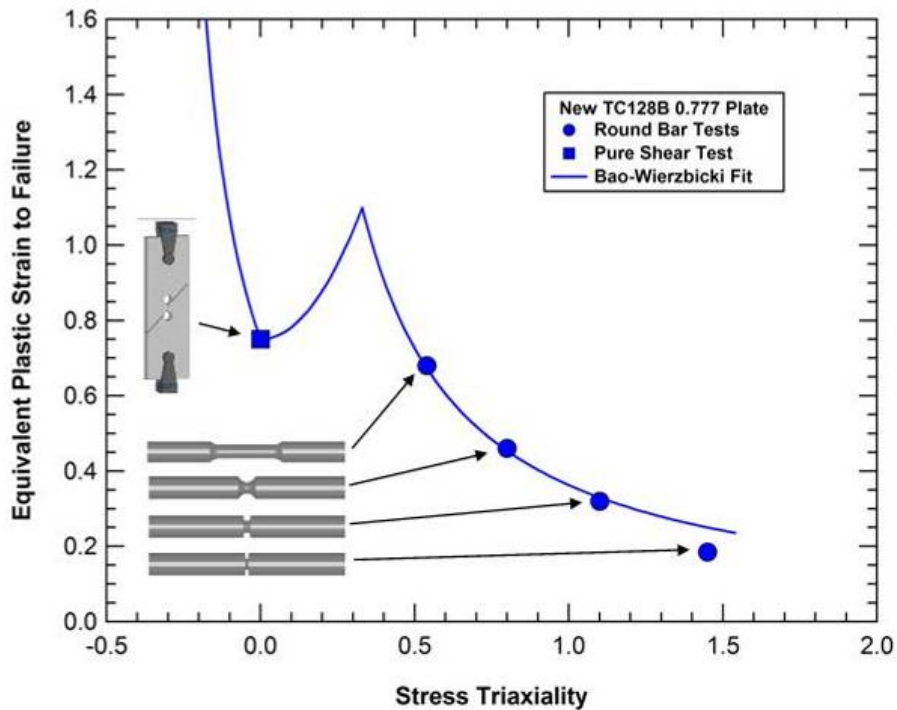
Figure 65. Bao-Wierzbicki failure surface and tests used for model calibration.

3.4   Material Characterization Testing and Analyses

A wide variety of material characterization tests were performed to calibrate and validate the material constitutive and failure models. These include material tests such as standard tensile testing to assess the material stress-strain behavior and testing under various stress states (notched tensile or tensile-shear tests) to obtain the characteristics of the failure surface. Subsequent tests under more general loading conditions, such as the punch test configuration, are

used to validate the models. The approach applied here is to perform detailed analyses all of the material testing conditions to assess the accuracy and validity of the models. The comparisons for the different testing conditions are provided in the following sections of this report.

3.4.1 Tensile Tests and Analyses

Standard tensile test methods were employed in accordance with ASTM E8 [27]. The thick TC128B allowed fabrication of a round tensile specimen (diameter of 0.505-inch). For all other materials a flat specimen, as shown in Figure 66, was utilized. The specimen had a gage length of 2-inch. No machining was performed in the thickness direction and it was tested as received.

Photographs of the TC128B round bar specimens that were tested are provided in Figure 67. An extensometer with a 2-inch gage length was mounted on the specimen during testing. In one case, the thickest TC128B condition, strain gages were also mounted (2 gages, oriented opposite of each other) on the specimen gage length. Due to the excellent agreement between the strain gage and extensometer results, strain gages were omitted in all subsequent testing.
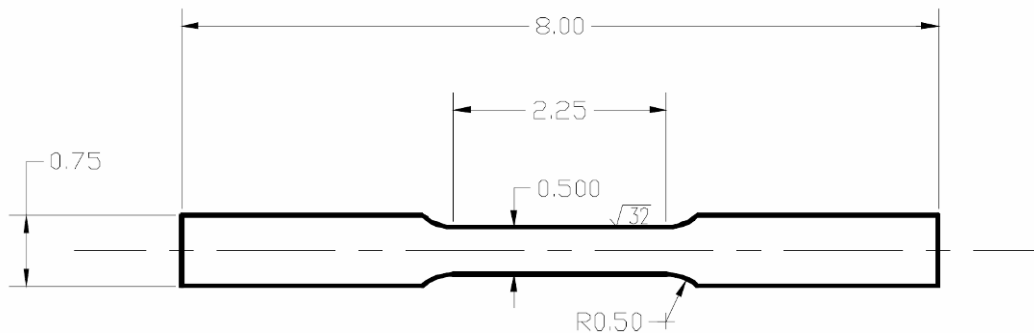
Figure 66. Dimensions of the specimen used in tensile testing.

Figure 67. Necking behavior observed in the TC128B round bar specimens.

All tests were performed in constant-rate displacement control. Two rates were used, either 0.035 or 0.050 inch/minute. Due to the large elongation observed in all of the steel materials, typical test times ranged from 15-30 minutes under the constant displacement testing. The data acquisition system was configured to record data at 3 Hz.

To confirm that the tensile test data reduction and material constitutive parameter extraction process was performed correctly, a model of the tensile specimen was generated and the tensile test was simulated using the constitutive model. The load and displacements were extracted from the analysis using consistent methodologies to the test. A comparison of the measured and calculated engineering stress-strain behaviors for TC128B is shown in Figure 68. The comparison shows that the model accurately reproduces the stress-strain behavior and captures the initialization of the necking response.

Similar comparisons were made for all of the materials characterized in this program. Examples of the A1011 jacket material and A516-70 are shown in Figure 69 and Figure 70, respectively.
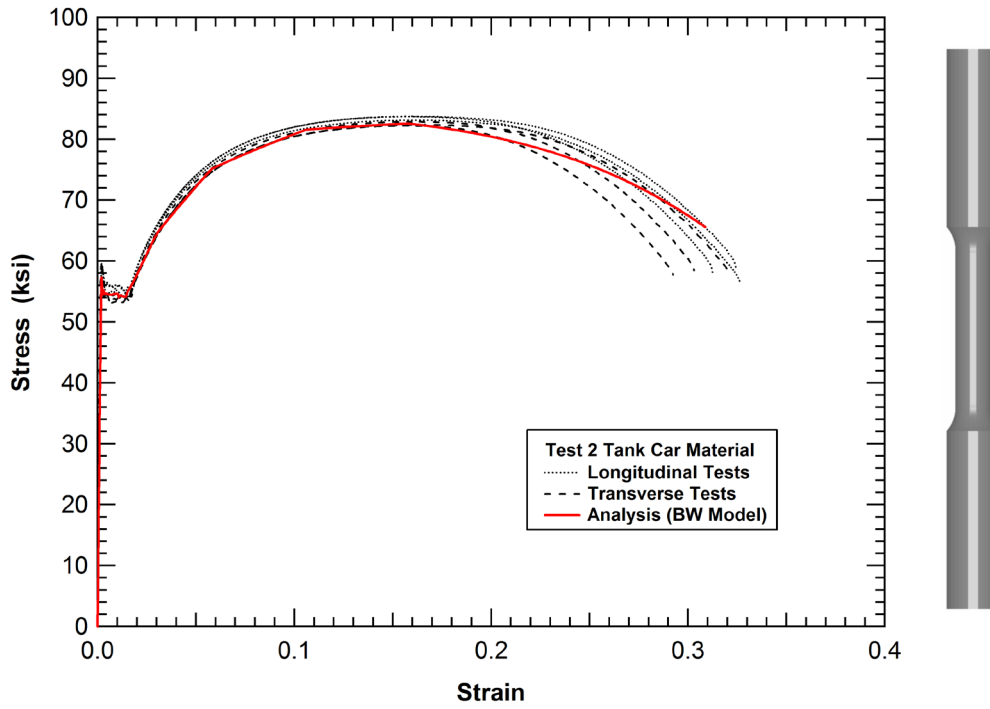
Figure 68. Validation of the tensile test behavior for TC128B.
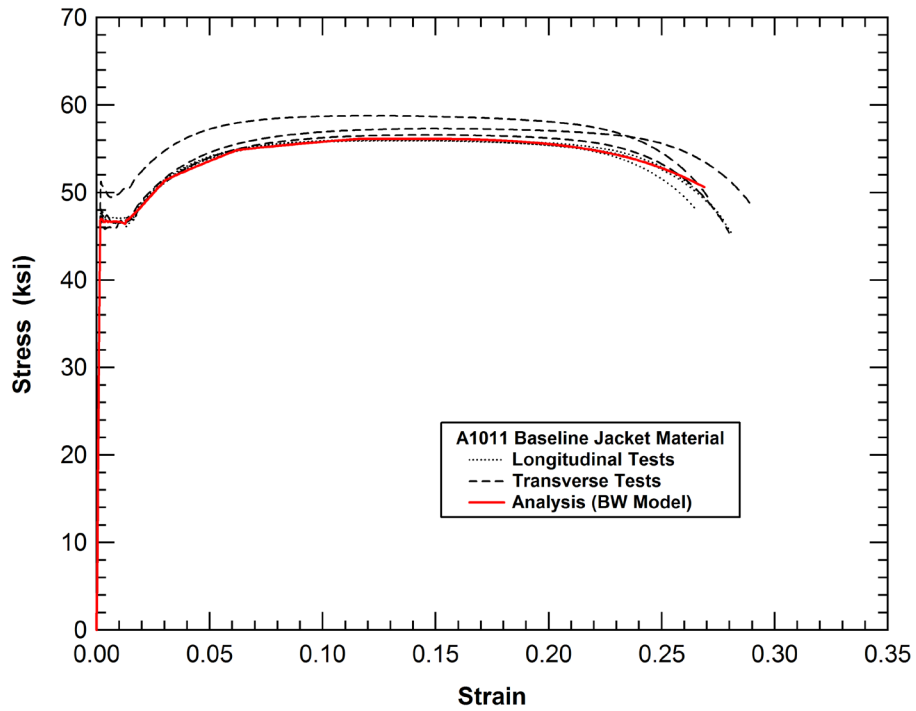
Figure 69. Validation of the tensile test behavior for A1011.
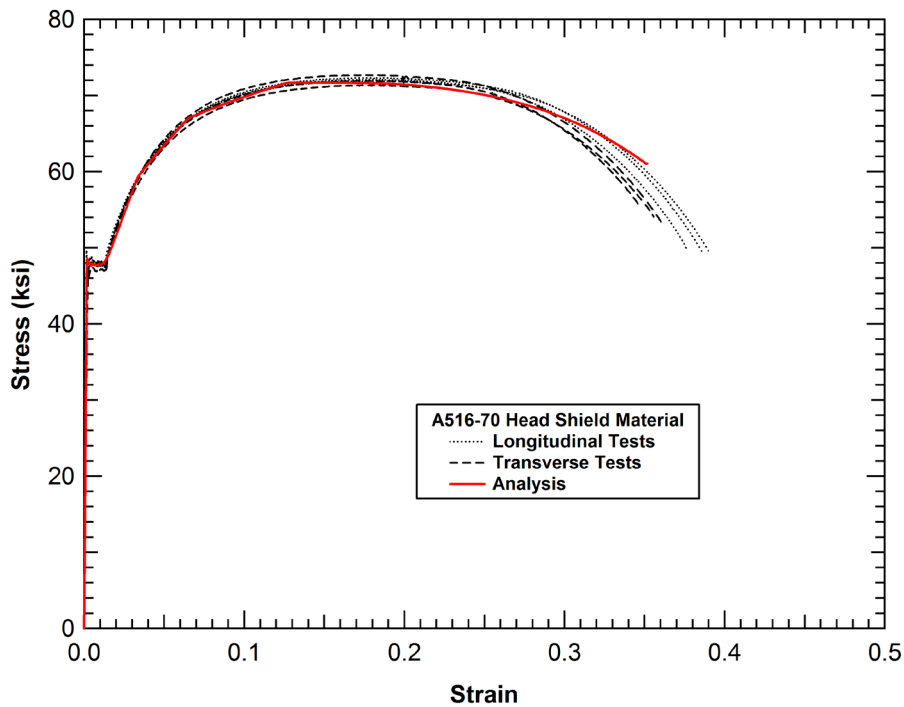
Figure 70. Validation of the tensile test behavior for A516-70.

3.4.2 Notched Round Bar Tensile Tests and Analyses

The notched round bar tensile tests were used to assess the performance of the BW failure model in the high stress triaxiality regime. The tests were performed using round bars with various notch radii [29] to achieve different levels of confinement at the notch root and thus different stress triaxiality levels. Models were created for the different notched round bar specimens and the tests were simulated.

Material was provided from the two full-scale tank shell test articles (Tests 1 and 2) in the form of 12x12-inch plates. These plates were taken from near the impact site and were fabricated from normalized TC128B with a thickness of 0.777-inch. Specimens were extracted from these plates for mechanical testing. All specimens were oriented in the transverse orientation relative to the original plate rolling direction. The transverse orientation of the plate used to fabricate a tank car ring segment corresponds to the axial direction of the tank.

The notched tensile testing was performed similar to the procedures of the conventional tensile test standard, ASTM E8. The inner net diameter of the notched specimen is 0.25-inch and the gross outer diameter is 0.5-inch. The three different notch geometries, with radii of 0.25, 0.10 and 0.05-inches, were all gripped in smooth clamping friction grips. A photograph of the test setup is shown in Figure 71.
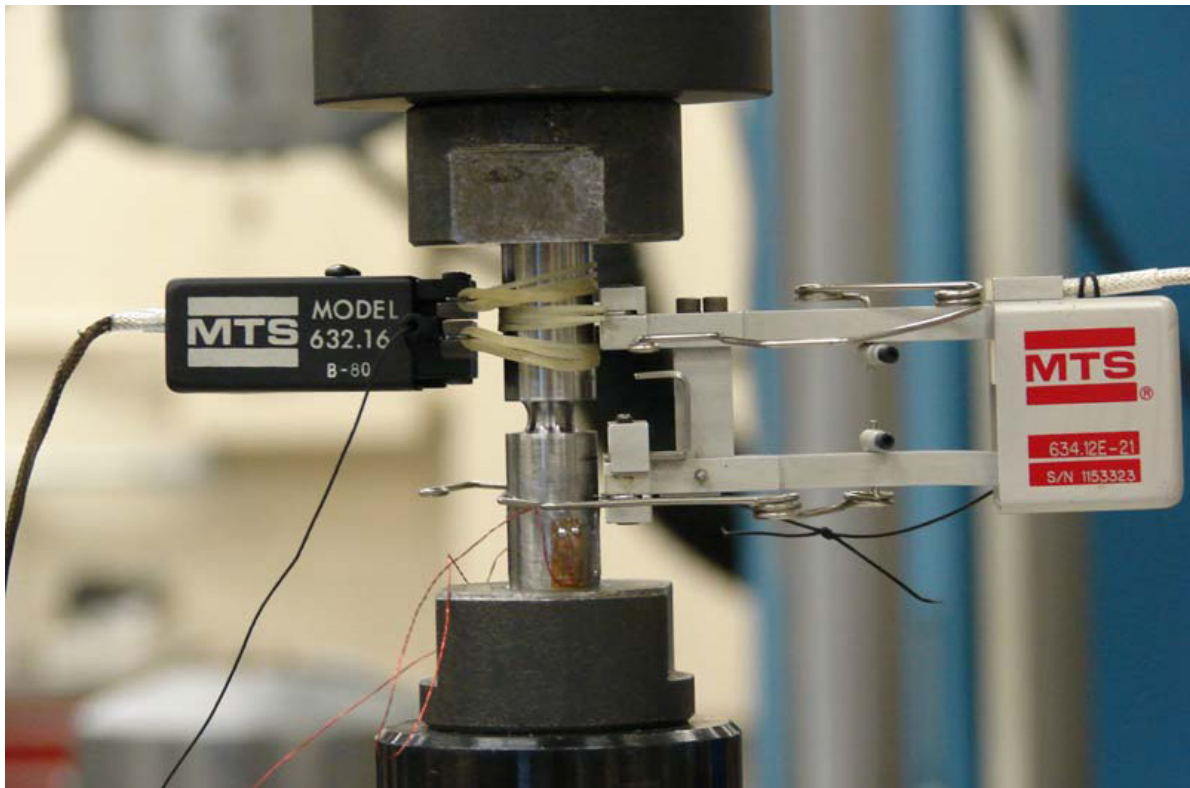
Figure 71. Test setup for the TC128B notched round bar specimens.

A comparison of the calculated and measured stress-strain behavior across the notch for the three different radii specimens is shown in Figure 72. The comparison shows that the constitutive and damage model were capable of reproducing both the increase in stress level and reduction in ductility that occur as the notch radius is reduced. The BW failure parameters used provide a good correlation to the observed failures of the specimens.
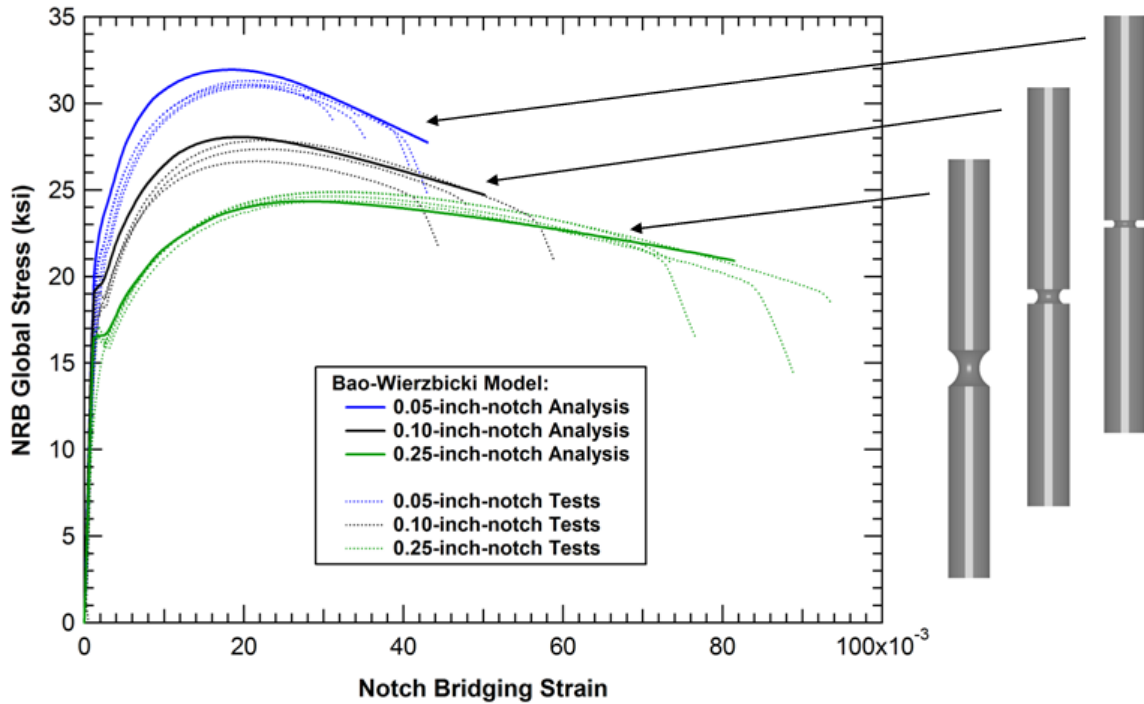
Figure 72. Validation of the notched round bar test behavior for TC128B.

3.4.3 Tensile-Shear Tests and Analyses

The combined tensile-shear tests were used to assess the performance of the BW failure model in the low stress triaxiality regime (stress triaxiality between 0 and 1/3). The tests were performed using a modified Arcan specimen [55] to achieve different ratios of tensile and shear by rotating the orientation of the gauge section relative to the loading axis, as shown in Figure 73. A photograph of the test setup is shown in Figure 74. Instrumentation includes clip gauges across both of the slots separating the upper and lower specimen sections, a string potentiometer to measure the displacement along the load path, the load ram LVDT, and the load cell. The tests were performed in a displacement control mode at a rate of 0.002 inch per second and data was collected at 5 Hz.

Simulations of the specimen geometry were initially performed to assess that a relatively uniform stress state could be achieved in the specimen gauge section, as shown in Figure 75. Models were then created for each of the specimens with different gauge section orientations and the tests were simulated. A comparison of the calculated and measured load-displacement behaviors are shown in Figure 76. The comparison shows again that the constitutive and damage model were capable of reproducing both the decrease in load level and increase in displacement

that occur as the orientation was rotated from pure tension to pure shear. The BW failure parameters used provide a good correlation to the observed failures of the specimens.
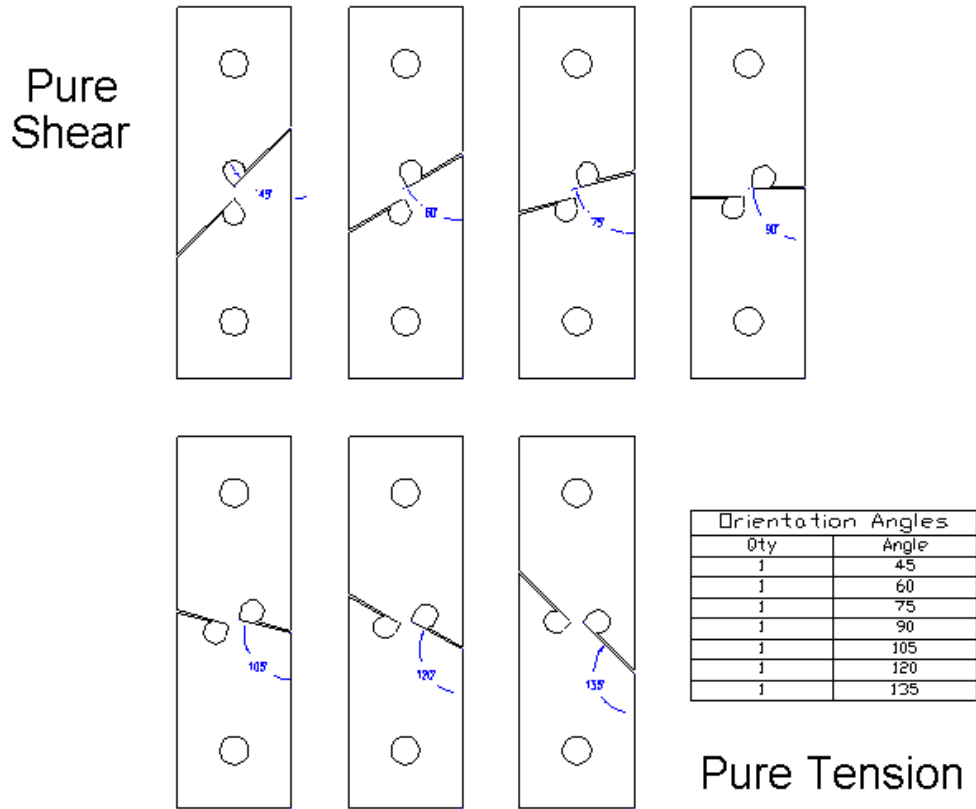
Figure 73. Specimen geometries for the combined tensile shear tests.
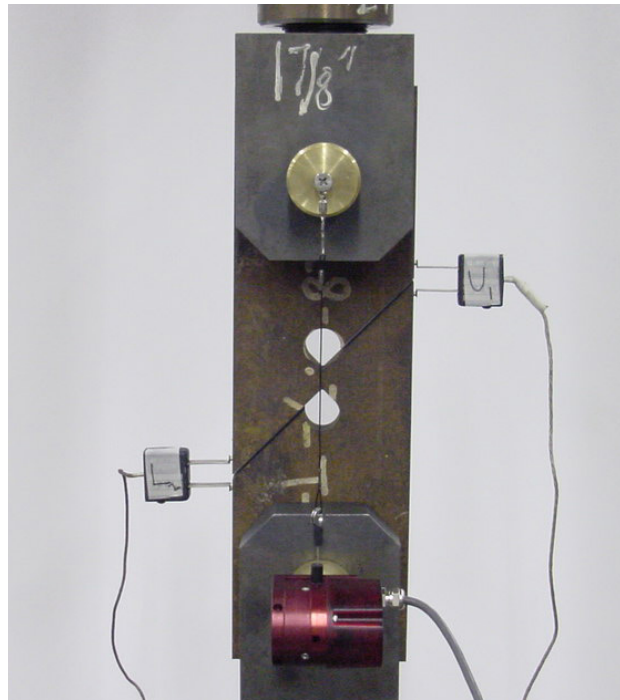
Figure 74. Photograph of the combined tensile shear test configuration.
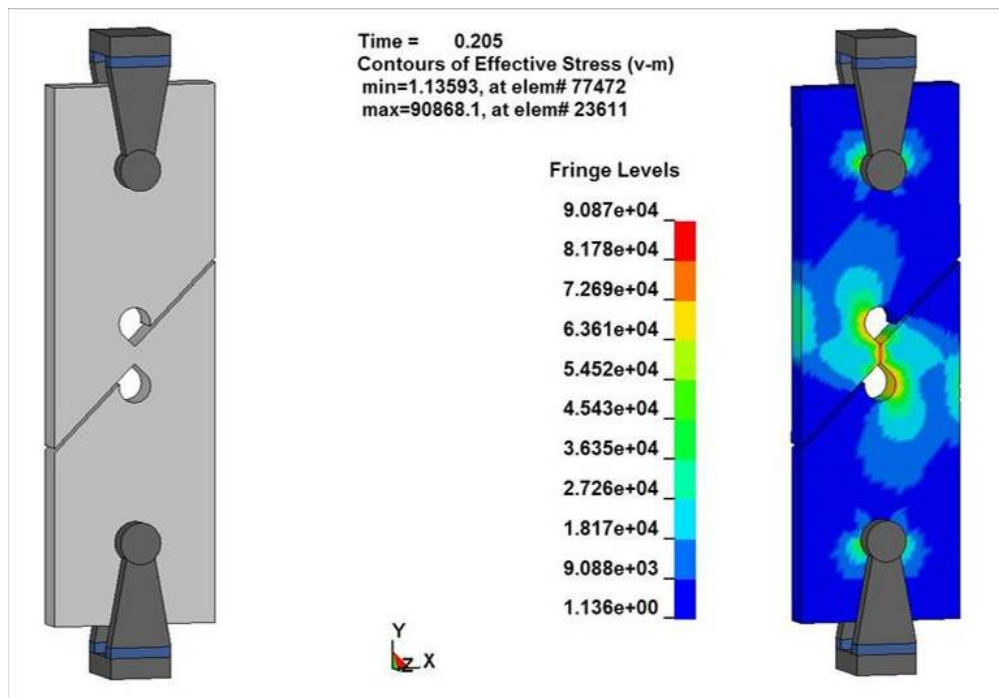
Figure 75. Analysis of the specimen behavior in the pure shear orientation.
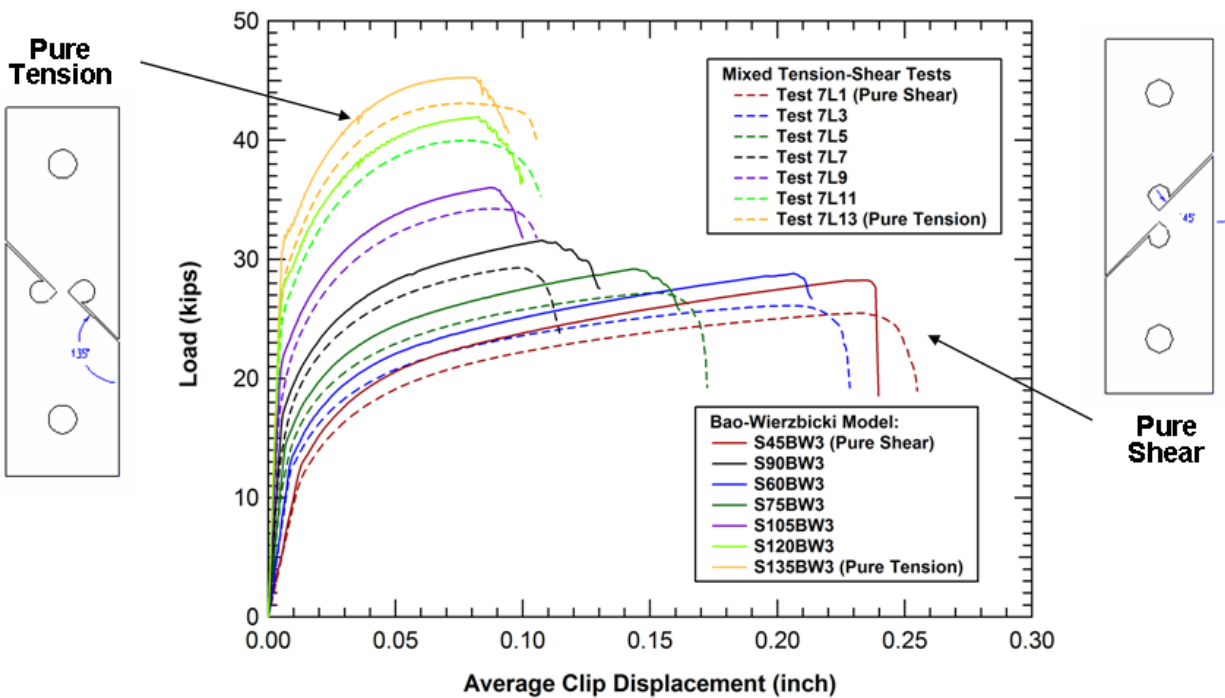
Figure 76. Validation of the combined tensile shear test behavior for TC128B.

3.4.4 Punch Tests and Analyses

The above notched round bar and tensile shear tests provide a good set of data to validate that the BW failure model can predict the damage development and failure of the TC128B material for a wide range of stress states. However, these tests were used to assess the failure parameters *A* and *B* in Equation 9. Therefore, an independent punch test was developed and applied to validate that the model could predict the failure of the material under a more general loading condition.

The specialized puncture fixture was developed for the NGRTC program at the SwRI Materials Test Lab and installed in a 220-kip test machine as shown in Figure 77. The punch test fixtures are shown with the 1.5-inch diameter punch and the 3-inch diameter receiving hole bore (so-called man hole cover). The fixture was designed so that different punch sizes and different man hole cover diameters can be used.

The punches were fabricated from hardened bar stock material. The punch contact face was flat with a 0.30-inch radius around the perimeter. Punches were fabricated with diameters of 1.0, 1.5, 2.0 and 3.0 inches. The dimensions of the 2.0-inch-diameter punch are shown in Figure 78. Man hole covers were fabricated with hole diameters of 2.0, 2.5, 3.0, 3.5, 4.5, and 5.5 inches

according to the dimensions shown in Figure 79. As a result, the punch test fixture was
applicable for evaluating the behavior of multiple materials and structural components [32-34].

Figure 77. Simulation of the punch test on the thin TC128B plate material.
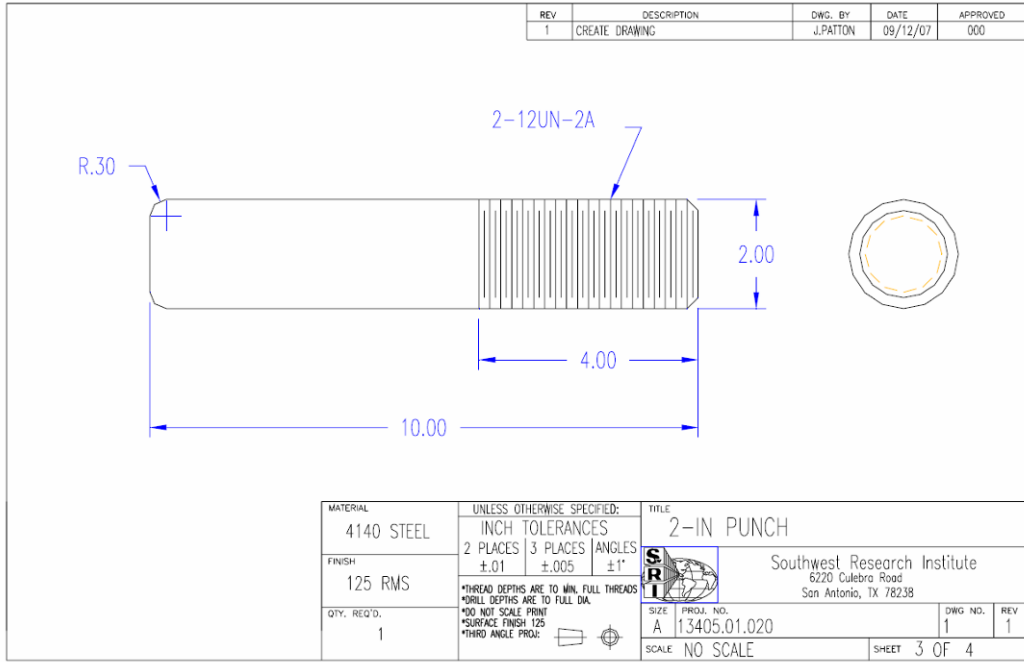
Figure 78. Dimensions of the 2-inch-diameter punch.
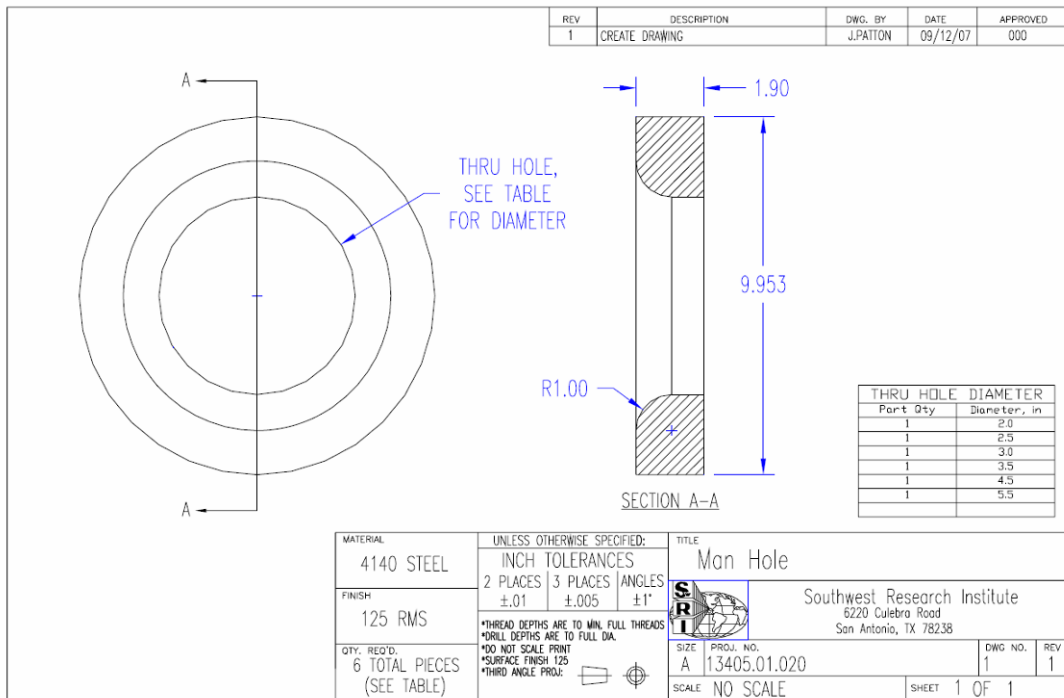
Figure 79. Dimensions of the man hole cover support plates.

During testing, the actuator (actually, the punch frame) displacement was measured with a remote LVDT mounted on the actuator. Three string pots were attached to the backside (opposite the punch) surface of the test specimen. These three string pots were all in a line with the middle location in the center of the punch and the two outer locations at the circumferential periphery of the punch. This provided additional measurements of the backside deformation opposite the punch on the front of the panel. Load was also measured from the load cell on the servohydraulic test frame. Tests were performed in displacement control at an applied rate of 1 inch/minute. The multiple data channels were recorded with a custom data acquisition system operating at 10 Hz. This typically provided total data files of anywhere from 500-2000 points.

The test series used for the validation of the TC128B constitutive and failure model was performed on 0.488-inch-thick plate specimens with various combinations of ram and man hole diameters [32]. The three tests performed used the 1.0, 1.5, and 2.0-inch diameter punches in combination with the 2.5, 3.0, and 3.5-inch diameter man hole covers, respectively. Photographs of the specimen failure behavior in these punch tests are shown in Figure 80. In all cases, the punch test sheared out a plug of material with a diameter approximately equal to the punch diameter.
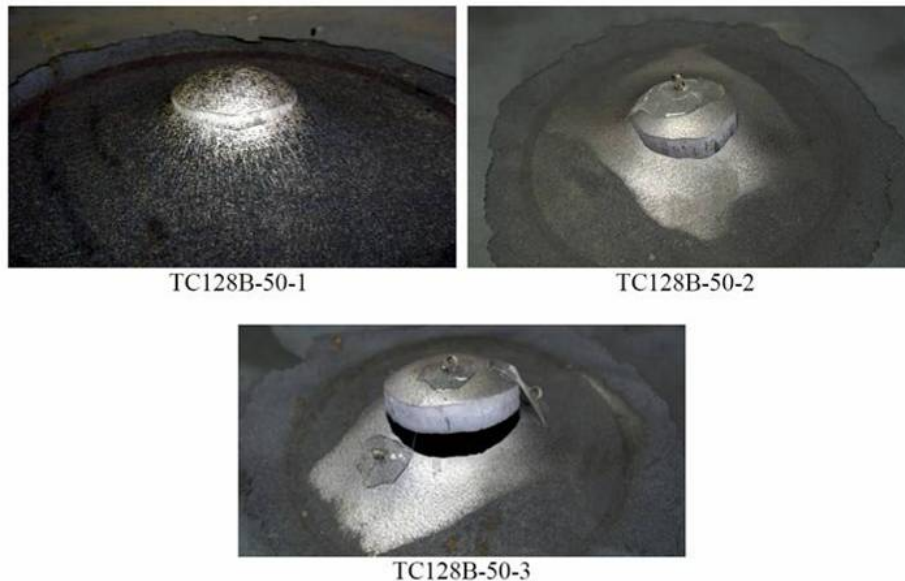
Figure 80. Punch test failure mode for the thin TC128B plate material.

An example of a model and simulation of a punch test on a 0.488-inch-thick TC128B plate is shown in Figure 81. The corresponding comparison of measured and calculated punch force-displacement curves for a series of three different tests on the TC128B plate is provided in Figure 82. In addition to the force-deflection curve the final profile of the plate specimens after

the punch tests were digitized and compared to the analyses. A representative profile comparison is shown in Figure 83.
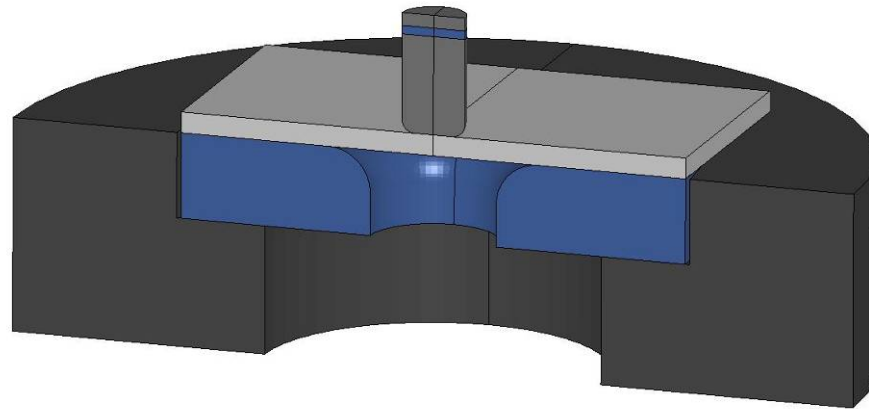
(a) Cross section of punch test geometry
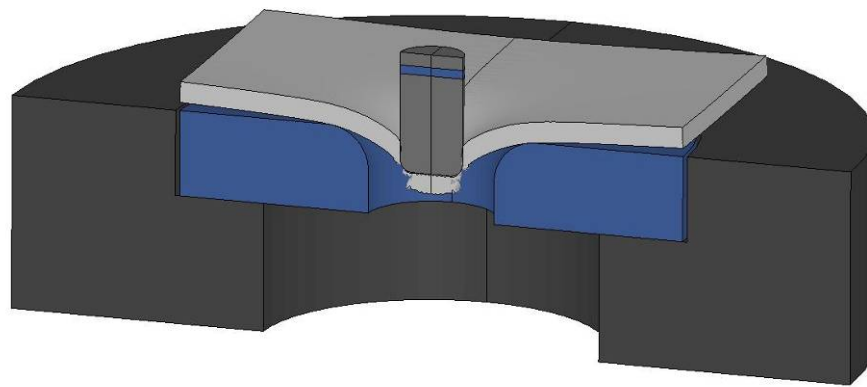
(b) Punch test response
Figure 81. Simulation of the punch test on the thin TC128B plate material.

The agreement of the measured and calculated behaviors for this punch test provides an additional validation that the BW failure model is appropriate for predicting puncture of the tank cars. The application of the failure model for assessing puncture energies for different tank geometries and impact conditions is provided in the following section of this report.
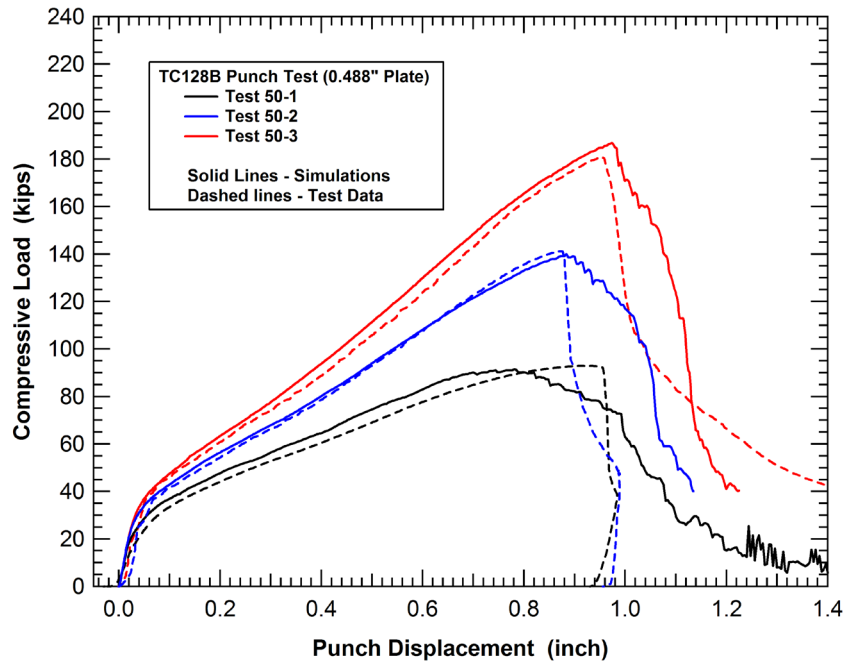
Figure 82. Force-deflection curves for three punch test configurations on TC128B.
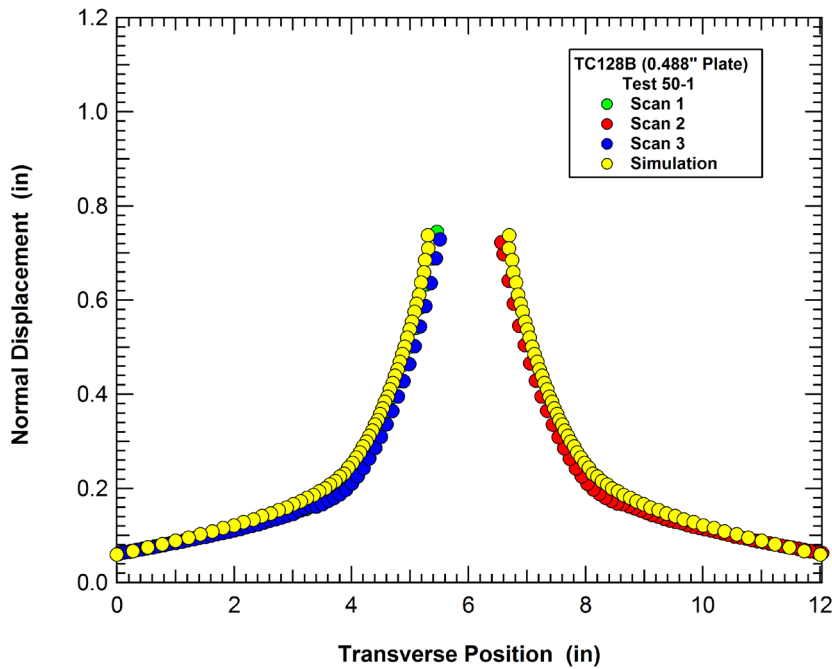
Figure 83. Comparison of the calculated and measured punch test plate profile.

Punch test on 90 XF plate material

In addition to the punch test on the TC128B plate material, the punch test fixture was used to evaluate other material and component configurations. One of these components was a foam sandwich structure proposed as part of a layered foam protection system. The testing and analyses of this foam core panel is described in Section 6.1.1 of this report. An additional punch test series of interest was the comparison of the punch behavior of a single plate and multiple plates of equivalent total thickness.

The two punch tests were performed using the HSLA 90 XF material. The first test was performed on a single 0.37-inch-thick plate and the second test was performed using three stacked 11 gauge sheets (nominally 0.12-inch-thick each) [34]. The comparison of the force-deflection behaviors for the two tests is shown in Figure 84. The initial portion of the loading on the monolithic plate is steeper due to the higher local bending stiffness. However, after approximately 0.1-inch displacement, the remainder of the force-deflection characteristics in the two tests were very similar. The peak puncture load in the monolithic plate was approximately 20 percent higher than that of the three layered 11 gauge sheets.
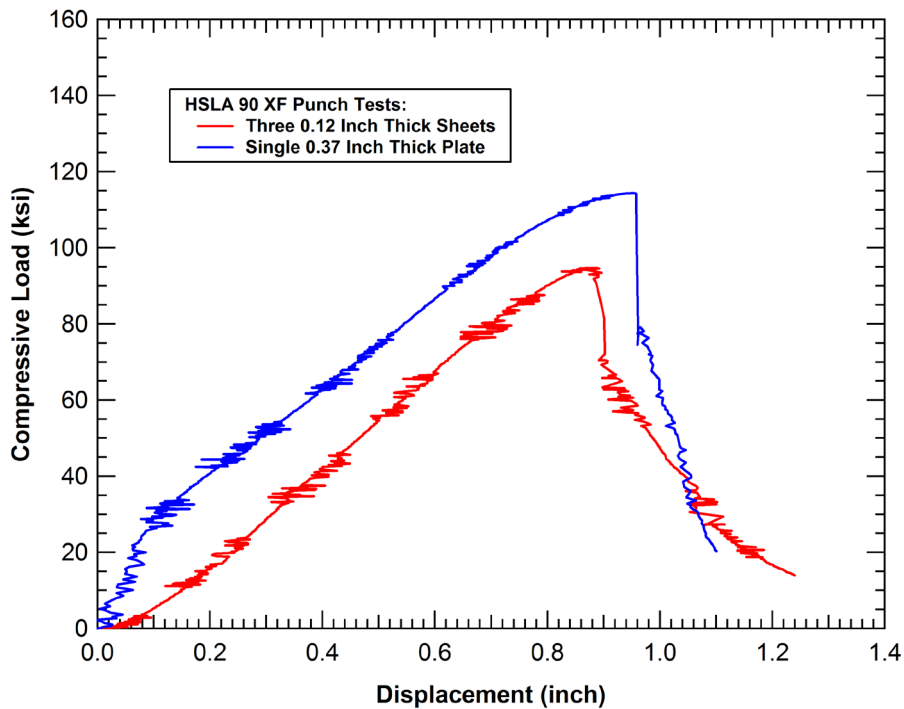
Figure 84. Comparison of the punch loads of the single and layered 90 XF specimens.

Analyses were performed for the two test configurations on the HSLA 90XF material. The material constitutive model included the Bao-Wierzbicki failure criterion applied in the same approach as for the TC128B material. The comparison of the measured and calculated punch test behaviors is shown in Figure 85. Again, the model was capable of predicting the overall characteristic and strength levels measured in the tests.
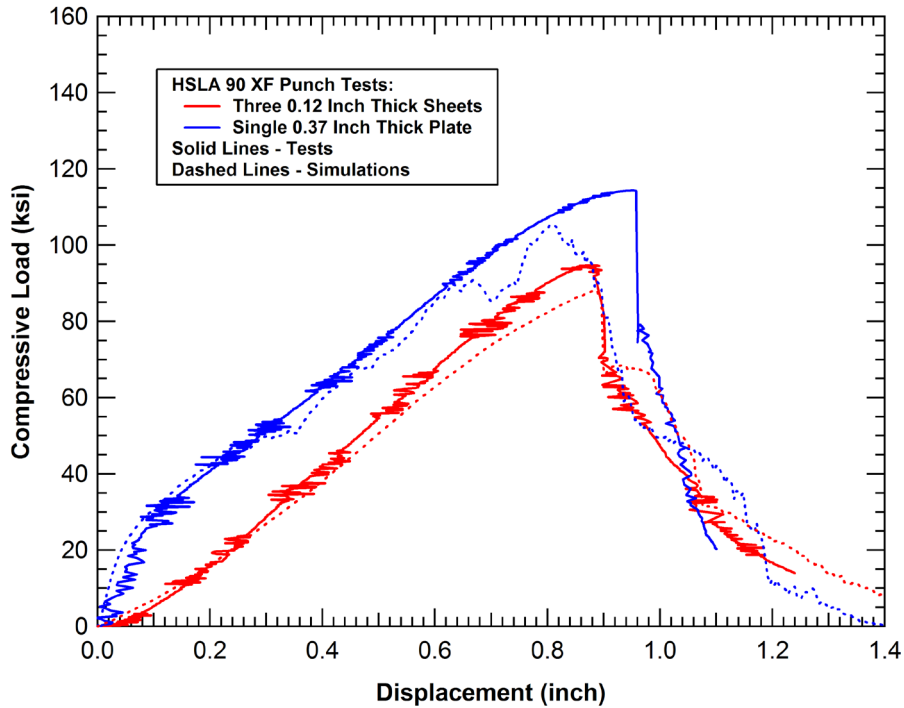
Figure 85. Comparison of the measured and calculated 90 XF punch behavior.

3.4.5 Bulk Fracture Charpy Machine (BFCM) Tests and Analyses

The majority of laboratory material tests used to validate the constitutive and failure models were quasistatic. One set of dynamic tests were performed for a previous research program using the Bulk Fracture Charpy Machine (BFCM) [56-59]. The BFCM facility, shown in Figure 86, consists of a large pendulum impactor retrofit with a heavy striker mass to increase the impact energy capacity needed to rupture the specimens. The BFCM test facility was designed to provide a comparative measure of energy to fracture in an unnotched specimen section. This test is a structural test and as such the results are dependent upon specimen and test apparatus dimensions.

The nominal span of the dog bone type specimens was 6 inches and the test section was full thickness of the plate material being tested by 1.0-inch wide. The dimensions of the specimens

used in the test series is shown in Figure 87. During pendulum impact, the specimen was subjected to a mixed axial and bending stress as well as the localized stress distributions around the contact face of the pendulum striker against the specimen.

Figure 86. Photograph of the Bulk Fracture Charpy Machine.

A variety of test conditions were evaluated that included different materials [56], different impact velocities [58], different specimen thicknesses [57], and different impactor geometries. The impactor geometries included both blunt and sharp striker tups with the dimensions provided in Figure 88 and Figure 89, respectively [56].
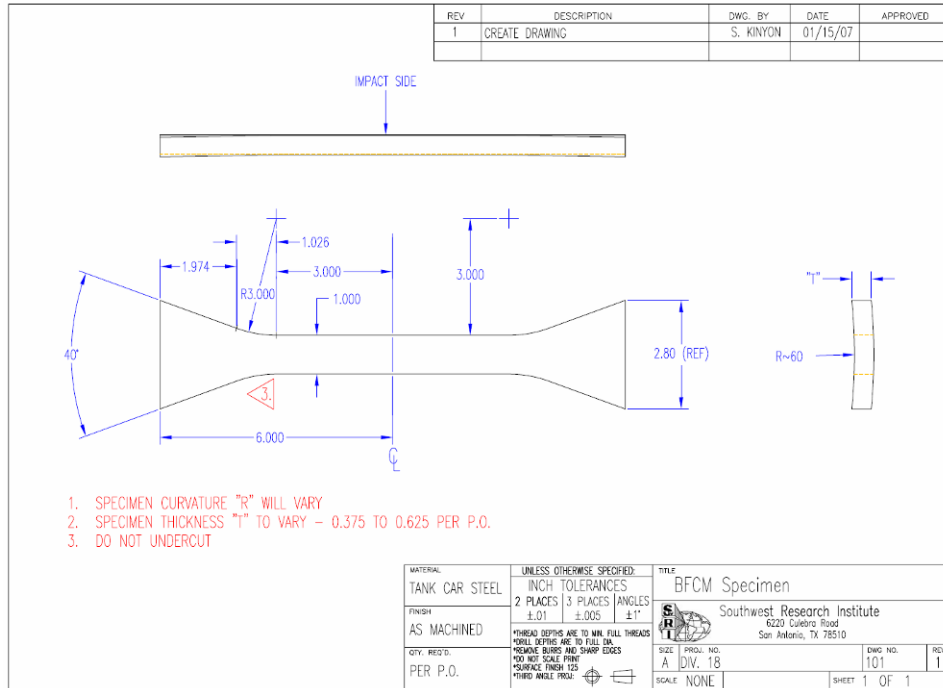
Figure 87. BFCM Test Specimen Dimensions.
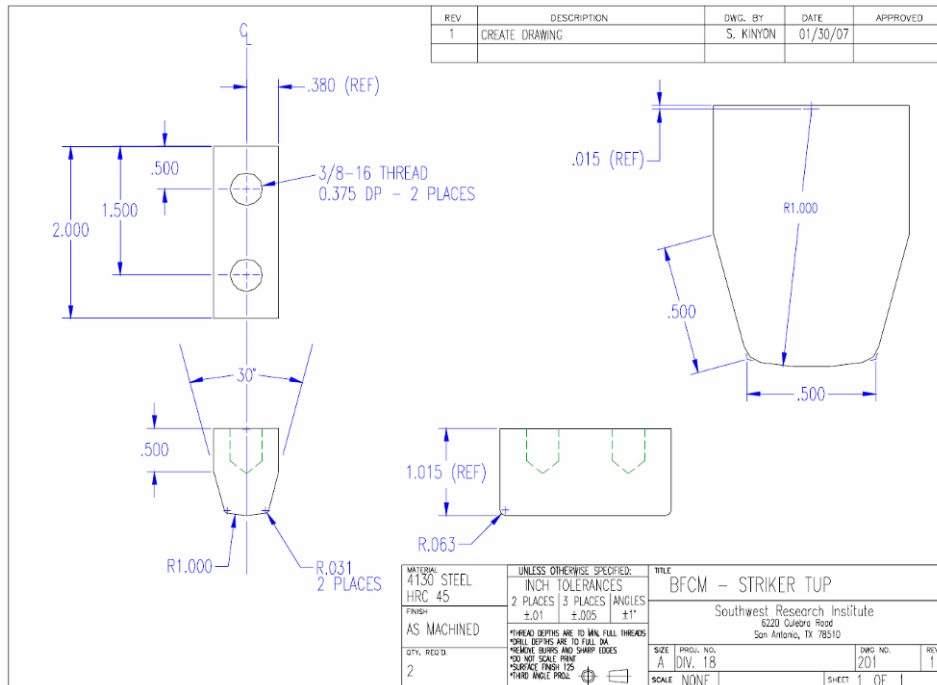
Figure 88. Dimensions of the blunt BFCM striker tup.
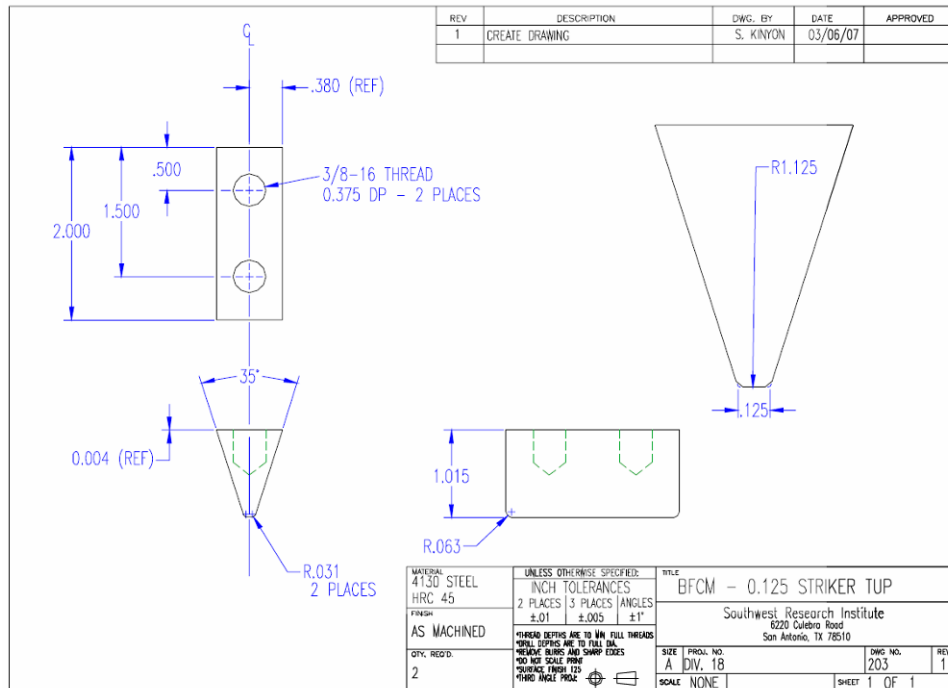
Figure 89. Dimensions of the sharp BFCM striker tup.

A preliminary model was generated to analyze the BFCM tests and applied to assess a set of impact analyses at various impact speeds that bounded the fracture energy for the specimen [58]. The model consisted of the test specimen, rigid grip blocks that are tightly fit to the specimen tapered tab geometry, and a rigid tup model with the total striker mass and initial striker velocity that is constrained to move in a pure translational motion. The preliminary model and impact response for an impact energy below the fracture energy is shown in Figure 90.

In the BFCM test series, the fracture of the specimen was bounded by striker impacts at 8.4 mph and 9.4 mph. The specimens for these two impact conditions are shown in Figure 91. The corresponding analyses of these two impact conditions with the preliminary BFCM model produced the deformed specimen geometries shown in Figure 92. Overall the comparison is favorable. The model was able to reproduce the bounds on the specimen fracture conditions between 8.4 and 9.4 mph. In addition, the deformation and failure modes appear to be consistent.

A picture of the observed failure mode captured in a high speed video of a BFCM test is shown in Figure 93. A region of material ahead of the blunt tup face is mostly undeformed and a pair of converging shear planes develop at the impact face near the edges of the tup face that converge as they propagate across the specimen thickness. This general deformation and failure behavior was captured in the calculations, as shown in Figure 94.

61

(a) Initial geometry

(b) Calculated impact response
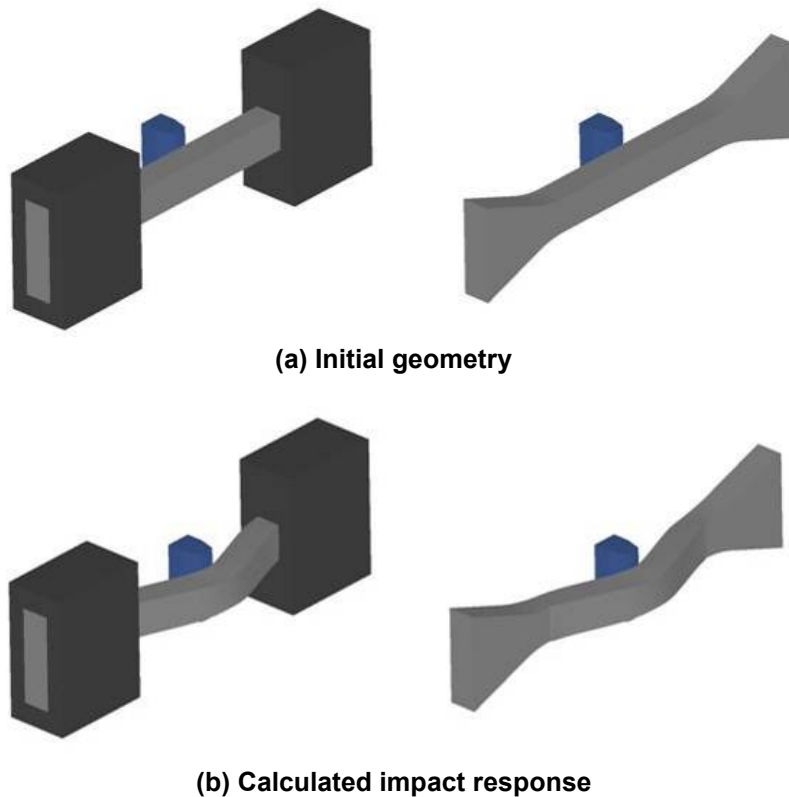
Figure 90. Preliminary finite element analysis of a BFCM test.

Figure 91. Observed BFCM specimen deformations at different impact velocities.

One significant difference was observed between the measured and calculated behaviors in the preliminary BFCM analyses. The test specimen final deformations, shown in Figure 91, have tab sections that are no longer aligned with the original specimen axis. This deformation indicates that the tabs were allowed to rotate within the tapered grip. The tabs in the preliminary model were very tightly constrained and this rotation within the grip was not allowed.
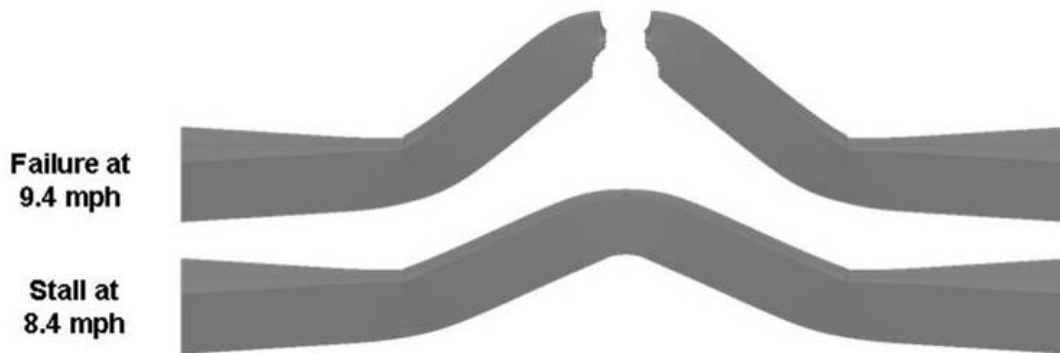
Figure 92. Calculated BFCM specimen deformations at different impact velocities.
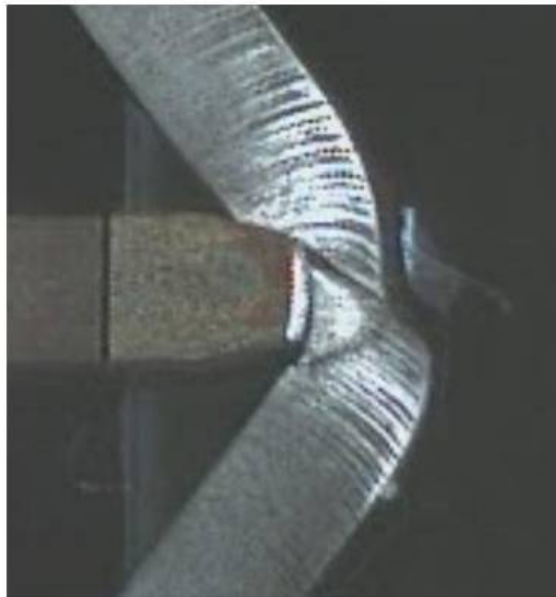
Figure 93. Observed BFCM specimen failure mode for the blunt striker.

An updated model was developed of the BFCM test configuration, as shown in Figure 95. This model contains a much more accurate representation of the specimen constraint conditions. The specimen is gripped by a 1-inch deep tapered slot machined into the grip block. The specimen is pushed forward in the slot and is initially in contact with the resisting face inside the grip block. A retaining plate is then bolted across the open side of the grip block. However, there is a gap between the specimen and the retaining plate equal to the difference between the 1-inch depth of the grip slot and the thickness of the plate material used to fabricate the specimen. In addition, the specimen taper does not have a tight tolerance relative to the grip taper and the specimen fits loosely in the grip fixture. As a result, some slip of the specimen relative to the grip block can occur in the tests.
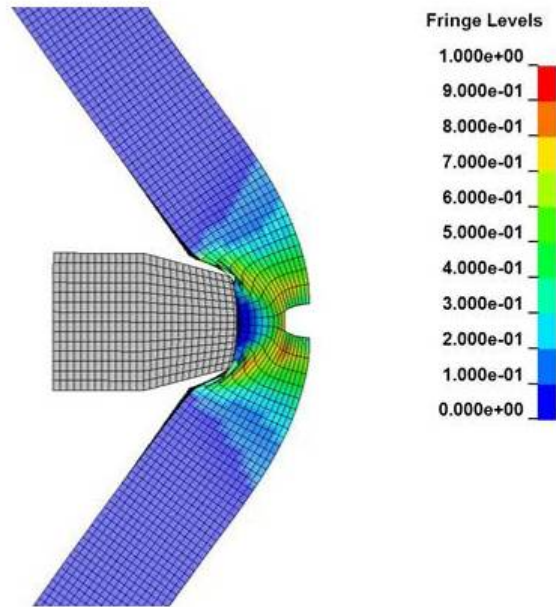
Figure 94. Calculated BFCM specimen failure mode for the blunt striker.
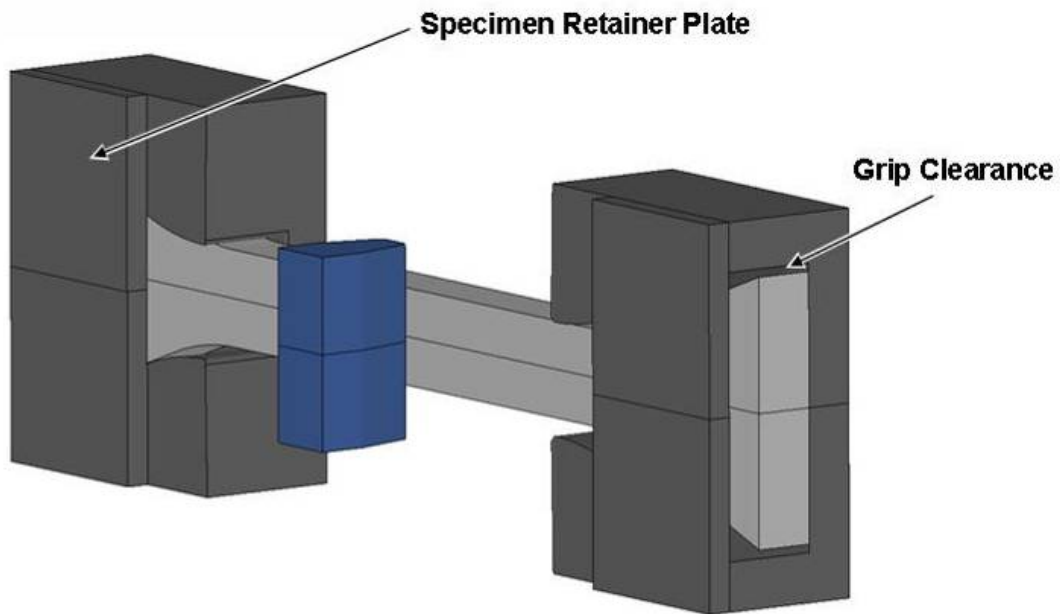
Figure 95. Finite element model of the BFCM test.

The series of BFCM tests on various thickness TC128B plate specimens was used to validate the model for a dynamic impact test condition [57]. A separate set of analyses on these tests were previously performed by the Volpe National Transportation Systems Center [60]. The model

was used to vary the test conditions and found that the fracture energies and impact response was sensitive to many parameters including:

- Gap tolerances between the specimen and grip.
- Model of the specimen retaining plate (rigid, deformable, or not included,).
- Friction coefficient between the specimen and the grip block.

The comparison of the measured and calculated fracture energies as a function of the specimen thickness with the blunt and sharp impactor tups are shown in Figure 96 and Figure 97, respectively. The analyses in these comparisons used the baseline TC128B material properties (shown in Figure 57) without any rate effects. All of the analyses using the rate effects models tended to over predict the fracture energies in the BFCM tests. In addition, these analyses used a 0.06-inch gap between the specimen tab and grip tapers and a rigid retaining plate on the back of the grip block. Overall the comparison of the calculated and measured fracture energies are reasonably good.
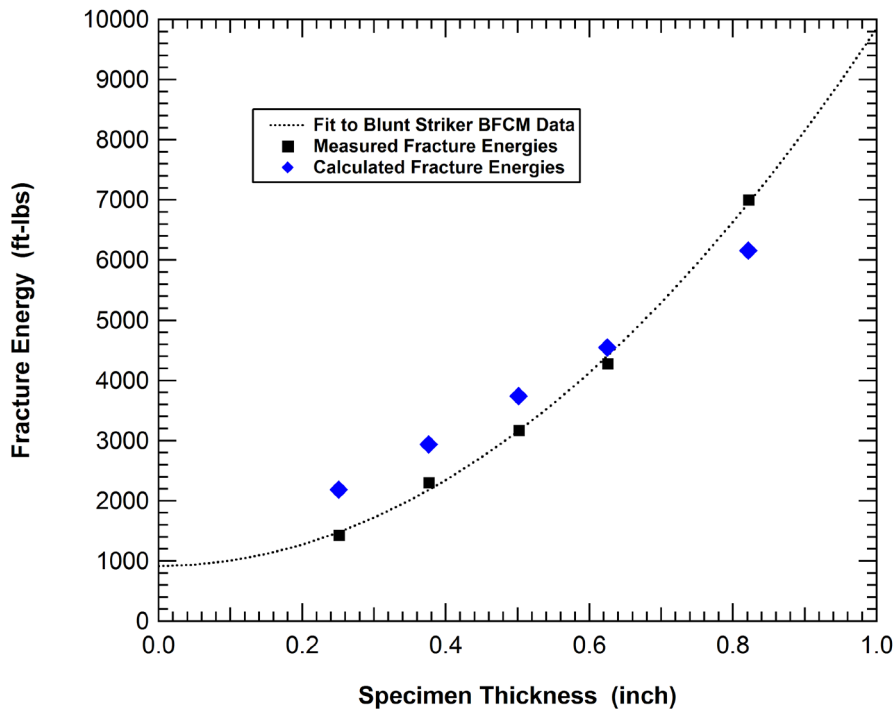
Figure 96. BFCM blunt striker fracture energy for different specimen thicknesses.
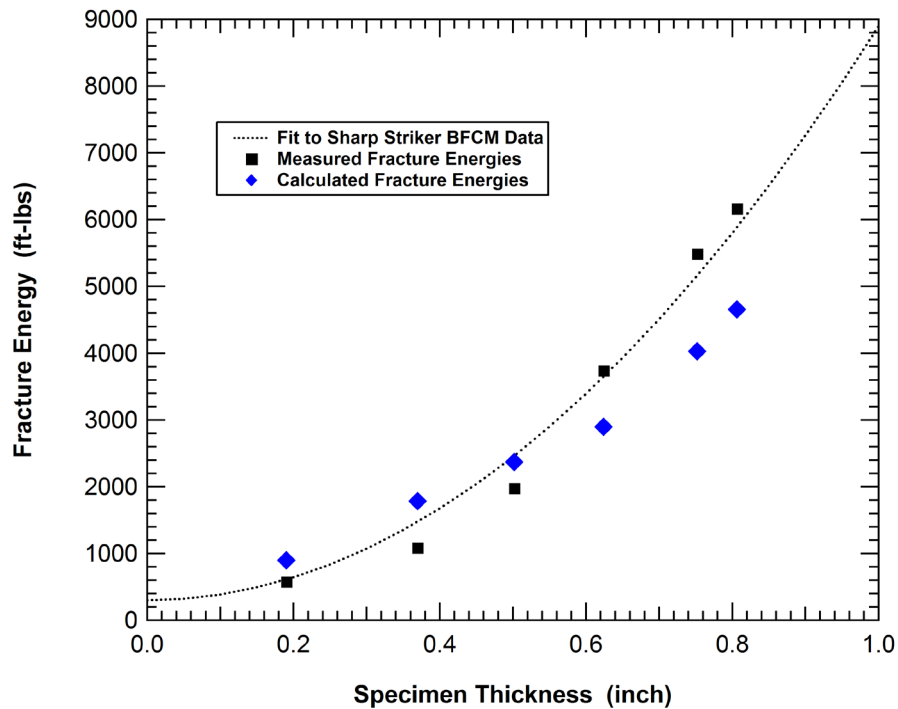
Figure 97. BFCM sharp striker fracture energy for different specimen thicknesses.

In addition to the fracture energies, the measured and calculated profiles of the broken specimens were compared. Representative examples for tests with the blunt and sharp impactors are shown in Figure 98 and Figure 99, respectively. The measured and calculated deformed shapes are very consistent.

The one trend observed in the BFCM testing that was not reproduced in the analyses is the increasing fracture energies for the thicker specimens above a linear fit (e.g. the data conforms to a quadratic fit). None of the parameter variations evaluated in the analyses were capable of reproducing this trend to the extent seen in the test data. Determination of the physical characteristics that are responsible for the effect is difficult since there are no active measurements (e.g. striker acceleration) that can be used to evaluate discrepancies in the testing and analyses. An attempt was made to assess the impact force history from the high speed video. However, there was not sufficient resolution to accurately assess the striker acceleration history.

It is suspected that the test fixture compliance may have contributed to the fracture energy nonlinearity. In high speed videos of the thicker specimen impact response, a significant amount of flexing is observable in the grip blocks. This would potentially allow for the test fixture to dissipate some of the impact energy and the amount would be greater for the higher loads associated with the thicker specimen. No attempt was made to introduce a similar level of test fixture compliance in the analyses to evaluate this effect.
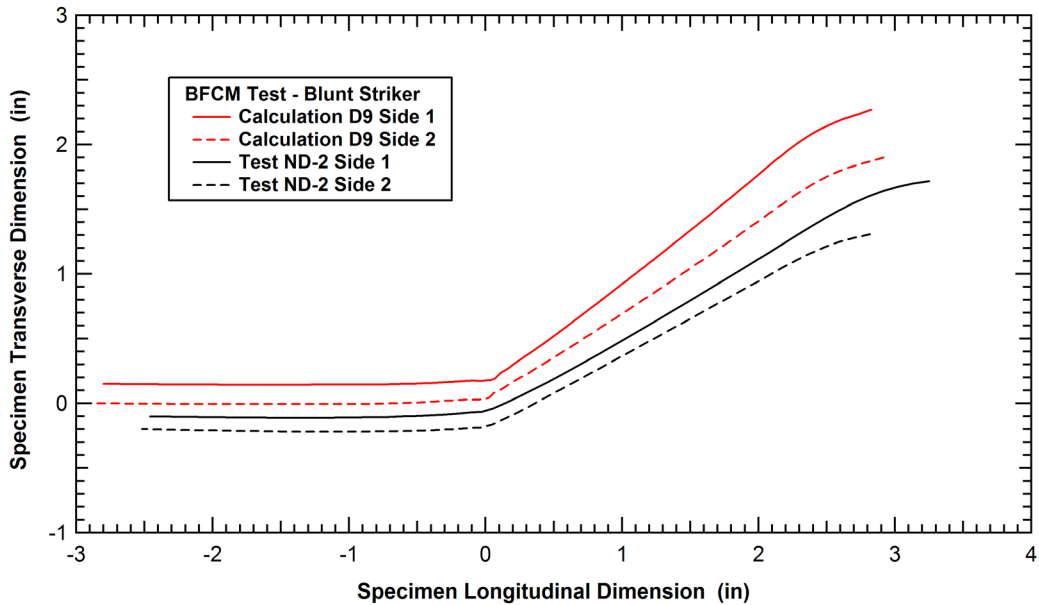
Figure 98. Calculated and measured BFCM blunt striker specimen deformations.
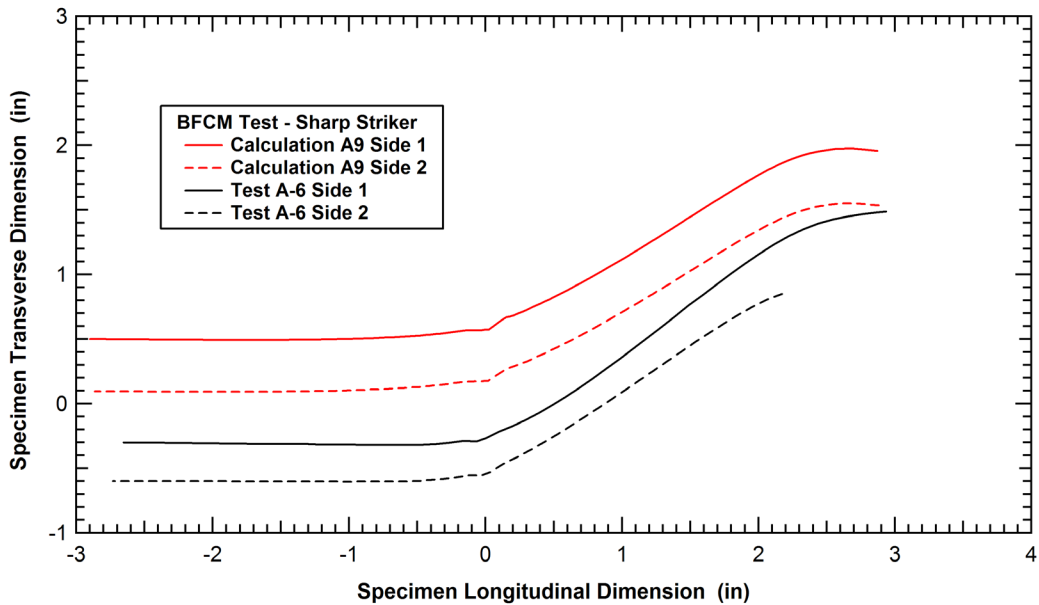
Figure 99. Calculated and measured BFCM sharp striker specimen deformations.

3.4.6 Characterization of Other Structural and Energy Absorbing Materials

The above sections describe the characterization of the mechanical and failure behaviors of traditional tank car materials (steels). These are the materials used in the baseline tank puncture analyses and for the majority of the retrofit protective designs. However, additional energy

absorbing materials (structural foams) and advanced structural materials (e.g. composite materials) were considered for protective system designs. Analyses of these concepts required similar efforts to characterize the material behaviors and develop associated material models.

The structural foams are primarily characterized by the foam density and associated unconfined compressive crush curve. An example of a measured unconfined compressive crush curve and associated analysis for a 5.4 pound per cubic foot (pcf) foam is shown in Figure 100. However, additional properties such as the tensile strength, interface behaviors and response under more general triaxial loading can also be important. As a result, additional tests such as foam sandwich panel bend and punch tests were also performed and analyzed. The characterization testing performed on foams and associated model development and validation are described in Section 6.1.1 of this report.
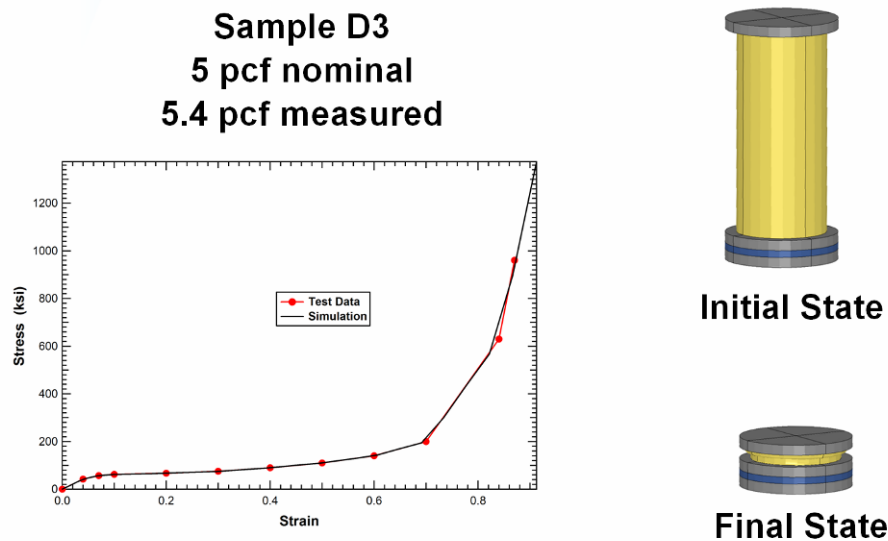
Figure 100. Unconfined compression testing and analysis of foam.

Composite materials were thought to be a potential candidate material for a tank protective system since composites have many strength characteristics similar to steels but with densities that are approximately ¼ of the steel density. Thus a significantly thicker composite protective structure could be applied on a tank car without exceeding a comparable weight. Composites have also been applied in armor systems for military vehicles achieving significant levels of impact and penetration protection [e.g. 61-64]. This also suggests the potential of a composite tank car system for significantly increasing the puncture resistance over current tank cars.

The mechanical and failure behaviors of composites are more complex than many engineering materials as a result of the material anisotropy and inhomogeneity. Composites are typically fabricated of very strong fibers (e.g. glass, carbon, kevlar) embedded in a polymer matrix material (e.g. epoxy). The fibers can typically be either continuous straight fibers arranged in

layers (plies) with various orientations or with woven fabric layers. As a result many different composite systems exist and these systems cover a wide range of material behaviors.

The composite system considered for this application uses woven glass fibers in a toughened matrix. This material system has been analyzed as part of a program to develop lightweight armor systems. The composite damage model development and validation against composite characterization tests is described in Section 6.4.1 of this report.

4   Detailed Tank Puncture Analyses

4.1   Introduction

In this section, the detailed BW failure model described in Section 3 is applied to assess various tank puncture conditions

4.2   Tank Car Puncture Model

As described in Section 3, the detailed failure model uses a fine mesh of brick elements in the impact zone with an element dimension of approximately 0.040 inch (1 mm). The model of the commodity tank and BW impact zone mesh used in these puncture analyses is shown in Figure 101. An algorithm in LS-DYNA is used to tie the edge of the shell elements to the solid elements around the edge of the impact zone.
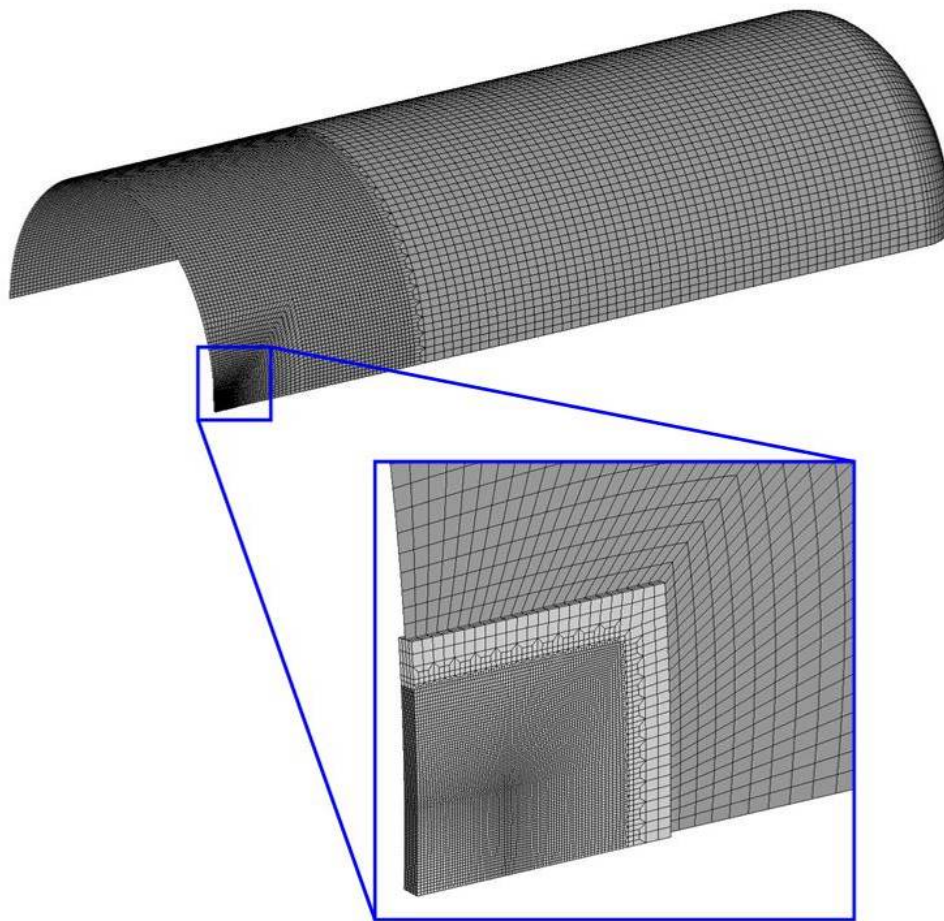
Figure 101. Tank model and impact zone mesh used for side impact puncture analyses.

As a result of the very fine mesh in the impact zone, the puncture models were significantly larger and have correspondingly longer run times. To allow for the evaluation of a wide range of impact conditions and tank geometries, some simplifications in the tank model were implemented.

The first simplification was the use of symmetry planes. For the analyses described here, two symmetry planes were used to reduce the model to one-quarter of the full tank (a half model was used for the offset head impacts). This had a small effect since some tank car structural details could not be included in the quarter model (e.g. manway and bolsters). The primary effect of this approximation was that a side impact centered on the tank may have a slightly reduced stiffness for large dent sizes since the manway and surrounding structures are stiffer than the bare commodity tank.

Another simplification in the tank puncture model was in the modeling approach used for the fluid lading. In the analyses presented in Section 2 an explicit model was used for the lading. However, this explicit model required a significant increase in the model size and also was not ideally compatible with a quarter symmetry model. An alternate modeling approach was to smear the weight of the lading uniformly into the commodity tank wall. A comparison of the full tank car impact response using the two different lading modeling methodologies is shown in Figure 102. The comparison shows that the simplification of the smeared lading approach did not have a large influence on the impact behavior.
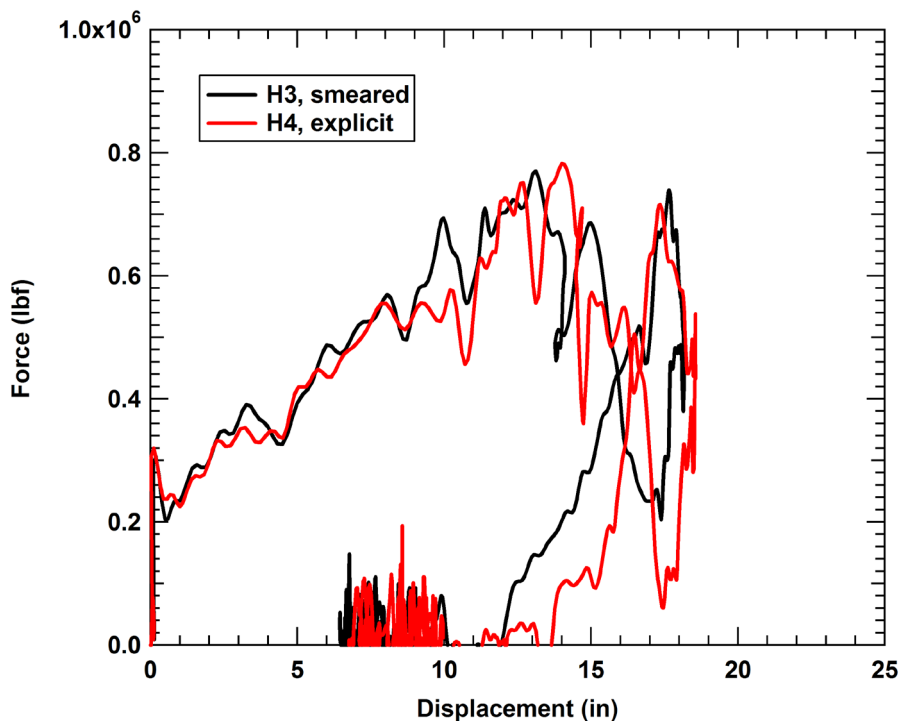
Figure 102. Calculated tank car impact behavior using two different lading models.

The final simplification of the impact modeling was that the ram car was not used in the analyses. Instead, a rigid model of the ram head was used with the mass of the entire ram car. This was a reasonable simplification since the measurements of ram car acceleration at distributed measurement locations were all in good agreement.

The simulation of the Test 2 impact conditions using the tank puncture model is shown in Figure 103. The model shown was reflected vertically about the symmetry plane (seen as a line in the figure) for improved visualization of the impact behavior. The impactor in this analysis was a rigid 6x6 inch ram with a 0.5-inch radius around the edges and a total weight of 286,000 lbs. The small rectangular patch of elements under the impactor (already punctured in Figure 103) is the fracture zone where the BW failure model was applied. The remainder of the tank structure was again modeled with 4-node shell elements and a tied shell-to-solid constraint was used at the interface of the two model regions.

The comparison of the measured and calculated force-deflection behavior for Test 2 with the tank puncture model is provided in Figure 104. The comparison shows overall good agreement between the calculation and test. The peak load at which the tank was punctured was very accurately captured by the model. The primary discrepancy of the test and model was a slightly more compliant behavior in the model at large displacements. This difference in compliance could primarily be attributed to the removal of the manway from the tank model.
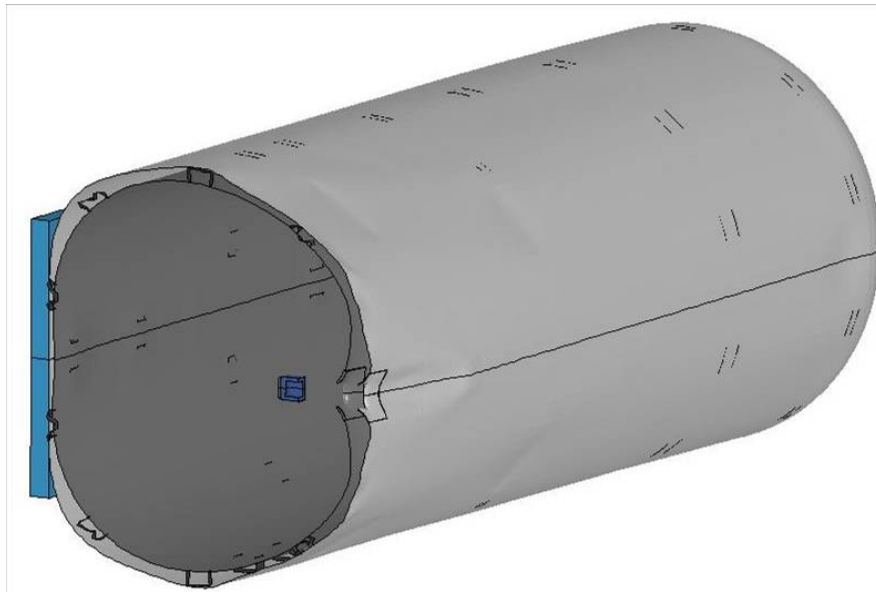
Figure 103. Simplified tank model analysis with Bao-Wierzbicki failure assessment.
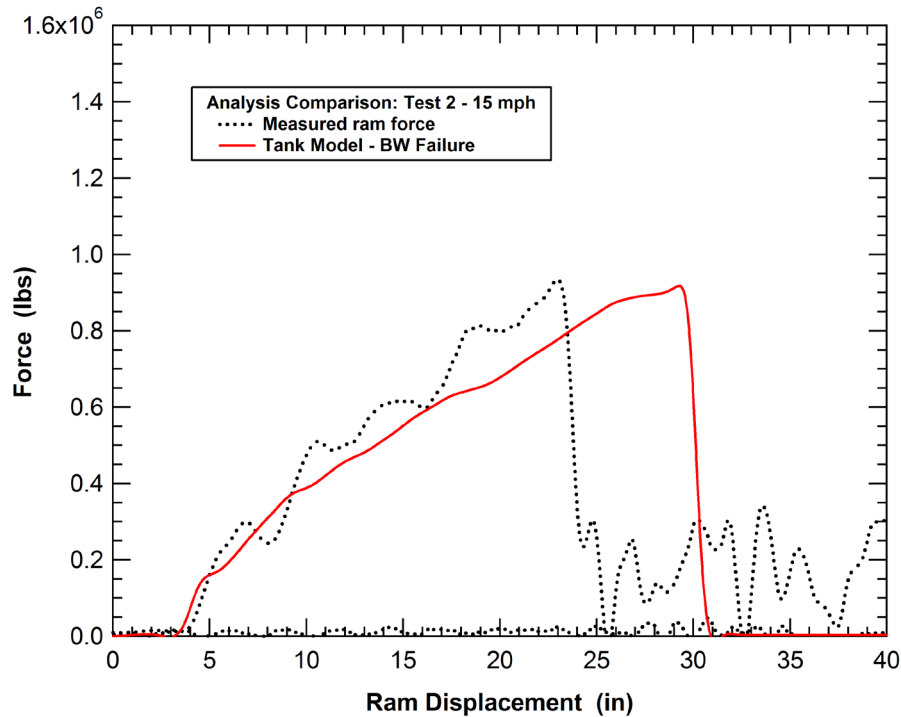
Figure 104. Tank puncture model Test 2 analysis with Bao-Wierzbicki failure assessment.

4.3 Assessment of Baseline Tank Puncture Conditions

The tank puncture model was used to assess the puncture energies for a wide range of tank car design variations and impact conditions. A variety of tank cars were evaluated including chlorine (Cl) and Ethylene Oxide (EO) tank car designs. As a result, the tank parameters investigated include tank diameter (100 and 119 inches), tank thickness (between 0.5625 and 1.102 inches), internal pressure (50 psi and 100 psi), jacket thickness, foam insulation, and impactor size. A summary of the tank geometric parameters used in the various analyses is provided in Table 3. The dimensions listed for the tank in the second column in Table 3 correspond to the diameter and length of the cylindrical portion of the tank. In addition, 2:1 ellipsoidal heads were used to complete the tank structure. The material used for the commodity tank shell and/or heads in all of the analyses was TC128B if the thickness was less than one inch and A516-70 if greater than one inch.

An example puncture response is shown in Figure 105. The analysis shown corresponds to the 300 lb Cl tank geometry (note: the 300 lb tank designation is used in the industry and refers to a tank with a 300 psi test pressure). The ram head model was updated in these analyses to include the tapered geometry used in the full-scale testing and an updated weight of 295,000 lbs. The tapered geometry included a 6x6 inch contact face but flared out to more closely duplicate the initial puncture response seen in the impact tests of the NGRTC program. Although the ram

head was tapered in the analyses, the contact patch remained the 6x6 inch face until the protective layers and/or tank were punctured. As a result, the tapered geometry did not play a significant role in the prediction of the puncture energies reported in this report.

Table 3. Parameters used for the tank impact analyses

Tank Type	Tank Shell Dimensions (D x L)	Shell/Head Thickness (Inches)	Shell/Head Material
300 lb CI	100 x 472 inches	0.5625 / 0.6030	TC128B
500 lb CI	100 x 472 inches	0.7770 / 0.8281	TC128B
600 lb CI	100 x 472 inches	0.9810 / 1.1360	TC128B / A516-70
300 lb EO	119 x 505 inches	0.5625 / 0.6030	TC128B
423 lb EO	119 x 505 inches	0.7770 / 0.8281	TC128B
500 lb EO	119 x 505 inches	0.9180 / 0.9784	TC128B
534 lb EO	119 x 505 inches	0.9810 / 1.1360	TC128B / A516-70
600 lb EO	119 x 505 inches	1.1020 / 1.2760	A516-70

The progression of the fracture behavior in the BW failure patch is shown in Figure 106. The fracture initiated near the corners of the impactor and propagated initially along the side of the impactor face. The crack subsequently ran along the top and bottom of the ram face. Finally, the edges of the puncture site are petaled inward as the tapered ram was forced through the tank wall. It should be noted that the use of two symmetry planes would potentially influence the fracture behavior since asymmetric crack propagation, such as was observed in Test 2, can not develop in the model.

The calculated force-deflection behaviors and puncture energies for the 300, 500, and 600 lb chlorine tanks are shown in Figure 107. These analyses used a tank diameter of 100 inches and an internal pressure of 100 psi. An 11 gauge jacket of A1011 steel was included with a 4-inch standoff. The shell thicknesses for the 300, 500, and 600 lb tanks were 0.5625, 0.777, and 0.981 inch, respectively. TC128B Material was used for all of the commodity tanks. The impact speed for all three analyses was 20 mph. The calculated puncture loads for the chlorine cars were approximately 0.7, 0.9, and 1.1 million lbs and the puncture energies were 0.67, 1.26, and 1.74 million ft-lbs for the 300, 500, and 600 lb tanks, respectively.
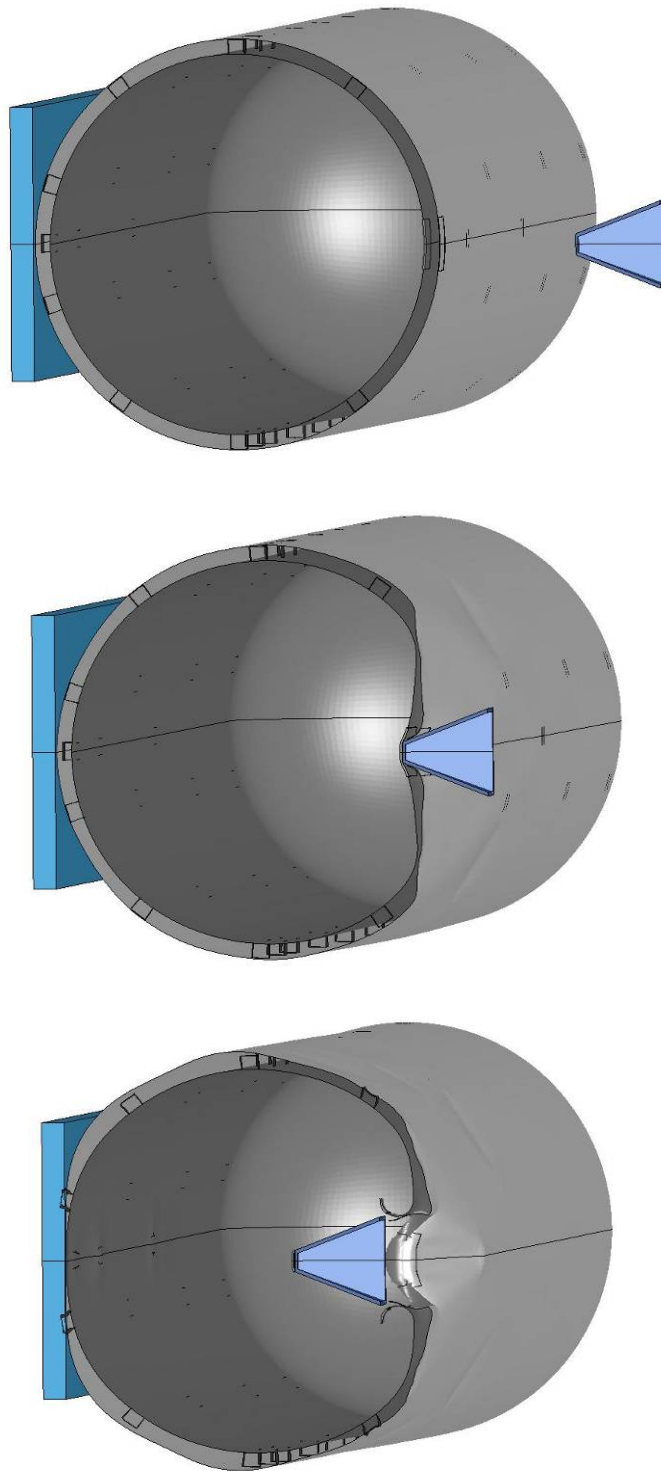
Figure 105. Detailed impact and puncture sequence for a 300 lb chlorine car.
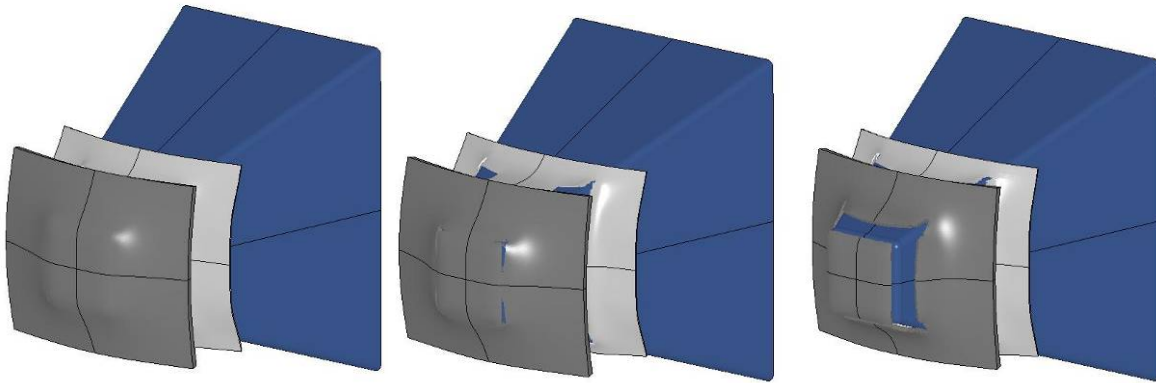
Figure 106. Calculated puncture initiation and fracture progression.
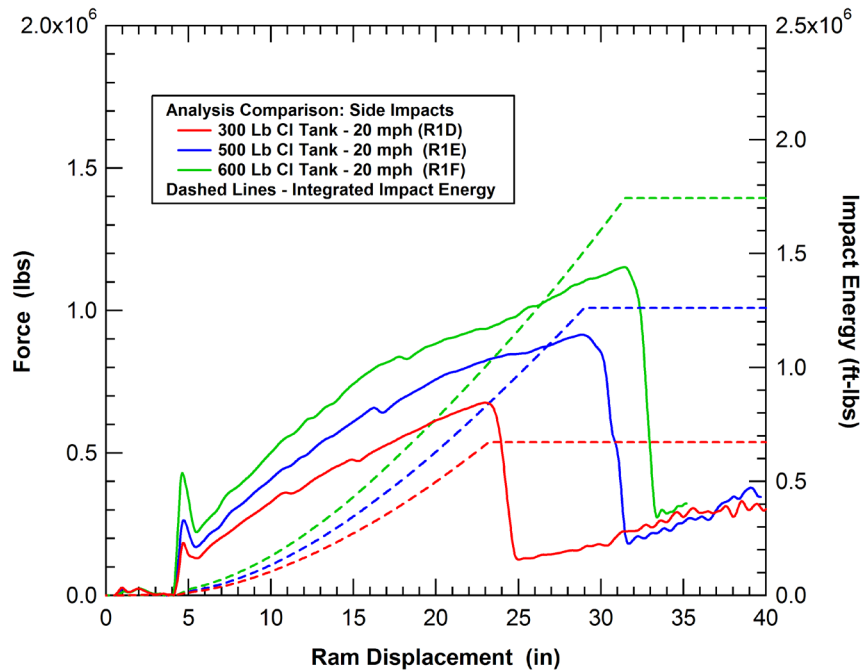
Figure 107. Side impact force-deflection curves and puncture energies for chlorine tank cars.

The energy balance for the 600 lb chlorine car impact is shown in Figure 108. The initial impact energy is approximately 4 million ft-lbs (all in the kinetic energy). As the impact progresses, the ram is decelerated and the kinetic energy drops off. The energy transfer is from the kinetic energy of the ram to the internal energy of the tank (plastic deformations of the tank material) and the pressure-volume work caused by the indentation reducing the total tank volume. The internal energy of the tank at rupture is approximately one million ft-lbs and the pressure volume work is between 500,000 and 600,000 ft-lbs. The hourglass energy and sliding energy in the calculation are both negligible indicating that the calculation is stable and does not have any numerical energy losses.
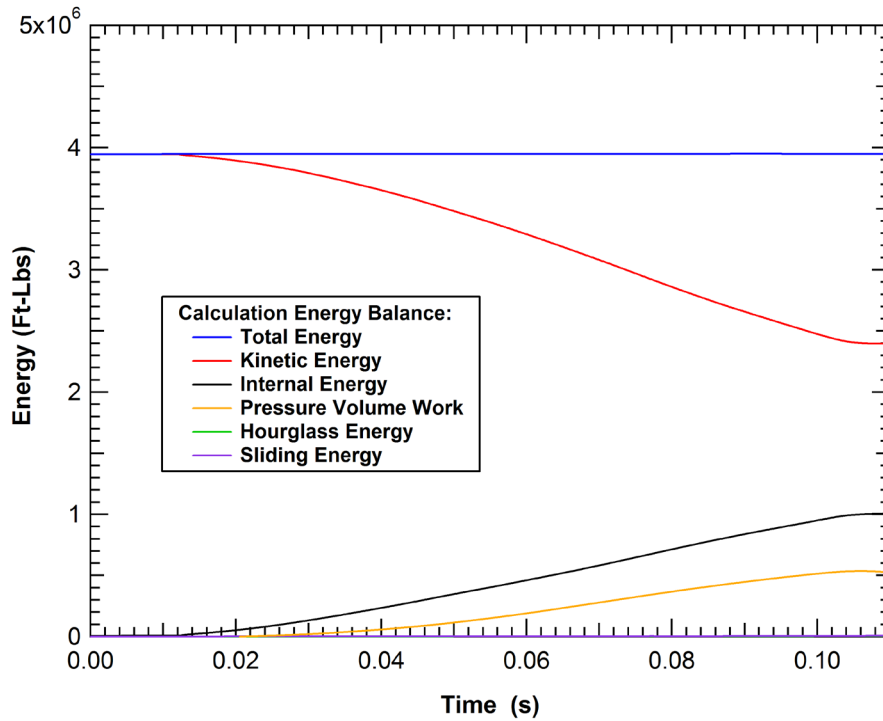
Figure 108. Calculated energy balance for the 600 lb chlorine tank car impact (R1F).

The design selected for the EO tank car has a 119-inch commodity tank diameter. From the Code of Federal Regulations (CFR §179.100-6), the wall thickness after forming of the tank shell and heads must not be less than that specified in §179.101, nor that calculated by the following formula:

$$t = Pd / 2SE \tag{10}$$

Where:

d = Inside diameter in inches

E = 1.0 welded joint efficiency; except for heads with seams = 0.9

P = Minimum required bursting pressure in psi

S = Minimum tensile strength of plate material in psi, as prescribed in §179.100–7

t = Minimum thickness of plate in inches after forming

Equation 10 was used to calculate the thickness of the 500 and 600 lb EO tanks to obtain the values provided in Table 3. The 300 lb EO tank thickness is from a required minimum thickness of 0.5625 inch and is the same as for the smaller diameter 300 lb Cl tank. In addition, EO tanks were analyzed with the 500 and 600 lb Cl tank wall thicknesses of 0.777 and 0.981 inches. The corresponding test pressures for these shell thicknesses when applied on the 119-inch diameter

EO tank were 423 and 534 lbs, respectively, from Equation 10. These analyses for additional intermediate EO tank shell thicknesses provides additional data since other EO tank car designs were of smaller diameter (e.g. 106 and 110 inches) and would therefore have correspondingly thinner tank shells for the equivalent test pressure.

The calculated force-deflection behaviors and puncture energies for the 300, 423, 500, 534, and 600 lb Ethylene Oxide (EO) tanks are shown in Figure 109. The significant differences between these analyses and the previous set for chlorine cars was that the tank diameter was increased to 119 inches and the internal pressures were reduced to 50 psi (there was also a small difference in the length of the tank shell). The calculated puncture loads were approximately 0.6, 0.9, 1.06, 1.1, and 1.17 million lbs and the puncture energies were 1.14, 1.66, 2.13, 2.7, and 2.87 million ft-lbs for the 300, 423, 500, 534, and 600 lb tanks, respectively.

The comparison shows that there was only a small difference in the puncture loads between the EO and chlorine cars, but there was a significant difference in the puncture energies. The comparison shows that the EO cars had larger displacements before they reached the puncture load and, as a result, had the higher energy dissipation levels. The puncture energies in the EO cars were approximately 50% higher than those in the chlorine cars.
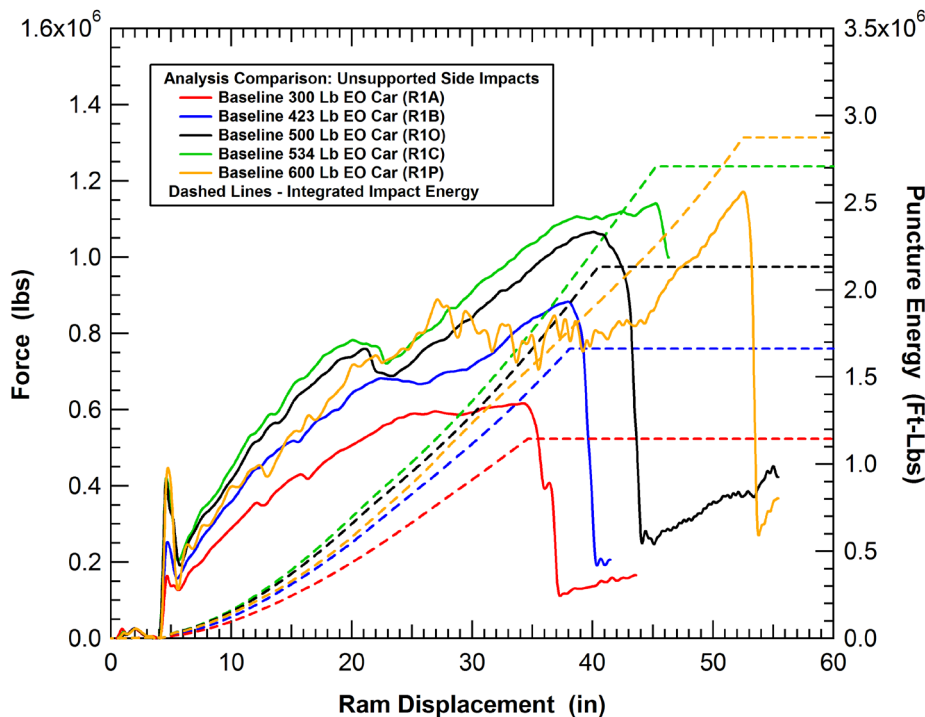
Figure 109. Side impact force-deflection curves and puncture energies for the EO Tank Cars.

4.3.1 Effects of Tank Pressure and Diameter

The primary parameters that can create the difference in the puncture energies seen between the EO and Cl tank cars are the tank diameter and the internal pressure. To resolve which of these two parameters was primarily responsible, an additional analysis was performed using the 300 lb EO car with a 100 psi internal pressure. The comparison of this analysis with the two previous analyses on the 300 lb EO car (50 psi) and the 300 lb chlorine car (100 psi) are shown in Figure 110. The comparison shows that the internal pressure was clearly the dominant parameter that contributes to the differences in the previous two sets of analyses. The force-deflection behavior and puncture energies of the 300 lb EO and chlorine cars with 100 psi internal pressure were virtually identical. Thus, the larger tank diameter of the EO car (119 inches versus 100 inches) had significantly less influence on the response for this tank geometry.
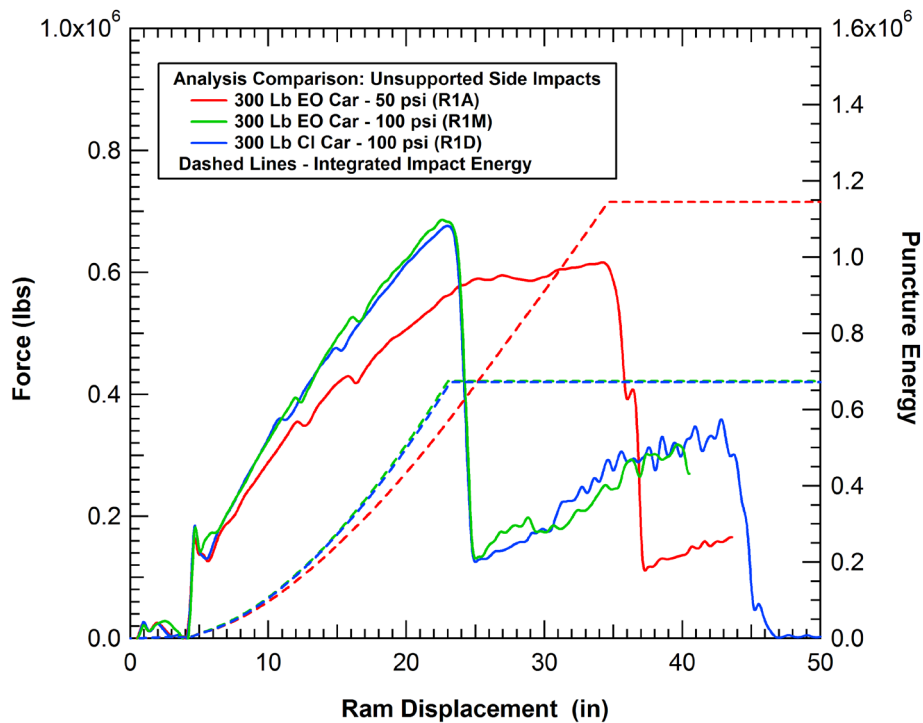
Figure 110. Side impact comparison for tank cars at different pressures and diameters.

Similar analyses of the effects of internal pressure for the 500 lb chlorine tank were performed at 50 and 100 psi. The calculated force-deflection curves are shown in Figure 111. Again the internal pressure had little effect on the side impact puncture force but the puncture energy increased by 60% from 1.26 to 2.01 million ft-lbs. A comparison of the force-deflection characteristics and puncture energies for the 500 lb chlorine tank car and the 423 lb EO tank car (both with a 0.777 in shell thickness) as well as the 500 lb EO car, all at 50 psi, are shown in Figure 112. The comparison shows some effect from changing the tank diameter (both at a

constant thickness or a scaled thickness), but the effects were much smaller than those created by the change in pressure levels.
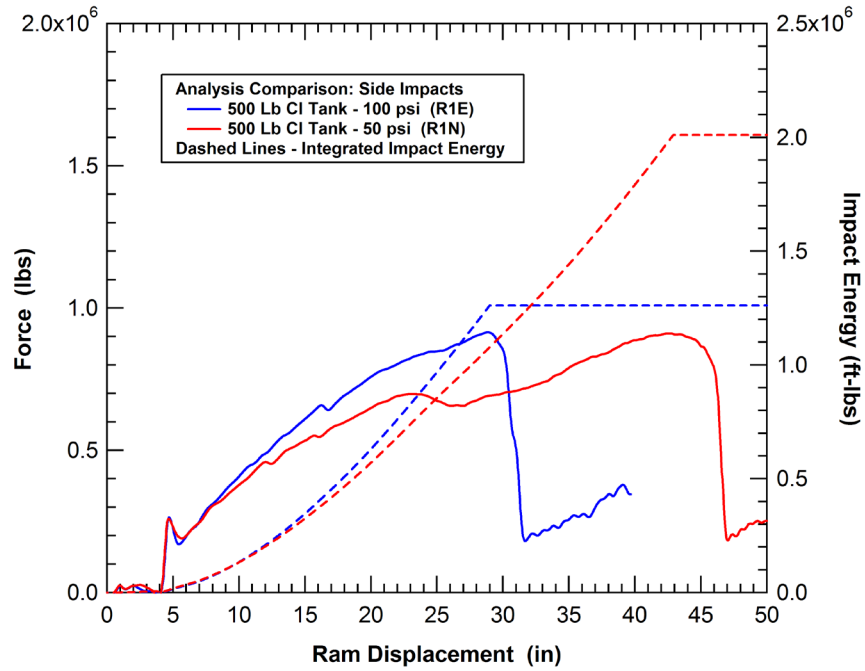
Figure 111. Evaluation of the effects of pressure on a 500 lb Cl tank.
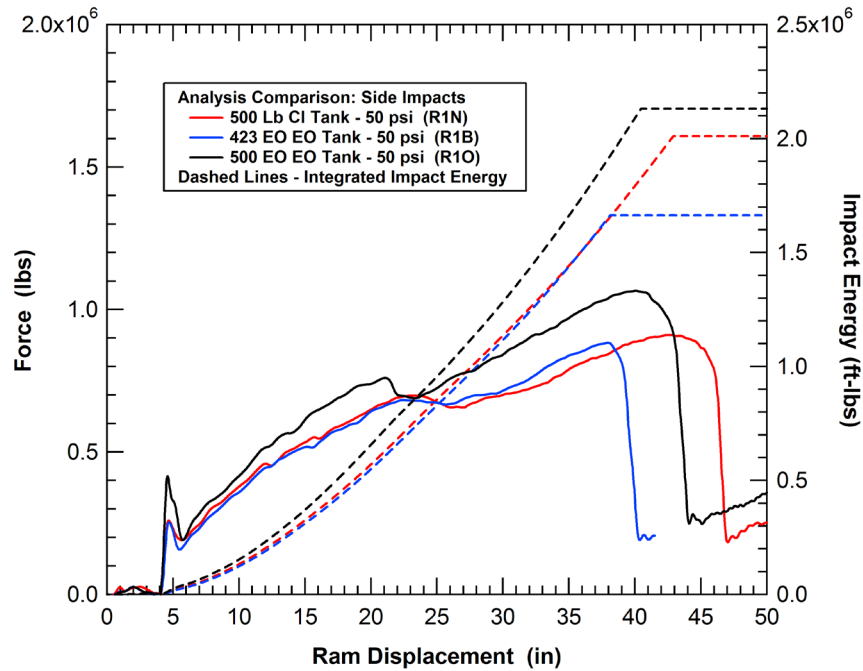
Figure 112. Evaluation of the effects of diameter and thickness at 50 psi.

4.3.2 Analyses of Tank Jacket Retrofit Designs

A proposed approach to increasing the puncture resistance of tank cars is to require commodities currently shipped in 300 lb tanks to be moved to 500 lb tank cars and commodities currently in 500 lb cars be shipped in 600 lb tank cars. A simple alternative to achieve the same puncture protection levels that may allow for retrofit solutions is to maintain the current thickness of the commodity tank and to add the additional thickness to the jacket to increase the puncture resistance. A series of side impact analyses was performed to evaluate this approach.

Chlorine Tank Cars

A comparison of a 500 lb chlorine tank cars retrofit with a 0.375-inch and 0.5625-inch jackets is shown in Figure 113. The comparison includes the baseline 500 and 600 lb chlorine cars for reference. The 500 lb chlorine tank car retrofit with the 0.375-inch jacket has a puncture energy of 1.73 million ft-lbs compared to 1.74 million ft-lbs for the 600 lb chlorine car. Therefore, the 0.375-inch jacket retrofit provides an equivalent level of puncture resistance at roughly equivalent weight for the chlorine tank cars. When retrofit with a 0.5625-inch jacket, the puncture energy increases to 2.17 million ft-lbs which is significantly greater than the baseline 600 lb chlorine tank car.
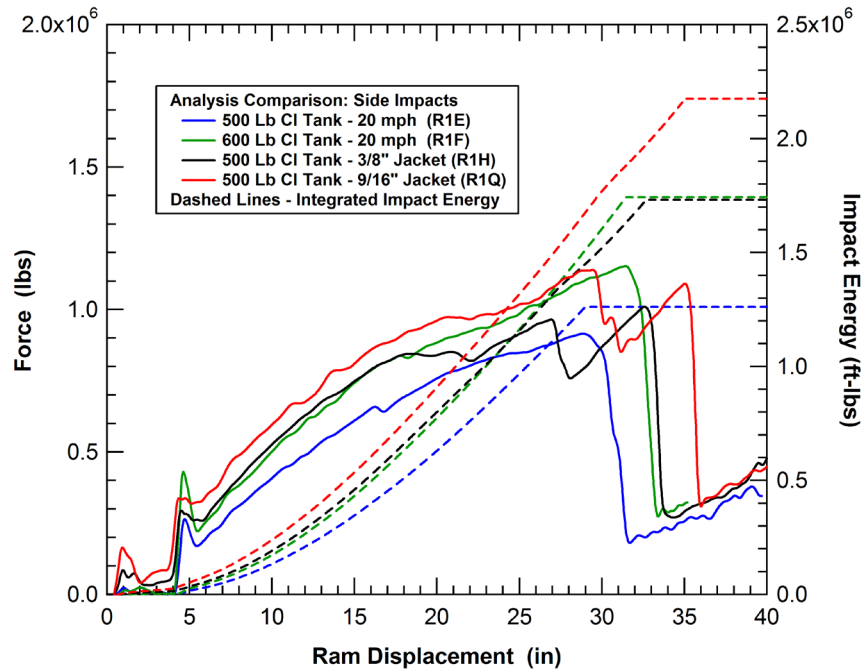
Figure 113. Evaluation of a 500 lb chlorine tank cars retrofit with thicker jackets.

A topic of interest for increasing the puncture resistance of tank cars is the relative efficiency of adding material to the jacket as opposed to adding material to the commodity tank. An indication of this can be obtained from these side impact analyses. The 500 lb Cl tank shell is 0.204 inch thinner than the 600 lb tank shell. The 0.375-inch retrofit jacket was modified by adding 0.256 inch to the original 11 gauge jacket thickness (0.119 inch, nominally) and switching the jacket material to something similar to TC128B. As a result, the total thickness of the tank shell and 0.375-inch jacket were approximately 0.050 inches thicker than the baseline 600 lb Cl tank with the 11 gauge jacket. The two analyses had approximately equivalent puncture energies. Thus, these analyses indicate that there is not a large difference in efficiency of using the additional material to reinforce either the jacket or the commodity tank.

A summary of the analyses of the 500 lb Cl tank with various jacket thicknesses is provided in Figure 114. The graph provides a fit to the analyses to illustrate the relationship between the retrofit jacket thickness and the puncture energy. The comparison shows that a retrofit jacket thickness of 0.375-inch is required for the 500 lb Cl tank to provide a similar level of puncture resistance as a 600 lb tank car with the 11 gauge jacket (as confirmed by the analysis with the 0.375-inch jacket).
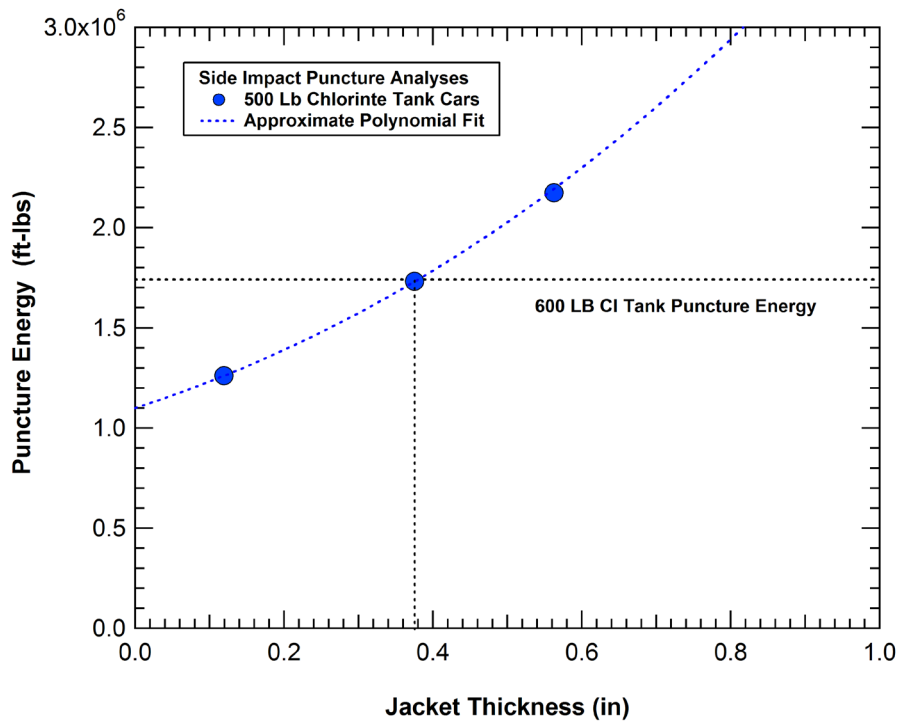
Figure 114. The effects of jacket thickness on puncture energy for a 500 lb Cl tank.

Ethylene Oxide Tank Cars

Similarly, analyses of a 300 lb EO tank car retrofit with a 0.375-inch jacket and with a 0.5625-inch jacket (i.e. double tank configuration) are compared to the baseline 300 lb EO car in Figure 115. The 300 lb EO tank car retrofit with the 0.375-inch and 0.5625-inch jackets have puncture energies of 1.85 million and 2.86 million ft-lbs, respectively. These compare to the 2.13 million ft-lbs for the 500 lb EO car.

A summary of the analyses of the 300 lb EO tank with various jacket thicknesses is provided in Figure 116. The comparison illustrates that a retrofit jacket thickness of approximately 7/16 inch would be required for a 300 lb EO tank to provide a similar level of puncture resistance as the 500 lb EO car. However, the puncture energy levels calculated for the 500 lb and 600 lb Cl tank cars are also indicated in Figure 116. We see from the comparison that the 300 lb EO tank car retrofit with a 0.375-inch jacket has a puncture energy that is higher than that of the 600 lb chlorine car as a result of the lower pressures in EO tanks. Thus, the 0.375-inch retrofit jacket on EO cars will provide a protection level equivalent to or better than that of retrofit designs of other commodities.
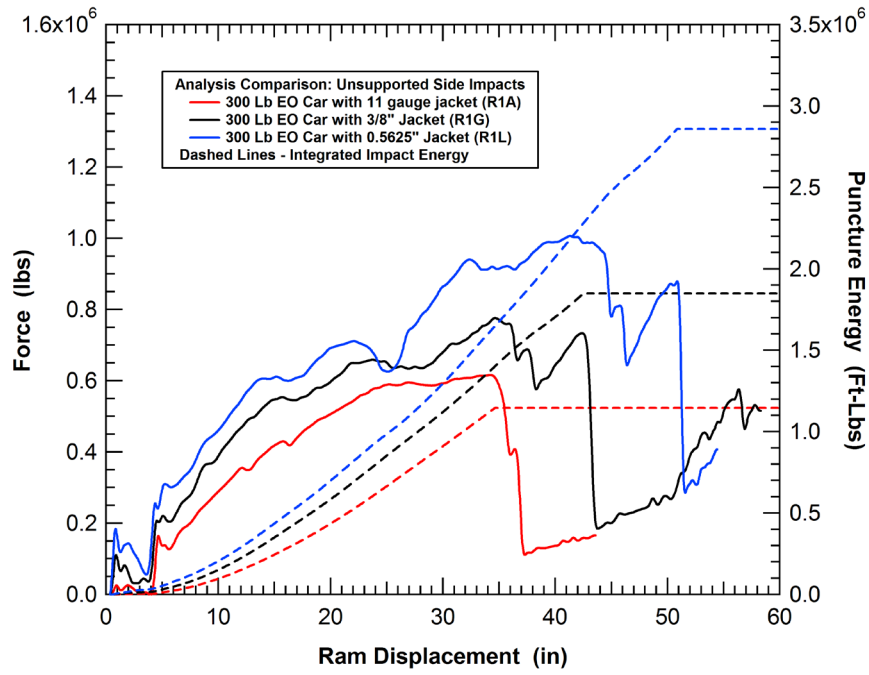
Figure 115. Analyses of 300 lb EO tanks with different thickness jackets.
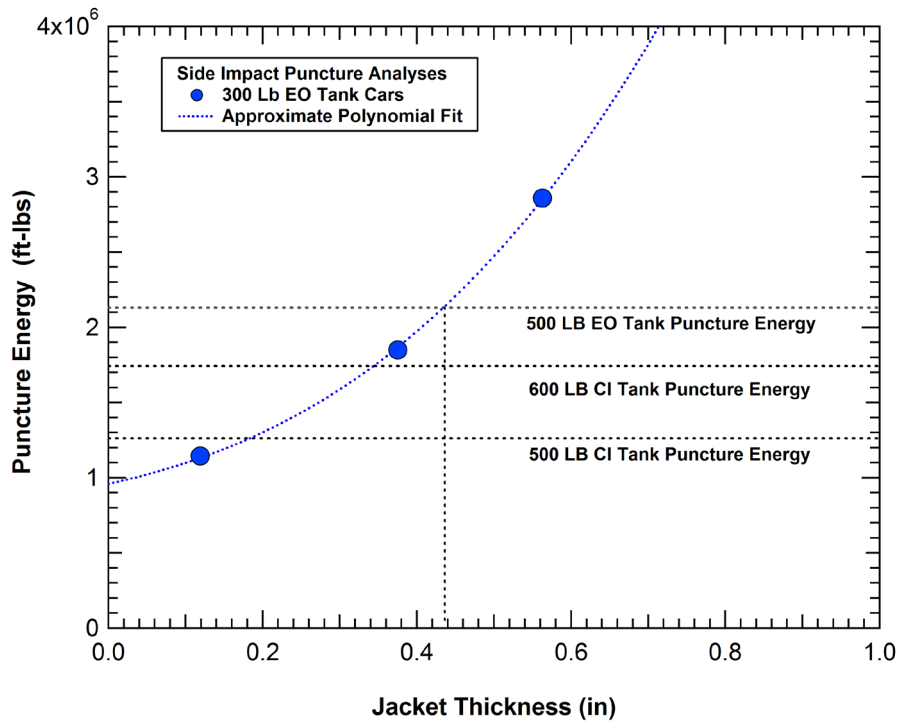
Figure 116. The effects of jacket thickness on puncture energy for a 300 lb EO tank.

Based on these results, the relative efficiency of adding material to the jacket as opposed to adding material to the commodity tank was assessed for the EO tank cars. The 300 lb EO tank shell is 0.3555-inch thinner than the 500 lb EO tank. The retrofit requirement of a 0.4375-inch jacket for the 300 lb EO tank car to achieve equivalent puncture resistance of the 500 lb EO tank adds 0.3185 inches when compared to the original 11 gauge jacket. As a result, the total thickness of the tank shell and 0.4375-inch jacket were approximately 0.037 inches thinner than the baseline 500 lb EO tank with the 11 gauge jacket. As was the case for the Cl tank, these analyses indicate that there is not a large difference in efficiency when using additional material to reinforce either the jacket or the commodity EO tank.

4.3.3 Effects of Impactor Size

A potential concern is that the selection of the 6x6 inch ram, as the primary threat used to assess puncture resistance, could prevent the adaptation of a concept that could provide significant benefit for impacts with larger contact areas. To evaluate the effects of the ram impactor size, analyses were performed on the 500 lb chlorine tank car being impacted by both 9x9 inch and 12x12 inch ram impactors with a 0.50-inch radius around the edges.

The model of the commodity tank and BW impact zone mesh used in the 12x12 inch impactor analyses is shown in Figure 117. Again, the refined zone is maintained along the perimeter of the impactor face with a characteristic element dimension of approximately 0.040 inch (1 mm).

A comparison of the force-deflection behaviors and puncture energies with the 6 inch, 9 inch, and 12 inch square impactors is shown in Figure 117. The higher impact speeds noted in the calculations with the 9 inch and 12 inch impactors were required to achieve the higher puncture energies associated with the larger impactors. Since the impact behavior is insensitive to impact speed (within a limited range), the impact velocities were not considered to be a relevant factor in the comparison. The increase to a 9x9 inch impactor increases the puncture load from 0.9 to nearly 1.3 million lbs and the corresponding puncture energy from 1.26 to 2.86 million ft-lbs. Similarly, the 12x12 inch impactor increases the puncture load from 0.9 to over 1.5 million lbs and the corresponding puncture energy from 1.26 to 4.95 million ft-lbs. The puncture initiation behavior at the interface of the ram and tank shell for the 12x12 ram are shown in Figure 119.
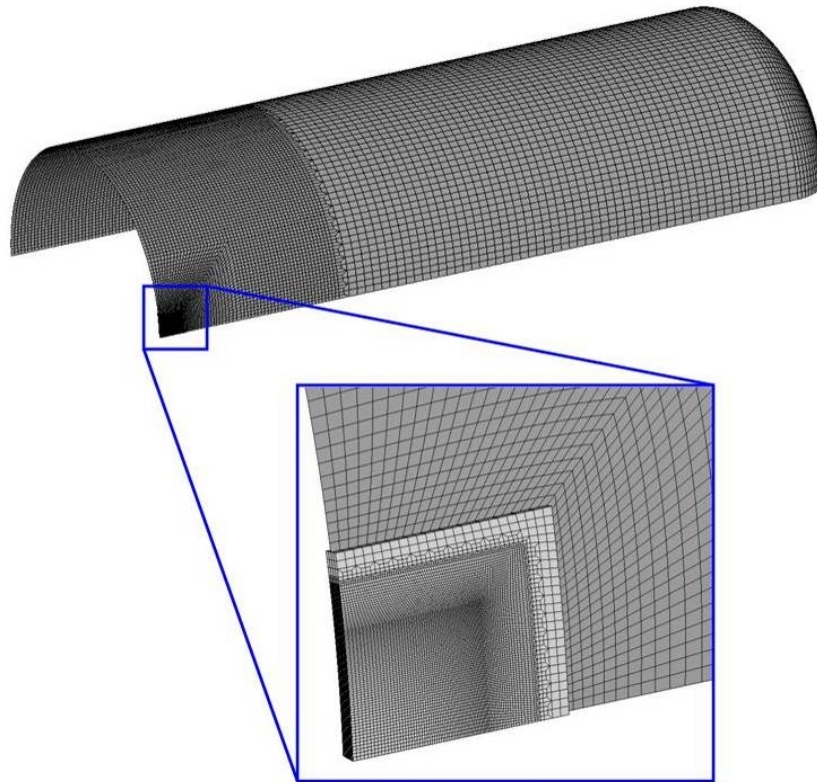
Figure 117. Tank model and impact zone mesh used for the 12x12 inch impactor.
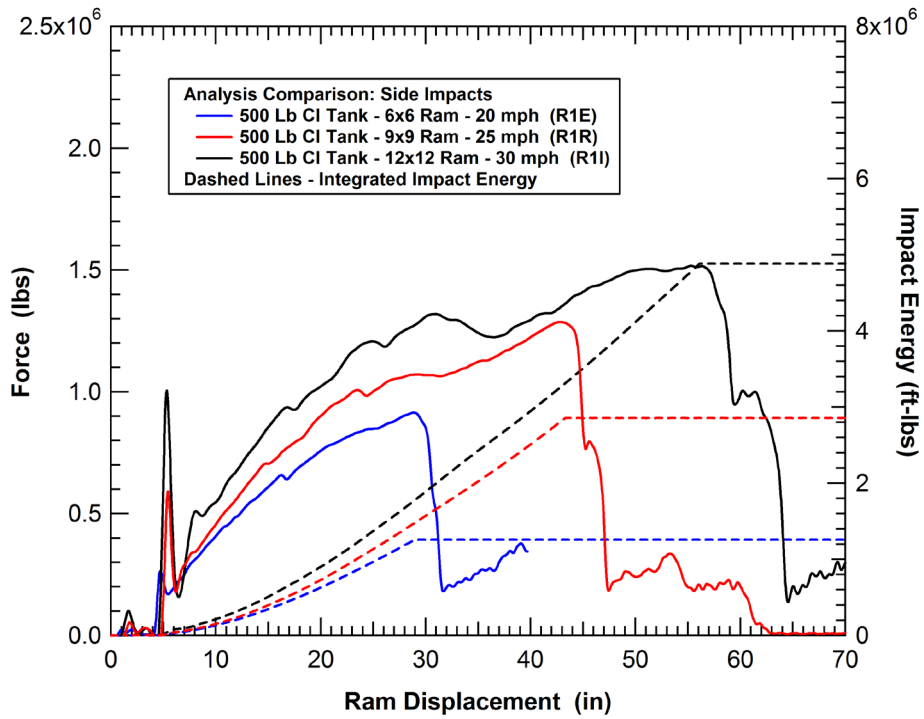
Figure 118. Evaluation of the effects of the ram size on a 500 lb chlorine tank.
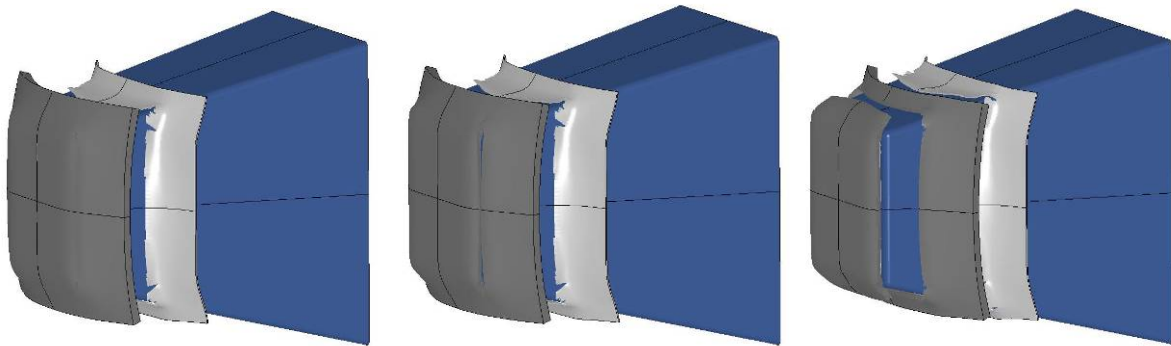
Figure 119. Calculated puncture initiation and fracture progression (12 inch x12 inch ram).

A similar set of analyses were performed on the 600 lb chlorine tank car being impacted by both the 9 inch and 12 inch impactors. A comparison of the force-deflection behaviors and puncture energies with the 6 inch, 9 inch, and 12 inch square impactors are shown in Figure 120. The 9 inch impactor increases the puncture load from 1.15 to 1.7 million lbs and the corresponding puncture energy from 1.74 to 3.94 million ft-lbs. The 12 inch impactor increases the puncture load from 1.15 to over 2.0 million lbs and the corresponding puncture energy from 1.74 to over 8.5 million ft-lbs.
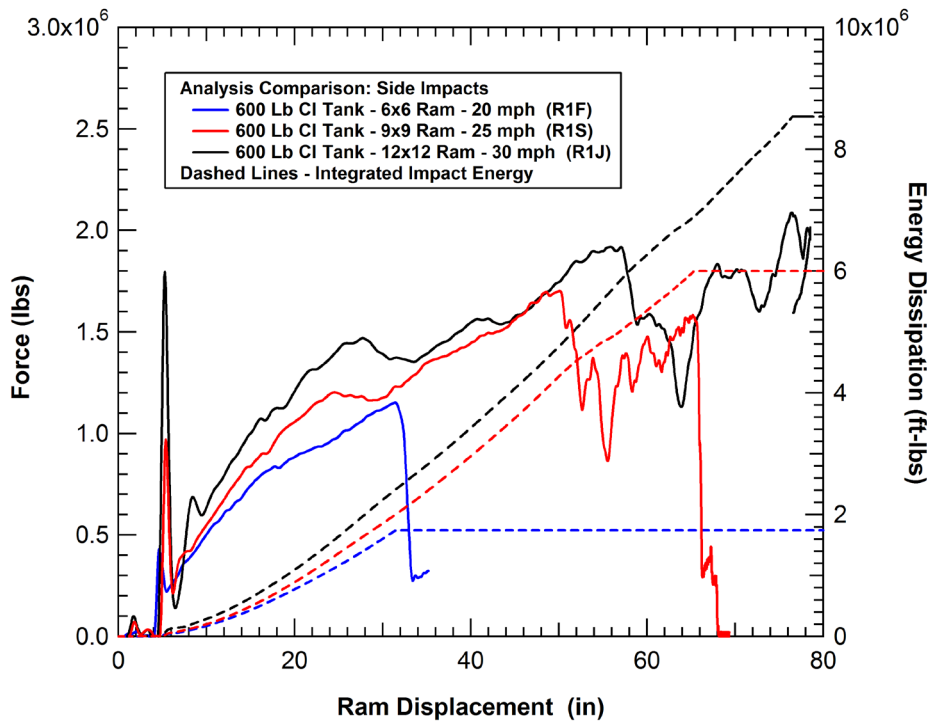
Figure 120. Evaluation of the effects of the ram size on a 600 lb chlorine tank.

One parameter in these analyses that can potentially influence the response is the impact velocity. In general we expect that the impact velocity will not have a large influence on the puncture behavior. However, the impact dynamics of the dent formation and the relative timing of the forces between the ram and the tank and between the tank and the reaction wall will be influenced by the impact velocity. An example comparison of the impact behavior for the 600 lb tank with the 9x9 inch impactor at 25 and 30 mph is shown in Figure 121. The impact speed has little effect on the puncture force. However, in this example, the impact speed has a significant effect on the puncture energy since the 30 mph impact fails right before the first peak of the force-deflection curve and the 25 mph impact fails in the second peak.
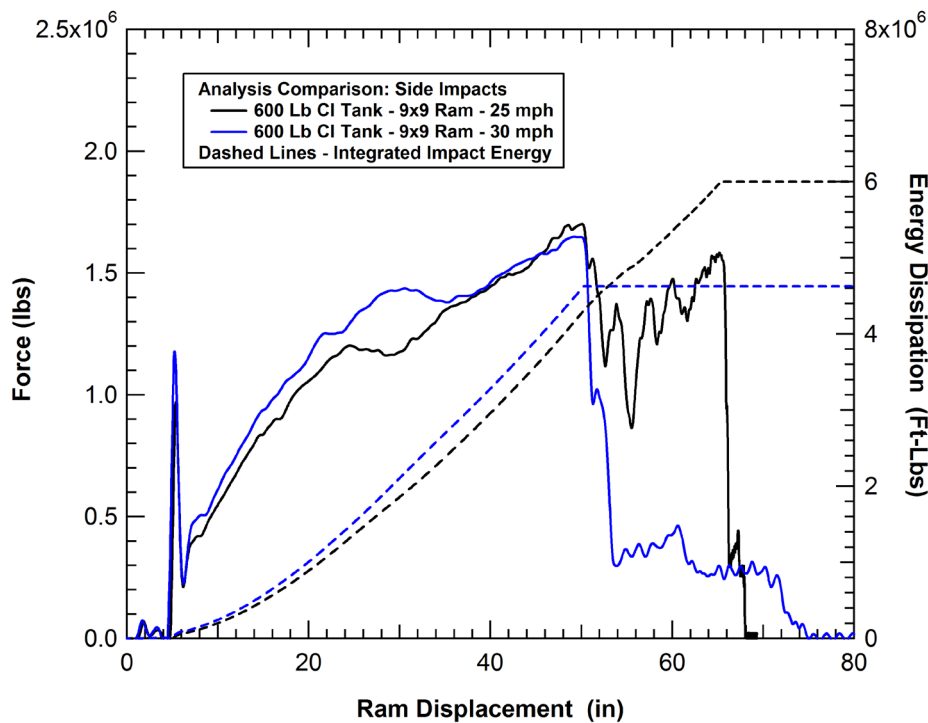
Figure 121. Effect of impact speed on the puncture behavior of the 600 lb CI tank.

The larger displacements and force levels associated with the larger ram open new opportunities to incorporate alternative protection systems to increase puncture resistance and energy dissipation. The simple retrofit design with the 0.375-inch jacket impacted by the 12x12 inch ram is shown in Figure 122. The thicker retrofit jacket increases the puncture energy to over 8 million ft lbs with the 12 inch impactor (a 77 percent increase over the 11 gauge jacket). This large increase results from the flattening of the force-deflection profile for ram displacements greater than 25 inches. Larger impactors, such as a coupler head, are often seen as a hazard in severe collisions or derailments. The effective dimensions of the coupler head are difficult to define due to the complex geometry. The external dimensions of the coupler head are approximately 13x22 inches. The contact area of the knuckle that would be the initial contact is

approximately 7x11 inches. By considering a wider range of impactors and collision conditions, a more optimized protection design may result that can further reduce the probability of a hazardous material release.
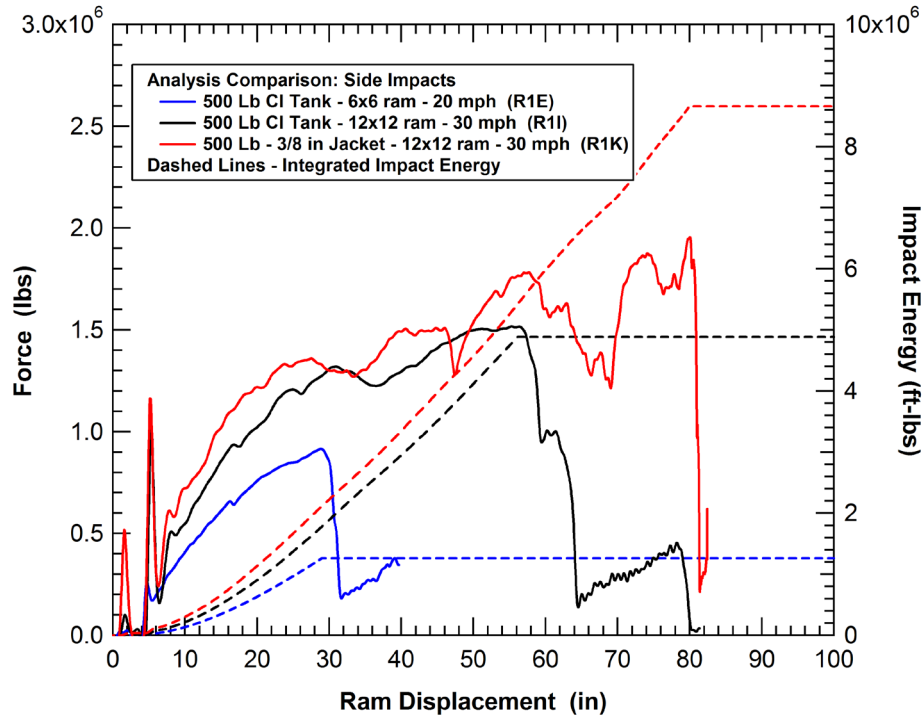
Figure 122. Evaluation of the effects of the reinforced jacket with the large ram size.

A summary of the effect of the impactor size on the puncture force and puncture energy for the 500 lb and 600 lb Cl tank cars are shown in Figure 123 and Figure 124, respectively. The two points plotted for the 600 lb tank car and 9-inch ram size represent the results for the analyses at 25 and 30 mph impact speeds, compared previously in Figure 121. The puncture force for the various impactors is compared to linear extrapolations through the forces produced by the 6 inch impactor. If the failure mode was dominated by the shear stress around the perimeter of the impact face, we would expect that the analyses would approximately follow these linear fits (this failure mode is discussed for the 6-inch impactor analyses below in Section 0). The drop off in the puncture force at larger impactor sizes (compared to the linear fits) indicates that different failure mechanisms are being introduced. The simplest explanation is that the load around the perimeter of the impactor was not uniform and that there was a less uniform distribution with increasing impactor size (e.g. a greater concentration of the load at the corners of the impactor).
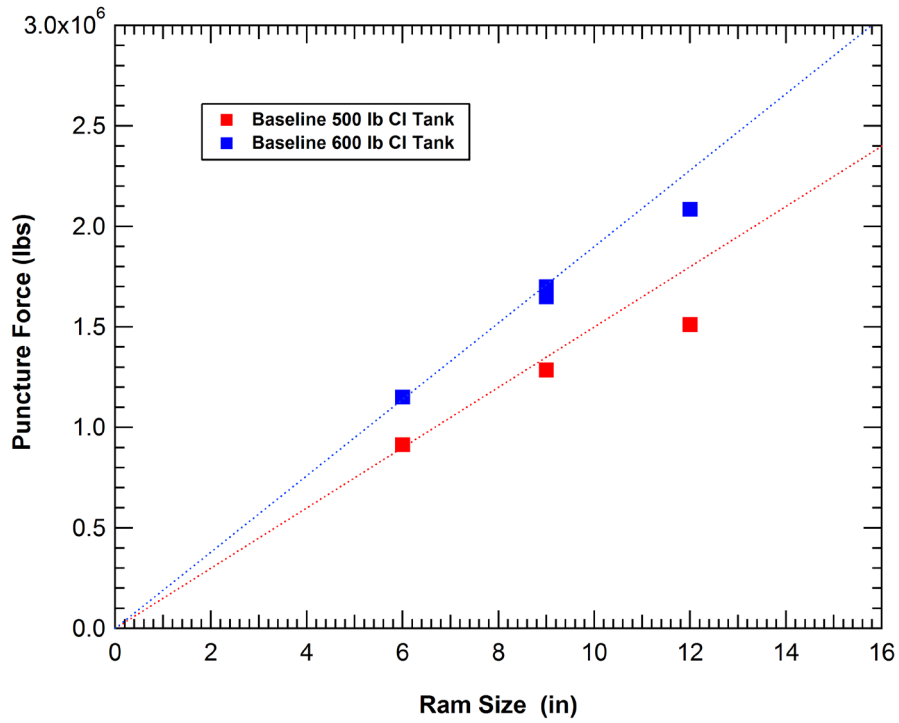
Figure 123. Summary of puncture forces for chlorine tank cars for various impactor sizes.
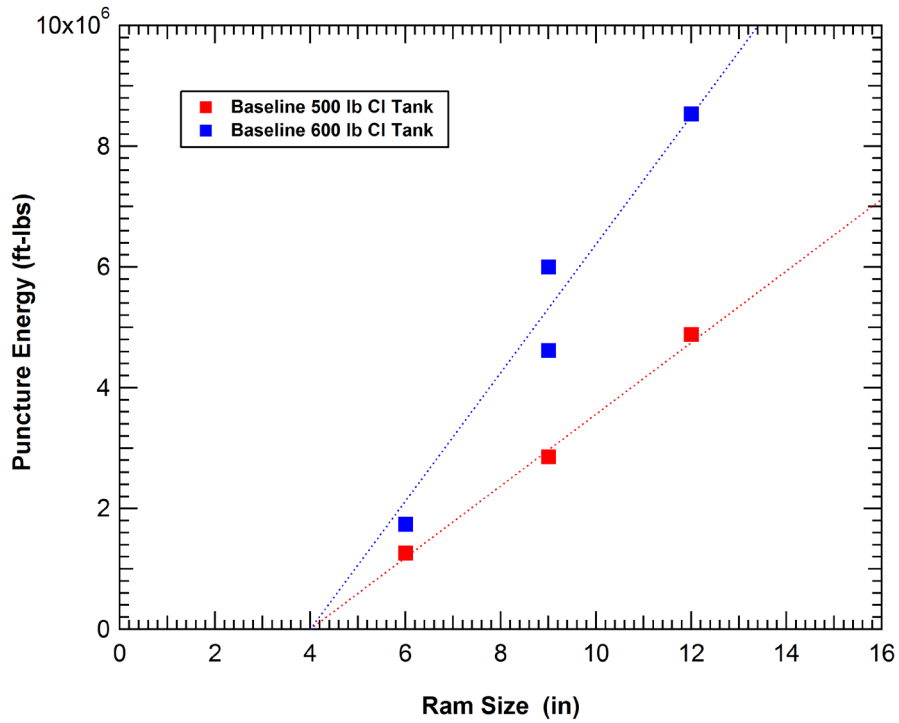
Figure 124. Summary of puncture energies for chlorine tank cars for various impactor sizes.

The comparison of puncture energies in Figure 124 shows that the increasing impactor size has a strong influence on the puncture energy. Note that the linear fit to the puncture energies shown in do not pass through the origin of the graph. Higher energies result from the significant increases in the displacement prior to puncture as the puncture force was increased (as seen in Figure 117 and Figure 120). This shows that any protective system that could blunt the loads and make the ram act like a larger impactor against the commodity tank would be an effective protection system.

One potential modeling approximation that could influence the above assessment of impactor size was the simplified modeling of the internal pressure. In these analyses the internal pressure was a constant 100 psi. However, with the formation of the dent in the tank during impact there will be an increasing hydrostatic internal pressure level. For the 6 inch impactor this increase in pressure was relatively small (10%-15%). However, the larger dents produced by the larger impactor sizes would result in a larger internal pressure increase.

The energy balance for the 600 lb chlorine car impact and the 12x12 inch impactor is shown in Figure 125. In this analysis, the tank was not fully punctured. However, threshold fracture initiation at the inside surface of the tank shows that puncture was very near. The initial impact energy is nearly 9 million ft-lbs (initial kinetic energy). As the impact progresses the ram is decelerated and the kinetic energy drops off nearly to zero. The energy transfer is from the kinetic energy of the ram to the internal energy of the tank (plastic deformations of the tank material) and the pressure-volume work caused by the indentation reducing the total tank volume. The internal energy of the tank at the end of the calculation is approximately four million ft-lbs and the peak pressure volume work is approximately 4.7 million ft-lbs. The hourglass energy and sliding energy in the calculation are both small.

Based on the energy transfer to the pressure-volume (PV) work, the effects of the tank volume change can be assessed. The 4.7 million ft-lbs PV work corresponds to a change in volume of 326 cubic feet (2438 gallons) with a constant 100 psi (14400 psf) pressure assumption. Using a tank nominal capacity of 17,300 gallons, the change in volume is approximately 14%. Therefore, the change in volume (ΔV) is more than the original outage volume (approximately 10%) and the pressure would increase significantly during the response.

To determine the influence of the variable internal pressure during the impact an additional series of analyses was performed. In these analyses, a control volume was established for the tank and the change in volume was used to calculate a corresponding change in pressure. The assumption in these analyses is that the tank has a 10.6% outage and the gas in the outage follows an ideal constant temperature compression behavior during impact. The resulting relationship between the relative volume and pressure in the tank is shown in Figure 126.

91
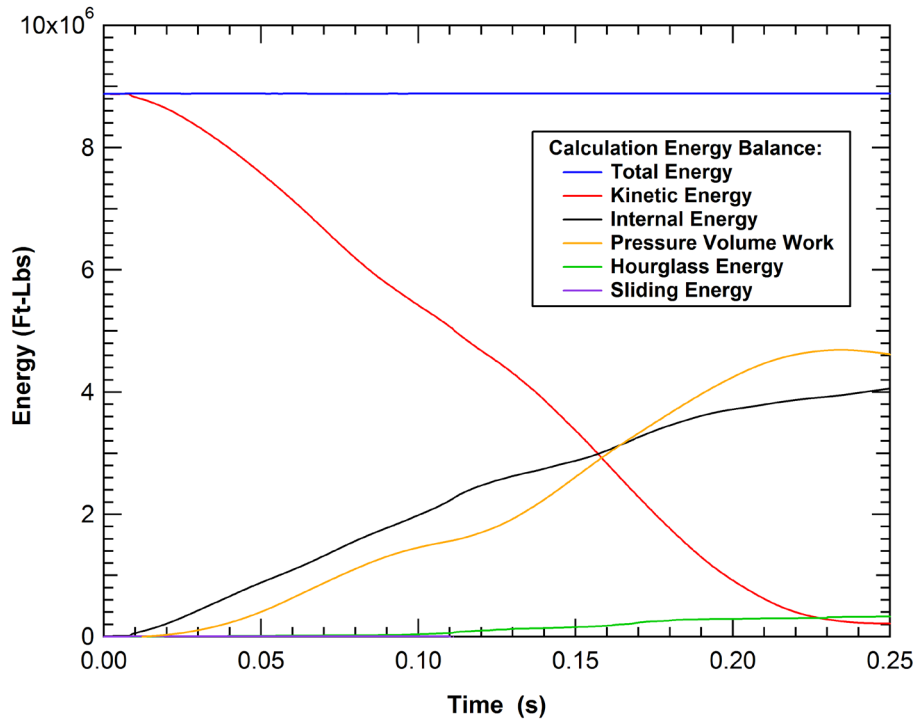
Figure 125. Calculated energy balance for the 600 lb Cl tank car 12x12 impact (R1J).
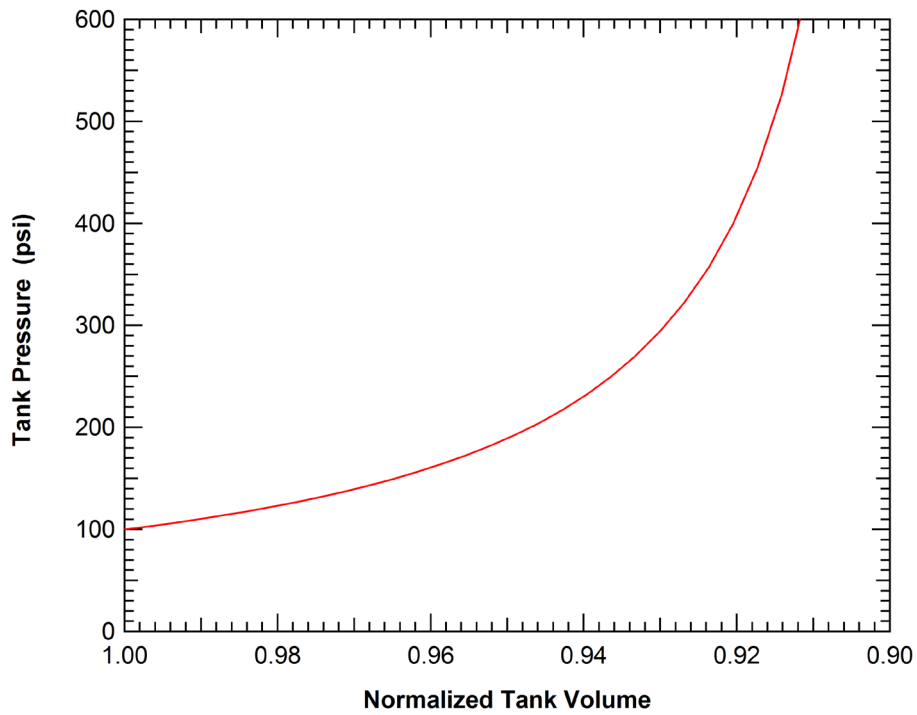
Figure 126. Pressure-volume relationship used for the tank control volume (10.6% outage).

The force-deflection curves with both constant and variable internal pressure for the 500 lb and 600 lb Cl tanks and the three different impactor sizes are shown in Figure 127 and Figure 128, respectively. For the updated analyses with the variable pressure, the impact velocities were also reduced by 5 mph to be closer to the expected puncture threshold velocity. Adding variable pressure to the model results in a stiffening of the later portions of the force-deflection curve and a reduction in the ram displacements prior to the tank puncture. The reductions are more significant for the larger ram sizes. This is expected since the larger rams have larger displacements prior to the puncture with a larger associated pressure change inside the tank.
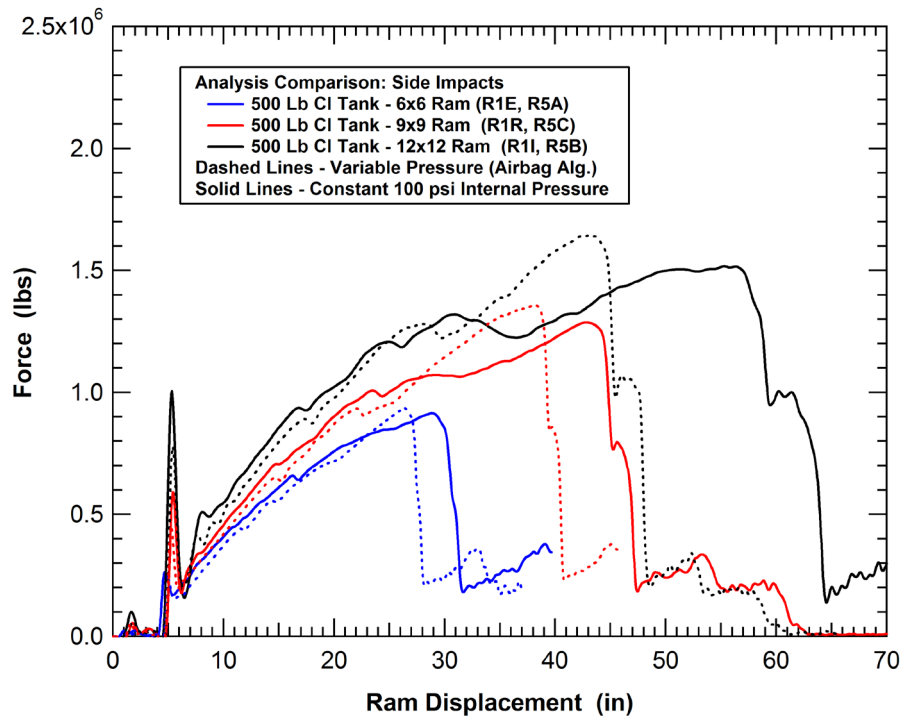
Figure 127. Effect of variable internal pressure on 500 lb tank impact response.

The control volume pressure histories for the three 500 lb Cl tank impact analyses are plotted as a function of the ram displacement in Figure 129. In the 6x6 inch impactor analysis the pressure change is less than 10% and the previous approximation of a constant 100 psi internal pressure is a reasonable simplification for the analyses. For the 9x9 and 12x12 inch impactors, the internal pressures increase to approximately 120 psi and 140 psi, respectively, at the point of the puncture initiation. These pressure increases are becoming sufficiently large to influence the tank effective stiffness during the impact.
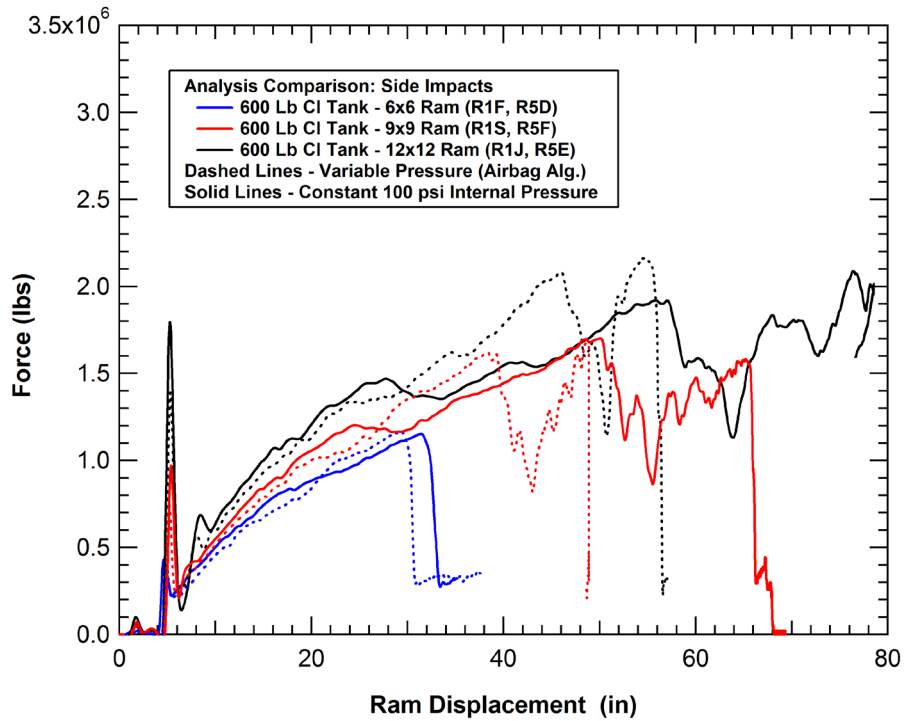
Figure 128. Effect of variable internal pressure on 600 lb tank impact response.
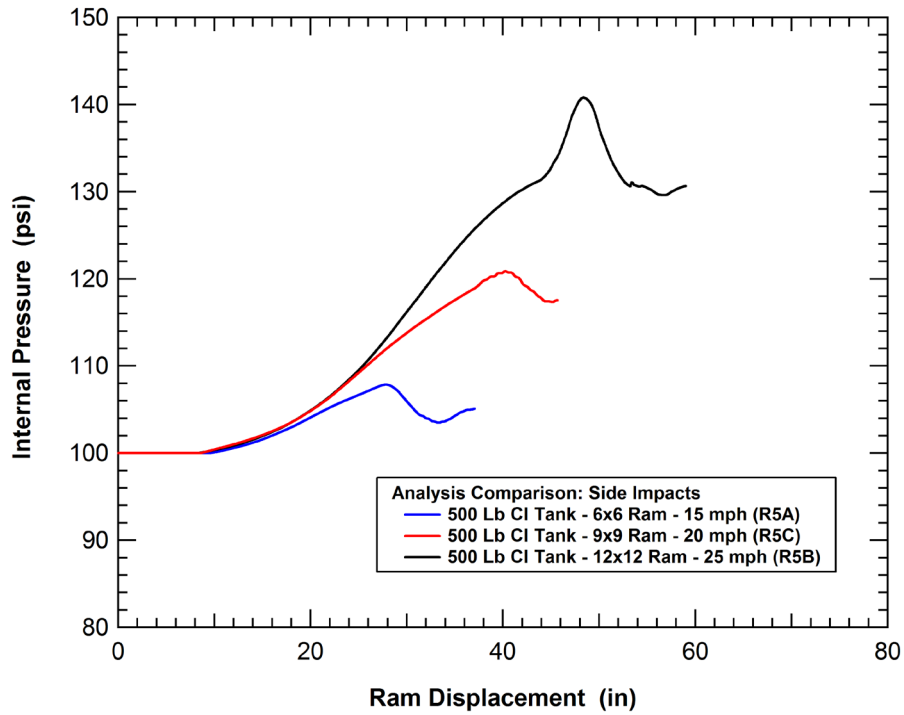
Figure 129. Calculated internal pressure variations in the 500 lb tank impact analyses.

The control volume pressure histories for the three 600 lb Cl tank impact analyses are plotted as a function of the ram displacement in Figure 130. The pressure histories for the 500 lb tank impact analyses are also included as the dashed lines in the figure for comparison. In the 6x6 inch impactor analysis, the pressure change is again less than 10% and the approximation of a constant pressure remains reasonable simplification. However, for the 9x9 and 12x12 inch impactors, the internal pressures increase to approximately 160 psi and 215 psi, respectively, at the point of the puncture initiation. These pressure increases are sufficiently large to significantly influence the tank effective stiffness during the impact.
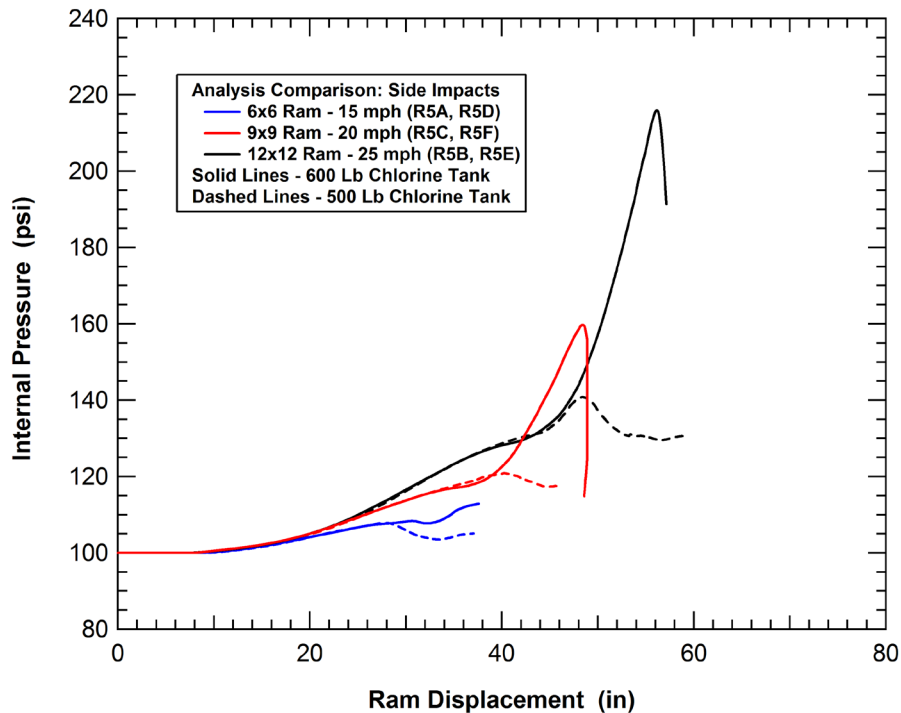
Figure 130. Calculated internal pressure variations in the 600 lb tank impact analyses.

The rate of pressure rise dramatically increases after about 40 inches of ram displacement, as seen in Figure 130. This change in behavior corresponds to the time when the commodity tank begins to significantly engage the reaction wall and the back side of the tank (opposite the ram impact point) begins to deform. This corresponds to the development of the second peak in the force-deflection curve.

The updated force-deflection curves and integrated puncture energies with the different size impactors are summarized in Figure 131 and Figure 132. The addition of the control volume and variable internal pressure produces a more linear relationship between the force and deflection than obtained with the constant internal pressure (shown previously in Figure 118 and Figure 120). The corresponding updated summaries of the peak puncture forces and puncture energies

for all of the analyses at different ram sizes are provided in Figure 133 and Figure 134, respectively. The comparisons show that the variable internal pressure does not have a significant influence on the puncture forces but does reduce the puncture energies by approximately 25-30% in the analyses with the 9x9 and 12x12 inch impactors.
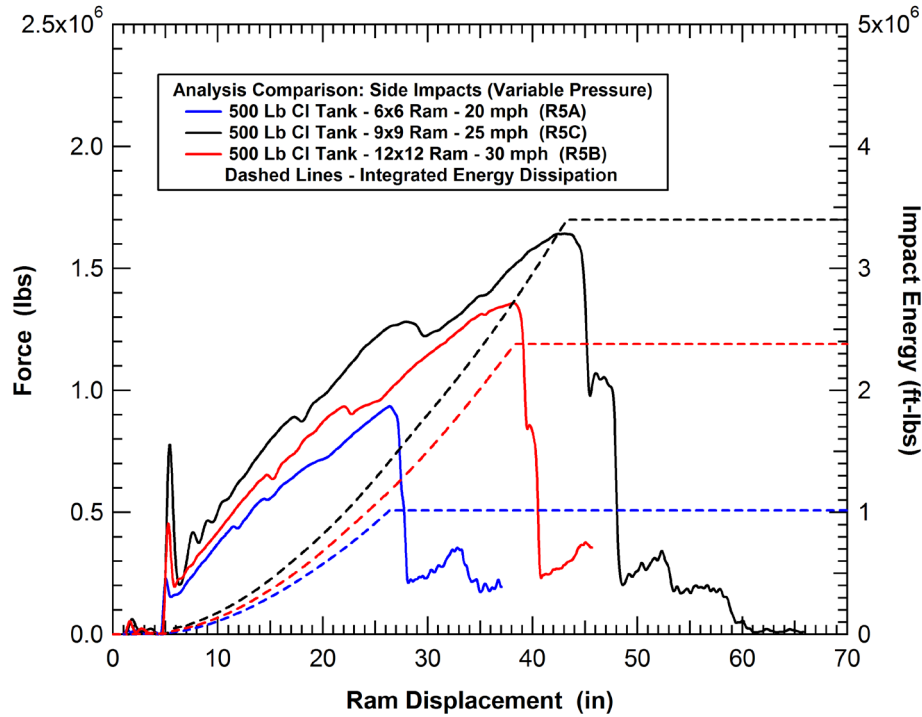
Figure 131. Updated 500 lb tank impact analysis with different size impactors.
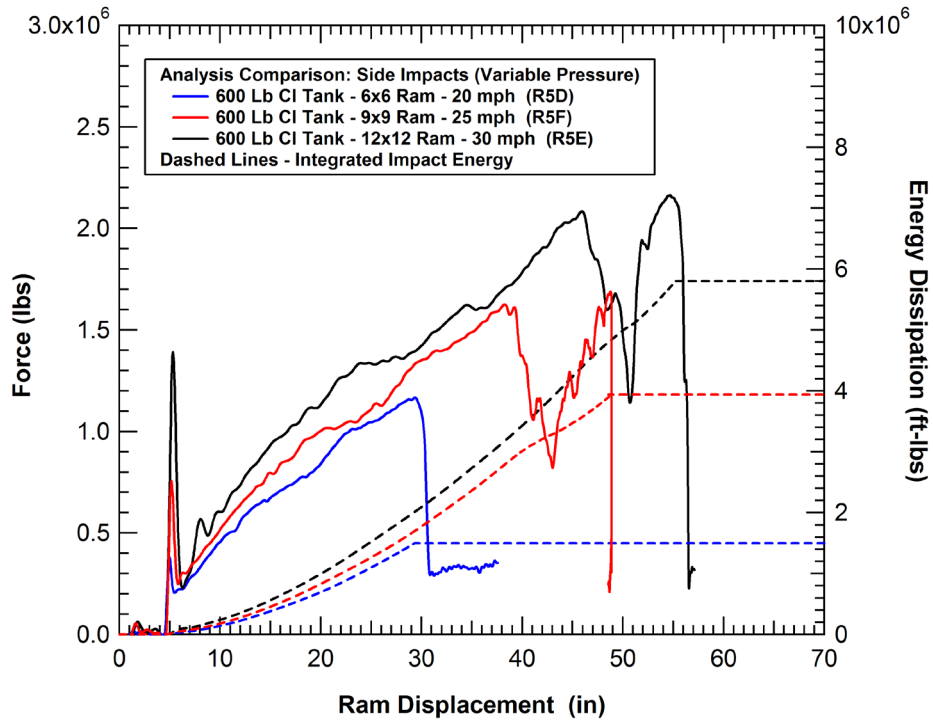
Figure 132. Updated 600 lb tank impact analysis with different size impactors.
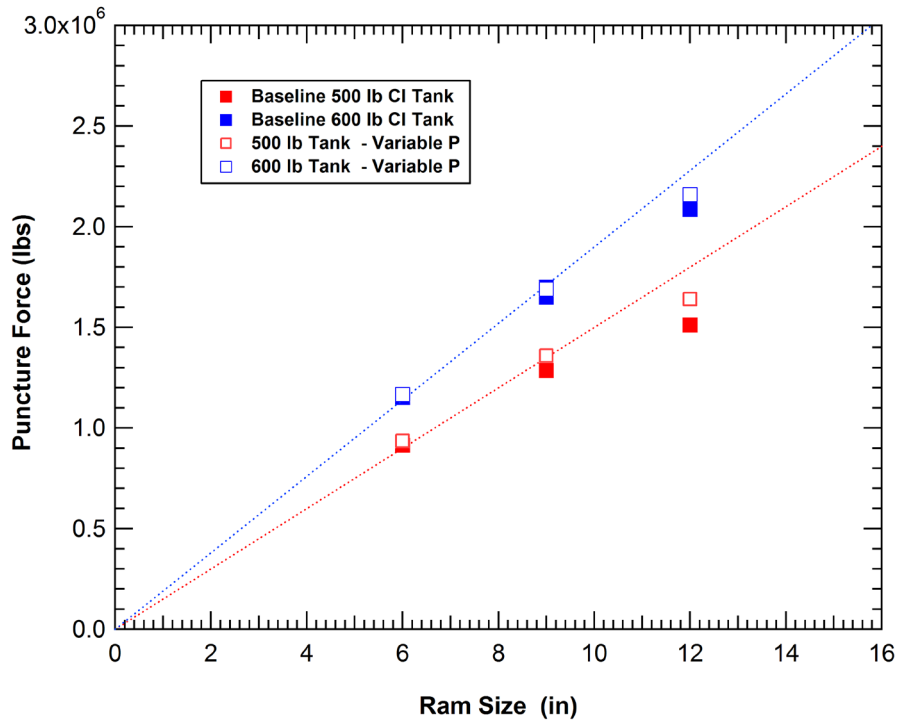
Figure 133. Summary of puncture forces for chlorine tank cars for various impactor sizes.
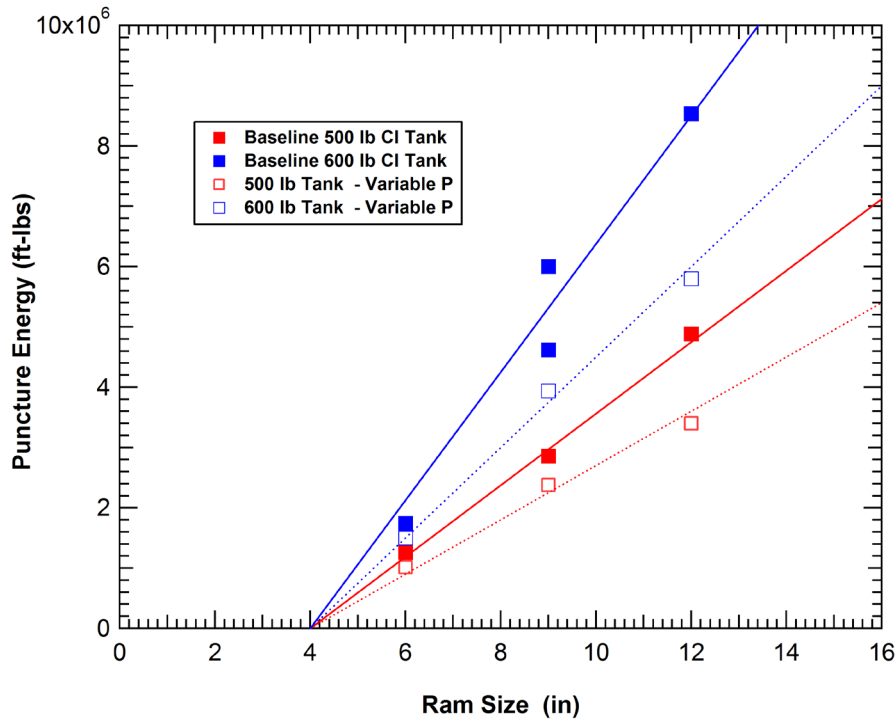
Figure 134. Summary of puncture energies for chlorine tank cars for various impactor sizes.

4.3.4 Effects of Outage Volume

An additional factor that can influence the puncture energy is the percentage of the tank volume that is reserved as the outage volume. To evaluate the effects of the outage volume a series of impact calculations were performed on an unpressurized tank with a geometry corresponding to a DOT-111A100W tank car (no jacket). The specific geometry modeled is a 23,000 gallon tank shown in Figure 135. The tank is 110-inches in diameter with a 44-foot 7-inch long cylindrical shell and 2:1-ellypsoidal heads. The tank is constructed with a 0.4375-inch-thick A516-70 steel tank shell. The tanks are impacted by the standard 6x6 inch impactor (286,000 lbs) at a speed of 16.2 mph corresponding to an initial 2.5 MJ impact energy.

The tanks in the analyses were modeled as initially unpressurized with a control volume algorithm used to include the pressure-volume effects. Control volume curves were generated representative of a tank filled with an incompressible liquid to various levels up to as much as 99 percent of the tank capacity (1 percent outage). The control volume pressure curves (gauge pressure) for outage volumes between 1 and 18 percent are shown in Figure 136 and are generated assuming the outage volume contains an ideal gas initially at one atmosphere (absolute pressure).
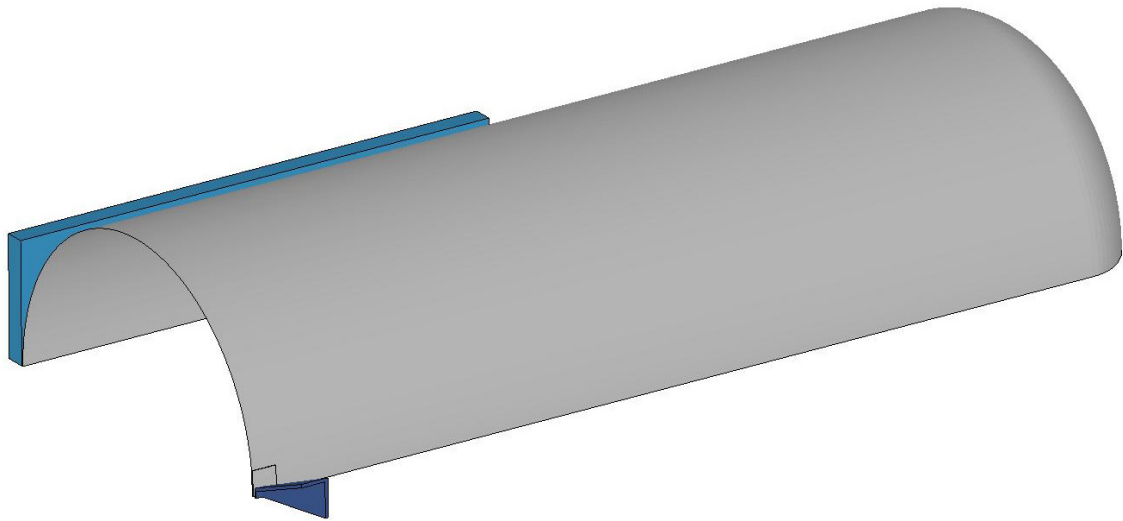
(a) ¼-symmetry model of tank, ram, and reaction wall
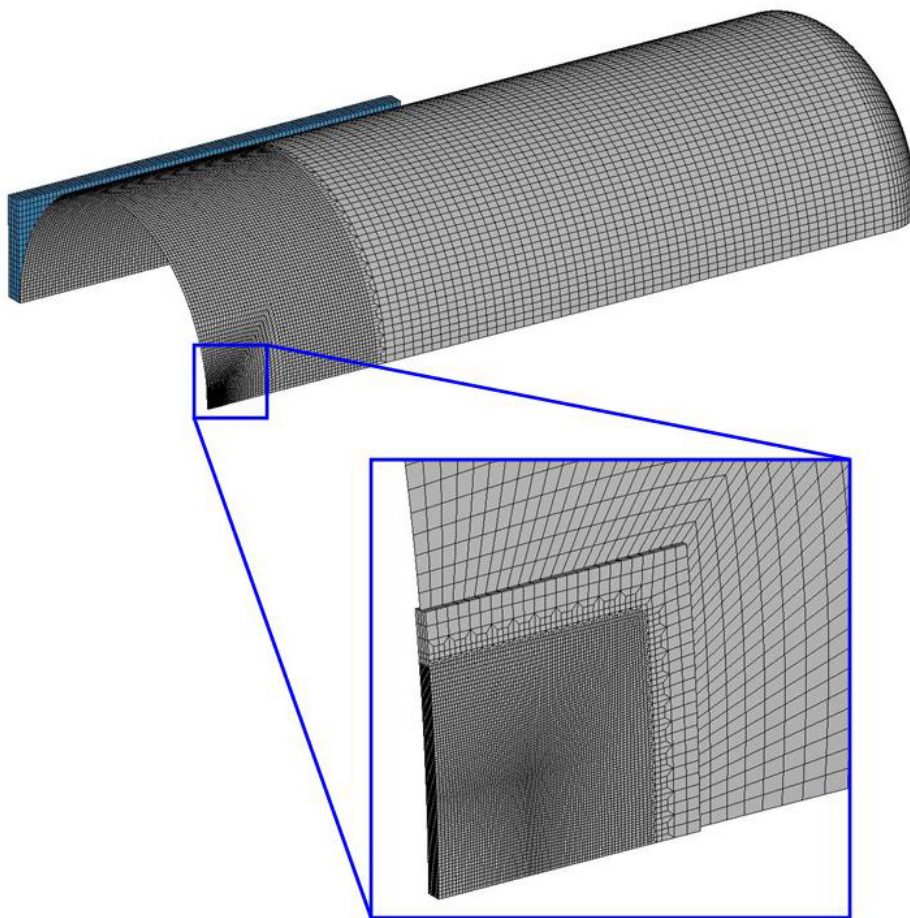
(b) Mesh resolution of the tank and impact patch

Figure 135. Model of a 23,000 gallon DOT-111A100W tank for analysis of outage volume effects.
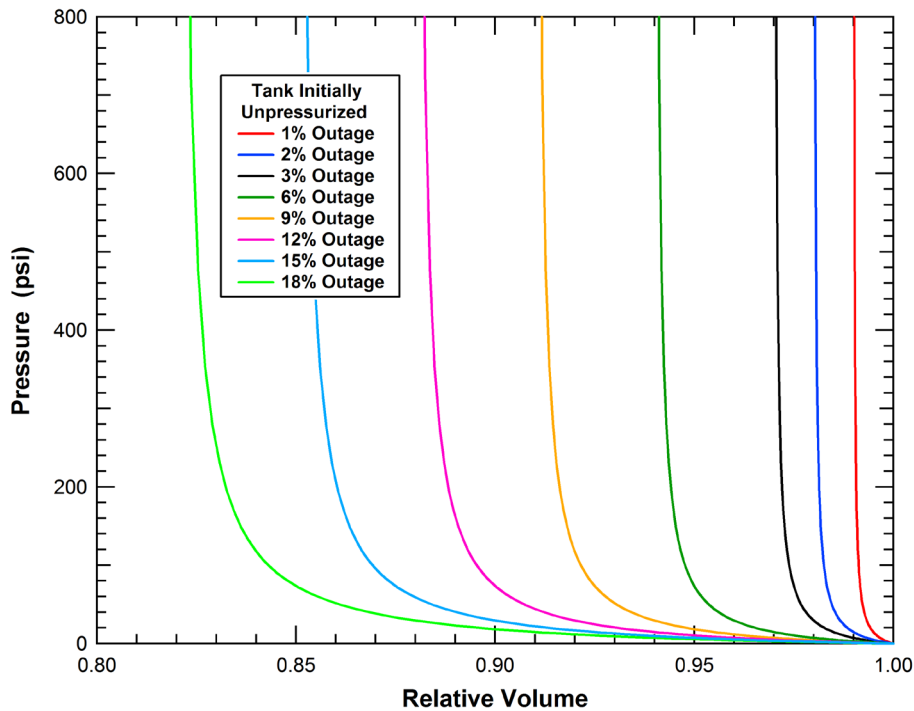
Figure 136. Control volume pressure curves for various outages between 1 and 18 percent.

A comparison of the impact deformations at the point of the tank shell penetration (puncture) for the 1, 3, and 9 percent outage volumes are shown in Figure 137. The comparison clearly shows that the larger outage volumes allow for a larger ram displacement before the tank is punctured. The comparison of the corresponding force-deflection behaviors and puncture energies with the different outage volumes is shown in Figure 138. A summary of the results from all of the calculations is provided in Table 4. The comparison shows that tanks with outage volumes between 1 and 18 percent are punctured at similar force levels (392,000 to 467,000 lbs) but at significantly different displacements (16 to 65 inches) resulting in puncture energies between 256,000 and 1,370,000 ft-lbs.

The calculated control volume pressures in the various analyses are compared in Figure 139 and the corresponding pressures at the time of tank puncture are included in Table 4. As expected, the displacement required to develop an internal pressure increase is significantly larger for the larger outage volumes. Another interesting find is that the calculated pressure levels at the point of the tank puncture is significantly reduced for the larger outage volumes. Thus, the fraction of the impact force resulting from the impact deformations is larger as the puncture deformation is increased and the effects of increasing the outage volume would be expected to have a diminishing return.
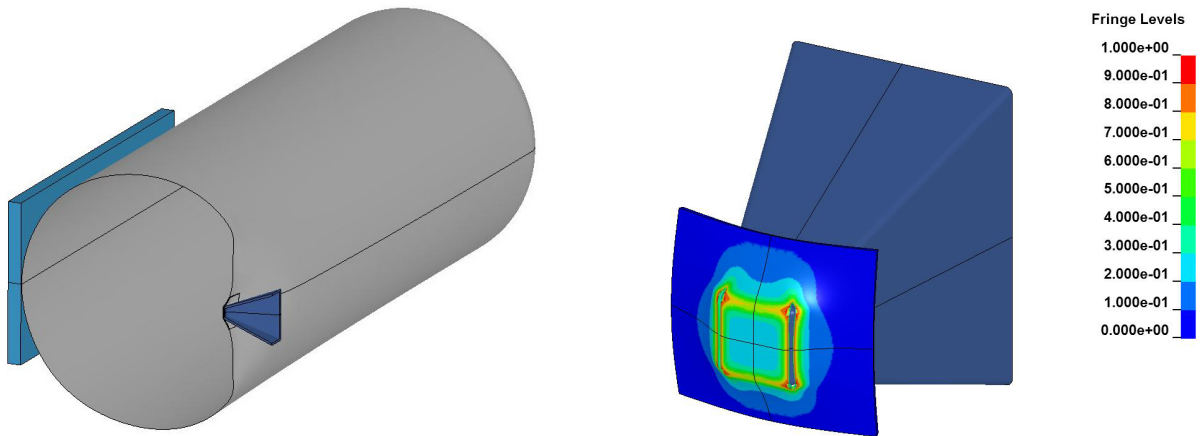
(a) Deformation at puncture for 1% outage
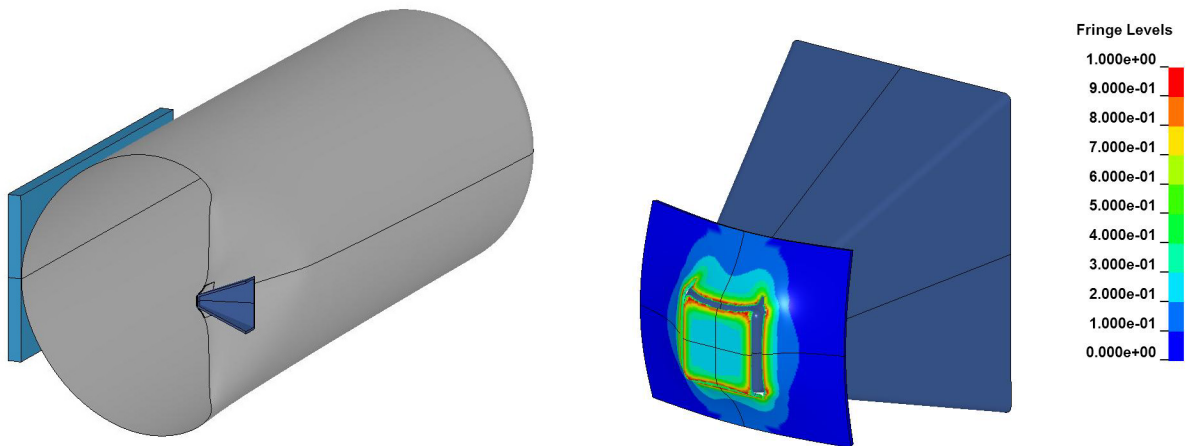
(b) Deformation at puncture for 3% outage
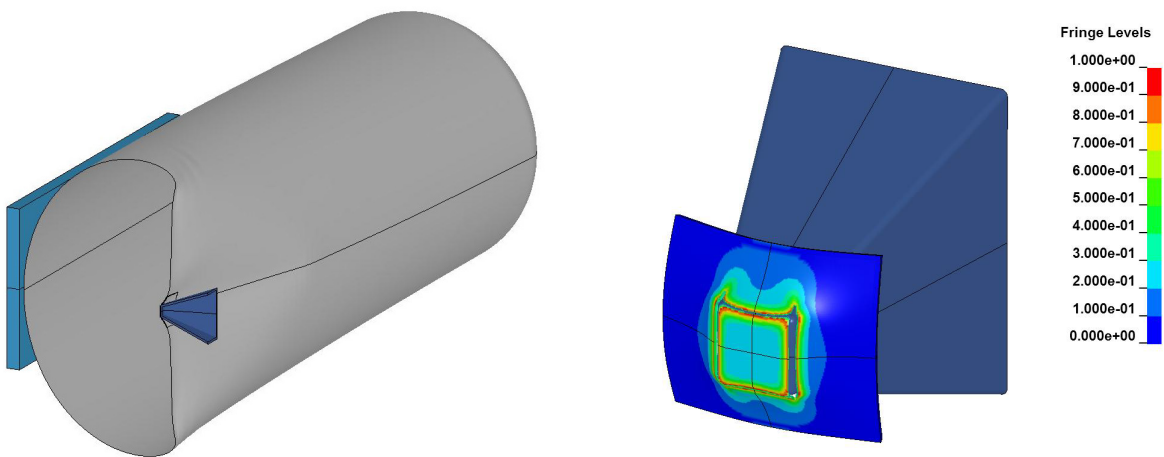
(c) Deformation at puncture for 9% outage

Figure 137. Calculated impact and puncture behaviors for different outage volumes.
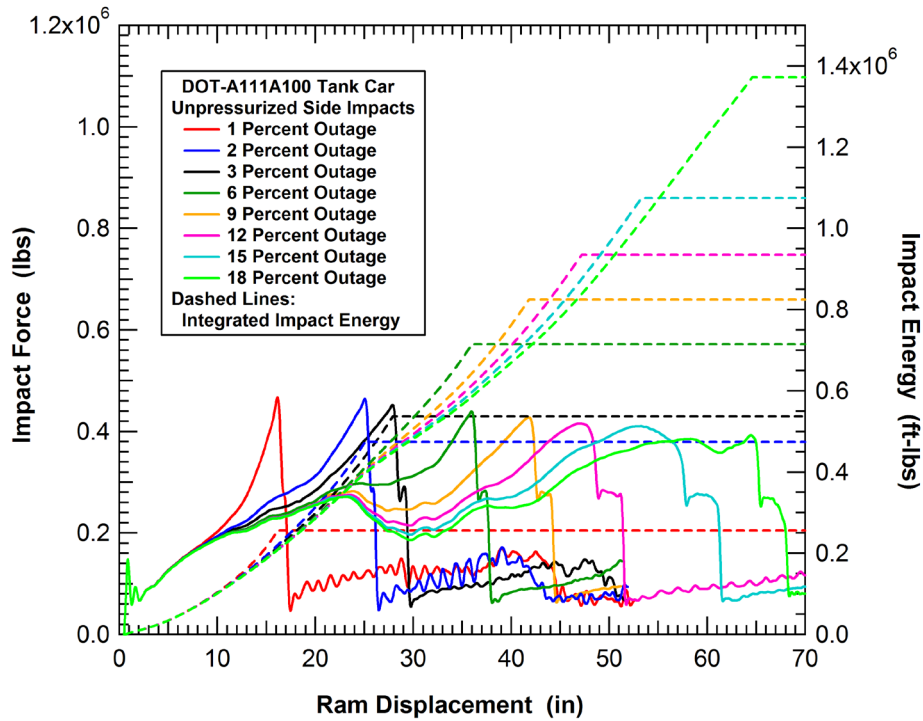
Figure 138. Force-deflection curves and puncture energies for different outage volumes.

Table 4. Summary of impact analyses to assess outage volume effects

Outage Volume	Tank Shell	Impact Conditions	Ram Puncture Displacement	Puncture Force (lbs)	Puncture Energy (ft-lbs)	Pressure at Puncture
1 %	0.4375 in A516-70	16.2 mph 6"x6" ram	16 inches	467,000	256,000	178 psi
2 %	0.4375 in A516-70	16.2 mph 6"x6" ram	25 inches	464,000	474,000	89 psi
3 %	0.4375 in A516-70	16.2 mph 6"x6" ram	28 inches	452,000	537,000	53 psi
6 %	0.4375 in A516-70	16.2 mph 6"x6" ram	36 inches	439,000	715,000	29 psi
9 %	0.4375 in A516-70	16.2 mph 6"x6" ram	42 inches	428,000	825,000	22 psi
12 %	0.4375 in A516-70	16.2 mph 6"x6" ram	47 inches	415,000	935,000	18 psi
15 %	0.4375 in A516-70	16.2 mph 6"x6" ram	53 inches	410,000	1,075,000	17 psi
18 %	0.4375 in A516-70	16.2 mph 6"x6" ram	65 inches	392,000	1,370,000	21 psi
100 %	0.4375 in A516-70	16.2 mph 6"x6" ram	>110 inches	n/a	>1,800,000	n/a
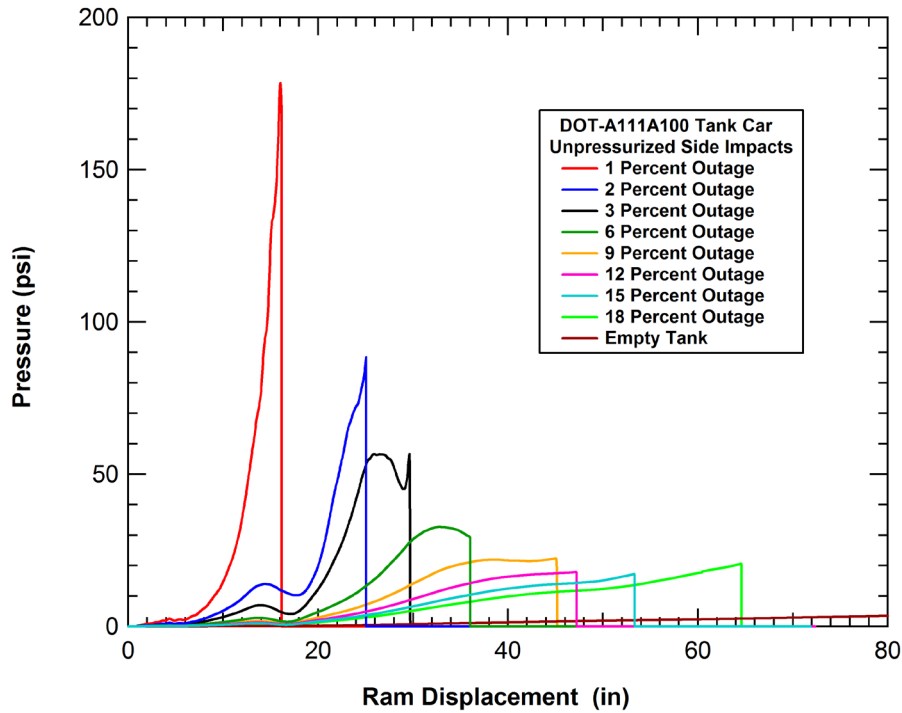
Figure 139. Control volume pressures for impacts with different outage volumes.

The calculated puncture energies are plotted against the outage volume in Figure 140. Also included in the figure is an approximate fit to the calculated energies. The functional form of the fit is a puncture energy that is proportional to the square root of the outage volume. Thus, the effect of an incremental increase of the outage volume results in a corresponding smaller increase in the puncture energy as the outage volume grows larger.

The calculated puncture energies have some natural variability about the functional fit. This variability can be seen by considering the impact behavior of an empty tank as shown in Figure 141. In the empty tank analysis the impactor dents the side of the tank and the dent continues to grow until the impactor eventually impacts the far side of the tank and impact wall (greater than 110 inch dent depth. As the side of the tank collapses the resistance of the tank dent oscillates between 150,000 and 300,000 lbs as the dent grows, never reaching a level that is sufficient to puncture the tank wall. The timing of the puncture for the different outage levels would be influenced by these natural variations in the impact resistance and as a result the calculated puncture energies do not fall directly on the smooth functional fit.
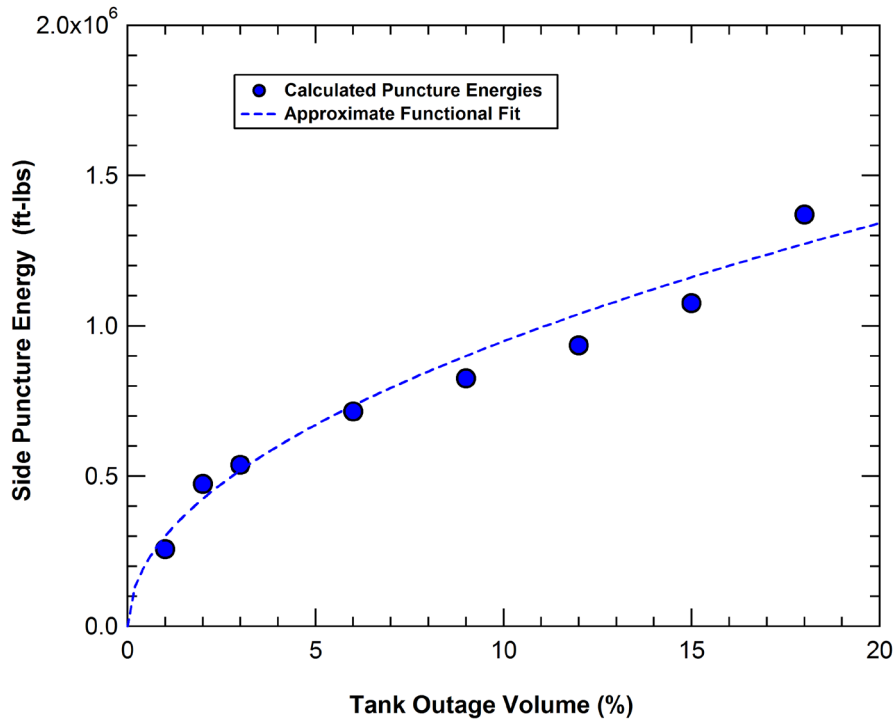
Figure 140. Effect of the outage volume on the puncture energy in side impacts.
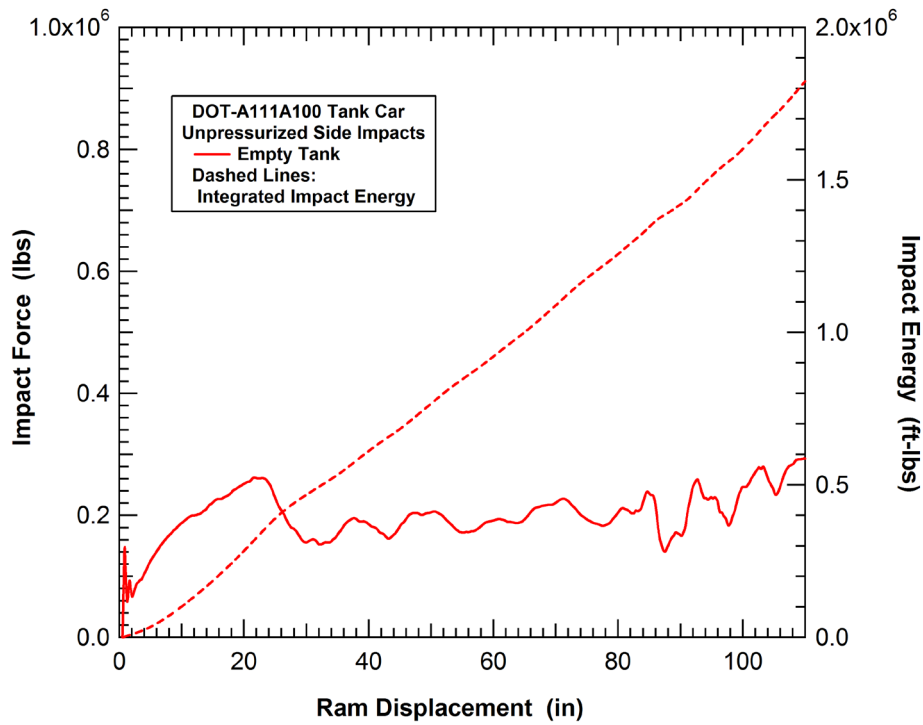
Figure 141. Force-deflection curve and impact energy dissipation for an empty tank.

An inspection of the puncture results in Table 4 indicates a trend of modest reduction in the puncture force as the outage volume is increased. The mechanisms believed responsible for this is the uniformity of the stresses around the edge of the impact face. The profile of the impact damage during the indentation process for both the 1 percent and 18 percent outage calculations is shown in Figure 142. When the tank has a 1 percent outage volume the damage development is relatively uniform around the perimeter of the contact patch other than the slight concentrations of damage at the corners of the impact face. However, for the 18 percent outage the damage along the top and bottom of the impact face is greater than that along the sides of the impactor. In addition, the larger dent depths would allow for more plastic bending around the edges and corners of the impact face which could result in a less uniform stress state and damage development through the thickness of the tank wall.

(a) Damage Profile for 1% outage　　　　**(b) Damage Profile for 18% Outage**
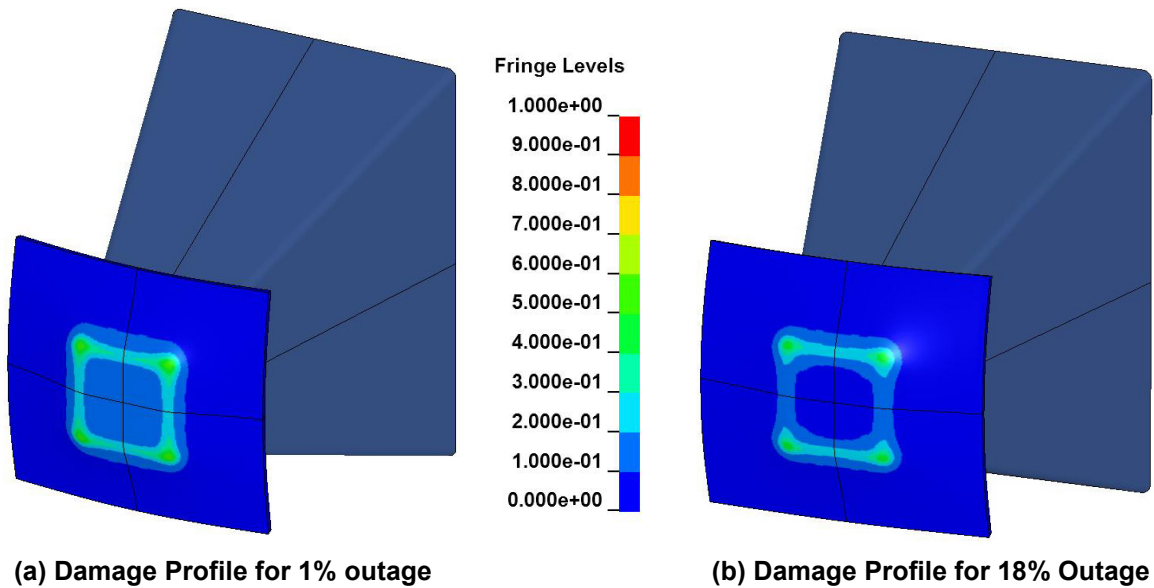
Figure 142. Side impact damage distribution for 1% and 18% outage volumes.

4.3.5 Effects of Impact Speed

A potential factor for assessing the impact conditions that will puncture a tank is the speed of the impacting object. As a reference, the lower bound of impact speed was assessed by performing a quasistatic loading of the tank car using the 6x6 inch impactor as a punch. The comparison of the dynamic impact response with the quasistatic behavior is shown in Figure 143.
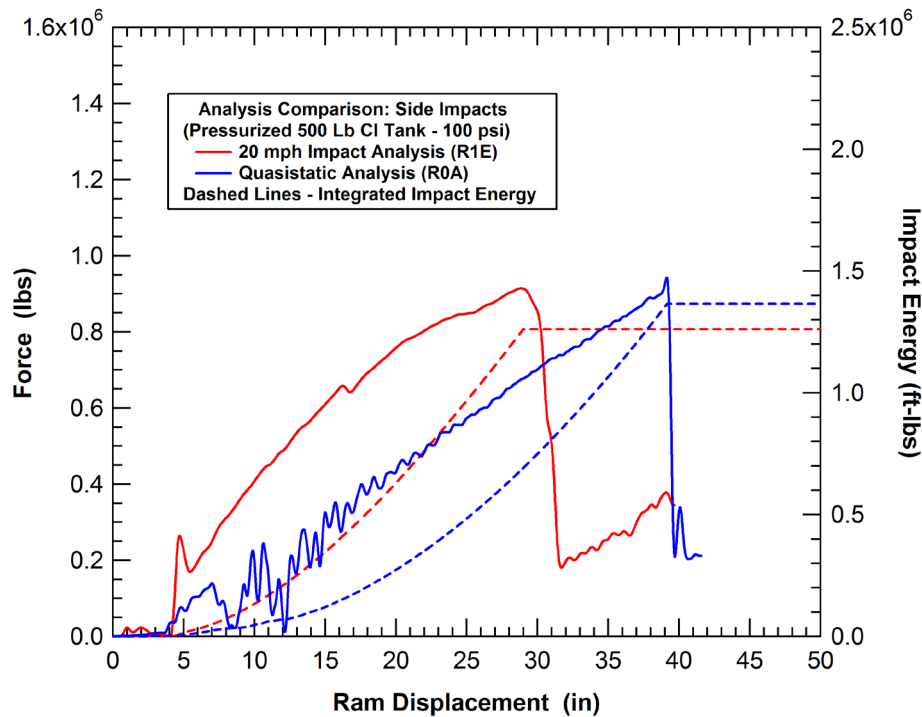
Figure 143. Effect of impactor speed on the puncture of a 500 lb CI tank.

The comparison shows that there are significant differences in the force deflection behavior in the dynamic and quasi-static loading. The quasistatic loading results in a lower force level for a given indentation depth and a much more linear force deflection characteristic where the reaction force is nearly proportional to the indentation depth. The higher force level in the dynamic impact is due to the inertial force contribution prodeuced by the need to rapidly accelerate portions of the tank to develop the indentation at 20 mph.

The reduced slope at late time in the dynamic analysis is produced by the drop in the relative speeds between the impactor and the tank. This contains contributions from both the impactor decelerating and the acceleration of the impacted tank.

4.3.6 Summary of the Side Impact Analyses

A summary of the NGRTC side impact analyses including the impact conditions and calculated puncture forces and energies is provided in Table 5 (excluding the outage effects analyses summarized in Table 4). The table includes the tank geometry, impact conditions, and the calculated puncture force and energy for each tank impact simulation.

The calculated puncture forces for all of the tank impact analyses using the 6x6 inch impactor are plotted against the combined thickness of the tank shell and jacket in Figure 144. The figure indicates a linear relationship between puncture force and total thickness of the protective layers.

The linear relationship between the puncture force and total tank system thickness provides an indication of the primary failure mechanism initiating the tank puncture. The geometry of the ram impacting and indenting a pressurized tank shell is shown in Figure 145(a). A force-balance analysis in the direction of the impact on a patch of tank shell material is shown in Figure 145(b). The forces resisting the impact loads are the pressure on the inside surface of the contact patch and the shear stress around the perimeter of the contact patch. For a 100 psi tank pressure and a 6x6 inch impactor, the total pressure load is less than 4 kips on the contact patch. Thus, the average shear stress is approximately equal to the impact force divided by the area of the perimeter of the impactor face divided by the tank thickness.

Table 5. Summary baseline side impact analyses

Calculation	Tank Type	Tank Shell	Shell Jacket	Impact Conditions	Internal Pressure (psi)	Puncture Force (lbs)	Puncture Energy (ft-lbs)
R1A	300 lb EO	0.5625 in TC128B	0.119 in A1011	20 mph 6"x6" ram	50 psi	616,000	1,145,000
R1B	423 lb EO	0.777 in TC128B	0.119 in A1011	20 mph 6"x6" ram	50 psi	883,000	1,663,000
R1C	534 lb EO	0.981 in TC128B	0.119 in A1011	20 mph 6"x6" ram	50 psi	1,141,000	2,709,000
R1D	300 lb CI	0.5625 in TC128B	0.119 in A1011	20 mph 6"x6" ram	100 psi	676,000	673,000
R1E	500 lb CI	0.777 in TC128B	0.119 in A1011	20 mph 6"x6" ram	100 psi	915,000	1,261,000
R1F	600 lb CI	0.981 in TC128B	0.119 in A1011	20 mph 6"x6" ram	100 psi	1,152,000	1,742,000
R1G	300 lb EO	0.5625 in TC128B	0.375 in TC128B	20 mph 6"x6" ram	50 psi	776000	1,849,000
R1H	500 lb CI	0.777 in TC128B	0.375 in TC128B	20 mph 6"x6" ram	100 psi	1,010,000	1,732,000
R1I	500 lb CI	0.777 in TC128B	0.119 in A1011	30 mph 12"x12" ram	100 psi	1,512,000	4,885,000
R1J	600 lb CI	0.981 in TC128B	0.119 in A1011	30 mph 12"x12" ram	100 psi	(2,085,000)[1]	(8,536,000)[1]
R1K	500 lb CI	0.777 in TC128B	0.375 in TC128B	30 mph 12"x12" ram	100 psi	1,948,000	8,660,000
R1L	300 lb EO	0.5625 in TC128B	0.5625 in TC128B	20 mph 6"x6" ram	50 psi	879,000	2,859,000
R1M	300 lb EO	0.5625 in TC128B	0.119 in A1011	20 mph 6"x6" ram	100 psi	686,000	675,000
R1N	500 lb CI	0.777 in TC128B	0.119 in A1011	20 mph 6"x6" ram	50 psi	909,000	2,011,000
R1O	500 lb EO	0.918 in TC128B	0.119 in A1011	20 mph 6"x6" ram	50 psi	1,066,000	2,131,000
R1P	600 lb EO	1.102 in A516-70	0.119 in A1011	20 mph 6"x6" ram	50 psi	1,171,000	2,874,000
R1Q	500 lb CI	0.777 in TC128B	0.5625 in TC128B	20 mph 6"x6" ram	100 psi	1,090,000	2,175,000
R1R	500 lb CI	0.777 in TC128B	0.119 in A1011	25 mph 9"x9" ram	100 psi	1,286,000	2,857,000
R1S	600 lb CI	0.981 in TC128B	0.119 in A1011	25 mph 9"x9" ram	100 psi	1,701,000	3,941,000
R1T	500 lb CI	0.777 in TC128B	0.375 in TC128B	25 mph 9"x9" ram	100 psi	1,476,000	3,878,000

Note (1) Tank was not fully punctured at this impact velocity.
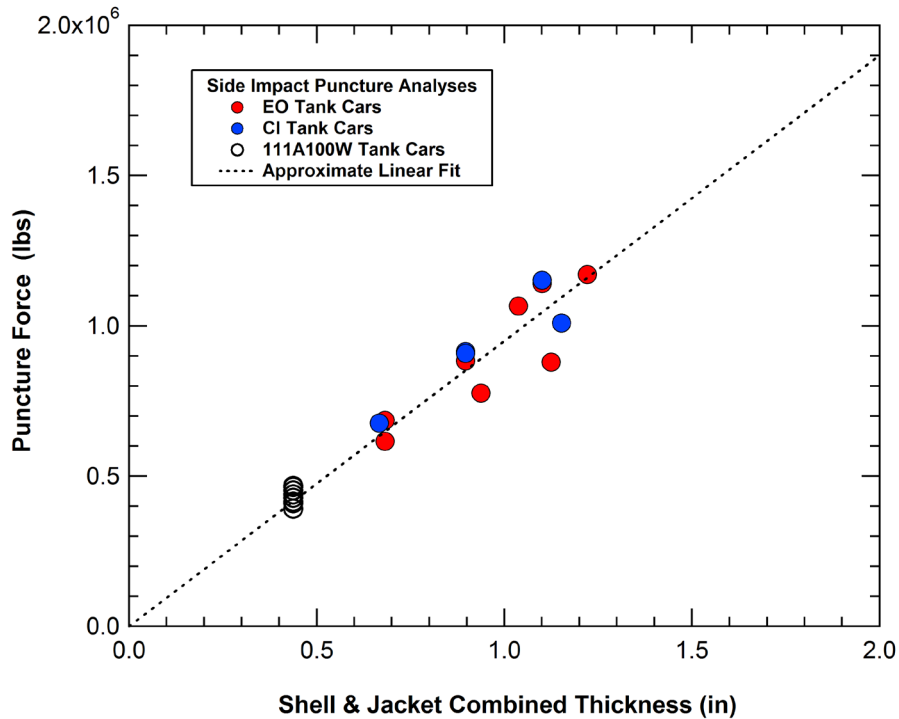
Figure 144. Side impact puncture force as a function of system thickness.

The slope of the linear fit in Figure 144 corresponds to an average shear stress in the tank layers around the perimeter of the impactor of 39 ksi. By comparison, the yield and ultimate stress levels of the TC128B in pure shear are 33 ksi and 49 ksi, respectively (approximately 58% of the stress values in pure tension using a Von Mises yield criterion). Thus, the failure mode is primarily exceeding the shear capacity around the perimeter of the impact patch.

The calculated puncture energies for all of the analyses using the 6x6 inch impactor are plotted against the combined thickness of the tank shell and jacket in Figure 146. When comparing puncture energy the data falls into two separate groups that are distinguished by the tank pressure. Again, the comparison indicates that the total thickness was the dominant parameter that determines puncture energy for a given pressure level and indicates that a retrofit design with an increased jacket thickness should provide equivalent protection.

A similar comparison of the puncture energy of the retrofit 300 lb EO cars and 500 lb Cl cars as a function of thickness is shown in Figure 147. The comparison illustrates that the addition of material to the jacket was much more efficient at increasing puncture energy for the more compliant EO tank cars (resulting from the thinner baseline tank shell thickness and lower pressure).
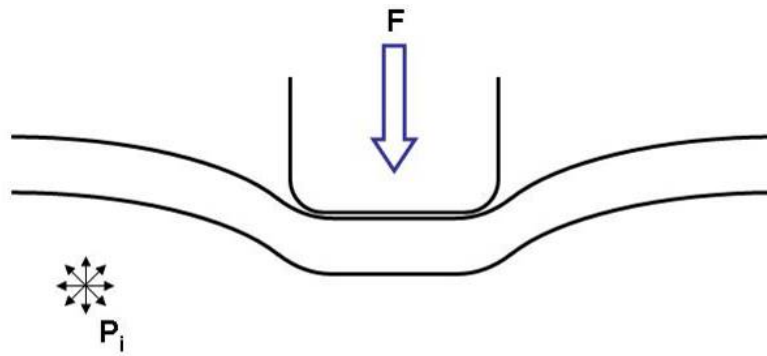
(a) Geometry of the tank indentation
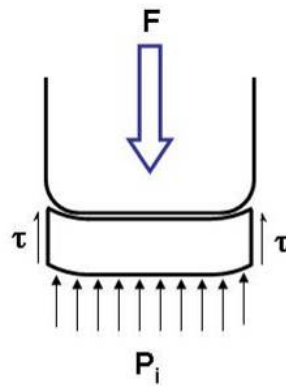
(b) Free body diagram for the tank contact patch

Figure 145. Loading and failure mechanism for the tank impact and puncture.

More advanced solutions to increasing the puncture resistance of tank cars includes the use of multi-layer steel and foam systems or engineered metal structures (EMS) such as a corrugated steel system being evaluated in the NGRTC program or the egg crate EMS concept proposed by the Volpe Transportation Systems Center and FRA [11, 65]. Several of these advanced concepts have been analyzed and results are provided in Section 6 of this report. However, of the systems analyzed to date, none are providing side impact protection levels that would survive a 25 mph impact with a 6x6 inch impactor (approximately 6 million ft-lbs). The principal challenge is that the small impactor face concentrates too large a load around the small perimeter of the impactor face and as a result, punctures through the protection system.
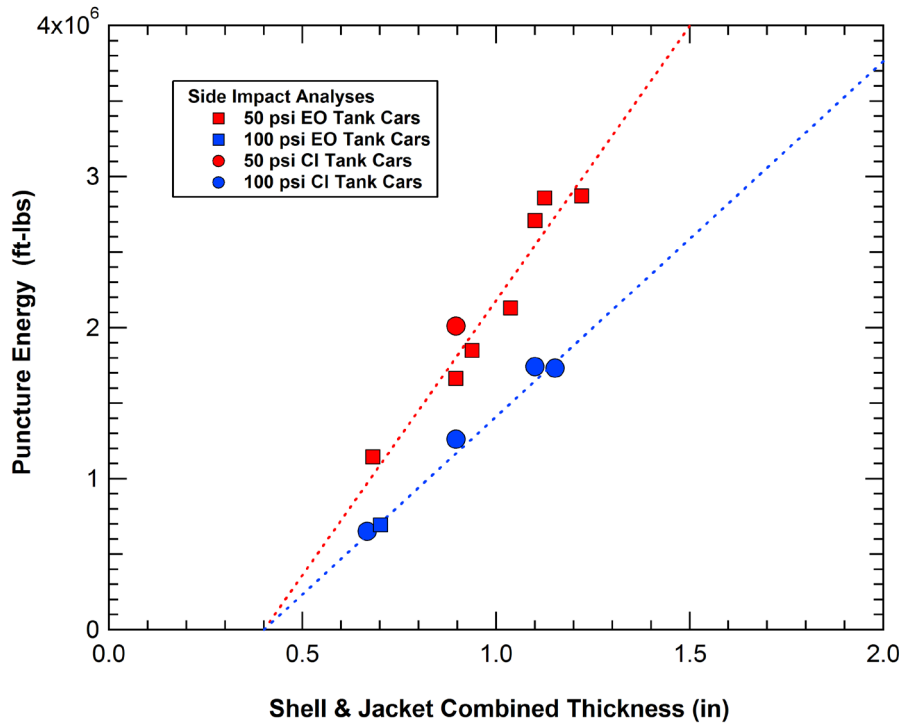
Figure 146. Side impact puncture energy as a function of system thickness.
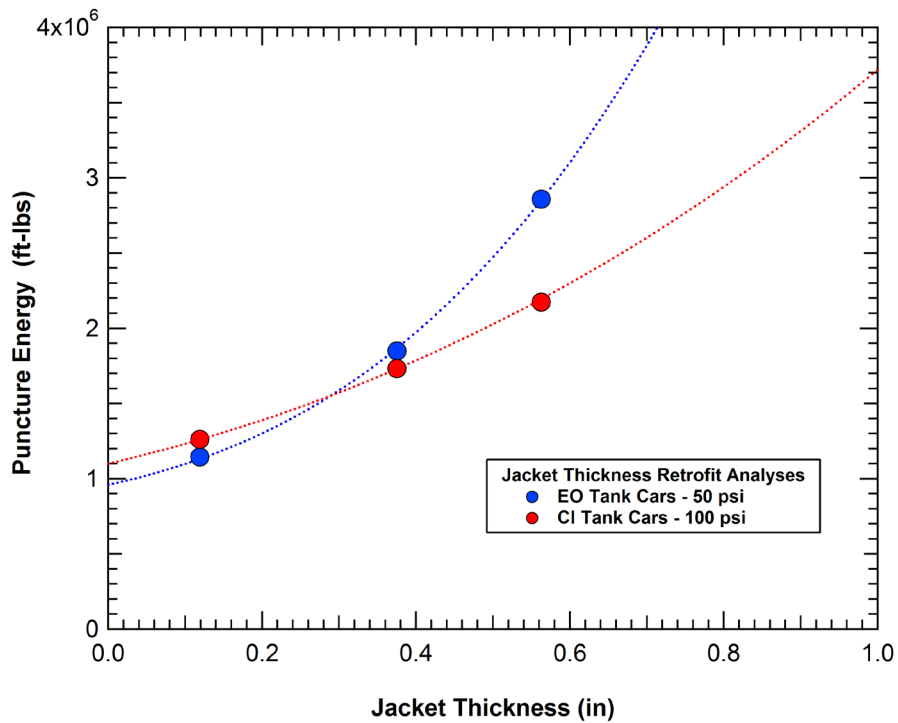
Figure 147. Puncture energy of retrofit tank cars as a function of jacket thickness.

5   Detailed Head Impact Analyses

5.1   Introduction

The tank head is subjected to a significant percentage of the overall impacts in collisions and derailments. The significant number of head impacts justifies additional protection compared to the sides of the tank. For this reason, head shields have been used for many years to provide an increased protection against head impacts. Thus, greater head impact protection offers the opportunity for substantial improvements in tank car safety. Additionally, the tank head comprises a small percentage of the overall tank surface area, so the weight penalty for additional protection is not as severe.

5.2   Head Impact Analyses and Model Validation

In addition to the full-scale side impact tests, three full-scale head impact component tests were performed under the NGRTC project. In these tests, only the tank head and external protective structures were used to simplify the test from a full tank car impact test. Tank heads were unpressurized in these tests and the test head and support structure were ventilated to atmospheric pressure. The tests did, however, use an off-center impact point which adds some complexity to the impact response. Baseline head impact testing and analyses are described here.

5.2.1   Head Test 1 – Baseline Head Impact Behavior

The first component test of a baseline tank car head test article was performed as part of the Next Generation Rail Tank Car project on October 30, 2007, at the Transportation Technology Center, Inc. (TTCI) in Pueblo, Colorado [66]. This test involved a 289,550-pound ram car impacting the baseline tank head at 8.66 mph. The target impact point was offset approximately 29 inches vertically downward from the center of the head. The ram car was equipped with a 6-inch square indenter with ½-inch radius around the edges. The tank head was affixed to the Transportation Technology Center impact barrier with a rigid fixture.

The test article and the ram car staged in position prior to the test are shown in Figure 148. The test article was bolted to the wall-offset fixture. The wall-offset fixture was bolted to the impact wall and an energy absorbing arrestor system was added to dissipate residual energy if the head was punctured. The arrestor system consists of four hydraulic cushion units, two on each side, placed to engage the ram car shortly after the head penetration. To withstand any potential loads from the arrester system, additional reinforcement was added to the underframe structures on the impacting end of the ram car. Some of this reinforcement on the side sills is seen in Figure 148.

Figure 148. Pretest conditions of the test article and ram car for Head Test 1.

Prior to the baseline Head Test 1, the ram car was weighed to determine the increase from the reinforcements. The A-end weight (ram end) was 163,300 lbs and the B-end weight was 126,250 lbs for a total weight of 289,550 lbs. The impact speed, measured by the reflector speed trap, was 8.66 mph. The ram punctured the jacket. The commodity tank was significantly deformed, but it did not puncture.

The damage to the jacket and tank head after the impact is shown in Figure 149. A close up view of the impact damage to the tank head is shown in Figure 150. The impact behavior shows that the ram initially contacts a point approximately 6 inches higher than the contact position at the end of the impact behavior. The head indentation in the offset impact geometry results in a vertical local displacement and sliding of the head material relative to the inward motion of the ram. Ultrasonic thickness testing showed that there was thinning of the tank head material in the region of the impact. The peak longitudinal acceleration was about 2.8 g after processing through a 60 Hz channel frequency class filter (CFC 60).
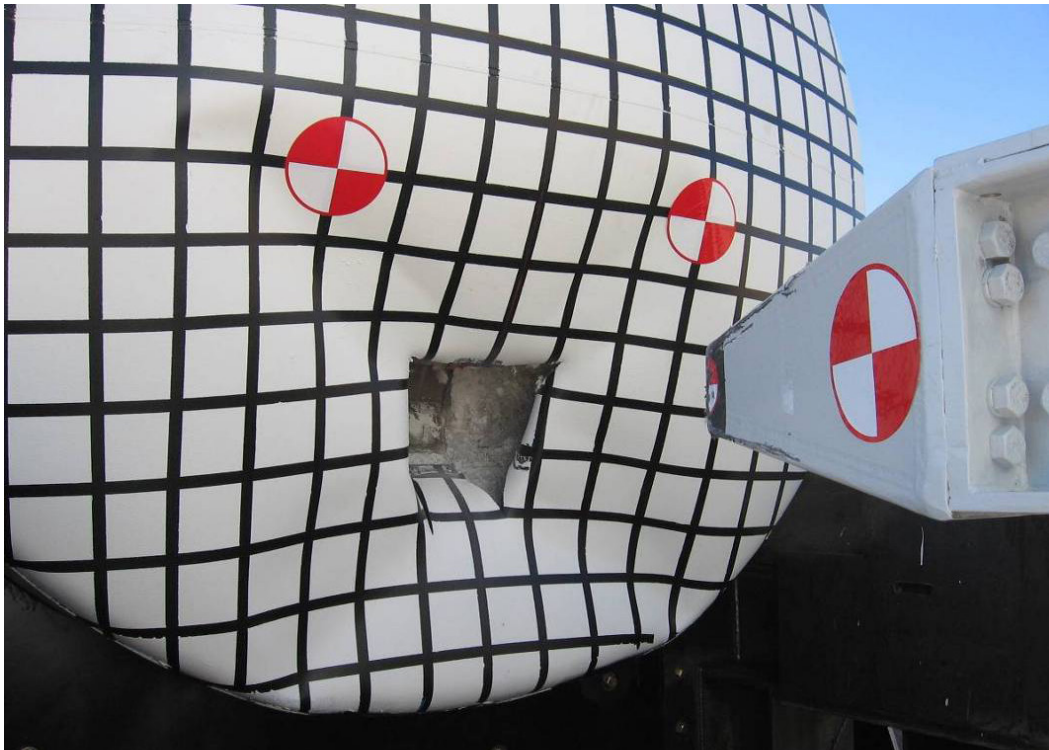
Figure 149. Post-test damage of the test article for Head Test 1.

Initial contact of the ram face on the head

Final position of the ram face on the head
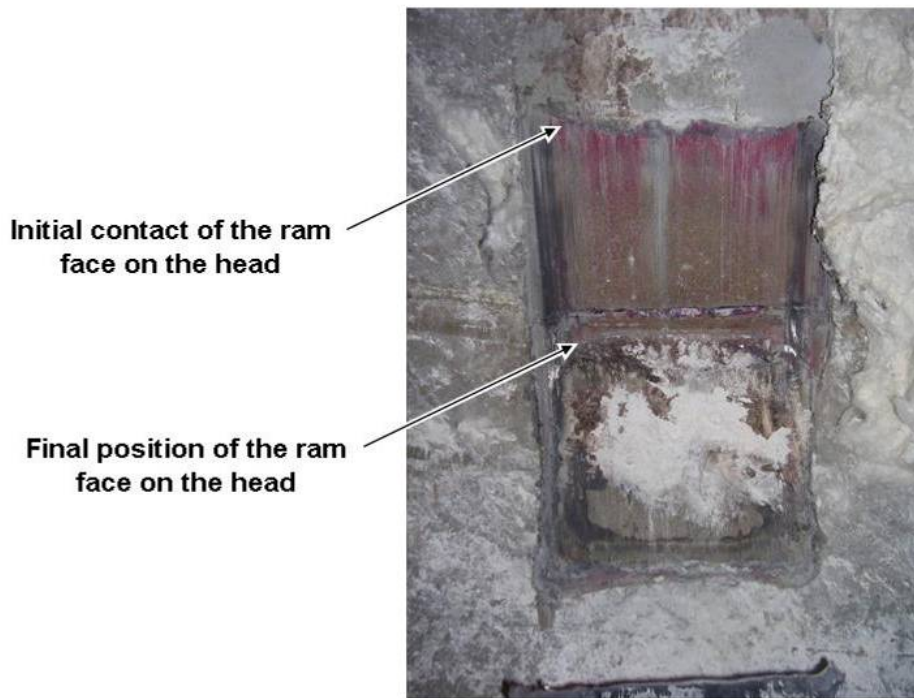
Figure 150. Impact damage on the tank head in Head Test 1.

5.2.2 Head Puncture Model

The head puncture modeling approach was identical to that of the tank side impact puncture analyses with a fine mesh of brick elements in the impact zone (both in the head and head shields) with an element dimension of approximately 0.040 inch (1 mm). The head impacts analyzed matched the Test 1 impact condition (impact point offset below the tank head center). As a result, the problem had only 1 symmetry plane running vertically through the test specimen. This symmetry plane was used in most of the head impact simulations to reduce the model size by one half compared to the full head model.

5.2.3 Comparison of Head Test 1 with Analyses

The damage to the head was calculated for the Head Test 1 impact conditions, as shown in Figure 151. The calculated impact behavior included the puncture of the jacket, shown in Figure 151 (a), and impact damage that did not fully puncture the head, seen in Figure 151 (b). The head damage included the sliding of the head material relative to the impactor as seen in the test. The predicted damage shows that this impact velocity was very nearly sufficient to puncture the tank head. All of these calculated impact responses are in good agreement with the observed Head Test 1 response.
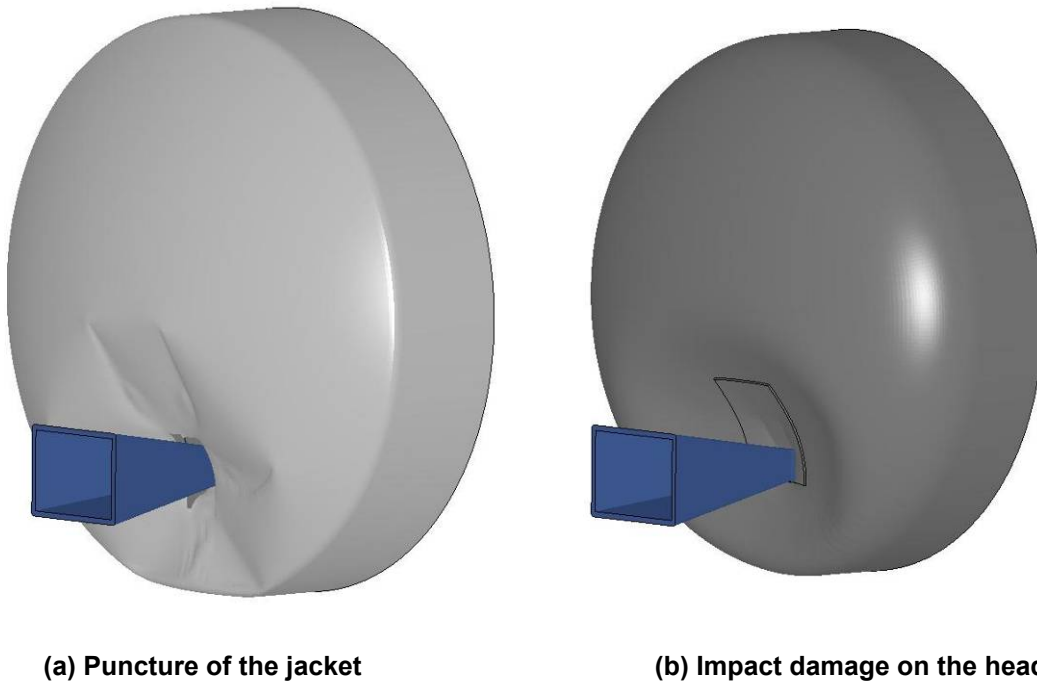
(a) Puncture of the jacket   (b) Impact damage on the head
Figure 151. Calculated impact response in Head Test 1.

The measured and calculated force-deflection characteristics are shown in Figure 152. The response shows a very linear behavior for the head impact and the peak load was approximately 800,000 lbs at a ram displacement of approximately 24 inches. The agreement between the force-deflection behaviors for the test and analysis is excellent. This comparison contributes to the further validation of the modeling procedures used to assess the puncture energies of tank cars under various impact conditions.
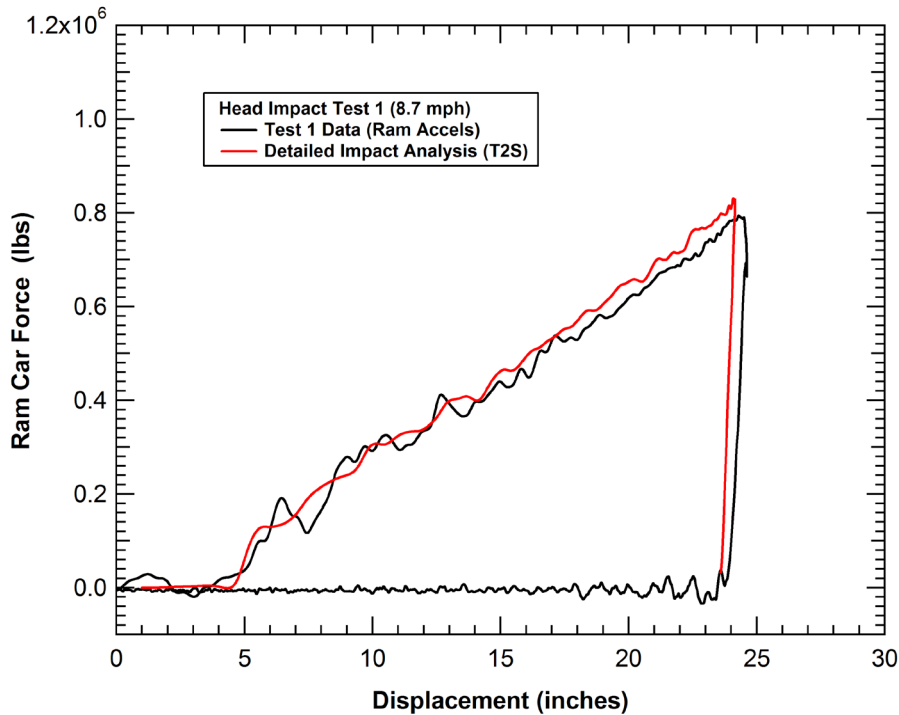
Figure 152. Calculated and measured force-deflection behaviors for Head Test 1.

5.3   Assessment of Head Impact Puncture Conditions

The head puncture model was used to assess the puncture energies for a wide range of tank car design variations and impact conditions. The Cl tank head parameters investigated included head thickness (300, 500, and 600 lb tank heads), internal pressure (unpressurized and 100 psi), jacket thickness, foam insulation, and impactor size. The head geometry was a 2:1 ellipsoid with a major diameter of 100 inches, consistent with the chlorine car dimensions. The jacket was a flanged and dished geometry with a 4 inch standoff at the head center and a 108 inch diameter at the transition to the jacket.

The model of the commodity tank head and BW impact zone mesh used in the head puncture analyses is shown in Figure 153. Due to the offset impact condition, only one vertical plane of symmetry exists and the model is for one half of the tank head. Again, the refined zone is

maintained along the perimeter of the impactor face with a characteristic element dimension of approximately 0.040 inch (1 mm).
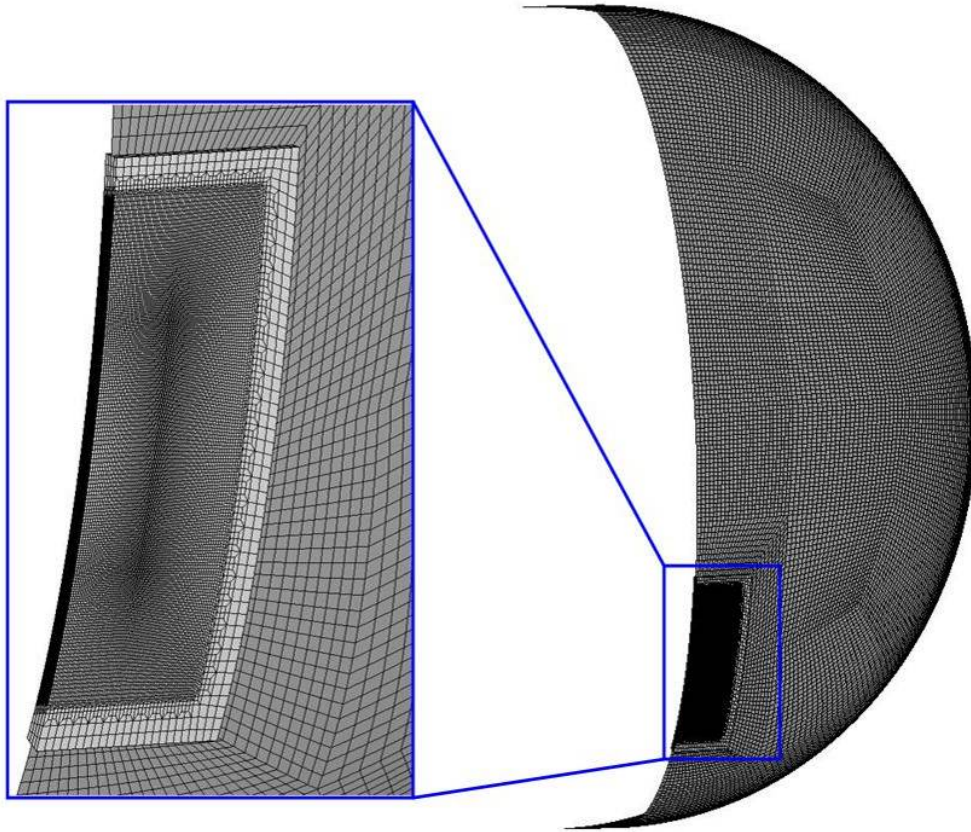
Figure 153. Tank head model and impact zone mesh used for the head puncture analyses.

An example head impact puncture response is shown in Figure 154. The ram head model had the same tapered geometry used in the full-scale testing and had an updated weight of 295,000 lbs. The tapered geometry included a 6x6 inch contact face but flares out to more closely duplicate the initial puncture response seen in the impact tests. The tank head in this analysis was a 500 lb head (0.8281 inches thick) with a 0.50-inch thick A516-70 full height head shield. The fractures of the tank and head shield initiate near the upper corners of the impactor and propagate along the sides and top edge of the impactor face forming a flap in the head.

(a) Initial impact conditions   (b) Puncture response of the head
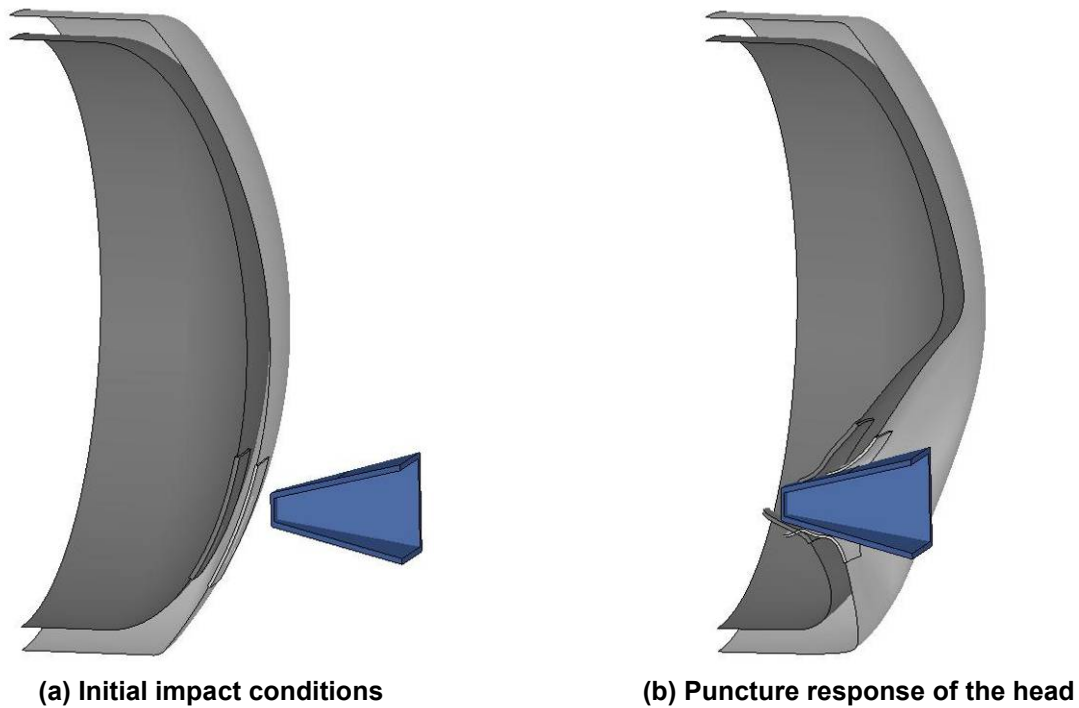
Figure 154. Calculated puncture behavior of a head and head shield.

The energy balance for the 500 lb head with a 0.50-inch thick A516-70 head shield is shown in Figure 155. In this analysis, the tank head is unpressurized. The initial impact energy is 2.85 million ft-lbs (all in the kinetic energy). As the impact progresses the ram is decelerated and the kinetic energy drops off to approximately 1.64 million ft-lbs. The energy transfer is from the kinetic energy of the ram to the internal energy of the tank deformations. There is no pressure-volume work since the tank head is unpressurized. The internal energy of the tank at the end of the calculation is approximately 1.2 million ft-lbs (equal to the drop in kinetic energy). The hourglass energy and sliding energy in the calculation are both small. This energy balance is typical for these analyses of the unpressurized head impacts.
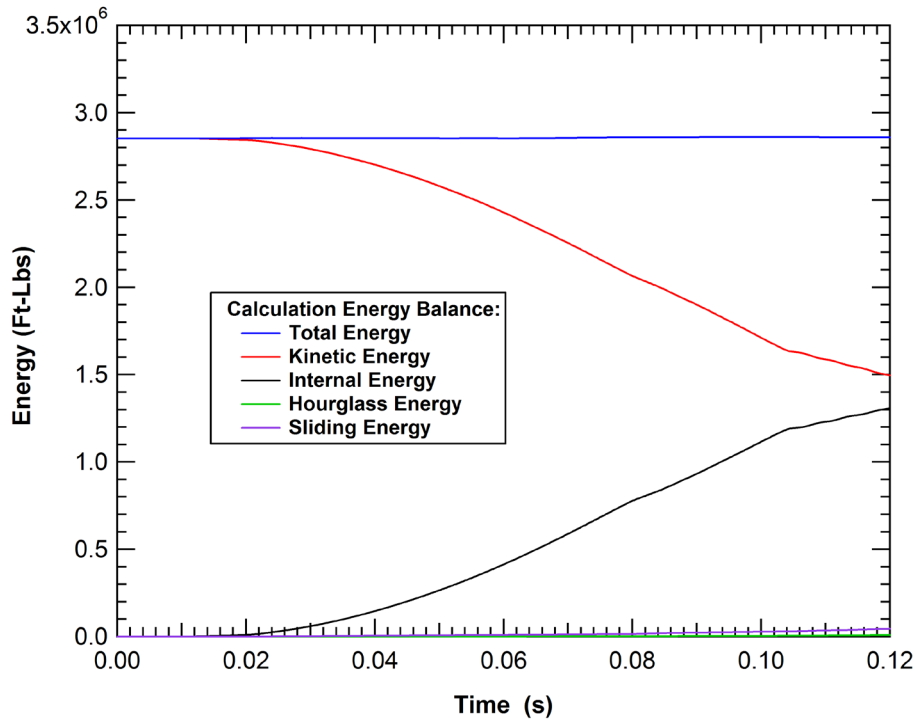
Figure 155. Calculated energy balance for the 500 lb CI tank head and Head Shield (R1C).

5.3.1 Baseline Impact Analyses on Unpressurized Heads

The calculated impact loads for a set of calculations on unpressurized heads is shown in Figure 156. The head geometries include the baseline 300, 500, and 600 lb tank heads with 11 gauge jackets and additional analyses for the 500, and 600 lb tank heads with 0.50-inch full height head shields. In this set of analyses, TC128 was used in modeling the 600 pound commodity tank for comparative purposes. It was recognized that TC128 is not available in plates over one inch thick. Subsequent head impact analyses on the 600 lb head used A516-70 as the head material.

A summary of these analyses on unpressurized heads, including the impact conditions and calculated puncture forces and energies, is provided in Table 6. The calculations shown in Figure 156 are summarized in the first five rows of the table.
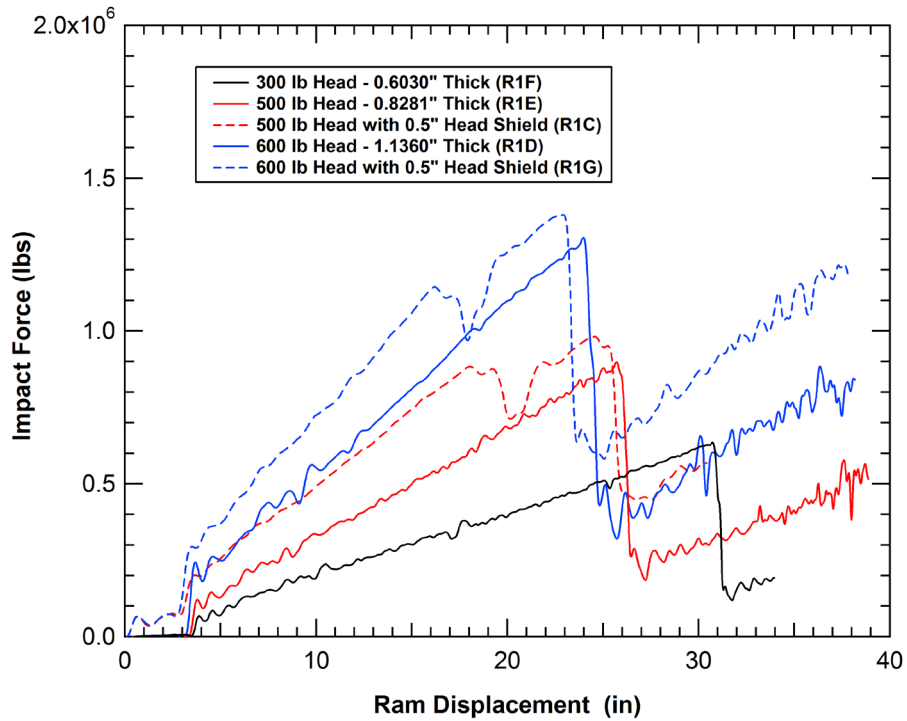
Figure 156. Calculated force-deflection behaviors for baseline head geometries.

Table 6. Summary of unpressurized head impact analyses

Calculation	Head Thickness	Jacket or Head Shield	Shell Jacket	Impact Velocity	Puncture Force (lbs)	Puncture Energy (ft-lbs)
R1F	0.6030	11 gauge A1011	11 gauge A1011	10 mph	636,000	783,000
R1E	0.8281	11 gauge A1011	11 gauge A1011	12 mph	898,000	903,000
R1C	0.8281	0.500" A516-70	0.500" A516-70	17 mph	981,000	1,196,000
R1D	1.1360	11 gauge A1011	11 gauge A1011	15 mph	1,305,000	1,274,000
R1G	1.1360	0.500" A516-70	0.500" A516-70	18 mph	1,380,000	1,455,000
R1H	0.8281	0.8281" TC128B	0.8281" TC128B	17 mph	1,430,000	1,842,000
R1I	0.8281	0.500" A516-70	11 gauge A1011	17 mph	955,000	1,140,000
R1J	0.6030	0.8281" TC128B	0.375" TC128B	17 mph	1,288,000	1,983,000

One feature of the design that can potentially impact the head impact response is the stiffness of the head shield support provided by the side jacket shell. In the example shown in Figure 154, the 0.50-inch head shield thickness was extended to the reaction frame providing a high stiffness support (Calculation R1C). This would be more representative of the support in a retrofit design where the jacket is significantly thicker than the baseline 11 gauge A1011 jacket.

For comparison, a second head impact analysis was performed under identical impact conditions where the only difference was the substitution of an 11 gauge A1011 jacket in the cylindrical section behind the head shield (Calculation R1I). The calculated impact behavior for this head geometry is shown in Figure 157. The initial impact and indentation of the head was identical. However, after approximately one foot of ram displacement, the loads were sufficiently high to initiate the buckling response in the jacket seen in Figure 157. The comparison of the force-deflection curves for the two corresponding analyses are shown in Figure 158. The comparison shows that the bucking of the jacket had little effect on the head impact response (either impact force or the puncture energy).
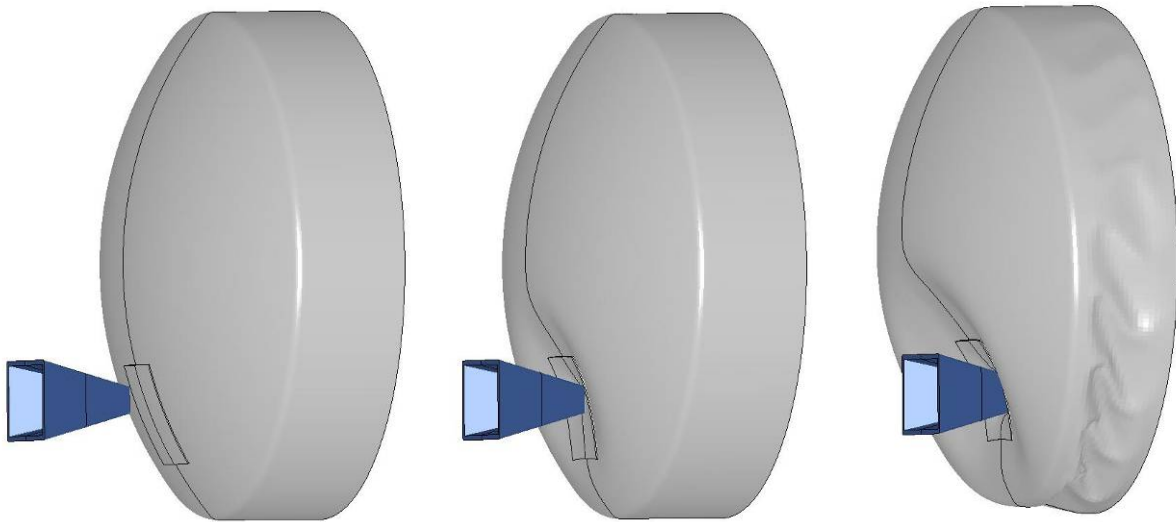
Figure 157. Buckling behavior for the 11 gauge jacket in the offset head impact.
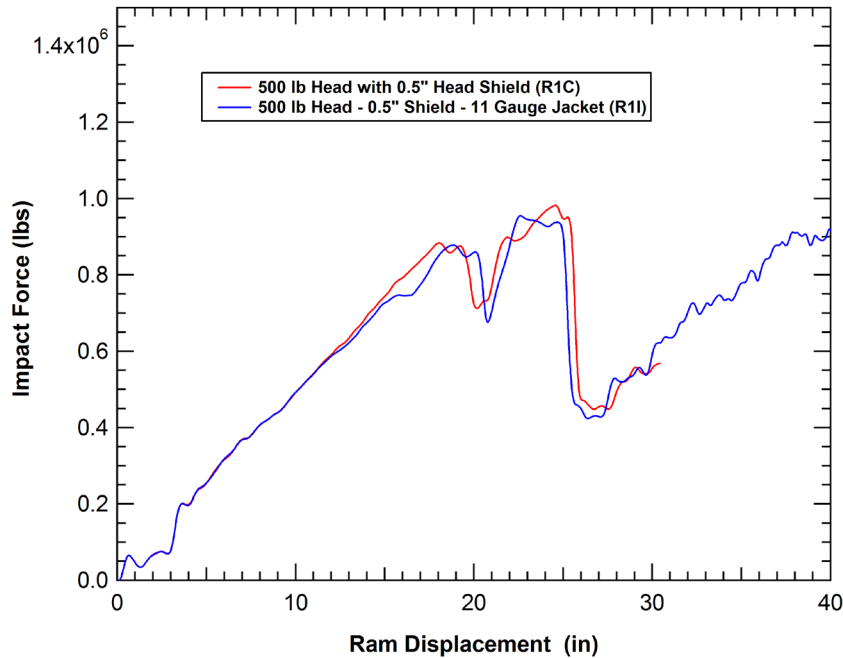
Figure 158. Effect of jacket stiffness on the calculated head impact response.

5.3.2 Baseline Impact Analyses on Pressurized Heads

The above head impact analyses were performed using a configuration similar to the head impact component tests in the NGRTC program. Although these analyses are representative of the full-scale tank head impact behavior, a concern was that neglecting the internal pressure in the head impacts will influence the response and potentially change some of the resulting conclusions. As a result, a series of analyses with internal pressure were also performed.

A summary of the pressurized head impact analyses is provided in Table 7. In all of these analyses the internal pressure was 100 psi. In this series of analyses, the material used for the tank head was TC128B when the thickness was less than one inch and A516-70 when the thickness was greater than one inch. The baseline 0.5 inch head shield material was also switched to A572-50. The relative stress-strain behaviors for these materials were previously provided in Section 3.2.3 of this report. The calculated force-deflection behaviors and puncture energies for the pressurized 300, 500, and 600 lb heads, all with a 0.5 inch A572-50 head shield, are shown in Figure 159. The 300, 500, and 600 lb heads were Calculations R1K, R1L, and R1P, respectively, in Table 7.

Table 7. Summary of pressurized head impact analyses. [1]

Calculation	Head Thickness	Jacket or Head Shield	Shell Jacket	Impact Velocity	Puncture Force (lbs)	Puncture Energy (ft-lbs)
R1K	1.1360	0.500" A572-50	11 gauge A1011	14 mph	1,206,000	1,121,000
R1L	0.8281	0.500" A572-50	11 gauge A1011	10 mph	966,000	916,000
R1M	0.8281	0.8281" TC128B	11 gauge A1011	14 mph	1,289,000	1,321,000
R1N	1.1360	0.500" A572-50	11 gauge A1011	11 mph	1,229,000	1,110,000
R1O	0.6030	0.8281" TC128B	0.375" TC128B	11 mph	>1,240,000	>1,190,000
R1P	0.6030	0.500" A572-50	11 gauge A1011	10 mph	813,000	782,000
R1Q	0.6030	0.8281" TC128B	0.375" TC128B	14 mph	1,316,000	1,537,000
R1U	0.8281	0.8281" TC128B	11 gauge A1011	14 mph	1,311,000	1,482,000
R1Y	0.8281	0.680" TC128B	0.375" TC128B	14 mph	1,292,000	1,390,000
R1Z	0.8281	11 gauge A1011	11 gauge A1011	10 mph	813,000	610,000
R0A [2]	0.8281	0.8281" TC128B	11 gauge A1011	10 mph	1,218,000	1,494,000
R0B [2]	0.8281	0.680" TC128B	0.375" TC128B	14 mph	1,195,000	1,252,000
R0C [2]	0.8281	0.500" A572-50	11 gauge A1011	14 mph	952,000	1,100,000
R0D	0.8281	0.680" TC128B	11 gauge A1011	14 mph	1,189,000	1,281,000
R0E	0.8281	0.8281" TC128B	0.375" TC128B	14 mph	1,466,000	1,661,000

Notes: (1) All analyses performed on chlorine tank heads using the 6x6 inch impactor

(2) Analyses with the shallow head shield profile.
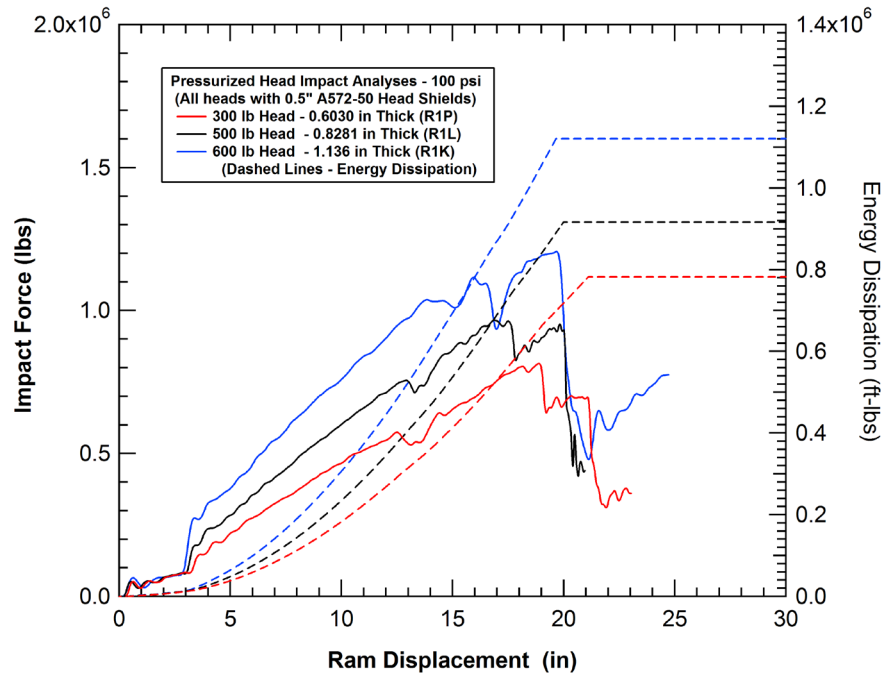
Figure 159. Calculated force-deflection behaviors for pressurized heads.

The comparison of the calculated force-deflection curves for the unpressurized and pressurized 500 lb head configurations is shown in Figure 160. The solid red lines are for the analysis of the unpressurized head and the blue lines are the pressurized head. The differences in the two analyses were the addition of 100 psi internal pressure and the head shield material was switched from A516-70 to A572-50. The comparison of these two analyses show nearly identical puncture forces but the puncture energy was reduced from 1.20 to 0.92 million ft-lbs in the pressurized head. The higher stiffness of the head resulting from the internal pressure resulted in the puncture occurring at approximately 5 inches less ram displacement.

The calculated force-deflection characteristics for a pressurized 500 lb Cl head (100 psi) with various thickness head shields is shown in Figure 161. In the figure, the thicker retrofit head shields (0.68 and 0.8281 inch thick) also have a thicker 0.375 inch retrofit jacket supporting the head shields. A similar comparison where the 11 gauge jacket was used to support all of the head shields is shown in Figure 162. As expected, the increasing thickness of the head shield increases the overall stiffness of the system, the peak puncture forces, and the puncture energies. The magnitudes of the puncture forces and puncture energies are summarized in Table 7. The side jacket thickness was also seen to have a significant contribution, as shown in Figure 163.
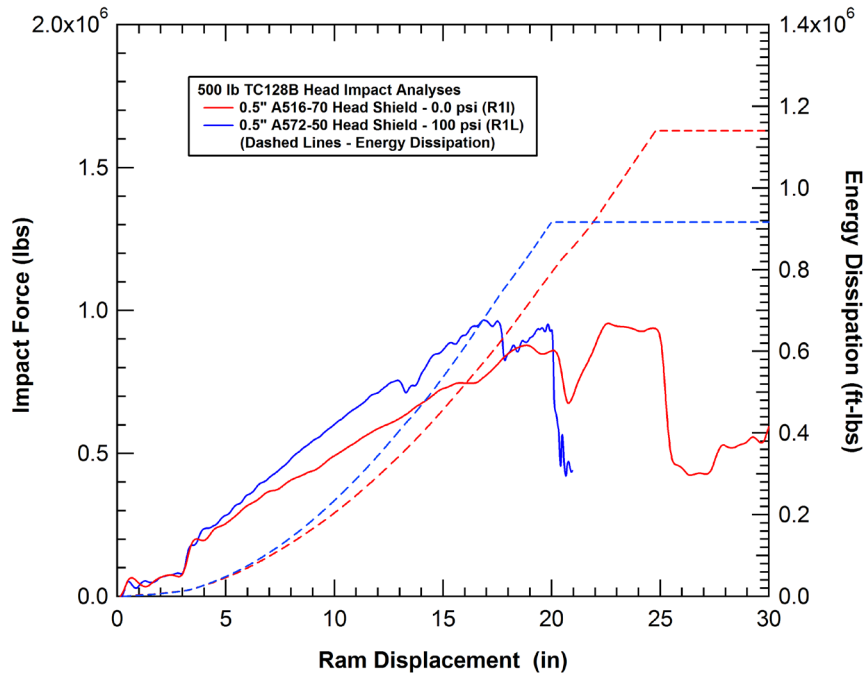
Figure 160. Force-deflection comparison for pressurized and unpressurized heads.
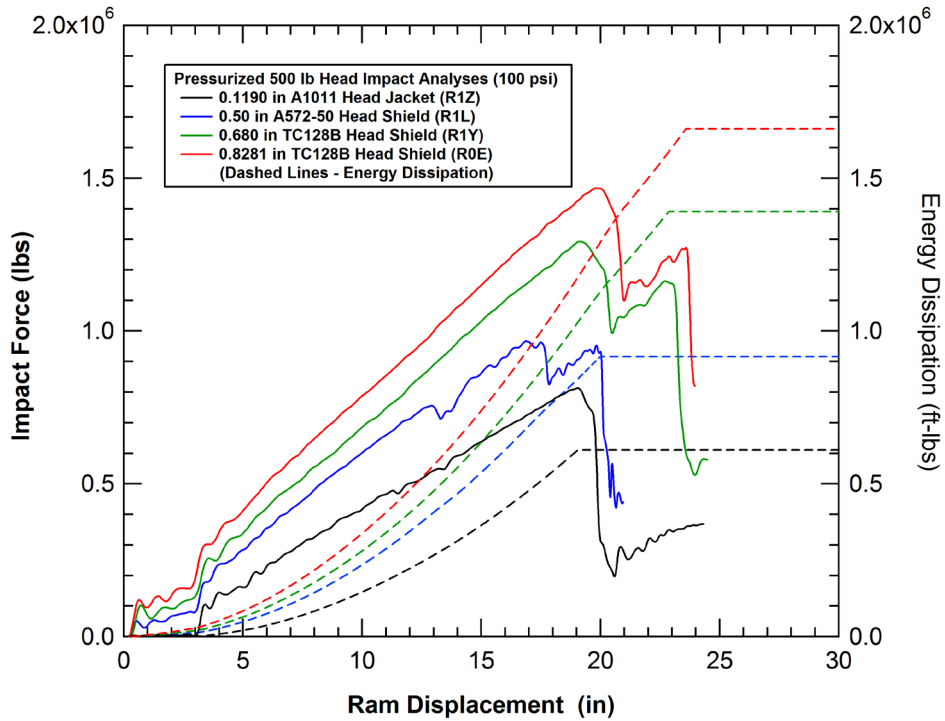
Figure 161. Force-deflection comparison for pressurized heads and various head shields (0.375-inch retrofit jacket thicknesses).
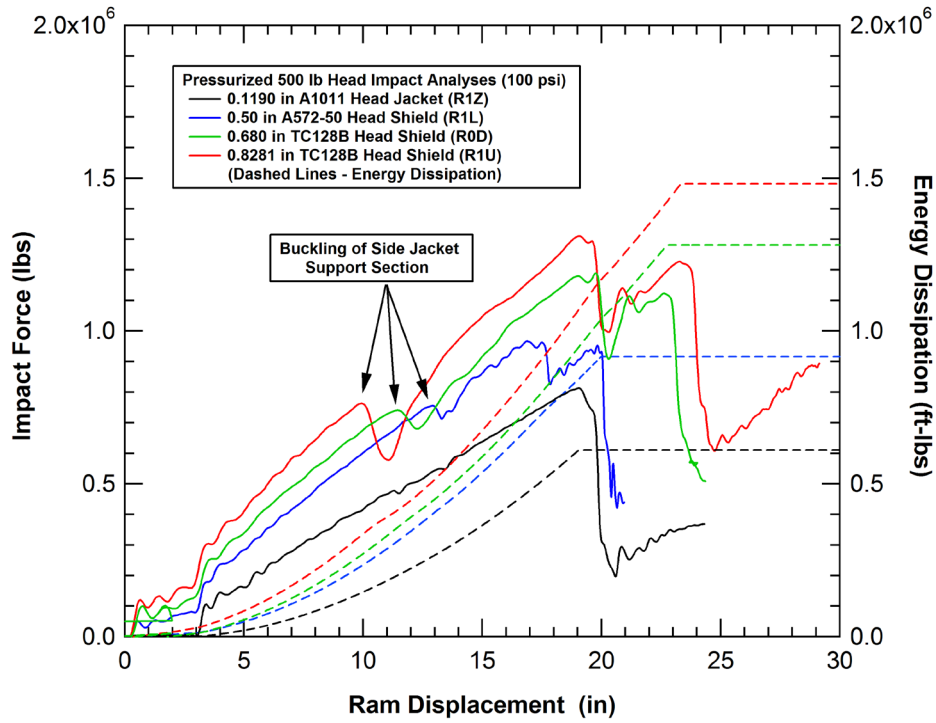
Figure 162. Force-deflection comparison for pressurized heads and various head shields (11 gauge jackets).
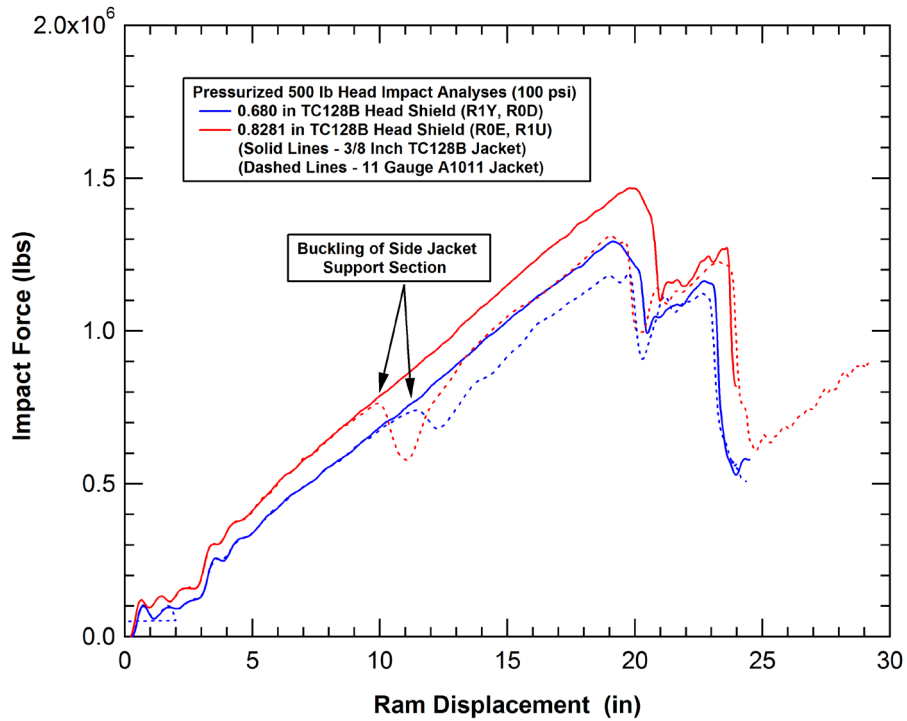
Figure 163. Force-deflection comparisons with different jacket thicknesses.

Ram Impact Speed Effects

An assumption of the analyses presented in this report is that the impact response is relatively insensitive to the impact speed within a limited range. As a result, each system is evaluated by selecting a collision speed that is between 25% and 50% higher than the estimated threshold puncture speed. The impact energy is then obtained from the resulting force-deflection characteristics prior to the point of puncture initiation. The magnitude of the residual kinetic energy in the ram is not considered to be significant. In this section, comparisons are made of analyses at different impact speeds to assess the validity of this assumption.

An analysis of a 300 lb tank head with the 0.8281 inch TC128B head shield found that an 11 mph impact velocity was too low to rupture the head (Calculation R1O). A repeat analysis was performed at a 14 mph impact velocity. A comparison of the force-deflection characteristics for the analyses at the two different impact speeds are shown in Figure 164. The comparison shows that the analyses follow a nearly identical force-deflection curve. Thus, the deflection behavior was independent of the collision speed within the range of impact speeds investigated.
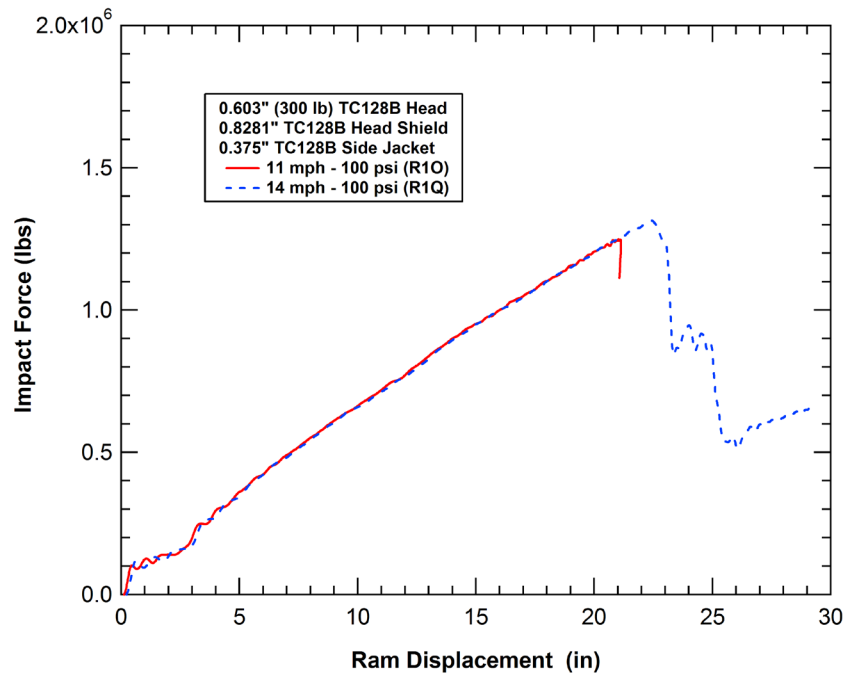
Figure 164. Calculated force-deflection behaviors at different impact speeds (300 lb head).

A similar set of analyses for the baseline 600 lb head geometry were performed at 11 and 14 mph impact speeds. A comparison of the corresponding force-deflection behaviors and impact energies is provided in Figure 165. The comparison again illustrates that there was very little difference in the impact response or puncture energies within this limited range of impact

velocities. Thus, the methodology was considered to be valid and additional analyses at impact speeds closer to the threshold puncture speed were not considered to be necessary.
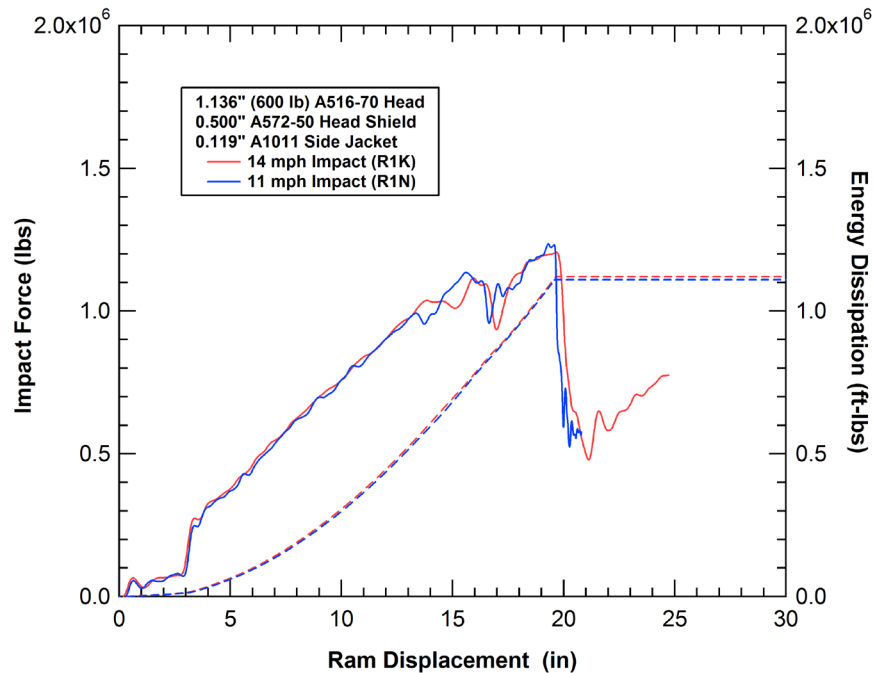
Figure 165. Calculated force-deflection behaviors at different impact speeds (600 lb head).

Head Shield Profile Effects

Another tank car design parameter that can potentially influence the head impact behavior and puncture resistance is the shape of the head shield. Head shields traditionally have a flanged and dished construction. However, the parameters of this head shield profile are not as uniform or as tightly constrained as the tank head profiles. An example of two different head shield profiles are shown in Figure 166. The first profile has a deeper dish profile that more closely conforms to the head geometry. This deep dish profile has been used for the majority of the head impact analyses in this report. The second profile has a shallower dish and results in a larger standoff distance from the head at locations other than at the center of the head.

(a) Deep head dish profile   **(b) Shallow head dish profile**
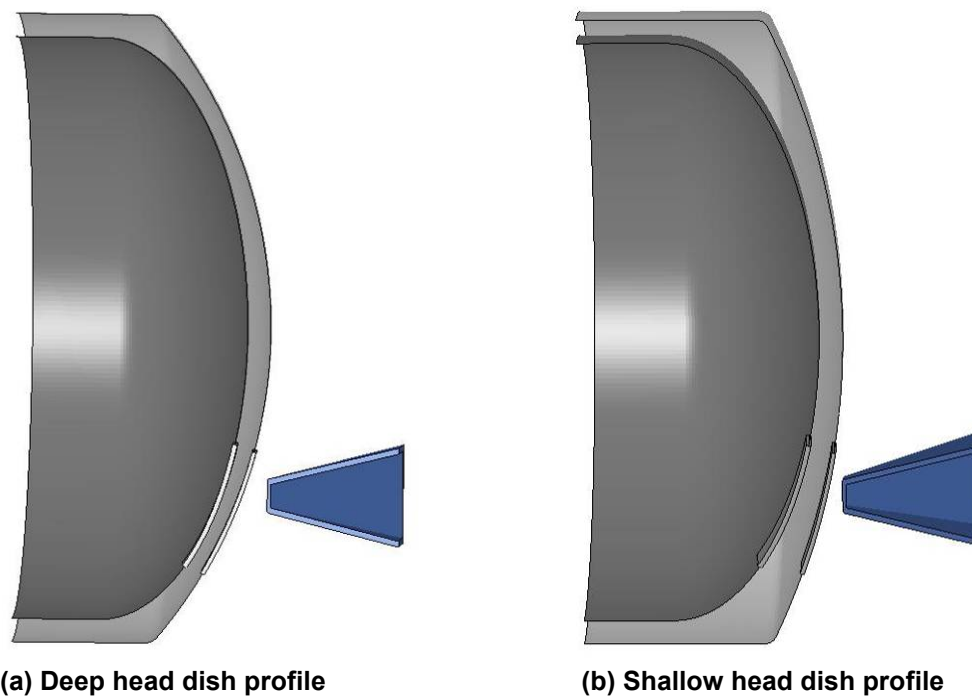
Figure 166. Models developed to assess the effects of the head shield profile.

Three different head shield thicknesses were evaluated with the two different dish profiles.
These were a 0.50-inch-thick A572-50 head shield and 0.680-inch-thick and 0.8281-inch-thick
TC128B head shields. An example of the calculated deformation response is shown in Figure
167. The comparisons of the calculated force-deflection characteristics and impact energy
dissipation for the 0.500, 0.680, and 0.8281-inch-thick head shields are provided in Figure 168,
Figure 169, and Figure 170 respectively. There are significant effects of the head shield profile
on the details of the impact response in each comparison. However, no significant consistent
trends were observed on the relative impact protection performance between the two designs.
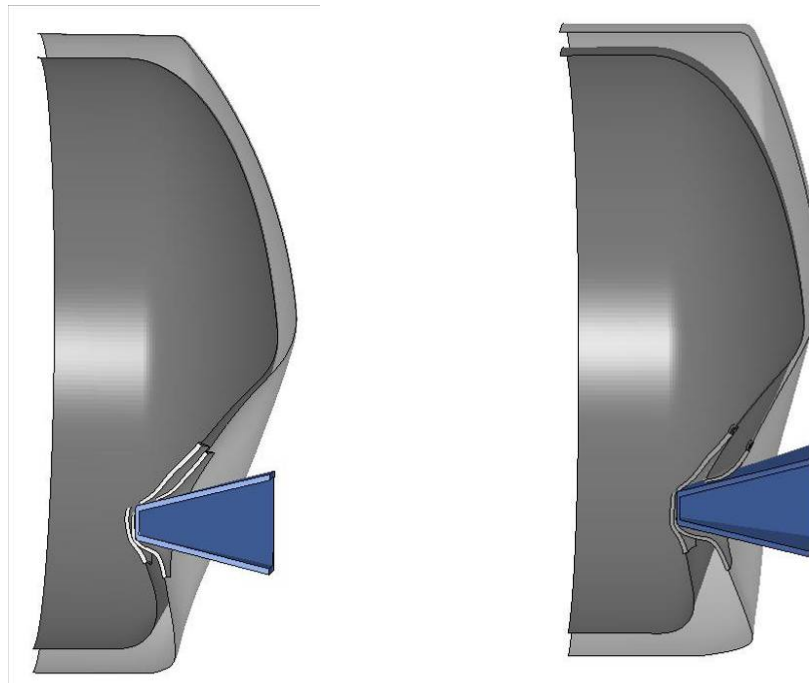
(a) Deep head dish profile　　　　　**(b) Shallow head dish profile**

Figure 167. Calculated Puncture response for the two head shield profiles.
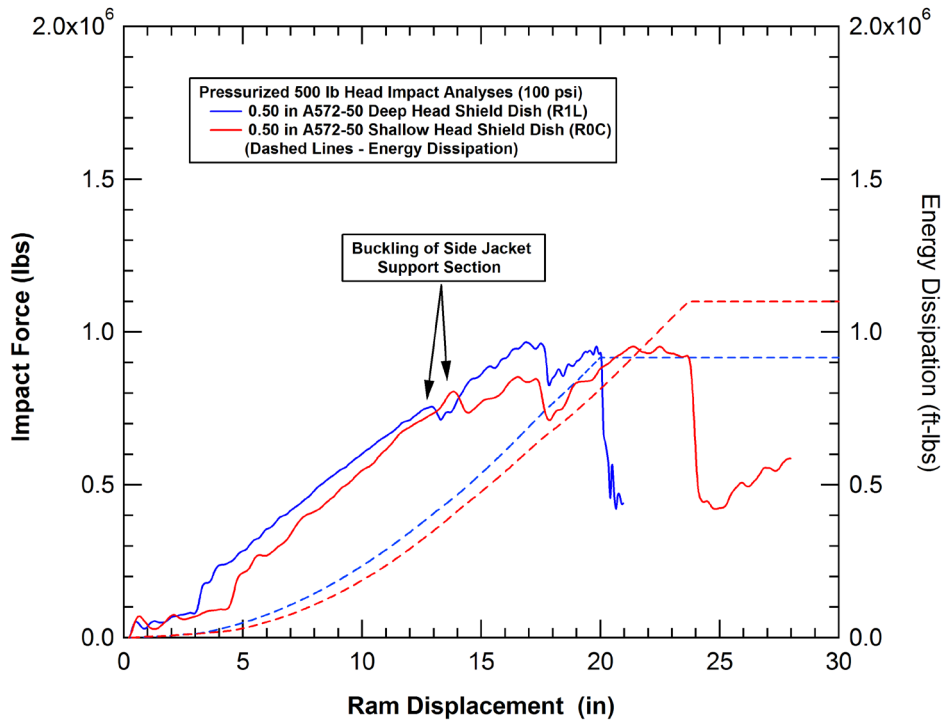
Figure 168. Calculated effects of the head shield profile (0.500-inch-thick shield).

130
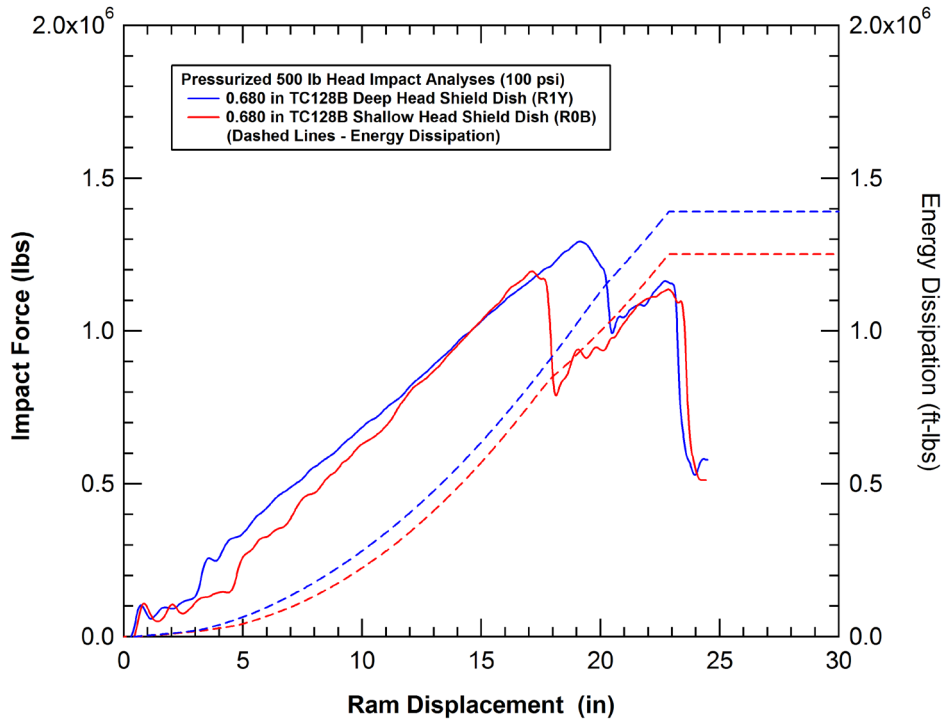
Figure 169. Calculated effects of the head shield profile (0.680-inch-thick shield).
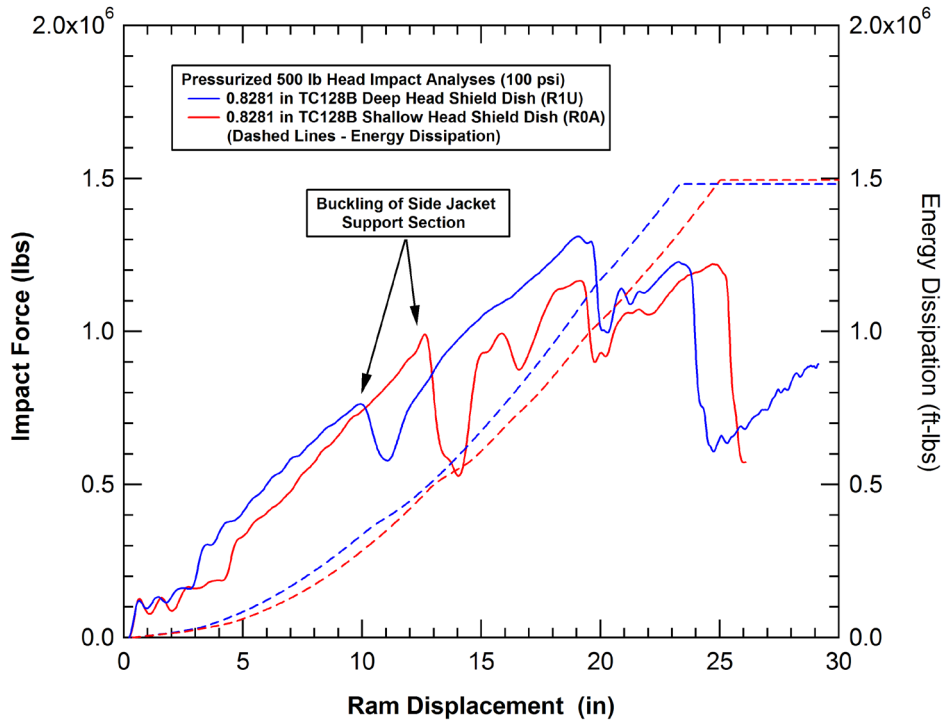
Figure 170. Calculated effects of the head shield profile (0.8281-inch-thick shield).

5.3.3 Analyses of Head Retrofit Designs

In addition to the baseline analyses with either an 11 gauge jacket or 0.5 inch head shield, analyses of retrofit head systems were performed with 0.680 and 0.8281 inch thick TC128B head shields. Force-deflection characteristics for unpressurized 500 lb tank heads with various head shields are compared to the baseline 600 lb head with 0.5 inch A516-70 head shield in Figure 171. The comparison shows that the 0.8281 inch thick TC128B head shield significantly increases the puncture resistance of the head. For the 500 lb tank head, the increase from the 0.50-inch head shield to the 0.8281 inch head shield produced greater than a 50% increase in puncture energy (1.14 to 1.84 million ft-lbs). The retrofit 500 lb head also has a higher puncture energy than the baseline 600 lb head with a 0.5 inch head shield.
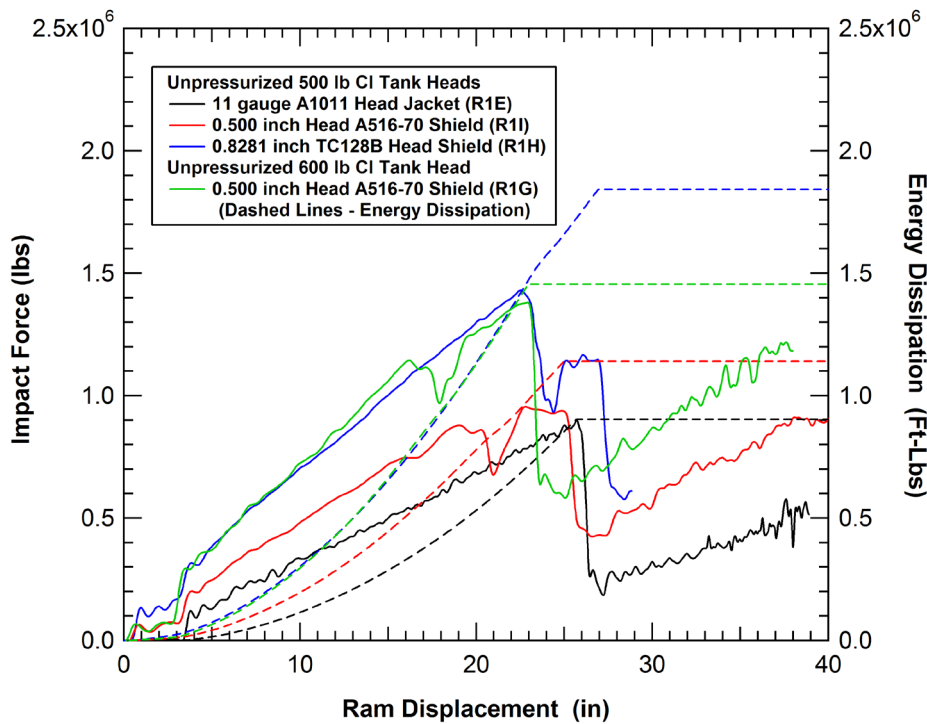
Figure 171. Calculated force-deflection behaviors for various unpressurized head designs.

The analyses of the unpressurized retrofit 300 lb head with a 0.8281 inch thick TC128B head shield is compared to the baseline 600 lb heads with 0.5 inch A516-70 head shields in Figure 172. The comparison shows that the 300 lb tank head with the thick head shield is punctured with a lower peak impact force but sustains larger overall displacements before the head is punctured. As a result, the retrofit 300 lb head has a higher puncture energy than the baseline 600 lb head with a 0.5 inch head shield (1.45 versus 1.98 million ft-lbs).
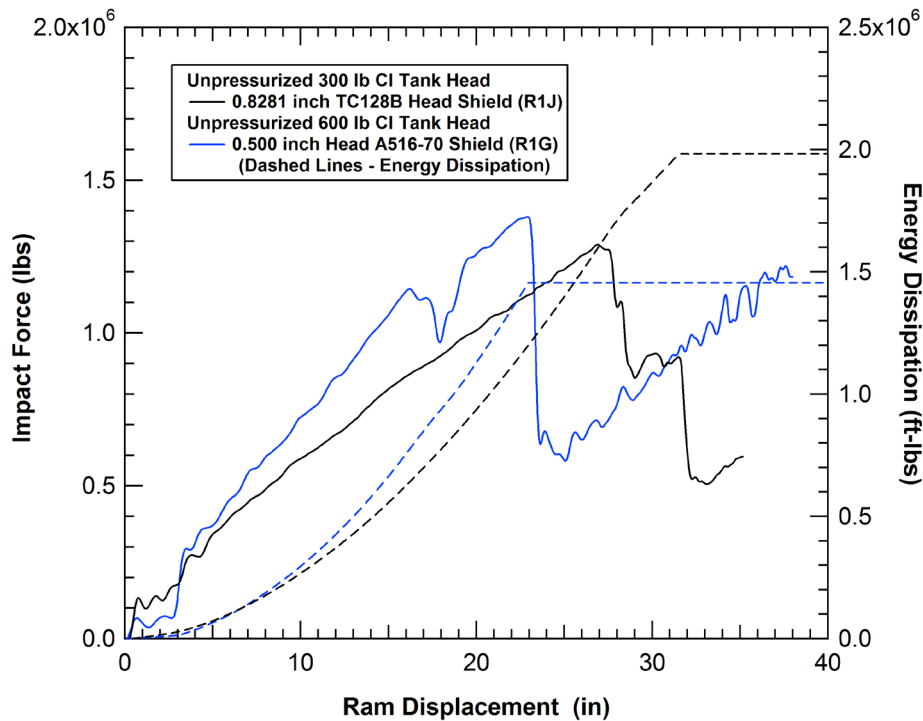
Figure 172. Comparison of unpressurized 600 lb and retrofit 300 lb tank head impacts.

Force-deflection characteristics for the pressurized 500 lb tank heads with various head shields are compared to the pressurized 600 lb head with 0.5 inch A516-70 head shield in Figure 173. The comparison shows that both the 0.680 inch and the 0.8281 inch TC128B head shields significantly increases the puncture resistance of the pressurized head.

For the 500 lb tank head, the increase from the 0.50-inch head shield to the 0.8281 inch head shield produced greater than a 50% increase in puncture energy (0.92 to 1.48 million ft-lbs). Similarly, the increase from the 0.50-inch head shield to the 0.680 inch head shield produced greater than a 30% increase in puncture energy (0.92 to 1.28 million ft-lbs). Both of the retrofit 500 lb heads have higher puncture energies than the baseline 600 lb head with a 0.5-inch head shield (1.48 and 1.28 versus 1.11 million ft-lbs).

The analyses of the pressurized retrofit 300 lb head with a 0.8281-inch-thick TC128B head shield are compared to the baseline 600 lb heads with 0.5-inch A516-70 head shields in Figure 172. When the 100 psi internal pressure is added to the head systems the overall stiffness of the two designs is much closer. The pressurized head comparison shows that the 300 lb tank head with the thick head shield is punctured with both higher peak impact force and larger overall displacements before the head is punctured. As a result, the retrofit 300 lb head has a higher puncture energy than the baseline 600 lb head with a 0.5 inch head shield (1.54 versus 1.12 million ft-lbs).
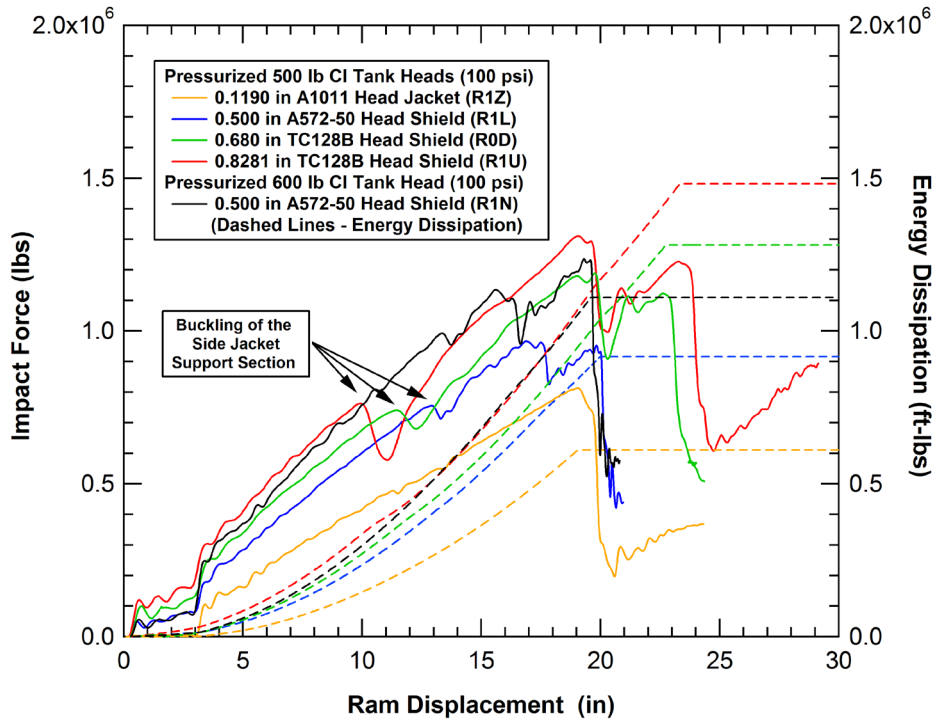
Figure 173. Calculated force-deflection behaviors for various pressurized head designs.
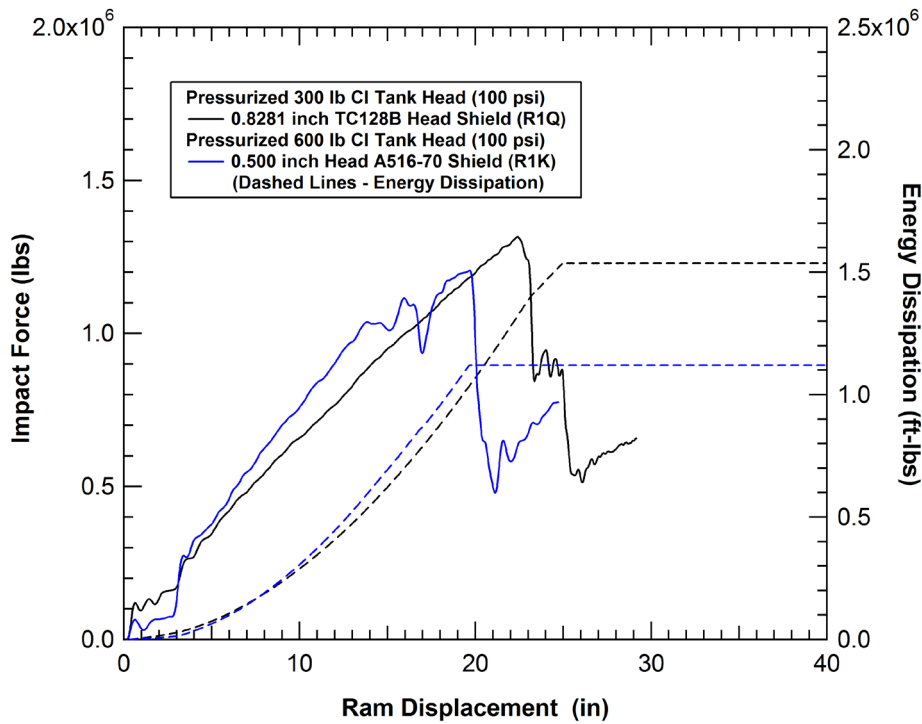
Figure 174. Comparison of pressurized 600 lb and retrofit 300 lb tank head impacts.

A summary of the analyses of the unpressurized 500 lb tank head with the various head shield thicknesses is provided in Figure 175. The puncture energy levels calculated for the 600 lb head with the baseline jacket and head shield are also indicated in the figure. The comparison shows that a retrofit head shield thickness of approximately 0.65 inch would be required for a 500 lb head to provide a similar level of puncture resistance as the 600 lb head with a 0.5 inch A516-70 head shield. The conclusions are similar for both the unpressurized and pressurized heads as shown in Figure 175.
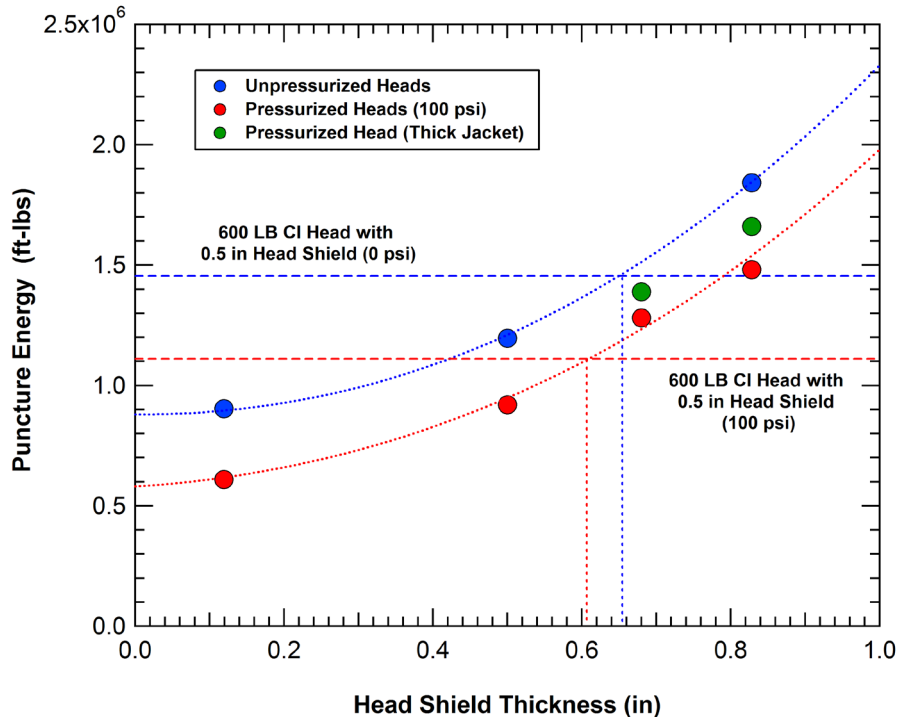
Figure 175. The effects of head shield thickness on puncture energy for a 500 lb head.

A secondary effect, not shown in the figure, is the effect of the head shield material. The 11 gauge (0.119 inch) head jacket was made of A1011 Steel, the 0.50 inch head shield was made of A516-70, and the 0.675 and 0.8281 inch head shield was made of TC128B. However, these material effects are believed to be small compared to the effect of the head shield thickness. Another effect illustrated in Figure 175 is that when a thicker retrofit head shield is supported by a thicker retrofit jacket over the tank shell (0.375-inch TC128B in this example), the head shield provides a greater level of puncture protection (calculations indicated by the green dots).

5.3.4 Head Impact Analyses on Ethylene Oxide Tank Heads

All of the above head impact analyses were performed using the chlorine tank head geometry (2:1 ellipsoid with a 100 inch major diameter). A set of three additional head impact analyses

were performed on EO tank configurations to confirm that the response is consistent with those from the above analyses on Cl tank heads. The dimensions of the Cl and EO tank heads were previously provided in Table 3. A summary of these EO tank head impact analyses is provided in Table 8. The analyses include the baseline 300 and 500 lb EO heads, each with a 0.5 inch head shields and a 300 lb head retrofit with a 0.8281 TC128B Head Shield. The calculated force-deflection characteristics for the EO heads are shown in Figure 176.

Table 8. Summary of pressurized EO head impact analyses

Calculation	Head Thickness	Jacket or Head Shield	Shell Jacket	Impact Velocity	Puncture Force (lbs)	Puncture Energy (ft-lbs)
R1R	0.6030	0.500" A572-50	11 gauge A1011	14 mph	929,000	1,116,000
R1S	0.6030	0.8281" TC128B	0.375" TC128B	14 mph	1,347,000	1,931,000
R1T	0.9784	0.500" A572-50	11 gauge A1011	14 mph	1,218,000	1,419,000
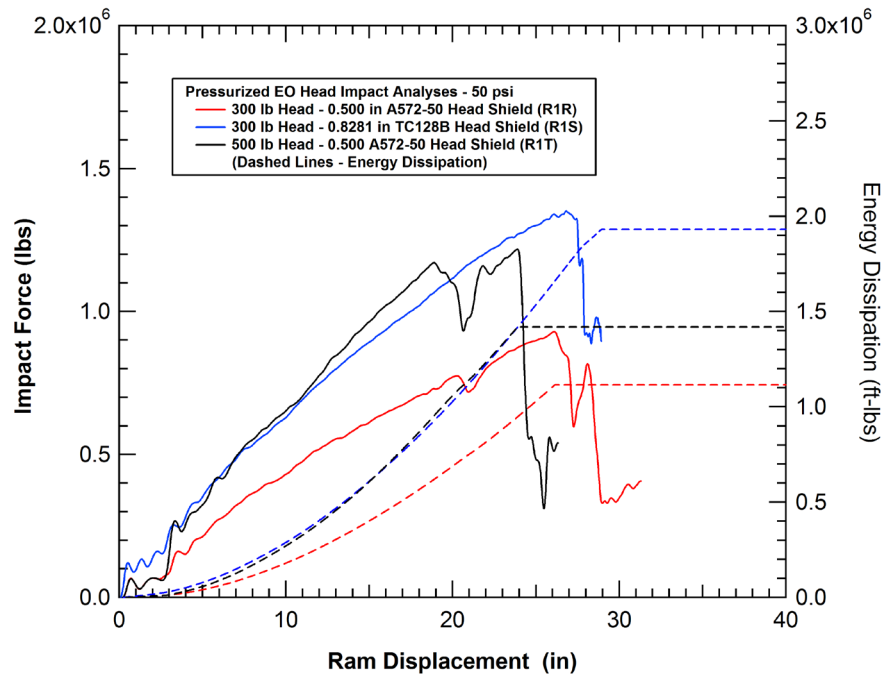
Figure 176. Calculated force-deflection behaviors for EO Tank head geometries.

The calculated puncture energy of the retrofit 300 lb EO tank head with the 0.8281 inch head shield was over 1.9 million ft-lbs and was approximately 35% higher than the puncture energy for the 500 lb EO head with the 0.5 inch head shield. Once again, a simple retrofit of adding additional thickness to the head shield was capable of providing a higher protection level than the tank with the higher test pressure head thickness.

The comparison of the relative impact responses of EO and Cl heads are provided in Figure 177 and Figure 178 for 500 lb and 300 lb configurations, respectively. The 500 lb comparison is difficult since a number of parameters were different. The EO tank head has a diameter of 119 inches compared to 100 inches for the chlorine head. The 500 lb EO tank head has a thickness of 0.9784 inch compared to 0.8281 inch for the chlorine head. Finally, the EO was pressurized to 50 psi where analyses were performed for unpressurized and 100 psi pressure levels for the chlorine head. However, it was clear that the 500 lb EO tank head had a higher puncture force and puncture energy than the 500 lb chlorine head.
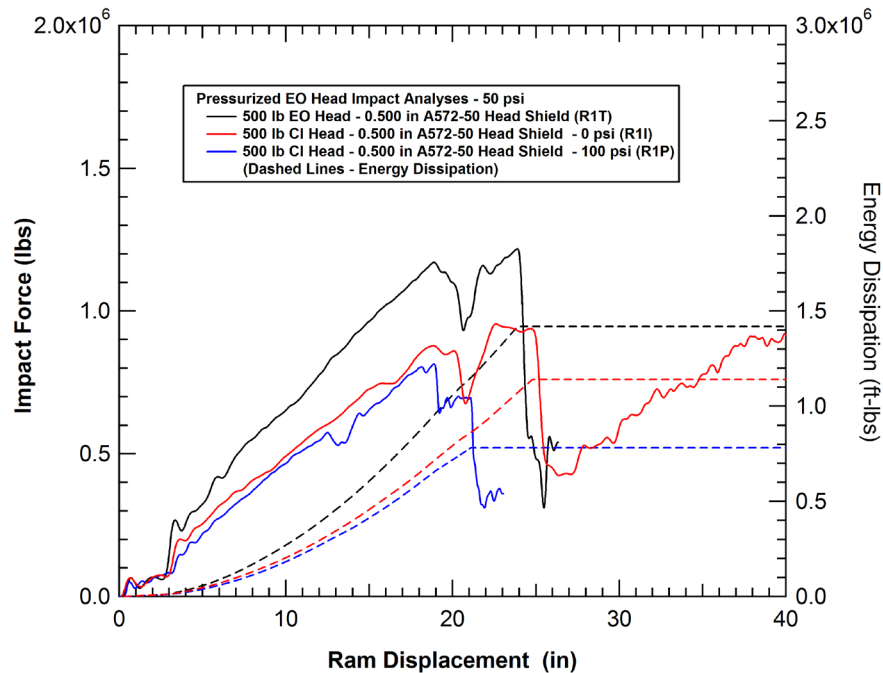
Figure 177. Calculated force-deflection behaviors for 500 lb EO and Cl Tank heads.

The comparison of the 300 lb EO and Cl tank heads is shown in Figure 178. In the 300 lb head configurations, both tank heads have the same thickness (0.5625-inch). Thus, the only differences were the head diameters (119 vs. 100 inches) and the internal pressure (50 vs. 100 psi). Again, for the 300 lb configuration, the EO tank head had a higher puncture energy than the chlorine head. However, in this case the head systems had equivalent thicknesses and as a result had nearly equivalent puncture forces. The additional energy resulted from the lower compliance of the EO head and correspondingly larger indentations before the puncture initiation.
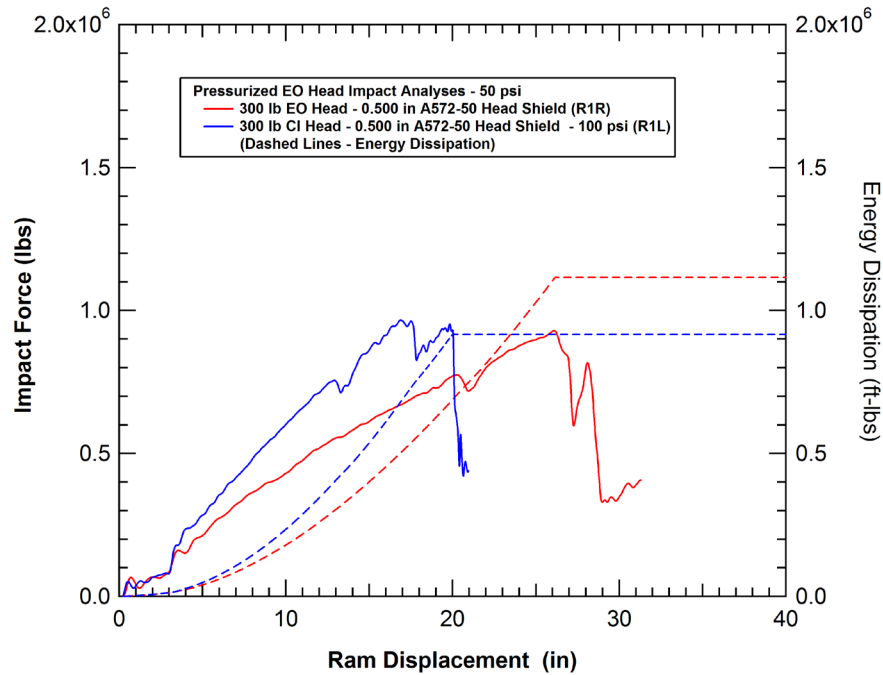
Figure 178. Calculated force-deflection behaviors for 300 lb EO and CI Tank heads.

5.3.5 Effects of Impactor Size

An important factor for assessing the impact conditions that will puncture a tank head is the size of the impacting object. The baseline impactor used in the analyses for this report is the square 6x6 inch impactor. However, we want to assess other impactors to make sure that any protective concepts that are developed will be appropriate for general impact conditions.

To evaluate the effects of the ram impactor size, analyses were performed on head geometries being impacted by both 9x9 inch and 12x12 inch ram impactors with a 0.50-inch radius around the edges. A summary of the impact analyses are shown in Table 9. The analyses include both the 500 lb and 600 lb chlorine tank head configurations with the 0.5 inch thick A572-50 full height head shield. A summary of the head impact analyses with the different impactor sizes is provided in Table 9.

The force-deflection characteristics for the various 500 lb and 600 lb tank head impact analyses are provided in Figure 179 and Figure 180, respectively. All of these head impact analyses included a 0.50-inch-thick A572-50 head shield. The comparisons show that the force-deflection characteristics are mostly independent of the impactor size, up to the point of head shield puncture initiation. However, the load level at which the penetration is initiated is strongly influenced by the impactor size.

Table 9. Summary head impact analyses with various impactor sizes. [1]

Calculation	Head Thickness	Jacket or Head Shield	Impactor Size	Impact Velocity	Puncture Force (lbs)	Puncture Energy (ft-lbs)
R1K	1.1360	0.50-inch A572-50	6 x 6 inch	14 mph	1,206,000	1,121,000
R1L	0.8281	0.50-inch A572-50	6 x 6 inch	10 mph	966,000	916,000
R1V	1.1360	0.50-inch A572-50	9 x 9 inch	25 mph	1,868,000	2,450,000
R1W	0.8281	0.50-inch A572-50	9 x 9 inch	25 mph	1,325,000	2,010,000
R0F	1.1360	0.50-inch A572-50	12 x 12 inch	25 mph	2,334,000	3,672,000
R0G	0.8281	0.50-inch A572-50	12 x 12 inch	25 mph	1,746,000	3,515,000

Notes: (1) All analyses performed on chlorine tank heads pressurized to 100 psi.
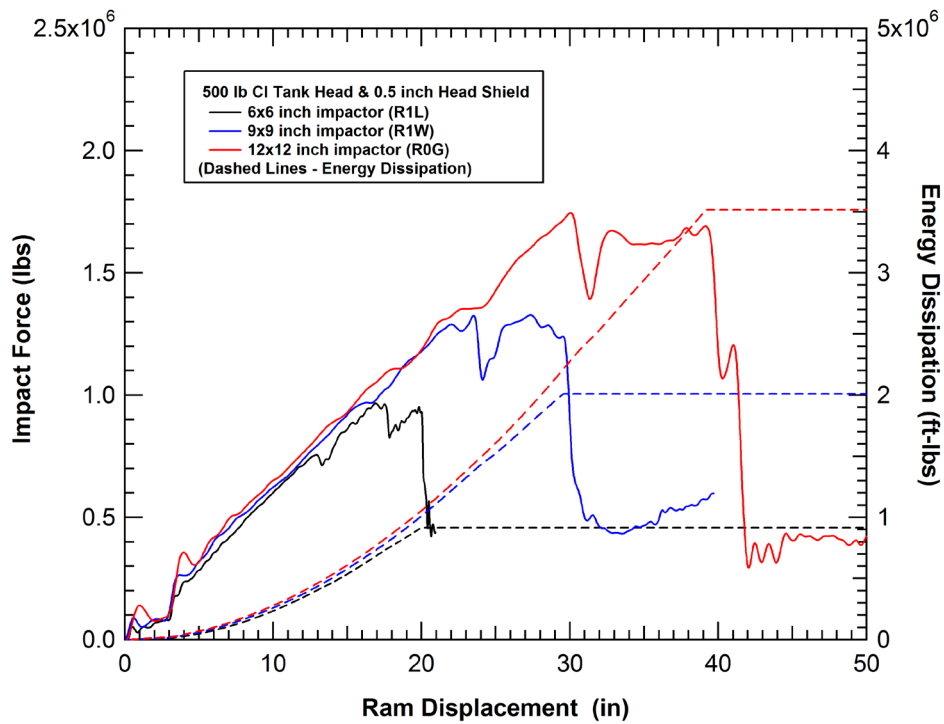
Figure 179. Impactor size effects on the 500 lb Cl tank head.
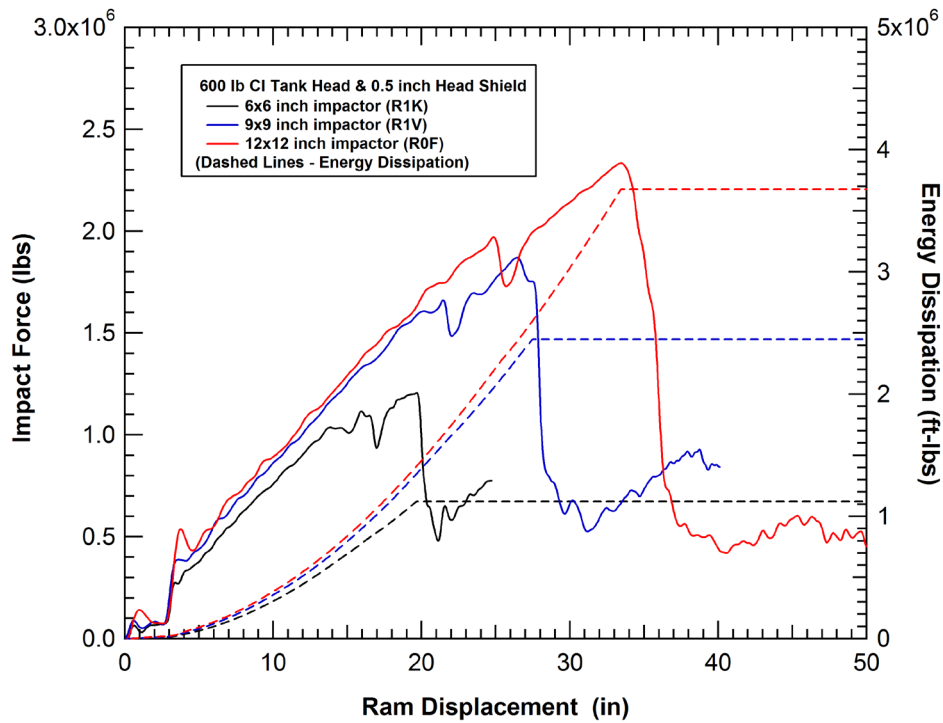
Figure 180. Impactor size effects on the 500 lb CI tank head.

The calculated puncture forces and puncture energies for both the 500 lb and 600 lb tank heads as a function of the ram size are summarized in Figure 181 and Figure 182, respectively. The puncture forces correlate closely to a linear function of the ram size. This again is consistent with the puncture initiation resulting from the local shear stresses at the perimeter of the ram contact face. The puncture energies also are close to a linear relationship to ram size over the range analyzed but the correlation does not go through the axis of the plot. As a result, the puncture energies are significantly increased when a larger impactor size is used.

The calculated energy balance for the 12-inch impactor and 600 lb tank head is shown in Figure 183. The initial impact energy is approximately 6.2 million ft-lbs (all in the kinetic energy). As the impact progresses, the ram is decelerated and the kinetic energy drops off. The energy transfer is from the kinetic energy of the ram to the internal energy of the tank head (plastic deformations of the tank material) and the pressure-volume work caused by the indentation reducing the total tank volume. The internal energy of the tank at rupture is approximately 3.8 million ft-lbs and the pressure volume work is approximately 400,000 ft-lbs. The hourglass energy and sliding energy in the calculation are both negligible indicating that the calculation is stable and does not have any numerical energy losses.
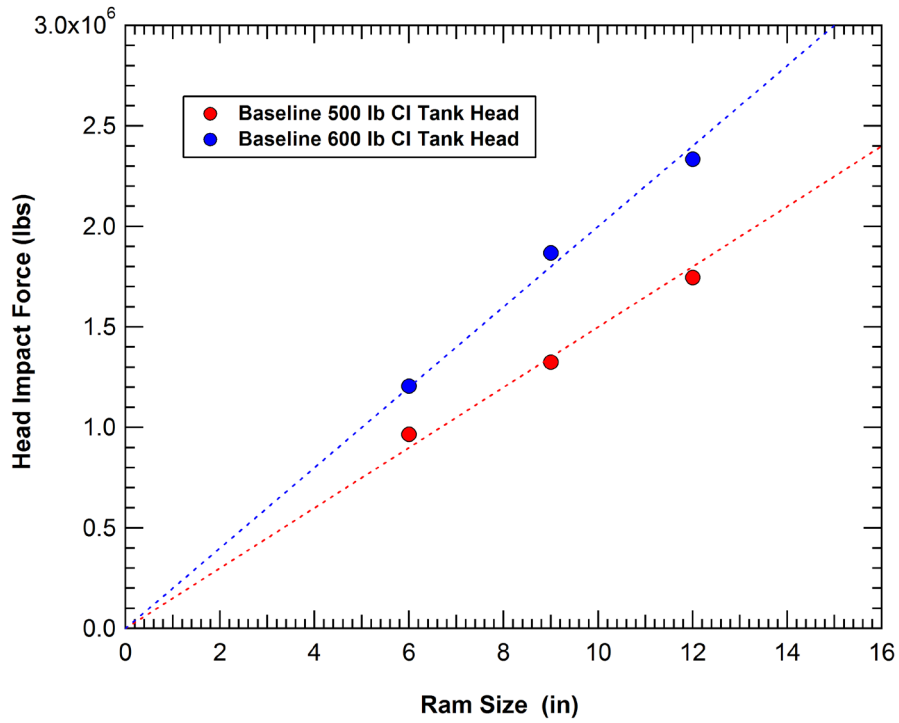
Figure 181. Summary of impactor size effects on the puncture forces for CI tank heads.
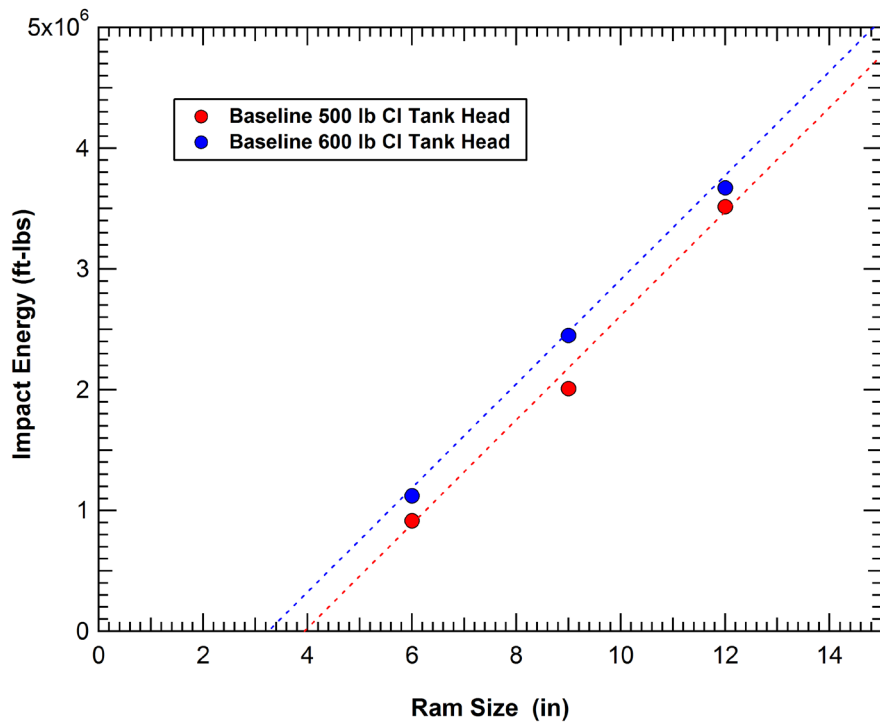
Figure 182. Summary of impactor size effects on the puncture energies for CI tank heads.
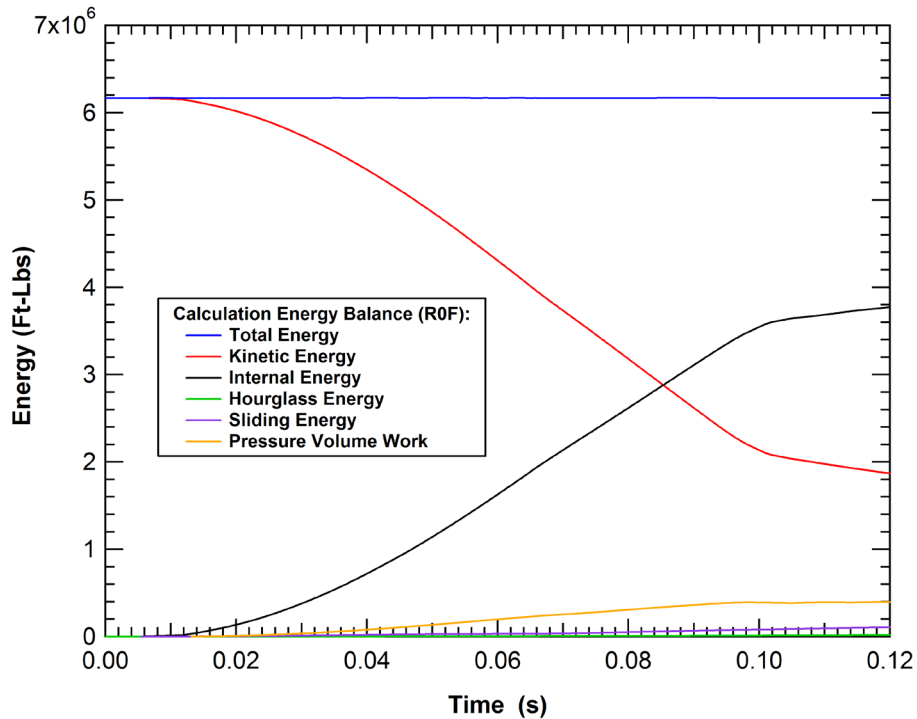
Figure 183. Energy balance for the 12-inch impactor and 600 lb CI tank head.

Based on the energy transfer to the pressure-volume (PV) work, the effects of the tank volume change can be assessed. The 400,000 ft-lbs PV work corresponds to a change in volume of 28 cubic feet (207 gallons) with a constant 100 psi (14400 psf) pressure assumption. Using a tank nominal capacity of 17,300 gallons, the change in volume is approximately 1.2%. Therefore, the change in volume (ΔV) is much smaller than the original outage volume (approximately 10%) and the constant pressure assumption of these analyses is a reasonable approximation. The hydrodynamic effects of the longitudinal sloshing of the lading in a head impact was not evaluated.

5.3.6 Effects of Impact Speed

A potential factor for assessing the impact conditions that will puncture a tank head is the speed of the impacting object. As a reference, the lower bound of impact speed was assessed by performing a quasistatic loading of the tank car using the 6x6 inch impactor as a punch. The comparison of the dynamic impact response with the quasistatic behavior is shown in Figure 184. The comparison shows that for this tightly constrained test condition there is little effect of the impact speed on the force deflection behavior or puncture energy.
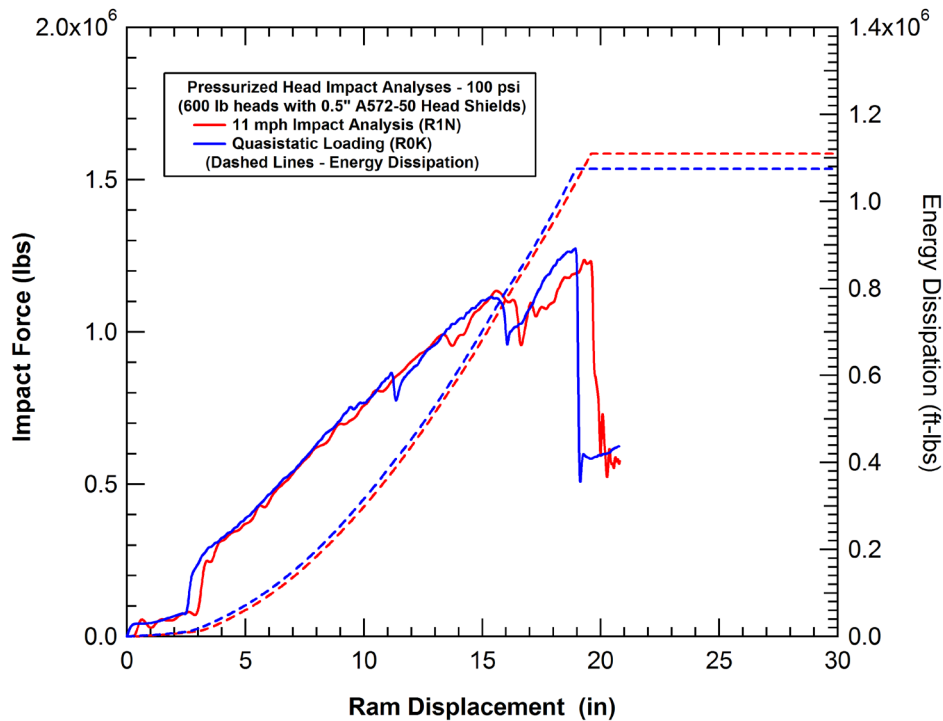
Figure 184. Effect of impactor speed on the puncture of a 500 lb CI tank head.

5.3.7 Summary of the Head Impact Analyses

The calculated head impact forces as a function of the combined head and head shield thickness are shown in Figure 185. The head impact analyses are added to the previous calculated forces for the side impacts, shown previously in Figure 144. The figure shows the analyses are mostly consistent with a linear relationship between puncture force and total thickness of the protective layers. However, the pressurized heads and the thicker head systems failed at forces that were on average a little lower than the linear fit to the side impact analyses.

The proposed failure mechanism for the lower puncture forces is that, for the stiffer head systems, the offset impact creates a larger stress concentration along the upper edge of the impactor face and the failure initiates at that location at a lower total force. The more compliant head systems allow for a larger dent to form and the impactor develops a more uniform stress distribution around the perimeter for the impact patch at the bottom of the indentation.
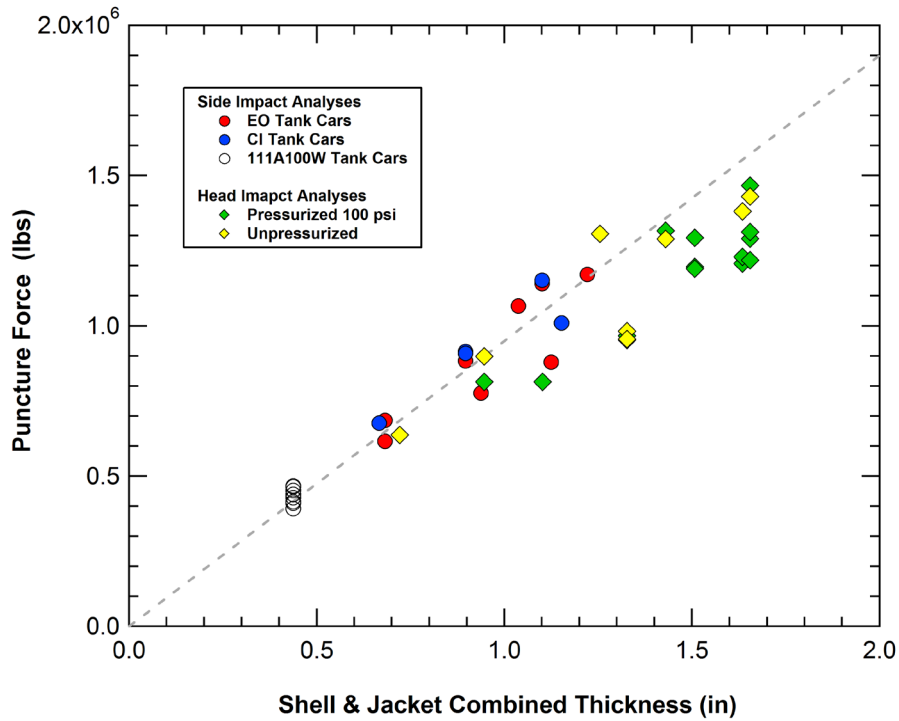
Figure 185. Calculated puncture forces as a function of system thickness.

The calculated puncture energies for all of the side and head impact analyses are plotted against the combined thickness of the system in Figure 186 (6x6 inch impactor only). When comparing all of the puncture energies, the data falls into four separate groups that are distinguished by the impact type (side or head) and the tank pressure. Again, the comparison indicates that the total thickness is the dominant parameter that determines puncture energy for a given impact condition and pressure level. This shows that a retrofit design with an increased jacket thickness should provide equivalent protection to thicker commodity tank systems with equivalent combined shell and jacket thicknesses.
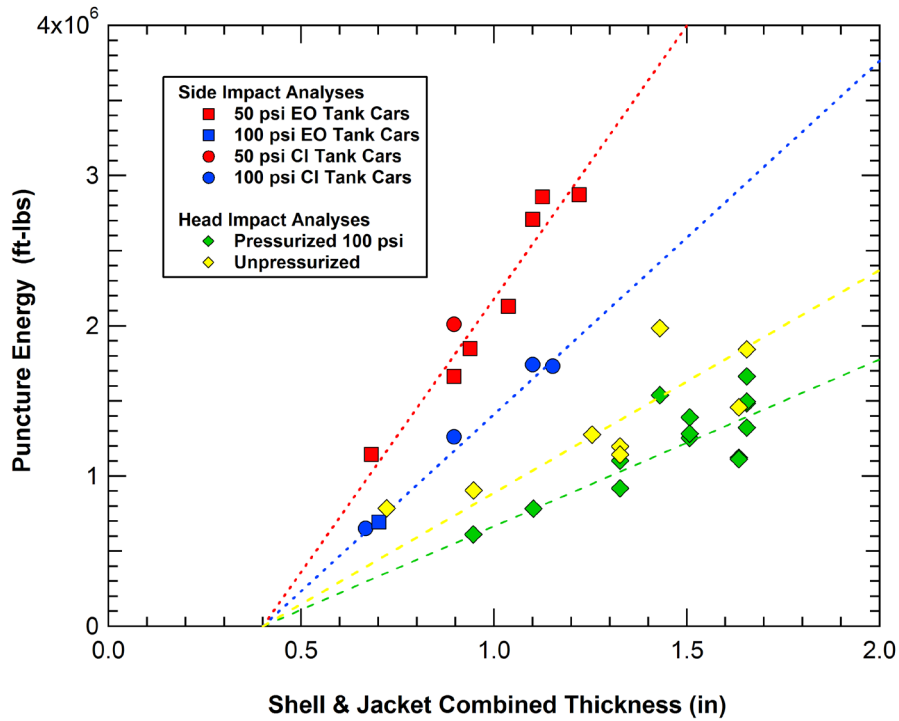
Figure 186. Calculated puncture energies as a function of system thickness.

The above summary of the puncture energies from the various analyses can be applied to assess the system requirements for more severe impact scenarios. For example, we can assess the head or side protection requirements to resist a puncture by the ram car with the 6x6 inch ram head at an impact speed of 18 mph. The impact energy for the 295,000 lb ram car at 18 mph is slightly over 3 million ft-lbs. If we extrapolate the impact energy summary, as shown in Figure 187, we would predict that the 3 million ft-lb puncture energy requires approximately 2.4 inches of steel for an unpressurized head and 3.1 inches of steel for a pressurized head (100 psi).

To check the validity of these estimates, a pair of analysis was performed for thicker head systems. The first analysis was on a pressurized head system that had a 1.6 inch head and 1.6 inch head shield for a total thickness of 3.2 inches. The second analysis was on an unpressurized head system that had a 1.2 inch head and 1.2 inch head shield for a total thickness of 2.4 inches. For both analyses, the head and shield were supported by a side cylindrical shell sections that were one inch thick. The heads and shields were assumed to have the baseline TC128B constitutive and failure properties used for the majority of tank shells and head analyses in this report.
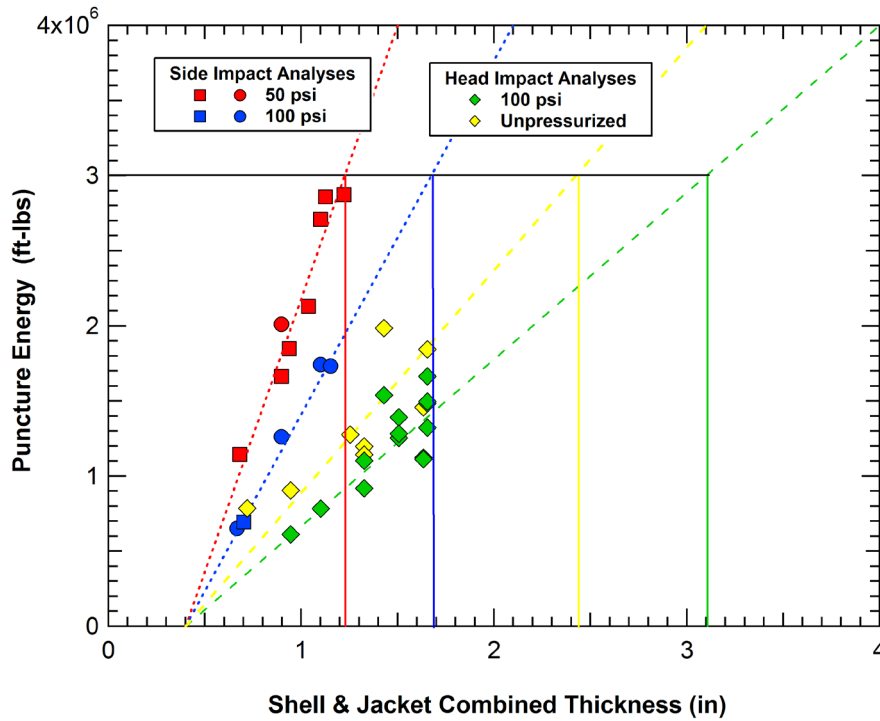
Figure 187. Extrapolated requirements for a 3 million ft-lb puncture energy.

The model and calculated impact behavior for the 18 mph impact on the pressurized head is shown in Figure 188. The head shield was punctured and fractures were initiated in the head, but a full penetration did not occur. The calculated damage in the impact zone is shown in Figure 189. The calculated level of damage indicates that the 18 mph impact is very close to the puncture threshold for this response (material is failed at a damage magnitude of 1.0).

The model and calculated impact behavior for the 18 mph impact on the unpressurized head is shown in Figure 190. The head and head shield were both punctured in this impact with only a very small fraction of residual kinetic energy at the time the head is punctured. The ram forward motion has been completely stopped in the deformed state shown in Figure 190.
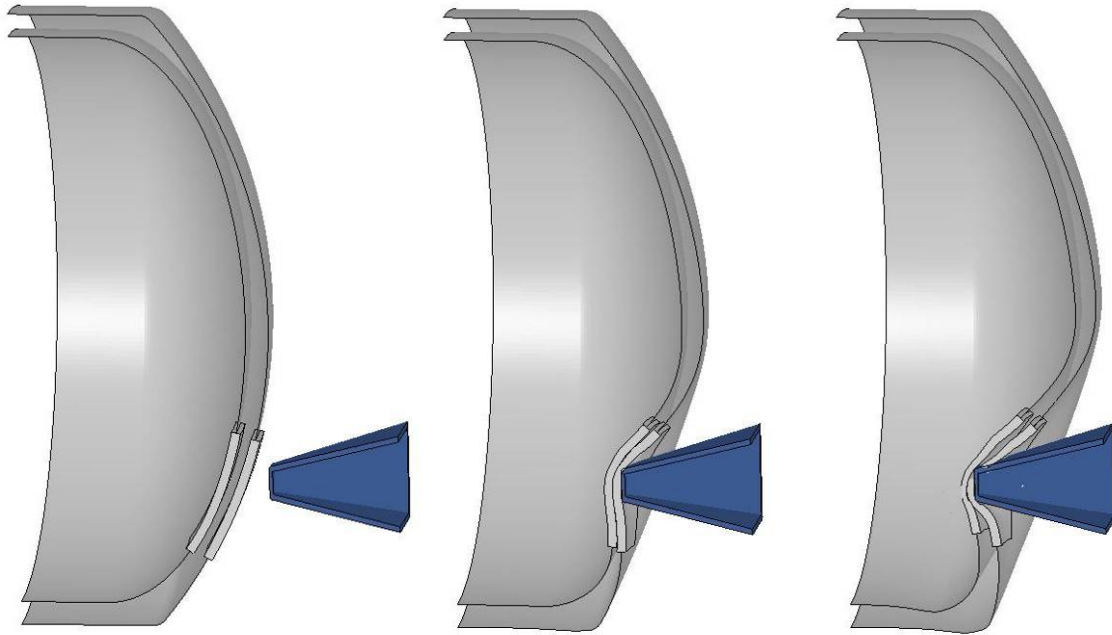
Figure 188. Calculated 18 mph impact response for the thick pressurized head system.
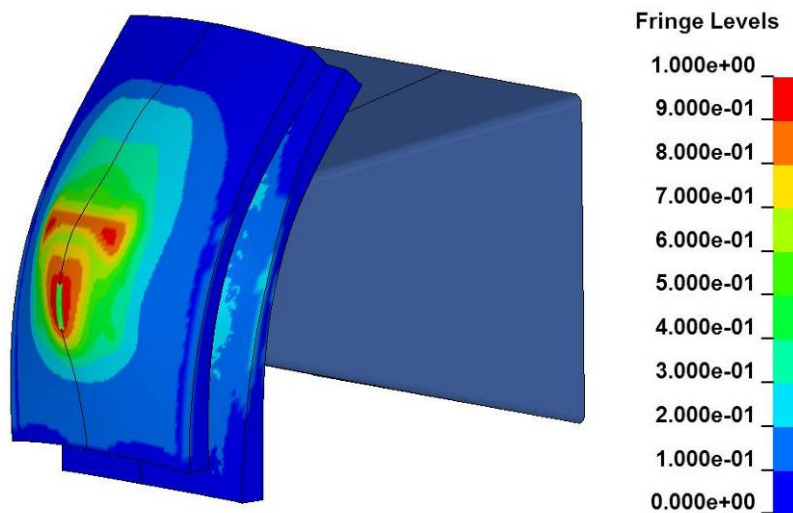
Figure 189. Calculated Bao-Wierzbicki damage levels in the thick head impact zone.

The updated puncture energy summary including the results of these thick head system analyses is shown in Figure 191. These analyses agree well with the expected values based on the extrapolation of previous results on thinner systems. Similarly, the updated punch force summary including these analyses is shown in Figure 192. Again, the forces agree very well with the linear fit to the total system thickness.
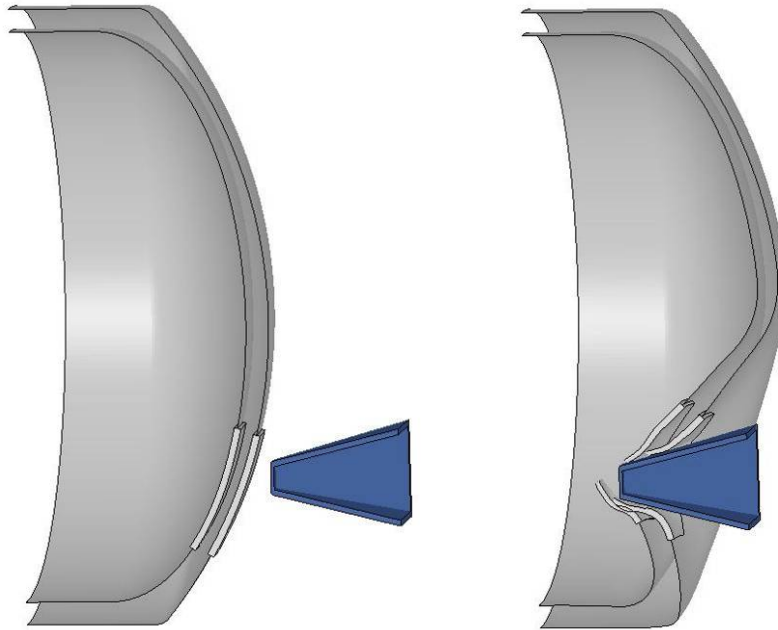
Figure 190. Calculated 18 mph impact response for the thick unpressurized head system.
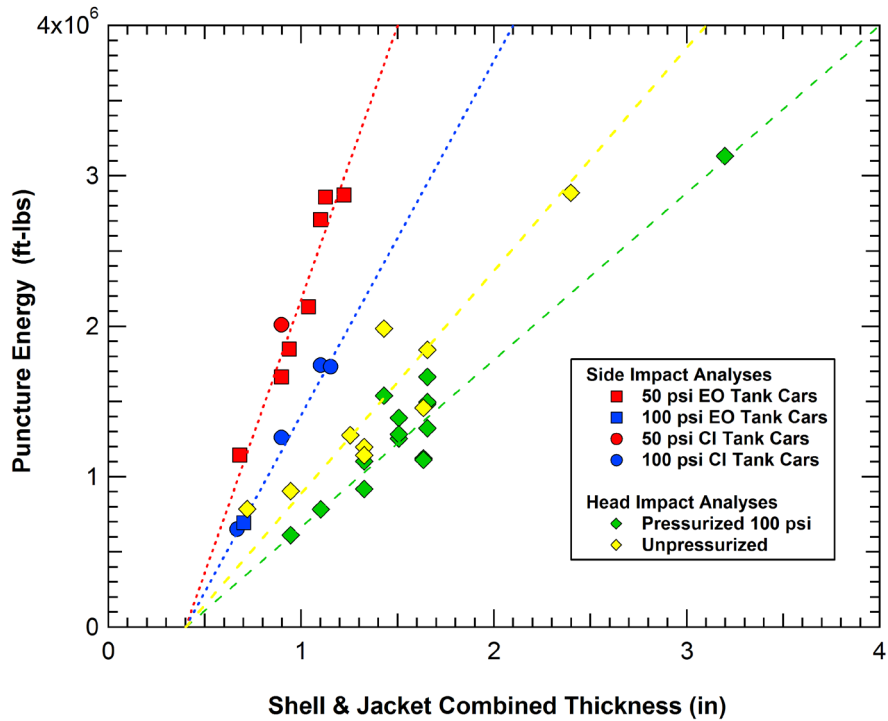
Figure 191. Calculated puncture energies as a function of system thickness.
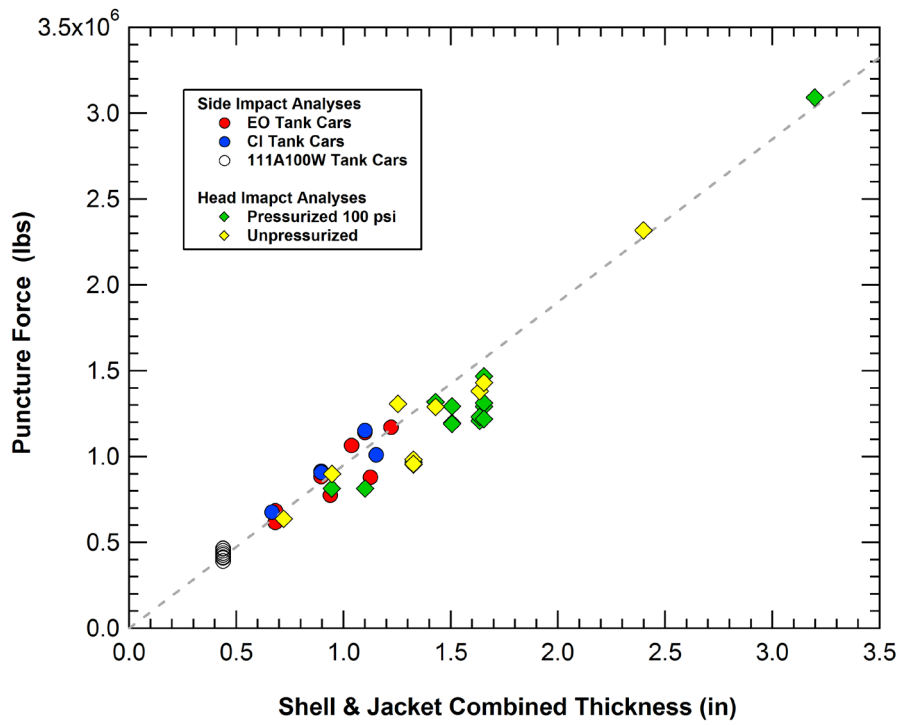
Figure 192. Calculated puncture forces as a function of system thickness.

6   Detailed Evaluation of Alternate Protection Concepts

In the previous sections of this report, the tank geometries and protection systems evaluated were either designs currently in operation or simple variations on those designs where the thickness and or materials used for the tank, jacket, or head shields was varied. This section provides information on the development of advanced tank car protection strategies. The primary approach was to adapt crash, energy absorption, and impact protection technologies to develop tank car puncture protection systems that could be adapted on to an existing tank car. Technologies investigated included energy absorbing materials (e.g. crushable foams) and advanced structural designs (e.g. sandwich structures with various core designs).

6.1   Evaluation of Foam Protection Systems

Structural foams have been applied to structures for crash safety and energy dissipation applications. They can easily be added to complex enclosed spaces and typically perform well in crushing when the foam remains confined [e.g. 67, 68].

This use of foams for the advanced tank car protection concept has several advantages. The tank car and confining jacket layers can be fabricated and assembled using the same facilities and equipment used for current tank car designs. The foams can be added to the tank cars relatively easily using available foaming equipment. Finally, the foam has beneficial properties for insulation and thermal protection of the tank, in addition to the energy absorbing characteristics.

The primary foam used in this effort was a Dow BETAFOAM™. This foam is classified as a rigid, all-water blown molded foam. BETAFOAM™ is designed to produce large, highly contoured, thin parts. In tank cars, the proposed concept was to add structural foams between the jacket and commodity tank. The foam would dissipate energy through crushing when impacted and could potentially act as a core material to couple the tank and jacket layers as a sandwich structure for improved performance. In some designs, multiple layers were used with two jackets applied to the tank and different density foams applied between the jackets and between the inner jacket and the tank. Variations in the thicknesses of the various layers and foam densities could be used to optimize the system.

In the following sections, the testing and analysis on structural foams and foam protection concepts are described. These efforts include a preliminary set of characterization tests on a range of foam densities and strengths and associated preliminary analyses to develop foam protection system concepts. Subsequently, a more detailed set of material characterization tests and component tests were performed using both a low density foam and a high density foam. These foams had nominal densities of 5 and 18 pounds per cubic foot (pcf) and corresponding crush strengths of approximately 100 psi and 1000 psi, respectively. A more accurate foam

constitutive model was developed and validated against the updated characterization testing and used in subsequent analyses of the foam system performance.

6.1.1 Validation of Foam Modeling

There are several constitutive models available in LS-DYNA that are appropriate for different types of foam materials. Many of these models are developed to include a strong dependence of the strength on the level of hydrostatic confining stress. This behavior is seen in some types of foam and is common to soils and geologic materials. Determination of the constitutive parameters for this type of model requires a series of triaxial material characterization tests as described in Reference 69.

For much of this effort, the primary information available on the foam materials was a preliminary set of unconfined compression tests to measure the crush curves. As a result, a simple crushable foam constitutive model was used where the behavior was fit to the unconfined compression test only. The specific model was the Material Type 63 constitutive model (*MAT_CRUSHABLE_FOAM or *MAT_63 in Reference 15) and the crush behaviors were obtained from the unconfined compression tests described below.

As the evaluation of foam systems progressed, a more comprehensive series of foam characterization tests were performed to allow the constitutive parameters to be determined for more complex foam models. These tests include unconfined compression tests, uniaxial compression tests, and triaxial compression tests as well as tensile testing. These tests were performed on both low density (nominally 5 pcf) and high density (nominally 18 pcf) BETAFOAM™ late in this development effort. Results of these characterization tests are also presented in this section.

Following the more comprehensive material characterization, some deficiencies were identified in the constitutive behaviors in the Material Type 63 model (referred to as Mat_63 in the remainder of the report). As a result, the Material Type 75 constitutive model (*MAT_BILKHU/DUBOIS_FOAM or *MAT_75 in Reference 15) was fit to the data and used in subsequent foam impact simulations. This model allows for a more accurate representation of the tensile behavior compared to the Mat_63 model and was considered to be appropriate since the characterization testing found that the BETAFOAM™ crush strength has a small dependence on the level of triaxial confinement. Results with both models are presented in the following sections.

Preliminary Foam Compression Testing

The preliminary characterization of the foam materials was performed using a set of unconfined compression tests. These tests were performed at SwRI for a range of foam densities [70, 71].

The specimen geometry utilized during testing was a solid cylinder approximately 1.3-1.4 inch in diameter and of varying heights depending upon the thickness of the original foam block (nominally 1- or 3-inch for the Dow BETAFOAM™). A photograph of the unconfined compression test conditions for a tall (3-inch thick) specimen is shown in Figure 193. Tests were performed under laboratory air conditions with no environmental preconditioning. All of the tests were performed in a displacement control mode.

Figure 193. Dual platen setup for unconfined compression testing of foam [70].

The local measurement of displacement was made by string pots on the loading platens. The displacement rate applied during testing was on the order of 0.5-inch/minute. Data was recorded at a 2 Hz sampling rate for the load cell, LVDT on the actuator, and the string pots. A dual-condition criterion was utilized to terminate the test. The two criteria included a 90-95% total strain limit and a 5000 psi stress limit.

An example test on a short (1-inch thick) foam specimen is shown in Figure 194 [70]. The specimen is compacted to a large extent to measure the full compaction curve into the region where the foam approaches a fully compacted state. After the load is removed the specimen remains in a compacted state with little recovery as seen in Figure 194(d).
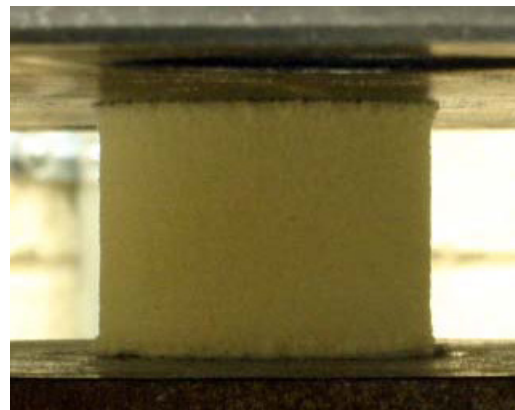
(a) 10 percent Compression

(b) 50 percent compression
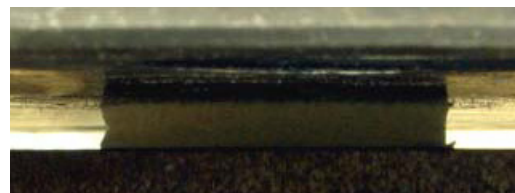
(c) 90 percent compression

(d) Post-test configuration

Figure 194. Compression test of a short (1-inch height), 5 pcf foam specimen [70].

A similar test on the tall (3 inch thick) foam specimen is shown in Figure 195. Many of these specimens developed a buckling instability as a result of the more slender specimen geometry. As a result, the corresponding crush curves for these tests will exhibit structural effects instead of a uniform material constitutive response. As much as possible, the constitutive model development efforts attempted to use the data from tests where buckling of the specimen was not significant.

(a) 8 percent Compression
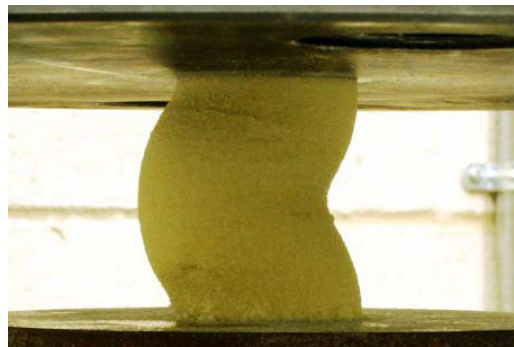
(b) 33 percent compression
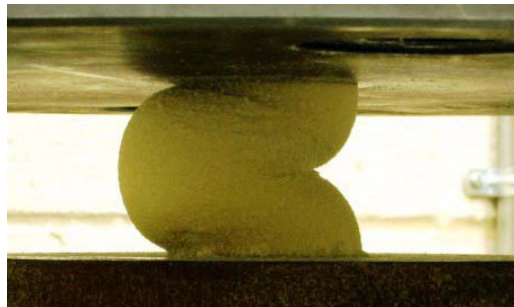
(c) 50 percent compression

Figure 195. Compression test of a tall (3-inch height), 7.5 pcf foam specimen [70].

The crush curves measured in the unconfined compression tests on the different foam densities are shown in Figure 196. These crush curves are the primary data requirement needed for the Mat_63 model. The objective of the testing was to obtain a family of crush curves for various strength foams that could be applied in the design study for the foam protection system. Two primary modifications were required for use in the constitutive models. First, the behavior under high levels of compaction needed to be extrapolated. In the severe impact events, the foam will

be compressed to load levels significantly greater than those in the unconfined compression tests. Information about the foam solid density and the analyses of the foam sandwich panel punch test were used to develop and assess the extrapolated behavior. The extrapolated behavior is indicated by the dotted line extension sections of the curves in Figure 197.
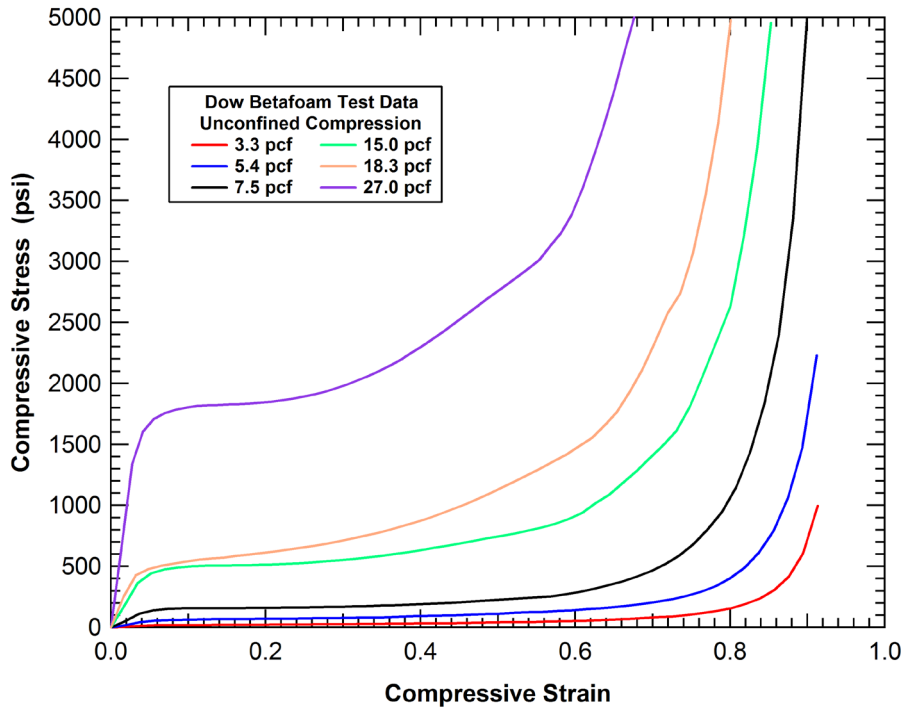
Figure 196. Unconfined compression curves for different density foams.

The second modification to the foam data required was to interpolate between some of the measured foam densities to obtain different desired crush strengths. These interpolated curves are indicated by the dashed lines in Figure 197. The interpolated data curves correspond to approximately 4.75 pcf and 22 pcf foam densities. The addition of these two interpolated foam densities results in a set of crush strengths that cover the range of interest and can be applied in different combinations to improve the puncture resistance.

The Mat_63 constitutive models developed using the unconfined compression crush curves were then used to simulate the compression tests to validate that the model parameters were properly defined. An example simulation of an unconfined compression test for the 5.4 pcf foam is shown in Figure 198. The corresponding comparison of the fit to the test data and the simulation of the test are shown in Figure 199. The comparison shows that the model is capable of accurately reproducing the measured unconfined compression behavior for the foam. In addition, when the specimens were given a small initial imperfection, the buckling behaviors could also be reproduced as shown in Figure 200.
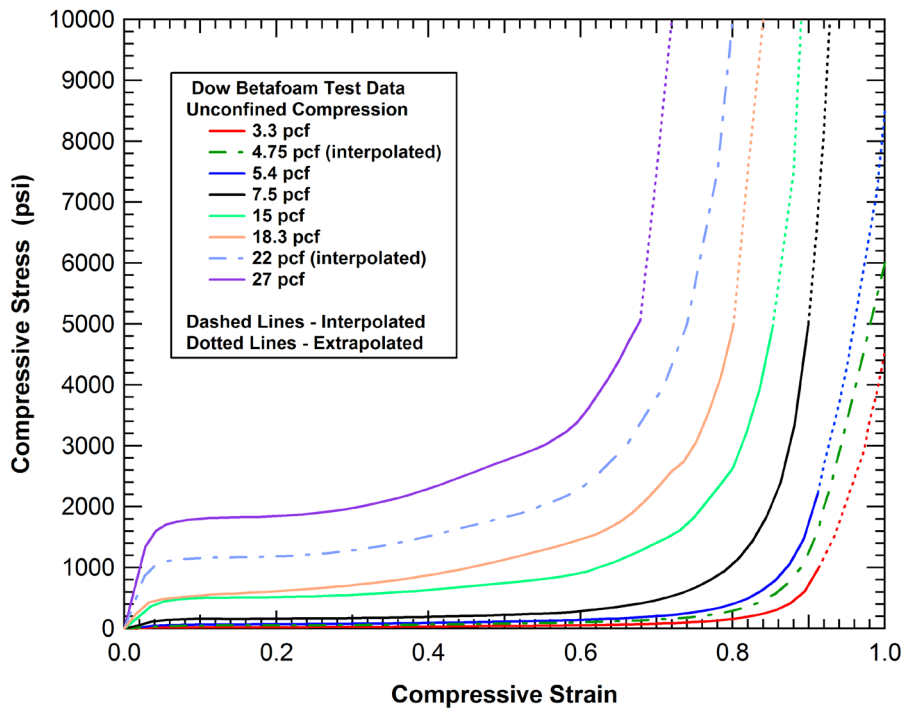
Figure 197. Unconfined compression curves for different density foams.

(a) Initial state   **(b) Fully compacted**
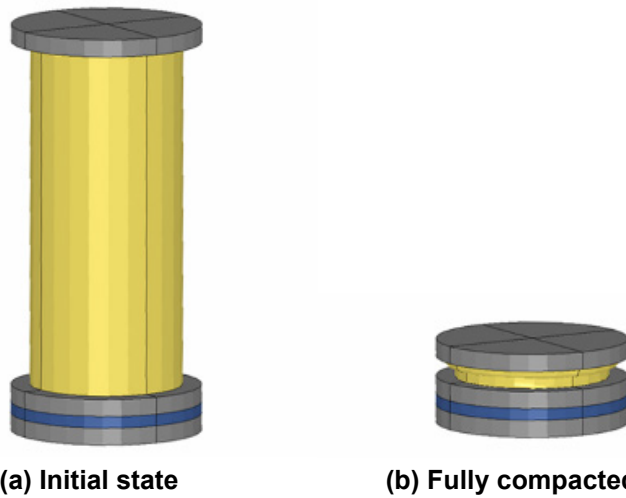
Figure 198. Simulation of an unconfined compression test (5.4 pcf foam).
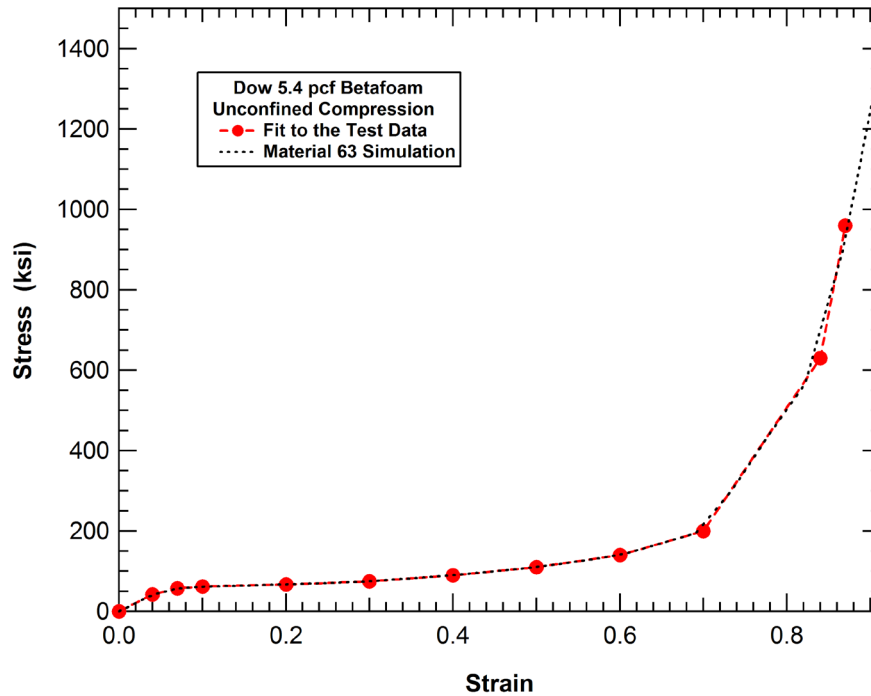
Figure 199. Constitutive model fit and compression test simulation (5.4 pcf foam).

(a) Initial state   **(b) Buckled specimen**
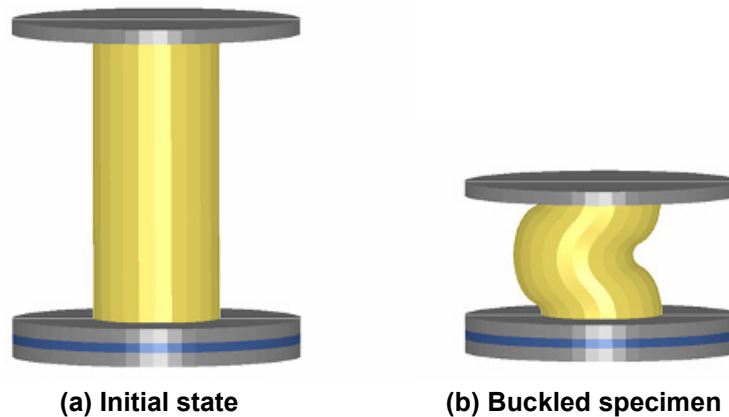
Figure 200. Simulation of the specimen buckling in unconfined compression tests.

Updated Foam Characterization Testing

To allow for a more comprehensive modeling and validation of the foam response, a detailed set of foam characterization tests were performed. These tests include unconfined compression tests, uniaxial compression tests, and triaxial compression tests as well as tensile testing. These tests were performed on both low density (nominally 5 pcf) and high density (nominally 18 pcf) BETAFOAM™. Results of these characterization tests are presented in this section.

The new set of unconfined compression tests and uniaxial tension tests were performed by The Dow Chemical Company. The compaction curves from the unconfined compression tests on the 5 pcf and 18 pcf foams are shown in Figure 201 and Figure 202, respectively. The test specimens were either 1.5 or 2.0 inches in diameter and 2.0 inches long. Both specimen geometries resulted in a uniform compression behavior (without significant lateral buckling) and the compaction curves all fall within a narrow band. From the series of 10 tests on the 5 pcf foam, the average density was 4.97 pcf and the crush strength is approximately 100 psi. From the series of 10 tests on the 18 pcf foam, the average density was 19.1 pcf and the crush strength is approximately 1000 psi.

A comparison of the crush strength for the 18.3 pcf foam in the initial test series (SwRI data of Reference 70) is compared to the new Dow data in Figure 203. The crush curve in the initial test series has a significantly lower steady state crush strength. However, much of this discrepancy may be the result of the lateral buckling of the specimen in this test.
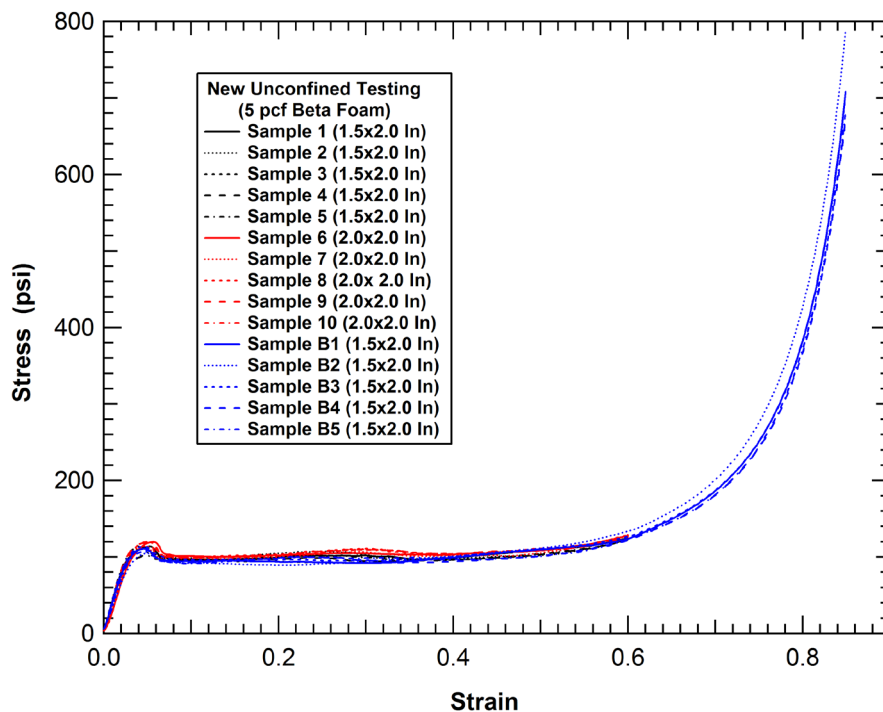
Figure 201. New unconfined compression testing on the 5 pcf foam.
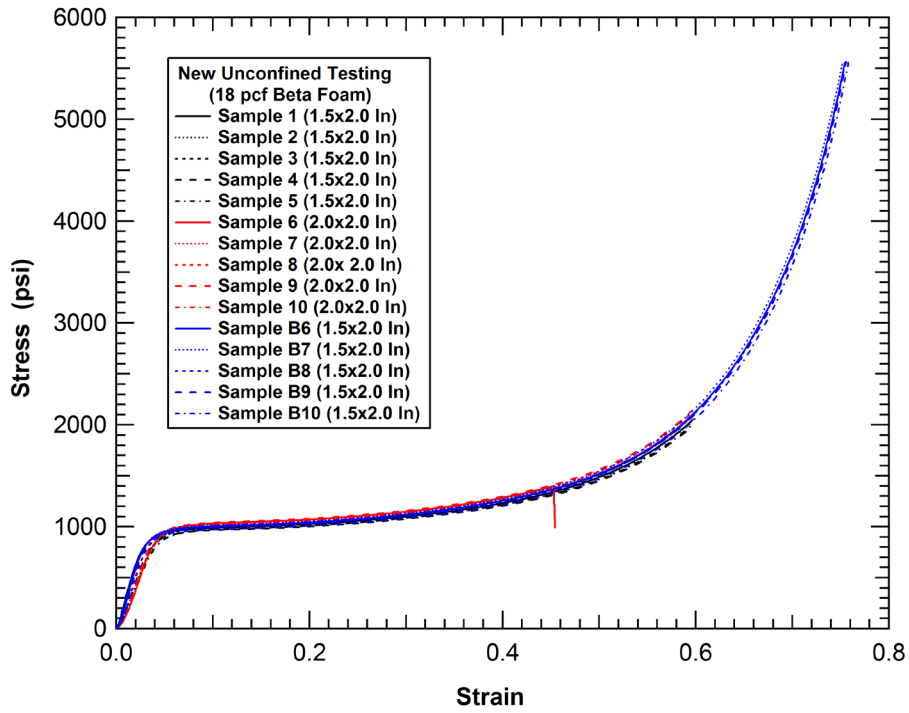
Figure 202. New unconfined compression testing on the 18 pcf foam.
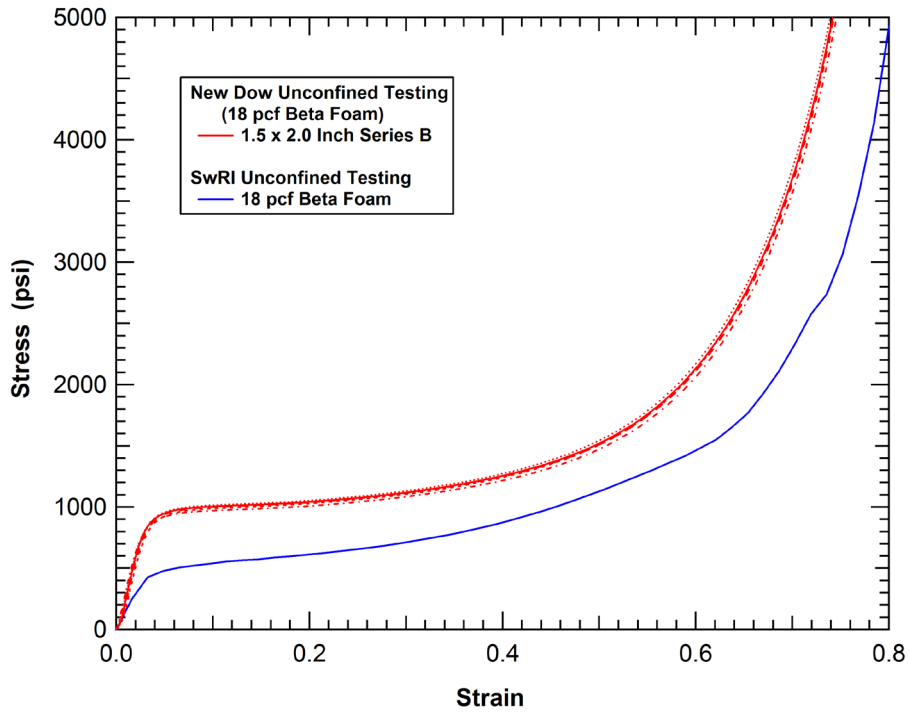
Figure 203. Comparison of unconfined compression test series on 18 pcf foams.

The tensile tests were performed on dog bone specimens with gauge section cross sectional dimensions of approximately 0.36 by 0.12 inch (9.2 mm W X 3.0 mm) and tested at a rate of approximately 2 inches per minute). The 5 pcf foam did not have sufficient strength to support the attachment of the grips and loads imparted in the setup of the testing. The tensile tests on the 18 pcf foam are shown in Figure 204. The high density foam has a tensile strength of approximately 1200 psi and fail at a tensile strain of approximately 7-8%. A comparison of the uniaxial tension and unconfined compression tests for this foam is provided in Figure 205. The comparison shows that the tensile stresses are approximately 20% higher than the compressive stresses up to the point of tensile failure.

The triaxial compression tests are commonly used to determine the strength envelope, or yield surface as it's referred to in LS-DYNA, of materials like soil and foams. The testing system used for the triaxial foam characterization testing is shown in Figure 206 [69]. For each test, a cylindrical specimen of foam is first prepared inside a fluid-tight membrane to prevent infiltration of the confining fluid (air). In the triaxial apparatus, it is possible to apply two independently controlled components of load to the test specimen, as appropriate to each individual test. Pressurized fluid (air) in the vessel is used to impose a hydrostatic stress. The other component of load is derived from a piston, which extends through a seal in the top of the pressure vessel, loading the cylindrical specimen in the axial direction. Electronic instrumentation is used to measure both the applied loads and the resulting deformations of the foam specimens.
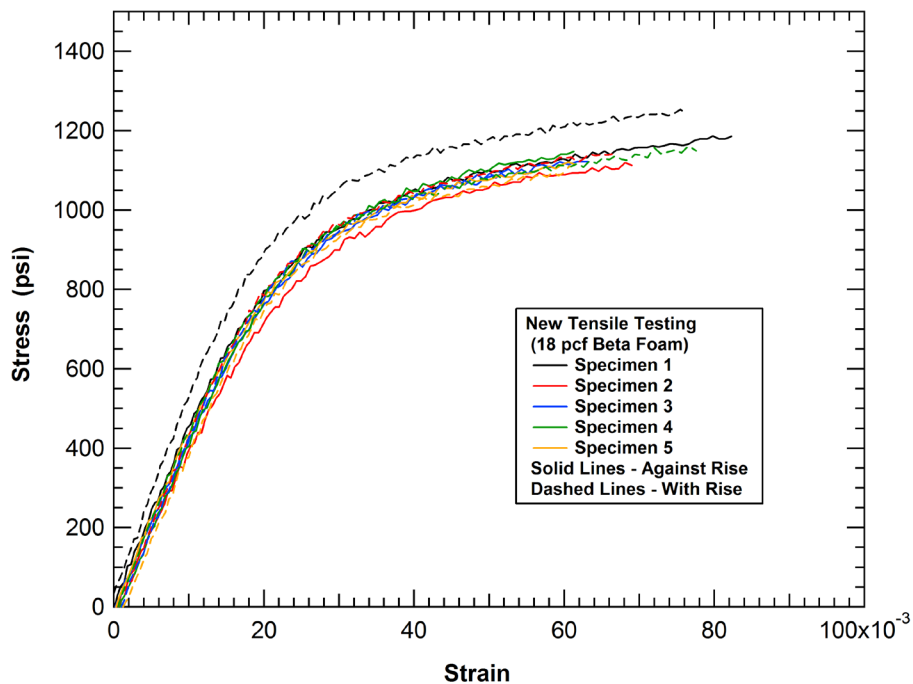
Figure 204. Uniaxial tension test results for the 18 pcf foam.
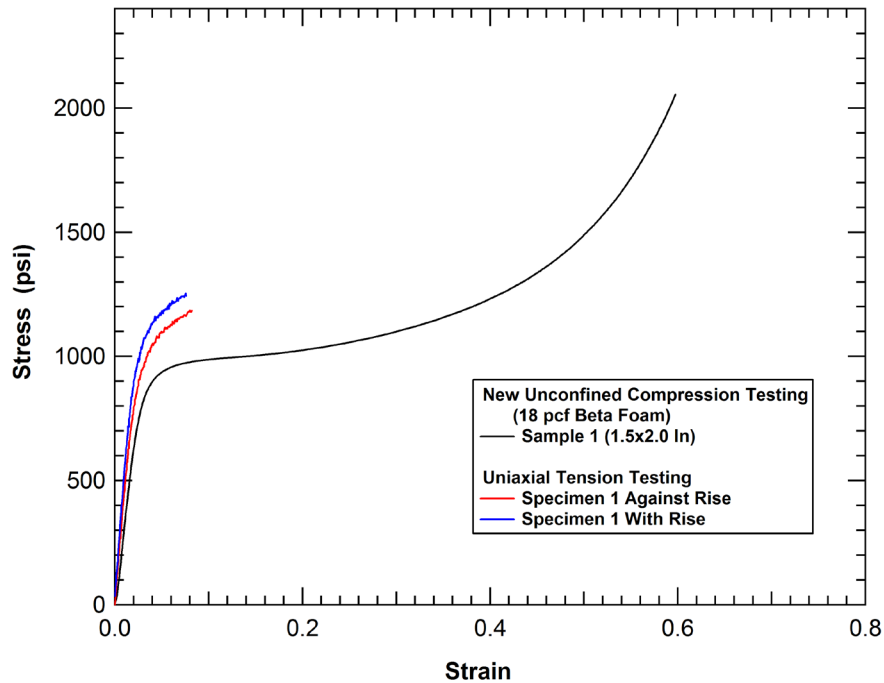
Figure 205. Comparison of the measured uniaxial stress behavior in tension and compression.
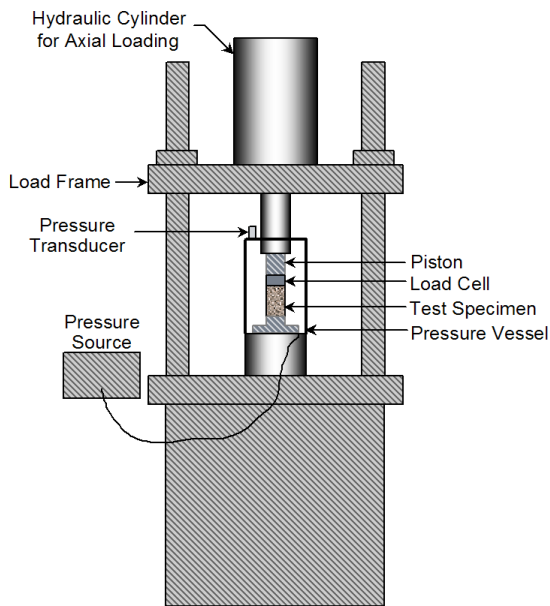
Figure 206. Schematic and photograph of the triaxial compression test apparatus.

The first series of tests performed are the basic triaxial tests on the foam specimens. In these tests, different levels of confining hydrostatic pressures are applied and then the specimen is subsequently compressed axially while the constant confining pressure is maintained. For the

high density foam (18 pcf), a series of hydrostatic tests was performed with confining pressures of 5, 10, 20, 50, 400, and 800 psi.

The true stress difference in the triaxial tests on the 18 pcf foam specimens are plotted against the measured axial and radial strains in Figure 207. In these tests, the stress difference is the additional axial compressive load applied in addition to the confining hydrostatic pressure. From the figure, we see that the low levels of confinement (below 50 psi) have a negligible effect on the response and would be expected to be equivalent to the unconfined compression test. However, when we plot these low confinement tests against the results of the unconfined compression tests we see that the two test series have a discrepancy in the crush strength of approximately 20% as shown in Figure 208. The source of this discrepancy is not known.

An alternative approach to present the results of the triaxial tests is to add the hydrostatic stress to the stress difference and plot the total axial stress against the axial compressive strain as shown in Figure 209. The graphs of the triaxial testing show that the foam does exhibit some stiffening under an increasing confining pressure. However the sensitivity of the behavior to the triaxiality of the load is smaller than seen in many other types of foams.
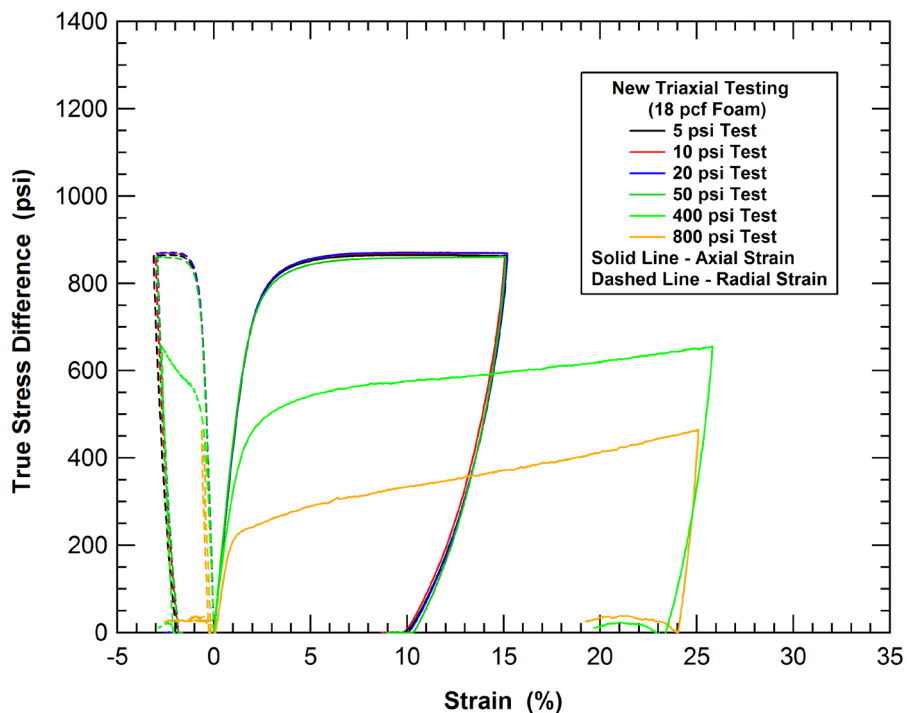
Figure 207. Triaxial test results for the 18 pcf foam.
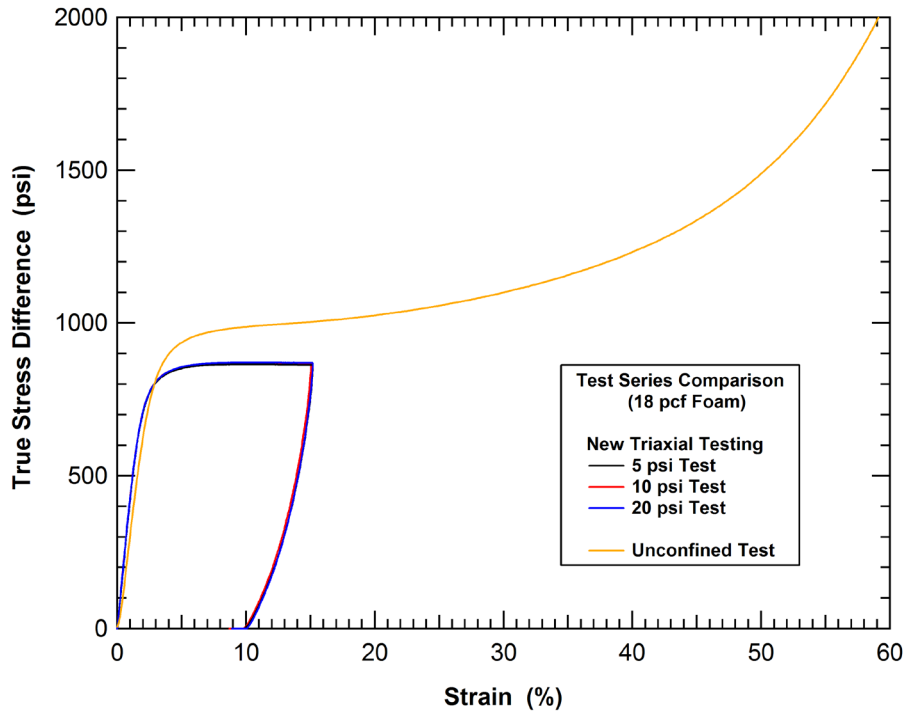
Figure 208. Comparison of unconfined and low confinement triaxial tests for 18 pcf foam.
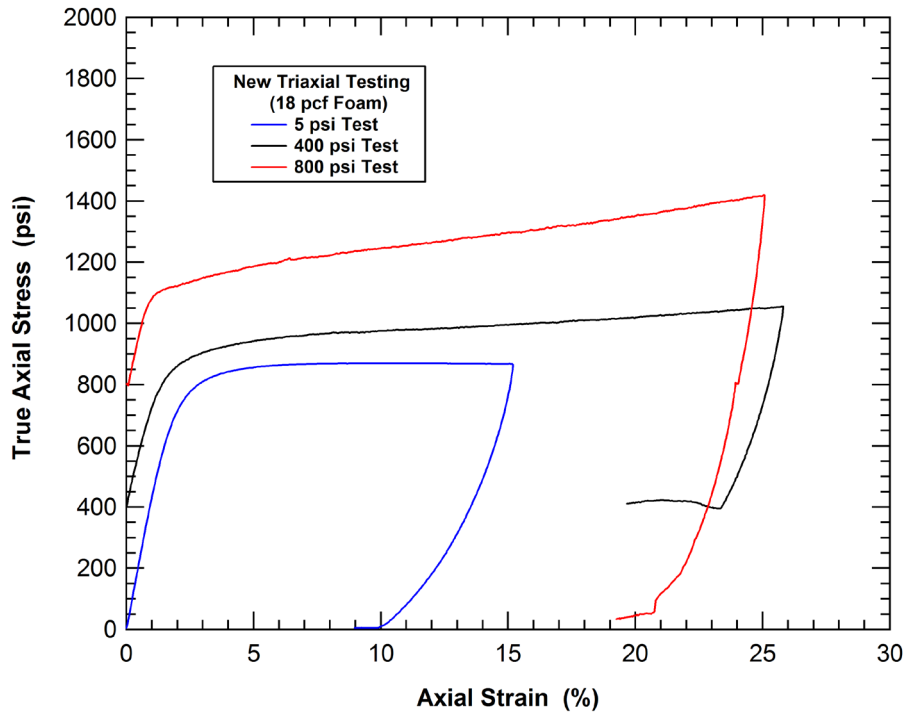
Figure 209. Triaxial test results for the 18 pcf foam.

163

The other foam characterization tests performed were a hydrostatic compression test and a uniaxial strain compression test. The hydrostatic and uniaxial strain compression tests are also conducted using the triaxial device. In the hydrostatic compression test, the cylindrical foam specimens are loaded only by fluid (air) pressure, without any piston loading. The stresses on the specimen are the same in all directions and there is no shear stress on any plane. This is referred to as the hydrostatic state of compression. The results of this test are used to define the volumetric deformation behavior of the material. When unloaded, the foam expands on a different path (slope). This unloading path yields the bulk unload modulus required for some constitutive models. LVDT measurements are used to record the axial and radial deformations (defining the volume strain). The data from the hydrostatic compression test on the 18 pcf foam is shown in Figure 18.

In the uniaxial strain test, the axial stress and confining pressure are applied in such a way that the specimen undergoes compressive axial strain with no strain in the radial direction. The uniaxial strain loading is accomplished with an automated loading control system using the radial deformation measurement as feedback in the control loop. If the radial strain increases, the confining pressure is increased to return the radial strain to zero. Because no radial strain is allowed in a uniaxial strain test, the axial strain is equal to the volumetric strain in the specimen. There is a difference between axial and radial stress, and hence shear stresses exist in the specimen. The results of the uniaxial compression tests on the 18 pcf foam is shown in Figure 211.
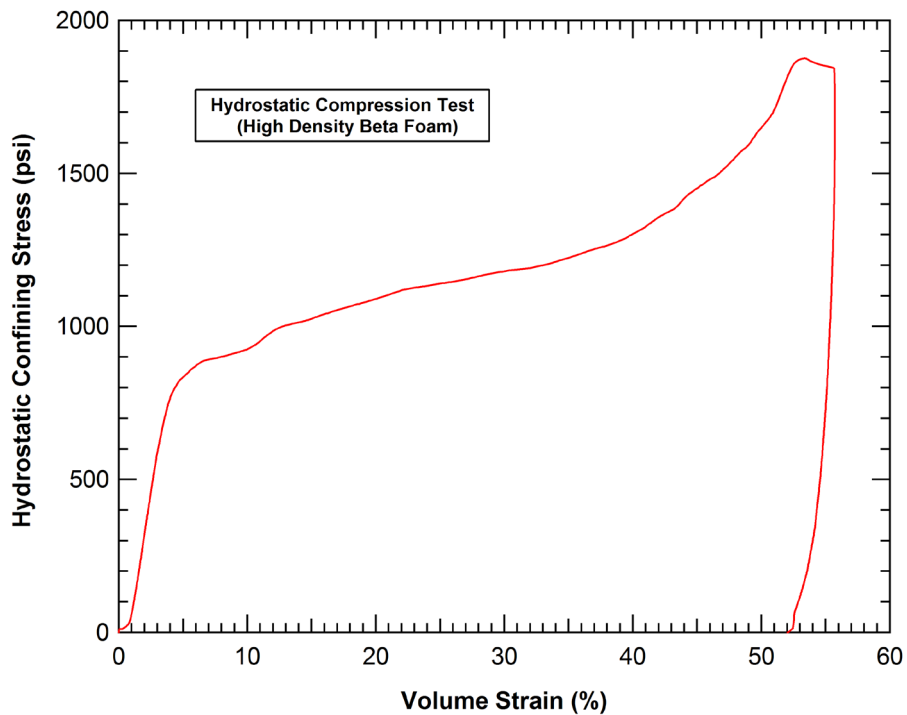
Figure 210. Hydrostatic compression test results for the 18 pcf foam.

A similar set of material characterization tests were performed on the low density (5 pcf) foam. The triaxial compression tests were performed at 2, 5, 10, 20, and 50 psi confining pressures. The results of those triaxial tests in terms of the true stress difference and the true axial stress are shown in Figure 212 and Figure 213, respectively. Again, the triaxial tests on the low density foam shows that the foam crush behavior is relatively insensitive to a confining pressure. In addition, the comparison of the triaxial compression tests with the unconfined compression tests show that the two test series are in reasonable agreement on the measured crush strength within the scatter of behaviors seen between tests, as seen in Figure 214. Potentially the steady state crush strength is lower in the unconfined compression test, which is opposite of the variation observed in the test series on the high density foam (Figure 208).

The final characterization tests performed on the low density BETAFOAM™ were the hydrostatic compression test and a uniaxial strain compression test. The results from the hydrostatic and uniaxial compression test on the 5 pcf foam are shown in Figure 215 and Figure 216, respectively.
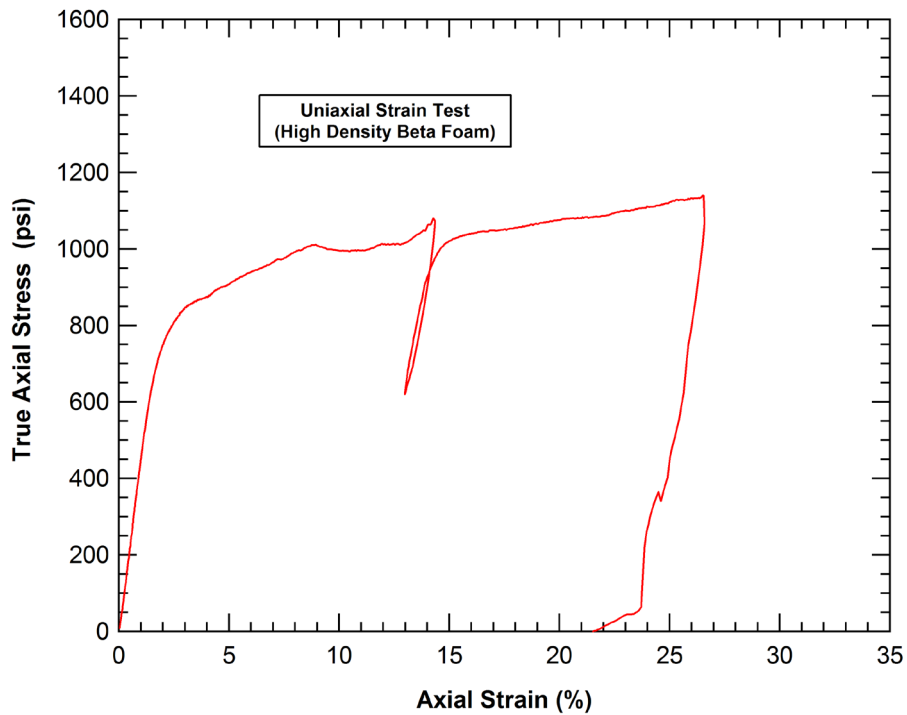
Figure 211. Uniaxial strain test results for the 18 pcf foam.
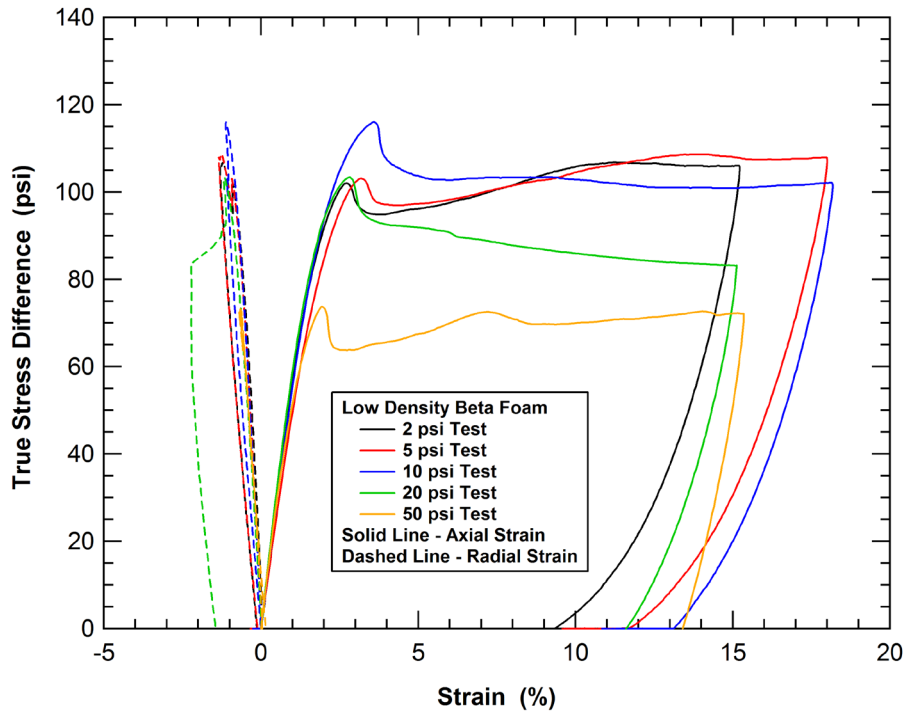
Figure 212. Triaxial test results for the 5 pcf foam (stress difference).
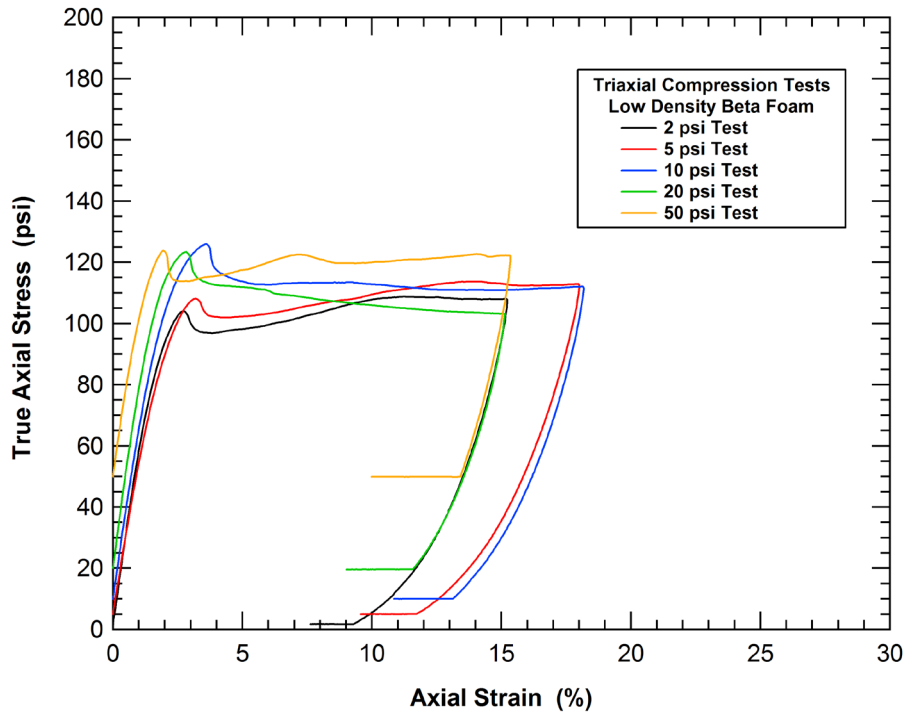
Figure 213. Triaxial test results for the 5 pcf foam (axial Stress).
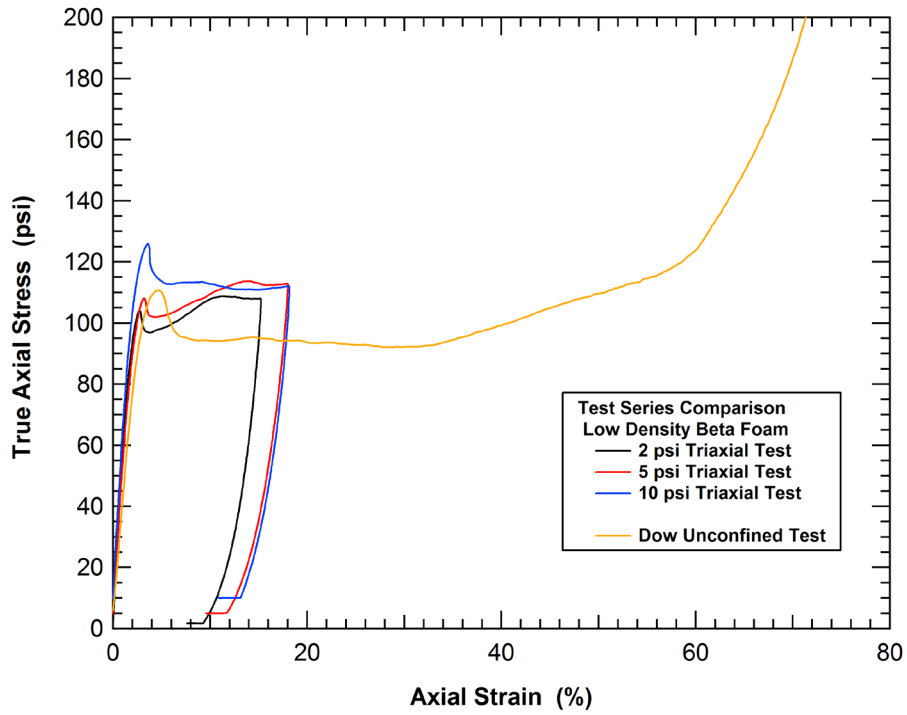
Figure 214. Triaxial test results for the 5 pcf foam (axial Stress).
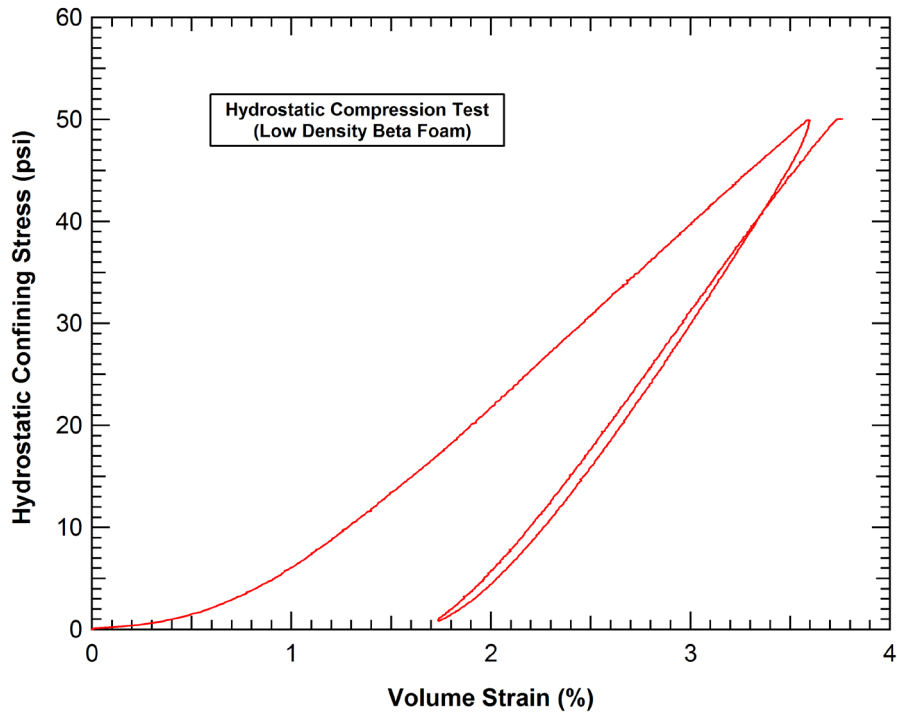
Figure 215. Hydrostatic compression test results for the 5 pcf foam.
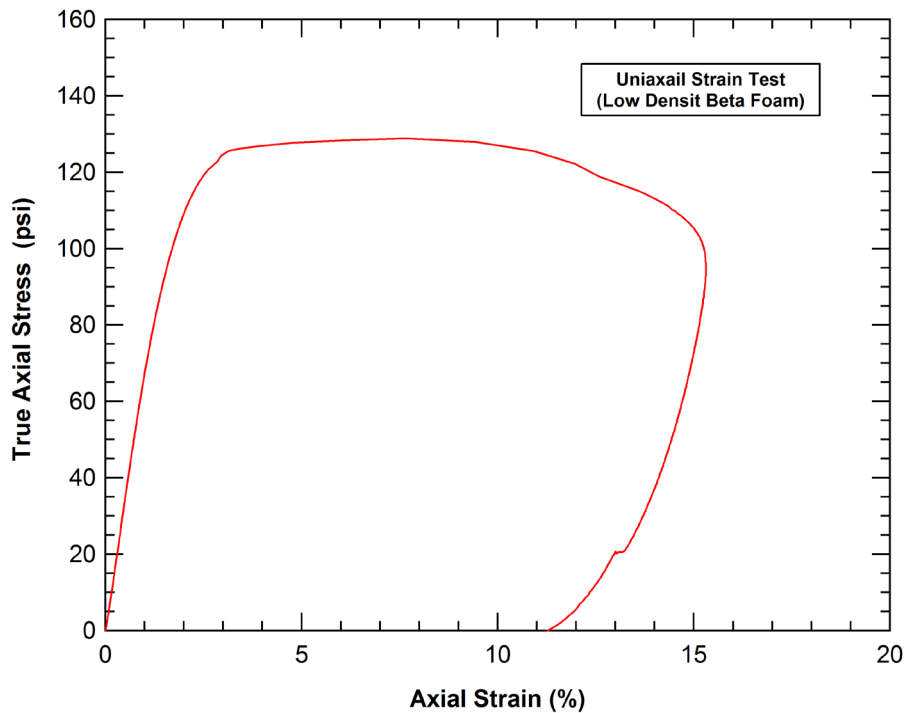
Figure 216. Uniaxial strain test results for the 5 pcf foam.

Foam Model Development and Validation

The updated foam characterization test data was initially applied to further evaluate and validate the Mat_63 constitutive model. The model constitutive parameters were fit to the new unconfined compression crush curves and the compression test was simulated. The comparison of the measured and calculated unconfined crush behaviors is provided in Figure 217. The comparison shows very good agreement showing that the crush curves were properly implemented into the constitutive model.
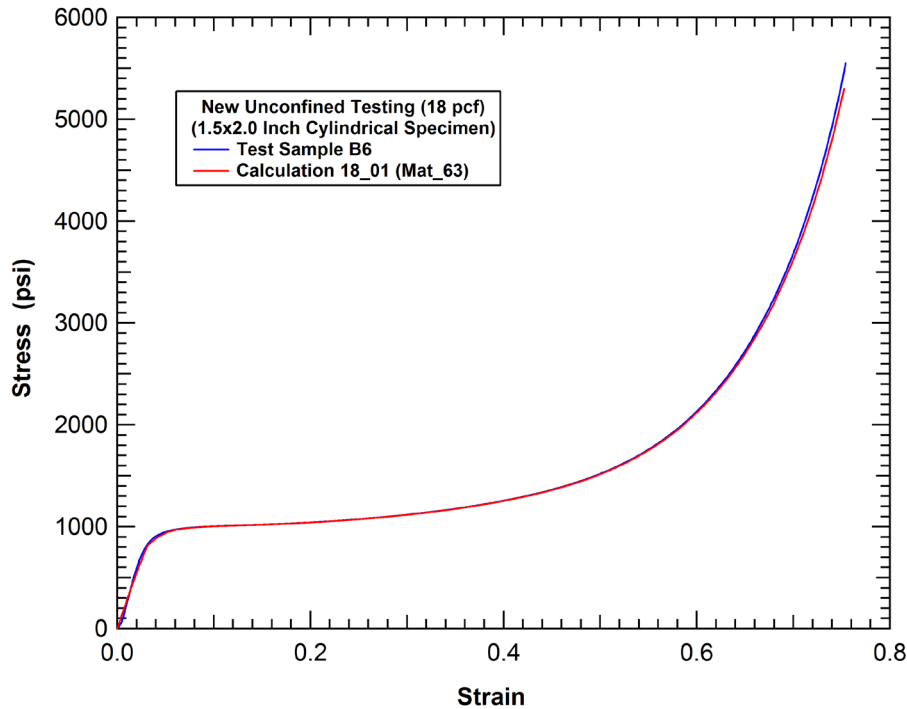
Figure 217. Calculated and measured unconfined compression behavior (18 pcf foam Mat_63).

The tensile tests on the 18 pcf foam were subsequently analyzed and a problem with the Mat_63 model was immediately identified. When the specimen was pulled in tension, the model did not develop any stresses, even though a nonzero tensile cutoff strength was specified. This was not the expected behavior from the model.

To further investigate the behavior of the Mat_63 model in tension, a series of analyses were performed where the model was first loaded into compression then the load direction was reversed and loaded into tension. The load deflection histories for two of these analyses are provided in Figure 218. The figure shows a behavior where the foam can support a tensile load equal to the magnitude of the maximum compressive load developed in the initial compressive phase of the cyclic loading. A physical mechanism that would produce this behavior was not clear and we believed this may be the result of a bug in the implementation of the Mat_63 model. However, LSTC confirmed that this is the behavior of this model and that there were not plans to modify the model behavior. They recommended that we try using the Material Type 75 model (referred to as Mat_75 in the remainder of the report) for our application.
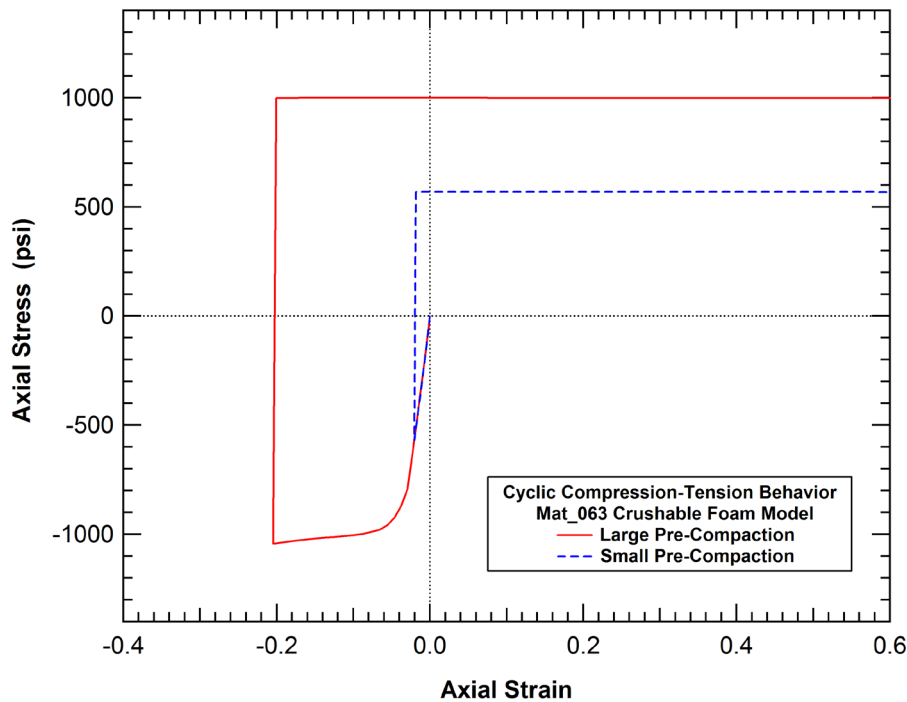
Figure 218. Calculated cyclic compression-tension behavior (18 pcf foam Mat_63).

The Mat_75 model requires the specification of both a pressure yield stress versus volumetric strain curve and a uniaxial yield stress versus volumetric strain curve (e.g. crush curve). The uniaxial yield curve can be extended in both the tensile and compressive directions to fit different measured behaviors. This capability is a significant improvement over the capabilities of the Mat_63 model.

The Mat_75 constitutive parameters were fit to the updated foam data and the unconfined compression test was simulated. Initially, the uniaxial crush curve applied previously in the Mat_63 model was used for the compression uniaxial yield stress curve in the Mat_75 model. The calculated response for this model is compared to the test and Mat_63 calculated behavior in Figure 219. The comparison shows poor agreement of the Mat_75 model in the large deformation compaction response where the calculated stiffening of the foam material occurs prematurely. This occurs because the Mat_63 model is designed to use an engineering stress-strain crush curve as an input and the Mat_75 model is designed to use the true stress-strain crush curve as an input.
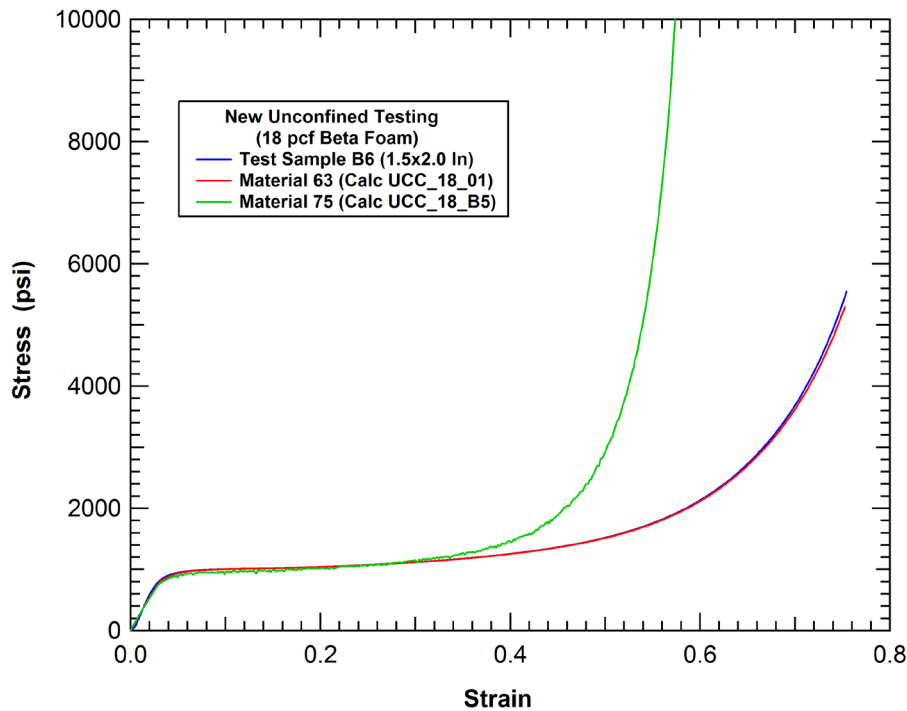
Figure 219. Calculated and measured unconfined compression behavior (18 pcf foam Mat_63).

The Mat_75 uniaxial yield curves were subsequently corrected to the true volumetric strain using the approach described in Section 3.2.1. The comparison of the engineering and true strain crush curves for the 18 pcf foam is provided in Figure 220. The true strain crush curve is then adapted by adding on the tensile test phase to create the uniaxial yield curve required for the Mat_75 model, shown in Figure 221. The tensile behavior is that defined in the negative volume strain section of the yield curve.

Also shown in Figure 221 is a pressure yield versus true volumetric strain curve required as a material model input. The comparison of the measured hydrostatic compression stress-strain curve with the compression curves obtained in the other characterization tests is shown in Figure 222. In general, all of the curves are similar in magnitude. Potentially, the hydrostatic curve can be as much as 20 percent above the other curves in different regions of the crush response. To investigate the effect of this variability, a sensitivity study was performed using pressure yield curves that were scaled from the uniaxial yield curve by factors of 1.0 and 1.2. There was little difference in the calculated results for most of the analyses. However, in the triaxial compression tests (described below) the pressure curve equal to the uniaxial yield curve (100 percent pressure yield model) provided a better correlation to the measured response than the analyses using the 120 percent pressure yield model. As a result, the 100 percent pressure yield model was used in the subsequent Mat_75 analyses of the component and large scale impact tests.
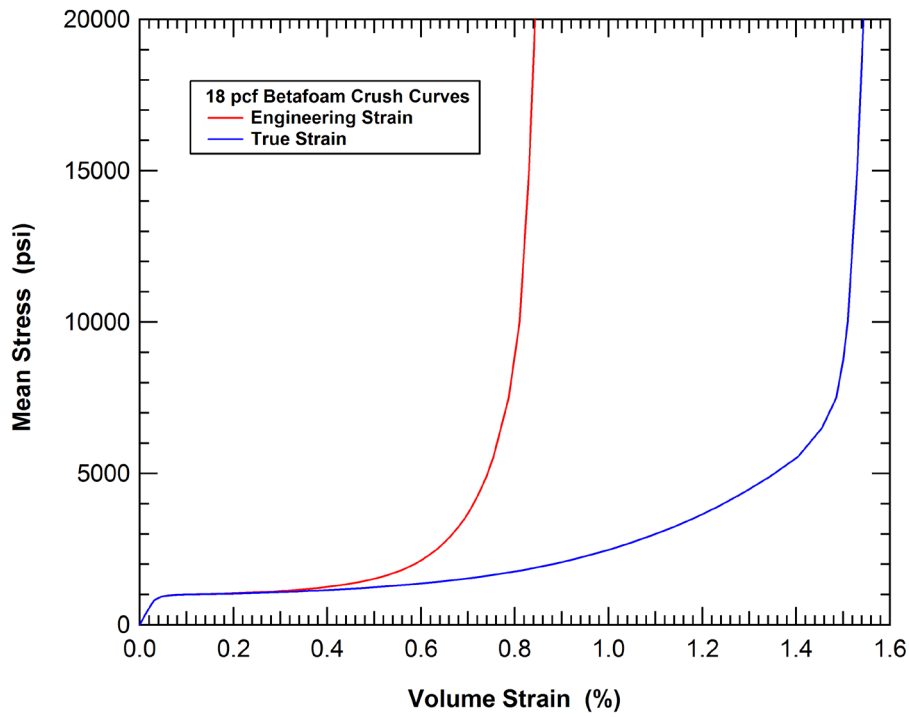
Figure 220. True stress correction of the crush curve (18 pcf foam).
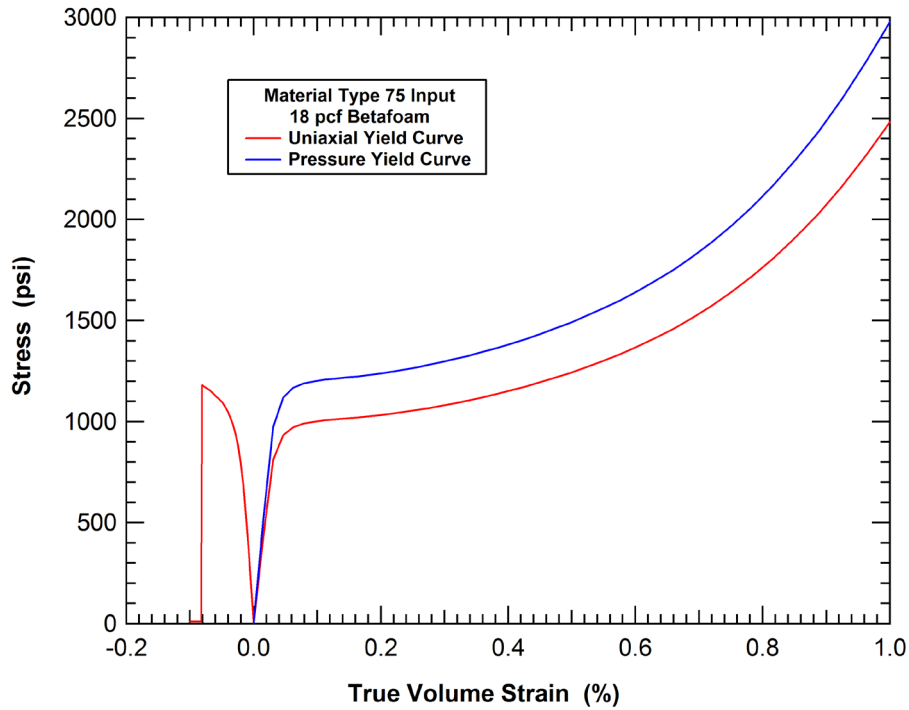
Figure 221. True stress correction of the crush curve (18 pcf foam Mat_75).
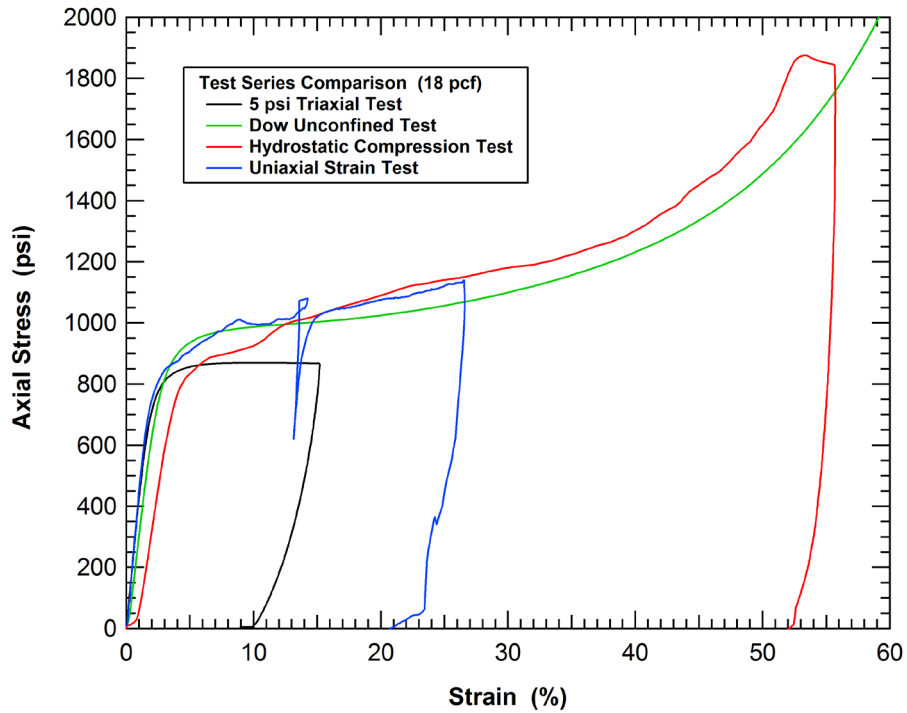
Figure 222. Comparison of measured foam crush curves from the various tests (18 pcf).

The first analysis performed with the corrected Mat_75 model was the unconfined compression test. The comparison of the measured and calculated crush curves is shown in Figure 223. After the correction of the Mat_75 material input parameters to the true volumetric strain, the constitutive model is able to accurately reproduce the unconfined compression response. Included in the figure are the analyses using both the 100 percent and 120 percent pressure yield curve models. The variation in the pressure yield curve strength has a small effect on the calculated unconfined compression response.

The calculated response of a cylindrical foam specimen in tension using the Mat_75 model is shown in Figure 224. In the initial phase of the loading the specimen stretches uniformly. However, at approximately 7 percent strain, the damage localizes to a plane of elements and the load drops to a very low level. The corresponding calculated tensile stress-strain behavior is compared to the measured tensile behavior in Figure 225. The comparison shows good agreement in the measured and calculated tensile response.
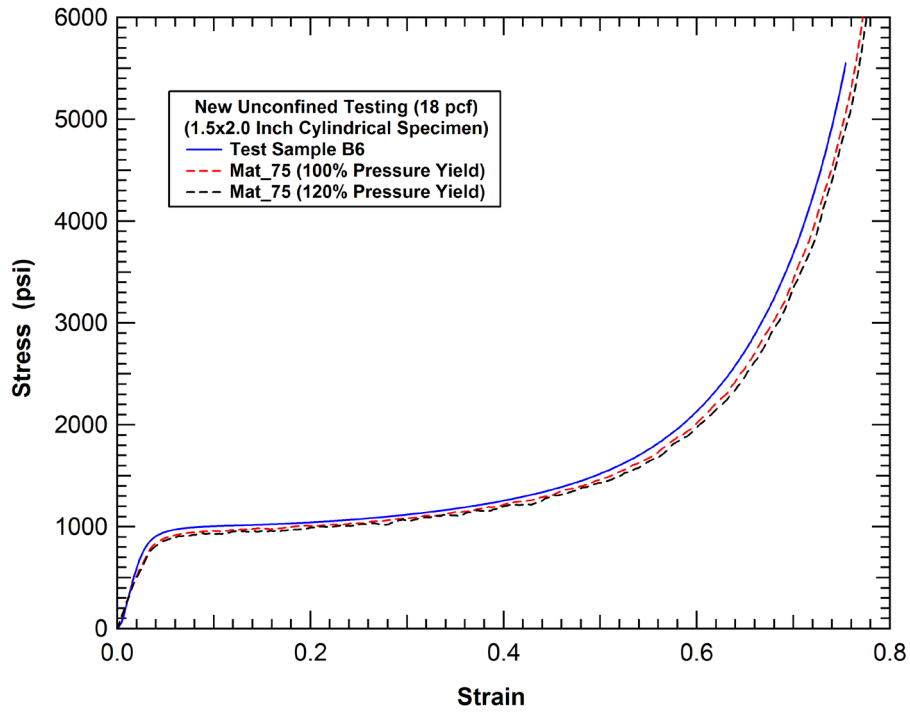
Figure 223. Calculated and measured unconfined compression behavior (18 pcf foam Mat_75).
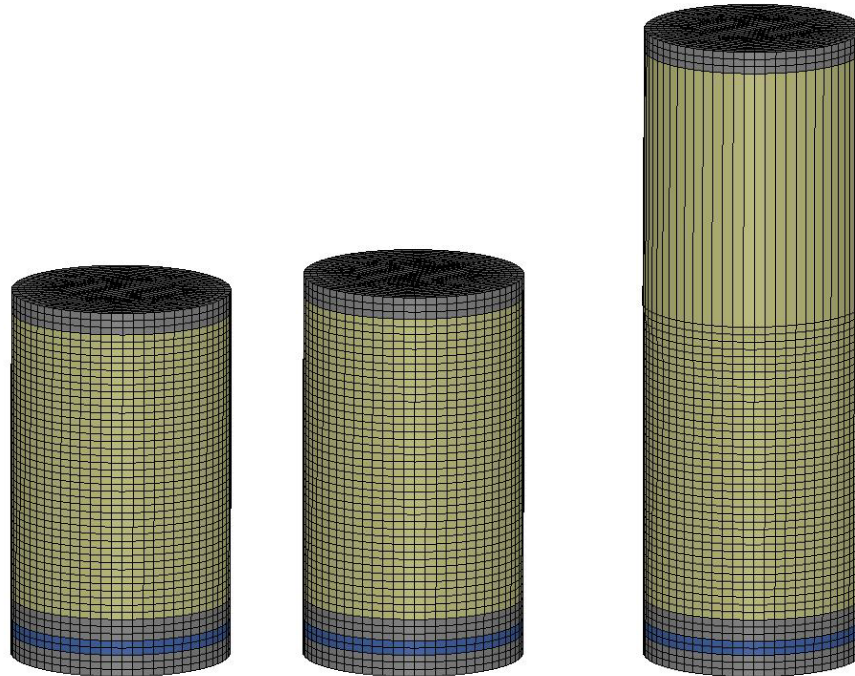
Figure 224. Calculated tensile behavior of a cylindrical foam specimen (18 pcf foam Mat_75).
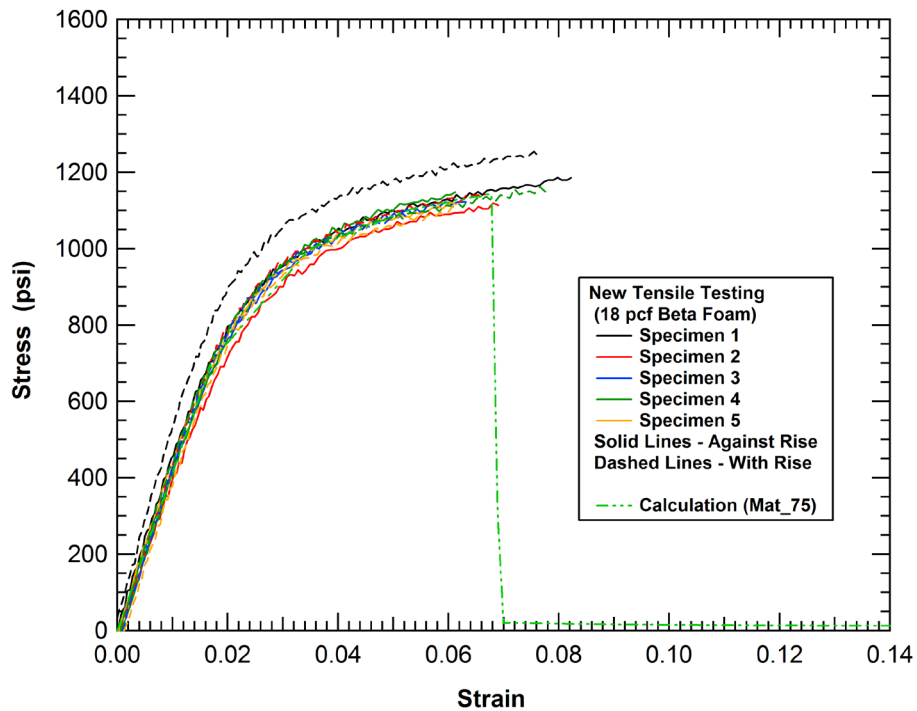
Figure 225. Comparison of measured and calculated tensile behavior (18 pcf foam Mat_75).

The triaxial compression tests were analyzed using the Mat_75 model with both the 100 percent and 120 percent pressure yield curve models. The comparison of the calculated and measure response for the 120 percent pressure yield curve is shown in Figure 226. The agreement between the measured and calculated response for the low and confinement tests (5 psi and 400 psi) is pretty good. However, the calculated response for the high confinement (800 psi) test has almost no increase in the strength during the crush behavior (hardening in the crush curve) as seen in the test. The calculated response for the triaxial compression tests with the 120 percent pressure yield curve also had an unstable behavior and filtering of the calculated crush forces was required to produce the smooth crush curves seen in Figure 226.

The comparison of the calculated and measure response for the 100 percent pressure yield curve is shown in Figure 227. The agreement between the measured and calculated response for the low and confinement tests is similar to that of the 120 percent pressure curve analyses. However, the calculated behavior for the high confinement (800 psi) test has improved and includes a hardening behavior in the crush curve as seen in the test. In addition, the calculated response for the triaxial compression tests with the 100 percent pressure yield curve were more stable and resulted in smoother calculated crush forces compared to the 120 percent pressure yield analyses. As a result of these differences, the 100 percent pressure curve was used for the remainder of the Mat_75 analyses.
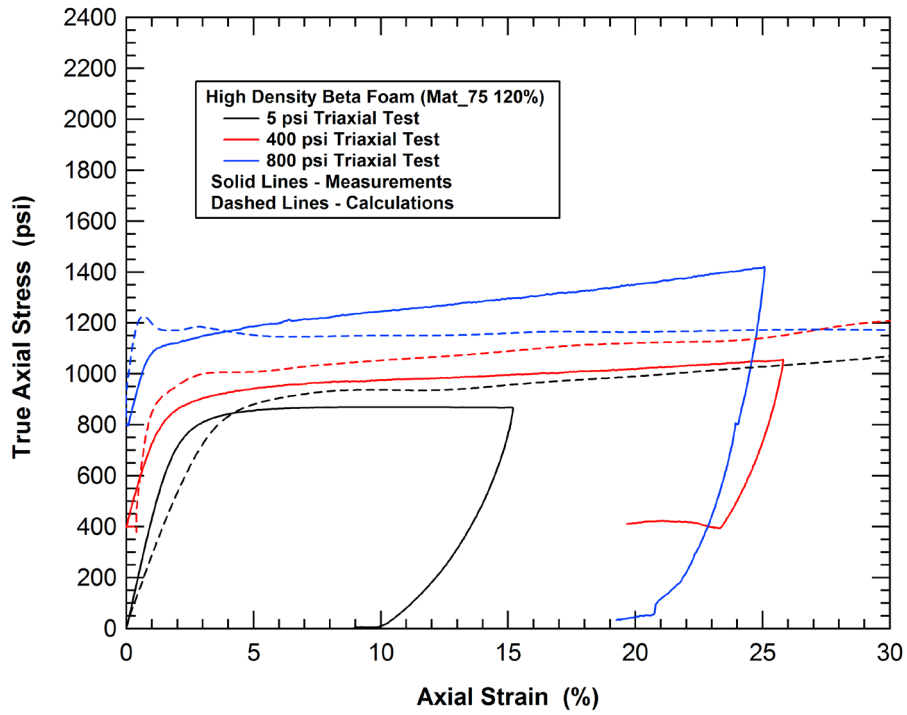
Figure 226. Comparison of measured and calculated triaxial test behaviors (Mat_75 - 120 percent).
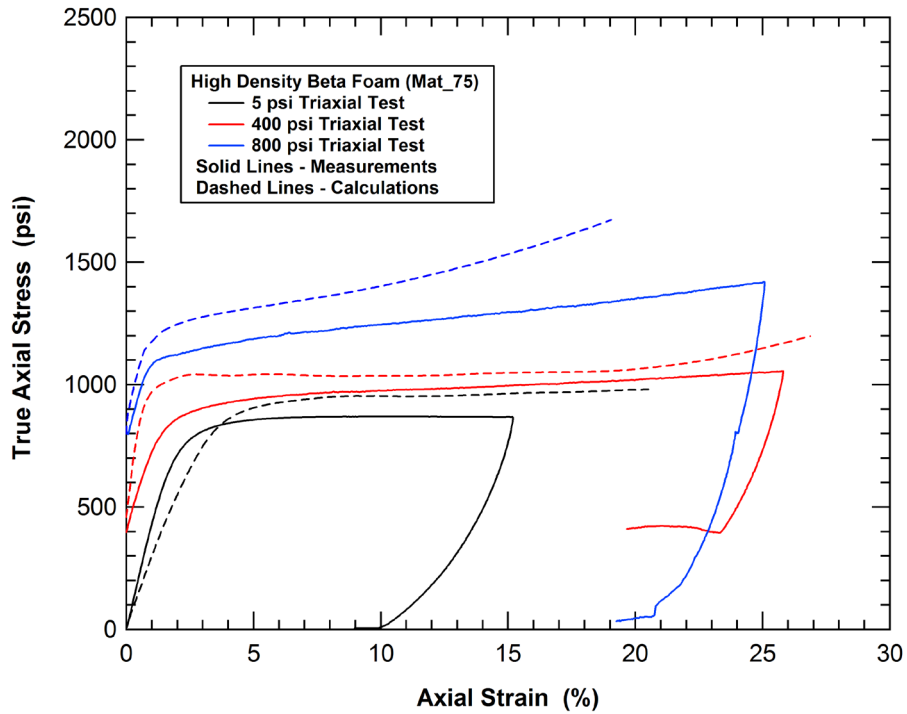
Figure 227. Comparison of measured and calculated triaxial test behaviors (Mat_75 - 100 percent).

A similar set of analyses were performed for the 5 pcf foam. The analyses were able to achieve a similar level of correlation between the calculations and the tests. A representative comparison of the predicted and measured unconfined compression behaviors is shown in Figure 228. This model was applied for the analyses of the low density foams in the component tests described below.
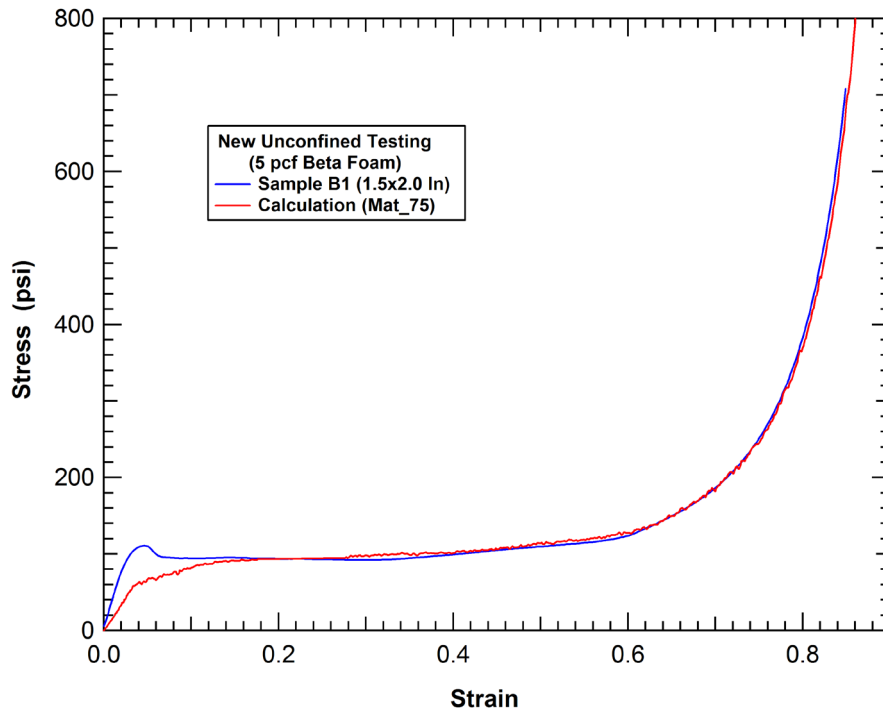
Figure 228. Calculated and measured unconfined compression behavior (5 pcf foam Mat_75).

Foam Laboratory Component Testing

In addition to the unconfined compression tests to characterize the material behavior, laboratory component tests were performed on foam sandwich panels to validate the foam models. These tests included a panel bend test and punch testing on the sandwich panel [34, 72-74].

Foam Sandwich Panel Punch Test

The configuration for the foam sandwich panel punch test is shown in Figure 229 [34]. Test samples were placed in the specialized puncture fixture available in the SwRI Materials Test Lab and used previously for validation of the steel constitutive and damage models as described in Section 3.4.4 of this report. The punch was 1.5-inch diameter and the receiving hole bore (man hole cover) was 3-inch diameter. During testing, the actuator displacement was measured with a remote LVDT mounted on the actuator. Load was measured from the load cell on the servohydraulic test frame. Tests were performed in displacement control at an applied rate of 1

inch/minute. Data was recorded with a custom data acquisition system operating at 10 Hz. This typically provided total data files of anywhere from 500-2000 points.
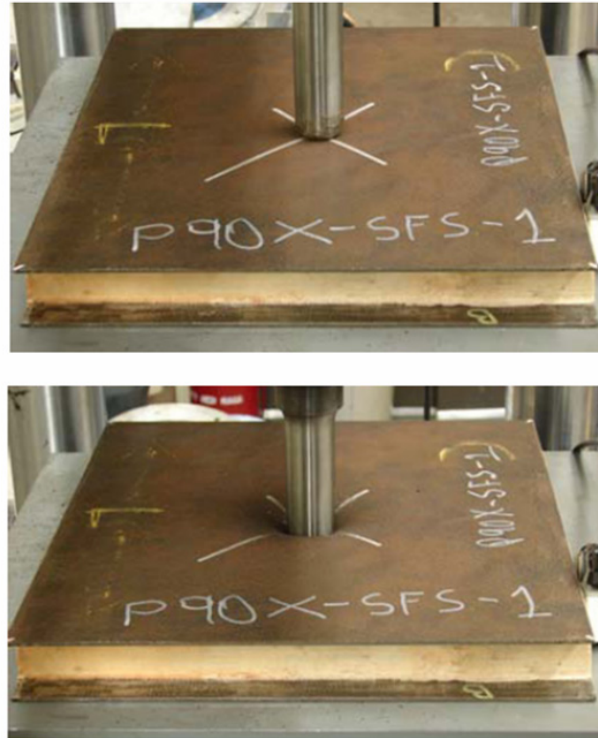
Figure 229. Photographs of the foam sandwich panel puncture test.

The analyses of the foam panel punch test was performed using both the Mat_63 and Mat_75 models. A comparison of the measured and calculated (Mat_63) punch behaviors are shown in Figure 230. The comparison shows very similar deflections and deformation modes. The only discrepancy was the visible cracking on the foam seen in the test. This type of discrete tensile crack formation was not possible with the simple foam model applied in the analyses.
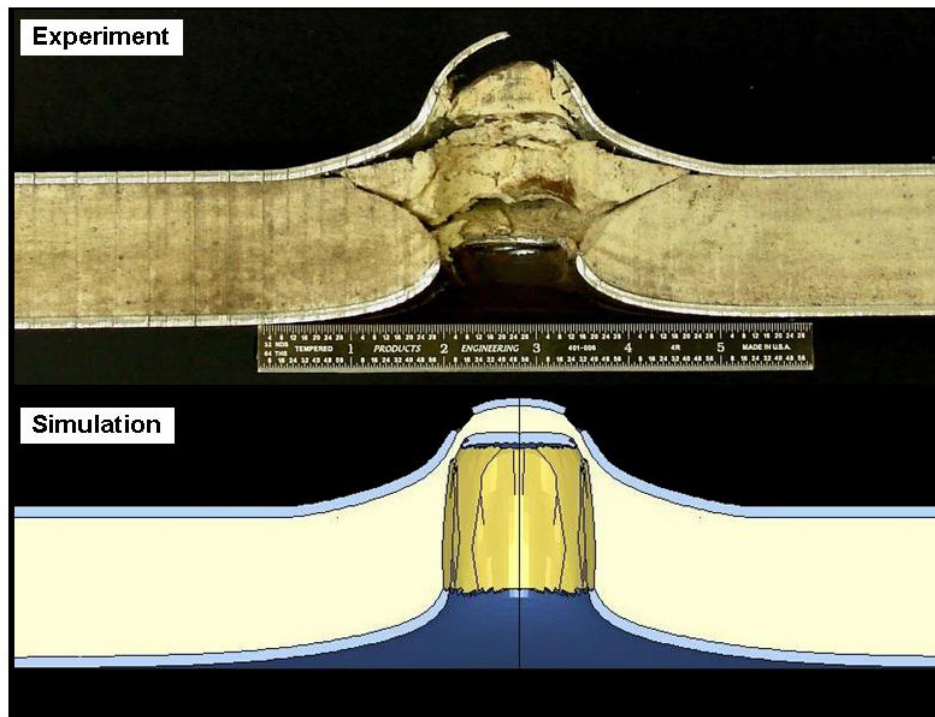
Figure 230. Measured and calculated foam sandwich panel punch test behavior (Mat_63).

The comparison of the measured and calculated force-deflection characteristics for the punch test is shown in Figure 231. The load-displacement behavior exhibits two peaks, corresponding to penetration of the two steel layers. The peak load for this test can be compared to the load when a single layer of the HSLA 90 XF face sheet was tested. The panel results exhibit a 20% increase in peak load suggesting that the interaction of the foam and face sheets provide a combined response to resist puncture. However, this overall increase in puncture force levels was relatively modest.

Two different Mat_63 analyses were performed with different tensile cutoff strengths. The comparison shows that a high tensile cutoff stress (1000 psi) results in an over prediction of the forces after the upper face sheet was penetrated. When the tensile cutoff stress was reduced to 100 psi a much better agreement was obtained for the full force-deflection behavior in the punch test. The characterization testing performed subsequent to these analyses found that the 1000 psi tensile cutoff is much closer to the actual tensile strength but the improved correlation with the lower tensile cutoff may be an indication of the stress reduction after the formation of the discrete cracks in the test. In addition, the Mat_63 model was shown to have deficiencies in the modeling of the tensile behavior as described above.
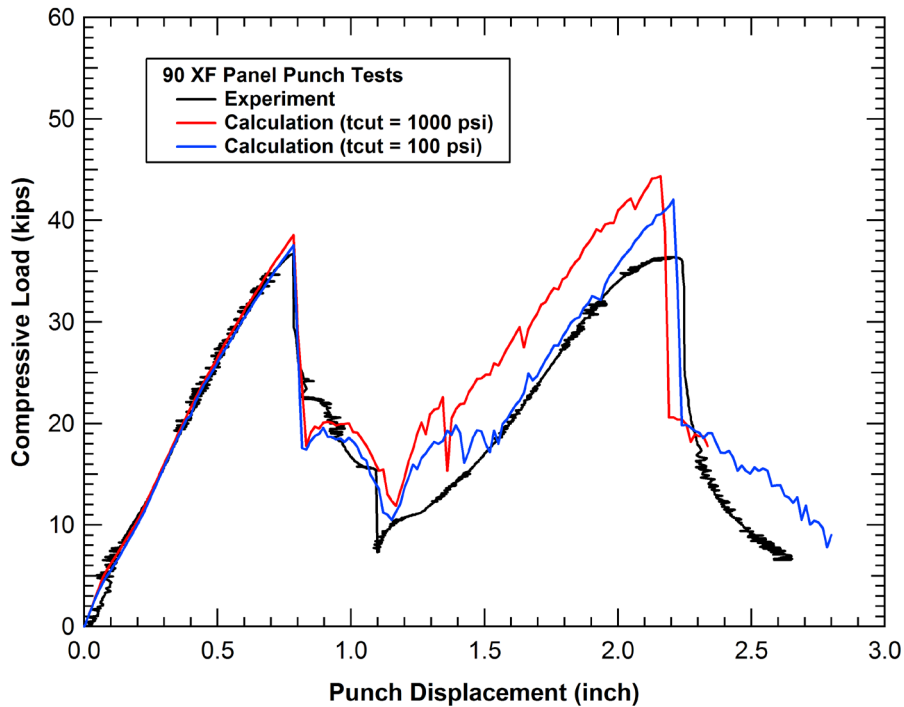
Figure 231. Comparison of measured and calculated foam sandwich panel punch forces (Mat_63).

The comparison of the measured and calculated (Mat_75) punch behaviors are shown in Figure 232. The comparison shows very similar deflections and deformation modes. Again the model does not show discrete tensile crack formation. However, the mat_75 model has the capability to reduce the tensile strength in regions of the foam where the tensile strain is exceeded. Thus the local reduction in tensile stresses around the punch can be modeled.

The comparison of the measured and calculated force-deflection characteristics for the punch test is shown in Figure 233. The overall agreement for the analysis with the Mat_75 model is pretty good indicating that the improved modeling of the tensile behavior is helpful for simulating the punch test response. The slight discrepancy in the character of the second peak in the force deflection is probably a result of the symmetry conditions used in the model. By applying a quarter symmetry model in the analysis, the response forms a plug type failure of the second face sheet rather than the asymmetric flap failure observed in the test.
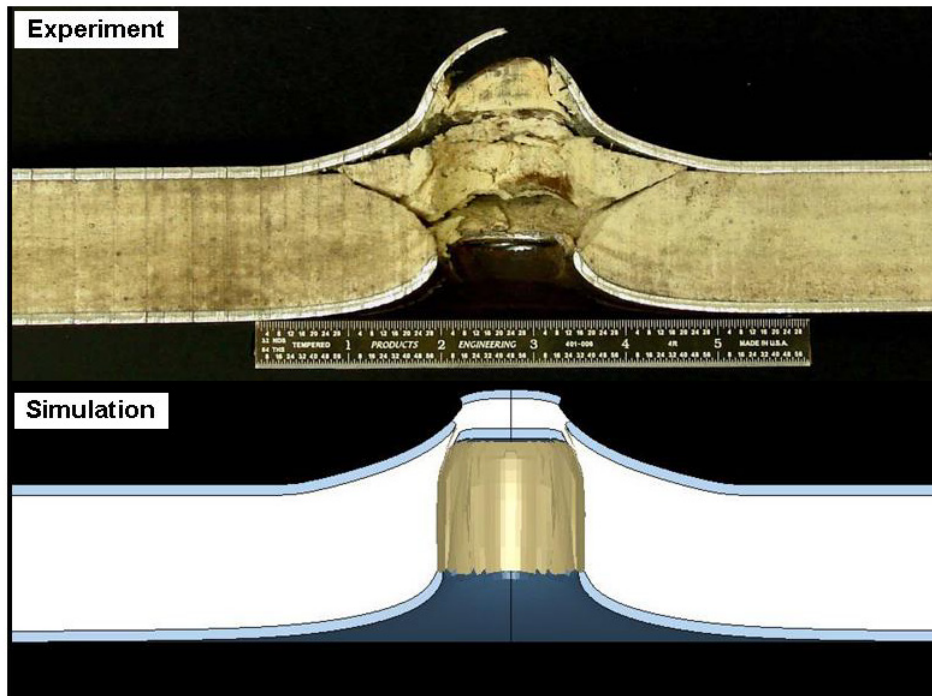
Figure 232. Measured and calculated foam sandwich panel punch test behavior (Mat_75).
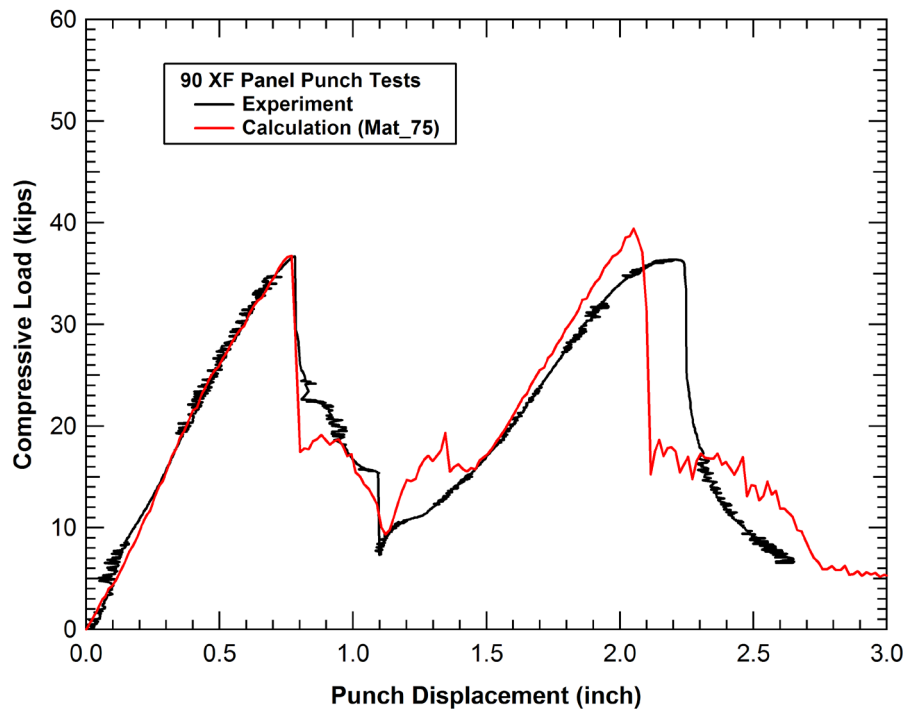
Figure 233. Comparison of measured and calculated foam sandwich panel punch forces (Mat_75).

Foam Sandwich Panel Flexure Testing

Two sets of flexure tests were performed on sandwich panels. In the preliminary set of flexure tests, the specimens were fabricated by bonding face sheets to existing foam blocks [72, 73]. These preliminary tests were analyzed with the Mat63 model. The subsequent sandwich panel specimens were fabricated by expanding foam between face sheets with different surface treatment conditions [74]. These tests were analyzed using the Mat_75 model.

In the preliminary test series, two foam sandwich panels were tested in a bend test fixture to evaluate the performance. The steel face sheets for the panels were nominally cut 17-inch long by 15-inch wide. The foam core was constructed from a foam block that was split on the thickness centerline in a band saw and after trimming it was essentially 15x15 inch (the steel pieces overhung on each end by 1-inch nominally). In one case, the foam was bonded on both surfaces and in the second case no adhesive was used. The adhesive used was 3M scotch-weld 2216 B/A gray. The cure cycle that was applied was 120 minutes at 150° F. Foam surfaces that were sprayed with release agent during original foam fabrication (several months prior to testing) were sanded and cleaned with isopropyl alcohol prior to adhesive bonding.

A loading approximating a three-point flexure was applied, with the two lower flexure supports being cylinders 3.5-inch in diameter. The upper loading point, or pusher, was a 5x1.5 inch pusher with a 0.5-inch radius around the contact face. The nominal span (outer-to-outer loading line distance) was 12 inches. The longitudinal axis of the test panel was located along the 12-inch span as was the major axis of the 5x1.5 pusher.

A 200-kip servohydraulic test machine was used for the flexure testing. The loading was applied with a 2-inch per minute displacement rate to the test specimen. A custom data acquisition system was connect to record data from the LVDT, load cell (200 kip capacity) and four other string pots also included in the setup.

The measured load-displacement behaviors for both the bonded and unbonded sandwich panels are shown in Figure 237. Initially the bonded panel was much stiffer in flexure than the unbonded panel. However, within approximately the first one-half inch of the loading, the bond between the face sheets and foam core fails and the behavior approaches that of the unbonded panel. In addition, the load-displacement behaviors for both panels have numerous load drop-offs. These load drops likely correspond to where the foam cracked.
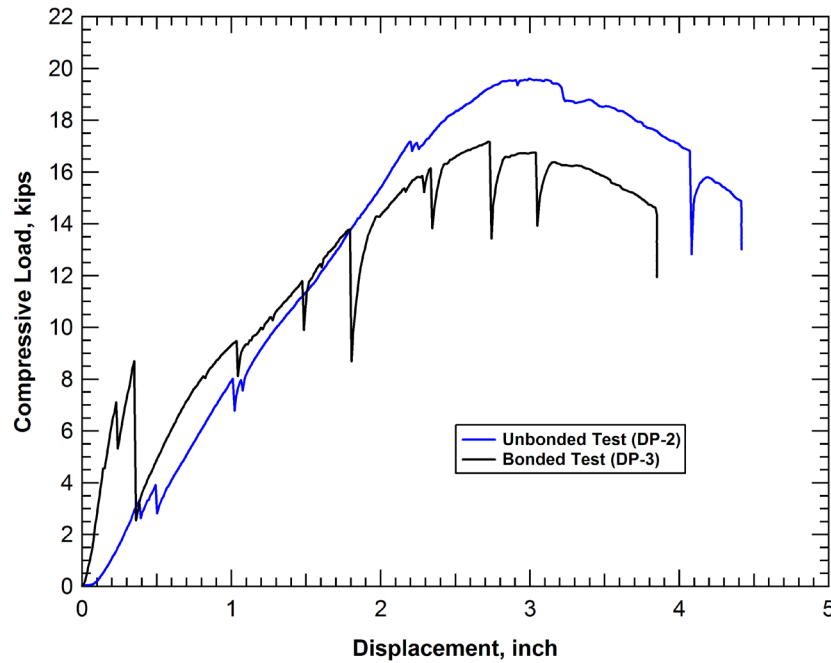
Figure 234. Comparison of bonded and unbonded foam sandwich panel bend tests.

A series of calculations were performed with the Mat_63 model to investigate the sandwich panel performance in the bend test. A comparison of the measured and calculated bend test response is shown in Figure 235. The variations evaluated in the analyses included the effect of a bonded or unbonded interface, the friction between foam and steel when the unbonded condition was used, the tensile cutoff strength for the foam, and modeling characteristics such as the contact algorithm between the various panel and test fixture components. Several of these parameters were found to have little effect on the behavior. The contact algorithms (e.g. automatic, surface to surface) had no effect on the behavior. The variation of the tensile cutoff strength had a small effect, even for very low values of tensile strength. However, the interface between the foam and the steel face sheets was found to be very important.

The comparisons of the measured and calculated (Mat_63) force-deflection behaviors for the bonded sandwich panel flexure tests are shown Figure 236. The analyses show a similar behavior in the initial portion of the curves. However, the model does not include the failure of the bonded interface that occurs at approximately 0.4 inch. As a result the calculation was much stiffer than the test after the face sheets debond from the foam.

A comparison of the calculated and measured force-deflection behaviors for the unbonded sandwich panel is shown in Figure 237. The calculated response was found to be sensitive to the friction coefficient at the foam-metal interface and the analysis shown was for a high friction coefficient of 0.8 which provided the best correlation to the measured response. These tests and

analyses show that the behavior of the foam-steel interface (both strength and interaction after debonding) will be important to optimize the performance of the foam based tank protection systems.
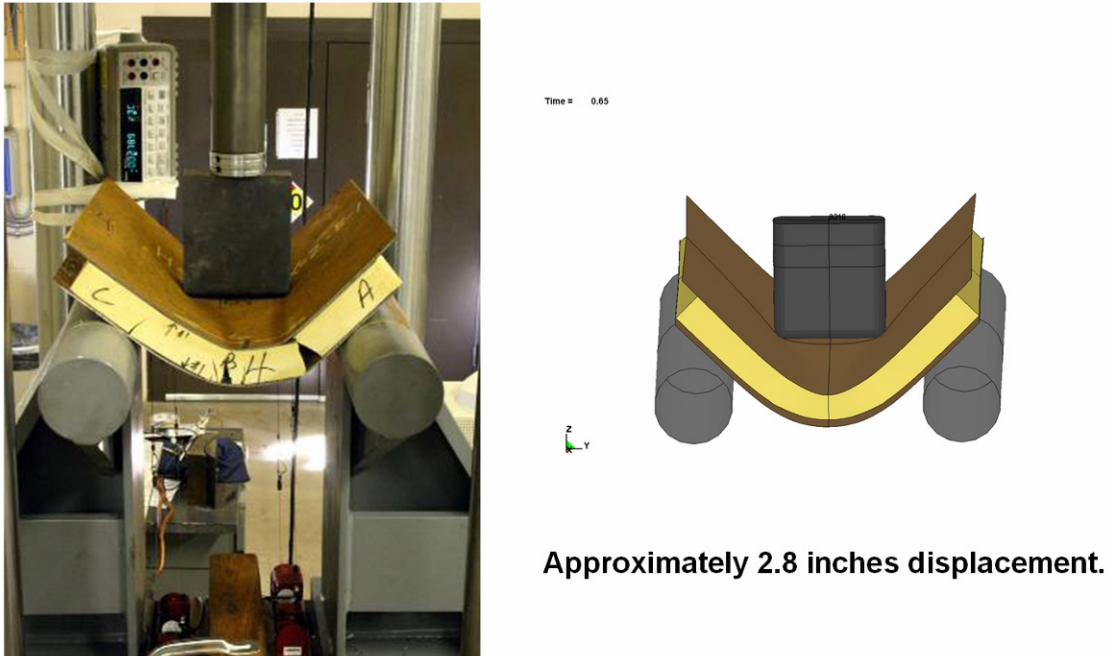
Figure 235. Comparison of a foam sandwich panel bend test and analysis (Mat_63).
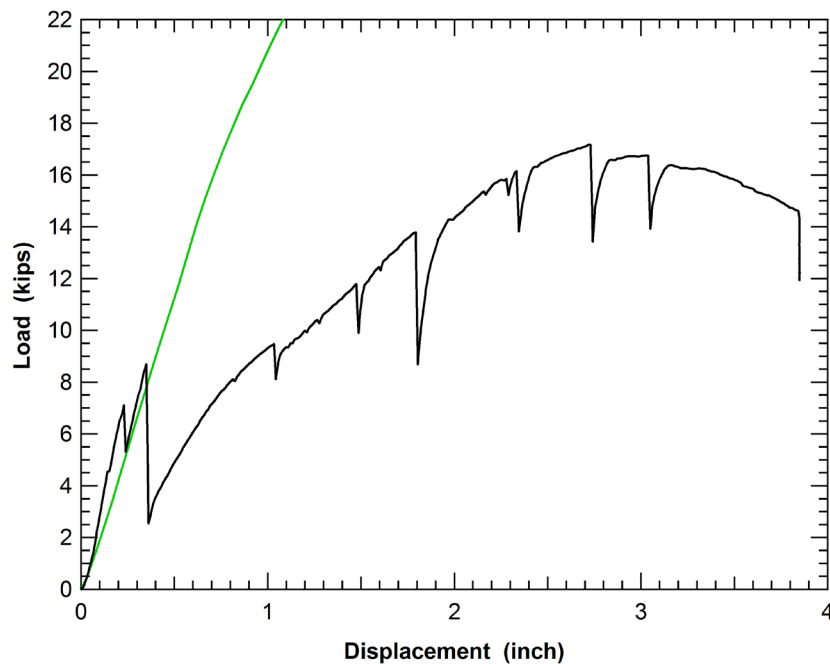
Figure 236. Measured and calculated response for the bonded foam sandwich panel (Mat_63).
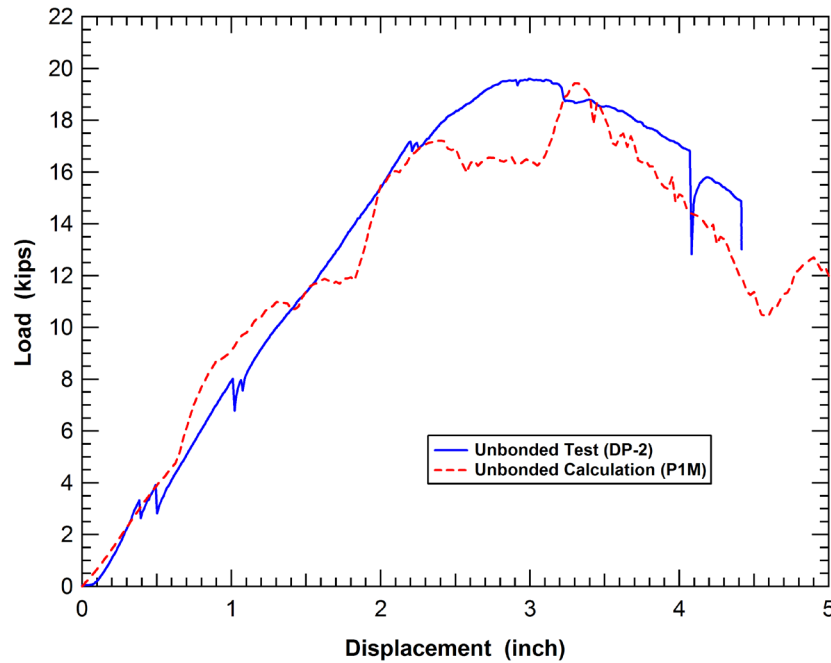
Figure 237. Measured and calculated response for the unbonded foam sandwich panel (Mat_63).

In the second set of panel flexure tests, the foams evaluated included both 5 pcf and 18 pcf BETAFOAM™. The steel face sheet surface preparations investigated included untreated, sand-blasted, coated, and sand-blasted and coated. Each foam and surface preparation combination was repeated three times to establish the variability in the performance, with a total of 24 tests conducted. The repeatability within test groups was good both in terms of the load displacement behavior and the magnitude of the maximum loads.

Panels were fabricated by The Dow Chemical Company and were supplied in the ready-to-test condition. The test conditions were the same as those used in the preliminary panel flexure test series. The specimens were loaded with the constant displacement rate of 2 inches per minute.

The measured force-deflection curves from representative tests on the 18 pcf and 5 pcf panels with the various surface treatments are shown in Figure 238 and Figure 239, respectively. As expected, the 18 pcf foam panels all sustained higher loads than the 5 pcf panels. Within the 18 pcf group, the non-treated and sand-blasted conditions displayed significantly higher loads than the other two coated surface preparation conditions. The peak load in these tests is two to three times higher than that of the coated surface specimens and the load does not drop off until a ram displacement of approximately one inch. This failure mode was significantly different from other conditions and was marked by a loud audible 'crack' as the foam layer failed. These tests show that the foam-steel interface conditions can have a large effect on the panel (or tank car system) response. In post-test specimen inspections, a notable separation between the foam and

steel layers was found for the coated and sand-blasted with coating conditions for both the 5-pcf and 18-pcf foams, indicating a lack of adhesion.
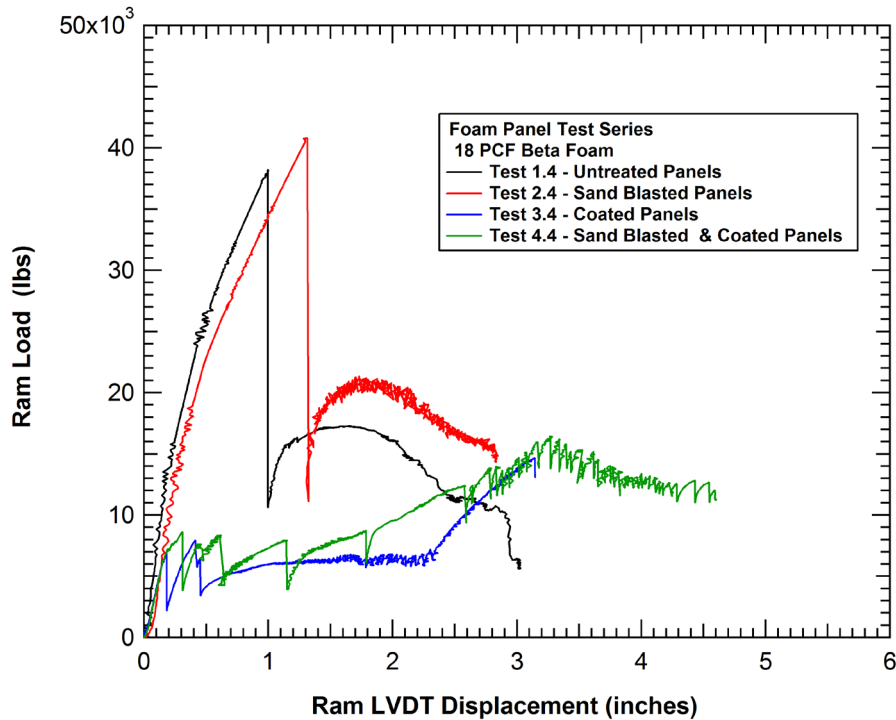
Figure 238. Measured behaviors for the new 18 pcf foam sandwich panel tests.

The results from the preliminary panel flexure tests are compared to the second test series on the 18 pcf foam specimens in Figure 240. The preliminary tests agree reasonably well wit the tests using the coated face sheet surface treatments.

The comparisons of the Mat_75 calculated and measured panel flexure behaviors for the 18 pcf and 5 pcf foam panel specimens are shown in Figure 241 and Figure 242, respectively. In the analyses, the foam is perfectly bonded to the face sheets and any delamination failure would be modeled as a failure through the foam elements adjacent to the face sheets. The comparisons show that the correlation is best in the early portion of the response before the delamination is initiated in the specimens with good bond characteristics. Using this modeling approach with a perfect bond would provide an upper bound to the strength and energy dissipation that could potentially be achieved with further development of the interface bonding methodologies.
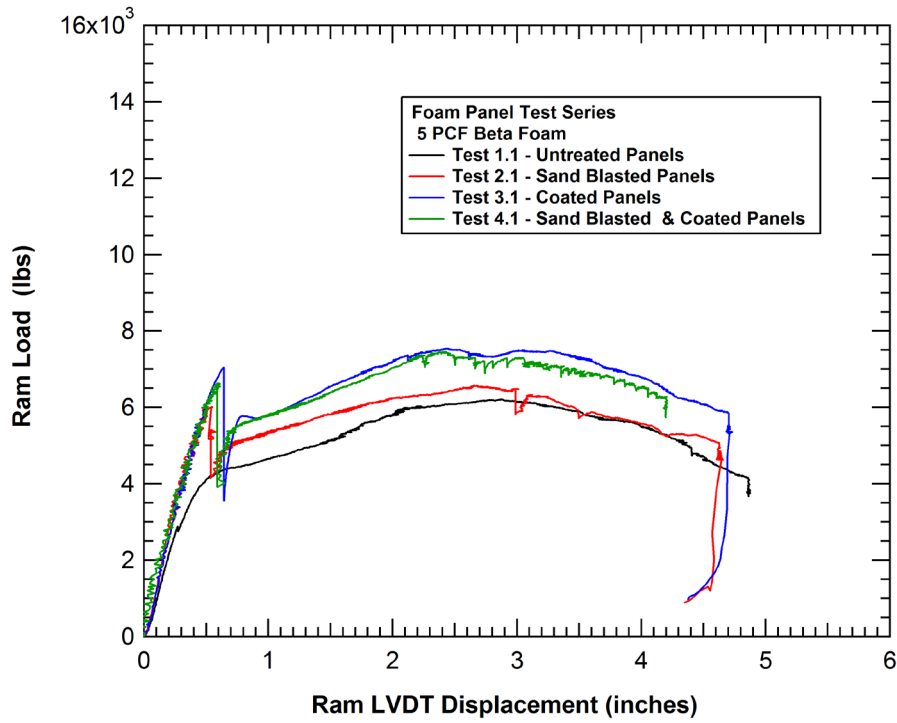
Figure 239. Measured behaviors for the new 5 pcf foam sandwich panel tests.
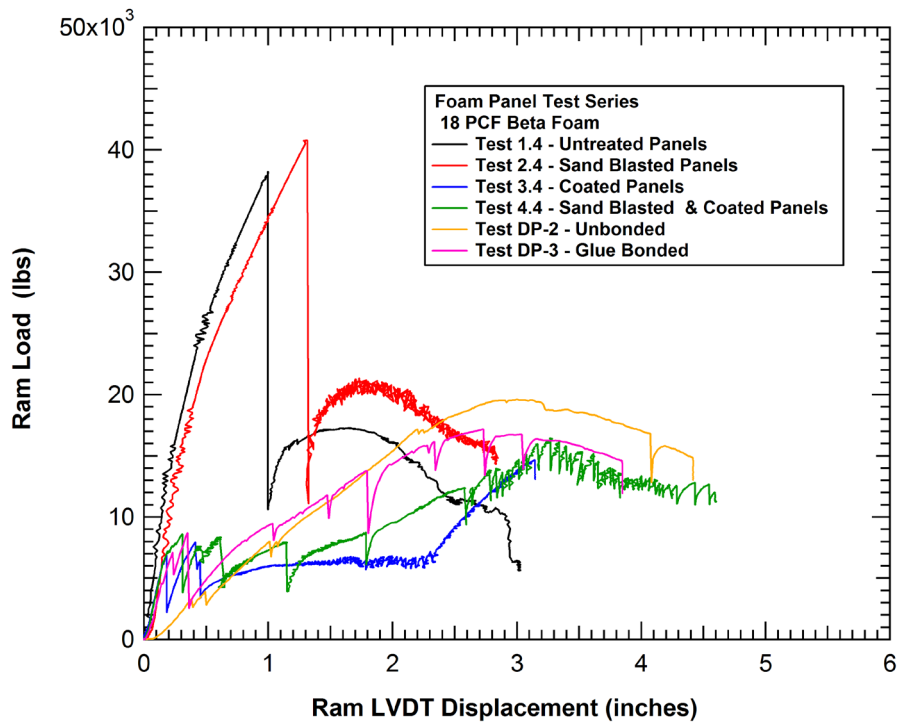
Figure 240. Comparison of the new and original foam sandwich panel tests.
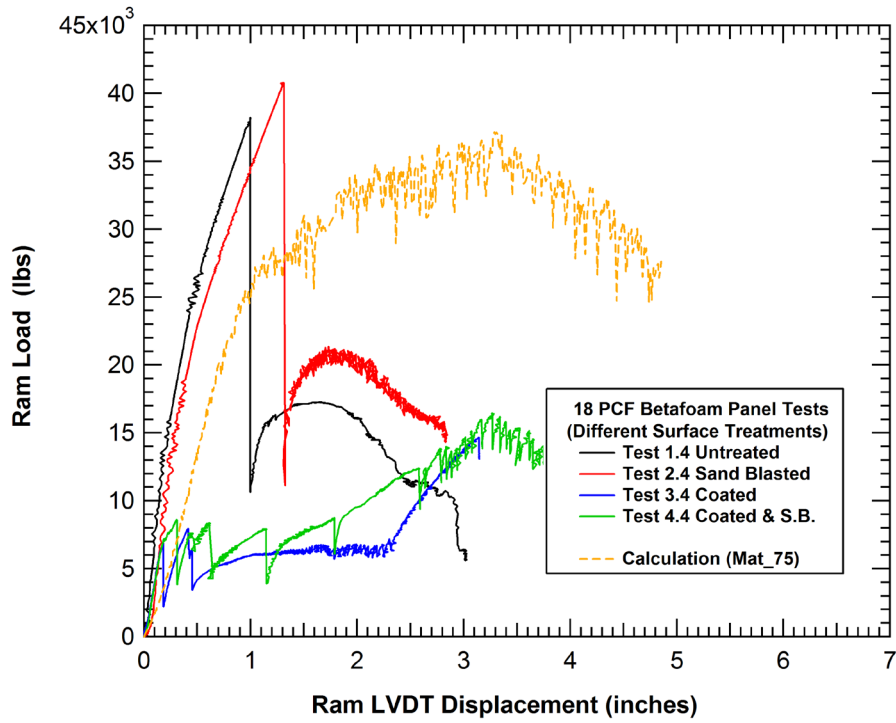
Figure 241. Measured and calculated behaviors for the new 18 pcf foam sandwich panel tests (Mat_75).
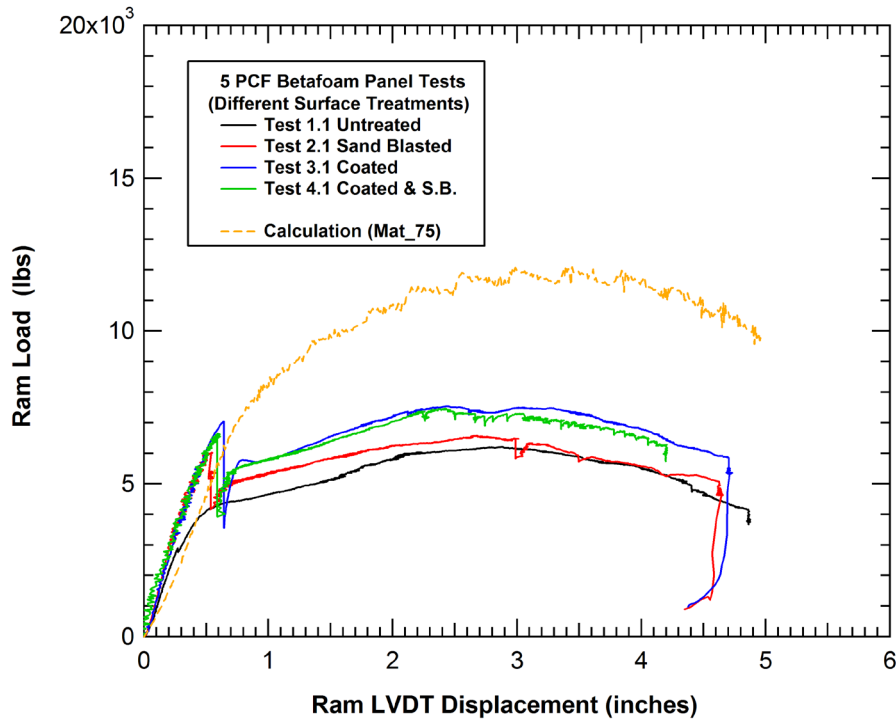
Figure 242. Measured and calculated behaviors for the new 5 pcf foam sandwich panel tests (Mat_75).

6.1.2 Head Test 2 Measurements and Analyses (Foam System)

The second component test of a tank car head test article was performed as part of the Next Generation Rail Tank Car project on April 30, 2008, at the Transportation Technology Center, Inc. (TTCI) in Pueblo, Colorado [75]. This test involved a 295,200-pound ram car striking the Option 2 prototype design tank head at 16.9 mph. The ram car was equipped with a 6-inch square indenter with 0.50-inch radius around the edges. The tank head was affixed to the Transportation Technology Center impact barrier with a rigid fixture. The indenter punctured the outer head shield, inner jacket, and the tank head. The ram car was then slowed to a stop by the arrestor system mounted on the barrier. The peak longitudinal acceleration before the arrestor system engaged was about 3.9 g (CFC60).

The test article and the ram car staged in position prior to the test are shown in Figure 243. The test article was bolted to the wall-offset fixture. The wall-offset fixture was bolted to the impact wall and an energy absorbing arrestor system was added to dissipate residual energy if the head is punctured. The arrestor system consists of four hydraulic cushion units, two on each side, placed to engage the ram car shortly after the indenter penetrates the head.

Figure 243. Pretest configuration of the test head and ram car.

The Option 2 prototype consisted of three steel layers enclosing two foam layers. The outer layer was a 0.50-inch A516-70 head shield that was 127 11/16 inches in diameter. The inner jacket was an 11-gage A1011 jacket head that was 121 5/8 inches in diameter. The inner layer

was a 0.777 inch TC128 commodity head that was 102 inches in diameter. The inner foam layer was about 10-inches thick at the apex of the head and consisted of 4 lb/ft^3 foam. The outer foam layer was about 2-inches thick at the apex of the head and consisted of 18 lb/ft^3 foam.

The ram car was modified before this test in anticipation of higher peak loads expected for the new prototype head designs. Support was added behind the ram to resist bending, the ram was strengthened, and a new hardened indenter was installed.

Prior to head test 2, the ram car was weighed to determine the increase from modifications. The A-end weight (ram end) was 168,050 lbs and the B-end weight was 127,150 lbs for a total weight of 295,200 lbs. The impact speed, measured by the reflector speed trap, was 16.9 mph. The ram punctured the outer jacket, inner jacket, and tank head. The damage to the outer jacket after the impact is shown in Figure 244. An interior view of the impact damage to the tank head is shown in Figure 245.

Figure 244. Puncture of the external protective layers in Head Test 2.
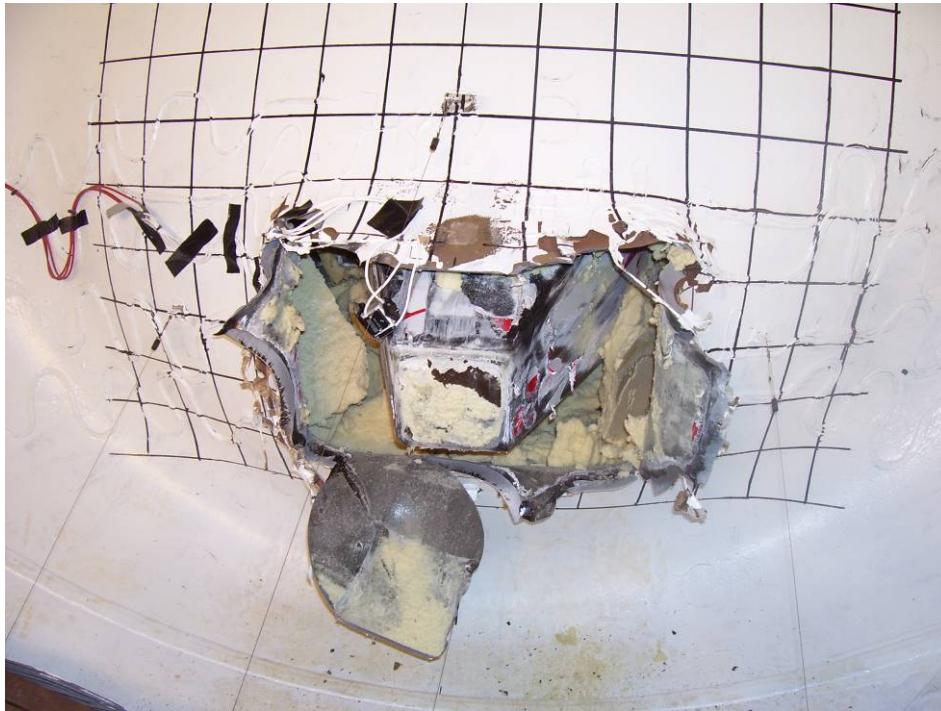
Figure 245. Internal puncture of the tank head in Head Test 2.

Head Test 2 was performed prior to the detailed characterization testing of the foams and the pretest analyses were performed using the Mat_63 foam models. A comparison of the predicted and measured force-deflection behaviors for Head Test 2 is shown in Figure 246. The pretest prediction did a very good job of predicting the initial behavior and the puncture of the outer head shield which occurs at a force level of approximately 500,000 lbs and a ram displacement of approximately 10 inches. However, in the subsequent loading, the pretest prediction over predicts the force levels by 200,000 to 300,000 lbs.
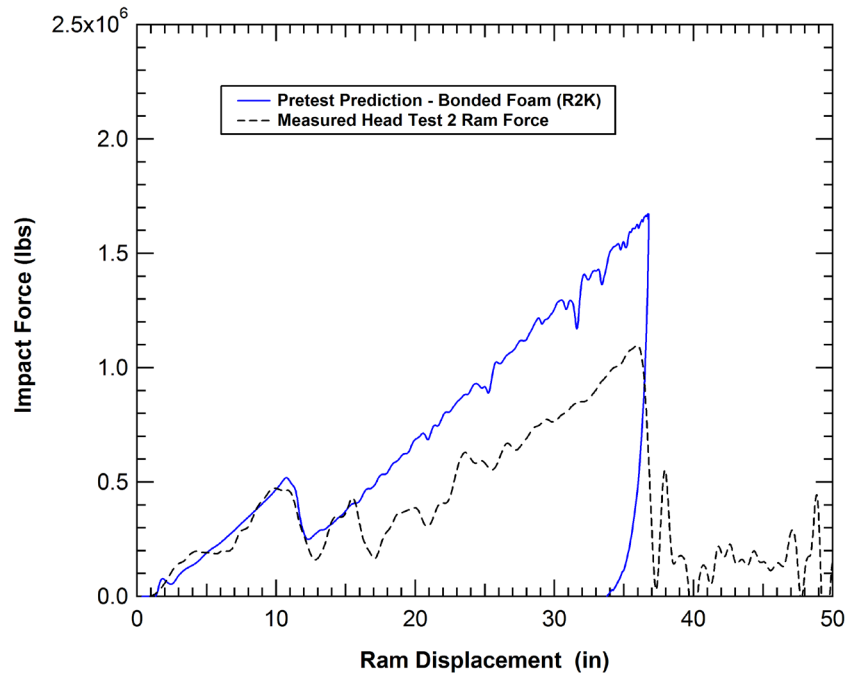
Figure 246. Comparison of predicted and measured behavior for Head Test 2.

The behavior measured in Head Test 2 can be better understood by comparing to the impact behavior for Head Test 1, as shown in Figure 247. We see that the later portion of the curve was nearly identical to that of the baseline head. As a result, we know that the foam had either significantly debonded from the head or had developed tensile cracks and was not resisting any loads. In contrast, the pretest prediction was performed using a perfect bond between the foam and the metal layers. In addition, the prediction was performed with a high estimate of the tensile cutoff stress. As a result, the model of the layered foam protective system holds together and continues to work as a system after the outer head shield layer was penetrated in the pretest analysis.
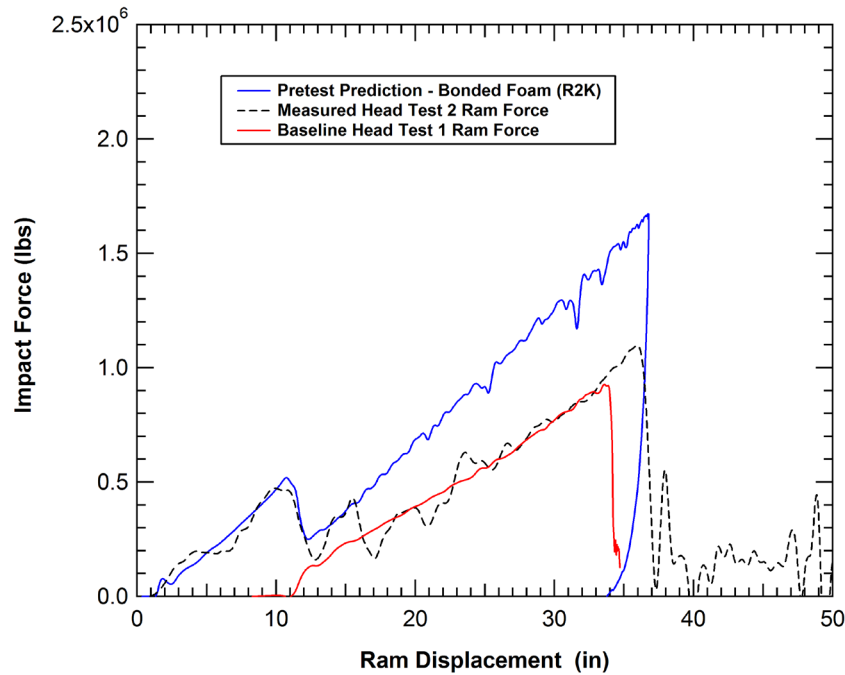
Figure 247. Comparison of predicted and measured behavior for Head Test 2.

The results of this test produced the following observations:

1. The models of the foam and detailed puncture models of the steel can accurately predict the penetration of the outer layers.

2. With the current formulation of the foam and foam-metal interface bonding, the system contributes very little to the puncture resistance after the outer layers were penetrated. Additional development of the foam and interface is needed to improve the performance.

Subsequent to the detailed foam characterization testing, a post test analysis was performed using the Mat_75 foam models. The other significant change to the post test analysis was that a Bao-Wierzbicki failure patch was added to the head to calculate the point at which the head is punctured. The comparison of the calculated and measured force-deflection behaviors is shown in Figure 248. Again there is overall good agreement in the puncture of the outer foam system protective layers and the forces at which the head is punctured. The primary difference is that the calculated forces begin to increase more quickly after the puncture of the outer layers. Again, this potentially is a result of large scale debonding at the foam-steel interfaces.

The calculated and measured force-deflection behaviors are integrated to obtain the puncture energies shown in Figure 249. The comparison shows that the calculated puncture energy is approximately 12 percent higher than measured in Head Test 2.
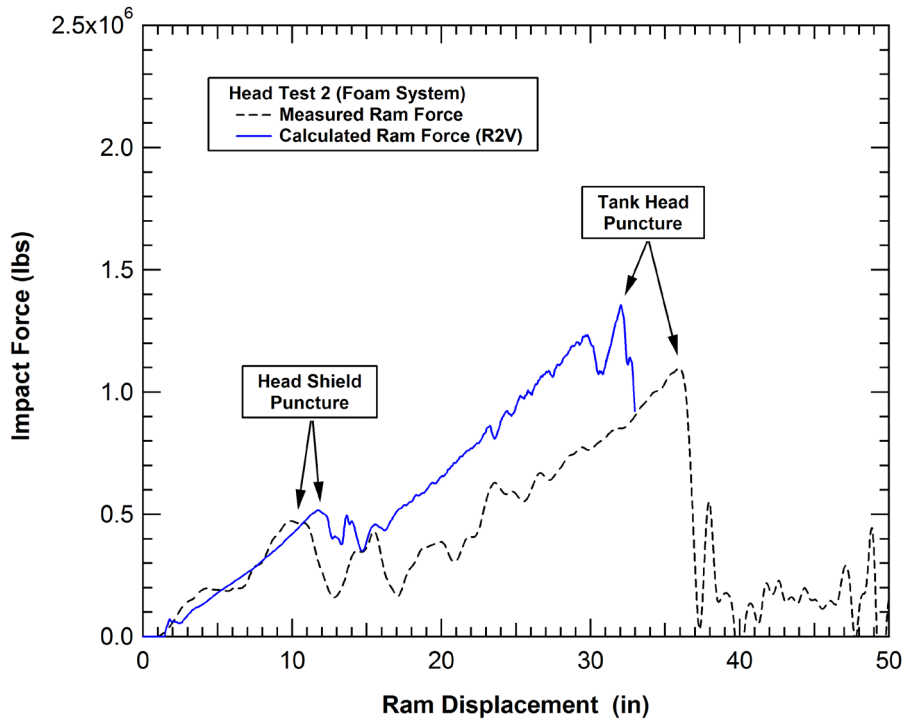
Figure 248. Comparison of calculated and measured behavior for Head Test 2 (Mat_75).
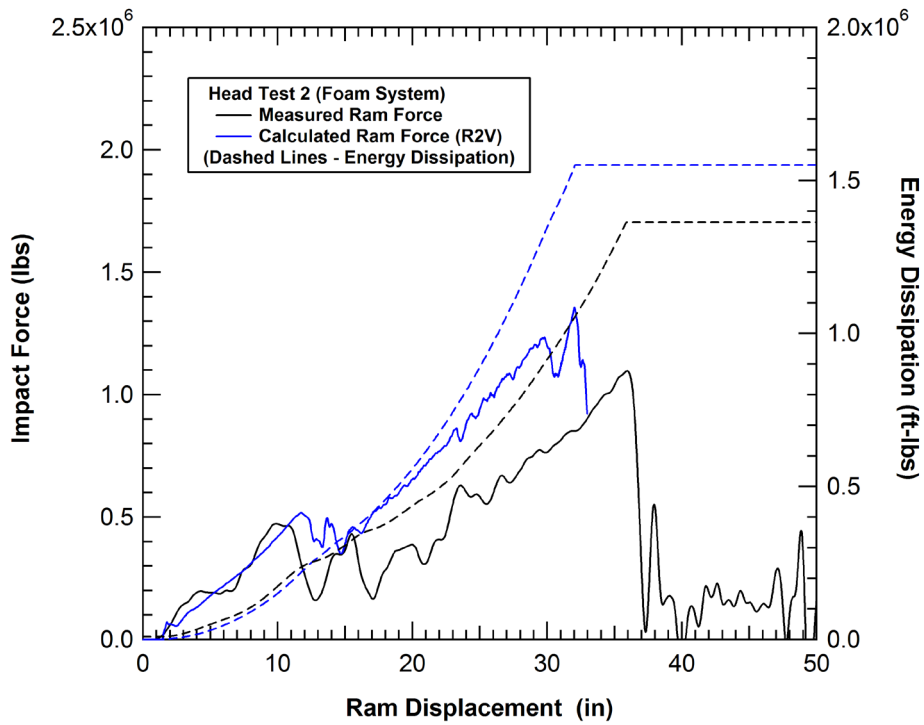
Figure 249. Comparison of calculated and measured behavior for Head Test 2 (Mat_75).

For this head impact test geometry, the influence of the foam modeling is seen primarily in the early time response. The later time forces are dominated by the internal tank head response. A comparison of the analyses with the Mat_63 and Mat_75 models is shown in Figure 250. The calculated response with the Mat_63 model is stiffer in the early indentation of the head shield. This probably results from the fact that tensile failures are not properly modeled. In addition, the behavior of the Mat_63 model after the head shield transitions directly to the loading of the internal head with no indications of the contribution of the inner head shield visible in the calculated force-deflection response. The calculated response with the Mat_75 model more closely matches the characteristics of the measured early time behavior.
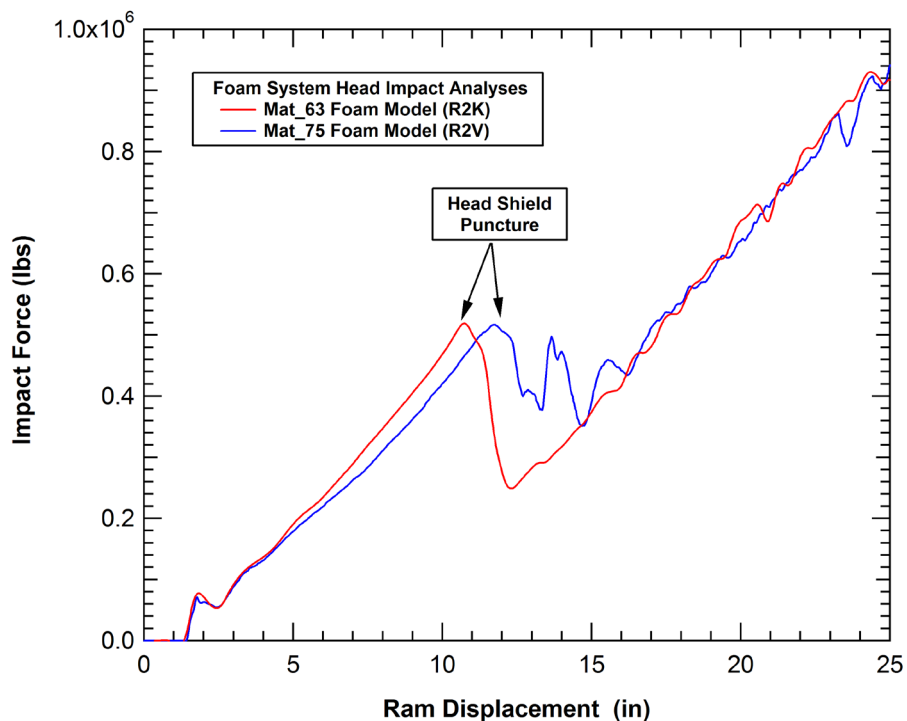
Figure 250. Comparison of calculated head impact response with different foam models.

6.1.3 Side Impact Puncture Analyses of Foam Systems

A series of additional analyses were performed to investigate the influence of different foam system design parameters on the protection performance. These analyses were performed prior to the detailed foam characterization and as a result were performed with the Mat_63 foam models.

An example of the difficulties of developing structural systems to protect against the 6x6 inch impactor can be demonstrated by adding low density structural foam between the jacket and tank in the 300 lb EO car with the thicker outer jacket. A 3.3 pound per cubic foot (pcf) structural

foam was added to the 4 inch space between the tank and jacket. The system concept was to couple the shell and jacket layers as a sandwich structure and to dissipate some of the impact energy with the crushing of the structural foam. The crush strength for the 3.3 pcf foam was roughly 50 psi [70].

The force-deflection curve and puncture energy for this concept using structural foam is shown in Figure 251. Without the foam the puncture force was 780,000 lbs and the puncture energy was 1.85 million ft lbs. The addition of the foam causes the punch to penetrate the outer jacket at approximately 15 inches displacement and the commodity tank was punctured at approximately 33 inches. Without the foam the 0.375-inch jacket was not punctured until 36 inches of ram displacement and the tank ruptures at 43 inches. As a result, the overall puncture energy in the commodity tank drops from 1.85 million ft lbs to 1.27 million ft-lbs with the addition of the foam. The early failure of the outer jacket appears to result from the foam increasing the overall stiffness of the outer jacket behavior and concentrating the localized loads around the perimeter of the ram head.
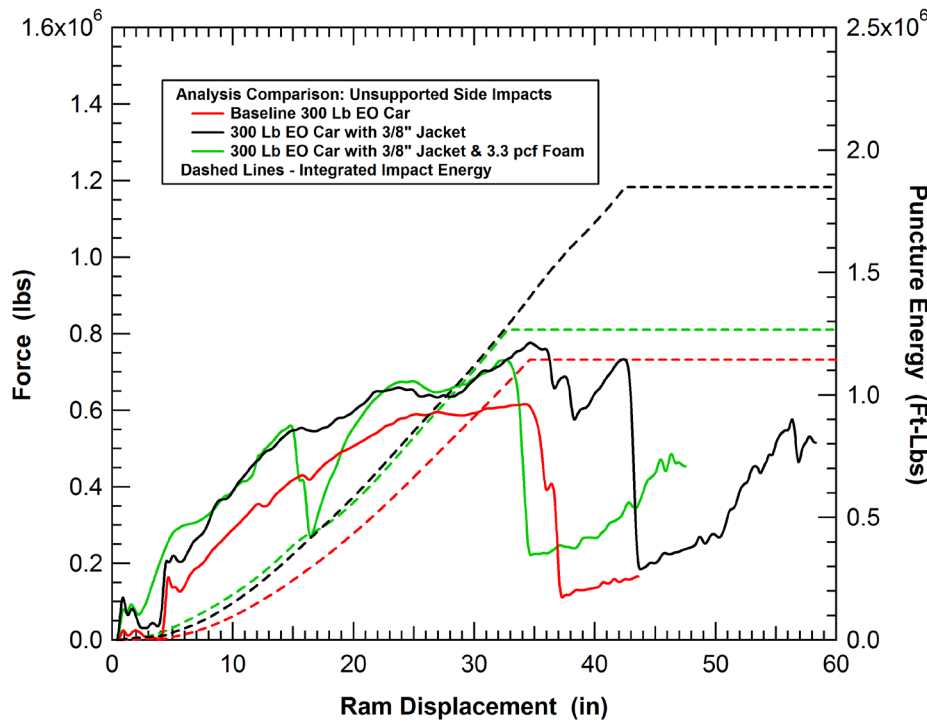
Figure 251. Evaluation of a retrofit EO tank car with a 0.375-inch jacket and foam.

Another example of a foam system side impact analysis was performed with the 12x12 inch impactor to see if the larger contact area improves the performance of foam systems. An analysis was performed for a 500 lb Cl tank with a 0.375 inch jacket and 4 inches of 3.3 pcf foam impacted by the 12 inch impactor. The calculated impact response is shown in Figure 252. The

corresponding force-deflection characteristics for this analysis are compared to other tank systems in Figure 253. The comparison shows that the system performs better than the baseline tank with an 11 gauge jacket. However, again the foam results in an earlier jacket penetration and lower puncture energies than the system retrofit with the 0.375 inch jacket but without any foam.
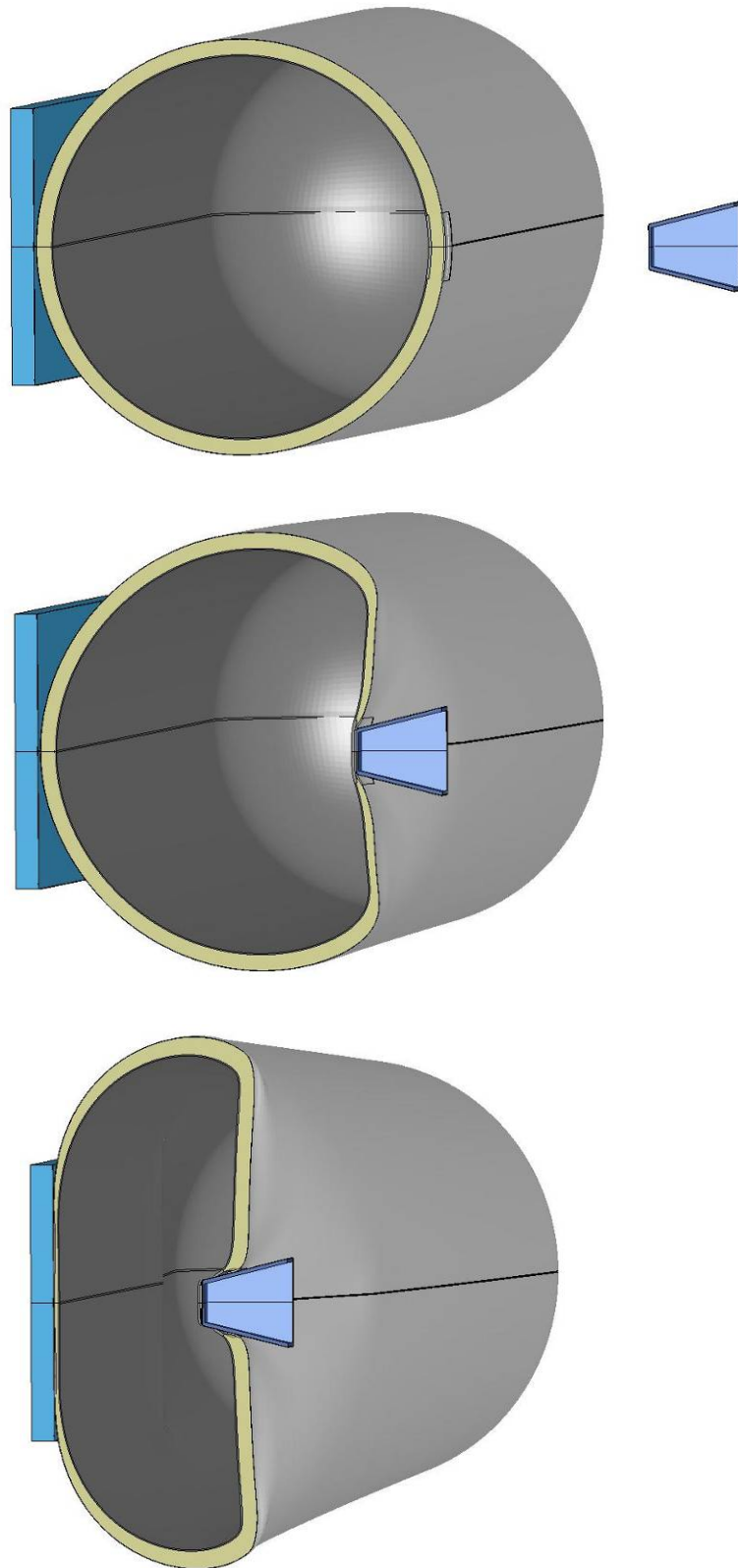
Figure 252. Impact response of a foam retrofit tank with the large ram (12" by 12").
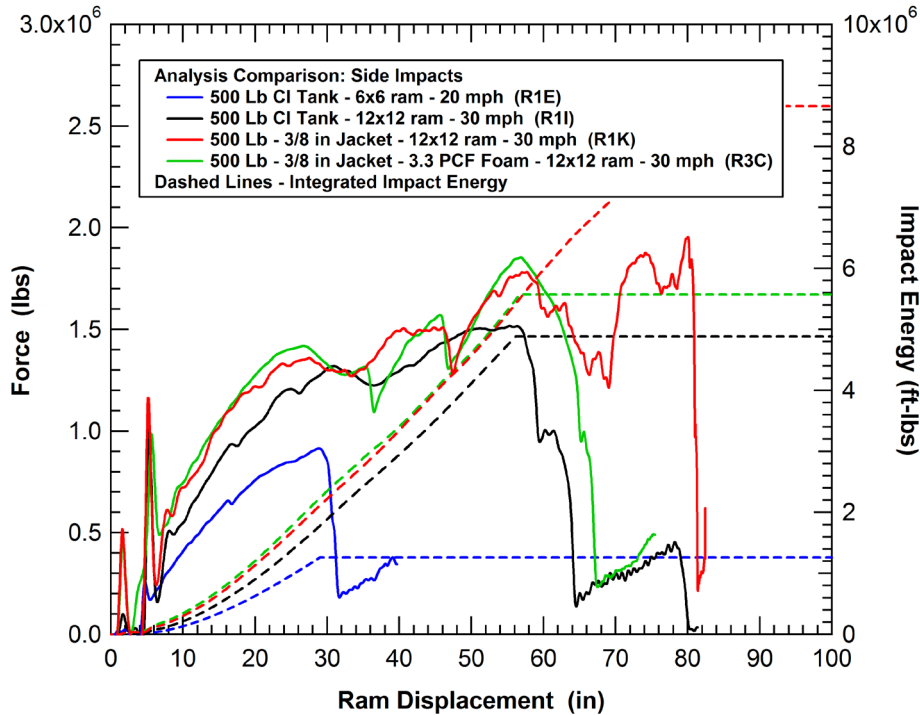
Figure 253. Evaluation of the effects of the ram size on a 500 lb chlorine tank.

6.1.4 Head Impact Puncture Analyses of Foam Systems

A series of additional layered foam head protection combinations were analyzed. The combinations of jacket thicknesses, materials, and foam densities analyzed are summarized in Table 10. These analyses were primarily performed using foam models with high estimates of the tensile cutoff stress and good bonding between the layers. As a result, the primary information developed from these analyses was the response up to the point of the outer head shield penetration.

Table 10. Multilayer foam protection system analyses

Calculation	Head Thickness	Inner Foam	Inner Head Jacket/Shield	Outer Foam	Outer Head Shield
R2K	0.8281	10" 4.75 pcf	11 gauge A1011	2" 18.3 pcf	0.50" A516-70
R2N	0.8281	10" 4.75 pcf	11 gauge A1011	2" 18.3 pcf	0.50" A516-70
R2P	0.8281	10" 4.75 pcf	0.25" 90XF	2" 3.30 pcf	0.50" 90XF
R2Q	0.8281	10" 3.30 pcf	0.25" 90XF	2" 7.50 pcf	0.75" 90XF
R2S	0.8281	10" 3.30 pcf	0.25" TC128B	2" 7.50 pcf	0.75" TC128B

An example of the calculated impact behavior of a foam protection system is shown in Figure 254. The initial response was as desired for the system where the outer high density foam layer and the inner jacket and head shield act together as a sandwich structure. As the outer layers were driven inward by the ram, a larger volume of the low density inner foam was crushed. However, at relatively small displacements the outer layer was penetrated and the protection system was defeated.
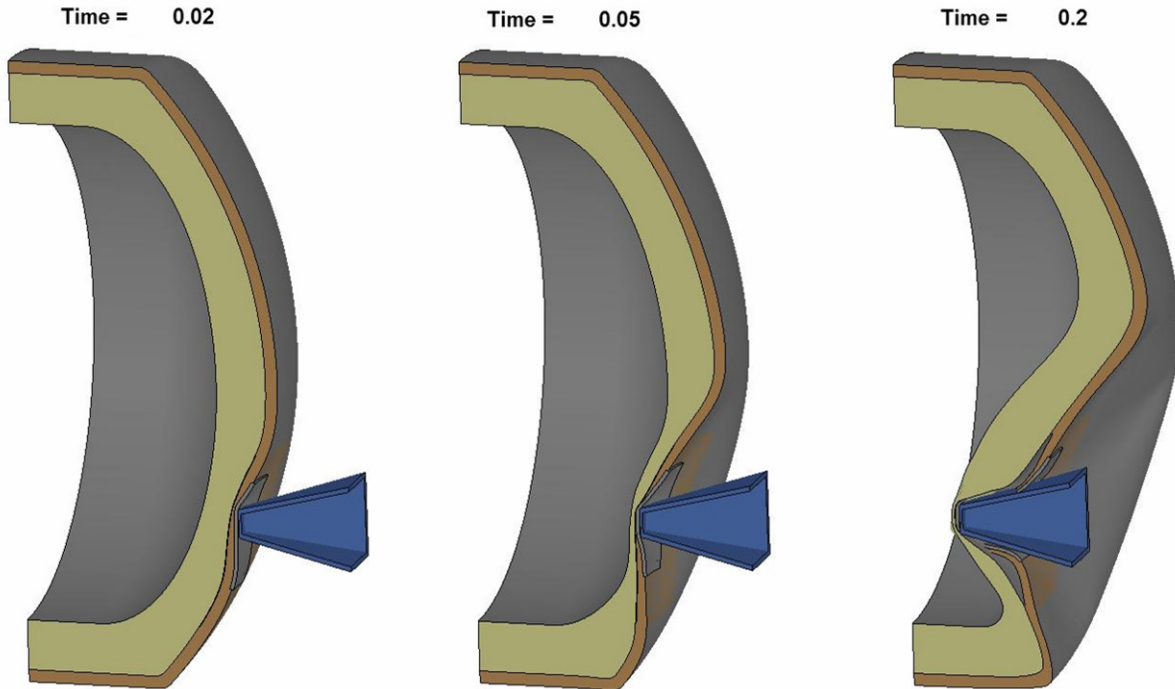
Figure 254. Impact behavior of a multi-layer foam head protection system (R2S).

A series of force-deflection characteristics for various foam head protection systems is shown in Figure 255. Note that the detailed puncture modeling was only included in the outer layer so the large forces developed at late times by the resistance of the head were not realistic. However, the initial puncture of the outer head shield as indicated in the figure should be accurately captured.

The calculated impact forces to puncture the outer layer were compared to those of previous analyses in the plot of the puncture force versus system thickness in Figure 256. The difference in the data for the foam systems was plotted against the outer head shield thickness only rather than the sum of the head and jacket thicknesses. This shows that the foam had the effect of making each layer act independently rather than coming in contact and working together to resist the high shear stresses around the edge of the impactor. As a result, the maximum achievable puncture forces were reduced and the system does not reach the desired puncture energies.
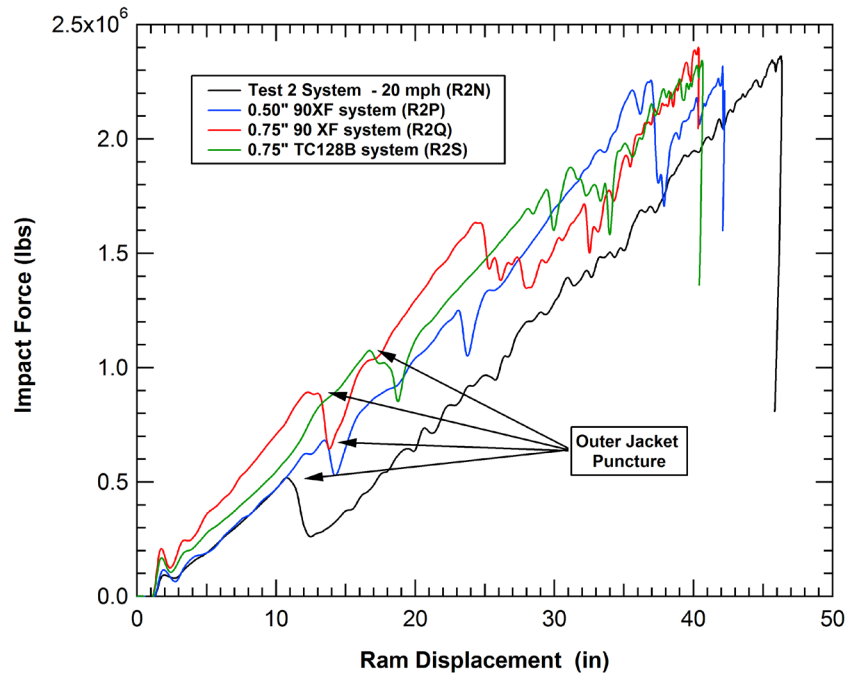
Figure 255. Impact behavior of multi-layer foam head protection systems.
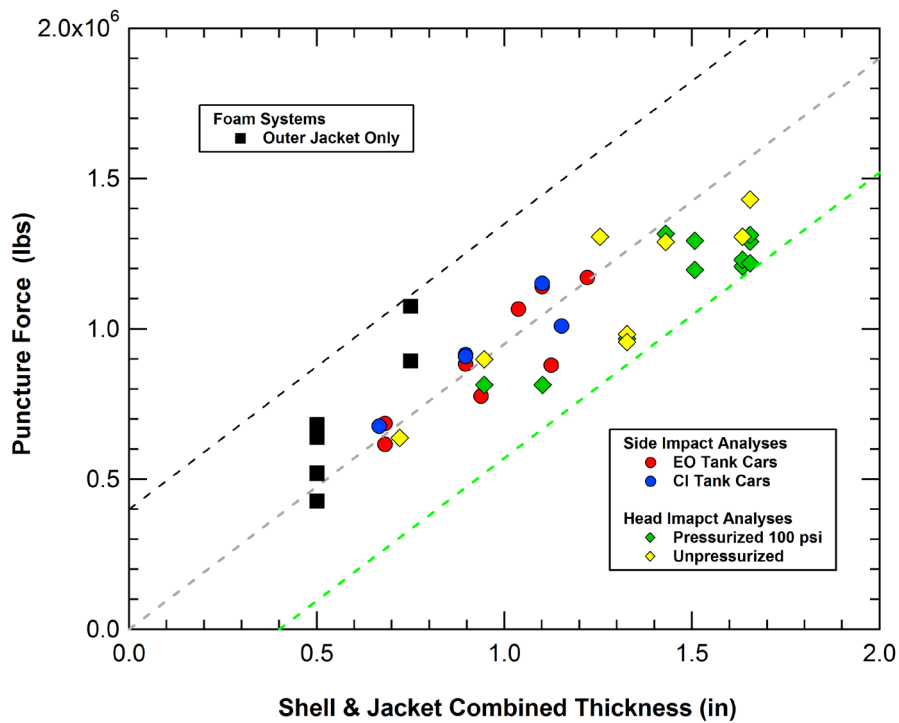
Figure 256. Comparison of foam protection puncture forces to baseline systems.

6.2   Evaluation of EMS Protection Systems

Another proposed protection concept is to use external engineered metal structures (EMS) to protect the tank structure and dissipate the impact energy. These EMS concepts have a wide range of potential geometries and fabrication techniques. However, the primary concepts analyzed here were structures with inner and outer face sheets and a metal core structure that creates a metal sandwich structure. The core should maintain the spacing between the face sheets to improve the efficiency and stiffness of the EMS system and at sufficiently high loads, deform in a mode to dissipate energy.

There are a large variety of core structures including truss core geometries [76], hexagonal, rectangular, and triangular cellular cores [77-79], corrugated geometries, and metallic foam cores [80]. These structures were subjected to a range of loading conditions from static loading to impact and blast loading. In general, the testing and analyses concentrated on loads distributed over an area that is large compared to the characteristic length of the cellular core or core thickness. One study investigated cellular sandwich panels subjected to both distributed and localized blast loads. The study found that a stiff core panel is superior to a solid plate when subjected to a planar impulse, but inferior when the load was localized [81]. The performance under a localized loading is very important for the puncture performance for a tank subjected to a 6-inch impactor.

The two primary core structures investigated here were a corrugated core sheet and an egg-crate design where an orthogonal grid of webs, normal to the face sheets, creates square cell geometry.

6.2.1   Head Impact Puncture Analyses of a Corrugated EMS Systems

A series of analyses were performed on a corrugated head protection EMS system. The nomenclature for the corrugated EMS structures is shown in Figure 257. The primary EMS structure is a 6 inch deep corrugated structure with the face sheets and corrugated core sheet all made of 11 gauge 90 XF material. A detail of the end EMS corrugation geometry is shown in Figure 258. A drawing of the initial proposed EMS structure for Head Test 3 is shown in Figure 259. An objective of these analyses was to further develop this head protection configuration prior to Head Test 3 using the corrugated EMS structures as the structural foundation.
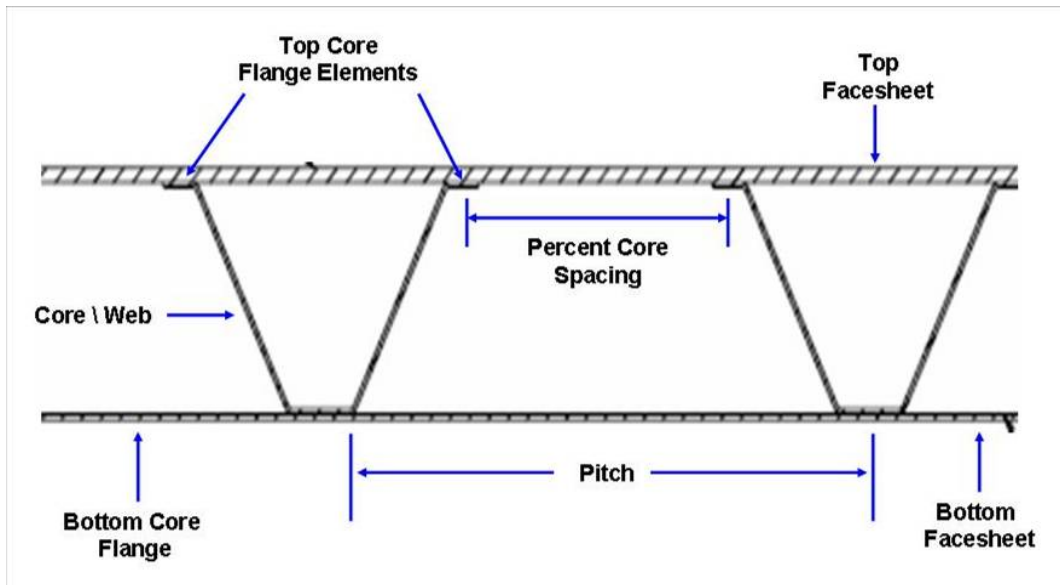
Figure 257. Nomenclature for corrugated EMS structures.
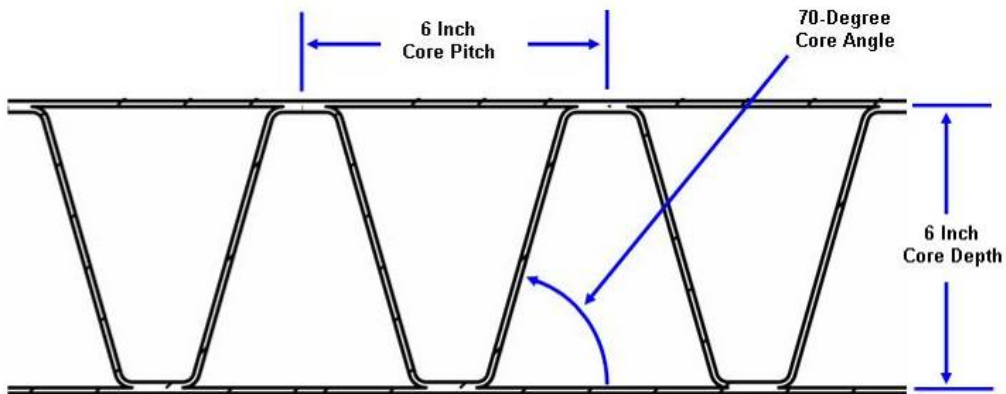
Figure 258. Detail of the corrugated EMS corrugation geometry.
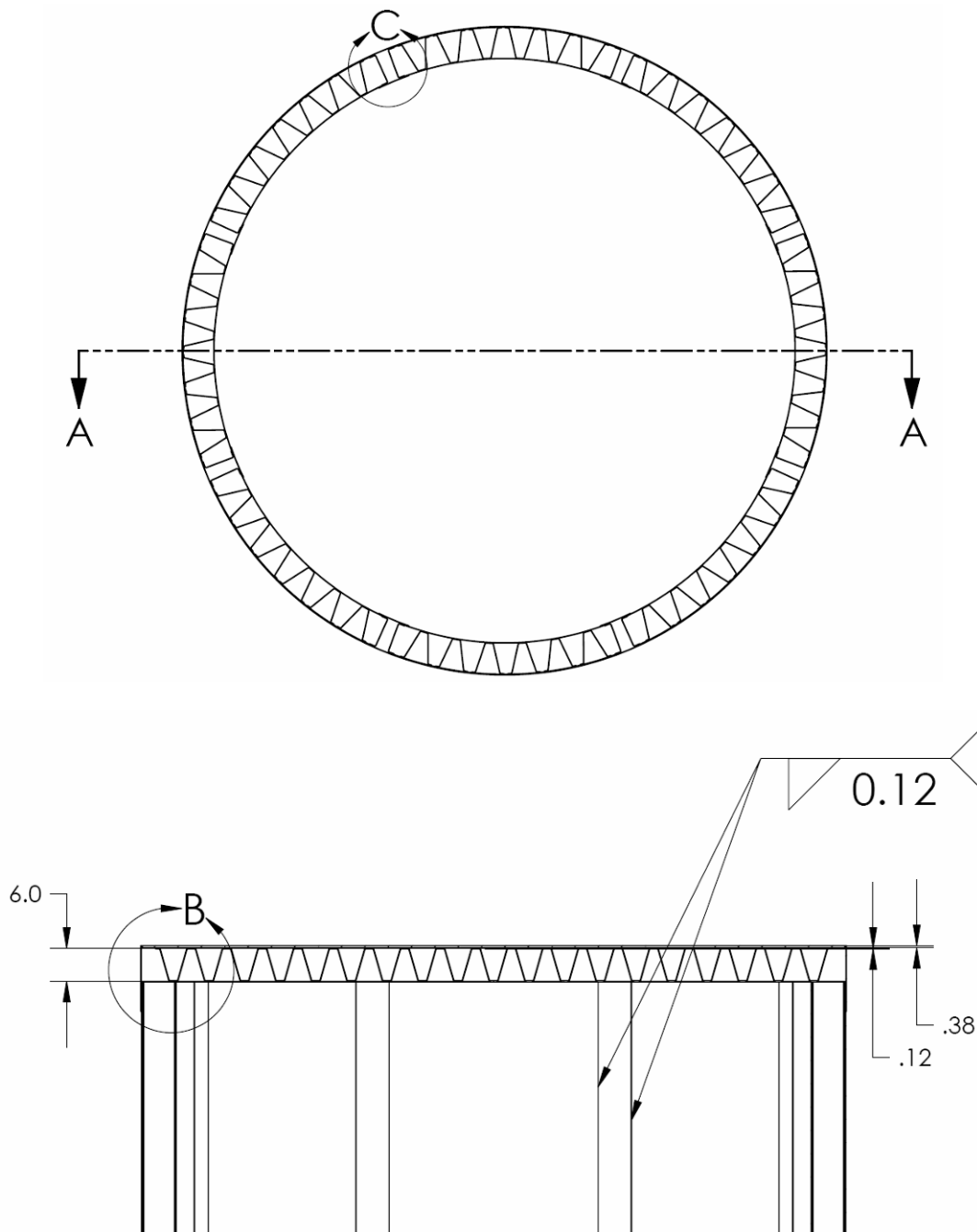
Figure 259. Drawing of the proposed corrugated EMS structure for Head Test 3.

The baseline concept was to create a cylindrical side EMS structure and flat end EMS with a thicker cover plate to resist puncture. An example of the calculated behavior for this concept with a 0.375-inch thick 90 XF end cover plate is shown in Figure 260. The system was penetrated with approximately 5 inches of indentation caused by the ram with an impact force of

586,000 lbs. To improve the performance of this system, the end plate needs to be significantly thicker and/or the overall compliance of the system needs to be increased.

The proposed modification to the system is to extend the outer face sheet on the side EMS structure and separate the end EMS structures from the stiff side EMS. The calculated performance of this concept with an 8 inch extension of the side face sheet is shown in Figure 261. This system still uses a 0.375-inch 90 XF end cover plate. The added extension reduces the system compliance and some crushing of the side extension was observed before the end EMS was penetrated.
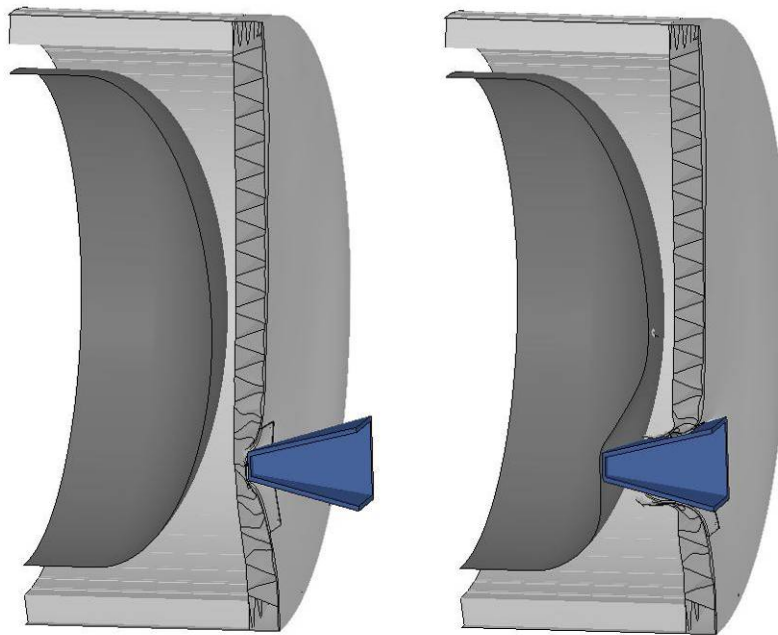
Figure 260. Calculated response of the baseline corrugated EMS system (R3A).
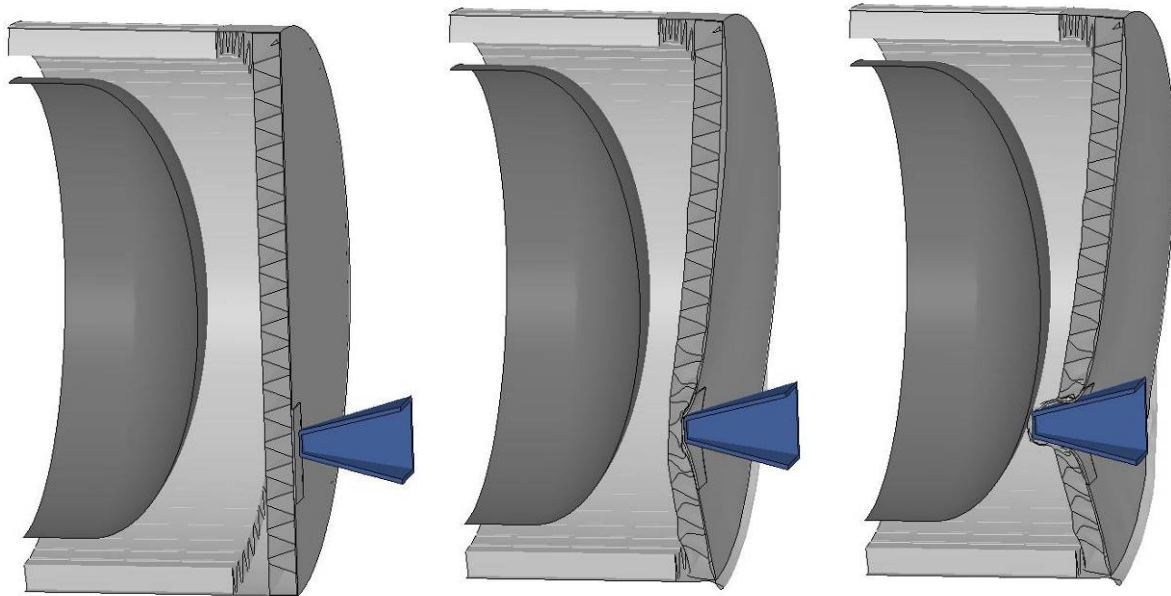
Figure 261. Calculated response of the corrugated EMS with an 8 inch standoff (R3D).

The second proposed modification to the system was to increase the thickness of the end cover plate to allow for larger impact forces and greater energy dissipation prior to the puncture of the protective structures. The calculated performance of this concept, with the 8 inch extension of the side face sheet and 0.777 inch thick TC128B cover plate, is shown in Figure 262. The addition of the end cover plate significantly improves the performance and allows for significantly more deflection and impact energy dissipation before the system was punctured.
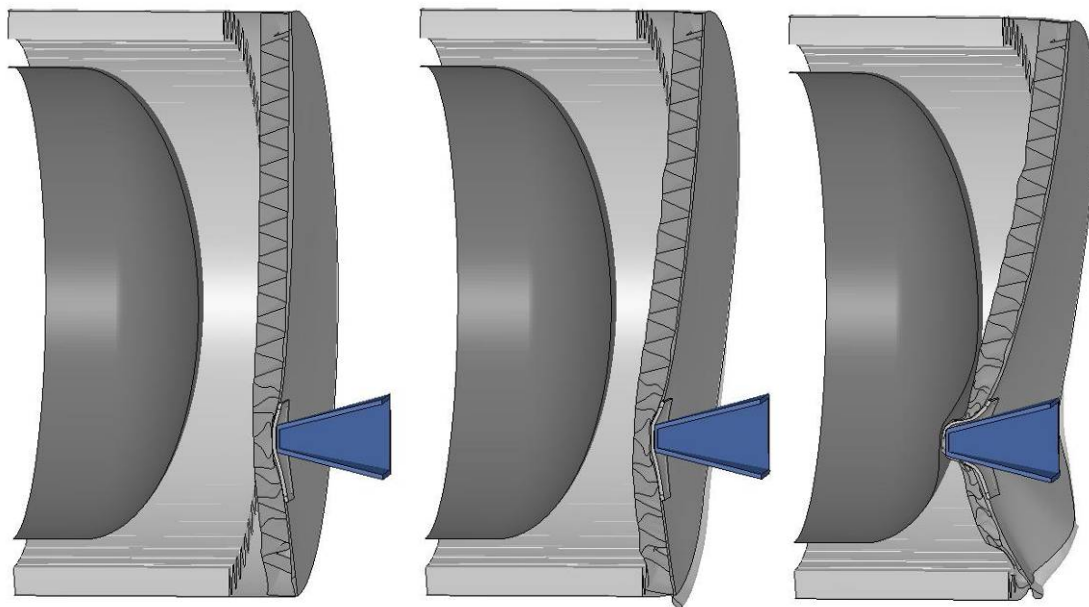
Figure 262. Calculated response of the corrugated EMS and thick cover plate (R3E).

The calculated force-deflection behaviors of these three EMS systems are shown in Figure 263. The initial system without an end extension was punctured at a displacement of approximately 5 inches and a force of 587,000 lbs. Adding the end extension of 8 inches does not significantly change the peak force the system resists, however the collapse of the extension allows for approximately 12 inches of ram travel before the end EMS was penetrated. The thicker end plate (0.777 TC128B) response produces approximately two feet of deflection and a force of 864,000 lbs before the EMS system was penetrated. Thus, the combined effects of increasing the system compliance and increasing the load capacity of the outer layers results in a significant increase in the energy dissipation capability.
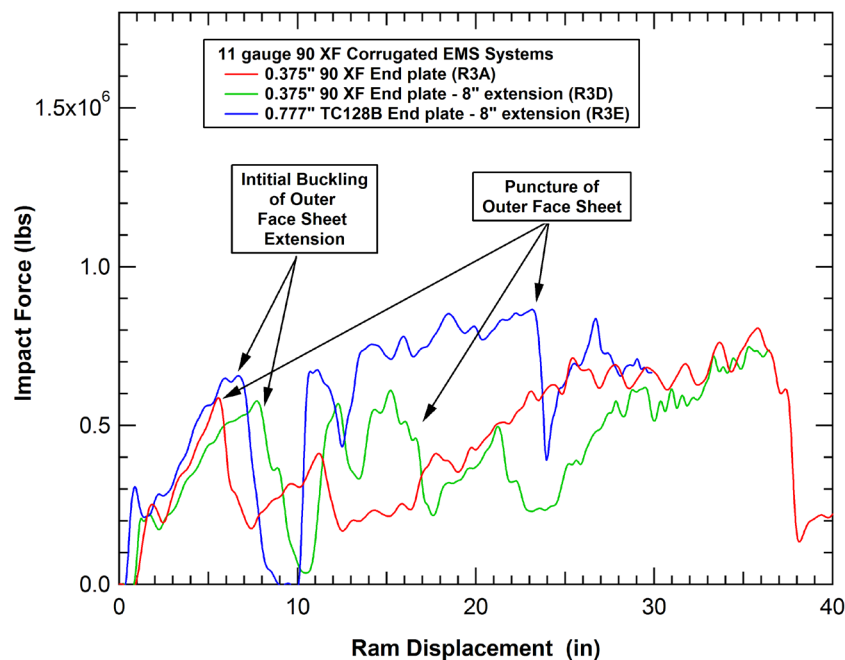
Figure 263. Head impact analyses on corrugated EMS end structures.

A summary of the corrugated EMS head protection design analyses is given in Table 11. All of the corrugated EMS structures were fabricated from the 90XF steel that was 11 gauge thick in both the face and core sheets. The variations in the design were the end plates added at the outer surface of the system to resist the initial system puncture and the standoff distance added between the end EMS section and the side cylindrical curved EMS structures. In all cases, the extended end EMS was supported by an extension of the side EMS outer 11 gauge face sheet.

Table 11. Summary corrugated EMS head impact analyses

Calculation	End Plate Thickness & Material	End EMS Standoff	EMS Puncture Force (lbs)	EMS Puncture Energy (ft-lbs)
R3A	3/8 in 90 XF	0.0 Inch	587,000	130,000
R3B	15/32 in TC128B	0.0 Inch	625,000	191,000
R3C	3/8 in 90 XF	8 Inches	515,000	433000
R3D	15/32 in TC128B	8 Inches	610,000	495,000
R3E	0.777 in TC128B	8 Inches	861,000	1,068,000
R3F	0.777 in TC128B	12 Inches	953,000	1,425,000
R3G	0.777 in TC128B	12 Inches	1,059,000	1,313,000
R3H	2X 3/8 in 90 XF	12 Inches	941,000	1,410,000
R3I	2X 3/8 in 90 XF	12 Inches	944,000	1,395,000
R3J	0.777 in TC128B	12 Inches	964,000	1,410,000

The system can be improved by further extending the end EMS to 12 inches of separation. The calculated response for this system is shown in Figure 264. A comparison of the force-deflection characteristics for the 8 inch and 12 inch extensions with the 0.777 inch end plate are shown in Figure 265. By increasing the standoff the end structure undergoes a larger deflection before penetration and dissipates correspondingly larger impact energy. This 12-inch extension is the configuration selected for the EMS structure to be used in Head Test 3.

A final comparison of the original and modified EMS system performance is shown in Figure 266. The original EMS design was punctured at a displacement of approximately 5 inches and force of 600,000 lbs. By reinforcing the end plate and extending the end EMS structure by 12 inches, the EMS system now has a displacement of approximately 30 inches and a force of approximately 1 million pounds before the EMS structure is penetrated. As a result, the EMS puncture energy is increased from 130,000 ft-lbs to over 1.4 million ft-lbs.

After selecting the EMS configuration for Head Test 3, additional analyses were performed as pretest predictions. The primary difference in these analyses is that a patch of refined solid elements was added to the head impact zone (BW failure patch) to allow for the detailed assessment of both the EMS and head puncture levels. The calculated impact behaviors at both 15 and 18 mph impact speeds are shown in Figure 267 and Figure 268, respectively. At 15 mph the impactor is arrested before the head puncture is initiated. At 18 mph, the head is also punctured with negligible residual kinetic energy.
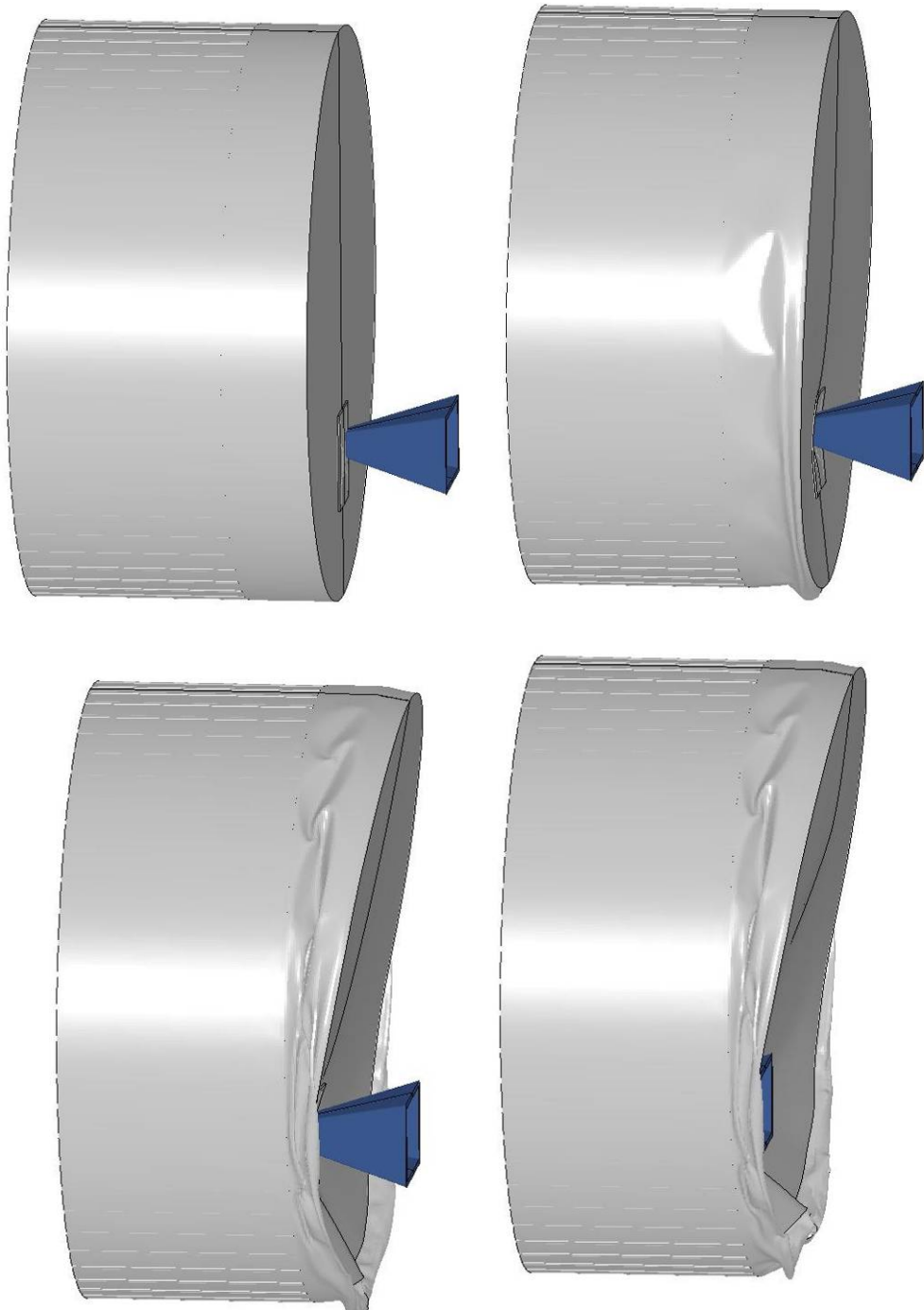
Figure 264. Calculated response of the corrugated EMS with a 12 inch standoff (R3F).
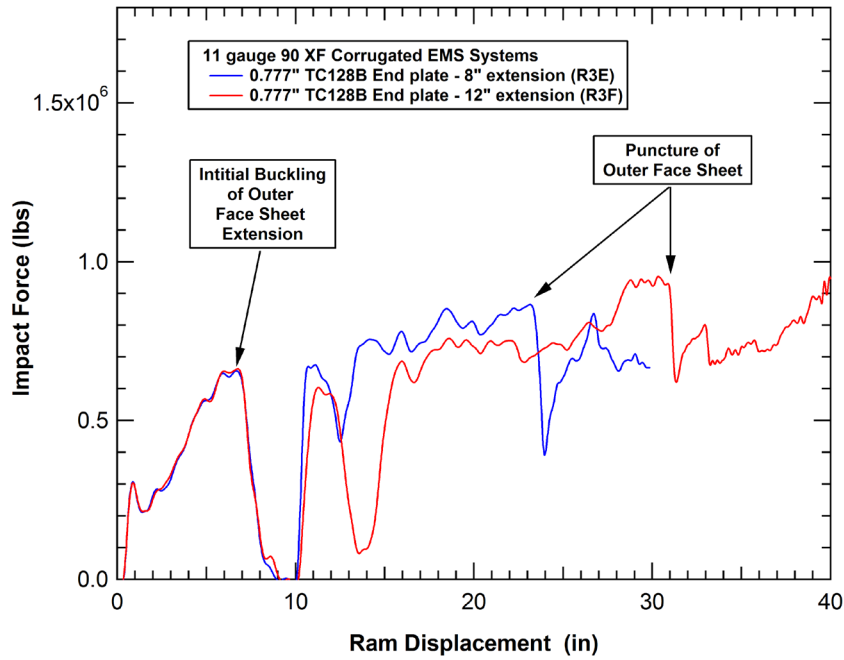
Figure 265. Performance of corrugated EMS end structures with various standoffs.
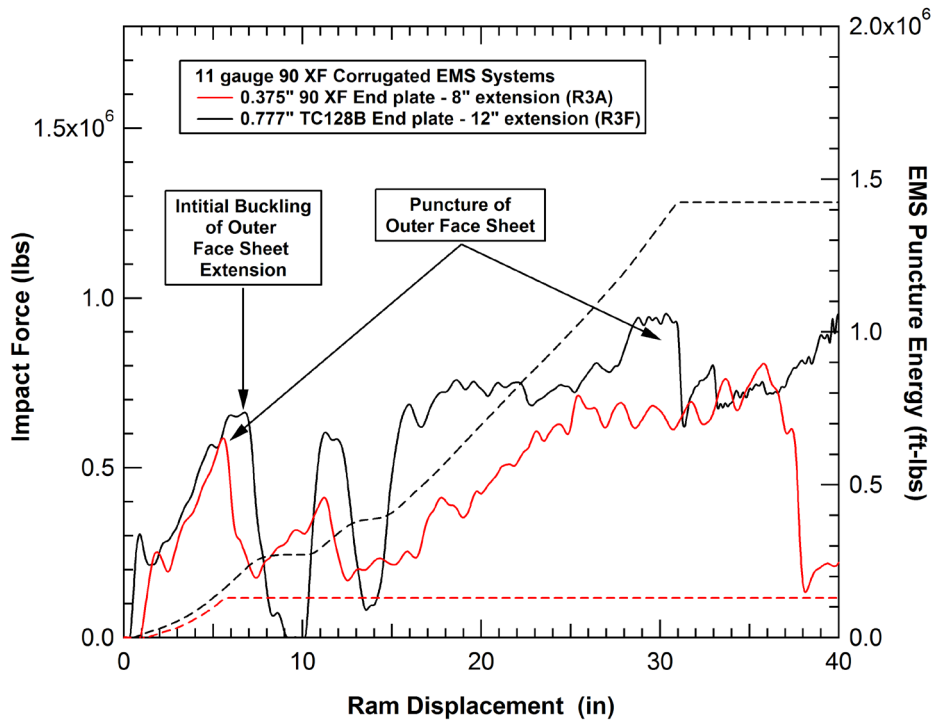
Figure 266. Performance of corrugated EMS end structures with various standoffs.
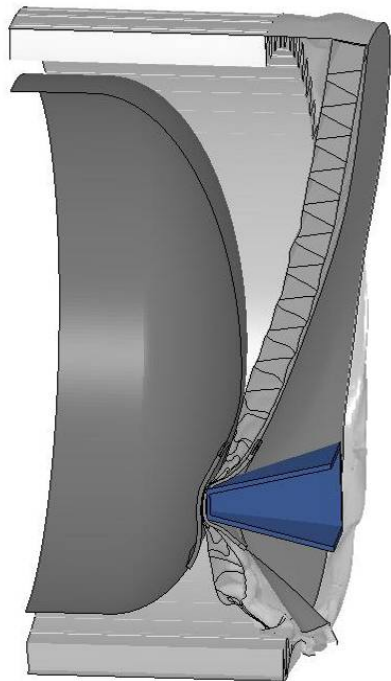
(a) EMS puncture state   **(b) Final deformation state**
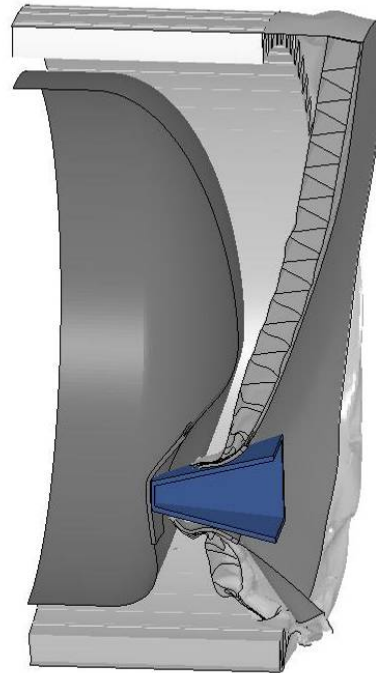
Figure 267. Predicted Head Test 3 impact response at 15 MPH.
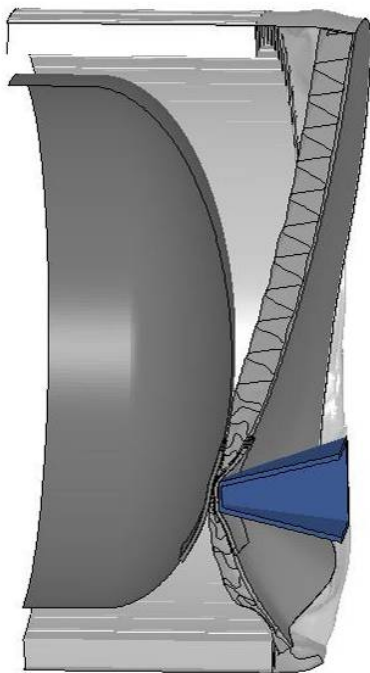
(a) EMS puncture initiation state   **(b) Head puncture state**
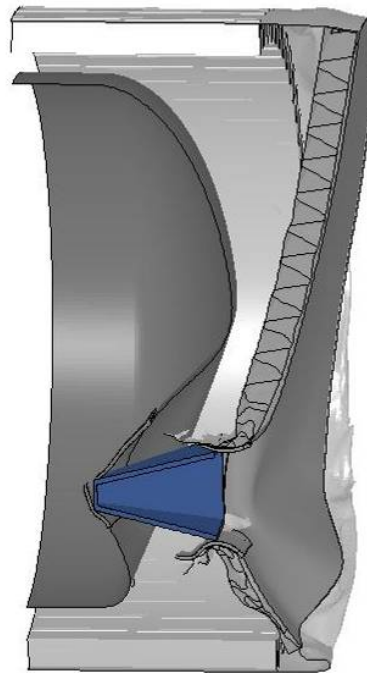
Figure 268. Predicted Head Test 3 impact response at 18 MPH.

211

A comparison of the predicted force-deflection characteristics and energy dissipation for the Head Test 3 configuration at 15 and 18 mph are shown in Figure 269. The two impact behaviors are very similar for displacements up to approximately 40 inches where the 15 mph impact response is complete. In both calculations the EMS structure is punctured at a displacement of approximately 30 inches and a peak load of approximately one million pounds. This also corresponds closely to the time that the inner EMS structure engaged the tank head. In the 18 mph impact response, the ram undergoes approximately an additional 20 inches (50 inches total) before the head is punctured.
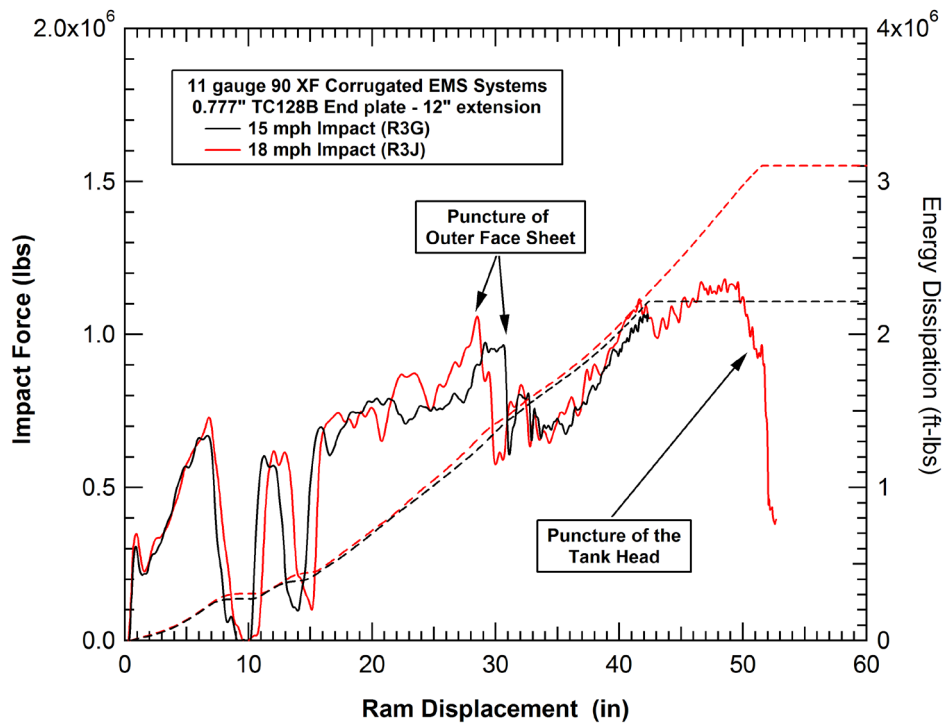
Figure 269. Performance of corrugated EMS end structures with various standoffs.

6.2.2 Head Test 3 Measurements and Analyses (EMS System)

The third component test of a tank car head test article was performed as part of the Next Generation Rail Tank Car project on July 30, 2008, at the Transportation Technology Center, Inc. (TTCI) in Pueblo, Colorado [75]. This test involved a 296,225-pound ram car striking the Option 3 prototype design tank head and EMS protection structures at 18.2 mph. The ram car was equipped with a 6-inch square indenter with 0.50-inch radius around the edges. The tank head was affixed to the Transportation Technology Center impact barrier with a rigid fixture.

The test article in position prior to the test is shown in Figure 270. The test article was bolted to the wall-offset fixture. The wall-offset fixture was bolted to the impact wall and an energy

absorbing arrestor system was added to dissipate residual energy if the head is punctured. The arrestor system consists of four hydraulic cushion units, two on each side, placed to engage the ram car shortly after the indenter penetrates the head.

Figure 270. Pretest configuration of the test head and corrugated EMS system.

The Option 3 prototype consisted of a 6-inch corrugated EMS structure with a 0.777 inch thick TC128B protective end plate. The EMS structure was fabricated from 11 gauge 90 XF material with the geometry shown in Figure 258. A 12-inch extension of the outer jacket was added between the side and end EMS structures to incorporate a lower strength crush zone and improve the overall energy dissipation.

The ram car was again modified before this test to allow for the testing with the larger protective EMS system. The energy absorbing buffers in the test fixture were repositioned to fit the larger external diameter of the EMS and the ram car end structures were reinforced to resist the new buffer load application points. The modified ram car prior to the test is shown in Figure 271 and the weight of the ram car was 296,225 lbs.

The target test speed was 18 mph. The impact speed, measured by the reflector speed trap, was 18.2 mph. The ram punctured the EMS head protective structures and the inner 500 lb tank head. The damage to the outer EMS structure after the impact is shown in Figure 272. An interior view of the impact damage to the tank head is shown in Figure 273. Both the EMS structures and head were fully penetrated by the ram head.

Figure 271. Pretest configuration of the test head and corrugated EMS system.
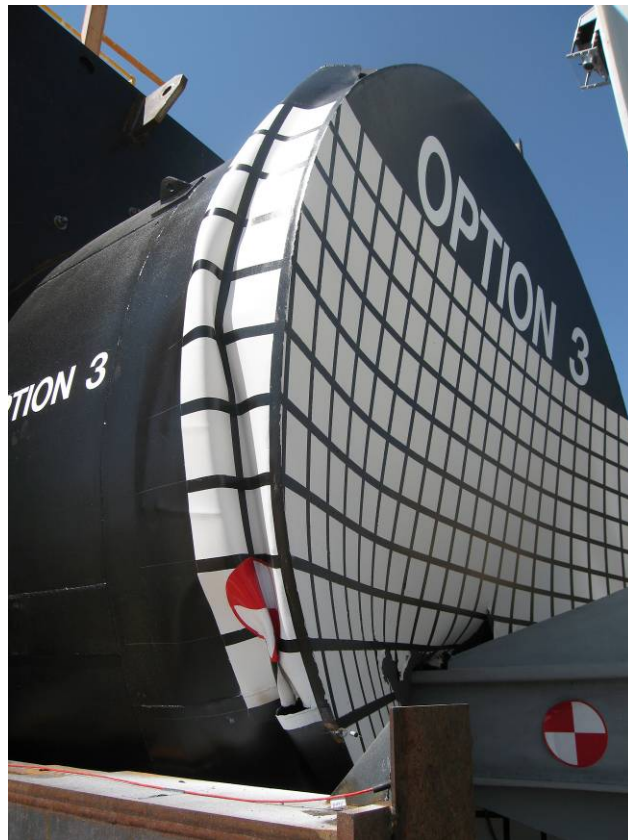
Figure 272. Impact damage to the external EMS protection system in Head Test 3.

Figure 273. Internal puncture of the tank head in Head Test 3.

A comparison of the predicted and measured force-deflection behaviors for Head Test 3 is shown in Figure 274. The pretest prediction did a good job of predicting the characteristics of the force-deflection curve and the displacement levels at which the EMS structures and the head are punctured. However, the measured impact forces are on average approximately 30 percent lower than predicted by the pretest analysis.

The discrepancies between the pretest analysis and the test are indicated by the inspection of the post-test damage to the structures. After the test, the end EMS corrugation was fully separated from the outer EMS face sheet as seen in Figure 275. Post-test inspection of the corrugation welds indicated that the separation initiated near the impact location and the weld fractures subsequently propagated outward to the edge of the end EMS structure. The result of this debonding would be to lower the forces and energy dissipation from the EMS deformations with significant reductions in the extent of core buckling as seen in Figure 276.

Another damage mechanism not expected in the pretest analysis was a fracture in the outer EMS end plate (0.777-inch TC128B) that extends from the impact point downward to the edge of the plate. The post-test fracture of the EMS end plate is seen in Figure 277. Post test inspection determined that this fracture initiated via a shear crack and propagated as a Mode I tensile fracture [82]. Thus, the crack appeared to occur after the 6-inch impactor had pierced the 0.777-inch end plate and was opened up by the wedging effect of the tapered impactor. Shear lips on

the Mode I fracture indicate some ductility. Chevron markings on the fracture surface indicate a fracture in the transition region of the Charpy energy curve. This fracture would lower the post penetration resistance and energy dissipation predicted for the tapered ram head. It was subsequently identified that the TC128B end plate was not normalized. However, the potential effect of normalization on the formation of this fracture was not assessed.
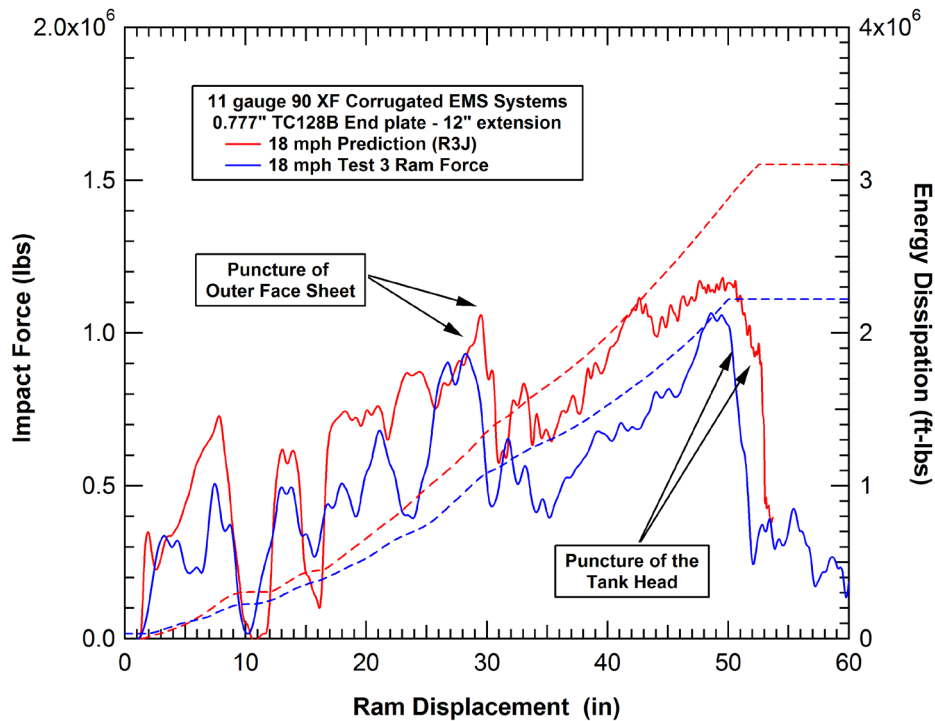
Figure 274. Comparison of predicted and measured behavior for Head Test 3.

A post-test analysis was performed to bound the effects of the EMS corrugation weld failures on the impact behavior. In the analysis, the end EMS corrugation was fully separated from the outer face sheet prior to the impact. The force-deflection characteristics for this analysis are compared to both the test and the pretest analysis in Figure 278. We see that the post-test analysis agrees well with the measured forces in the initial portion of the impact response. As the later deformations develop the characteristics of the test structures and post-test analyses begin to diverge. This indicates that the corrugation probably debonded from the face sheet locally under the impact at an early time but the progression to the edge of the end EMS structure probably occurred as the EMS deformations grew larger.

Figure 275. Separation of the outer face sheet on the end EMS structure.

Figure 276. Buckling of the end EMS corrugation in Head Test 3.

Figure 277. Fractured EMS end cover plate in Head Test 3.
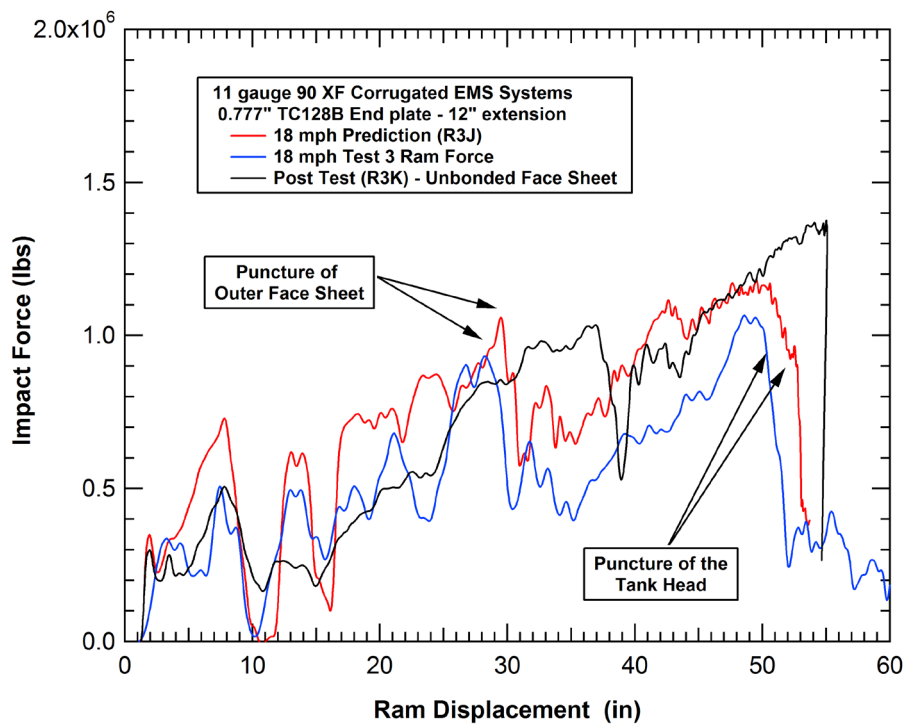
Figure 278. Comparison of Post-test analysis and measured behavior for Head Test 3.

The results of this test produced the following observations:

1. Head Test 3 was successful in providing high quality test data for model validation on EMS structures and evaluating the impact response of a non-optimized EMS head protection concept.

2. The agreement between the predicted and measured impact response was reasonable and the primary discrepancies between the model and the test are known (primarily failures of the EMS corrugation welds).

3. With a modified design of the corrugation attachment (e.g. adhesive bonding or new welding protocols), the predicted level of impact protection for this system should be achievable (approximately three million ft-lbs or three times energy absorption for the baseline 500lb head impact).

4. The total EMS structure mass in Head Test 3 is approximately two times that of the 500 lb head used in the test (thus the total test specimen weight is approximately three times that of a bare head).

5. The weight of the end EMS structures (0.777-inch end plate and corrugation) is equivalent to a steel plate with an effective thickness of 1.325 inches. Adding a more traditional head shield, or multiple layered head shields, with a combined thickness of 1.325 inches would result in the head test configuration puncture energy of approximately 2.5 million ft-lbs (for the unpressurized 500 lb tank head).

6. Implementation of this design would be more difficult on a traditional tank car due to the end EMS extension added to achieve a lower force level crush zone (12-inch end EMS extension). The extension of the end EMS structures would require a redesigned and extended draft sill to allow clearance between adjacent cars.

7. The normalized effectiveness (energy dissipation/unit weight) of this EMS structure is similar to approach of adding additional thickness to a traditional head and head shield design. The additional complexity of implementing this EMS design with an energy absorbing crush zone is not warranted for the 6x6 impactor threat. However, with further optimization (other core designs, optimized layer thicknesses, improved crush zone performance) and for other impactor threats, there is still potential for significantly improved tank car protection performance with EMS systems.

6.2.3 Side Impact Puncture Analyses of a Corrugated EMS Systems

The design of the EMS structure used in Head Test 3 was based on a non-optimized 6-inch corrugation design constructed from 11 gauge 90 XF steel. The system was modified to have an

increased puncture resistance and higher puncture energy in a head impact. However, no efforts were made to change the design for a side impact.

An analysis was performed to assess the side impact response using this baseline 6-inch corrugated EMS design. The geometry of this design was shown previously in Figure 258 and Figure 259. The model for the side impact analysis is shown in Figure 279. The system is applied over a baseline 500 lb chlorine tank pressurized to 100 psi. The standoff from the tank to the inside of the EMS structure is 4 inches. The total weight of the 6-inch EMS structure was 32,000 lbs which is approximately equal to the weight of a 0.59-inch thick tank.
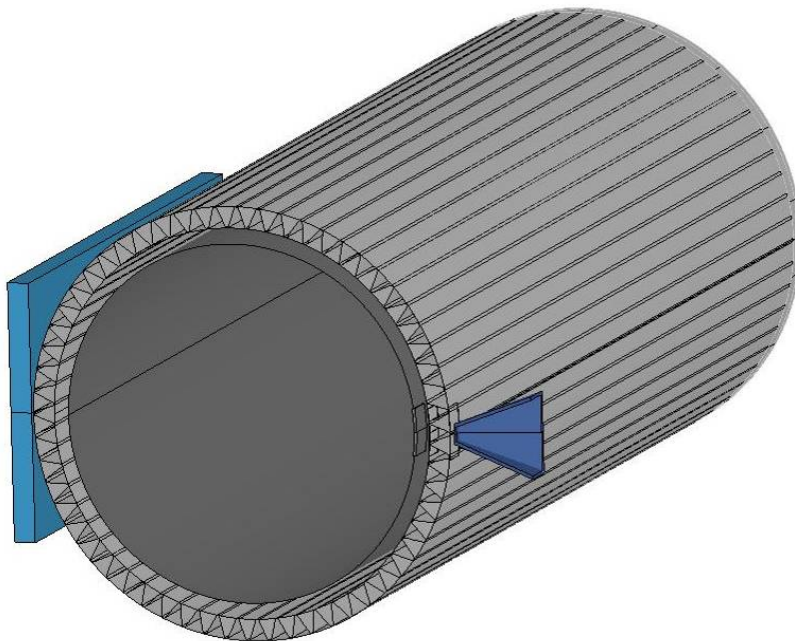
Figure 279. Model for the 6-inch corrugated EMS side impact analysis.

The calculated puncture behavior of the baseline 6-inch corrugated EMS structure is shown in Figure 280. The ram punches through the EMS structure at a load of approximately 200,000 lbs and a ram displacement of approximately 6 inches. Thus, the energy dissipation of this EMS structure is quite small compared to that of a single thicker jacket of equivalent weight.

Based on the lessons learned from the previous detailed analyses, we can propose a corrugated EMS structure for the tank car side protection. We know we need to increase the thickness of the outer face sheet as much as is reasonably practical. To achieve this, the core depth was reduced to three inches. The proposed design is shown in Figure 281. Effectively, this design is a ½-scale reproduction of the preliminary corrugated EMS design but with a 0.25-inch-thick outer face sheet. The core sheet and inner face sheet have been reduced to 16-gauge (0.060-inch-

thick). The construction material is not specified but any medium to high strength steel with good ductility can be used (e.g. TC128B, A516-70, A572-50).

The model for the side impact analysis with this modified 3-inch EMS design is shown in Figure 282. The system is again applied over a baseline 500 lb chlorine tank pressurized to 100 psi. The standoff from the tank to the inside of the EMS structure is 3.5 inches. The total weight of the 3-inch EMS structure was 28,000 lbs which is approximately equal to the weight of a 0.51 inch thick tank. This new design is a weight reduction of more than 4,000 lbs from the original 6-inch corrugated EMS concept.
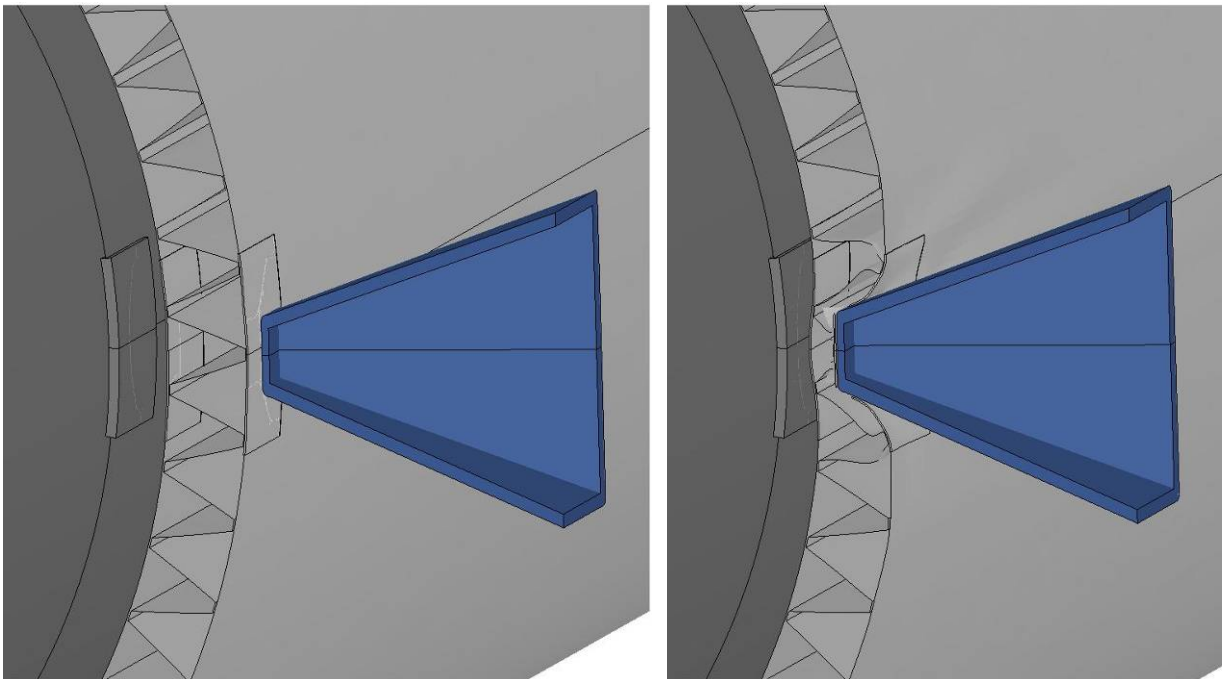
Figure 280. Calculated 6-inch EMS puncture behavior.
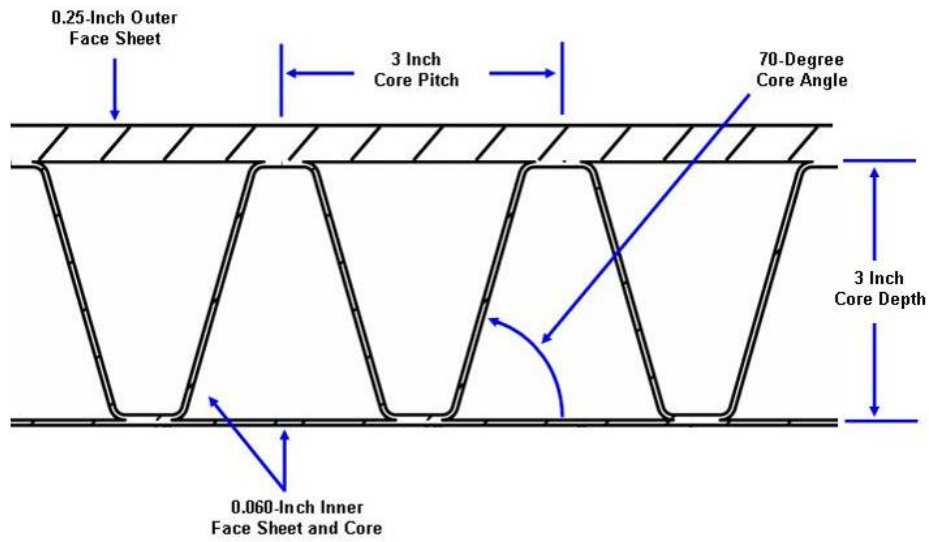
Figure 281. Detail of the modified EMS corrugation geometry.
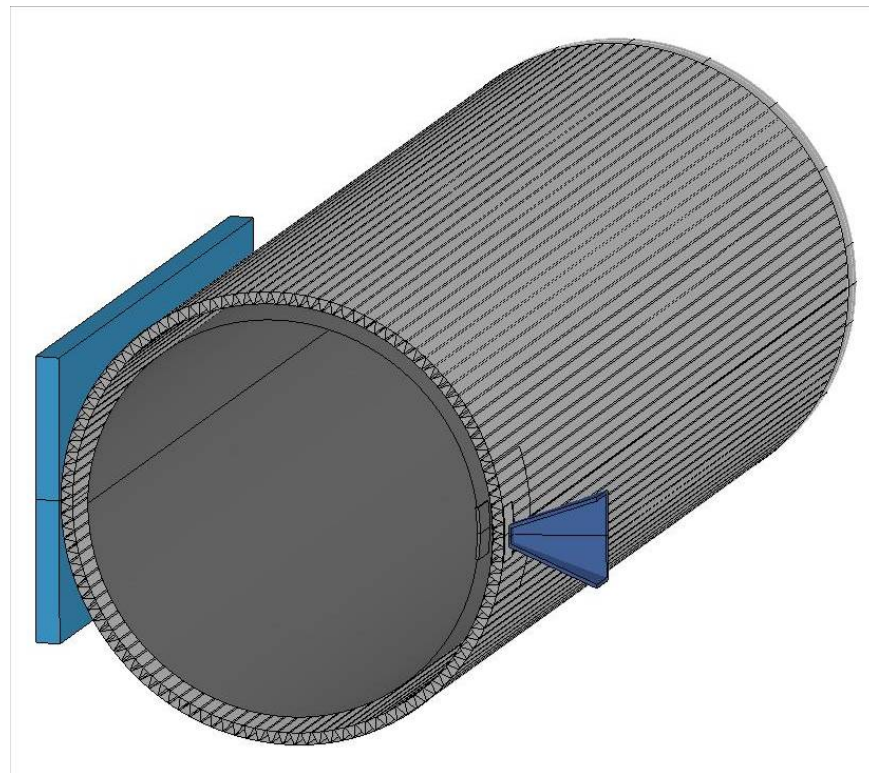
Figure 282. Model for the 3-inch corrugated EMS side impact analysis.

The calculated puncture behavior of the modified 3-inch corrugated EMS structure is shown in Figure 283. In this case, the EMS structure deforms under the impactor and engages the inner

tank structure well before the outer EMS face sheet is penetrated. The ram punches through the EMS structure at a load of approximately 600,000 lbs and a ram displacement of approximately 12 inches. Thus, the energy dissipation of this EMS structure is approximately 5 times that of the original 6-inch EMS concept. The comparison of the force-deflection characteristics of the 3-inch and 6-inch corrugated EMS structures for these side impact analyses is shown in Figure 284.

This example of the performance of different corrugated EMS designs illustrates that the approaches required to optimize this type of system are to remove weight from the inner face sheet and core structure to lower the system stiffness and to increase the outer face sheet thickness to improve the penetration resistance. The extreme extrapolation of this concept is to move all of the EMS weight into a single thicker outer jacket as shown in Figure 285. The weights of the corrugated EMS systems are comparable to the 0.5625-inch thick jacket analyzed previously and described in Section 4.3.2 (analysis R1Q). The total weight of this jacket with a 4-inch standoff was 29,500 lbs.
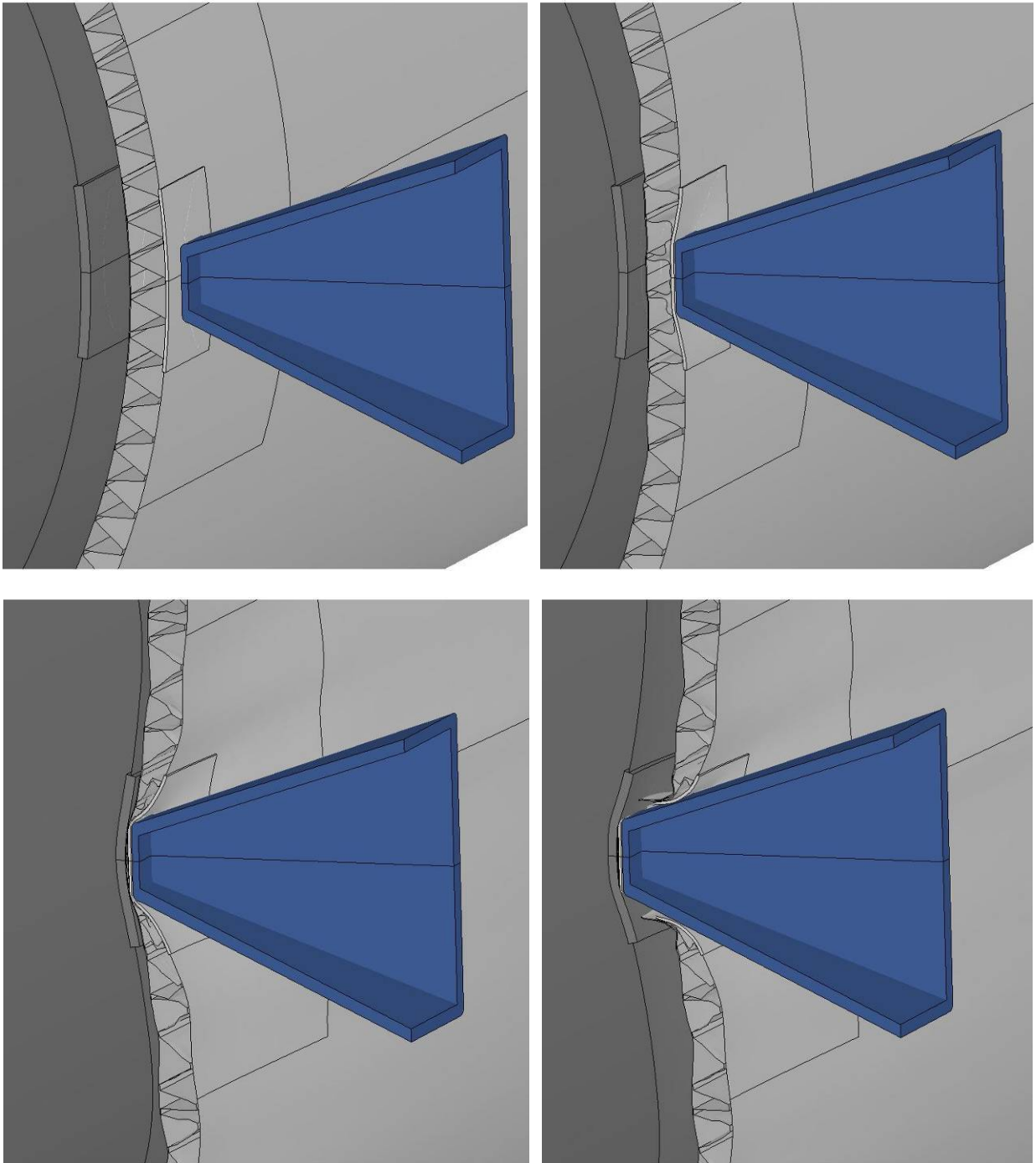
Figure 283. Calculated 3-inch EMS puncture behavior.
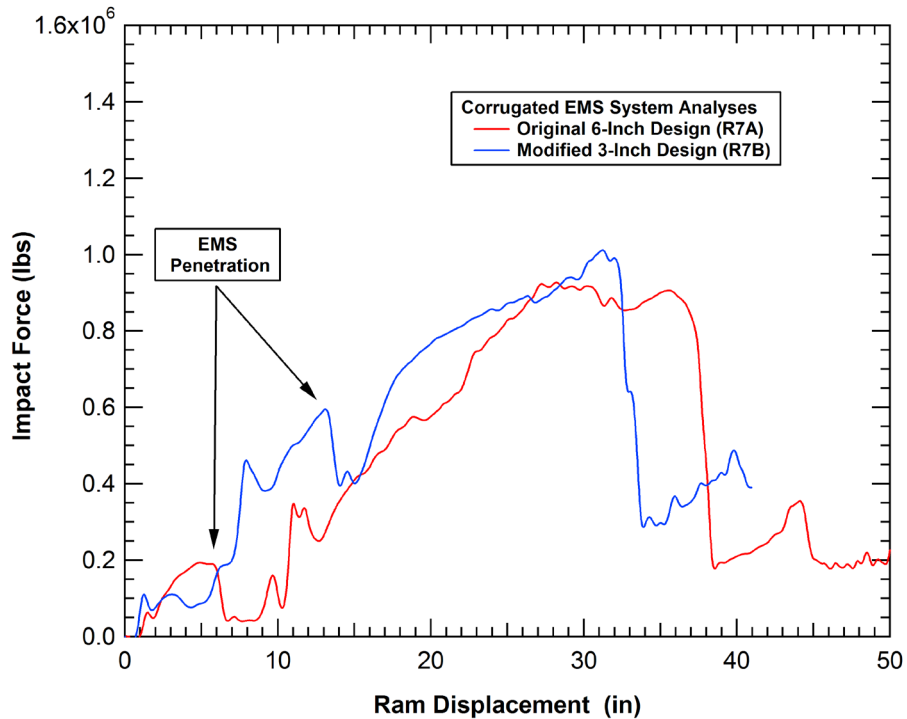
Figure 284. Comparison of the force-deflection behaviors for the corrugated EMS concepts.

The calculated force-deflection behavior for the 0.5625-inch-thick jacket is compared to those of the corrugated EMS structures in Figure 286. The largest difference with this design is that the thick jacket is not penetrated until a force of approximately 1.1 million lbs and an impactor displacement of approximately 30 inches. Thus, the jacket absorbs significantly more impact energy than the corrugated EMS structures for the 6-inch impactor.

Although the monolithic jacket performs better than the corrugated EMS structures in this example, the conclusion can not be generalized to all EMS designs and impact scenarios. The EMS structures would be expected to perform significantly better under a more distributed loading. Other benefits of the EMS concepts are that the structural stiffness can be used to efficiently carry the train service loads in a "tank within a tank" design. Further analysis of other EMS concepts (e.g. core geometries, materials) and more general impact conditions would be required to obtain an optimized design.
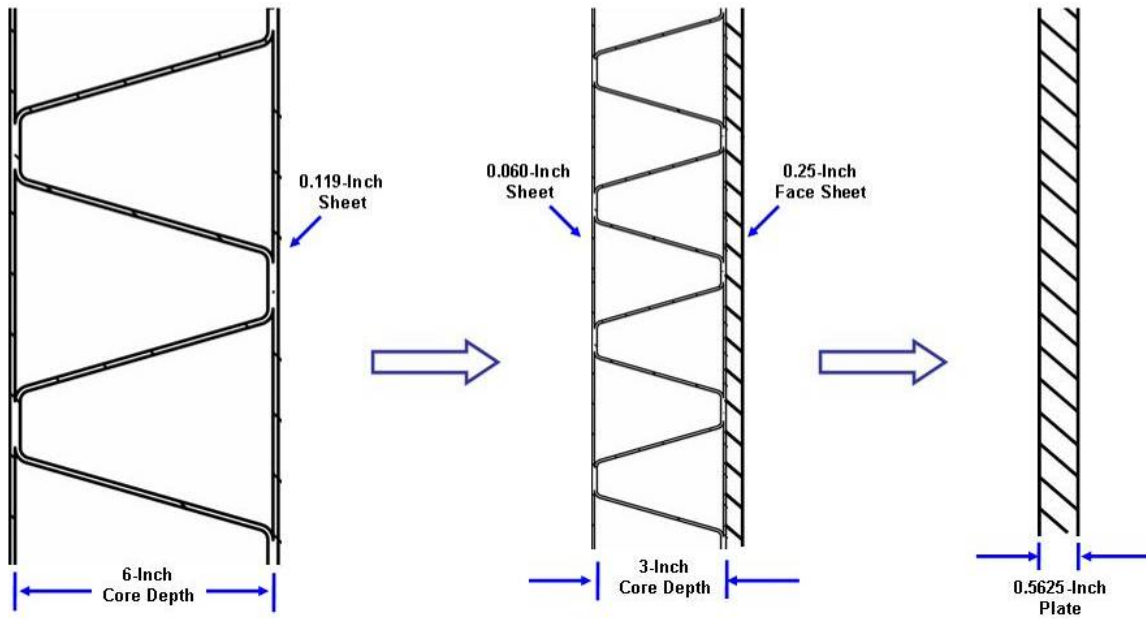
Figure 285. Extrapolation of the corrugated EMS concept.
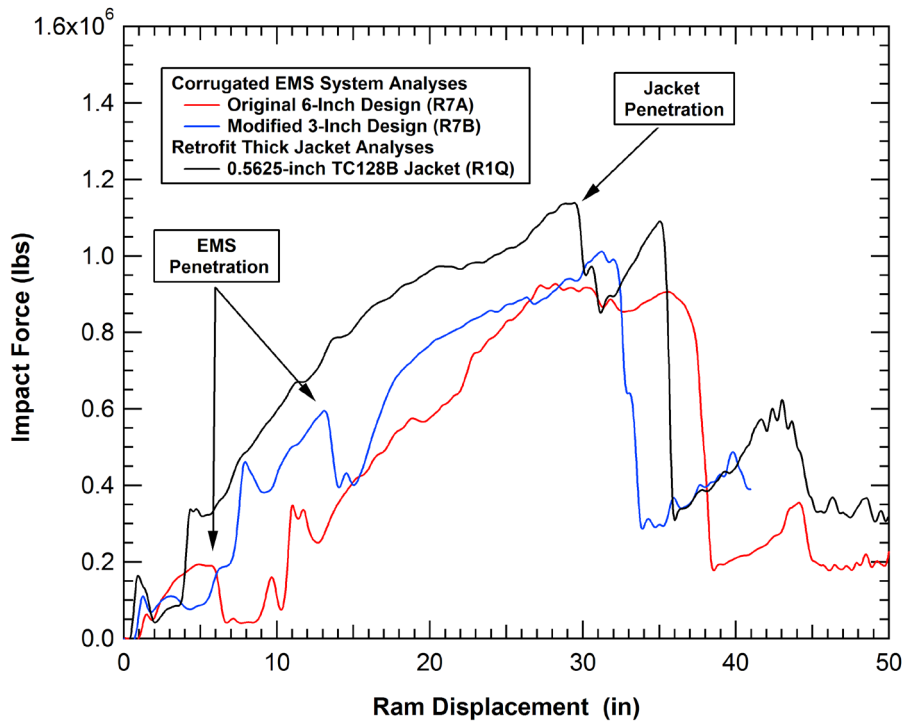
Figure 286. Comparison of the force-deflection behaviors for the corrugated EMS concepts.

6.2.4 Side Impact Puncture Analyses of an Egg Crate EMS Systems

An analysis was performed for the side impact of an egg-crate EMS system. The parameters of the analyses were:

- 500 lb TC128B tank
- 0.777 inch tank thickness
- 4 inch egg crate EMS
- 8 gauge (0.1644") face sheets
- 5 gauge (0.2092") core
- 100 psi internal pressure
- Smeared lading

The model used for the egg crate EMS is shown in Figure 287. The impact condition used was a 20 mph impact of a 295,000 lb rigid 6x6 inch ram. A 4-inch cell size was selected so that the 6-inch square ram face could not punch between the ribs. The calculated force-deflection characteristics and the impact behavior are shown in Figure 288 and Figure 289, respectively. The response was a localized denting and crushing of the EMS structure that continues to a full penetration of the EMS structure. The puncture of the outer face sheet occurs at a total displacement of 6 inches and a force of 439,000 lbs.

The puncture force plotted against the face sheet thickness for the egg crate system is compared to the other structural concepts in Figure 290. The puncture resistance of the outer face sheet was marginally more efficient than other systems. However, the total effective thickness of this EMS system was approximately equivalent to a 0.7 inch plate. As a result, this system again results in the individual layers resisting the impact forces and penetration independently, which significantly reduces the performance of the overall system.
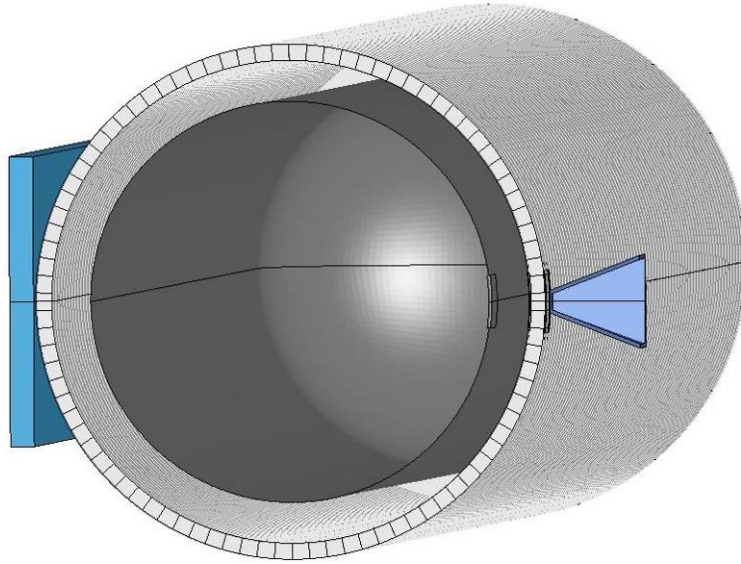
Figure 287. Side impact model for a 4-inch egg crate EMS system.
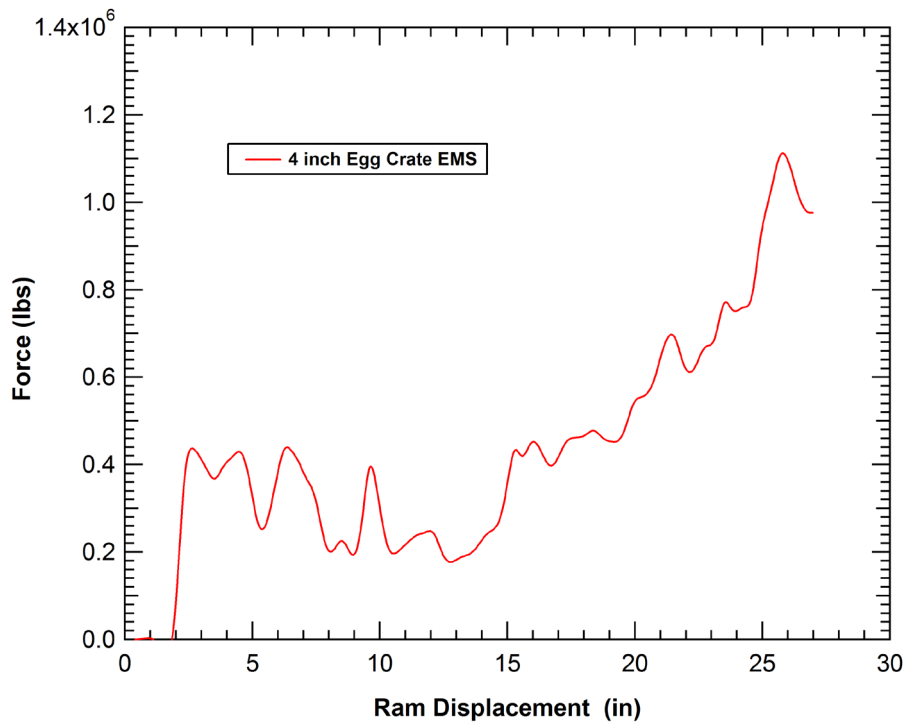
Figure 288. Calculated impact forces for a 4-inch egg crate EMS system.

(a) Initial impact **(b) EMS penetration**

(c) Detail of EMS crush
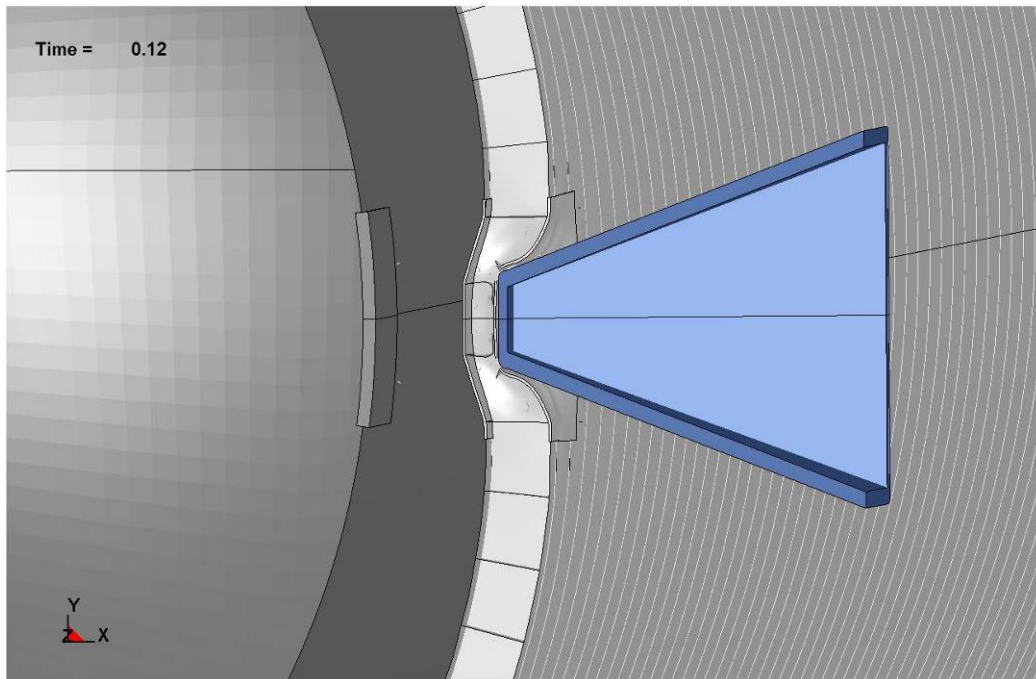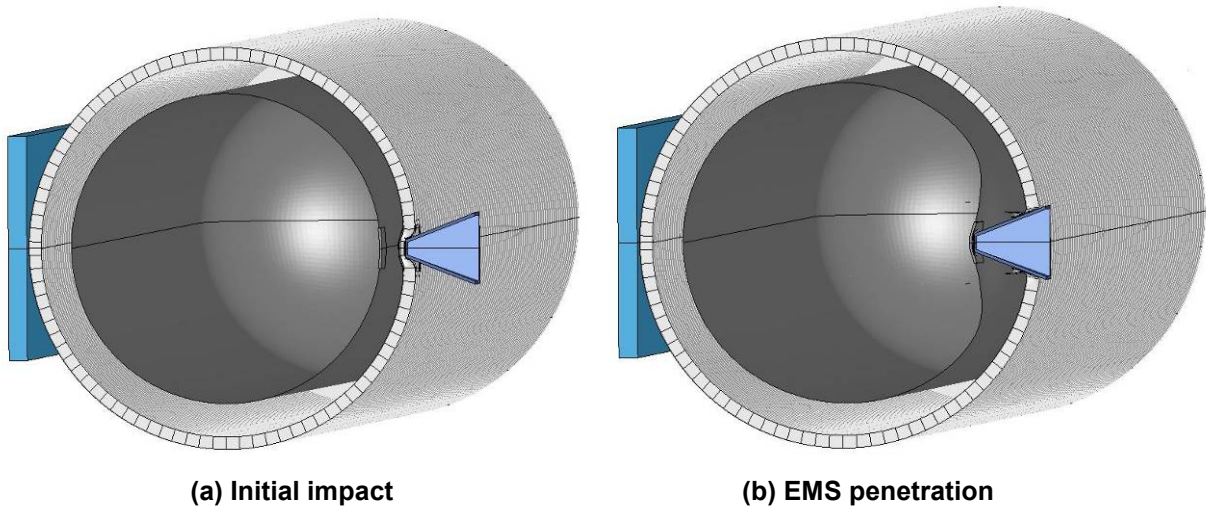
Figure 289. Calculated side impact damage for a 4-inch egg crate EMS system.
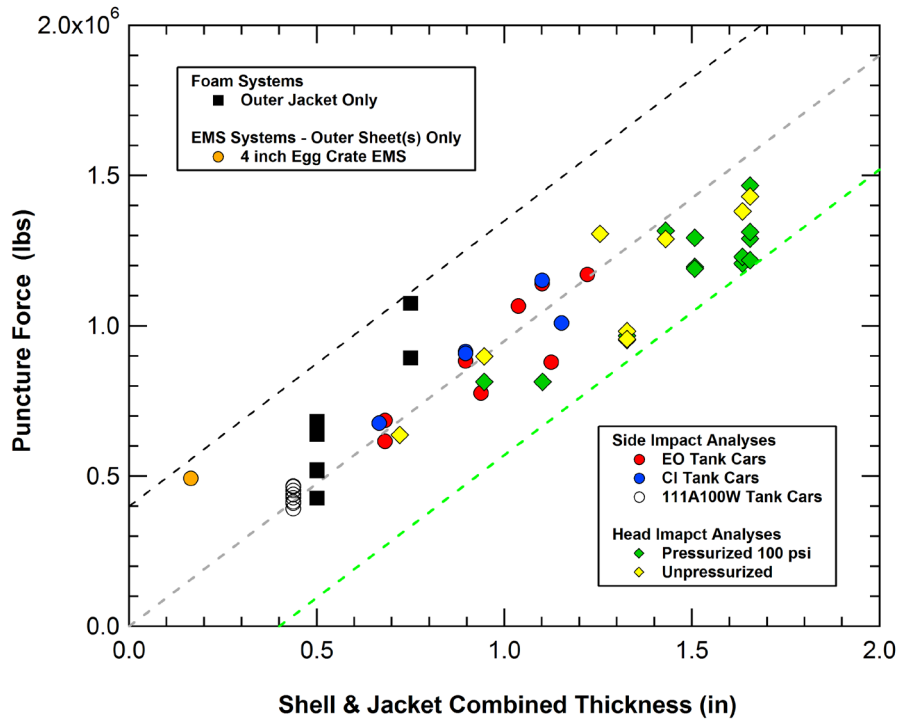
Figure 290. Puncture force versus face sheet thickness for the egg crate EMS.

6.2.5 Summary of the EMS Puncture Analyses

A summary of the puncture forces plotted against the end plate and outer EMS face sheet thickness for the corrugated systems are compared to the other structural concepts in Figure 291. The puncture resistance of the outer layers (summing the thickness of the flat layers in contact outside the core structure) was consistent with that of other systems. However, by extending the end EMS structure from the side structure, the required impact force levels to crush the system were reduced and significantly more energy was dissipated before the puncture force capacities were exceeded.
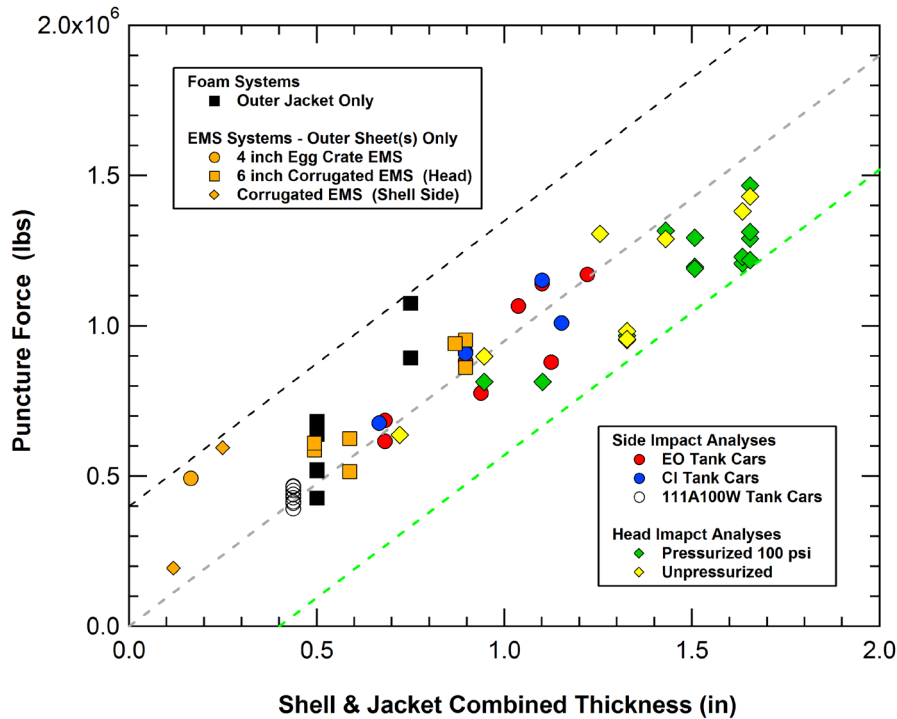
Figure 291. EMS puncture forces as a function of outer layer thickness.

6.3 Double Tank Head Concept Puncture Analyses

One proposed concept for improving the tank head puncture resistance is to use a double head system. This idea is similar to a double hull concept for large tanker transport ships to reduce the potential for an oil spill in a grounding accident. The Geometry for the double head concept is relatively simple with an extension of the side shell of variable length and a second head added with an identical 2-to-1 ellipsoidal geometry. An example of a model used for a double head analysis is shown in Figure 292. In this model a 12-inch standoff distance between the heads is obtained by the extension of the tank shell.

The idea proposed for this double head concept is that the standoff distance, the relative thickness of the inner and outer heads, and the pressure between the two heads could all be varied to optimize the puncture resistance. A summary of the double head analyses is provided in Table 12. The sum of the total thickness of the two heads was maintained at 1.6 inches but the thickness of the individual heads was varied between 0.6, 0.8, and 1.0 inch. The inner tank pressure was maintained at 100 psi but the pressure between the inner and outer heads was varied between 0, 50, and 100 psi. The standoff distance between the inner to outer heads was varied between 2, 6, 12, and 18 inches. The calculated peak puncture force and puncture energies are also provided in the table.
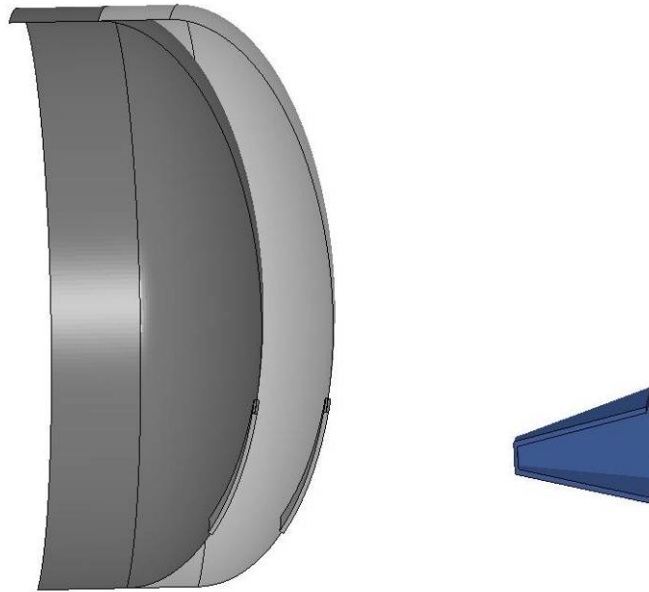
Figure 292. Model for the double head puncture protection concept.

Table 12. Summary of the double head impact analyses

Calculation	Inner/Outer head Thickness	Inner/Outer head pressure	Outer Head Standoff	EMS Puncture Energy (ft-lbs)	EMS Puncture Force (lbs)
R5A	0.80/0.80 inch	100/50 psi	12 Inches	1,775,000	1,243,000
R5B	1.00/0.60 inch	100/50 psi	12 Inches	1,925,000	1,451,000
R5C	0.60/1.00 inch	100/50 psi	12 Inches	1,720,000	1,533,000
R5D	0.80/0.80 inch	100/0 psi	12 Inches	1,625,000	1,319,000
R5E	0.80/0.80 inch	100/100 psi	12 Inches	1,900,000	1,049,000
R5F	0.80/0.80 inch	100/50 psi	6 Inches	1,670,000	1,365,000
R5G	0.80/0.80 inch	100/50 psi	18 Inches	1,920,000	1,087,000
R5H	0.80/0.80 inch	100/50 psi	2 Inches	1,650,000	1,475,000
R5I	0.80/0.80 inch	100/0 psi	2 Inches	1,500,000	1,490,000
R5J	1.00/0.60 inch	100/50 psi	2 Inches	1,550,000	1,406,000

The summaries of the peak puncture forces and puncture energies for the double head concepts compared to other puncture analyses are provided in Figure 293 and Figure 294, respectively. In general, the puncture forces are consistent with those of other head and tank systems. In two cases, the puncture forces fall below the lower bound of the previous analyses. In these two analyses, the outer head is punctured before the inner head is significantly engaged due to either the largest standoff distance (18 inches in calculation R5G) or the combination of a large standoff and high pressure between the heads (12-inch standoff and 100 psi between heads in

calculation R5E). Thus, these calculations have a puncture force that is controlled by the separate head thicknesses instead of the combined system thickness.
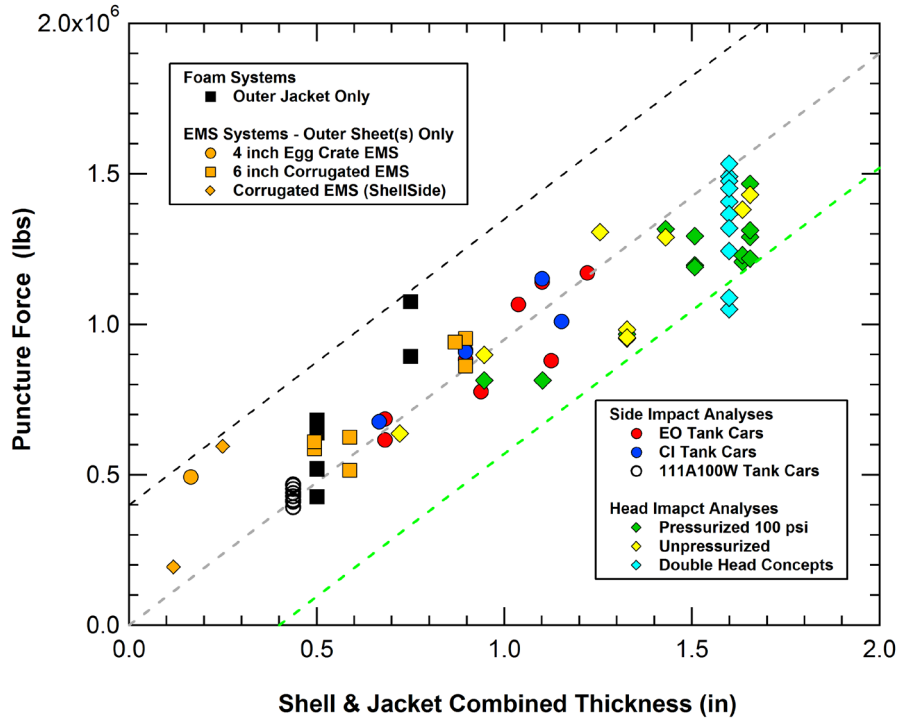
Figure 293. Summary of the double head concept puncture forces.

The puncture energies for the double head system are higher than that of a traditional pressurized head and head shield system and more consistent with the previous analyses on unpressurized heads. This would indicate that there is at least some benefit to this type of optimized double head system for head impact protection.

A parameter that was found to have a significant trend with respect to the puncture energy in the analyses was the head standoff distance. The double head models with the various standoff distances analyzed are shown in Figure 295. The corresponding impact behaviors for these models with balanced 0.8-inch-thick heads and a 50 psi pressure between the inner and outer heads is shown in Figure 296. The analyses show consistent trends with larger peak force levels with the smaller standoff distance and larger total puncture energy with the larger standoff distance. The increase in peak force levels with smaller standoffs occurs since the inner head is more significantly deformed and develops a higher impact resistance force at the time the outer head is punctured. The larger total puncture energy with increased standoff is a result of the larger total ram displacement required before the system is penetrated.
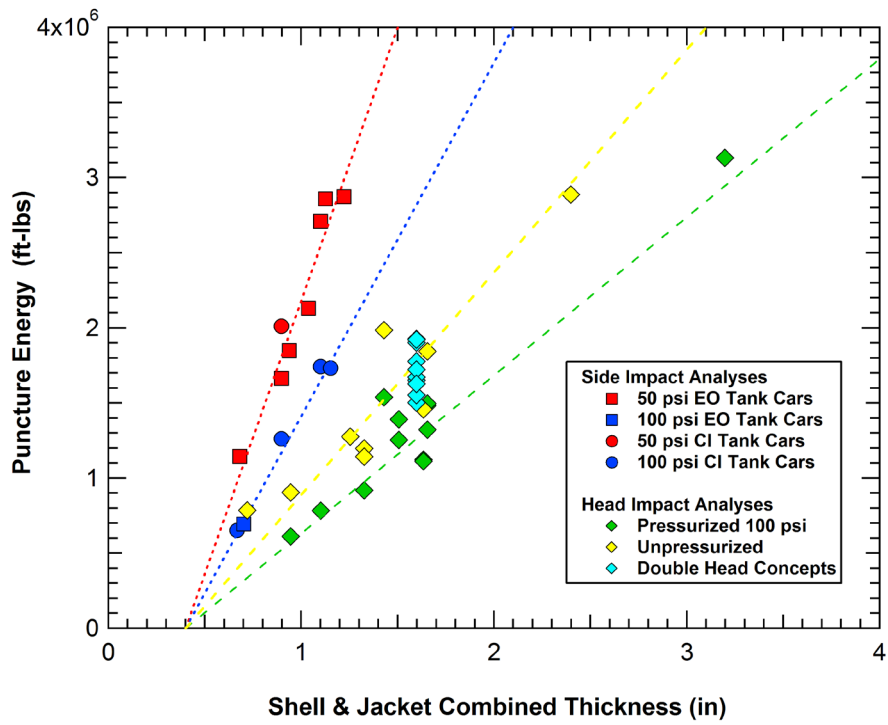
Figure 294. Summary of the double head concept puncture energies.
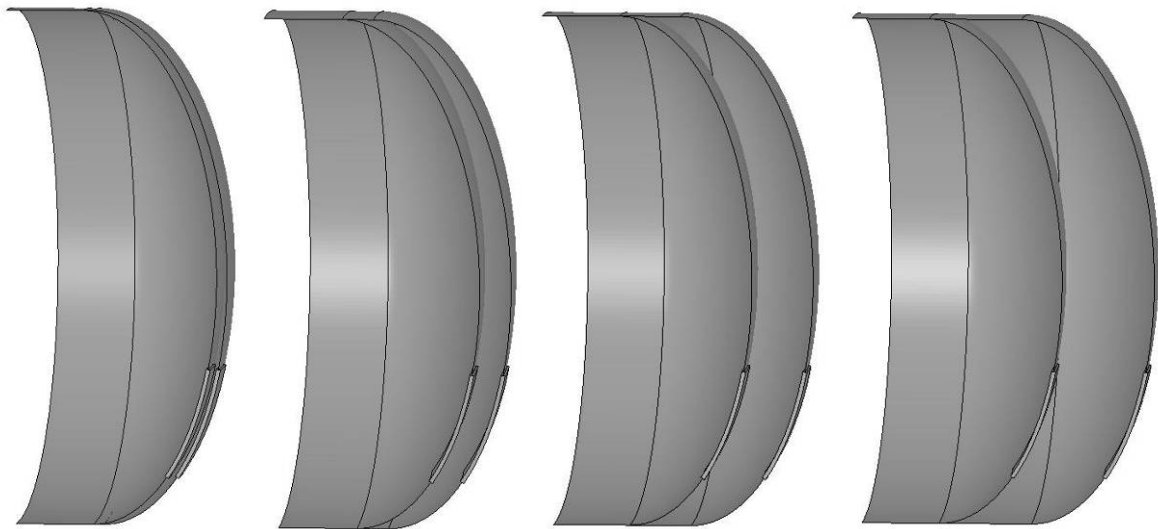
Figure 295. Double head models with different standoff distances (2, 6, 12, and 18 inches).
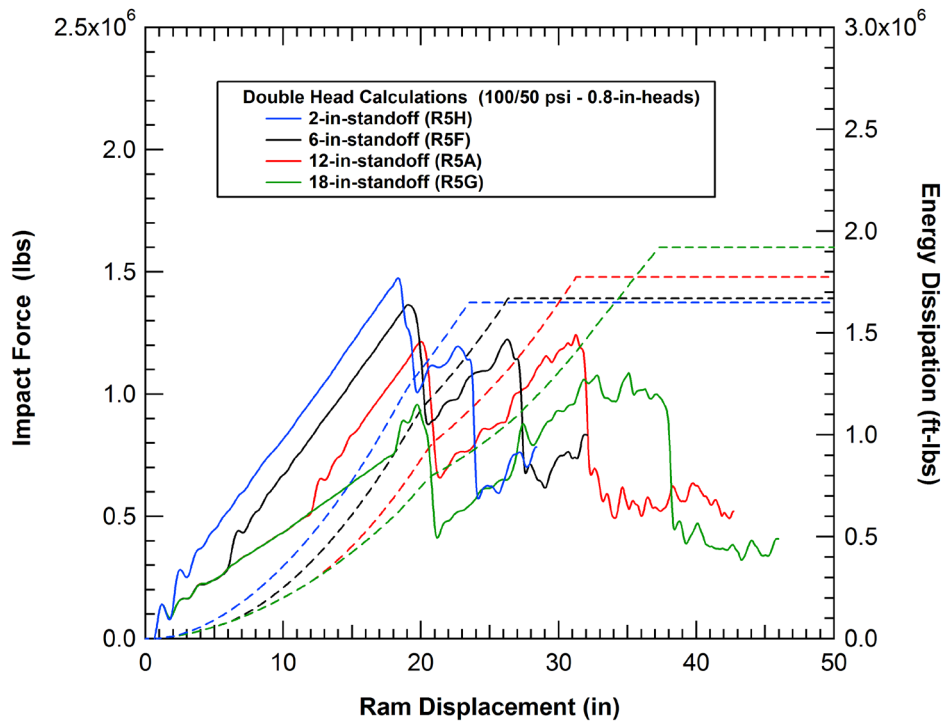
Figure 296. Effect of the standoff distance on the double head impact response.

A summary of the puncture energies as a function of the head standoff distance for all of the double head analyses is shown in Figure 297. A linear fit to the data is provided in the figure and the slope of the curve corresponds to a 250,000 lb force. This helps to explain the trend observed in the analyses. The force displacement curve for a single 0.80-inch head pressurized to 50 psi is shown in Figure 298. The head is punctured at a force of approximately 880,000 lbs and the average residual force developed as the tapered head is pushed through the punctured head is on the order of 250,000 lbs. As a result, the larger standoff distances would add a larger energy dissipation contribution of the punctured outer shell before the inner head is punctured. The trend of increasing total puncture energies is therefore primarily an artifact of the impactor geometry and would not be as significant for improving the puncture protection for other impactor geometries (such as a broken rail). This effect is partially responsible for the larger average puncture energy of the double heads compared to the baseline pressurized head analyses, illustrated in Figure 294.
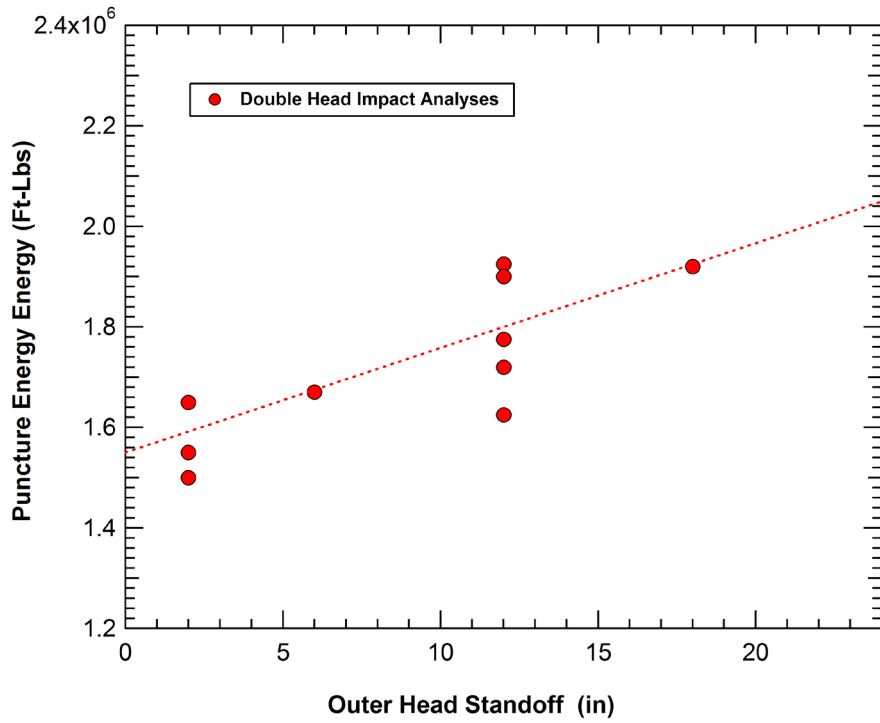
Figure 297. Summary of the standoff effects on the double head impact response.
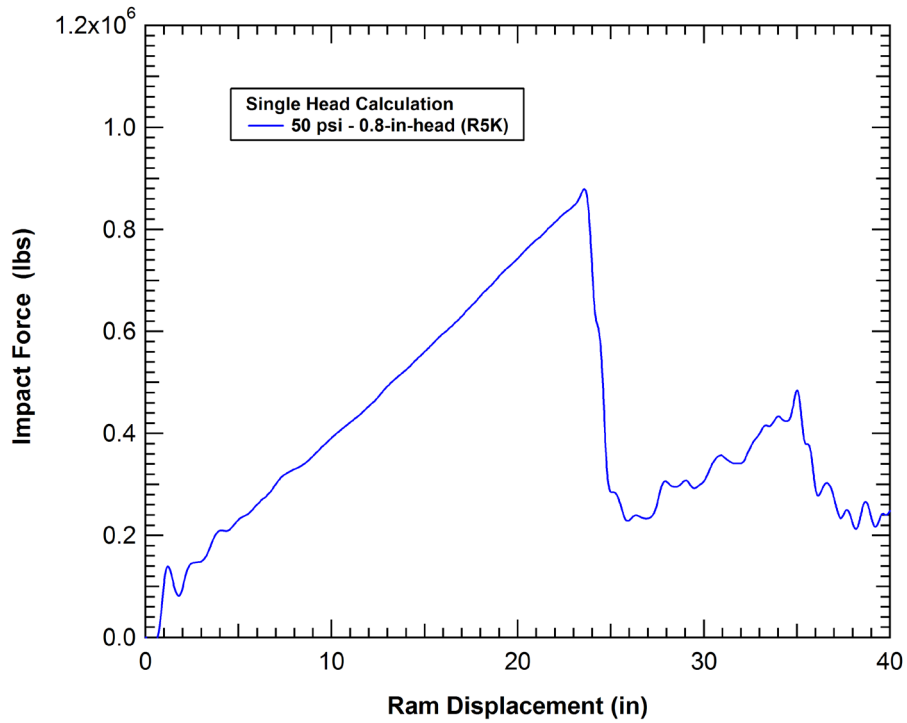
Figure 298. Calculated force-deflection curve for a single 0.8-inch-thick head.

The calculated impact behavior for analyses demonstrating the effects of changing the relative thickness of the two heads is shown in Figure 299 (analyses with the 12-inch standoff). The characteristics of the impact behavior are consistent with effectively summing the response of two independent heads. The system is slightly more efficient when the outer head is thicker than the inner head. However, again this trend may be influenced by the larger post puncture forces that develop in the thicker outer head geometry. A similar trend was observed in a pair of analyses with the 2-inch standoff distance as shown in Figure 300. For the smaller standoff distance, the difference in the total puncture energy is almost entirely due to the puncture of the internal head occurring at a ram displacement that is 1-2 inches larger with the thicker inner head configuration.
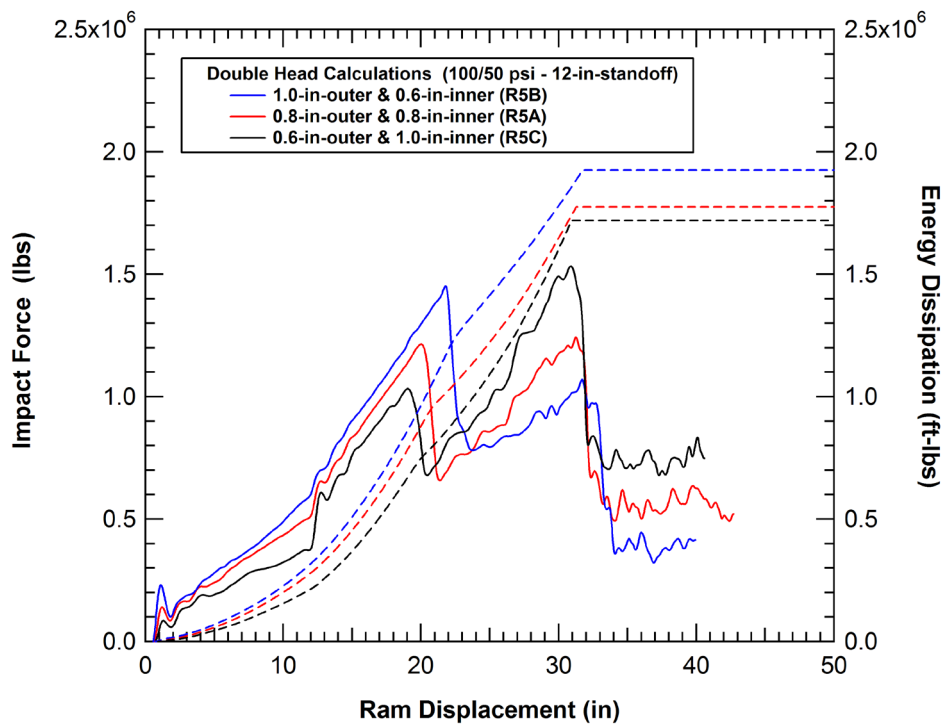
Figure 299. Effect of the head thickness on the double head impact response (12-inch standoff).
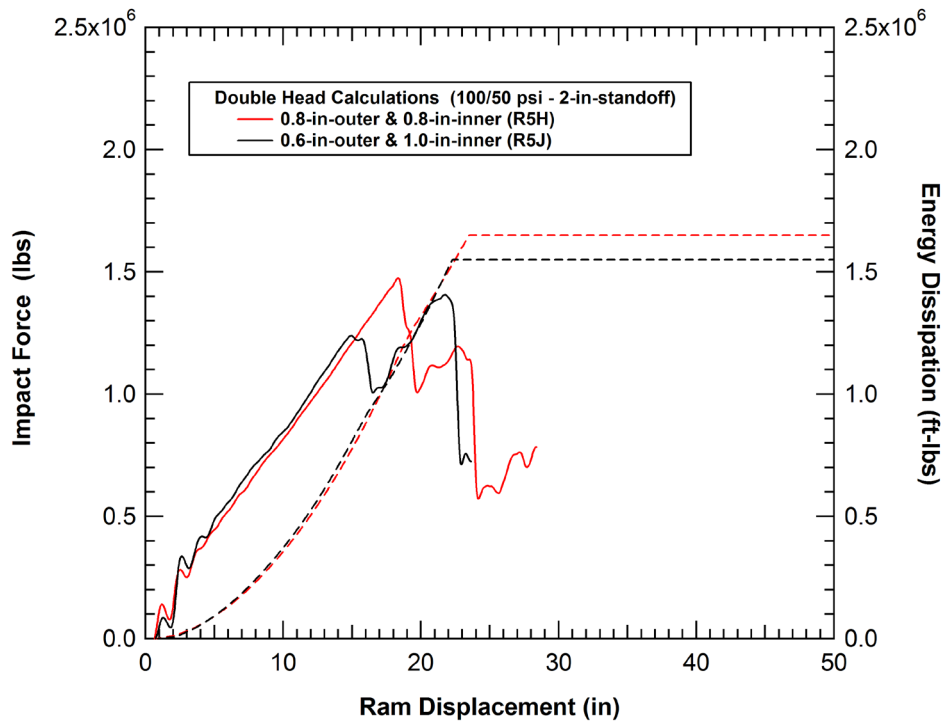
Figure 300. Effect of the head thickness on the double head impact response (2-inch standoff).

The calculated impact behavior for analyses demonstrating the effects of changing the pressure between the two heads is shown in Figure 301 (analyses with the 12-inch standoff). The higher pressures result in an earlier puncture of the outer head but a delayed puncture of the inner head. The larger total displacement before the inner head is punctured produces higher total system puncture energies when the pressure between the heads is increased. The assumption of these analyses is that the pressure between the heads remains constant throughout the impact and head puncture process. If the pressure drops rapidly after the outer head is punctured, the overall puncture energy of the double head system would be reduced as the pressure between the heads is increased.
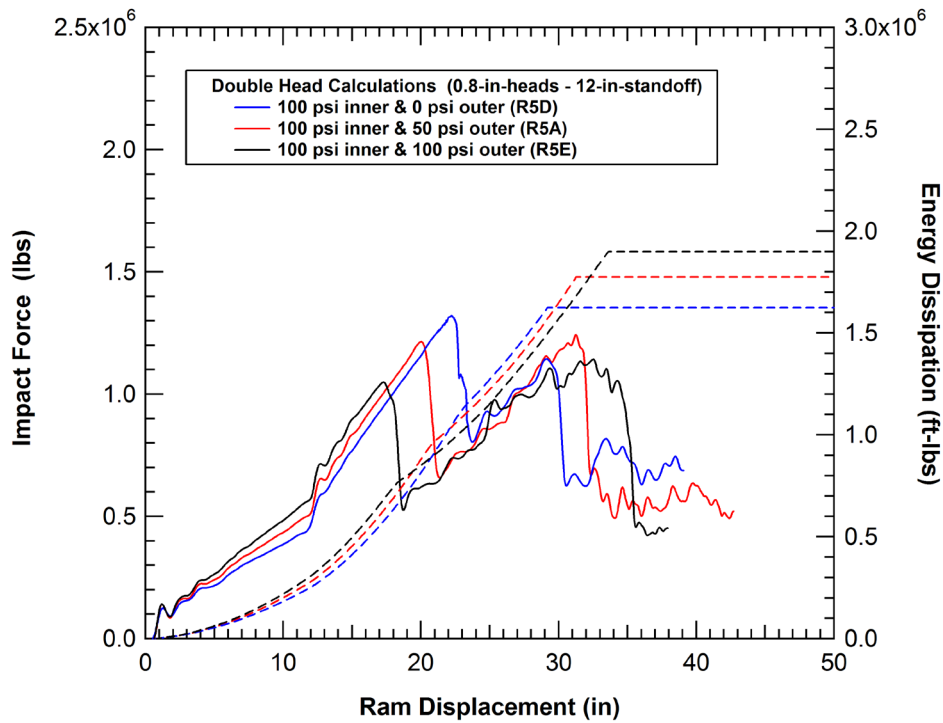
Figure 301. Effect of the pressure ratio on the double head impact response (12-inch standoff).

A similar effect of the pressure between the heads was observed in a pair of analyses with the 2-inch standoff distance as shown in Figure 302. For the smaller standoff distance, the difference in the total puncture energy is again almost entirely due to the puncture of the internal head occurring at a ram displacement that is approximately 2 inches larger with the increase pressure between the two heads.
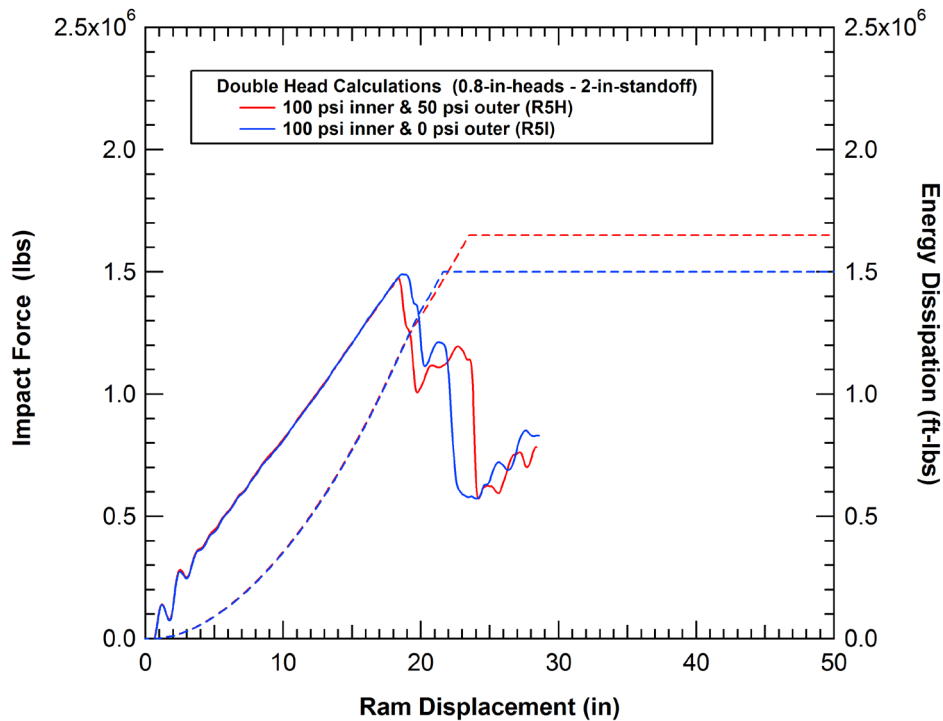
Figure 302. Effect of the pressure ratio on the double head impact response (2-inch standoff).

6.4 Analyses of Composite Tank Protection Concepts

The above analyses indicate that a tank protection system developed using only typical tank car materials (steels) will have difficulty reaching the protection goals of the NGRTC program. To achieve a five times increase in the puncture energy of tank cars while maintaining a comparable level of utility will require nontraditional tank car design approaches and advanced materials. These potential materials for advanced protection concepts include polymeric composite materials. The potential of these materials for increasing tank car puncture protection is described in this section.

6.4.1 Validation of Composite Modeling

Before composite material systems can be evaluated, a constitutive model for the composites including appropriate damage and failure behaviors needed to be developed and validated. The constitutive and damage behaviors of composites are more complex due to the material anisotropy, inhomogeneity, and the large number of resulting damage modes that can develop (e.g. matrix cracking, fiber breakage, and delamination).

There are several constitutive models available in LS-DYNA for composite materials. However, for the local impact and puncture behavior of the tank car protection requirements, an important

damage mechanism will be the delamination of the composite in the impact zone. Just as required for metals, the approach to accurately model this damage mode requires a local solid element patch with a detailed failure model capable of simulating the range of composite damage and failure behaviors.

After an evaluation of available modeling options, the LS-DYNA material type 162 was selected (*MAT_COMPOSITE_MSC_DMG) [83]. This model may be used to simulate progressive failure in composite materials consisting of unidirectional and woven fabric layers subjected to high strain-rate and high pressure loading conditions. The model is a generalization of the layer failure model reported in [84]. The Matzenmiller, Lubliner, and Taylor (MLT) damage mechanics approach [85] has been adopted to characterize the softening behavior after damage initiation. Failure models based on the 3D strains in a composite layer with improved progressive failure modeling capability are established for a unidirectional or a plain weave fabric composite layer. They can be used to effectively simulate the fiber failure and delamination behavior under impact conditions. This model was developed and is supported by the Materials Science Corporation (MSC) and requires an additional license to activate the model capabilities in LS-DYNA.

Composite Punch Testing

A composite punch test series was found in the open literature that was appropriate for the validation of the composite constitutive and damage model. The punch tests were performed at the University of Delaware Center for Composite Materials (UD-CCM) on a fiberglass/epoxy composite [86, 87]. The specific composite system used in the tests is one proposed for use in ballistic impact protection and has characteristics that make it a good candidate material for tank car impact protection (e.g. toughened matrix material system and relatively inexpensive constituent materials). The tests span a sufficient range of loading conditions to be a valuable data set for model validation.

The composites used in this study were fabricated from two-dimensional [2-D] woven S-2 Glass fabric and SC15 resin. Composite laminates were fabricated using 2, 4, 6, 11, and 22 layers of the plain weave fabric. Specimens made from these laminates are tested under punch shear loading with support-span to punch ratio (SPR) of 2.0 and 8.0, as shown in Figure 303. The quasi-static punch shear tests were conducted in the displacement-control mode at a cross-head displacement rate of 0.10 inch/min.

The punch shear test fixture consists of a square support plate (2 inches thick) with a circular hole at the center, a relatively thin cover plate (0.5 inch thick) with a central hole similar to the support plate, and a cylindrical punch. Sets of support plates and cover plates were fabricated with different support span (SS) diameters (D_S) of between 0.55 inch and 4.0 inches. Composite

plate specimens were bolted on the punch shear test fixture between the support plate and the cover plate. A cylindrical punch was used with a 0.5 inch diameter (D_P) and a flat tip. The combination of punch and support spans provides spans to punch ratios of between 1.1 and 8.0 (SPR = D_S/D_P). In addition, a test was performed against a support plate without a hole (SPR = 0). The calculated force-deflection behavior for a 22 layer thick composite plate and different span ratios is shown in Figure 304. The corresponding damage in these punch test specimens is shown in Figure 305. Force-deflection behavior of the tests with SPR=8 for various layer thicknesses are shown in Figure 306.
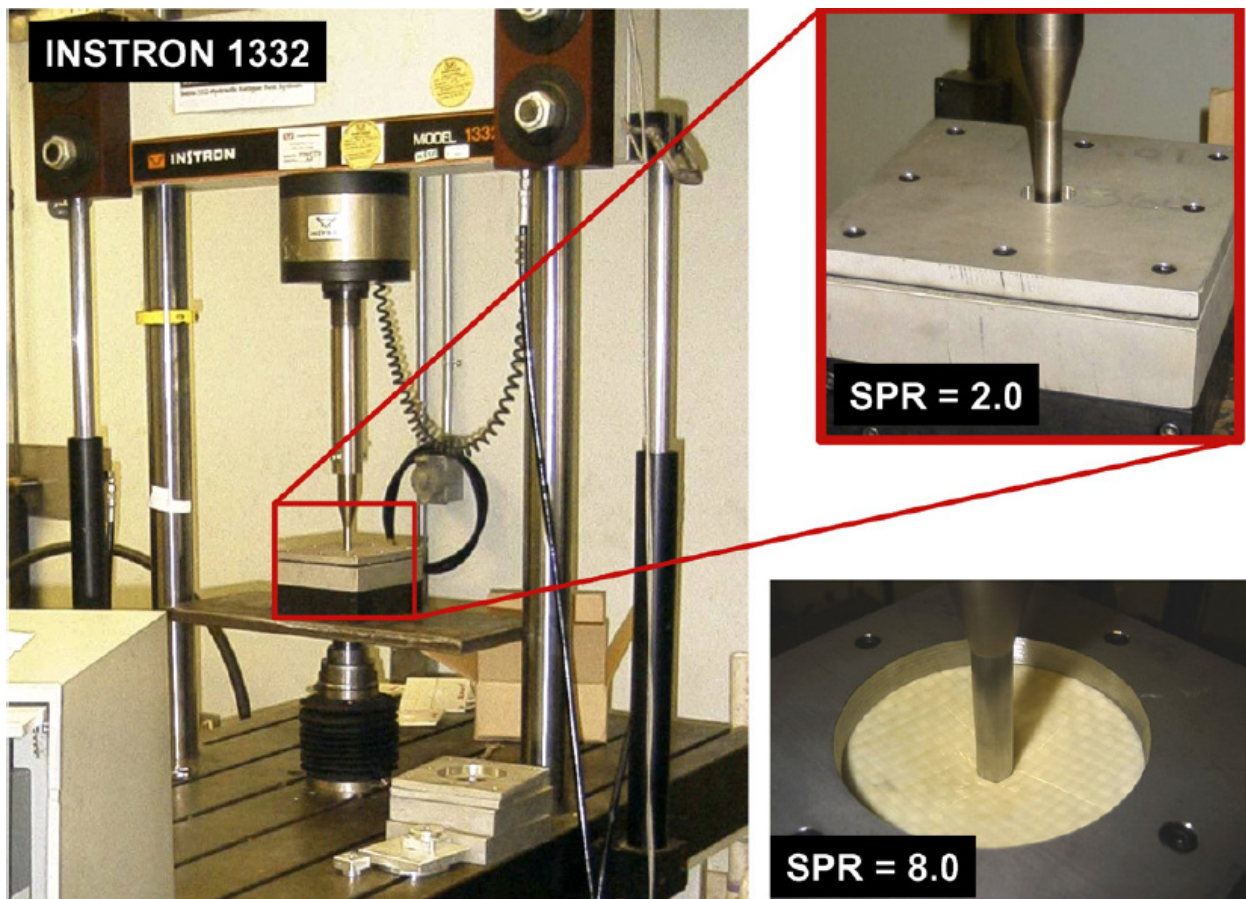
Figure 303. Experimental set-up for the quasi-static punch-shear experiment [86].
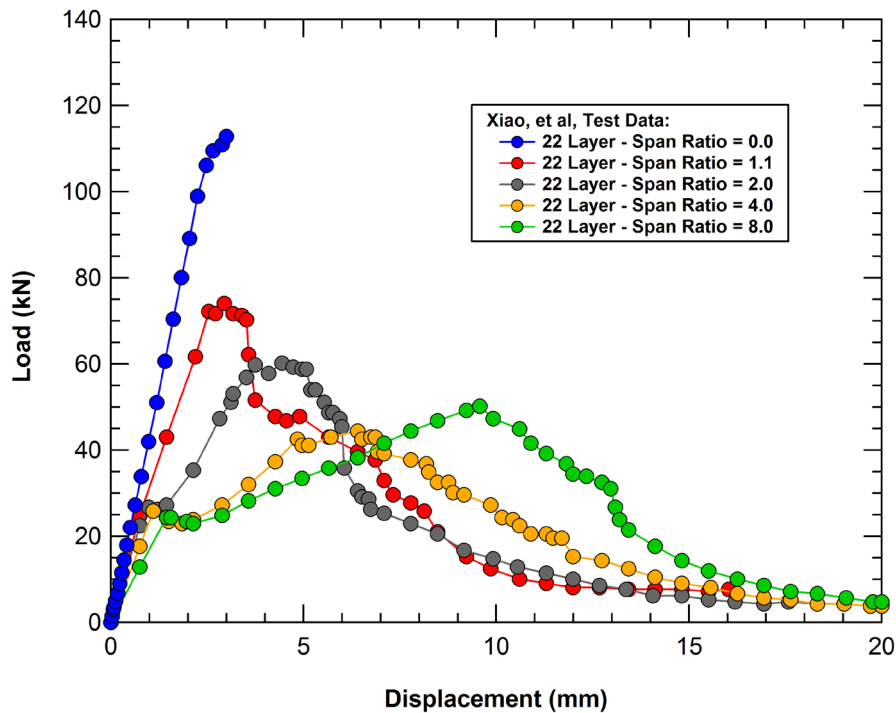
Figure 304. Effect of the span ratio on the composite punch force [87].

Composite Punch Modeling

Models of the punch tests were developed to validate the *MAT_COMPOSITE_MSC_DMG material model. Our approach was to model the same experiments performed by Xiao et al [86] and confirm the agreement between simulations and experiments reported, as shown in Figure 307. The LS-DYNA models of the punch simulations were developed based on descriptions provided by Xiao et al in Reference 86.

A resulting model of an 11-layer composite punch experiment is shown in Figure 308. The constraining ring was modeled as rigid and the punch as steel. Contact was specified between the ring and composite and the punch and composite with no friction. Eroding contact was defined between the composite layers. Constitutive properties of the composites used in this study are provided in Table 13.
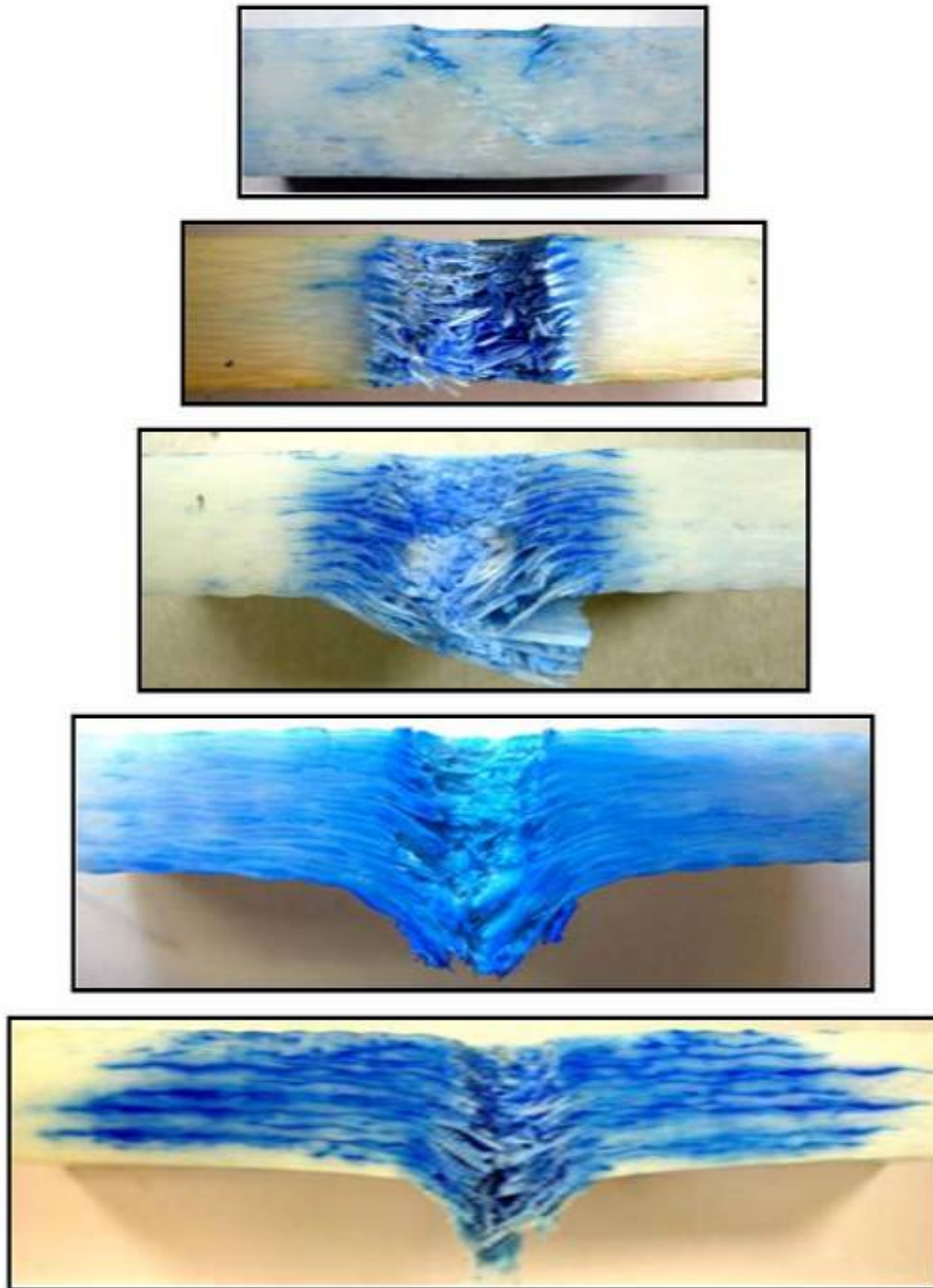
Figure 305. Effect of the span ratio on the composite punch test damage mode [87].
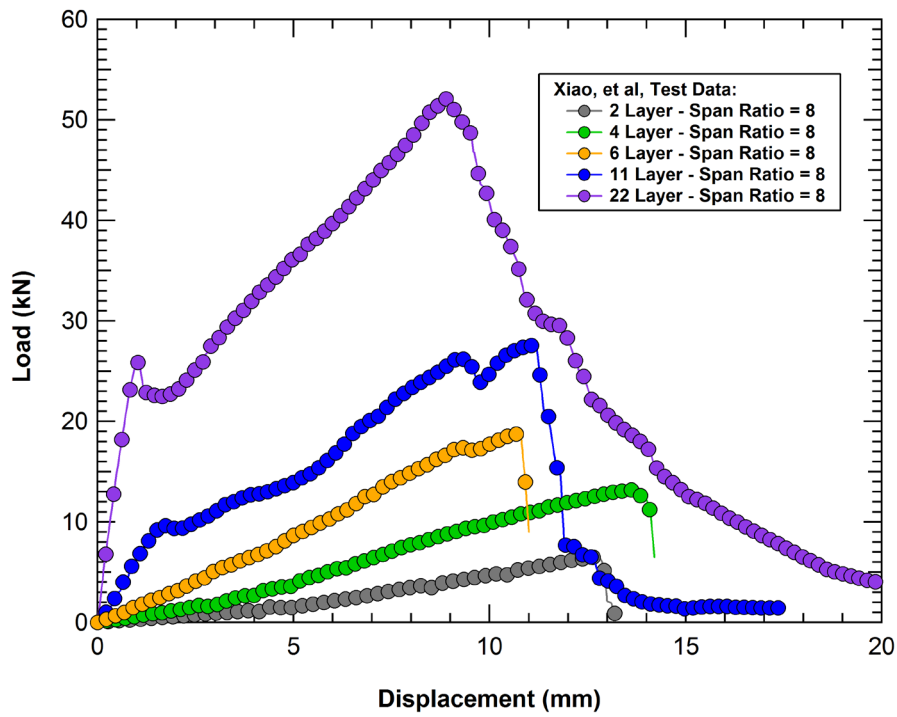
Figure 306. Effect of the specimen thickness on the composite punch force (SPR = 8) [86].
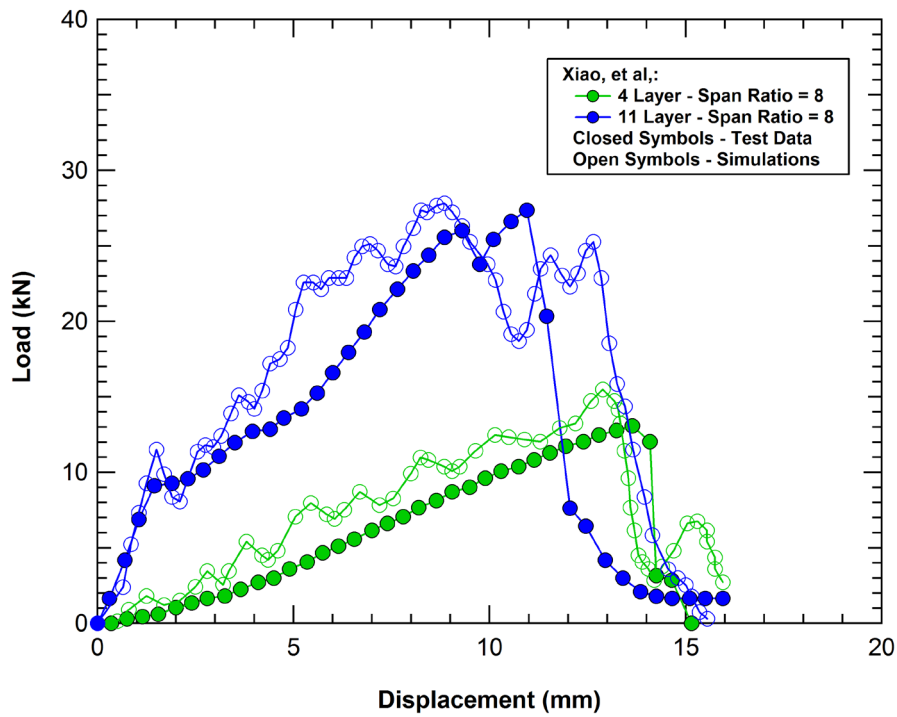
Figure 307. Comparison of the composite damage model with punch test data [86].
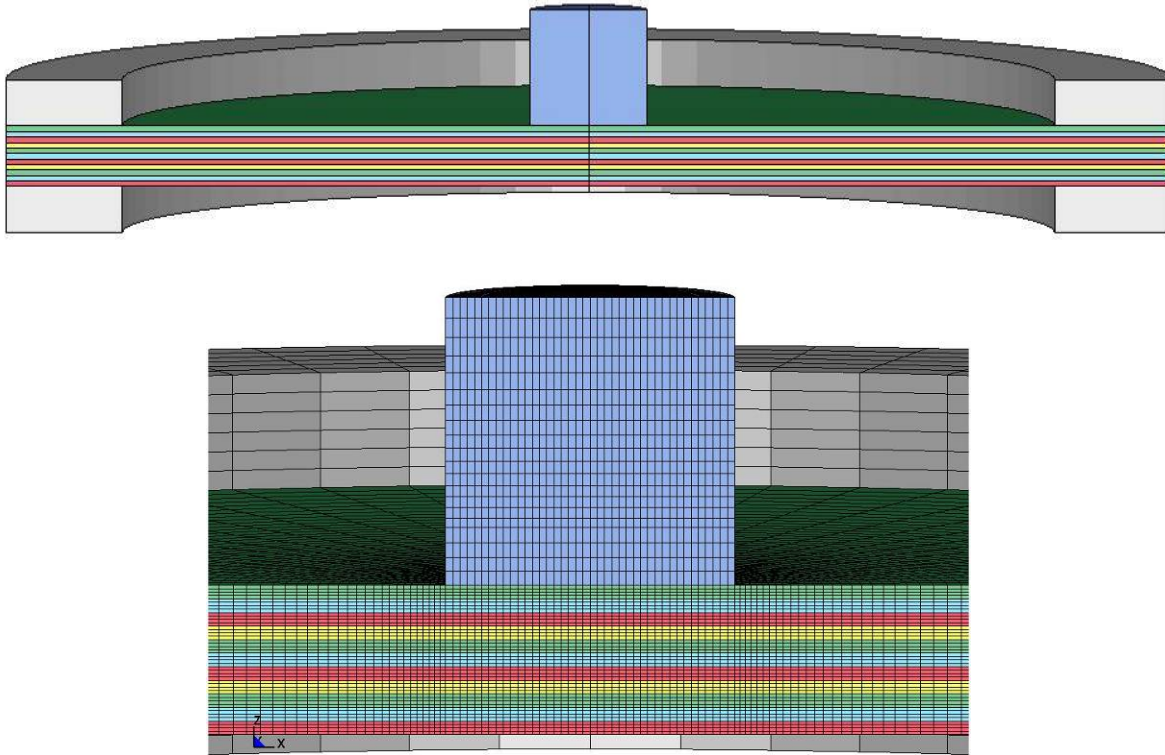
Figure 308. LS-DYNA model of an 11-layer composite punch experiment.

Table 13. Constitutive model parameters for woven S-2 Glass/SC15 resin composite

MID	ρ, kg/m3	EA	EB	EC	PRBA	PRCA	PRCB
1	1.85E+03	27.5 GPa	27.5 GPa	11.8 GPa	0.11	0.18	0.18
GAB	**GBC**	**GCA**	**AOPT**	—	—	—	—
2.9 GPa	2.14 GPa	2.14 GPa	2	—	—	—	—
XP	**YP**	**ZP**	**A1**	**A2**	**A3**	—	—
0	0	0	1	0	0	—	—
V1	**V2**	**V3**	**D1**	**D2**	**D3**	**beta**	—
0	0	0	0	1	0	0	—
SXT	**SXC**	**SYT**	**SYC**	**SZT**	**SFC**	**SFS**	**SXY**
604 MPa	291 MPa	604 MPa	291 MPa	58 MPa	850 MPa	300 MPa	75 MPa
SYZ	**SZX**	**SFFC**	**AMODEL**	**PHIC**	**E_LIMT**	**S_DELM**	—
58 MPa	58 MPa	0.3	2	10	0.2	1.2	—
OMGMAX	**ECRSH**	**EEXPN**	**CERATE1**	**AM1**	—	—	—
0.999	0.1	4	0	2.0	—	—	—
AM2	**AM3**	**AM4**	**CERATE2**	**CERATE3**	**CERATE4**	—	—
2.0	0.5	0.2	0	0	0	—	—

Note: Parameter definitions can be found in the LS-DYNA User's Manual [15].

Initial simulations using various shared-memory parallel processing (SMP) versions of LS-DYNA did not yield good results in predicting the experimental punch behavior. A sample of the runs performed with one of the LS-DYNA versions (ls971s_R2_7600, a formally released version) are shown in Figure 309. Initial loading of the composites agrees well with the experiments, but the simulated punch behavior consistently failed at lower load and displacements. Various modeling parameters that may affect the simulation results were considered, but were never adequate to achieve the load and displacements at failure seen experimentally. These included the following:

- Material constitutive parameters. Material 162 parameters for the plain weave S-2 Glass/SC15 composite vary some in the literature [e.g. 84, 88; 89]. Variations in the interlaminar shear stress concentration factor (S_DELIM) were also considered since this variable is mesh-dependent.

- Contact type between the punch and composite.

- Loading rate and time stepping.

- Number of elements per ply (1, 2, 4, 6 elements per ply considered).
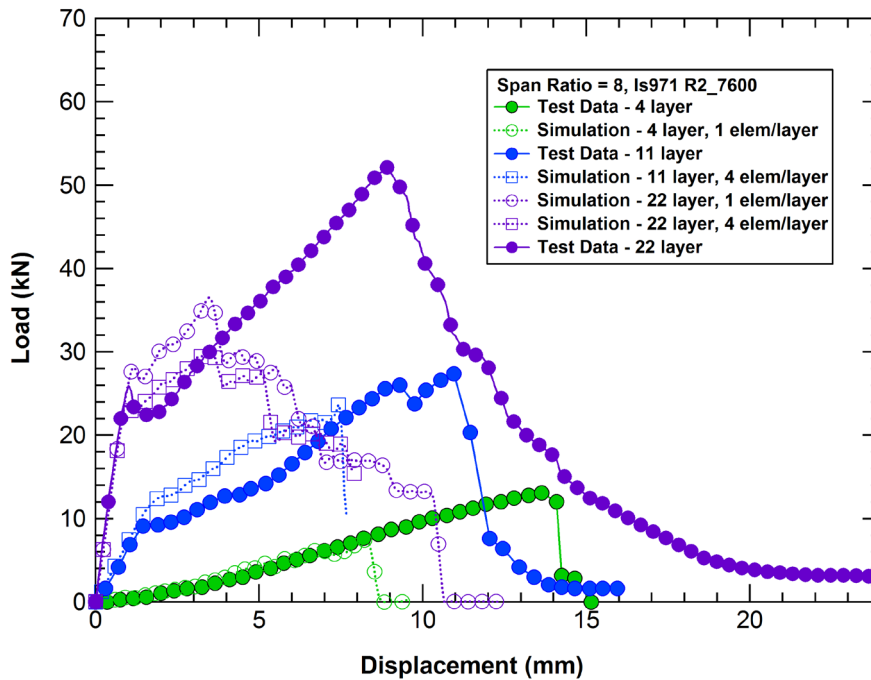
Figure 309. Comparison of initial punch simulations using ls971s_R2_7600.

A likely reason for the lack of agreement between simulations and tests was the functionality of material 162 in the versions of LS-DYNA built to run on ARA computers. Significant effort was expended in working with LSTC and MSC to have a version of LS-DYNA functioning correctly

with material 162. Material 162 is formally supported by MSC, but LSTC provides versions of LS-DYNA with this material model. A request was made to MSC for LS-DYNA models that could be used to validate that the material model was functioning correctly in the versions of LS-DYNA built for ARA. MSC provided single element models to proof various functions of the model. However, these single element tests do not provide a comprehensive way of assessing the models functionality as there is damage growth that occurs based on the state of surrounding elements. Several requests were made to MSC for additional models to test the functionality of material 162. Unfortunately, none were provided that could be validated against other results.

It was found that several SMP versions of LS-DYNA provided by LSTC did not pass all of these single element tests. In particular, when an element was loaded with through-the-thickness compression and shear, the nonlinear response was different than what is reported by UD-CCM [90], as shown in Figure 310. Ultimately, for the version ls971s_R4_47600 (all R4 builds of LS-DYNA provided by LSTC allow for user-defined materials to be used, which was need for the BW model), the response of all single element tests matched the results from UD-CCM. However, punch simulations with these versions still did not match experimental results.
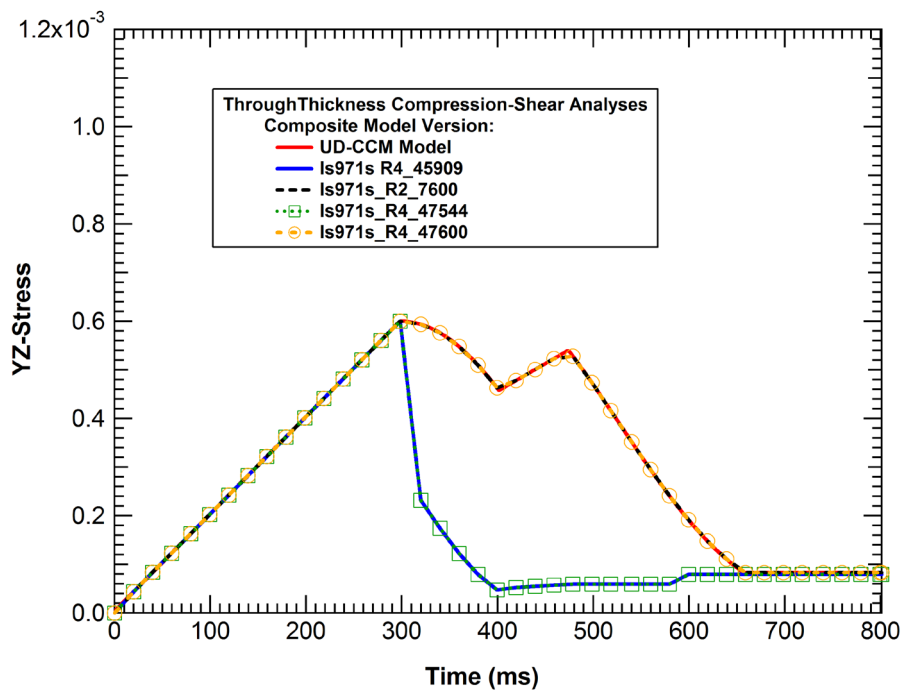
Figure 310. Single element response under through-the-thickness compression-shear for various SMP versions of LS-DYNA.

According to Xiao et al [86], successful comparisons between simulations and experiments were achieved using an older version of LS-DYNA, ls970. In a final attempt to get better agreement

with the punch experiments, 4-layer and 11-layer models were run using ls970s_6763. The comparison of the results from the ls970 and ls971 versions of the code for the 4-layer and 11-layer models are shown in Figure 311 and Figure 312, respectively. The load-displacement for the 4-layer simulations were very similar using both versions of the code. However, the 11-layer simulation was significantly different. The result using ls970s_6763 more closely matches the experimental and published simulation results, but still punches through the composite plate at roughly half the displacement.
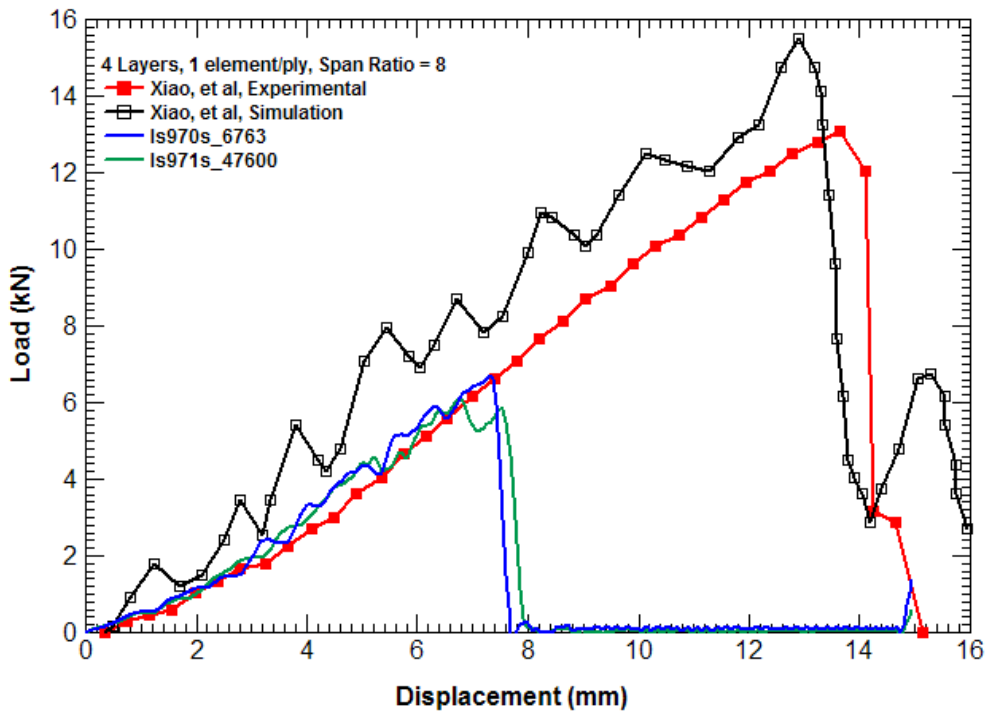
Figure 311. Comparison of 4-layer punch simulations using ls970 and ls971.
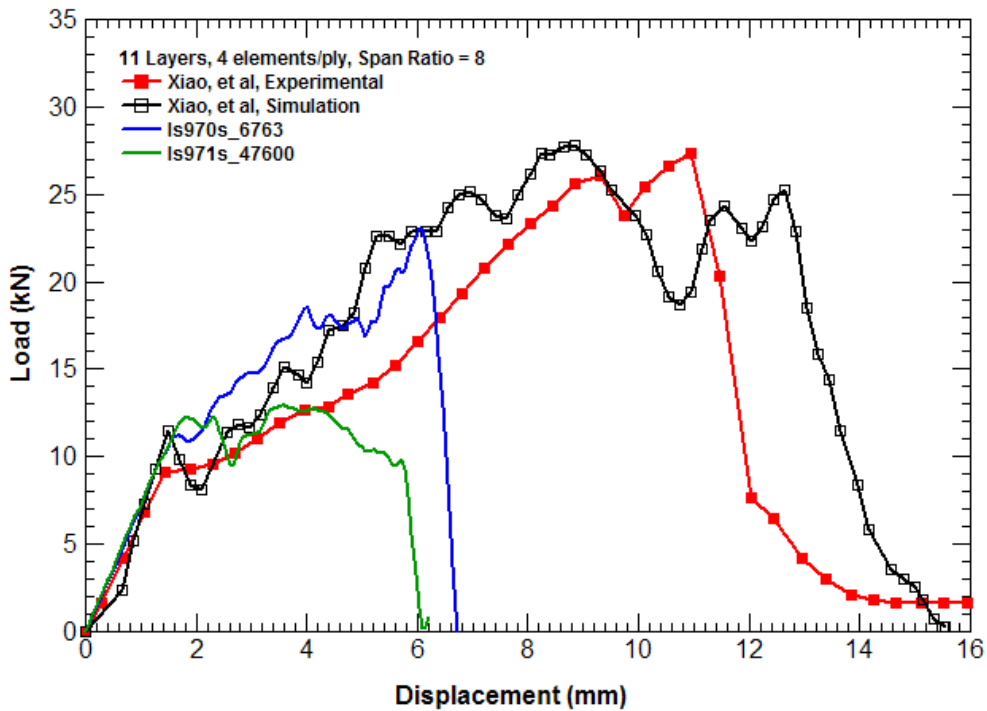
Figure 312. Comparison of 11-layer punch simulations using ls970 and ls971.

These results give no indication that the material 162 model implemented in any of the versions of LS-DYNA received from LSTC works correctly. It consistently produces lower force-displacements at failure than seen in experiments and other simulations. Identifying and correcting the error would require further collaboration with LSTC, MSC and possibly UD-CCM.

Although the punch test simulations consistently produced lower force-displacements at failure, the model for material 162 showed reasonably good agreement up to this point. Simulation of the composite jacket on a tank car should therefore provide a lower bound on its performance.

6.4.2 Tank Car Side Impact Analyses with a Composite Jacket

A model was developed to assess the puncture resistance of the 500 lb chlorine tank car with a composite jacket retrofit. A 1.5-inch thick composite jacket was placed around the commodity tank, as shown in Figure 313. A composite with this thickness has approximately the same weight as a steel jacket with a thickness of 0.355 inches (note that the same tank car retrofit with a 0.375-inch steel jacket was assessed in Section 4.3.2). A (0/90) layup with principal material directions coincident with the hoop and axial tank directions and equal numbers of 0 degree and 90 degree layers was used. The model for the commodity tank is the same as discussed in the previous analyses.

The model developed for the composite jacket is shown in Figure 314. Outside the impact zone, the jacket was modeled with shell elements. These were connected to solid elements in the impact zone, much like the approach used for modeling the commodity tank. Here, however, the solid mesh is made of two separate material models for the composite, material type 2 (*MAT_ ORTHOTROPIC_ELASTIC) for the coarser transition elements and material type 162 (*MAT_ COMPOSITE_MSC_DMG) in the path of the impactor. Material type 54 (*MAT_ ENHANCED_COMPOSITE_DAMAGE) was used to model the shell elements.

Material type 54 uses the ply-level constitutive properties to predict laminate properties by specifying the number of plies and their orientations by means of lamination theory. For these preliminary analyses, no damage was allowed in the model. The shell model therefore provides the correct elastic stiffness for a 1.5-inch thick composite prior to damage initiation. The transition elements, modeled with material type 2, also model the composite as linear elastic, but with the same through-the-thickness elastic properties used in material type 162. This transition region is necessary to reduce the number of nodes through the thickness of the jacket to be compatible with using the algorithm in LS-DYNA for connecting the shell elements to the solid elements.

The region in the path of the impactor was modeled with material type 162. To reduce the model size, this region was model with 12 thick plies of the composite fabric. In reality, a composite this thick would require approximately 64 plies of fabric where delamination could occur between each layer. To model each ply, a minimum of 64 elements would be needed through the thickness. Instead, the composite was modeled with 12 layers with 3 elements through the thickness of each ply, resulting in 36 elements through the thickness. Elements therefore have a characteristic length of about .042 inches (1 mm). Delamination can still occur in the model, but only between each of the 12 layers.
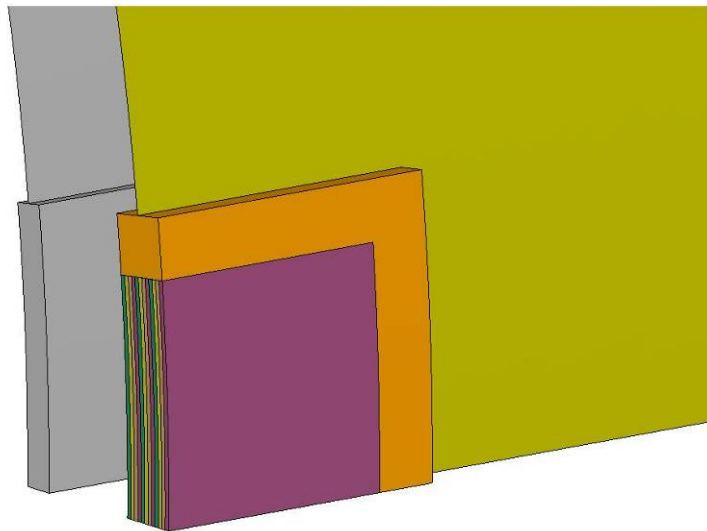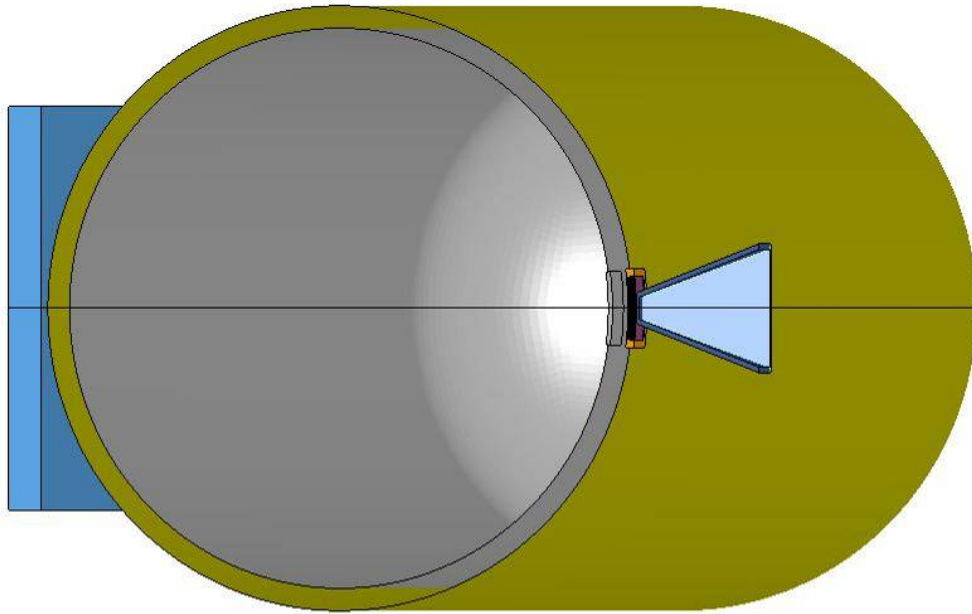
Figure 313. Side impact model with a composite jacket.
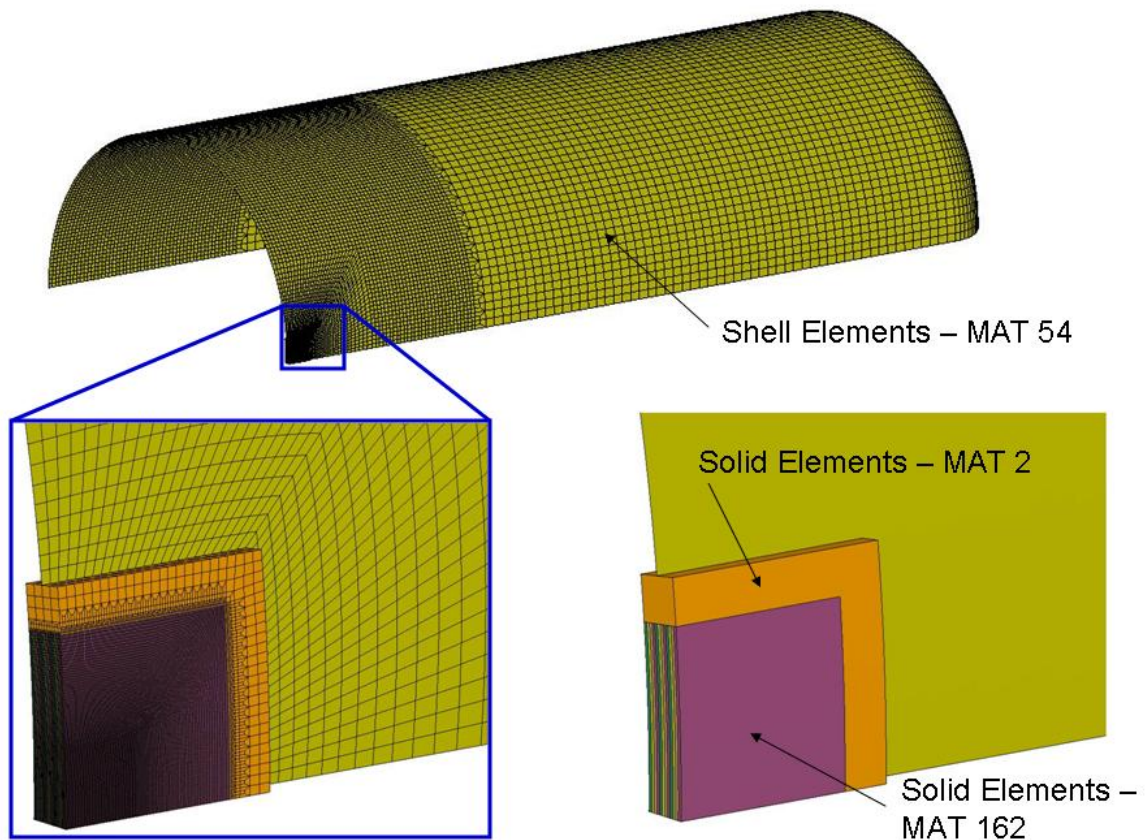
Figure 314. Composite tank model and impact zone mesh used for side impact puncture analyses.

Preliminary analyses with the tank model were performed without any internal pressure or the BW failure model for the steel implemented. This analysis is still ongoing. Currently, the analysis has progressed to a time of 36 ms (12.5 inch displacement), as shown in Figure 315. Impactor force-displacement is shown in Figure 316. For comparison, the force-deflection curve of a 500 lb chlorine tank car with an 11-gauge A1011 jacket and pressurized to 50 psi was added to the figure. This configuration was selected since it has a very similar stiffness to the unpressurized tank with the composite jacket.

The current impact load is in excess of 500,000 lbs and the composite jacket has significant damage but is still capable of resisting the impact loads around the perimeter of the contact patch. Based on the observed level of damage, it is not expected that the calculation would predict a puncture force that is significantly greater than that of an equivalent weight steel jacket. However, the composite model is also expected to under predict the composite strength in this analysis.
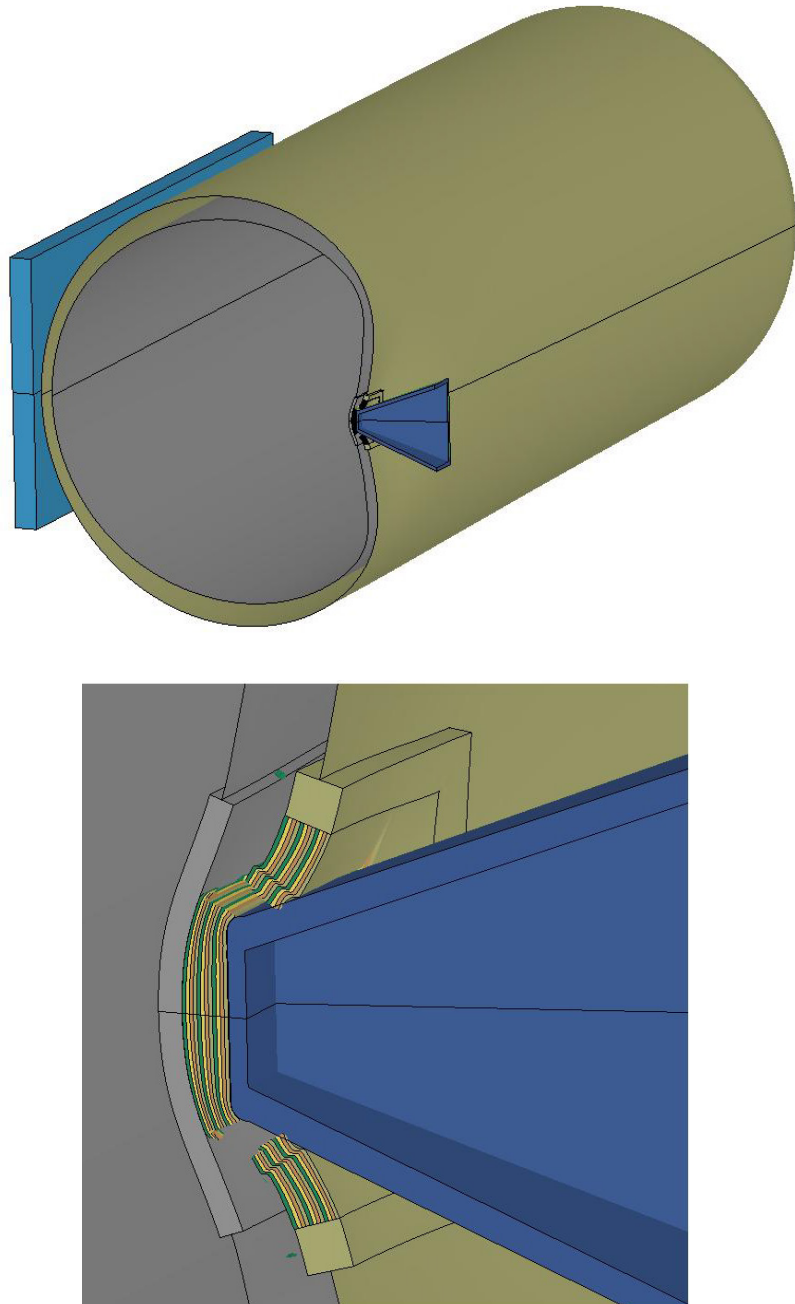
Figure 315. Punch-shear mode in composite jacket at 18 inches of displacement.

One effect seen in the analyses is the potential for the composite to provide a blunting of the impact loads on the commodity tank. A comparison of the impact behavior of a 1.5-inch thick composite jacket with an equivalent weight steel jacket is shown in Figure 317 and Figure 318. The comparison clearly shows a blunting of the loads on the commodity tank for the same level

254

of impact displacement and this effect has potential for delaying the development of damage and penetration of the tank. The magnitude of this blunting effect would be expected to increase as the thickness of the composite jacket becomes greater.
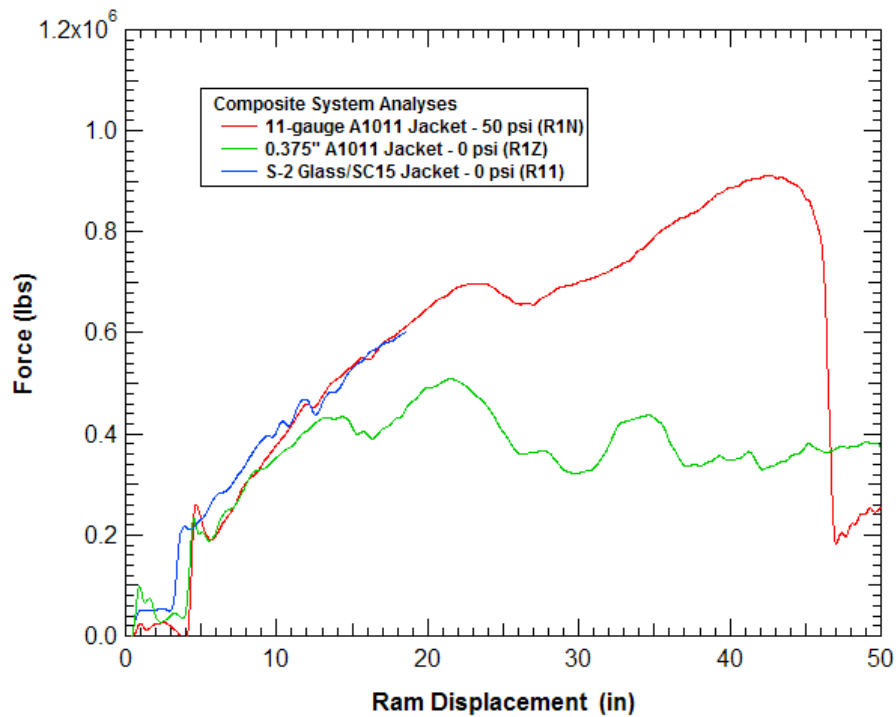
Figure 316. Side impact force-deflection curves for a 500 lb tank car with a composite jacket.
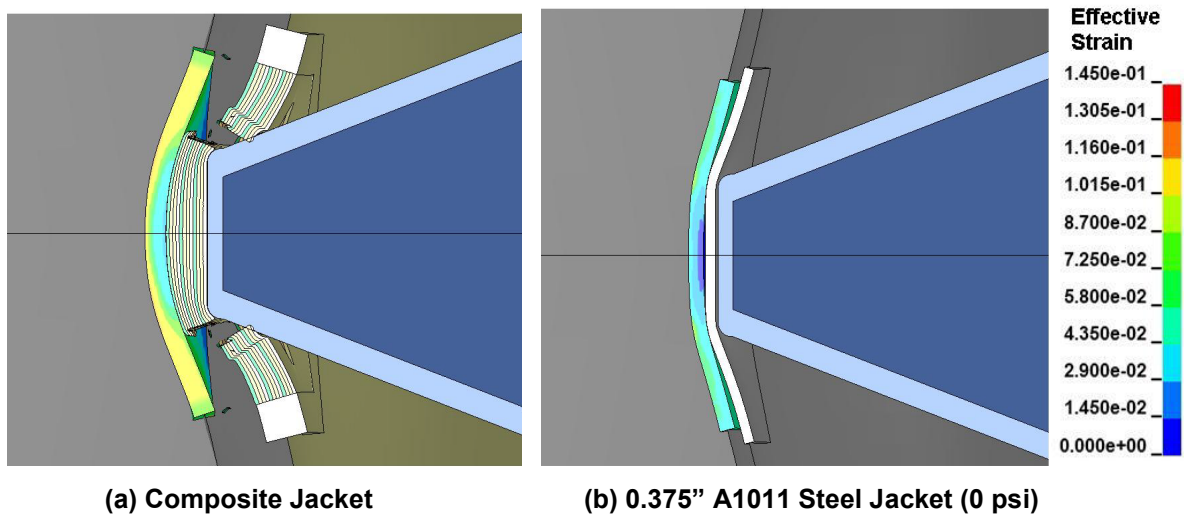
(a) Composite Jacket　　　　　　**(b) 0.375" A1011 Steel Jacket (0 psi)**

Figure 317. Composite jacket blunting effect at 50 ms (17-inch displacement).

(a) Composite Jacket   b) 0.375" A1011 Steel Jacket (0 psi)
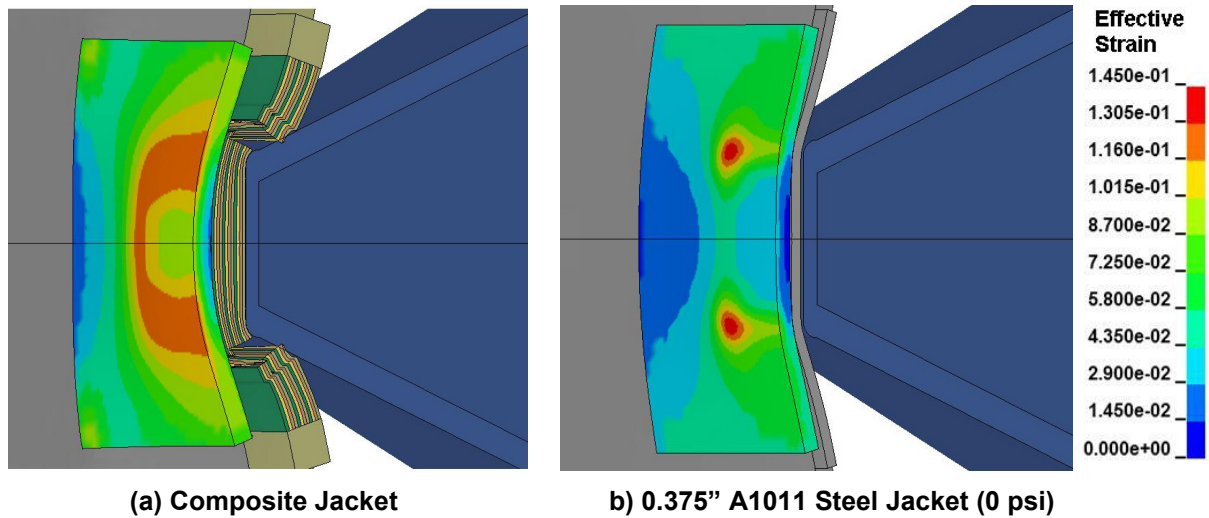
Figure 318. Effective strains in the 500 lb commodity tank at 50 ms (17-inch displacement).

Empirical Evaluation of Composite Puncture Protection Potential

The detailed finite element analyses did not produce a reliable assessment of the impact and puncture behavior of a tank car with a composite protection system. Alternatively, the data available in the open literature sources can be used to estimate the potential of a composite layer to enhance the tank car puncture resistance.

As was discussed in previous sections, the tank impact behavior is dominated by punch-shear through the jacket and commodity tank. By comparing normalized punch test peak loads from the composites and steel testing, an estimate can be made as to their relative performance. A normalized peak punch load was calculated as

$$F_n = \frac{F_p}{D_p \rho t} \tag{11}$$

where F_p is the peak punch load, D_p is the diameter of the punch, ρ is the material density and t is the plate thickness. Effectively, this is the shear stress around the punch perimeter scaled by the material density. As a result, the punch shear resistance is compared on an equivalent weight basis rather than an equivalent thickness basis.

Data were taken from the punch tests performed on A1011, HSLA 90x and TC128B steels by SwRI Materials Test Lab, discussed in Section 3.4.4, and normalized [32-34]. Data from the composite punch tests performed by Xiao et al [86] for SPR = 2 and SPR =8, as was shown for SPR=8 in Figure 306, were similarly normalized. These are plotted against aerial density in Figure 319. Steel data are an average of all span ratios tested, from 1.5 to 2.5. The ranges of results from different span ratios are also shown in the figure. The effectiveness of the

composite appears to drop as its thickness is increased. Some of this effect is the shift from a bending failure mode to a punch-shear mode. At larger thicknesses, and higher loads, this may also be due to stress concentrations at the sharp punch edges causing localized failure. Recall that the composite punch tests used a square punch where the steel tests used a punch with rounded edges. Therefore, in comparing the composite and shear punch data, we believe that these values provide a lower bound on the performance of the composite.
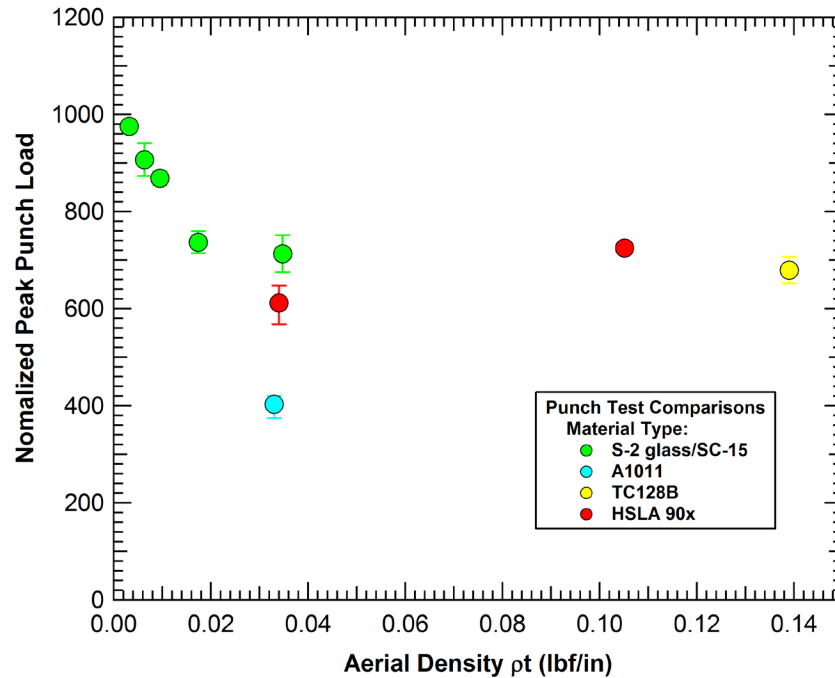
Figure 319. Normalized peak punch test loads versus aerial density for various materials.

At the largest aerial density testing for the composite, a direct comparison with A1011 and HSLA 90x can be made because the 11 gauge steels used in these tests had a similar aerial density. The composite out performs A1011 by approximately 70% and HSLA 90x by roughly 10%. However, if one assumes that the performance of the composite remains the same with larger thicknesses (aerial densities above 0.1), the HSLA 90x and TC128B show comparable performance.

The above comparison shows that a composite puncture protection layer could perform as well as a steel layer and potentially perform better. Improved performance of the composite system could likely be obtained by optimizing the composite material and/or layup for these types of impact conditions. For example, the simulated failure begins at the punch corner preferentially develops along the hoop direction. The current layups is a 0/90 plain weave, with equal numbers of layers in the hoop and axial directions. Layers oriented off the principal tank axes and with a

greater number in the axial direction may improve the performance. However, it is not expected that an optimized layup alone would result in drastic increases in performance. As a result, we have not yet identified any composite systems that could achieve a puncture resistance that approach a two times improvement over a comparable weight steel system.

7   Summary and Conclusions

This report describes the results of a research program to develop strategies for improving railroad tank cars so they can maintain tank integrity for more severe accident conditions than current equipment. The approach used in the research and development program was to develop a tank impact and puncture prediction capability using detailed finite element analyses. Along with the modeling efforts, an extensive test program was performed. The testing included both laboratory tests of materials and components and full scale impact testing of tank cars and tank protection concepts. The test program was critical for both the development and the validation of the puncture modeling capability.

This tank car impact and puncture modeling capability was applied to evaluate a wide range of tank/jacket and head/head shield geometries. The side impact condition was a normal impact centered on the belt line of the tank and the head impact was an offset impact point approximately 29 inches vertically downward from the center of the head. The calculated head and shell impact forces as a function of the combined head and head shield thickness are shown in Figure 320 (all analyses with the 6x6 inch impactor). The figure shows the analyses are in general consistent with a linear relationship between puncture force and total thickness of the protective layers.

The linear relationship between the puncture force and total tank system thickness provides an indication of the primary failure mechanism initiating the tank puncture. The 6x6 inch impactor produces a large shear stress in the tank wall around the perimeter of the contact patch. The slope of the linear fit in Figure 320 corresponds to an average shear stress in the tank layers around the perimeter of the impactor of 39 ksi. By comparison, the yield and ultimate stress levels of the TC128B in pure shear are 33 ksi and 49 ksi, respectively (approximately 58% of the stress values in pure tension using a Von Mises yield criterion). Thus, the failure mode is primarily exceeding the shear capacity around the perimeter of the impact patch.

The calculated puncture forces for pressurized heads and the thicker head systems tended to fall slightly below the linear fit in Figure 320. The proposed mechanism for these lower forces is that, for the stiffer head systems, the offset impact creates a larger stress concentration along the upper edge of the impactor face and the failure initiates at that location at a lower total force. The more compliant head systems allow for a larger dent to form and the impactor develops a more uniform stress distribution in the impact patch around the ram face perimeter.
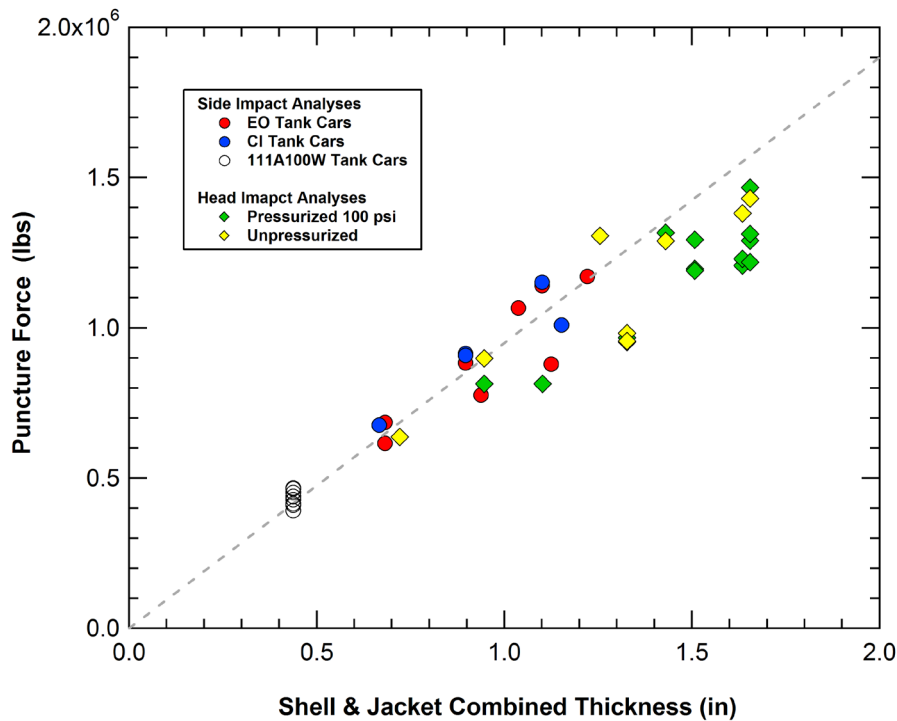
Figure 320. Calculated puncture forces as a function of system thickness.

The calculated puncture energies for all of the side and head impact analyses are plotted against the combined thickness of the system in Figure 321 (6x6 inch impactor only). When comparing all of the puncture energies, the data falls into four separate groups that are distinguished by the impact type (side or head) and the tank pressure. Again, the comparison indicates that the total thickness is the relative parameter that determines puncture energy for a given impact condition and pressure level, indicating that a retrofit design with an increased jacket thickness should provide equivalent protection to a thicker commodity tank system with equivalent combined shell and jacket thicknesses.

The puncture energy summary in Figure 321 illustrates the important effect of internal pressure. If we examine the results from side impact analyses, we find that the puncture energy is 50% to 75% higher when the internal pressure is reduced from 100 psi to 50 psi. This is a potential opportunity to reduce the probability of tank punctures by controlling the tank pressure (e.g. modify operational procedures to ship at a lower average temperature).

The correlation of the system thickness and puncture energy can also be converted to assess system requirements for a given impact scenario. The relationship between the impact speed and impact energy for the 295,000 lb ram car is provided in Figure 322. This impact energy is proportional to the mass of the object. A 286,000 ram car would have energies that are three percent lower than those in Figure 322. This relationship between speed and impact energy can

be combined with the linear fits between system thickness and puncture energy, shown in Figure 321, to determine the required system thickness to resist puncture for a specified impact speed.
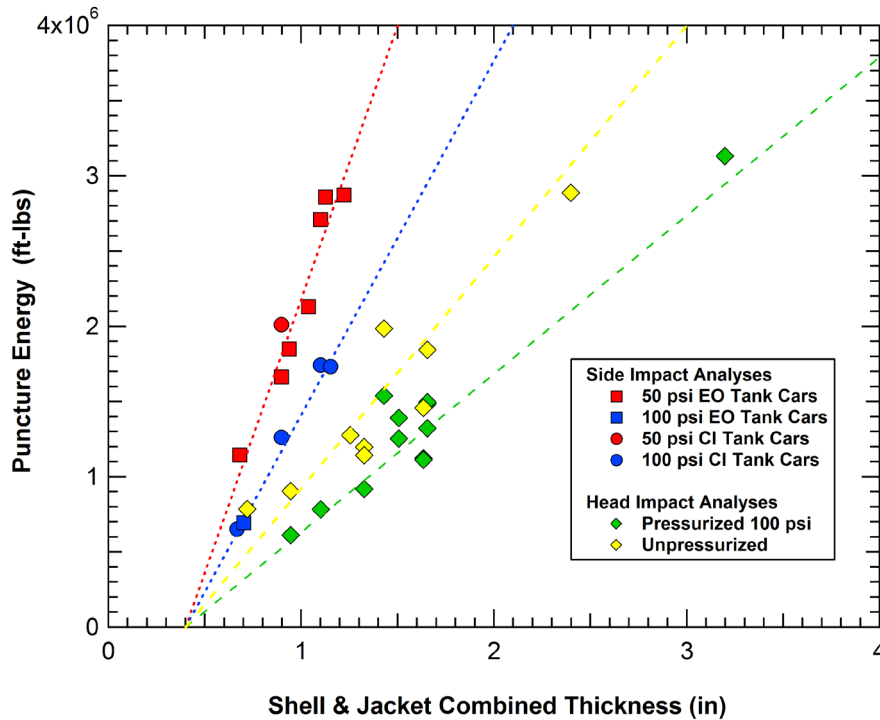
Figure 321. Calculated puncture energies as a function of system thickness.

Examples of the pressurized (100 psi) Cl tank car thickness requirements to resist a puncture of the 6x6 inch impactor at various impact speeds is shown in Figure 323 for both side and head impacts. The figure shows that as the impact speed increases, the system thickness required begins to increase rapidly. A 25 mph side impact would require approximately three inches of steel to prevent puncture and a 30 mph head impact would require more than six inches of steel. Obviously, these protection levels are not achievable with a traditional tank car design approach while maintaining a tank car that is economically viable as a result of both the initial tank car cost and the drastically reduced lading capacity.

The modeling capabilities developed in this program were applied to analyze a series of advanced tank car protective structure concepts. Included in these were multi-layered foam systems and engineered metal structures (EMS) systems. A variety of designs were investigated both with analyses and with full-scale head tests. However, neither of the foam or EMS systems was optimized.
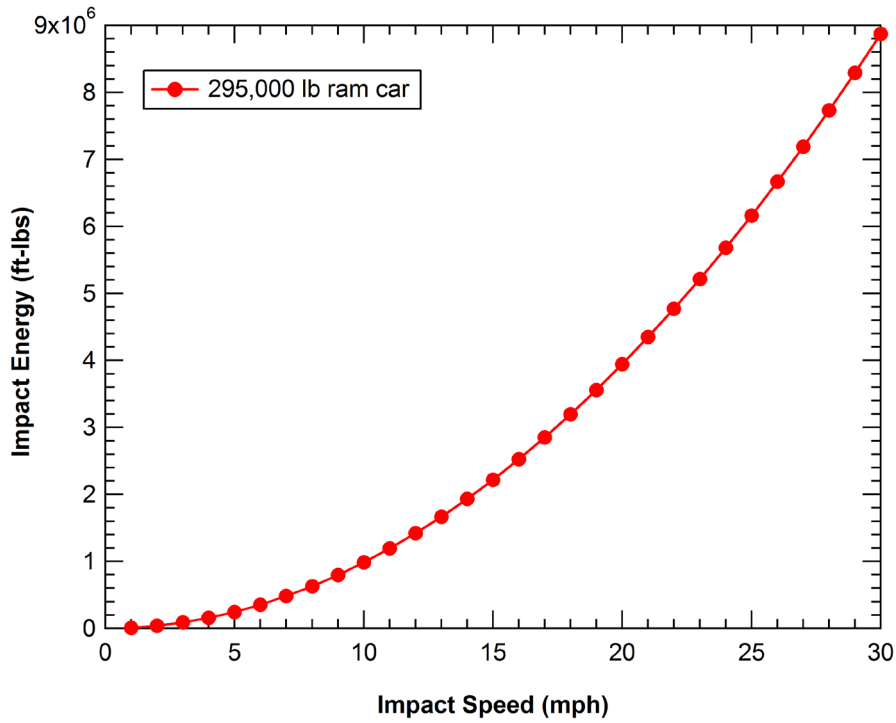
Figure 322. Relationship between impact speed and kinetic energy for the ram car.
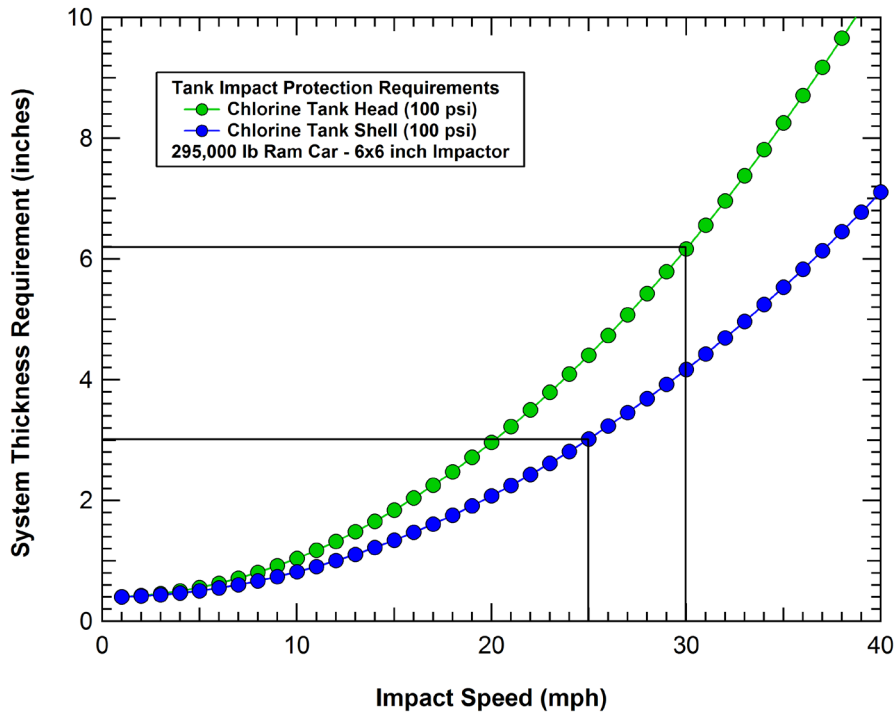
Figure 323. Puncture prevention thickness requirements for various impact speeds.

The failure mode of the advanced systems was similar to that of the baseline tank systems when impacted by the 6x6 inch impactor. When the load acting on a layer of the advanced protective system exceeded the shear capacity of the layer, the layer would be punctured. For many of the advanced concepts, the system design would increase the stiffness of the support for the outer layers. The increased support structure stiffness would result in outer layer penetration at reduced ram displacements. As a result, the protection system and commodity tank would be penetrated independently at lower peak forces and lower puncture energies than could be obtained in an optimized system. In general, the performance of advanced protective systems was typically improved when the thickness of the outer layer was increased to resist puncture and the stiffness of the supporting structure was reduced to increase the displacements of the system before the puncture level was exceeded.

The calculated forces to puncture the outer layer of foam and EMS systems are added to the plot of the puncture force versus system thickness in Figure 324. The difference in the data for the advanced systems is that the thickness used is the layer thickness only (e.g. outer head shield or outer face sheet thickness) rather than the sum of the total tank and jacket layer thicknesses. The comparison shows that the foam and EMS structures had the effect of making each layer act independently rather than coming in contact and working together to resist the high shear stresses around the edge of the impactor. As a result, the maximum achievable puncture forces were reduced and the systems do not reach the desired puncture energies.

Although the systems with a monolithic jacket performed better than the corrugated EMS structures in this example, the conclusion can not be generalized to all EMS designs and impact scenarios. The EMS structures would be expected to perform significantly better under a more distributed loading. Other benefits of the EMS concepts are that the structural stiffness can be used to efficiently carry the train service loads in a "tank within a tank" design. Further analysis of other EMS concepts (e.g. core geometries, materials) and more general impact conditions would be required to obtain an optimized design.

A similar set of observations was obtained from the analysis of layered foam systems. In general, the systems analyzed did not outperform a single monolithic plate of equivalent protection system weight for the 6x6 inch impactor. However, the performance for larger impactors and the optimum foam and interface properties to maximize performance were not fully explored. In addition, low density foams can contribute to improved thermal insulation. If a foam system can maintain a lower average shipping temperature (and thus a lower average tank pressure), the overall tank puncture energy could potentially be increased.

Figure 324. EMS puncture forces as a function of outer layer thickness.

A preliminary evaluation was also performed to assess the potential of composite materials for tank car puncture protection. Composite materials have densities that are typically one quarter to one third of the density of steel. Therefore, a much thicker composite system could be used to protect the tank car for the same added weight.

A comparison of punch test data indicates that there is potential for modest puncture resistance improvements using composite materials. For specific test conditions, the composite out performs A1011 by approximately 70% and HSLA 90x by roughly 10% on an equivalent weight basis. Further improvements in the performance of the composite system could likely be obtained by optimizing the composite material and/or layup for these types of impact conditions. However, we have not yet identified any composite systems that could achieve a puncture resistance that approach a two times improvement over a comparable weight steel system.

Impact Performance Summary

A summary of the current state of tank car side impact performance is provided in Figure 325. From the full scale side impact Test 2, described in Section 2.3.2, the 105J500W tank car puncture energy slightly less than one million ft-lbs. This corresponds to a 10 mph impact with a 286,000 lb ram car and the 6x6 inch impactor. From analyses, the puncture energies of the

105J300W and 105J600W tank cars are approximately 30 percent less and 40 percent greater than the 105J500W tank car, respectively.

The goal of the Next Generation Railroad Tank Car Project was to increase the puncture energy of the tank car by five to ten times over the baseline 105J500W tank car design. This target is outlined by the red box in Figure 325. The proposed TIH tank car standard falls within this range, requiring a puncture energy that is 6 times that of the baseline tank car. However, the levels that were found to be achievable with the first generation concepts in the NGRTC project are more consistent with two to three times the puncture energy of the baseline design.

Figure 325. Summary of side impact puncture performance and goals.

A similar summary of the current state of tank car head impact performance is provided in Figure 326. The calculated puncture energy for a pressurized (100 psi) 105J500W tank head with an 11-gauge head jacket is 610,000 ft-lbs (analysis described in Section 5.3.2). This corresponds to an 8 mph impact with the 286,000 lb ram car and the 6x6 inch impactor. For comparison, the

puncture energy of a 105J600W tank head with a 0.50 inch full height head shield is 1.1 million ft-lbs.

The goal of the Next Generation Railroad Tank Car Project was to increase the puncture energy of the tank car by five to ten times over the baseline 105J500W tank head as outlined by the red box in Figure 326. The proposed TIH tank car standard is above this range, requiring a puncture energy that is approximately 14 times that of the baseline tank head. However, the levels that were found to be achievable with the first generation concepts in the NGRTC project are more consistent with 2.5 to 4 times the puncture energy of the baseline design.

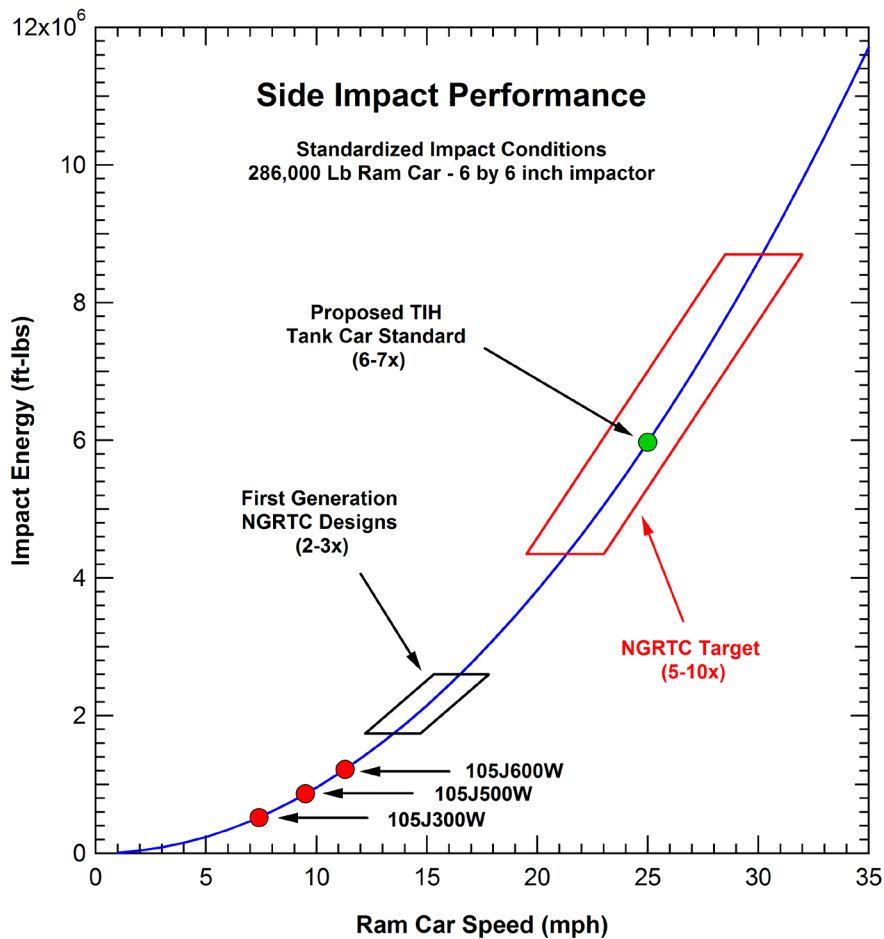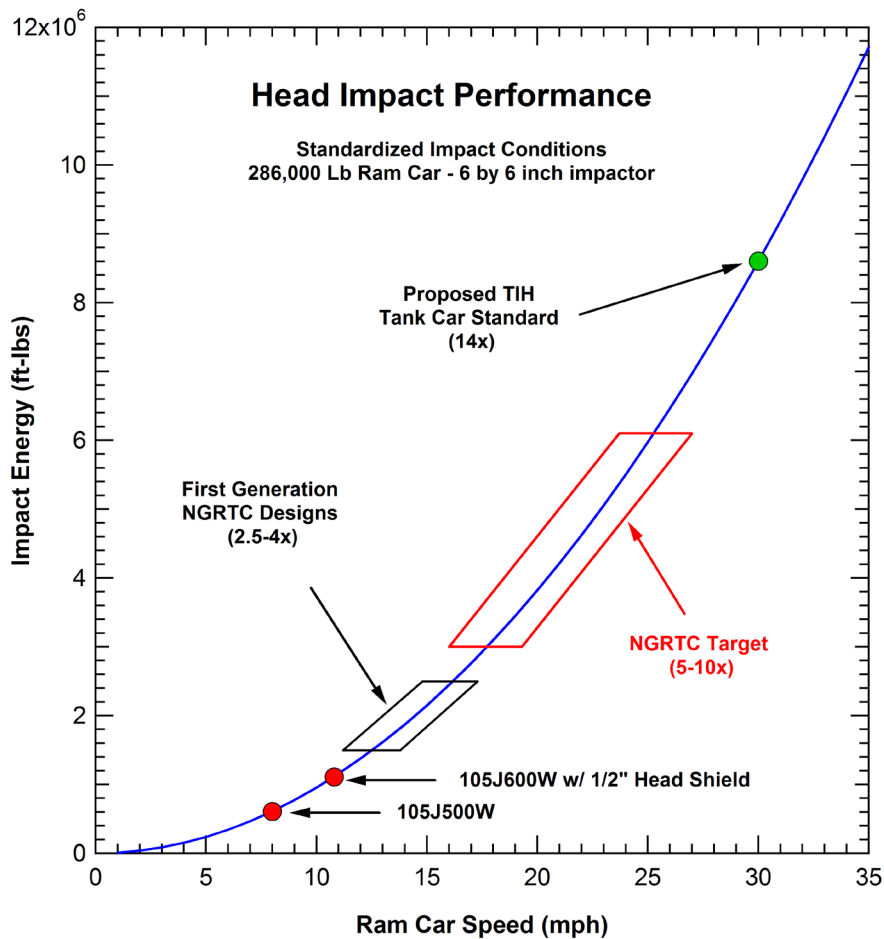**Figure 326. Summary of head impact puncture performance and goals.**

8   References

1. Tyrell, D.C., Jeong, D.Y., Jacobsen, K., Martinez, E., "Improved Tank Car Safety Research," Proceedings of the 2007 ASME Rail Transportation Division Fall Technical Conference, RTDF2007-46013, September 2007.

2. National Transportation Safety Board, 2004: "Derailment of Canadian Pacific Railway Freight Train 292-16 and Subsequent Release of Anhydrous Ammonia Near Minot, North Dakota; January 18, 2002," Railroad Accident Report NTSB/RAR-04/01.

3. National Transportation Safety Board, 2006: "Collision of Union Pacific Railroad Train MHOTU-23 with BNSF Railway Company Train MEAP-TUL-126-D with Subsequent Derailment and Hazardous Materials Release, Macdona, Texas, June 28, 2004," Railroad Accident Report NTSB/RAR-06/03.

4. National Transportation Safety Board, 2005: "Collision of Norfolk Southern Freight Train 192 with Standing Norfolk Southern Local Train P22 with Subsequent Hazardous Materials Release at Graniteville, South Carolina, January 6, 2005," Railroad Accident Report NTSB/RAR-05/04.

5. Barkan, Christopher P.L., Satis V. Ukkusuri, S. Travis Waller, "Optimizing the design of railway tank cars to minimize accident-caused releases", Computers & Operations Research, (2005 Elsevier Ltd).

6. Saat, Mohd Rapik, Christopher P.L. Barkan, "Release Risk and Optimization of Railroad Tank Car Safety Design", Transportation Research Record: Journal of the Transportation Research Board (2005).

7. Saat, Mohd Rapik, Christopher P.L. Barkan, "Release Risk as Metric for Evaluating Tank Car Safety Performance", Saat & Barkan 05-1826.

8. Jeong, D.Y., Lyons, M.L., Orringer, O., Perlman, A.B., 2007: "Equations of Motion for Train Derailment Dynamics," Proceedings of 2007 ASME Rail Transportation Division Fall Technical Conference, RTDF2007-46009.

9. S.W. Kirkpatrick, B.D. Peterson, and R.A. MacNeill, "Finite Element Analysis of Train Derailments," ICrash2006. Proceedings of the International Crashworthiness Conference, July 4-7, 2006, Athens, Greece.

10. Association of American Railroads, Technical Services Division, Mechanical Section—Manual of Standards and Recommended Practices.

11. Tyrell, D.C., Jacobsen, K., Talamini, B., Carolan, M., "Developing Strategies for Maintaining Tank Car Integrity During Train Accidents," Proceedings of the 2007 ASME Rail Transportation Division Fall Technical Conference, RTDF2007-46015, September 2007.

12. S.W. Kirkpatrick and R.W. Klopp, "Risk Assessment for Damaged Pressure Tank Cars," 2003 COMPUTER TECHNOLOGY AND APPLICATIONS, ASME Publications, Proceedings of: PVP2003 - The 2003 ASME PVP Conference, July 20-24, 2003, Cleveland, Ohio, W. Reinhardt and D.J. Martin, Eds.

13. S.W. Kirkpatrick and R.W. Klopp, "Hazard Assessment for Pressure Tank Cars Involved in Accidents," ICrash 2000. Proceedings of the International Crashworthiness Conference, September 6-8, 2000, London, UK, E. C. Chirwa and D. Otte Eds., pp. 223-235.

14. R.W. Klopp, S.W. Kirkpatrick, and D.A. Shockey, "Damage Assessment of Tank Cars Involved in Accidents: Phase II - Modeling and Validation," Final Technical Report to the Federal Railroad Administration, FRA Report, June, 1999.

15. "LS-DYNA Keyword User's Manual," Livermore Software Technology Corporation, Version 970, April 2003.

16. "TrueGrid Manual, Version 2.1.0," XYZ Scientific Applications, Inc., September 2001.

17. Derailment of Canadian Pacific Railway Freight Train 292-16 and Subsequent Release of Anhydrous Ammonia Near Minot, North Dakota, January 18, 2002, NTSB Railroad Accident Report No. NTSB/RAR-04/01, March 2004.

18. Kirkpatrick, S. W., "Analysis of the Tank Car Response in the Minot ND Derailment," ARA Technical Report, June 17, 2005.

19. "Draft of NTSB Material Laboratory Factual Report [In reference to Canadian Pacific Railway Derailment and Anhydrous Ammonia Release, Minot, ND, January 18, 2002, DCA-02-MP-002]," Frank Zakar, Metallurgy Group Chairman, Feb. 14, 2003.

20. Matthew Witte and Satima Anankitpaiboon, "Fully Instrumented Side Impact Test of Tank Car 3069," Transportation Technology Center, Inc. Report No. P-07-033, October 8, 2007.

21. Matthew Witte and Satima Anankitpaiboon, "Second Fully Instrumented Tank Car Baseline Side Impact Test of Tank Car 3074," Transportation Technology Center, Inc. Report No. P-07-034, October 8, 2007.

22. Boscardin, Marco D., "Vehicle Impact Wall Evaluation Report, AAR Test Facility, Pueblo, Colorado" Boscardin Consulting Engineers, Inc. Report to TTCI, July 9, 2007.

23. Bao, Y., and Wierzbicki, T., "On Fracture Locus in the Equivalent Strain and Stress Triaxiality Space," International Journal of Mechanical Sciences 46, 81-98.

24. Bao, Y., and Wierzbicki, T., "A Comparative Study on Various Ductile Crack Formation Criteria," Journal of Engineering Materials and Technology 126, 314-324.

25. Young-Woong Lee and Tomasz Wierzbicki, "Quick Fracture Calibration for Industrial Use," Massachusetts Institute of Technology Impact & Crashworthiness Laboratory, Report No: 115, August 2004.

26. Tang, Y., Yu, H., Gordon, J., Jeong, D., and Perlman, A.B., "Analysis of Railroad Tank Car Shell Impacts Using Finite Element Method," Proceedings of the 2008 ASME/IEEE Joint Rail Conference, JRC2008-63014, April 2008.

27. Pete McKeighan, "Tensile Properties and Stress-Strain Behavior of Various Steel Products Used in Fabricating Test Specimen for the NGRTC Program," NGRTC Project Memorandum, Southwest Research Institute, 21 November 2007.

28. L.E. Malvern, Introduction to the Mechanics of a Continuous Medium, Prentice-Hall, 1969.

29. Pete McKeighan, "Notched Tensile Properties of Tank Car Material from Full Scale Test No. 1 (Car No. 3069) and Test No. 2 (3074) Oriented in the Transverse Direction," NGRTC Project Memorandum, Southwest Research Institute, 20 November 2007.

30. Pete McKeighan, "Notched Tensile Properties of Thickest TC128B Tank Car Material from Material Inventory for Fabricating Test Specimens," NGRTC Project Memorandum, Southwest Research Institute, 6 December 2007.

31. Pete McKeighan, "Shear Tests on TC128B Normalized Material of Two Different Thicknesses," NGRTC Project Memorandum, Southwest Research Institute, December 2007.

32. Pete McKeighan, "Puncture Tests on Jacket Material (A1011, 90X) and Normalized TC128B Shell Material (two thicknesses)- Revised," NGRTC Project Memorandum, Southwest Research Institute, 17 December 2007.

33. Pete McKeighan, "Puncture Behavior of 0.48-inch Thick A516 Material," NGRTC Project Memorandum, Southwest Research Institute, 12 April 2008.

34. Pete McKeighan, "Puncture Properties of Different 90x Stacked Layers and a Composite Structure," NGRTC Project Memorandum, Southwest Research Institute, 23 March 2008.

35. Kirkpatrick, S.W., Bocchieri, R.T., Sadek, F., Robert A. MacNeill, R.A., Holmes, B.S., Peterson, B.D., Cilke, R.W., and Navarro, C., "Analysis of Aircraft Impacts into the World Trade Center Towers," NIST NCSTAR 1-2B, National Institute of Standards and Technology (NIST) Investigation, October, 2005.

36. Materials Research & Engineering, Inc., "Room Temperature Tensile Tests at different Crosshead Speeds," Technical Report, Prepared for T.L. Anderson, Quest Reliability, LLC, MRE Report #R07-02-003, February 19, 2007.

37. Pete McKeighan, NGRTC Project Memorandum, Southwest Research Institute, 5 December 2007.

38. Cowper, G.R. and Symonds, P.S., "Strain-Hardening and Strain-Rate Effects in the Impact Loading of Cantilever Beams," Brown University, Division of Applied Mathematics Report, P. 28, September 1957.

39. Beremin, F. M., 1981, "Study of Fracture Criteria for Ductile Rupture of A508 Steel," in Advances in Fracture Research (ICF5), D. François, Ed., Pergamon Press , pp. 809-816.

40. Chaboche, J. L. et al., Editors, 1986, "Séminaire International sur l'Approche Locale de la Rupture," Conference Proceedings, Centre de Recherches EDF, "Les Renardières," Moret-sur-Loing, France.

41. Curran, D. R., Seaman, L. and Shockey, D. A, 1987, "Dynamic Failure of Solids," Physics Reports, Vol. 147, pp. 253-388.

42. Lemaitre, J., 1986, "Local Approach of Fracture," Engineering Fracture Mechanics, Vol. 25, pp. 523-537.

43. Mudry, F., 1985, "Methodology and Applications of Local Criteria for Prediction of Ductile Tearing," Elastic-Plastic Fracture Mechanics, L. H. Larson, ed., ECSC, EEC, EAEC, Brussels and Luxembourg, Belgium, pp. 263-283.

44. Hancock, J. W. and Mackenzie, A. C., 1976, "On the Mechanisms of Ductile Failure in High-Strength Steels Subjected to Multiaxial Stress States," Journal of the Mechanics and Physics of Solids, 24, pp. 147-169.

45. Rice, J. R., and Tracey, D. M., 1969, "On the Ductile Enlargement of Voids in Triaxial Stress Fields," J. Mech. Phys. Solids, 17, 201-217.

46. Giovanola, J. H., and Rosakis, A. J., Editors, 1992, Advances in Local Fracture/Damage Models for the Analysis of Engineering Problems, AMD-vol. 137, American Society of Mechanical Engineers, New York.

47. Giovanola, J. H., and Kirkpatrick, S. W., 1992, "Applying a Simple Ductile Fracture Model to Fracture of Welded T-Joints," in Advances in Local Fracture/Damage Models for the Analysis of

Engineering Problems, AMD Vol. 137, J. H. Giovanola and A. J. Rosakis, Eds., American Society of Mechanical Engineers, New York, pp. 285-303.

48. Giovanola, J.H., and Kirkpatrick, S.W., 1993, "Methodology for Evaluating Strength and Fracture Resistance of Weldments Using a Local Approach to Fracture," in Pressure Vessel Integrity-1993, PVP-Vol. 250, W. E. Pennel, S. Bhandari, G. Yagawa, Editors, American Society of Mechanical Engineers, New York, pp.157-171.

49. Giovanola, J.H., and Kirkpatrick, S.W., and Crocker, J.E., 1996, "Investigation of Scaling Effects in Elastic-Plastic Ductile Fracture Using the Local Approach," Proceedings of the First European Mechanics of Materials Conference on Local Approach to Fracture, Euromech-Mechamat '96, Fontainebleau-France, Sept. 9-11.

50. Gurson, A.L., "Continuum Theory of Ductile Rupture by Void Nucleation and Growth: Part 1—Yield Criteria and Flow Rules for Porous Ductile Media." Journal of Engineering Materials and Technology, Vol. 99, 1977, pp. 2-15.

51. Tvergaard, V., "On Localization in Ductile Materials Containing Spherical Voids." International Journal of Fracture, Vol. 18, 1982, pp. 237-252.

52. Tvergaard, V., "Material Failure by Void Growth to Coalescence." Advances in Applied Mechanics, Vol. 27, 1990, pp. 83-151.

53. T.L. Anderson and S.W. Kirkpatrick, "Quantifying and Enhancing Puncture Resistance in Railroad Tank Cars Carrying Hazardous Materials," Technical Report, Prepared for The Chlorine Institute, August 7, 2006.

54. Mackenzie, A. C., Hancock, J. W., and Brown, D. K., 1977, "On the Influence of State of Stress on Ductile Failure Initiation in High-Strength Steels," Eng. Fracture Mechanics, 9, 167-188.

55. M. Arcan, Z. Hashin and A. Voloshin, "A Method to Produce Uniform Plane-stress States with Applications to Fiber-reinforced Materials," Experimental Mechanics, pp. 141-146, April 1978.

56. Pete McKeighan, "BFCM Testing on Five Current/Candidate Tank Car Materials," Project Memorandum, Southwest Research Institute, Prepared for Quest Reliability, 10 may 2007.

57. Pete McKeighan, "Revised Role of Specimen Thickness on BFCM Energy – Blunt Tup," Project Memorandum, Southwest Research Institute, Prepared for Quest Reliability, 17 May 2007.

58. Pete McKeighan, "Influence of Initial Energy Level on BFCM Energy," Project Memorandum, Southwest Research Institute, Prepared for Quest Reliability, 24 May 2007.

59. Pete McKeighan, "Initial BFCM Results and the Role of Specimen Dimensions," Project Memorandum, Southwest Research Institute, Prepared for Quest Reliability, 3 April 2007.

60. Yu, H., Jeong, D.Y., Gordon, J.E., Tang, Y.H., "Analysis of Impact Energy to Fracture Un-Notched Charpy Specimens Made from Railroad Tank Car Steel," Proceedings of the 2007 ASME Rail Transportation Division Fall Technical Conference, RTDF2007-46038, September 2007.

61. Hogg, P.J., "Composites for Ballistic Applications," Composites Processing 2003, CPA, Bromsgrove, U.K. 21st March 2003.

62. AMPTIAC Quarterly, Volume 8 No. 4, Army Materials Research: Transforming Land Combat through New Technologies, 2004.

63. AMPTIAC Quarterly, Volume 9 No. 2, High Performance Fibers for Lightweight Armors, 2005.

64. Skaggs, R., Cheeseman, B., Yen, C.F., Dooley, R., Boyd, K., Walsh, S., Campbell, J., Hoppel, C., and Goetz. R., "Development of Mine Blast Protected Vehicle Structures for Future Combat Systems," Proceedings for the Army Science Conference (24th), Orlando, Florida, 2005.

65. Carolan, M., Talamini, B., and Tyrell, D.C., "Update on Ongoing Tank Car Crashworthiness Research: Predicted Performance and Fabrication Approach," Proceedings of the 2008 IEEE/ASME Joint Rail Conference, Paper No. JRC2008-63052, Wilmington, Delaware, USA, April 2008.

66. Russell Walker, Greg Garcia, Satima Anankitpaiboon, and Kari Gonzales, "Tank Car Head Baseline Component Test," Transportation Technology Center, Inc. Report No. P-08-009, April 2008.

67. B.-J. Kim And S.-J. Heo, "Collapse Characteristics of Aluminum Extrusions Filled With Structural Foam for Space Frame Vehicles," International Journal of Automotive Technology, Vol. 4, No. 3, pp. 141−147 (2003).

68. B.S. Holmes and J.K. Gran, "Developing a Research Safety Vehicle Structure with Scale Modeling Techniques," Stanford Research Institute Final Technical Report to Minicars, Inc., U.S. DOT, National Highway Traffic Safety Administration, Subcontract No. DOT-HS-5-01215, 1976.

69. Thomas, M.A., Chitty, D.E., Gildea, M.L., and T'Kindt, C.M., "Constitutive Soil Properties for Cuddeback Lake, California and Carson Sink, Nevada," Draft NASA Report No. NASA/CR—2008–215345, Prepared by Applied Research Associates, Inc., February 2008.

70. Pete McKeighan, "Foam Material Properties - Free Compression Stress-Strain Behavior," NGRTC Project Memorandum, Southwest Research Institute, 19 October 2007.

71. Pete McKeighan, "Foam Material Properties - Effect of Humidity and Different Specimen Sizes on the Free Compression Stress-Strain Behavior," NGRTC Project Memorandum, Southwest Research Institute, 26 November 2007.

72. Pete McKeighan, "Three Preliminary Experiments Examining the Flexure Properties of Composite and Solid Steel Sub-size Panels," NGRTC Project Memorandum, Southwest Research Institute, 21 December 2007.

73. Pete McKeighan, "Fourth Small Panel Experiment - Flexure Properties of a Steel-Foam Composite," NGRTC Project Memorandum, Southwest Research Institute, 12 February 2008.

74. Pete McKeighan, "Experiments Examining the Effect of the Steel Surface Preparation on the Flexural Properties of Bonded Composite Sub-size Panels," NGRTC Project Memorandum, Southwest Research Institute, 27 August 2008.

75. Fries, R., Walker, R., Anankitpaiboon, S., and Garcia, G., " Tank Car Head Impact Tests: Option 2 - Multilayer Foam Head Protection; Option 3 - Nonoptimized EMS Head Protection," Transportation Technology Center, Inc. Report No. P-08-Draft, Sept. 2008.

76. Queheillalt, D.T., Murty, Y., and Wadley. H.N.G., "Mechanical Properties of an Extruded Pyramidal Lattice Truss Sandwich Structure," Scripta Materialia 58, pp. 76–79, (2008).

77. Wadley, H. N. G., Fleck, N. A., Evans, A. G., "Fabrication and structural performance of periodic cellular metal sandwich structures," Comp. Sci. and Tech., 63, 2331-2343, 2003.

78. Fleck N.A., Deshpande V.S., "The resistance of clamped sandwich beams to shock loading," Journal of Applied Mechanics, ASME; 71: 1-16, (2004).

79. H.J. Rathbun, D.D. Radford, Z. Xue, M.Y. He, J. Yang, V. Deshpande, N.A. Fleck, J.W. Hutchinson, F.W. Zok, A.G. Evans, "Performance of Metallic Honeycomb-Core Sandwich Beams Under Shock Loading," International Journal of Solids and Structures 43, 1746–1763, (2006).

80. Tagarielli, V.L., Fleck N.A., Deshpande V.S., "The Collapse Response of Sandwich Beams with Aluminum Face Sheets and a Metal Foam Core," Advanced Engineering Materials, Vol. 6, No. 6, pp. 440-443 (2004).

81. Z. Wei, V.S. Deshpande, A.G. Evans, K.P. Dharmasena, D.T. Queheillalt, H.N.G. Wadley, Y.V. Murty, R.K. Elzey, P. Dudt, Y. Chen, D. Knight, K. Kiddy, "The Resistance of Metallic Plates to Localized Impulse," Journal of the Mechanics and Physics of Solids 56, 2074–2091, (2008).

82. Fries, R., Hybinette, C., Douglas, P., and Toms, R.., "Inspection of NGRTC Option 3," NGRTC Project Memorandum, Sept. 10, 2008.

83. "User's Manual for LS-DYNA MAT162 Unidirectional and Plain Weave Composite Progressive Failure Models," Univ. of Delaware Center for Composite Materials, Materials Sciences Corporation, November, 2005.

84. Yen, C.F., "Ballistic impact Modeling of Composite Materials," Proceedings of the 7th International LS-DYNA Users Conference, Dearborn Michigan, May 19-21, 2002.

85. Matzenmiller, A., Lubliner, J., and Taylor, R.L. (1995). "A Constitutive Model for Anisotropic Damage in Fiber-Composites," Mechanics of Materials, 20, pp. 125-152.

86. Xiao, J.R., Gama, B.A., and Gillespie, J.W. Jr., "Progressive Damage and Delamination in Plain Weave S-2 Glass/SC-15 Composites Under Quasi-Static Punch-Shear Loading," Composite Structures Vol. 78, pp. 182–196, 2007.

87. Waliul Islam, S.M., "A Quasi-Static Penetration Model for Ballistic Energy Absorption of Thick Section Composite," Univ. of Delaware Center for Composite Materials, presented at the UD-CCM 2005 research Reviews, March 2, 2005.

88. Deka, L.J., S.D. Bartus, U.K. Vaidya, "Numerical Modeling of Simultaneous and Sequential Multi-Site Impact Response of S-2 Glass/Epoxy Composite Laminates", Composites and Polycon 2007, Oct. 17-19, 2007.

89. Gama, B.A., Xiao, J.R., and Haque, Md. J., "Experimental and Numerical Investigations on Damage and Delamination in Thick Plain Weave S-2 Glass Composites Under Quasi-Static Punch Shear Loading," Army Research Laboratory Report No. ARL-CR-534, Prepared by the Univ. of Delaware Center for Composite Materials, February 2004.

90. http://www.ccm.udel.edu/Tech/MAT162/SingleElement.htm